Microswimmers: dynamical density functional theory and discrete particle models

Inaugural-Dissertation

zur Erlangung des Doktorgrades
der Mathematisch-Naturwissenschaftlichen Fakultät
der Heinrich-Heine-Universität Düsseldorf

vorgelegt von

Christian Georg Hoell
aus Moers

Düsseldorf, Oktober 2019

aus dem Institut für Theoretische Physik II: Weiche Materie
der Heinrich-Heine-Universität Düsseldorf

Gedruckt mit der Genehmigung der
Mathematisch-Naturwissenschaftlichen Fakultät der
Heinrich-Heine-Universität Düsseldorf

Referent: Prof. Dr. Hartmut Löwen

Korreferent: Priv.-Doz. Dr. Andreas M. Menzel

Tag der mündlichen Prüfung: 25.10.2019

Abstract

The study of active matter concerns physical systems that take up energy from their environment and use it to drive themselves out of equilibrium, e.g., self-propelled particles. This work specifically focuses on microswimmers, i.e., force- and torque-free particles that are suspended in a viscous fluid and induce fluid flows in order to propel themselves. For this purpose, we here model individual swimmers by introducing an extended force dipole consisting of two discrete force centers that co-move with the spherical swimmer body. Both pushers (extensile microswimmers) and pullers (contractile microswimmers) can be described. The resulting motion is determined in the limit of far-field hydrodynamics at low Reynolds numbers. On this premise, minimal models for straight-propelling and circle-swimming microswimmers, as well as similar active rotators are created. Additionally, pairwise hydrodynamic interactions between swimmers are described.

The corresponding minimal models are then taken as an input to develop statistical descriptions for (semi)dilute suspensions of straight-propelling microswimmers and circle swimmers. Here, also the influences of external potentials and thermal noise, as well as pairwise steric and hydrodynamic interactions between the swimmers, are included in the resulting dynamical density functional theory (DDFT) that describes the temporal evolution of the one-swimmer density. As a test, the DDFT for straight-propelling microswimmers is applied to a planar arrangement of swimmers in a circularly symmetric external trapping potential, for which results qualitatively compare with those of particle-based computer simulations. In particular, the self-propulsion leads to a high-density ring structure of radially oriented swimmers, when hydrodynamic interactions are neglected. With them included, the swimmers can aggregate into a single high-density spot at one spontaneously chosen position on the ring. Our numerical evaluations show a further instability of this spot against reorientations of the swimmers away from the radial direction, which leads to movement of the spot along the circular trap. In contrast to that, for circle swimmers, a sufficiently strong curvature of their trajectories leads to localizations near the center of the trap.

Additionally, our DDFT serves as the basis for a statistical theory describing, for planar swimmer systems, the possible onset of collective orientational order due to hydrodynamic interactions. We here obtain approximations for the swimmer–swimmer pair distribution function by combining our DDFT with a newly introduced adaptation of Percus' equilibrium test-particle method to active systems. These results are taken as an input for a linear stability analysis of the disordered

state against collective polar orientational order. We find that (pure) puller systems can develop such order on the considered length scale if their hydrodynamic couplings can overcome rotational diffusion, while pushers do not spontaneously develop such order from a linear instability. We derive a quantitative criterion for the onset of ordering, which compares qualitatively with existing particle-based computer simulations of microswimmer systems in periodic boxes.

A further extension of our statistical framework to binary mixtures of microswimmers is presented. In particular, this multi-species DDFT for microswimmers is applied to the previously mentioned trap, showing that, typically, one species transfers its behavior onto the other species, if two species are considered that only differ by their type of propulsion mechanism (pusher vs. puller). Moreover, unconfined pusher–puller mixtures in large periodic boxes are shown to spontaneously develop orientational order through a linear instability, if there are enough, sufficiently strong pullers in the system. Additionally, we introduce a circular shear-cell model, in which a microswimmer species is confined within a ring of externally driven passive particles. Here, the driving induces a fluid flow that consistently rotates the swimmers on the inside. Thus, the swimmers can propel less efficiently against the trapping potential and tend to be localized further towards the center of the trap.

Next, in terms of a discrete-particle model, simple three-sphere swimmers that propel by shape changes (relative distance changes between the spheres) are discussed in two special cases. First, the behavior of a “neutral” (i.e., neither pusher nor puller) swimmer near a hard wall is described, with thermal noise neglected. Depending on its initial orientation and distance from the wall, the swimmer either escapes, gets trapped by the wall, or undergoes a perpetual oscillatory gliding motion. When an additional relative mutual rotation of the spheres is included, the swimmer starts circling if it is close to the wall, which mimics behavior reported for some flagellated bacteria. Additionally, the dynamics of a three-sphere swimmer between two parallel hard walls is discussed. For this purpose, approximate mobility tensors for this setup are derived. In addition to neutral swimmers, also variants that have pusher or puller signatures are considered. Depending on the initial parameters, either trapped, sliding, or (oscillatory) gliding states are reached.

Finally, interactions of (active) particles with elastic interfaces are studied. We introduce a simple model membrane and discuss, e.g., under which circumstances an approaching active particle penetrates it, in the absence of induced fluid flows. Furthermore, the interplay between hydrodynamic interactions and the elastic response of an interface is discussed in two cases. First, a passive particle within an elastic spherical cavity is driven in a non-axisymmetric setup, which leads to non-trivial dynamics of the particle and the cavity. Second, an infinite planar interface influences the behavior of a general microswimmer that is represented by different terms of a force multipole expansion. In particular, we find that the contribution of a rotlet dipole leads to circling motions, theoretically underpinning the behavior of the modified three-sphere swimmer mentioned above.

Eidesstattliche Versicherung

Ich versichere an Eides Statt, dass die Dissertation von mir selbständig und ohne unzulässige fremde Hilfe unter Beachtung der „Grundsätze zur Sicherung guter wissenschaftlicher Praxis an der Heinrich-Heine-Universität Düsseldorf“ erstellt worden ist.

Düsseldorf, ____________________ _________________________

Preface

The content of this dissertation is based on articles that I co-authored, and that have been published in / submitted to peer-reviewed scientific journals. These articles are reproduced in Chapter 5 and are listed in the following (in topical order):

- **P1** A. M. Menzel, A. Saha, C. Hoell, and H. Löwen, *Dynamical density functional theory for microswimmers*, J. Chem. Phys. **144**, 024115 (2016).
- **P2** C. Hoell, H. Löwen, and A. M. Menzel, *Dynamical density functional theory for circle swimmers*, New J. Phys. **19**, 125004 (2017).
- **P3** C. Hoell, H. Löwen, and A. M. Menzel, *Multi-species dynamical density functional theory for microswimmers: derivation, orientational ordering, trapping potentials, and shear cells*, J. Chem. Phys. **151**, 064902 (2019).
- **P4** C. Hoell, H. Löwen, and A. M. Menzel, *Particle-scale statistical theory for hydrodynamically induced polar ordering in microswimmer suspensions*, J. Chem. Phys. **149**, 144902 (2018).
- **P5** A. Daddi-Moussa-Ider, M. Lisicki, C. Hoell, and H. Löwen, *Swimming trajectories of a three-sphere microswimmer near a wall*, J. Chem. Phys. **148**, 134904 (2018).
- **P6** A. Daddi-Moussa-Ider, M. Lisicki, A. J. T. M. Mathijssen, C. Hoell, S. Goh, J. Bławzdziewicz, A. M. Menzel, and H. Löwen, *State diagram of a three-sphere microswimmer in a channel*, J. Phys.: Condens. Matter **30**, 254004 (2018).
- **P7** A. Daddi-Moussa-Ider, S. Goh, B. Liebchen, C. Hoell, A. J. T. M. Mathijssen, F. Guzmán-Lastra, C. Scholz, A. M. Menzel, and H. Löwen, *Membrane penetration and trapping of an active particle*, J. Chem. Phys. **150**, 064906 (2019).
- **P8** C. Hoell, H. Löwen, A. M. Menzel, and A. Daddi-Moussa-Ider, *Creeping motion of a solid particle inside a spherical elastic cavity: II. Asymmetric motion*, Eur. Phys. J. E **42**, 89 (2019).
- **P9** A. Daddi-Moussa-Ider, C. Kurzthaler, C. Hoell, A. Zöttl, M. Mirzakhanloo, M.-R. Alam, A. M. Menzel, H. Löwen, and S. Gekle, *Frequency-dependent higher-order Stokes singularities near a planar elastic boundary: implications for the hydrodynamics of an active microswimmer near an elastic interface*, Phys. Rev. E **100**, 032610 (2019).

My contributions to these scientific articles are specified in Chapter 5.

Acknowledgments

It is a great pleasure to acknowledge and thank all the people who helped and supported me during my doctoral studies. My sincerest gratitude here belongs to Prof. Dr. Hartmut Löwen for the sustained guidance and encouragement I was given, already since my Bachelor and Master theses. It has been a great honor to work together on interesting (and positively challenging) physical problems, and I will look back fondly on my time at the Institut für Theoretische Physik II.

Cordially, I thank Priv.-Doz. Dr. Andreas M. Menzel for the continuous supervision during my doctoral studies, for mapping out the DDFT research problems, for many helpful discussions, as well as for the close and most enlightening re-reading of and commenting on drafts, abstracts, proofs, etc.

In addition to my doctoral adviser and my co-supervisor, my heartfelt thanks also go to everyone with whom I had the incredible privilege to co-author papers. Especially, I would here like to point out Dr. Abdallah Daddi-Moussa-Ider who initiated and managed several joint publications with a great spirit and friendliness.

I also thank Prof. Dr. Dr. Carsten Müller, whose work in the role of the formal mentor and thus designated mediator in case of a student–adviser conflict should not be lessened by the absence of such conflicts.

None of my studies and learning would have been possible without all the people working at Heinrich-Heine-Universität Düsseldorf, in particular at our institute. Specifically, I thank Claudia Stader, Joachim Wenk, and Karin Wildhagen, who all have facilitated my work in our group immensely.

With great sympathy I think of all the (doctoral) students with whom I have crossed paths at seminars, courses, lectures, and conferences. Explicitly, I would here also like to thank all the different school and university teachers who worked hard to let us learn.

My special thanks go to my fellow doctoral candidates with whom I shared a very significant time, in particular Soudeh Jahanshahi, Sonja Tarama, Mate Puljiz, Urs Zimmermann, Giorgio Pessot, Christoph Sitta, and Peet Cremer.

An additional big "Thank you!" is appropriate for all of my smart and great colleagues at our institute. In particular, I thank Abdallah, Lukas, Mate, and Peet, with whom I amiably shared an office during the last years.

With respect to this dissertation, I thank Soudeh Jahanshahi, Sonja Tarama, Abdallah Daddi-Moussa-Ider, and Lukas Fischer for commenting on diverse drafts.

Finally, I thank my loved ones for the continued support during my studies, in the hope that I can give back even only half of what I got from you.

Contents

Chapter 1

Introduction

In this chapter, starting in Sec. 1.1, active microswimmers are discussed with regard to their prospective importance in biological, medical, and technical applications, as well as how they fit into the context of (active soft matter) physics, see Sec. 1.2. Additionally, Sec. 1.3 emphasizes the importance of statistical theories for describing the collective behavior in suspensions of microswimmers, which motivates the interest in this topic. A short review over previous studies on self-propelled particles with neglected hydrodynamic interactions is given in Sec. 1.4, which later allows us to compare our results for microswimmers to that simpler case.

1.1 Why we care about microswimmers

A working definition of *microswimmers* follows from listing their characteristic properties [1]. Specifically, a typical microswimmer is an approximately micrometer-sized physical object suspended in a viscous fluid medium, e.g., water. Taking up energy from its environment, such a swimmer creates its own self-propulsion, with the direction of locomotion determined by the orientation of the swimmer. The underlying self-propulsion mechanism induces fluid flows in the background medium, which can lead to interactions between the swimmer and nearby objects, including other swimmers, so-called hydrodynamic interactions.

Due to the underlying processes and the possible applications, the study of microswimmers is an interdisciplinary scientific field that includes aspects of biology, medicine, engineering, chemistry, and physics. In particular, this interest is rooted in the existence of biological microswimmers in nature, and in the idea to use (artificial) microswimmers as workhorses in diverse medical and technical applications.

Specifically, biological microswimmers exist in a plethora of aqueous environments on our planet [2–10]. This includes bacteria that live in the human body (particularly in the colon), constituting an estimated average fraction of 3×10^{-3} of the human body mass [11,12]. Prototypical examples for biological microswimmers are motile types of the common *Escherichia coli* (*E. coli*) bacterium species, which move by rotating a bundle of flagella [6].

Additionally, artificial microswimmer have been realized [13–18]. Here, a typical design is to take a colloidal sphere and to coat its half-spheres unequally, creating *Janus particles* (named with reference to a two-faced Roman deity). Under suitable external stimuli (e.g., introduction of reactants [16–18], irradiation with light [15]), such Janus particles may create around themselves a corresponding gradient of, e.g., the concentration of a chemical, which can lead to the creation of fluid flows and thus self-propulsion.

In principle, colloidal Janus particles can be imparted with a choice of desired properties by including appropriate steps in their synthesis, leading to wide-ranging possibilities in their use. Possible (future) applications of such designed active agents could be medical, e.g., precise delivery of pharmaceutical drugs to exactly those sites in the human body where they are needed [19–23], use in non-invasive surgery [21, 24, 25], or the guidance of sperm cells [26]. Additionally, they could also power microengines in further technical contexts [27–29].

1.2 Microswimmers in a physical context

In this work, I consider, in general, microswimmers in the following sense:

> *"Microswimmers are force-free and torque-free objects capable of self-propulsion in a (typically) viscous environment and, importantly, exhibit an explicit hydrodynamic coupling with the embedding solvent via flow fields generated by the swimming strokes they perform."* [1, p. 6]

Step by step, this definition renders microswimmers distinct from several adjacent types of physical objects, as detailed below.

First, even as the net force and the net torque that are directly related to its active motion vanish, a microswimmer can still achieve self-propulsion by creating, e.g., fluid flows, as detailed in Secs. 2.2 and 4.1 for specific swimmer models. A given orientation of the swimmer at a certain time then determines its swimming direction at that moment. This distinguishes microswimmers from *driven matter* [30], which moves, in general, along an externally specified direction.

Second, the *"(typically) viscous environment"* defines the surrounding of a microswimmer. Generally, the motion of a microswimmer is considered to be overdamped, i.e., its inertia can be neglected [1, 2]. The quality of this assumption can be quantified via the dimensionless *Reynolds number* [31]

$$\mathrm{Re} = \frac{\rho_\mathrm{f}\, a\, v_\mathrm{s}}{\eta}\,, \tag{1.1}$$

where ρ_f is the mass density of the fluid, η denotes its dynamic viscosity, a stands for the size of the hydrodynamic swimmer body, and v_s represents the (free-)swimming speed. Inserting specific values for motile *E. coli* bacteria leads to $\mathrm{Re} \approx 3 \cdot 10^{-5}$ [1].

For Re $\ll 1$, the resulting *creeping flow* of the fluid is mathematically described by the Stokes equation (as detailed in Sec. 2.1), for which a whole theoretical apparatus is at hand [31–33]. For example, Re $\ll 1$ is valid for typical swimmers of sizes $a \sim 1\,\mu\mathrm{m}$ and speeds $v_{\mathrm{s}} \sim 10\,\mu\mathrm{m}/s$ that are suspended in water [2]. Small Re can be achieved for larger objects as well, when, e.g, highly viscous silicone oil is used as a surrounding medium [34]. Inertial effects have to be considered for Re $\gtrsim 1$, as is the case for *underdamped* self-propelled particles (also called *microflyers*) [35–37], which could be realized in, e.g., complex plasma systems [38].

Third, the second half of the above quote (after *"importantly"*) defines a certain "wetness" of microswimmers, i.e., the self-propulsion mechanism of one swimmer can affect its environment and thus also other swimmers. This distinguishes microswimmers from the simpler *"dry" self-propelled particles* for which hydrodynamic interactions mediated by the background medium are neglected [1]. Additional complexity beyond the concept of microswimmers, and thus beyond the scope of this work, is introduced, e.g., by *chemically active colloids* [13, 14, 18, 39], for which phoretic interactions may also have to be considered [40].

Microswimmers, microflyers, dry self-propelled particles, and chemically active colloids all are covered by the more general term *active matter* [1,41]. Per definition,

> *"[a]ctive matter systems are able to take energy from their environment and drive themselves far from equilibrium."* [1, p. 2]

In principle, but beyond the scope of this work, such activity can also manifest itself via other means than self-propulsion, e.g., by cell division [42–45].

Since active matter systems are inherently out of equilibrium, their behavior can vary widely from equilibrium physics. For example, planar arrangements of self-propelled particles with orientational alignment interactions can show long-range orientational order (concerning their propulsion directions) [46, 47], which had previously been proven to be impossible for planar passive equilibrium systems [48].

Moreover, in non-equilibrium systems, hydrodynamic interactions can change even static properties of steady-state solutions, e.g., the one-body density. This stands in contrast to (ergodic) passive equilibrium systems, for which static properties are determined by the partition function, which in turn is independent of hydrodynamic interactions [49].

1.3 Importance of statistical theories

Setting out to find suitable statistical descriptions for suspensions of microswimmers, our work involves, in particular, the development of a corresponding statistical theory in the form of a dynamical density functional theory (DDFT) [**P1**–**P4**]. As discussed in Chapter 3, this versatile framework can be used in diverse situations. In the following, the importance of *statistical theories* in physics is briefly illustrated.

Given a system of N (interacting) particles, there are two routes that we refer to. The first one is to treat them individually as discrete particles, the overall motion of which is described by Nd_f coupled ordinary differential equations (each particle featuring d_f degrees of freedom) that are, in general, only solvable via numerical methods. For self-propelled particles, a typical choice here is to employ (overdamped) *Brownian dynamics* computer simulations [50].

However, the discrete-particle path can have disadvantages. For example, numerical evaluations may scale unfavorably with N, for instance as thermal noise can limit computational efficiency when hydrodynamic interactions are included [51], or many different realizations of the system must be performed to achieve statistically sound results. Starting analytical arguments based on the particle picture is frequently less convenient when compared to the density picture described below.

Specifically, a second route concerning many-body systems is to instead regard the *probability densities* with which the particles occupy the different phase-space configurations. However, the full N-particle probability distribution is typically too complicated for direct evaluations. Fortunately, many of the physical properties can be described via the coarse-grained one-body or two-body probability densities, even in non-equilibrium.

Accordingly, one switches to such *reduced n-body probability densities.* Mathematically, for identical particles this can be achieved by starting from an appropriate dynamical equation for the N-particle distribution and integrating out the corresponding degrees of freedom for all except for n particles, as is discussed in Sec. 3.1.1 within our theoretical framework. This way, a (dynamical) statistical theory is obtained, the evaluation of which directly leads to statistically relevant results. The strength of different influences affecting the system can then be thoroughly checked with relative ease, e.g., by comparing the associated probability density currents or by performing corresponding (approximate) analytical calculations.

Nevertheless, a (frequently necessary) approximate statistical theory should be compared with simulations (and/or experiments) to test whether the chosen level of description is sufficient. For example, Ref. 51 and Publication **P4**, as well as Sec. IV B of Publication **P3**, examined similar situations and were enriched by the possibility to crosscheck the results qualitatively. Sometimes, the discrete-particle picture is more intuitive than the frame provided by statistical theories. Consequently, statistical and discrete-particle-based approaches complement each other and enable us to consider physical problems from diverse points of views.

1.4 Dry self-propelled particles: a short review

This section gives a brief summary regarding previous studies on dry self-propelled particles, for individual (single) particles and for many-particle systems, allowing for a later comparison with our results. The corresponding prototypical model is given by the *active Brownian particle* (ABP) [1, 52]. Here, the well-established overdamped Langevin equations of motion for passive colloidal particles are modified by inserting effective forces [53] that correspond (in the absence of noise) to a propulsion in the direction of the particle orientation. Specifically, the resulting velocity $\mathbf{v}$ and angular velocity $\boldsymbol{\omega}$ of one spherical ABP are given by [1, 54]

$$\mathbf{v} = v_\mathrm{s}\hat{\mathbf{n}} + \boldsymbol{\xi}_\mathrm{t} + \mu^\mathrm{t}\mathbf{F}, \tag{1.2a}$$

$$\boldsymbol{\omega} = \boldsymbol{\xi}_\mathrm{r}\,. \tag{1.2b}$$

Here, v_s is the free-swimming speed, the unit vector $\hat{\mathbf{n}}$ represents the current orientation of the particle, μ^t is its mobility, and $\mathbf{F}$ denotes the (optional) force acting on the particle. This force can be induced externally and/or via steric interactions between particles. Additionally, the vectors $\boldsymbol{\xi}_\mathrm{t}$ and $\boldsymbol{\xi}_\mathrm{r}$ (for the translational and, respectively, rotational degrees of freedom) are zero-mean Gaussian noise terms, with variances chosen such that thermal Brownian motion is reproduced in the limit of passive systems involving $v_\mathrm{s} = 0$ [1].

For $\mathbf{F} = \mathbf{0}$, a free self-propelled particle is obtained. The motion of a single ABP can be described qualitatively as follows: after a ballistic part at very small times [that is not covered by Eqs. (1.2)], the particle undergoes diffusive motion at small times, then a ballistic motion in the approximate direction of $\hat{\mathbf{n}}$ at intermediate times, again transforming into diffusive motion when the direction of motion is lost due to rotational diffusion. In particular, this leads to an effective long-time translational diffusion, which can be modeled as a random walk with step length $v_\mathrm{s}\tau_\mathrm{r}$ and time step $\tau_\mathrm{r} = (D_\mathrm{r})^{-1}$, where D_r is the thermal rotational diffusion constant [1]. More generally, the first four moments of the probability distributions of the position (at arbitrary times) that result from the above coupled Langevin equations have been analytically determined [55] (also for ellipsoidal self-propelled particles [56]).

Maybe surprisingly, even single-particle (or non-interacting many-particle) systems can show interesting properties. For example, ABPs tend to spend elevated times at repulsive walls [57–59], breaking the detailed balance found in equilibrium passive systems [49]. Moreover, it can take significant mathematical effort to describe even seemingly simple ABP problems, e.g., the sedimentation of self-propelled particles, for which non-trivial, locally polarized steady states have been found [60–62]. The motion of single self-propelled particles even in complicated flow fields can often be well-described via only small adjustments to Eqs. (1.2) [63, 64].

A major breakthrough in the study of active matter has been provided by the observation that spherical self-propelled particles (with sufficiently strong short-ranged repulsive steric interactions between each other) can spontaneously form clusters that are surrounded by gas-like regions [54, 65]. This is commonly known as *motility-induced phase separation* (MIPS) [66–71]. The basic mechanism for the growth of such clusters is a long-time local mutual blockade of colliding ABPs, with additional incoming particles being hindered in their propulsion by these blocked clusters [65]. While a full statistical theory from first principles for MIPS is still missing, several helpful approaches have been carried out [66, 67, 72–74].

On a more coarse-grained level, ABPs have also been treated in scalar field theories [75, 76] and via effective equilibrium approaches [77–79]. Moreover, under some circumstances, the behavior of ABPs can be mapped on Ornstein-Uhlenbeck processes [80–83].

Furthermore, the model of ABPs can be generalized to *circle swimmers* when neglecting the possible influence of a surrounding fluid, which feature an additional self-rotation term in Eq. (1.2b) [84], see also the wet equivalent in Sec. 2.2. Another model similar to ABPs are *run-and-tumble* self-propelled particles that replace the smooth rotational diffusion of Eq. (1.2b) with discrete reorientation events (that are triggered randomly) [85], which mimics the swimming behavior of wild-type motile *E. coli* bacteria [6]. The addition of explicit orientational alignment interactions between particles following the famous Vicsek model can trigger orientational ordering and the formation of moving density bands [46, 47, 86–88].

Next, we transition from dry self-propelled particles to active microswimmers. Chapter 2 presents our force-dipole-based model of microswimmers, including its theoretical foundation via low-Reynolds-number hydrodynamics.

Chapter 2

Force-dipole-based microswimmers

Historically, an early theoretical description of a microswimmer has been the now-standard *squirmer* model [89–91]. It assumes that the swimmer prescribes a velocity field on its surface to achieve self-propulsion, as is conceivable for cilia-covered microorganisms. Another simple model are three-sphere swimmers [92, 93]. The behavior of a such a swimmer in the vicinity of hard walls [**P5**, **P6**] is described in Sec. 4.1.2. Furthermore, the possibility of more abstracted models based on an appropriate driving force dipole had previously been mentioned in Refs. 94–97.

In this section, our discrete force-dipole-based minimal model of a microswimmer is discussed. Specifically, Sec. 2.1 lays the ground for the mathematical description of fluid flows at low Reynolds numbers. On this premise, minimal models for *straight-propelling* (sometimes: *linear*) microswimmers [**P1**], *circle swimmers* [**P2**], and *active rotators* are introduced in Sec. 2.2. In Chapter 3, the first two of these models are taken as input for corresponding statistical theories [**P1**–**P4**].

2.1 Fluid flow at low Reynolds number

A (simple) fluid consists of incredibly many small particles, e.g., a typical glass of water contains 10^{25} water molecules. Appropriately, one does not account for each molecule by itself, but instead transitions to a continuum description of the fluid (and its internal flows). In particular, this type of description is also valid for fluid flows around a suspended mesoscopic colloidal particle [31–33], which includes microswimmers [1]. Furthermore, the motion of colloidal particles of such size in, e.g., water is typically characterized by the overdamped regime, as the Reynolds number introduced in Eq. (1.1) is significantly smaller than 1 [2].

In this case, the famously hard-to-solve Navier-Stokes equations for the fluid flow reduce to the much simpler equations

$$-\eta\,\nabla_{\mathbf{r}}^2\,\mathbf{u}(\mathbf{r}) + \nabla_{\mathbf{r}}\,p(\mathbf{r}) = \mathbf{f}_b(\mathbf{r}), \tag{2.1a}$$

$$\nabla_{\mathbf{r}}\cdot\mathbf{u}(\mathbf{r}) = 0, \tag{2.1b}$$

which describe the *Stokes flow* that results from the bulk force density $\mathbf{f}_b(\mathbf{r})$ applied to an incompressible fluid [31, 32]. Here, η is the dynamic viscosity of the fluid,

$\nabla_{\mathbf{r}}$ denotes the spatial gradient with respect to the position $\mathbf{r}$, $\mathbf{u}(\mathbf{r})$ stands for the flow field, and $p(\mathbf{r})$ represents the local (scalar) pressure field of the fluid.

Equations (2.1) are instantaneous in time and linear in their response to the force density $\mathbf{f}_b(\mathbf{r})$. The latter property implies that if the force density consists of a sum of discrete point-like force centers (mathematically described by delta distributions), the effects of these force centers can be regarded separately and afterwards be superimposed.

This procedure is facilitated by the knowledge of the corresponding Green's function to Eqs. (2.1). For an unbounded three-dimensional fluid that is quiescent (i.e., non-moving) infinitely far away from the origin, this fundamental solution is the well-established Oseen tensor $\mathbf{O}(\mathbf{r})$ that connects a delta-distributed force density $\mathbf{f}_b(\mathbf{r}') = \mathbf{F}_0\, \delta(\mathbf{r}')$ located at the origin to the resulting fluid flow field by [31–33]

$$\mathbf{u}(\mathbf{r}) = \mathbf{O}(\mathbf{r}) \cdot \mathbf{F}_0 := \frac{1}{8\pi\eta} \frac{\mathbf{1} + \hat{\mathbf{r}}\,\hat{\mathbf{r}}}{r} \cdot \mathbf{F}_0, \tag{2.2}$$

where $\mathbf{1}$ is the unity matrix, $r = |\mathbf{r}|$ denotes the norm of $\mathbf{r}$, and $\hat{\mathbf{r}} = \mathbf{r}/r$ stands for the corresponding unit vector.

The response of a rigid particle to an existing surrounding fluid flow is described by Faxén's laws. For a spherical particle of radius a that enforces a no-slip boundary condition on the fluid flow at its surface, these laws read [31]

$$\mathbf{v} = \left(1 + \frac{a^2}{6}\, \nabla_{\mathbf{r}}^2\right) \mathbf{u}(\mathbf{r}), \tag{2.3a}$$

$$\boldsymbol{\omega} = \frac{1}{2}\, \nabla_{\mathbf{r}} \times \mathbf{u}(\mathbf{r}), \tag{2.3b}$$

where $\mathbf{v}$ is the resulting translational velocity of the sphere and $\boldsymbol{\omega}$ is its resulting angular velocity. Together with the above framework, we can now introduce our force-dipole-based microswimmer models in Sec. 2.2.

As an aside, it should be mentioned that not all hydrodynamic processes regarding microswimmers take place in the overdamped regime. For example, a recent study discusses intermediate-Reynolds-number fluid waves that microorganisms of the species *Spirostomum ambiguum* generate to communicate with each other [98].

2.2 Construction of minimal microswimmer models

As a result of the conservation of momentum and angular momentum of the compound system consisting of a microswimmer and the surrounding fluid in the overdamped regime, any corresponding model has to effectively render the self-propelling swimmer force- and torque-free [1, 53]. Thus, the induced fluid flow due to self-propulsion does not result from a force monopole (and not from a torque monopole), but could (typically) be described to leading order as caused by a force dipole [1]. However, additional external potentials, e.g., due to gravity, can still lead to force and torque monopoles. Depending on the nature of the resulting fluid flows, a force-dipole swimmer is classified as either a *pusher* (which pushes away the fluid along the axis of self-propulsion, and draws it in from the perpendicular axes), or a *puller* (for which these flows are inverted) [94, 99], see also Fig. 2.1.

Below, we introduce corresponding minimal force-dipole-based microswimmer models [**P1**, **P2**]. As detailed in Chapter 3, we have also used them throughout Publications **P1**–**P4** as input for our statistical theories to describe (semi)dilute suspensions of microswimmers. Additionally, the same model was applied in many-swimmer particle-based computer simulations [51]. This allowed to qualitatively compare results from the statistical theory in Publications **P3** and **P4** with corresponding simulation results to support our approach.

2.2.1 Straight-propelling microswimmer

As detailed in Publication **P1**, we have constructed a minimal microswimmer model by rigidly attaching two discrete force centers $\mathbf{f}_\pm$ to a spherical swimmer body (of hydrodynamic radius a), see also Fig. 2.1. Specifically, they are parameterized as

$$\mathbf{f}_\pm = \pm f\,\hat{\mathbf{n}} \tag{2.4}$$

and are anchored at

$$\mathbf{r}_+ = \mathbf{r} + \alpha L\,\hat{\mathbf{n}}, \tag{2.5a}$$
$$\mathbf{r}_- = \mathbf{r} - (1-\alpha) L\,\hat{\mathbf{n}}, \tag{2.5b}$$

respectively. Here, $\mathbf{r}$ stands for the position of the swimmer body, $L > 2a$ is a constant length, α (with $a/L < \alpha \leq 1/2$) denotes a dimensionless parameter characterizing the asymmetry of the swimmer, and the unit vector $\hat{\mathbf{n}}$ describes the orientation of the swimmer. Additionally, the sign of the force parameter f distinguishes between pushers ($f > 0$) and pullers ($f < 0$). By construction, this model is force- and torque-free [**P1**].

The force centers now create a fluid flow, which is calculated by multiplying the Oseen tensor, see Eq. (2.2), with $\mathbf{f}_\pm$ and superimposing the results. Applying Eqs. (2.3), the motion of the swimmer is calculated . For $\alpha \neq 1/2$, a non-vanishing self-propulsion velocity parallel to $\hat{\mathbf{n}}$ is achieved, while the self-rotation is zero due to the axial symmetry of the setup. *Shakers* [94, 96], which do not self-propel but still stir the surrounding fluid, follow by choosing $\alpha = 1/2$ [**P1**].

From an abstracted physical point of view, the force centers can be seen as representations of an averaged (extended) force dipole that a microswimmer exerts [**P1**]. For example, the flow field around an *E. coli* bacterium contains a component resulting from a pusher-type force dipole [100]. The alga *Chlamydonas reinhardtii*,

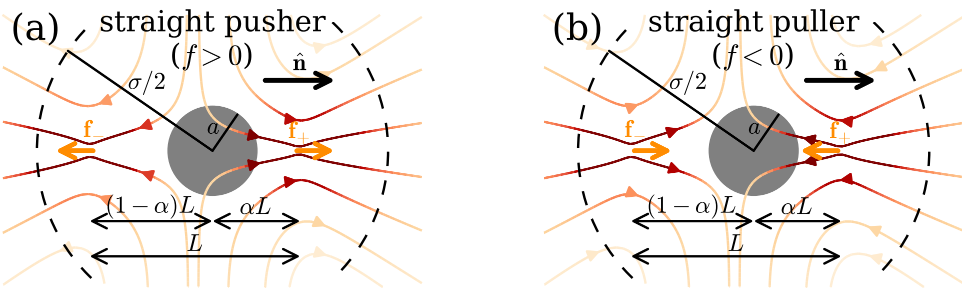

Figure 2.1: Sketch of our minimal microswimmer model [**P1**]. Two oppositely-oriented force centers co-move with the spherical swimmer body, as described in the main text. (a) For $f > 0$, a pusher is constructed, while (b) a puller follows for $f < 0$. Streamlines indicate the flow field, with color intensity representing its local strength. Dashed circular lines display the effective steric interaction radius of the swimmer.

however, has the signature of a puller, when the strokes of its two flagella are averaged over time [101].

Beyond a single swimmer, hydrodynamic interactions between swimmers are of utmost interest in many-body systems. For our model, we can develop pairwise "active mobility tensors" connecting the $\mathbf{f}_\pm$ of one swimmer to corresponding contributions to the velocity and angular velocity of a second swimmer, see also Eq. (3.2). For this purpose, Faxén's laws are applied, at the position of the second swimmer, to the flow field induced by the force dipole exerted by the first swimmer.

Concerning the fluid flows induced by $\mathbf{f}_\pm$, one should here, in principle, include corrections due to the finite radius of the no-slip swimmer body [33]. As a consequence, this rescales the leading-order contribution to the above pairwise active mobility tensors, as has been explicitly calculated for a similar force-dipole-based swimmer model [102]. The necessary changes make the mathematical description less tractable. In Publications **P1**–**P4**, we have neglected these corrections.

We require that both αL and $(1-\alpha)L$ are significantly larger than the radius a. For practical reasons, the singularities of the flow at $\mathbf{r}_\pm$ have to be shielded from other swimmers. We therefore introduce a repulsive steric interaction between the swimmers with an effective radius $\sigma/2 \gg \max\{\alpha L, (1-\alpha)L\}$ and a sufficiently high energy barrier [**P1**–**P4**], see also Fig. 2.1. This way, the swimmers are kept at large-enough distances from each other, even when they are heading for collision.

One advantage of our model is that we can extend it with relative ease to describe more complicated microswimmers. A corresponding model for circle swimmers is discussed next in Sec. 2.2.2, and one for only-rotating active particles in Sec. 2.2.3.

2.2.2 Circle swimmer

We now switch to swimmers that also *self-rotate* (with a constant angular velocity in the absence of any disturbances). In three dimensions, this potentially leads to helical trajectories, which become circular when planar confinement is introduced. Hence, these microswimmers are called *circle swimmers* [84, 103–107]. Typically, *dry* circle swimmers are modeled as ABPs (see Sec. 1.4) with an additional effective torque contributing to Eq. (1.2b) [84]. Rod-shaped circle swimmers can show consistent motion along a wall when their self-rotation is hindered by the wall due to steric interactions [108]. A more complicated model is the *Brownian spinning top,* which can feature a coupling between its translational and rotational motion [109]. In Publication **P2**, we introduce a minimal model for "wet" circle swimmers.

Here, the main change relative to the model for a straight-propelling microswimmer of Sec. 2.2.1 is that the extended force dipole now is positioned away from the previous symmetry axis, in a direction $\hat{\mathbf{u}}$ that is perpendicular to $\hat{\mathbf{n}}$, see also Fig. 2.2 (a). Specifically, Eqs. (2.4) and (2.5) are replaced by [**P2**]

$$\mathbf{f}_{\pm} = \pm f \hat{\mathbf{n}}, \tag{2.6a}$$

$$\mathbf{r}_{+} = \mathbf{r} + \alpha L \, \hat{\mathbf{n}} + \gamma L \, \hat{\mathbf{u}}, \tag{2.6b}$$

$$\mathbf{r}_{-} = \mathbf{r} - (1-\alpha) L \, \hat{\mathbf{n}} + \gamma L \, \hat{\mathbf{u}}, \tag{2.6c}$$

where the number γ quantifies the biaxiality of the swimmer and the straight-propelling microswimmer model is recovered for $\gamma = 0$, cf. Fig. 2.2 (a). The condition of vanishing net torque is maintained [**P2**].

For $\gamma \neq 0$, a microswimmer results that, if swimming freely, self-propels and self-rotates with an angular velocity $\boldsymbol{\omega}_{\mathrm{s}} \parallel (\hat{\mathbf{n}} \times \hat{\mathbf{u}})$ [**P2**]. This leads to circular trajectories, the radius of which is given by $R_{\mathrm{s}} = |\mathbf{v}_{\mathrm{s}}|/|\boldsymbol{\omega}_{\mathrm{s}}|$. As both $\mathbf{v}_{\mathrm{s}}$ and $\boldsymbol{\omega}_{\mathrm{s}}$ scale linearly with f, this *swimming radius* R_{s} is independent of f. The swimming radius can be tuned, however, by changing the geometrical parameters α and γ, as demonstrated in Fig. 2 of Publication **P2**.

The above circle swimmer propels on circular trajectories even if not confined to a plane, in contrast to many biological microswimmer which, when unconfined, rather self-propel on helical trajectories. In our approach, the latter behavior could be modeled by adding a second force dipole $\mathbf{f}'_{\pm}$, with, e.g., $\hat{\mathbf{n}}' = \hat{\mathbf{n}} \times \hat{\mathbf{u}}$ and $\gamma' = 0$.

2.2.3 Active rotator

Dry active rotators (see also their externally driven counterparts [110, 111]) are self-rotating particles that can be described by setting $v_{\mathrm{s}} = 0$ in Eq. (1.2) and adding an effective torque acting on each particle to Eq. (1.2b). In analogy to the models in Secs. 2.2.1 and 2.2.2, *wet active rotators* are introduced below, i.e., particles that actively induce fluid flows leading to self-rotation, but not to self-propulsion.

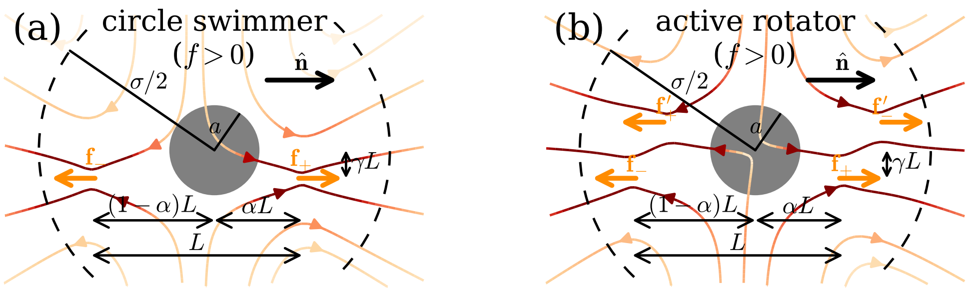

Figure 2.2: Force-dipole-based minimal models for two other types of microswimmer. (a) Circle swimmer [**P2**]. (b) Wet active rotator. Again, streamlines indicate the flow field and dashed lines the effective steric radius. Both objects are force- and torque-free. The circle swimmer self-propels and self-rotates, creating circular trajectories (in the absence of noise), while the active rotator only self-rotates.

For this purpose, the force dipole defined by Eqs. (2.6) is subjected to a point reflection with respect to the particle center $\mathbf{r}$. This creates a second pair of forces $\mathbf{f}'_\pm$ at $\mathbf{r}'_\pm$ given by

$$\mathbf{f}'_\pm = -\,\mathbf{f}_\pm = \mp f\hat{\mathbf{n}}, \tag{2.7a}$$
$$\mathbf{r}'_+ = \mathbf{r} - \alpha L\,\hat{\mathbf{n}} - \gamma L\,\hat{\mathbf{u}}, \tag{2.7b}$$
$$\mathbf{r}'_- = \mathbf{r} + (1-\alpha)L\,\hat{\mathbf{n}} - \gamma L\,\hat{\mathbf{u}}, \tag{2.7c}$$

see also Fig. 2.2 (b) for a sketch of the complete object. Due to the linearity of Eqs. (2.1), the (total) swimming velocity $\mathbf{v}_\mathrm{s}^\mathrm{tot}$ and angular velocity $\boldsymbol{\omega}_\mathrm{s}^\mathrm{tot}$ of the combined new object result from superposition of the respective contributions of the two force dipoles, i.e., $\mathbf{v}_\mathrm{s}^\mathrm{tot} = \mathbf{v}_\mathrm{s} + \mathbf{v}'_\mathrm{s}$ and $\boldsymbol{\omega}_\mathrm{s}^\mathrm{tot} = \boldsymbol{\omega}_\mathrm{s} + \boldsymbol{\omega}'_\mathrm{s}$.

In particular, the swimming velocity is a *true vector*, while the angular velocity is an *axial* vector. Thus, their different symmetry properties under point reflection lead to $\mathbf{v}_\mathrm{s}^\mathrm{tot} = \mathbf{v}_\mathrm{s} + \mathbf{v}'_\mathrm{s} = \mathbf{v}_\mathrm{s} - \mathbf{v}_\mathrm{s} = \mathbf{0}$ and $\boldsymbol{\omega}_\mathrm{s}^\mathrm{tot} = \boldsymbol{\omega}_\mathrm{s} + \boldsymbol{\omega}'_\mathrm{s} = 2\,\boldsymbol{\omega}_\mathrm{s}$. The latter is non-vanishing for $\gamma \neq 0 \wedge \alpha < 1/2$ [**P2**].

This way, a wet active rotator has been constructed, which is force- and torque-free. In principle, this model could now also be used as an input to a dynamical statistical theory similar to the ones discussed next in Chapter 3.

Chapter 3

Dynamical statistical theory for many-swimmer suspensions

As detailed in Sec. 1.3, (microscopic) statistical theories are versatile tools for describing many-particle systems. In particular, we have developed and applied a *dynamical density functional theory* (DDFT) for (semi)dilute suspensions of hydrodynamically interacting microswimmers [**P1**–**P4**]. Before discussing this new theory, I now briefly give an overview of the general concept of DDFT.

Historically, DDFT [112–122] is the non-equilibrium offspring of the *classical density functional theory* (DFT) that characterizes colloidal systems in equilibrium [123–127], which itself is the classical equivalent of the *quantum mechanical* density functional theory that is used to describe probability densities of electrons on the atomic scale [128–130]. In broad terms, DDFT acts as if the one-body density at a given time had been produced by a virtual external potential under the influence of which the system is in (instantaneous) equilibrium [**P1**]. Via this *adiabatic approximation*, detailed later in Sec. 3.1.2, DDFT transfers exact equilibrium relations to non-equilibrium situations in order to obtain the approximate dynamical evolution of the corresponding one-body densities. This procedure provides a quite powerful approach in many situations.

Formally, DDFT can be embedded in more general theories that additionally take into account non-adiabatic probability currents [131–134]. Instances of more coarse-grained descriptions, partially supported by DDFT, are phase-field crystal models [75, 135–139] or more-macroscopic hydrodynamic equations [140–142].

For (passive) overdamped colloidal particles, DDFT was first introduced as a semi-phenomenological extension of the (one-body-density) Smoluchowski equation [112]. Later, a firmer foundation was laid via diverse theoretical frameworks [114–118]. Conceptually, our statistical approach for microswimmers combines two previous DDFT strands that describe dry self-propelled particles [121, 143] and hydrodynamically interacting passive colloidal particles [144–149].

Next, in Sec. 3.1, I sketch the derivation (and application) of our DDFT for the basic case of straight-propelling microswimmers with a spherical body shape. Then, circle swimmers and mixtures of different microswimmer species are discussed as incrementally more complex cases in Sec. 3.2. An adaptation of our statistical theory that probes the possible onset of orientational order on larger scales is described in Sec. 3.3, introducing a test-particle method to obtain swimmer–swimmer pair distribution functions on the way. Finally, Sec. 3.4 discusses possible further extensions of our DDFT approach.

3.1 DDFT for straight-propelling microswimmers

A suspension of identical straight-propelling microswimmers, based on the model described in Sec. 2.2.1, is the simplest of the system that we set out to describe and thus has been the starting point of our work on this topic in Publication **P1**. In this section, I sketch how a dynamical density functional theory (DDFT) describing the collective behavior of interacting swimmers is developed in a two-step process. Specifically, a hierarchy of equations is derived from first principles in Sec. 3.1.1. Then, the associated dynamic equation for the one-body density is closed via DDFT methods in Sec. 3.1.2. Furthermore, Secs. 3.1.3 and 3.1.4 discuss the application of our DDFT to exemplary planar arrangements.

3.1.1 From conservation of probability to a hierarchy of equations

In Publication **P1**, we consider N straight-propelling microswimmers of the kind introduced in Sec. 2.2.1. At time t, the system is described by the probability density function $P = P(\mathbf{X}_1, \ldots, \mathbf{X}_N, t)$ of finding the system in a certain configuration, where $\mathbf{X}_i = (\mathbf{r}_i, \hat{\mathbf{n}}_i)$ denotes the configuration of the ith swimmer, $i = 1, \ldots, N$, and comprises its position $\mathbf{r}_i$ and its orientation $\hat{\mathbf{n}}_i$. Assuming overdamped dynamics (i.e., a low Reynolds number) and local conservation of probability, the many-particle Smoluchowski equation [150]

$$\frac{\partial P}{\partial t} = -\sum_{i=1}^{N} \Big(\nabla_{\mathbf{r}_i} \cdot (P\,\mathbf{v}_i) + \nabla_i^{\mathrm{or}} \cdot (P\,\boldsymbol{\omega}_i) \Big) \tag{3.1}$$

follows, on which we base our approach, in analogy to the derivation in Ref. 116. Here, $\nabla_i^{\mathrm{or}} = \hat{\mathbf{n}}_i \times \nabla_{\hat{\mathbf{n}}_i}$ is the orientational gradient operator for uniaxial particles, while $\mathbf{v}_i$ denotes the velocity and $\boldsymbol{\omega}_i$ the angular velocity of the ith swimmer. For pairwise hydrodynamic interactions between swimmers, $\mathbf{v}_i$ and $\boldsymbol{\omega}_i$ are given by [**P1**]

$$\begin{bmatrix} \mathbf{v}_i \\ \boldsymbol{\omega}_i \end{bmatrix} = \sum_{j=1}^{N} \left(\begin{bmatrix} \boldsymbol{\mu}_{ij}^{\mathrm{tt}} & \boldsymbol{\mu}_{ij}^{\mathrm{tr}} \\ \boldsymbol{\mu}_{ij}^{\mathrm{rt}} & \boldsymbol{\mu}_{ij}^{\mathrm{rr}} \end{bmatrix} \cdot \begin{bmatrix} \mathbf{F}_j \\ \mathbf{T}_j \end{bmatrix} + \begin{bmatrix} \boldsymbol{\Lambda}_{ij}^{\mathrm{tt}} & \mathbf{0} \\ \boldsymbol{\Lambda}_{ij}^{\mathrm{rt}} & \mathbf{0} \end{bmatrix} \cdot \begin{bmatrix} f\hat{\mathbf{n}}_j \\ \mathbf{0} \end{bmatrix} \right), \tag{3.2}$$

where we call the different $\boldsymbol{\mu}_{::}^{::}$ passive mobility tensors and the different $\boldsymbol{\Lambda}_{::}^{::}$ active mobility tensors. Additionally, f is the force parameter according to Eq. (2.4).

In Eq. (3.2), the force $\mathbf{F}_j$ and the torque $\mathbf{T}_j$ acting on swimmer j comprise the effects of thermal noise (via of an effective entropic potential [150]), external potentials, and pairwise steric interactions between swimmers [**P1**]. The mobility tensors have been determined on the basis of the microswimmer model introduced in Sec. 2.2.1 and inserted accordingly [**P1**–**P4**]. For the passive mobility tensors, we have used the Rotne-Prager level of hydrodynamic interactions [151, 152], which beyond the Oseen tensor includes corrections resulting from the non-vanishing size a of the swimmer body up to the order $\sim (a/r_{ij})^{-3}$, with r_{ij} being the distance between the two corresponding swimmers i and j [**P1**].

To explicitly solve for the full probability density $P(\mathbf{X}_1, \ldots, \mathbf{X}_N, t)$ in Eq. (3.1) is, in general, not possible in non-equilibrium. Therefore, we at this point start focusing on the one-swimmer density $\rho^{(1)}(\mathbf{X}, t)$, with the reduced n-swimmer densities being defined via [123]

$$\rho^{(n)}(\mathbf{X}_1, \ldots, \mathbf{X}_n, t) = \frac{N!}{(N-n)!} \int \mathrm{d}\mathbf{X}_{n+1} \, \ldots \int \mathrm{d}\mathbf{X}_N \, P(\mathbf{X}_1, \ldots, \mathbf{X}_N, t). \qquad (3.3)$$

Here, the prefactor arises because the swimmers are identical and we do not distinguish between them. Accordingly, the argument of the above n-swimmer density depends on the coordinates of “any” first swimmer, “any” second swimmer, and so on, so that we from now on denote them as $\mathbf{X}, \mathbf{X}', \ldots, \mathbf{X}^{(n)}$ instead of the numbering of the original swimmers.

The next step consists of reducing Eq. (3.1) by integrating out the coordinates of all swimmers except for those for one swimmer. The result reads [**P1**]

$$\frac{\partial \rho^{(1)}(\mathbf{X}, t)}{\partial t} = -\nabla_{\mathbf{r}} \cdot \left(\boldsymbol{\mathcal{J}}^{\mathrm{tt}} + \boldsymbol{\mathcal{J}}^{\mathrm{tr}} + \boldsymbol{\mathcal{J}}^{\mathrm{ta}} \right) - (\hat{\mathbf{n}} \times \nabla_{\hat{\mathbf{n}}}) \cdot \left(\boldsymbol{\mathcal{J}}^{\mathrm{rt}} + \boldsymbol{\mathcal{J}}^{\mathrm{rr}} + \boldsymbol{\mathcal{J}}^{\mathrm{ra}} \right), \qquad (3.4)$$

where each current density $\boldsymbol{\mathcal{J}}^{\cdot\cdot}$ corresponds to one of the mobility tensors in Eq. (3.2), with $\boldsymbol{\mathcal{J}}^{\cdot \mathrm{a}}$ referring to the respective $\boldsymbol{\Lambda}^{\cdot \mathrm{t}}$. The concrete $\boldsymbol{\mathcal{J}}$’s, given by Eqs. (32)–(37) of Publication **P1**, involve two- and three-swimmer densities, so that Eq. (3.4) is not closed at this level of the description. In principle, similar dynamical equations could now be derived for those densities, but these would again depend on densities of even-higher order [**P1**]. Neglecting hydrodynamic interactions and setting $f = 0$ in our framework, this escalating sequence of equations becomes the usual BBGKY hierarchy that is well-established in the theory of liquids [123, 153–157].

In order to obtain a closed dynamical equation for $\rho^{(1)}(\mathbf{X}, t)$, approximations must be introduced. First, DDFT suggests to transfer equilibrium relations to the non-equilibrium situation at hand, providing partial closure, as explained below in Sec. 3.1.2. Second, known relations between the remaining two-swimmer densities and the one-swimmer density can be inserted via pair distribution functions. The latter route is chosen in Publication **P4**, as discussed in Sec. 3.3.1.

3.1.2 An appropriate closure: the adiabatic approximation

As detailed in the preceding section, a dynamical equation for the one-swimmer density can be derived by integrating the many-body Smoluchoswki equation over the phase-space coordinates for all swimmers except for one swimmer. However, this equation still features dependencies on two- and three-swimmer densities, which prevents (numerical) evaluations. In this section, I explain how DDFT methods [112–122] can be used to overcome this problem, as has been discussed and applied in Publications **P1**–**P4**.

The central step here is the *adiabatic approximation*. In particular, DDFT acts as if the density at time t had been created by a virtual external potential $\Phi_{\mathrm{ext}}(\mathbf{X},t)$ under the influence of which the system is in (instantaneous) equilibrium, leading to the one-swimmer density observed at time t [114–116, **P1**]. In effect, this transfers exact equilibrium density correlations to the present non-equilibrium situation. Instead of determining the virtual quantity $\Phi_{\mathrm{ext}}(\mathbf{X},t)$ explicitly, two different expressions containing it can be derived using properties of thermodynamic equilibrium, as detailed below. Combining these two relations then eliminates $\Phi_{\mathrm{ext}}(\mathbf{X},t)$ from the mathematical description, and we obtain a closed set of equations.

First, we employ *Yvon-Born-Green (YBG) relations*, which result from the equilibrium limit of the BBGKY hierarchy [123,158]. Their nth level can be derived by taking into account the definition of the n-swimmer density in Eq. (3.3) under the assumption of [158, **P2**]

$$P \propto \exp(-\beta\mathcal{H}), \tag{3.5}$$

with $\beta = (k_{\mathrm{B}}T)^{-1}$, k_{B} denoting the Boltzmann constant, T the temperature, and $\mathcal{H}$ the (virtual) Hamiltonian

$$\mathcal{H} = \sum_{k=1}^{N-1}\sum_{l=k+1}^{N} U_{\mathrm{int}}(|\mathbf{r}_k - \mathbf{r}_l|) + \sum_{k=1}^{N} \Phi_{\mathrm{ext}}(\mathbf{X}_k, t). \tag{3.6}$$

At this point, the virtual external potential $\Phi_{\mathrm{ext}}(\mathbf{X},t)$ takes the role of the actual physical external potential and $U_{\mathrm{int}}(|\mathbf{r}_k - \mathbf{r}_l|)$ denotes the steric interaction potential acting between swimmers k and l. As an example, one corresponding formula (needed to eliminate some two-swimmer densities) reads

$$k_{\mathrm{B}}T\,\nabla_{\mathbf{r}}\,\rho^{(1)}(\mathbf{X},\mathbf{t}) = -\,\rho^{(1)}(\mathbf{X},t)\nabla_{\mathbf{r}}\,\Phi_{\mathrm{ext}}(\mathbf{X},t) - \int \mathrm{d}\mathbf{X}'\,\rho^{(2)}(\mathbf{X},\mathbf{X}',t)\nabla_{\mathbf{r}}\,U_{\mathrm{int}}(|\mathbf{r}-\mathbf{r}'|) \tag{3.7}$$

For the second route, the corresponding virtual grand potential functional $\Omega[\rho^{(1)}]$ is considered, which is minimal for the equilibrium (one-swimmer) density. By splitting the functional $\Omega[\rho^{(1)}]$ into the contribution of $\Phi_{\mathrm{ext}}(\mathbf{X},t)$, the (exactly known) ideal gas part, and the (generally unknown) interaction-induced *excess free-energy functional* $\mathcal{F}_{\mathrm{exc}}[\rho^{(1)}]$, the relation

$$-\Phi_{\mathrm{ext}}(\mathbf{X},t) = k_{\mathrm{B}}T \ln\left(\lambda^3\rho^{(1)}(\mathbf{X},t)\right) + \frac{\delta\mathcal{F}_{\mathrm{exc}}}{\delta\rho^{(1)}(\mathbf{X},t)} \tag{3.8}$$

is obtained from the minimization condition that is here transferred to the present non-equilibrium situation [**P1**], with λ being the thermal de Broglie wavelength. While the unique existence of an exact $\mathcal{F}_{\mathrm{exc}}$ is proven for all suitable systems [117], its concrete form is unknown for most cases and has to be approximated. For, e.g., soft repulsive steric interactions, a mean-field ansatz, later introduced as Eq. (3.11), is well-accepted.

As an example, Eqs. (3.7) and (3.8) can be combined to eliminate $\Phi_{\mathrm{ext}}(\mathbf{X},t)$ and corresponding two-swimmer densities from our mathematical formalism. An analogous process for the terms featuring the three-swimmer density can also be performed, reducing the corresponding terms to contain only two-swimmer densities [**P1**].

Following the above route, all higher-order densities related to steric interactions are reduced by one order. However, the terms resulting from hydrodynamic interactions still contain two-swimmer densities [**P1**]. Accordingly, an additional assumption has to be introduced to express the remaining instances of $\rho^{(2)}(\mathbf{X},\mathbf{X}',t)$ in terms of $\rho^{(1)}(\mathbf{X},t)$.

In Publication **P1**, a mean-field approximation was chosen for this purpose, assuming $\rho^{(2)}(\mathbf{X},\mathbf{X}',t)=0$ for $\mathbf{r}-\mathbf{r}'\to\mathbf{0}$ to avoid hydrodynamic divergences. For a smoother treatment of the mobility tensors, the more refined Onsager-like [159] ansatz $\rho^{(2)}(\mathbf{X},\mathbf{X}',t)=\rho^{(1)}(\mathbf{X},t)\,\rho^{(1)}(\mathbf{X}',t)\exp\left(-\beta U_{\mathrm{int}}(\mathbf{r},\mathbf{r}')\right)$ for $|\mathbf{r}-\mathbf{r}'|>2a$ and $\rho^{(2)}(\mathbf{X},\mathbf{X}',t)=0$ otherwise was used in Publications **P2**–**P4**. This completes our presentation of a closed, (numerically) solvable set of equations [**P1**].

3.1.3 Reduction to planar arrangements

Together with the approximations introduced in Sec. 3.1.2, Eq. (3.4) describes the dynamical evolution of $\rho^{(1)}(\mathbf{X},t)$. In general, this one-swimmer density depends on the five-dimensional phase-space coordinate $\mathbf{X}=(\mathbf{r},\hat{\mathbf{n}})$. To reduce the complexity of numerically solving the corresponding higher-dimensional partial differential equations, we restrict our evaluations to planar arrangements of microswimmers.

For this purpose, the microswimmers are confined to the xy-plane in the bulk fluid. Furthermore, the orientation of each swimmer is analogously constrained and can thus be parameterized by a single angle ϕ measured relatively to the x-axis, with $\hat{\mathbf{n}}=(\cos\phi,\sin\phi,0)$ and $\hat{\mathbf{n}}\times\nabla_{\hat{\mathbf{n}}}=\hat{\mathbf{z}}\,\partial_\phi$. Accordingly, $\rho^{(1)}(\mathbf{X},t)$ thus depends only on the three-dimensional phase-space coordinate $\mathbf{X}=(x,y,\phi)$. Such a setup could possibly be realized, e.g., by introducing corresponding optical trapping fields or by constraining the swimmers to the interface between two immiscible fluids of the same viscosity [**P1**].

The resulting partial differential equation has proven to be well-solvable [**P1**–**P4**]. For Publications **P2**–**P4**, the corresponding equations were solved using the numerical partial differential equation solver *FiPy* [160]. An equidistant numerical grid allowed to use *Fast Fourier Transformation* methods to calculate the convolution terms that emerge from the hydrodynamic interactions [**P2**–**P4**].

A first application of this general setup, considering microswimmers in an external trapping potential, is described next in Sec. 3.1.4. Planar arrangements are also discussed in the more complex situations addressed in Sec. 3.2.

3.1.4 Application to radial external trapping potentials

In Publications **P1** and **P2**, we further let an external potential act on the swimmers in the basic planar arrangement described above in Sec. 3.1.3. Namely, this was a quartic radial trapping potential

$$U_{\mathrm{ext}}(r) = V_0 \left(\frac{r}{\sigma}\right)^4. \tag{3.9}$$

Additionally, the steric interaction between two swimmers (which are located at positions $\mathbf{r}$ and $\mathbf{r}'$) has been modeled via a soft, repulsive GEM-4 potential, which has the functional form [161, 162]

$$U_{\mathrm{int}}(|\mathbf{r}-\mathbf{r}'|) = \epsilon_0 \exp\left(-\left(\frac{|\mathbf{r}'-\mathbf{r}|}{\sigma}\right)^4\right), \tag{3.10}$$

where $\epsilon_0 > 0$ is the (finite, but typically high) interaction energy at complete overlap. We further use the mean-field excess free energy functional

$$\mathcal{F}_{\mathrm{exc}} = \int\!\mathrm{d}\mathbf{X}\int\!\mathrm{d}\mathbf{X}'\,\rho^{(1)}(\mathbf{X},t)\,\rho^{(1)}(\mathbf{X}',t)\,U_{\mathrm{int}}(\mathbf{r},\mathbf{r}'), \tag{3.11}$$

which has previously been found to be appropriate when considering the above interaction potential [162].

For this general setup, we could qualitatively compare our results with those from existing particle-based computer simulations that included hydrodynamic interactions as well [85, 163]. The favorable agreement between the results described below stresses the success of our approach [**P1**].

Specifically, for vanishing active drive $f = 0$, the behavior of passive particles is recovered, i.e., a center-heavy density distribution is formed in the radial trap. Switching on the active drive, but neglecting the hydrodynamic interactions, leads to an off-center ring-like pattern, with the direction of self-propulsion pointing radially outwards [**P1**]. Along this ring, which had previously been reported in several studies [85, 163–165], the outward self-propulsion approximately balances the restoring force exerted by the trapping potential.

When now the hydrodynamic interactions are reintroduced, the fluid flows induced by the trapping potential acting on the microswimmers can lead to the collapse of the above radially symmetric density distribution to one off-center high-density spot [**P1**–**P3**]. (Please note that the results shown in Publication **P1** here typically featured two of these spots, which we later could attribute to the fact that the applied cut-off distance of the hydrodynamic interactions was too short when compared to the diameter of the ring distribution.) The swimmers organized in the high-density spot feature some degree of polar orientational order. Thus, they collectively pump the surrounding fluid. The formation of this *hydrodynamic fluid pump* (with broken radial symmetry) had previously been reported in corresponding particle-based computer simulations [85, 163].

The above effect can in principle be observed for pushers and for pullers. However, for appropriate system parameters, differences can be observed. For the parameters chosen in Publication **P2**, pushers generally favor a collapse to a high-density spot, while puller systems show a symmetric ring-like density distribution [**P2**].

3.2 Increasing the complexity

Beyond the basic case of (semi)dilute suspensions of straight-propelling swimmers discussed above in Sec. 3.1, we have also worked on DDFTs for more complex systems. In particular, this included (semi)dilute suspensions of hydrodynamically interacting circle swimmers [**P2**], see Sec. 3.2.1, and situations in which multiple species of swimmers are present [**P3**], see Sec. 3.2.2.

3.2.1 DDFT for circle swimmers

In contrast to the straight-propelling microswimmers discussed above in Sec. 3.1, circle swimmers additionally show active self-rotation. Beyond initial one-swimmer studies [84, 104, 106, 108], several particle-based computer simulations involving many "dry" circle swimmers have been performed in recent years [103, 166–168].

We here discuss suspensions of "wet" circle swimmers, on the basis of the model introduced in Sec. 2.2.2. In Publication **P2**, a corresponding DDFT has been derived in analogy to the one reviewed in Sec. 3.1. Only slight modifications were necessary for this purpose. Specifically, one additional term enters the current density $\boldsymbol{\mathcal{J}}^{\mathrm{ra}}$ and the locations of the active force centers need to be adjusted [**P2**].

Again, we have numerically evaluated our theory for a planar configuration of active circle swimmers under the influence of a radial external trapping potential. We find that an increased curvature of trajectories of our circle swimmers generally lets the swimmers self-propel less effectively against the external trapping force.

Accordingly, the corresponding steady-state density distributions become more localized towards the center of the trap [**P2**]. In particular, when varying the biaxiality parameter γ, we find a smooth transition between an off-center ring-like distribution and a center-heavy one, approximately around the value of γ for which the swimming radius R_s is equal to the ring size [**P2**].

For small γ, the general structure of the steady-state solution for spherical microswimmers, as discussed in Sec. 3.1.4, is maintained. That is, for a certain (large) parameter range, pusher microswimmers form a high-density spot with aligned radial orientation. Nevertheless, even a small self-rotation (for $0 < |\gamma| \ll 1$) can here induce a consistent movement of that spot along the rim of the external trapping potential [**P2**].

3.2.2 Mixtures of microswimmers

Another natural extension of the DDFT for one-species microswimmer systems is to allow for mixtures of distinct species of active swimmers (and also passive particles). This could find application in the description of biological systems, which often many species exposed to complex environments, and in medical contexts, in which artificial microswimmers are supposed to interact, e.g., with human cells of similar size. As an additional benefit, such multi-species statistical descriptions can enable to develop certain test-particle methods that determine correlation functions in one-component systems [169, 170].

Consequently, a multi-species DDFT for microswimmers was developed in Publication **P3**. There, we were able to build on existing DDFT descriptions for mixtures of passive particles [171–175], in combination with our DDFT for one-species microswimmer suspensions [**P1**].

The corresponding theoretical derivation starts once more from the many-particle Smoluchowski equation, see Eq. (3.1), in combination with a mobility-matrix formalism as in Eq. (3.2). Here, we now allow the swimmers to differ from each other in their model parameters, constituting multiple species [**P3**]. Then, in close analogy to the one-species case [**P1**], two coupled DDFT equations are derived to describe a binary mixture. They quantify the dynamical evolution of the respective one-swimmer densities of the two constituents [**P3**]. Subsequently, the theory has been applied to three different exemplary situations [**P3**], as detailed below.

First, a radial external trapping potential, similar to the situation described in Sec. 3.1.4, is populated with a pusher–puller binary mixture, with the two species only differing in the sign of the active force parameter f. It is found that in these systems, under the chosen system parameters, the majority species imposes its behavior onto the minority species [**P3**]. For an approximately equal number of pushers and pullers, the hydrodynamic currents induced by the self-propulsion of the two species feature similar magnitudes, but are oppositely oriented, and thus nearly cancel each other. Nevertheless, fluid flows that are induced by the action of the external trapping potentials can still lead to the formation of a high-density spot, if this effect overcomes thermal diffusion [**P3**].

Second, mixtures of pushers and pullers in a planar arrangement in the absence of the trapping potential have been studied with regard to the possible onset of orientational ordering due to hydrodynamic interactions between the swimmers, using the general method described below in Sec. 3.3. In reasonable agreement with corresponding results from particle-based computer simulations [51], it is found that a system of pullers can spontaneously develop orientational order on a larger scale even when it is doped with pushers [**P3**]. For a system in which pushers and pullers only differ by the sign of the force parameter f, we obtain a quantitative criterion necessary for the onset of polar orientational order. Specifically, it requires that more pullers than pushers are present and that the hydrodynamic ordering effects overcome the rotational diffusion of the swimmers [**P3**].

Third, we have constructed a *shear cell* model. For this purpose, one species of passive particles ($f = 0$) is confined to a ring by an external potential. Driving those particles with an appropriate external force field along the contour of the ring then creates an internal circular flow field [**P3**]. When we now confine straight-propelling microswimmers as a second species to the plane inside this ring, the induced shear flow continuously rotates them. This prevents an efficient swimming towards the boundary of the confinement [**P3**], similarly to the situation of circle swimming that we have investigated in Publication **P2**.

The successful application to these three examples shows the rich possibilities of description that our DDFT for mixtures of microswimmers offers. In principle, it could also be combined with the ideas of Publication **P2** to describe mixtures including circle swimmers.

3.3 Refinement of the theory for untrapped planar systems

Publication **P4** was inspired by previous particle-based simulations that showed orientational ordering due to hydrodynamic interactions for microswimmers endowed with mutually repulsive steric interactions [51, 176]. We have thus considered a similar situation in the context of our statistical theory. For this purpose, we followed a somewhat modified route including an additionally determined expression for the pair distribution function, see Sec. 3.3.1, obtained from a test-particle method for active particles, see Sec. 3.3.2. This more refined procedure became necessary because our previous mean-field treatment in the context of DDFT [**P1**–**P3**] turned out to be too simplified to answer the questions mentioned below [**P4**].

In particular, we find that the interplay of the active motion and the steric interactions between the swimmers creates pair distribution functions that depend on the swimmer orientations in a non-trivial way [**P4**]. Using corresponding functional forms as an input to our statistical framework, the linear stability of the disordered state against uniform orientational order resulting from hydrodynamic interactions has been tested, as discussed below in Sec. 3.3.3. For (semi)dilute suspensions of our puller microswimmers, it is found that hydrodynamic interactions between swimmers can establish polar orientational ordering on larger scales through linear order, in contrast to our pusher microswimmers [**P4**]. In further works, this method has been extended to multi-species mixtures of microswimmers [**P3**], as indicated in Sec. 3.2.2.

3.3.1 Involving the pair distribution function

In Sec. 3.1.1, Eq. (3.4) constitutes the first order of a BBGKY-like hierarchy of equations and still contains two- and three-swimmer densities [**P1**]. Applying the adiabatic approximations of DDFT, see Sec. 3.1.2, the three-swimmer densities can be replaced, which involves two-swimmer densities. The remaining two-swimmer densities can then be approximated in terms of one-swimmer densities, e.g., via the dilute limit of the pair distribution function, as described in Sec. 3.1.2. In the following, we skip the adiabatic approximation and instead sketch another route directly involving the pair distribution function.

In Publication **P4**, untrapped planar arrangements are studied with regard to the possible onset of global collective orientational ordering resulting from the hydrodynamic interactions induced by the swimming mechanisms. For a large periodic box of area A, we assume spatial homogeneity and introduce $\rho^{(1)}(\phi,t) = A\,\rho^{(1)}(\mathbf{X},t)$, with $\mathbf{X} = (x,y,\phi)$. Then, Eq. 3.4 reduces to approximately

$$\frac{\partial\rho^{(1)}(\phi,t)}{\partial t} = D_{\mathrm{r}}\,\partial_\phi^2\,\rho^{(1)}(\phi,t) - f\partial_\phi\left[\int\!\mathrm{d}\mathbf{r}\int\!\mathrm{d}\mathbf{X}'\,\hat{\mathbf{z}}\cdot\left(\mathbf{\Lambda}^{\mathrm{rt}}_{\mathbf{r},\mathbf{X}'}\,\hat{\mathbf{n}}'\right)\rho^{(2)}(\mathbf{X},\mathbf{X}',t)\right], \quad (3.12)$$

for sufficiently small overall densities [**P4**], with the rotational diffusion constant D_{r}. Here, the two-swimmer density can be rewritten using the pair distribution function $g(\mathbf{X},\mathbf{X}',t)$, which is defined via [123]

$$\rho^{(2)}(\mathbf{X},\mathbf{X}',t) = \rho^{(1)}(\mathbf{X},t)\,\rho^{(1)}(\mathbf{X}',t)\,g(\mathbf{X},\mathbf{X}',t). \quad (3.13)$$

This is particularly useful when considering fully disordered states, for which the one-body densities are of trivial forms [**P4**].

In general, knowledge of $g(\mathbf{X},\mathbf{X}',t)$ is important because it allows the direct calculation of many physical quantities in a system, e.g., the total average interaction energy caused by pairwise interactions between the particles [177]. Additionally, the pair distribution function can be used to easily differentiate between distinct states of matter [123]. Furthermore, $g(\mathbf{X},\mathbf{X}',t)$ can be related to several other (spatial) correlation functions, e.g., to the (static) structure factor accessible from light-scattering experiments [123].

Previous studies on ABPs determined typical forms of $g(\mathbf{X}, \mathbf{X}', t)$ [67, 178, 179]. The interplay between steric repulsive interactions and active self-propulsion creates front-back asymmetries and non-trivial variations as a function of the orientations of the swimmers [178]. First steps of calculating swimmer–swimmer pair distribution functions from computer simulations including hydrodynamic interactions have been performed [51, 180]. Our scope was to use an easily applicable method to determine pair distribution functions in active systems to an approximation degree sufficient for purposes.

Section 3.3.2 describes our test-particle method to find corresponding (orientation-dependent) swimmer–swimmer pair distribution functions. Taking these results as an input, the linear stability of Eq. (3.12) against the onset of collective polar orientational ordering is discussed in Sec. 3.3.3.

3.3.2 Active test-particle method

Our strategy has been to adapt a relation that is exact for passive equilibrium systems for the description of our active systems. Specifically, in equilibrium liquids, the pair distribution function is determined from the density around one particle that is fixed and treated as an (externally imposed) obstacle [123, 181]. For particles featuring an isotropic interaction potential $U_{\mathrm{int}}(|\mathbf{r}' - \mathbf{r}|)$ in a liquid state with average density $\bar{\rho}$, the pair distribution function follows as [123]

$$\bar{\rho}\, g(r) = \rho(r)\big|_{\mathrm{obstacle}}\,, \tag{3.14}$$

where the right-hand side represents the density distribution that the system forms around the one fixed particle, here located at $\mathbf{r}_0 = \mathbf{0}$. The influence of this one particle on the other particles is taken into account in the form of an external potential $U_{\mathrm{ext}}(\mathbf{r}) = U_{\mathrm{int}}(|\mathbf{r} - \mathbf{r}_0|) = U_{\mathrm{int}}(r)$. These relations can be evaluated using classical equilibrium density functional theory [182].

As Eq. (3.14) is exact in equilibrium [123], we consider it to be a reasonable starting point for obtaining a first-order approximation of the swimmer–swimmer pair distribution function in active systems, as detailed in Publication **P4** (and used in one of the applications discussed in Publication **P3**). Here, some ad-hoc adaptations are involved for active particles. Specifically, the position and orientation of one swimmer are fixed at $\mathbf{r}_0$ and, respectively, as $\hat{\mathbf{n}}_0$. Then, in order to account for the active self-propulsion of the fixed swimmer, we stream the other swimmers against the fixed swimmer with its free-swimming velocity $\mathbf{v}_0$ [**P4**]. The resulting (orientation-dependent) density distribution, stemming from the interplay between this streaming and the repulsive steric interaction between the swimmers, appears to lead to a reasonable approximation for the swimmer–swimmer pair distribution function [**P4**].

Hydrodynamic interactions have not been taken into account in this procedure [**P4**]. It is still unclear how they, also in combination with the thermal fluctuations of the fixed swimmer, could be included in the above method. Accordingly, the obtained pair distribution functions are, strictly speaking, valid approximations only for dry ABPs in a non-aligned state. However, our method should also provide reasonable approximations for cases in which hydrodynamic interactions do not overly affect the swimmer–swimmer pair distribution function. For different systems, hydrodynamic interactions might nevertheless significantly influence the pair distribution function [180].

3.3.3 Application to collective polar orientational ordering

In Publication **P4**, we have combined the reasoning of Sec. 3.3.1 with the Percus-type test-particle method described in Sec. 3.3.2. This way, *a priori* predictions are made for the onset of orientational order on larger scales in (semi)dilute suspensions of our model microswimmers, in the absence of additional external trapping potentials. In particular, using correspondingly determined forms of the pair distribution function and performing a first-order harmonic fit for an expression that involves it, cf. Fig. 2 of Publication **P4**, Eq. (3.12) leads to a partial differential equation of the form [**P4**]

$$\frac{\partial \rho^{(1)}(\phi,t)}{\partial t} = D_{\mathrm{r}}\, \partial_\phi^2 \rho^{(1)}(\phi,t) - Cf\partial_\phi \left[\rho^{(1)}(\phi,t)\!\int\! \mathrm{d}\phi' \rho^{(1)}(\phi',t)\, \sin(\phi-\phi')\right], \quad (3.15)$$

with $C > 0$ being a positive constant.

This functional form is further supported by a two-swimmer scattering approach (valid for very dilute suspensions) that is described in Appendix B of Publication **P4**. Additionally, Appendix C of the same article identifies a minimal orientation-dependent functional form of the pair distribution function leading to $C \neq 0$ on the right-hand side of Eq. (3.15). In particular, this minimal contribution describes an enhanced probability to find in the vicinity of the fixed swimmer other particles that propel in the approximately same direction [**P4**].

A linear analysis of the above equation for the stability of the orientationally disordered, spatially homogeneous state against the onset of large-scale polar orientational order has been performed [**P4**]. We find that orientational order in (semi)dilute suspensions, emerging from a linear instability, can only develop for sufficiently strong pullers, and not for (pure) pusher systems [**P4**]. This is in qualitative agreement with the results obtained from previous particle-based computer simulations using the same swimmer model [51]. In the future, our approach may be useful to characterize ordering effects in other systems as well, e.g., in (semi)dilute suspensions of rod-shaped swimmers.

3.4 Outlook

In the following, I provide an outlook concerning related physical situations that could be investigated via statistical theories similar to ours in the future. Some of these are, at least in principle, in the reach of the present framework, see Sec. 3.4.1, while others go well beyond it, see Sec. 3.4.2.

3.4.1 Extensions in the reach of our theory

I now present several additional situations the description of which is within reach of our theoretical framework. Moreover, I describe possible pathways to adjust our theory for the respective physical situations.

A first possible modification would be to use another model microswimmer, e.g., three-sphere swimmers or squirmers. Additional higher-order hydrodynamic singularities (e.g., force quadrupole, source dipole, rotlet dipole) could be included with corresponding model parameters extracted from experimental measurements on real microswimmers. If the hydrodynamic swimmer bodies remain spherical, solely the active mobility tensors that contribute to the corresponding $\boldsymbol{\mathcal{J}}^{\cdot\mathrm{a}}$ in Eq. (3.4) would have to be changed. In the same manner, near-field corrections to the mobility tensors could be incorporated.

Further changes in the hydrodynamic mobility tensors arise if nearby obstacles constrain the background fluid flow. For example, the Blake tensor replaces the Oseen tensor when a force is exerted in the vicinity of a planar no-slip boundary [183]. For microswimmers self-propelling near a wall or in a small-width channel, see also the corresponding studies of single three-sphere swimmers in Publications **P5** and **P6**, active and passive mobility tensors could be calculated and inserted into our formalism. Such a procedure could be combined with existing DDFT concepts for particles under confinement [184, 185]. Furthermore, the effects of elastic interfaces, as regarded in Publications **P8** and **P9**, could be included accordingly.

Another modification concerns different potentials for the steric interactions between the swimmers. Typically, such a change involves identifying an appropriate form of the excess free energy functional $\mathcal{F}_{\mathrm{exc}}$. For example, hard spheres are often treated using fundamental measure theory [186–191]. This method has also been generalized to anisotropic particle shapes [192–197]. The use of short-ranged hard steric interactions in our theoretical framework might affect the accuracy of our far-field treatment of hydrodynamic interactions, in particular if the swimmer bodies closely approach each other. However, this is avoided if the effective ranges of these interactions are significantly larger than the hydrodynamic radii of the swimmers. Another example could be strong but significantly screened repulsive electrostatic interactions (for instance, based on the typical Yukawa interaction potential [198–200]). Corresponding particle-based "dry" computer simulations for hard self-propelled particles have been performed, employing *event-driven* Brownian dynamics [179, 201, 202] or *kinetic Monte-Carlo* algorithms [203, 204].

The hydrodynamic mobility tensors in our framework could, in principle, be replaced to account for other, e.g., non-spherical, shapes of the swimmer body. While the corresponding low-Reynolds-number hydrodynamic theory is most straightforward for spherical particles [31, 33], extensions to non-spherical bodies exist. A particular example are (rod-like) prolate spheroids, for which analytic singularity solutions are at hand [33]. Moreover, at least the passive self mobility tensor [i.e., $\boldsymbol{\mu}_{ij}^{\cdot\cdot}$ for $i = j$ in Eq. (3.2)] can be determined for a large variety of rigid body shapes [205]. In particular, this can, for non-orthotropic bodies, lead to a coupling between translational and rotational components, e.g., a force exerted on that body could result in an angular velocity [32, 109]. Pair mobility tensors (both passive and active) for such arbitrarily-shaped particles, however, would probably need to be calculated numerically before evaluations of our DDFT equations and would there need to be inserted as a tabulated input.

In order to extend the statistical theory into another direction, it might be interesting to include Vicsek-type effective alignment interactions [46, 47, 86–88] between the microswimmers. Similarly, one could incorporate phoretic interactions between swimmers [206], which should be feasible when these are mapped to effective pairwise interactions [40].

An additional generalization could be to allow for varying motility fields [207, 208]. However, it is yet unclear how to extend the proof of existence for an exact excess free energy functional in DDFT [117] to such a system. Nevertheless, an effective DDFT for a corresponding coarse-grained model has already been proposed [209]. One could also allow for local variations of the viscosity of the background fluid, which indeed can induce interesting effects already for a single swimmer [210]. Furthermore, anisotropic background fluids might be taken into account [211, 212].

Another possible extension would concern feedback-controlled motility [213, 214]. Then the self-propulsion of the microswimmers is (externally) tuned according to prescribed rules. Conceptually, this problem is related to driven particles with (time-delayed) feedback, for which a DDFT has recently been formulated [215].

In biological microswimmer systems, death and reproduction play a role in the long-time dynamics and might be interesting to be incorporated into our framework. Such effects have already been treated via DDFT in the context of the growth of tumors [45]. Additionally, the transition of bacteria between, e.g, motile and non-motile states, might be included via coupled source and sink terms in the multi-species approach of Publication **P3**.

Our present numerical evaluations have been confined to relatively small systems, but can, in principle, be extended to truly periodic systems by corresponding periodic boundary conditions. Then, the hydrodynamic interactions between the periodic images of particles must be incorporated, see, for instance, the long-range nature of the Oseen tensor in Eq. (2.2). Here, a standard method is based on the Ewald summation technique [216], which separates short-range from long-range contributions and treats the latter in Fourier space. Corresponding results for passive mobility tensors are well-known [217–220] and could be considered for the different $\boldsymbol{\mu}_{::}$ in Eq. (3.2). In the case of the force-dipole-based microswimmer model of Ref. 102, corresponding Ewald summations have been carried out for the active parts as well [221]. Thus, it is to be expected that such calculations can also be performed for our model (and similar microswimmer models).

An addition extension could be to include externally imposed fluid flows [56, 222–228]. For example, it has been found that pusher microswimmers under shear at low densities can induce a strong decrease in the effective overall viscosity of the suspension [229, 230]. In our formalism, external flows call for two different adjustments beyond the limit of our shear cell in Publication **P3** (where the imposed flow is primarily inducing angular velocities of the confined microswimmers). First, increased fluctuations between particles in, e.g., shear flows, may induce changes in the one-swimmer density, as has been described by introducing a corresponding term in existing DDFT approaches [231–235]. Second, hydrodynamic interactions between particles/swimmers are changed when external flows are present [31, 33, 236, 237]. This could be accounted for by using adjusted mobility tensors in Eq. (3.2).

3.4.2 Further open problems

Our theory treated the influence of induced fluid flows on the basis of far-field pairwise hydrodynamic interactions, which is considered to be sufficient for (semi)dilute suspensions [238–242]. This approach is supported by the steric shielding that we have introduced to ensure large-enough distances between the individual swimmers. Nevertheless, hydrodynamic interactions are, in general, many-particle interactions and can feature significant near-field contributions [31–33], which is particularly important if swimmers come close to each other. In particle-based computer simulations, hydrodynamic near-field interactions can be included by explicitly taking into account fluid flows of the background medium at a corresponding computational cost, e.g., via multiparticle collision dynamics [91, 222, 243–246] / stochastic rotation dynamics [90, 247] or via Lattice-Boltzmann methods [85, 176, 248–250]. A future task might be to investigate how such many-particle effects can be treated in a statistical approach like ours, for active microswimmers or even only for passive colloidal particles. The main, yet unsolved problem would be to reduce the description in a way that leads to a closed equation for the dynamical evolution of the *one-body* density.

Another highly non-trivial task is the ongoing quest for a statistical description of motility-induced phase separation (MIPS) [54, 65–71], see also Sec. 1.4, from first principles, which would complement the existing theoretical approaches [66, 67, 72–74]. In addition to the description of similar MIPS-like effects in active–passive mixtures [74, 139, 251–253], the effect of hydrodynamic interactions on this kind of phase separation forms an interesting aspect [91].

One promising approach in this regard has been the extension of power functional theory (PFT) to describe systems of self-propelled particles [254–256]. The further inclusion of hydrodynamic interactions in PFT has not been realized yet and might require input similarly to our DDFT approaches for microswimmers discussed in Publications **P1**–**P4**.

In principle, it should also be possible to derive dynamical statistical descriptions for systems of many microflyers, i.e., underdamped active particles [35–37]. There, it would be particularly interesting to include hydrodynamic fluid flows as well. For this purpose, one could maybe build on existing DDFTs for passive particles with hydrodynamic interactions and inertia [147–149].

Real background media, e.g., complex fluids in the human body, can feature viscoelastic properties, which can heavily change the behavior of microswimmers [257–263]. The thus-introduced memory effects mediated by the background fluid might be incorporated using concepts of statistical approaches that were developed for systems with time-delayed feedback [215, 264].

Our DDFT principally is valid only for (semi)dilute suspensions of active microswimmers, i.e., for not-too-high swimmer densities [**P1**]. Alternatively, mode-coupling theories for systems of self-propelled particles describe the behavior in very dense suspensions [265, 266], with applications to, e.g., active glasses [267]. Detailed comparison between the two approaches may determine which one works better at intermediate densities, and if there is a need for a crossover theory. Here, the answer might depend on the specific microswimmer system that is investigated.

In a much broader picture, one might look for applications beyond condensed matter physics. Our dynamical statistical approach for non-equilibrium active agents was developed from Eq. (3.1), which expresses the local conservation of probability. Such general conservation laws might also hold to good approximation for a variety of processes studied by different disciplines, e.g., for the flux of goods in economic systems. Consequently, related problems might be studied by similar methods.

Chapter 4

Discrete-particle models

In this chapter, different discrete models for single (active) particles and microswimmers are introduced and evaluated to study their behavior when confined by explicit boundaries. Specifically, the motion of a three-sphere swimmer near rigid walls is described in Sec. 4.1 and the interaction between (active) particles and elastic interfaces is discussed in Sec. 4.2. It is to be remarked that the corresponding works [**P5**–**P9**] are independent of our statistical investigations of many-swimmer suspensions [**P1**–**P4**] discussed in Chapter 3.

4.1 Three-sphere swimmers

One standard model for a microswimmer is the *three-sphere swimmer* consisting of three connected spheres that perform prescribed periodic relative motions [92]. The general concept is briefly discussed in Sec. 4.1.1. For correctly chosen parameters, the induced fluid flows lead to a self-propelled net "forward" motion. As described in Sec. 4.1.2, we have described the behavior of a single such swimmer near a planar no-slip boundary [**P5**] and inside a channel consisting of two parallel no-slip walls [**P6**].

4.1.1 General concept

In the following, I briefly establish the principle of a *three-sphere swimmer* as introduced by Najafi and Golestanian [92, 268–271]. Specifically, three colloidal particles are placed along a line and linked via rigid connections, the lengths of which can be tuned dynamically in a controlled way. As in Sec. 2.1, a low Reynolds number [and thus Stokes fluid flow as described by Eqs. (2.1)] is assumed so that one moving sphere leads, via hydrodynamic interactions, to an instantaneous motion of the other spheres. For the moment, it is assumed that this swimmer is situated in a three-dimensional bulk viscous fluid.

As the next step, periodic relative motions between the outer spheres and the central sphere are prescribed. If a phase difference between these two motions is present, each periodic cycle can lead to a net translation of the central sphere along the direction of the symmetry axis (but, in this free-swimming case, a change of the orientation of the swimmer is not present) [92, **P5**]. Dividing this translated distance by the duration of one period, we obtain the effective swimming velocity v_{s}.

When evaluating the corresponding equations under the assumption that the net force and net torque acting on the three spheres vanish and averaging over one cycle of the prescribed motion, v_{s} can be calculated analytically for the current situation of a free swimmer suspended in a bulk fluid [92, **P5**]. The three-sphere model is versatile with diverse variants, e.g., circle swimmers [93]. Furthermore, experimental realizations have been outlined [269, 270]. Next, I discuss how three-sphere swimmers behave near one [**P5**] or two [**P6**] planar no-slip boundaries that constrict the fluid flow.

4.1.2 In the vicinity of planar walls

Addressing three-sphere swimmers near walls, we again need to start with the Stokes equations in Eqs. (2.1). The fundamental solution of a partial differential equation generally depends on the specific boundary conditions. In the presence of one infinitely-extended planar wall, the Oseen tensor is replaced by the Blake tensor, which is derived by introducing appropriate "mirror images" that ensure that the no-slip boundary condition at the surface of the wall is met [183]. From this, the hydrodynamic self and pair mobility tensors describing the translational and rotational response to forces applied to one sphere can be obtained [272, 273] so that, again, a full physical description of the dynamics of a low-Reynolds-number three-sphere swimmer is possible [274, **P5**]. In Publication **P5**, we have studied swimmers composed of three equally sized spheres. This symmetry lets the force-dipole term of the (averaged) induced hydrodynamic flow field vanish. Accordingly, a *neutral swimmer*, being neither a pusher nor a puller, is constituted.

Considering vanishing thermal noise, we have found via numerical simulations using the above hydrodynamic input that, depending on its initial orientation and height above the wall, the dynamics of a neutral three-sphere-swimmer falls into one of three categories [**P5**]. First, the swimmer can escape from the wall, particularly when its swimming direction initially points away from the wall. Second, it can move towards a trapped state, in which the orientation points straight towards the wall and the swimmer hovers at a fixed height above the wall. Third, the swimmer can perform a gliding motion parallel to the wall, with coupled oscillations of its height above the wall and its orientation.

Furthermore, we introduced an additional relative rotation between the spheres [**P5**], which we consider as a coarse-grained model for the rotating flagella and counter-rotating head of, e.g., motile *E. coli* bacteria [6]. For these bacteria, a previous experimental study reported a circling motion near a wall [275], with the hydrodynamic coupling to the wall providing a plausible explanation [276]. We indeed find that the modified three-sphere swimmers show this behavior, with the sense of the circling flipping when the sense of the imposed relative rotations is switched [**P5**], indicating the suitability of our approach. In retrospect, this behavior seems to be closely related to the effect of a rotlet dipole near a wall, which is commented on in Sec. 4.2.2 and Publication **P9**.

In Publication **P6**, we have built upon the above framework to describe the behavior of a three-sphere swimmer inside a prototypical microfluidic channel consisting of two parallel planar no-slip-boundary walls. In contrast to the one-wall case, the Green's function connected to Eqs. (2.1) for the channel geometry cannot be provided in real-space coordinates by a closed formula. However, approximations, either using Fourier transforms [277] or via a formally infinite sum using the method of images [278], are available and have both been employed here, leading to consistent results [**P6**].

In addition to the "neutral" swimmers composed of three equally sized spheres, also the behavior of pushers (pullers) featuring an enlarged sphere at the front (rear) of the three-sphere chain [279] was investigated. The corresponding state diagrams of trajectories showed trapped, sliding, and (oscillatory) gliding states [**P6**].

4.2 Interactions with elastic interfaces

Typically, microswimmers in reality exist and operate in complex and confined environments [1]. One such complication, which is very interesting with regard to possible medical applications, results from the interaction of swimmers with elastic interfaces and, especially, membranes.

In Sec. 4.2.1, I discuss the one-dimensional minimal membrane model that we have introduced in Publication **P7** to describe its reaction to an approaching active particle. Section 4.2.2 concerns, first, hydrodynamic interactions between an active microswimmer and an elastic spherical cavity it is surrounded by [**P8**]. Second, the changes to the velocity and angular velocity of a swimmer that propels near an infinitely-extended planar elastic interface are discussed on the basis of a multipole decomposition of the fluid flows generated by the swimmer [**P9**].

4.2.1 Response of an elastic membrane to an approaching active particle: trapping and penetration

Biological cells are typically shielded from their environment via an elastic cell membrane that can hold back potentially harmful influences [280–282]. However, medical applications involving microscopic drug delivery may rely on active agents intruding into a cell to transport their medical cargo [283–285], so that strategies to overcome the cell membrane have to be developed. In Publication **P7**, a simple model membrane is introduced. We study under which circumstances an active particle can penetrate it.

The model membrane consists of a one-dimensional chain of spherical particles in two-dimensional space. The two particles on each end of the chain are fixed at positions $(\pm L/2, 0)$, with chain length L. Each particle i is endowed with a dipole moment $\mathbf{m}_i$ (of magnitude $m = |\mathbf{m}_i|$ for all i), which is assumed to be fixed to the orientation of the particle [**P7**]. Thus, $\mathbf{m}$ can be rewritten as $\mathbf{m}_i = m\,(\cos\phi_i, \sin\phi_i)$, where the angle ϕ_i parameterizes the particle orientation and is measured relatively to the x-axis. In addition to the resulting dipolar interactions, further short-ranged repulsive steric interactions and nearest-neighbor elastic interactions in form of harmonic springs (with a non-vanishing rest length) act between the membrane particles and keep them at finite distances from each other [**P7**]. Here, possible effects of thermal noise, hydrodynamic interactions, and changes in the propulsion direction of the active particle are neglected and left to future works.

By construction, the ground state of the above model membrane is a straight chain with all dipole moments oriented parallel to the chain axis [**P7**]. This particular arrangement is taken as the initial configuration. Assuming overdamped motion, the (perpendicular) approach of an active particle towards the center of the chain and the resulting response of the model membrane are investigated via Brownian dynamics simulations and analytical calculations. Depending on, e.g., the free-swimming self-propulsion speed of the active particle and the magnitude m of the dipole moment, either the membrane is able to hold back the active particle or the active particle can overcome the membrane and penetrate it, see also the corresponding state diagrams for different elasticity of the springs between neighboring membrane particles in Fig. 2 of Publication **P7**.

For only small deformations of the membrane, a linearized theoretical description is possible for a discrete-particle and for a continuum version of the model [**P7**]. In the latter case, the dynamical evolution of the local transverse displacement $\rho(x,t)$ of the membrane and its local (dipole) orientation $\phi(x,t)$ is specified by

$$\frac{1}{A}\,\partial_t\rho = \partial_x^2\rho - \frac{1}{2}\,\partial_x\phi + P_0\,\delta(x), \tag{4.1a}$$

$$\frac{1}{B}\,\partial_t\phi = \partial_x\rho - \phi, \tag{4.1b}$$

with Dirichlet-type boundary conditions $\rho(x = \pm L/2, t) = 0$ at all times t, assuming the chain to be fixed at its two ends [**P7**]. Additionally, $A \propto m^2$ has the dimension of a diffusion constant, $B \propto A$ is an inverse time, P_0 relates to the free-swimming speed of the active particle, and the initial conditions for a chain located at its undisturbed rest position read $\rho(x, t = 0) = \phi(x, t = 0) \equiv 0$ for all $x \in [-L/2, L/2]$.

Under the assumption that the dipole orientation $\phi(x,t)$ relaxes faster than the transverse displacement $\rho(x,t)$, we set $\partial_t\phi = 0$ in Eq. (4.1b). This implies $\phi = \partial_x\rho$ so that Eq. (4.1a) reduces to

$$\frac{1}{A}\,\partial_t\rho = \frac{1}{2}\,\partial_x^2\rho + P_0\,\delta(x), \tag{4.2}$$

which has the formal structure of the *diffusion/heat equation*, with a single source term at $x = 0$. The solution of this partial differential equation (with the above boundary conditions) is known and can be expressed via Jacobi theta functions [286]. At long times t, the result reproduces a triangular shape of the chain, which is also found from the full numerical solution [**P7**].

Publication **P7** constitutes a proof of concept that the above-described approach to a model membrane via particles featuring mutual steric, elastic and dipolar interactions is feasible and mathematically sufficiently facile. As an extension, a subsequent paper has introduced a more realistic two-dimensional model membrane spanned in three-dimensional space, again focusing on the question, under which circumstances an active particle can pass (and, possibly, damage) the membrane [287]. Further open problems that could be studied in future works are listed in Sec. 4.3. Next, Sec. 4.2.2 discusses (active) particles hydrodynamically interacting with elastic interfaces.

4.2.2 Hydrodynamic interactions with elastic interfaces

An elastic interface can constitute a hindrance to fluid flows, with typically time-dependent effects. For sufficiently simple models of elasticity, corresponding properties, e.g., the flow field resulting from a force acting on a nearby passive particle, can be obtained numerically via boundary integral methods [288]. Additionally, analytical calculations are feasible for suitable geometries [288–295]. In the past, Daddi-Moussa-Ider *et al.* have performed such studies on particles near infinitely extended [288, 290, 293] and finite [295] planar interfaces, between two parallel infinite planar interfaces [289], and near, but outside of, a spherical interface [291,292]. Here, all stated geometries refer to the initial undisturbed shape of the corresponding interface, which typically changes in response to the fluid flows.

Furthermore, the problem of hydrodynamic fluid flows resulting from a force exerted on a particle *inside* an elastic spherical cavity had been solved for the *axisymmetric* case, in which the force is oriented parallel to the distance vector between the centers of the cavity and the particle [294]. In Publication **P8**, we have additionally determined the complementing solution for the *asymmetric* case of a perpendicular force.

Technically, the analytic calculation is performed using an appropriate set of orthonormal basis functions, namely spherical harmonics [**P8**]. The respective resistances of the elastic interface towards shear and bending are incorporated using standard models of membrane elasticity [296, 297]. Analytical results are derived that compare favorably with the full numerical results obtained via boundary integral methods [**P8**]. In addition to the full fluid flow field, we obtain the resulting velocity of the encapsulated particle, the deformation of the elastic spherical interface, and the movement of the cavity in response to the application of the force. In particular, the cavity starts rotating due to the asymmetric force [**P8**].

Publication **P8** concerns an external force driving a passive particle and thus only constitutes a first step towards the description of a (force-free) microswimmer in the same situation. In Publication **P9**, we have performed a corresponding study for microswimmers in a simpler geometry, namely near an infinitely extended, initially planar elastic interface. To address the possible effect of the presence of the microswimmer, we formally perform a force multipole expansion and analyze the consequences resulting from applying a force dipole (with a bulk flow field decaying $\propto r^{-2}$, where r is the distance from the microswimmer), a force quadrupole, a source dipole, and a rotlet dipole (all featuring bulk fluid flows decaying $\propto r^{-3}$) [**P9**]. Additionally, corresponding treatments have also been performed for force and torque monopoles [**P9**], which might arise in the presence of external potentials, e.g., when gravitation acts on algae of the species *Volvox carteri*, the density of which is typically not closely matched to the surrounding fluid [100]. Since the superposition of appropriate terms of this multipole expansion can approximate arbitrary flow fields to the lower orders in the hydrodynamic far field, our description should be versatile in its adaption to a multitude of different microswimmers [**P9**].

Again, the resulting time-dependent changes to the velocity and angular velocity of the swimmer in the presence of an elastic interface have been calculated. As is typical for hydrodynamic interactions with an infinitely extended, initially planar elastic interface [288], the contributions of the resistance towards shear and bending can be treated separately here [**P9**].

In particular, the rotlet-dipole contribution was found to lead to a spontaneous rotation and thus to a circling motion of the swimmer when it is near the elastic interface [**P9**], in analogy to what we have observed for our modified three-sphere swimmer in Publication **P5**. For hard walls and only-shear-resistant interfaces, we find the same sense of rotation, which, however, is flipped for only-bending-resistant interfaces [**P9**]. We thus conclude that the rotlet dipole can be used as a minimal description of interface-induced circling [**P9**], which is an effect that has been reported for, e.g., motile *E. coli* bacteria [275]. Previously, this had been explained using specific microswimmer models [276, 298, **P5**].

In Sec. 4.3, I list related questions that could be addressed in future works. This includes possible extensions of the approaches described in Secs. 4.1 and 4.2.1.

4.3 Outlook

It should be stressed that most results of Publications **P5**–**P9** can be tested in possible experiments, indicating one very important next step. Apart from that, this section provides a brief outlook on possible further studies concerning the three-sphere swimmer near rigid walls introduced in Sec. 4.1 and the (active) particles interacting with elastic interfaces that are discussed in Sec. 4.2.

Biological microswimmers in nature and artificial microswimmers in possible medical applications often are confined by or propelling close to interfaces, e.g., sperm cells in the female reproductive tract or drug-carrying Janus particles in blood vessels. Typically, these interfaces are not planar so that the approaches discussed in Publications **P5**–**P7** and **P9** should be extended to arbitrary (or at least to more complex) geometries. Similarly, the elastic spherical cavity in Publication **P8** could be replaced by a cavity of, e.g., ellipsoidal shape.

The one-dimensional model membrane discussed in Sec. 4.2.1 has already been extended to a planar two-dimensional case (spanned in three-dimensional space) in a recent study [287]. The next step could now be to further transition to cell-like closed model membranes, e.g., of a spherical shape as a starting point. Moreover, the introduction of hydrodynamic interactions into the description might provide further connections to realistic situations.

Concerning our studies of interactions between particles and elastic interfaces, we have employed simple models for the resistance towards shear and bending by the interface [**P8**, **P9**]. Here, experiments could clarify when this level of description is sufficient. In any case, one might think about using more adjusted models, especially when modeling materials with very specific elastic properties.

Publications **P5**–**P9** discuss, in general, the behavior of single particles. This could be extended to many-particle systems, in particular for the three-sphere swimmers in the vicinity of rigid walls. Apart from treating this situation via discrete-particle-based simulations, one could also employ, for (semi)dilute microswimmer suspensions (and maybe using other swimmer models), the DDFT approach discussed in Chapter 3.

Chapter 5

Scientific publications

In the following, Publications **P1–P9** that form the basis of this dissertation are reproduced. For each publication, I present a summary of my contributions and a notice on copyright and licensing.

P1 Dynamical density functional theory for microswimmers

Reproduced from

A. M. Menzel, A. Saha, C. Hoell, and H. Löwen,
Dynamical density functional theory for microswimmers,
J. Chem. Phys. **144**, 024115 (2016),
with the permission of *AIP Publishing.*

Digital Object Identifier (DOI): `https://doi.org/10.1063/1.4939630`

Statement of contribution

AMM, HL, and I developed the theory. AS performed the numerical evaluations. AMM, AS, and HL wrote the paper.
Specifically, I contributed to the verification of the hydrodynamic description of the here-introduced model microswimmer and of the derivation of the dynamical density functional theory. Moreover, I participated in editing the corresponding equations and finalizing the manuscript.

Copyright and license notice

THE JOURNAL OF CHEMICAL PHYSICS **144**, 024115 (2016)

Dynamical density functional theory for microswimmers

Andreas M. Menzel,[a] Arnab Saha,[b] Christian Hoell, and Hartmut Löwen[c]
Institut für Theoretische Physik II, Weiche Materie, Heinrich-Heine-Universität Düsseldorf, 40225 Düsseldorf, Germany

(Received 26 October 2015; accepted 24 December 2015; published online 13 January 2016)

Dynamical density functional theory (DDFT) has been successfully derived and applied to describe on one hand passive colloidal suspensions, including hydrodynamic interactions between individual particles. On the other hand, active "dry" crowds of self-propelled particles have been characterized using DDFT. Here, we go one essential step further and combine these two approaches. We establish a DDFT for active microswimmer suspensions. For this purpose, simple minimal model microswimmers are introduced. These microswimmers self-propel by setting the surrounding fluid into motion. They hydrodynamically interact with each other through their actively self-induced fluid flows and via the common "passive" hydrodynamic interactions. An effective soft steric repulsion is also taken into account. We derive the DDFT starting from common statistical approaches. Our DDFT is then tested and applied by characterizing a suspension of microswimmers, the motion of which is restricted to a plane within a three-dimensional bulk fluid. Moreover, the swimmers are confined by a radially symmetric trapping potential. In certain parameter ranges, we find rotational symmetry breaking in combination with the formation of a "hydrodynamic pumping state," which has previously been observed in the literature as a result of particle-based simulations. An additional instability of this pumping state is revealed. © *2016 AIP Publishing LLC.* [http://dx.doi.org/10.1063/1.4939630]

I. INTRODUCTION

Microswimmers[1–4] are abundant in nature in the form of self-propelling microorganisms; moreover, they can be generated artificially in the laboratory. Prominent examples are sperm cells, usually propelling along helical paths,[5] bacteria like E. coli moving forward by a rotational motion of their spiral-shaped flagella,[6] or synthetic Janus colloids catalyzing a chemical reaction on one of their hemispheres.[7]

In recent years, there have been intense research activities on the individual as well as on the collective properties of such active particles.[1–4,8–10] As a central difference between active systems and conventionally driven passive ones, the active systems are driven locally on the individual particle level, whereas in passive cases an external field acts on the system from outside. This feature, together with the interactions between active particles, can result in highly correlated collective motion and intriguing spatiotemporal patterns, see, e.g., the transition from disordered motion to a state of collective migration,[11–17] the emergence of propagating density waves,[18–24] or the onset of turbulent-like behavior[25,26] and vortex formation.[27] Further collective phenomena comprise dynamic clustering and motility-induced phase separation,[28–38] crystallization,[39–41] as well as lane formation.[42–46] Novel experimental techniques, such as automated digital tracking[47,48] or the realization of active granular and artificial colloidal systems[49–53] are taking a major role in this research area. Often in modeling approaches, self-propulsion is implemented for "dry" objects by effective active forces acting on the particles.[54] In the present work, we explicitly take into account self-induced fluid flows of individual microswimmers, which they employ for propulsion. These self-induced fluid flows represent a significant contribution to the particle interactions.

Describing the collective behavior of many interacting self-propelled particles calls for statistical approaches.[17,21,55–60] These comprise Boltzmann theories[15,16,22] and master equations.[61] As a major benefit, it is typically relatively systematic to coarse-grain the resulting statistical equations. In this way, hydrodynamic-like equations to characterize the systems on a macroscopic level are obtained with specified expressions for the macroscopic system parameters. Alternatively, macroscopic equations can directly be derived from symmetry principles,[12–14,62,63] yet leaving the expressions for the macroscopic parameters undetermined.

The statistical approach that we introduce in the following to describe suspensions of interacting active microswimmers is dynamical density functional theory (DDFT).[64–66] It has turned out as highly effective to characterize passive systems that are determined by overdamped relaxation-type dynamics. Examples are spinodal decomposition,[66] phase separation of binary colloidal fluid mixtures,[67] nucleation and crystal growth,[68] colloidal dynamics within polymeric solutions,[69] mixtures exposed to a temperature gradient,[70] dewetting phenomena,[71] liquid-crystalline systems,[72] and rheology under confinement.[73,74]

In the past, on one hand, DDFT has been successfully extended for passive colloidal suspensions to include hydrodynamic interactions.[75–77] On the other hand, DDFT has been amended to model active self-propelled particle systems,

[a]Electronic address: menzel@thphy.uni-duesseldorf.de
[b]Electronic address: arnab@thphy.uni-duesseldorf.de
[c]Electronic address: hlowen@thphy.uni-duesseldorf.de

yet by directly assigning an effective drive to the individual constituents.[40,41,78,79] What is missing at the moment is a DDFT that brings together these two approaches and addresses suspensions of active microswimmers. This means, a DDFT that contains active propulsion via self-induced fluid flows, including the resulting hydrodynamic interactions between the swimmers. We close this gap in the present work.

For this purpose, as a first step, a simple minimum model microswimmer must be introduced that propels via self-induced fluid flows. This step is performed in Sec. II. Moreover, the resulting hydrodynamic and additional soft steric interactions between these swimmers are clarified, together with a confining trapping potential. In Sec. III, we derive our statistical theory in the form of a DDFT. Our starting point is the microscopic Smoluchowski equation for the interacting individual model microswimmers. Next, in Sec. IV, details of a two-dimensional numerical implementation are listed together with the numerical results presented for a system under spherically symmetric confinement. In agreement with previous particle-based simulations[80,81] we observe a rotational symmetry breaking in certain parameter ranges, which can be identified as a "hydrodynamic fluid pump." An additional novel instability of this state is identified. Finally, we conclude in Sec. V.

II. MODEL

To derive our theory, we consider a dilute suspension of N identical self-propelled microswimmers at low Reynolds number.[82] In particular, hydrodynamic interactions between these swimmers are to be included. The self-propulsion of a microswimmer is concatenated to self-induced fluid flows in the surrounding medium. This represents a major source of hydrodynamic interaction between different swimmers. To capture the effect, it is necessary to specify the geometry of the individual microswimmers, which sets the self-induced fluid flows. We proceed by first introducing a maximally reduced model microswimmer and then formulating the resulting interactions between pairs of such swimmers.

A. Individual microswimmer

To keep the derivation and presentation of the theory in the Secs. II and III as simple as possible, we introduce a minimum model microswimmer as depicted in Fig. 1. Similar setups were mentioned in Refs. 56 and 83–85. Each microswimmer consists of a spherical body of hydrodynamic radius a. The swimmer body is subjected to hydrodynamic drag with respect to surrounding fluid flows. In this way, the swimmer can be convected by external flow fields. One way of self-convection is to generate a self-induced fluid flow. For this purpose, each microswimmer features two active force centers. They are located at a distance L from each other on a symmetry axis that has orientation $\hat{\mathbf{n}}$ and runs through the center of the swimmer body. The two force centers exert two antiparallel forces $+\mathbf{f}$ and $-\mathbf{f}$, respectively, onto the surrounding fluid and set it into motion. Summing up the two forces, we find

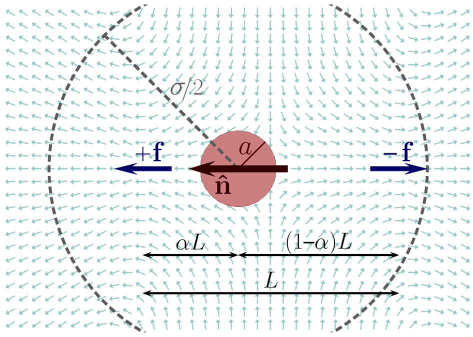

FIG. 1. Individual model microswimmer. The spherical swimmer body of hydrodynamic radius a is subjected to hydrodynamic drag. Two active point-like force centers exert active forces $+\mathbf{f}$ and $-\mathbf{f}$ onto the surrounding fluid. This results in a self-induced fluid flow indicated by small light arrows. L is the distance between the two force centers. The whole setup is axially symmetric with respect to the axis $\hat{\mathbf{n}}$. If the swimmer body is shifted along $\hat{\mathbf{n}}$ out of the geometric center, leading to distances αL and $(1-\alpha)L$ to the two force centers, it feels a net self-induced hydrodynamic drag. The microswimmer then self-propels. In the depicted state (pusher), fluid is pushed outward. Upon inversion of the two forces, fluid is pulled inward (puller). We consider soft isotropic steric interactions between the swimmer bodies of typical interaction range σ, implying an effective steric swimmer radius of $\sigma/2$.

that the microswimmer exerts a vanishing net force onto the fluid. Moreover, since $\mathbf{f}\|\hat{\mathbf{n}}$, there is no net active torque.[86] The force centers are point-like and do not experience any hydrodynamic drag.

Self-propulsion is now achieved by shifting the swimmer body along $\hat{\mathbf{n}}$ out of the geometric center. We introduce a parameter α to quantify this shift, see Fig. 1. The distances between the body center and the force centers are now αL and $(1-\alpha)L$, respectively. We confine α to the interval $[0, 0.5]$. For $\alpha = 0.5$, the body is symmetrically located between the two force centers, and no net self-induced motion occurs. This geometry is called shaker.[56,84] For $\alpha \neq 0.5$, the symmetry is broken. The swimmer body feels a net self-induced fluid flow due to the proximity to one of the two force centers. Due to the resulting self-induced hydrodynamic drag on the swimmer body, the swimmer self-propels. In the depicted state of outward oriented forces, the swimmer pushes the fluid outward and is called a pusher.[56] Inverting the forces, the swimmer pulls fluid inward and is termed a puller.[56]

B. Hydrodynamic interactions

We now consider an assembly of N interacting identical self-propelled model microswimmers, suspended in a viscous, incompressible fluid at low Reynolds number.[82] The flow profile within the system then follows Stokes' equation:[87]

$$-\eta\nabla^2\mathbf{v}(\mathbf{r},t) + \nabla p(\mathbf{r},t) = \sum_{i=1}^{N}\mathbf{f}_i(\mathbf{r}_i,\hat{\mathbf{n}}_i,t). \qquad (1)$$

Here, t denotes time and $\mathbf{r}$ any spatial position in the suspension, while, on the left-hand side, $\mathbf{v}(\mathbf{r},t)$ gives the corresponding fluid flow velocity field. η is the viscosity of the fluid and $p(\mathbf{r},t)$ is the pressure field. On the right-hand side, $\mathbf{f}_i$ denotes the total force density field exerted by the ith microswimmer onto the fluid. $\mathbf{r}_i$ and $\hat{\mathbf{n}}_i$ mark the current position and orientation of the ith swimmer at time t, respectively.

Obviously, on one hand, each microswimmer contributes to the overall fluid flow in the system by the force density it exerts on the fluid. On the other hand, we have noted above that each swimmer is dragged along by the induced fluid flow. In this way, each swimmer can transport itself via active self-propulsion. Moreover, all swimmers hydrodynamically tear on each other via their induced flow fields. That is, they hydrodynamically interact, which influences their positions $\mathbf{r}_i$ and orientations $\hat{\mathbf{n}}_i$.

Progress can be made due to the linearity of Eq. (1) and assuming incompressibility of the fluid, i.e., $\nabla \cdot \mathbf{v}(\mathbf{r},t) = 0$. We denote by $\mathbf{F}_j$ and $\mathbf{T}_j$ the forces and torques, respectively, acting directly on the swimmer bodies ($j = 1, \ldots, N$), except for frictional forces and frictional torques resulting from the surrounding fluid. The non-hydrodynamic body forces and torques may, for example, result from external potentials or steric interactions and will be specified below. From them, in the passive case, i.e., for $\mathbf{f} = \mathbf{0}$, the instantly resulting velocity $\mathbf{v}_i$ and angular velocity $\boldsymbol{\omega}_i$ of the ith swimmer body follows as

$$\begin{bmatrix} \mathbf{v}_i \\ \boldsymbol{\omega}_i \end{bmatrix} = \sum_{j=1}^{N} \mathbf{M}_{ij} \cdot \begin{bmatrix} \mathbf{F}_j \\ \mathbf{T}_j \end{bmatrix} = \sum_{j=1}^{N} \begin{bmatrix} \boldsymbol{\mu}_{ij}^{tt} & \boldsymbol{\mu}_{ij}^{tr} \\ \boldsymbol{\mu}_{ij}^{rt} & \boldsymbol{\mu}_{ij}^{rr} \end{bmatrix} \cdot \begin{bmatrix} \mathbf{F}_j \\ \mathbf{T}_j \end{bmatrix}. \tag{2}$$

Here, $\mathbf{M}_{ij}$ are the mobility matrices, the components of which ($\boldsymbol{\mu}_{ij}^{tt}$, $\boldsymbol{\mu}_{ij}^{tr}$, $\boldsymbol{\mu}_{ij}^{rt}$, $\boldsymbol{\mu}_{ij}^{rr}$) likewise form matrices. They describe hydrodynamic translation–translation, translation–rotation, rotation–translation, and rotation–rotation coupling, respectively.

This formalism is the same as for suspensions of passive colloidal particles.[88,89] We consider stick boundary conditions for the fluid flow on the surfaces of the swimmer bodies. The microswimmers are assumed to be suspended in an infinite bulk fluid, where the fluid flow vanishes at infinitely remote distances. Then, there are several methods to determine the mobility matrices, e.g., the so-called method of reflections[88,90] or the method of induced force multipoles.[91] In general, for N interacting suspended particles, there is no exact analytical solution to the problem. Yet, the mobility matrices can be calculated in the form of a power series in a/r_{ij}. Here, r_{ij} is the distance between the centers of the ith and jth swimmer body, i.e., $r_{ij} = |\mathbf{r}_{ij}|$ with $\mathbf{r}_{ij} = \mathbf{r}_j - \mathbf{r}_i$. The denser the suspension, the higher the orders in a/r_{ij} that need to be taken into account for a reliable characterization. In the following, we confine ourselves to relatively dilute and semi-dilute systems, taking into account pairwise hydrodynamic interactions up to and including order $(a/r_{ij})^3$. In contrast to this, see, for example, Refs. 92–94 for simulation approaches to dense suspensions of microswimmers.

To the order of $(a/r_{ij})^3$, hydrodynamic coupling is calculated in the following standard way. Since our system is overdamped, the forces $\mathbf{F}_j$ and torques $\mathbf{T}_j$ acting on the swimmer bodies are directly transmitted to the surrounding fluid. The fluid flow induced by each spherical swimmer body of hydrodynamic radius a is calculated on the Rodne-Prager level.[88] At the position of the ith swimmer, the flow field induced by swimmer $j \neq i$ reads[88]

$$\mathbf{v}(\mathbf{r}_i) = \frac{1}{6\pi\eta a}\left(\frac{3a}{4r_{ij}}\left(\mathbf{1} + \hat{\mathbf{r}}_{ij}\hat{\mathbf{r}}_{ij}\right) + \frac{a^3}{4r_{ij}^3}\left(\mathbf{1} - 3\hat{\mathbf{r}}_{ij}\hat{\mathbf{r}}_{ij}\right)\right) \cdot \mathbf{F}_j + \frac{1}{8\pi\eta r_{ij}^3}\mathbf{r}_{ij} \times \mathbf{T}_j, \tag{3}$$

where $\mathbf{1}$ is the unity matrix and $\hat{\mathbf{r}}_{ij} = \mathbf{r}_{ij}/r_{ij}$. The velocity $\mathbf{v}_i$ and angular velocity $\boldsymbol{\omega}_i$ resulting due to this flow field for the ith swimmer of hydrodynamic radius a follows from Faxén's laws[88,95]

$$\mathbf{v}_i = \left(1 + \frac{a^2}{6}\nabla_i^2\right)\mathbf{v}(\mathbf{r}_i), \tag{4}$$

$$\boldsymbol{\omega}_i = \frac{1}{2}\nabla_i \times \mathbf{v}(\mathbf{r}_i). \tag{5}$$

Due to the linearity of Stokes' equation, Eq. (1), the overall velocities and angular velocities are obtained by superimposing the influence of all other swimmer bodies $j \neq i$. In addition to that, the direct effect of $\mathbf{F}_i$ and $\mathbf{T}_i$ on the motion of the ith swimmer is given by Stokes' drag formulae[88]

$$\mathbf{v}_i = \frac{1}{6\pi\eta a}\mathbf{F}_i, \tag{6}$$

$$\boldsymbol{\omega}_i = \frac{1}{8\pi\eta a^3}\mathbf{T}_i. \tag{7}$$

Combining all these ingredients, the motion resulting for $\mathbf{f} = \mathbf{0}$ can be conveniently summarized in the form of Eq. (2) by setting[88,89]

$$\boldsymbol{\mu}_{ii}^{tt} = \mu^t\mathbf{1}, \quad \boldsymbol{\mu}_{ii}^{rr} = \mu^r\mathbf{1}, \quad \boldsymbol{\mu}_{ii}^{tr} = \boldsymbol{\mu}_{ii}^{rt} = \mathbf{0}, \tag{8}$$

for entries $i = j$ (no summation over i in these expressions) and

$$\boldsymbol{\mu}_{ij}^{tt} = \mu^t\left(\frac{3a}{4r_{ij}}\left(\mathbf{1} + \hat{\mathbf{r}}_{ij}\hat{\mathbf{r}}_{ij}\right) + \frac{1}{2}\left(\frac{a}{r_{ij}}\right)^3\left(\mathbf{1} - 3\hat{\mathbf{r}}_{ij}\hat{\mathbf{r}}_{ij}\right)\right), \tag{9}$$

$$\boldsymbol{\mu}_{ij}^{rr} = -\mu^r\frac{1}{2}\left(\frac{a}{r_{ij}}\right)^3\left(\mathbf{1} - 3\hat{\mathbf{r}}_{ij}\hat{\mathbf{r}}_{ij}\right), \tag{10}$$

$$\boldsymbol{\mu}_{ij}^{tr} = \boldsymbol{\mu}_{ij}^{rt} = \mu^r\left(\frac{a}{r_{ij}}\right)^3\mathbf{r}_{ij}\times, \tag{11}$$

for entries $i \neq j$. Here, we have introduced the abbreviations

$$\mu^t = \frac{1}{6\pi\eta a}, \qquad \mu^r = \frac{1}{8\pi\eta a^3}. \tag{12}$$

In this notation, the matrices $\boldsymbol{\mu}_{ij}^{tr} = \boldsymbol{\mu}_{ij}^{rt}$ in Eq. (11) represent operators with "×" the vector product.[89]

So far, only the influence of the passive swimmer bodies has been included. We now take into account the active forces. Again, because of the linearity of Eq. (1), their effect can simply be added to the swimmer velocities and angular velocities on the right-hand side of Eq. (2).

The concept to include the influence of the active forces is the same as summarized above for the passive hydrodynamic interactions. There is only one difference. We consider the active force centers as point-like, and not of finite hydrodynamic radius. Moreover, they do not transmit torques to the fluid. Thus, instead of Eq. (3), their induced flow fields are readily described on the Oseen level.[88] The flow fields induced by the two force centers of the jth microswimmer at the position of the ith swimmer body read

$$\mathbf{v}^{+}(\mathbf{r}_i) = \frac{1}{8\pi\eta r_{ij}^{+}} \left(\mathbf{1} + \hat{\mathbf{r}}_{ij}^{+}\hat{\mathbf{r}}_{ij}^{+}\right) \cdot f\hat{\mathbf{n}}_j, \tag{13}$$

$$\mathbf{v}^{-}(\mathbf{r}_i) = -\frac{1}{8\pi\eta r_{ij}^{-}} \left(\mathbf{1} + \hat{\mathbf{r}}_{ij}^{-}\hat{\mathbf{r}}_{ij}^{-}\right) \cdot f\hat{\mathbf{n}}_j. \tag{14}$$

These expressions are valid also for $i = j$, which leads to self-propulsion of a single isolated swimmer. We have defined

$$\mathbf{r}_{ij}^{+} = \mathbf{r}_{ij} + \alpha L\hat{\mathbf{n}}_j, \tag{15}$$

$$\mathbf{r}_{ij}^{-} = \mathbf{r}_{ij} - (1-\alpha)L\hat{\mathbf{n}}_j \tag{16}$$

to refer to the distance vectors between the active force centers of the jth swimmer and the center of the ith swimmer body. Moreover, we have parameterized

$$\mathbf{f}_j = f\hat{\mathbf{n}}_j \tag{17}$$

so that the sign of f now determines the character of the swimmer (pusher or puller).

In analogy to the passive case, the velocities and angular velocities of the swimmer bodies of finite hydrodynamic radius a that result from the active flow fields Eqs. (13) and (14) are calculated from Faxén's laws, Eqs. (4) and (5). The result can be written using mobility matrices

$$\boldsymbol{\mu}_{ij}^{tt\pm} = \frac{1}{8\pi\eta r_{ij}^{\pm}} \left(\mathbf{1} + \hat{\mathbf{r}}_{ij}^{\pm}\hat{\mathbf{r}}_{ij}^{\pm}\right) + \frac{a^2}{24\pi\eta r_{ij}^{\pm\,3}} \left(\mathbf{1} - 3\hat{\mathbf{r}}_{ij}^{\pm}\hat{\mathbf{r}}_{ij}^{\pm}\right), \tag{18}$$

$$\boldsymbol{\mu}_{ij}^{rt\pm} = \frac{1}{8\pi\eta r_{ij}^{\pm\,3}} \mathbf{r}_{ij}^{\pm} \times . \tag{19}$$

Within this framework, the corresponding active forces on the right-hand side of Eq. (2) have to be inserted as $\pm f\hat{\mathbf{n}}_j$. Since there are no active torques, we may set $\boldsymbol{\mu}_{ij}^{tr\pm} = \boldsymbol{\mu}_{ij}^{rr\pm} = \mathbf{0}$. Altogether, passive and active hydrodynamic interactions, including the self-propulsion mechanism, are now formulated up to third order in a/r_{ij}.

C. Body forces and torques

We now specify the non-hydrodynamic forces $\mathbf{F}_j$ and torques $\mathbf{T}_j$ acting directly on the swimmer bodies. In our case, these forces can be written as

$$\mathbf{F}_j = -\nabla_j U - \nabla_j \ln P. \tag{20}$$

Here, ∇_j denotes the partial derivative $\partial/\partial\mathbf{r}_j$. Throughout this work, we measure energies in units of $k_B T$ with k_B the Boltzmann constant and T the temperature of the fluid. Variations in temperature due to the non-equilibrium nature of our system are ignored. In Eq. (20), the first contribution results from a potential

$$U\left(\mathbf{r}^N\right) = \frac{1}{2}\sum_{\substack{k,l=1\\k\neq l}}^{N} u(\mathbf{r}_k,\mathbf{r}_l) + \sum_{l=1}^{N} u_{ext}(\mathbf{r}_l), \tag{21}$$

where we use the abbreviation $\mathbf{r}^N = \{\mathbf{r}_1,\mathbf{r}_2,\ldots,\mathbf{r}_N\}$. Accordingly, we will abbreviate $\hat{\mathbf{n}}^N = \{\hat{\mathbf{n}}_1,\hat{\mathbf{n}}_2,\ldots,\hat{\mathbf{n}}_N\}$ below. For simplicity and as a first step, we confine ourselves to soft pairwise steric interactions of the form

$$u(\mathbf{r}_k,\mathbf{r}_l) = \epsilon_0 \exp\left(-\frac{r_{kl}^4}{\sigma^4}\right). \tag{22}$$

ϵ_0 sets the strength of this potential and σ an effective interaction range, see Fig. 1. Such soft interaction potentials are frequently employed to describe effective interactions in soft matter systems, e.g., between polymers, star-polymers, dendrimers, and other macromolecules in solution.[96] One task for the future is to clarify more precisely the nature of the effective steric interactions between individual microswimmers, for instance, for self-propelling microorganisms featuring agitated cilia and flagella.[97] We prefer the so-called GEM-4 potential in Eq. (22) to a simple Gaussian interaction, because it can describe both liquid and solid phases within mean-field approximation, in contrast to the Gaussian potential.[98] The phase behavior depends on the parameter ϵ_0 as well as on the average density of the suspended particles. Here, we fix the parameters such that our system remains in the liquid phase. Moreover, the density is adjusted to avoid overlap of the swimmers. Properties of crystallized systems may be investigated in a later study.

In addition to that, we consider the microswimmers to be confined to a rotationally symmetric external trapping potential. It constitutes the second contribution on the right-hand side of Eq. (21) and reads

$$u_{ext}(\mathbf{r}_l) = k|\mathbf{r}_l|^4. \tag{23}$$

k sets the strength of the trap. We choose the quartic potential instead of a more common harmonic trap due to its lower gradient at smaller radii. Overlap of individual swimmers is reduced in this way.

The quantity $P \equiv P(\mathbf{r}^N,\hat{\mathbf{n}}^N,t)$ in Eq. (20) denotes the probability distribution to find the N microswimmers at time t at positions $\mathbf{r}^N$ with orientations $\hat{\mathbf{n}}^N$. Via the contribution involving $\ln P$, we consistently include entropic forces into our statistical characterization.[99] This term represents the effect of thermal forces acting on each swimmer as a result of thermal fluctuations.

Due to the spherical shape of the swimmer bodies, and for simplicity, we assume in the present work that non-hydrodynamic torques acting on the swimmer bodies solely result from thermal fluctuations. They can be included into our statistical formalism by setting[99]

$$\mathbf{T}_j = -\hat{\mathbf{n}}_j \times \nabla_{\hat{\mathbf{n}}_j} \ln P. \tag{24}$$

Further contributions to the torques, e.g., resulting from steric alignment interactions between different swimmers, may be considered in future studies.

III. DERIVATION OF THE DDFT FOR MICROSWIMMERS

Our starting point to derive the DDFT for active microswimmers including hydrodynamic interactions is the microscopic Smoluchowski equation[99] for N identical interacting swimmers. This continuity equation for the time evolution of the probability distribution $P(\mathbf{r}^N, \hat{\mathbf{n}}^N, t)$ reads

$$\frac{\partial P}{\partial t} = -\sum_{i=1}^{N} \Big(\nabla_i \cdot (\mathbf{v}_i P) + (\hat{\mathbf{n}}_i \times \nabla_{\hat{\mathbf{n}}_i}) \cdot (\omega_i P) \Big). \tag{25}$$

On the basis of Sec. II, we insert

$$\mathbf{v}_i = \sum_{j=1}^{N} \Big(\boldsymbol{\mu}^{tt}_{ij} \cdot \mathbf{F}_j + \boldsymbol{\mu}^{tr}_{ij} \mathbf{T}_j + \boldsymbol{\Lambda}^{tt}_{ij} \cdot \hat{\mathbf{n}}_j f \Big), \tag{26}$$

$$\omega_i = \sum_{j=1}^{N} \Big(\boldsymbol{\mu}^{rt}_{ij} \mathbf{F}_j + \boldsymbol{\mu}^{rr}_{ij} \cdot \mathbf{T}_j + \boldsymbol{\Lambda}^{rt}_{ij} \hat{\mathbf{n}}_j f \Big), \tag{27}$$

where we have introduced the abbreviations

$$\boldsymbol{\Lambda}^{tt}_{ij} = \boldsymbol{\mu}^{tt+}_{ij} - \boldsymbol{\mu}^{tt-}_{ij}, \tag{28}$$

$$\boldsymbol{\Lambda}^{rt}_{ij} = \boldsymbol{\mu}^{rt+}_{ij} - \boldsymbol{\mu}^{rt-}_{ij}. \tag{29}$$

Thus, the hydrodynamic interactions enter via the configuration-dependent expressions for $\mathbf{v}_i$ and ω_i. For a single, isolated microswimmer, i.e., for $N = 1$, the self-propulsion velocity becomes $\mathbf{v}_1 = \boldsymbol{\Lambda}^{tt}_{11} \cdot \hat{\mathbf{n}}_1 f$, which is directed along the swimmer axis and vanishes in the case of a shaker, where $\alpha = 0.5$.

Our scope is to derive from Eq. (25) a dynamic equation for the swimmer density $\rho^{(1)}(\mathbf{r}, \hat{\mathbf{n}}, t)$. In general, the n-swimmer density $\rho^{(n)}(\mathbf{r}^n, \hat{\mathbf{n}}^n, t)$ for $n \le N$ is obtained from the probability distribution $P(\mathbf{r}^N, \hat{\mathbf{n}}^N, t)$ by integrating out the degrees of freedom of $N - n$ swimmers,

$$\rho^{(n)}(\mathbf{r}^n, \hat{\mathbf{n}}^n, t) = \frac{N!}{(N-n)!} \int d\mathbf{r}_{n+1} \int d\hat{\mathbf{n}}_{n+1} \dots \int d\mathbf{r}_N \int d\hat{\mathbf{n}}_N \; P(\mathbf{r}^N, \hat{\mathbf{n}}^N, t). \tag{30}$$

Accordingly, we obtain a dynamic equation for $\rho^{(1)}(\mathbf{r}, \hat{\mathbf{n}}, t)$ by integrating out from Eq. (25) the degrees of freedom of $N - 1$ swimmers. This leads us to

$$\frac{\partial \rho^{(1)}(\mathbf{r}, \hat{\mathbf{n}}, t)}{\partial t} = -\nabla_{\mathbf{r}} \cdot (\mathcal{J}_1 + \mathcal{J}_2 + \mathcal{J}_3) - (\hat{\mathbf{n}} \times \nabla_{\hat{\mathbf{n}}}) \cdot (\mathcal{J}_4 + \mathcal{J}_5 + \mathcal{J}_6), \tag{31}$$

with the abbreviations

$$\begin{aligned} \mathcal{J}_1 = {} & -\mu^t \Big(\nabla_{\mathbf{r}} \rho^{(1)}(\mathbf{r}, \hat{\mathbf{n}}, t) + \rho^{(1)}(\mathbf{r}, \hat{\mathbf{n}}, t) \nabla_{\mathbf{r}} u_{ext}(\mathbf{r}) + \int d\mathbf{r}' d\hat{\mathbf{n}}' \rho^{(2)}(\mathbf{r}, \mathbf{r}', \hat{\mathbf{n}}, \hat{\mathbf{n}}', t) \nabla_{\mathbf{r}} u(\mathbf{r}, \mathbf{r}') \Big) \\ & - \int d\mathbf{r}' d\hat{\mathbf{n}}' \, \boldsymbol{\mu}^{tt}_{\mathbf{r},\mathbf{r}'} \cdot \Big(\nabla_{\mathbf{r}'} \rho^{(2)}(\mathbf{r}, \mathbf{r}', \hat{\mathbf{n}}, \hat{\mathbf{n}}', t) + \rho^{(2)}(\mathbf{r}, \mathbf{r}', \hat{\mathbf{n}}, \hat{\mathbf{n}}', t) \nabla_{\mathbf{r}'} u_{ext}(\mathbf{r}') \\ & + \rho^{(2)}(\mathbf{r}, \mathbf{r}', \hat{\mathbf{n}}, \hat{\mathbf{n}}', t) \nabla_{\mathbf{r}'} u(\mathbf{r}, \mathbf{r}') + \int d\mathbf{r}'' d\hat{\mathbf{n}}'' \rho^{(3)}(\mathbf{r}, \mathbf{r}', \mathbf{r}'', \hat{\mathbf{n}}, \hat{\mathbf{n}}', \hat{\mathbf{n}}'', t) \nabla_{\mathbf{r}'} u(\mathbf{r}', \mathbf{r}'') \Big), \end{aligned} \tag{32}$$

$$\mathcal{J}_2 = -\int d\mathbf{r}' d\hat{\mathbf{n}}' \, \boldsymbol{\mu}^{tr}_{\mathbf{r},\mathbf{r}'} (\hat{\mathbf{n}}' \times \nabla_{\hat{\mathbf{n}}'}) \rho^{(2)}(\mathbf{r}, \mathbf{r}', \hat{\mathbf{n}}, \hat{\mathbf{n}}', t), \tag{33}$$

$$\mathcal{J}_3 = f \Big(\boldsymbol{\Lambda}^{tt}_{\mathbf{r},\mathbf{r}} \cdot \hat{\mathbf{n}} \rho^{(1)}(\mathbf{r}, \hat{\mathbf{n}}, t) + \int d\mathbf{r}' d\hat{\mathbf{n}}' \, \boldsymbol{\Lambda}^{tt}_{\mathbf{r},\mathbf{r}'} \cdot \hat{\mathbf{n}}' \rho^{(2)}(\mathbf{r}, \mathbf{r}', \hat{\mathbf{n}}, \hat{\mathbf{n}}', t) \Big), \tag{34}$$

$$\begin{aligned} \mathcal{J}_4 = {} & -\int d\mathbf{r}' d\hat{\mathbf{n}}' \boldsymbol{\mu}^{rt}_{\mathbf{r},\mathbf{r}'} \Big(\nabla_{\mathbf{r}'} \rho^{(2)}(\mathbf{r}, \mathbf{r}', \hat{\mathbf{n}}, \hat{\mathbf{n}}', t) + \rho^{(2)}(\mathbf{r}, \mathbf{r}', \hat{\mathbf{n}}, \hat{\mathbf{n}}', t) \nabla_{\mathbf{r}'} u_{ext}(\mathbf{r}') \\ & + \rho^{(2)}(\mathbf{r}, \mathbf{r}', \hat{\mathbf{n}}, \hat{\mathbf{n}}', t) \nabla_{\mathbf{r}'} u(\mathbf{r}, \mathbf{r}') + \int d\mathbf{r}'' d\hat{\mathbf{n}}'' \rho^{(3)}(\mathbf{r}, \mathbf{r}', \mathbf{r}'', \hat{\mathbf{n}}, \hat{\mathbf{n}}', \hat{\mathbf{n}}'', t) \nabla_{\mathbf{r}'} u(\mathbf{r}', \mathbf{r}'') \Big), \end{aligned} \tag{35}$$

$$\mathcal{J}_5 = -\mu^r \hat{\mathbf{n}} \times \nabla_{\hat{\mathbf{n}}} \rho^{(1)}(\mathbf{r}, \hat{\mathbf{n}}, t) - \int d\mathbf{r}' d\hat{\mathbf{n}}' \, \boldsymbol{\mu}^{rr}_{\mathbf{r},\mathbf{r}'} \cdot (\hat{\mathbf{n}}' \times \nabla_{\mathbf{n}'}) \rho^{(2)}(\mathbf{r}, \mathbf{r}', \hat{\mathbf{n}}, \hat{\mathbf{n}}', t), \tag{36}$$

$$\mathcal{J}_6 = f \int d\mathbf{r}' d\hat{\mathbf{n}}' \, \boldsymbol{\Lambda}^{rt}_{\mathbf{r},\mathbf{r}'} \hat{\mathbf{n}}' \rho^{(2)}(\mathbf{r}, \mathbf{r}', \hat{\mathbf{n}}, \hat{\mathbf{n}}', t). \tag{37}$$

Eq. (31) represents the dynamic equation for our searched-for quantity $\rho^{(1)}$. However, as a consequence of the inter-swimmer interactions within our system, the equation contains the unknown two- and three-swimmer densities $\rho^{(2)}$ and $\rho^{(3)}$. Dynamic equations for these higher-n swimmer densities can likewise be derived from Eq. (25) by integrating out the degrees of freedom of $N - n$ swimmers. Yet, this only shifts the problem to higher n. It is found that the dynamic equation for $\rho^{(n)}$ contains $\rho^{(n+1)}$ and $\rho^{(n+2)}$ for $1 \le n \le N - 2$. Therefore, a reliable closure scheme is needed to cut this hierarchy of coupled dynamic partial differential equations, typically referred to as the

Bogoliubov-Born-Green-Kirkwood-Yvon (BBGKY) hierarchy.[100] DDFT provides such closure relations. In the following, we employ this approach to break the hierarchy already at $n = 1$. Thus, we derive a decoupled dynamic equation for $\rho^{(1)}(\mathbf{r},\hat{\mathbf{n}},t)$.

DDFT uses as an input the concepts from equilibrium density functional theory (DFT).[64–66,100–104] Most importantly, DFT implies that a certain observed equilibrium density $\rho^{(1)}_{eq}(\mathbf{r},\hat{\mathbf{n}})$ can only result from one unique external potential $\Phi_{ext}(\mathbf{r},\hat{\mathbf{n}})$ acting on the system. As a consequence, $\Phi_{ext}(\mathbf{r},\hat{\mathbf{n}})$ is set by an observed $\rho^{(1)}_{eq}(\mathbf{r},\hat{\mathbf{n}})$ and, moreover, the grand canonical potential Ω and the free energy $\mathcal{F}$ can be expressed as functionals of $\rho^{(1)}(\mathbf{r},\hat{\mathbf{n}})$. In our case, we may write

$$\Omega\left[\rho^{(1)}\right] = \mathcal{F}_{id}\left[\rho^{(1)}\right] + \mathcal{F}_{exc}\left[\rho^{(1)}\right] + \mathcal{F}_{ext}\left[\rho^{(1)}\right]. \tag{38}$$

Here,

$$\mathcal{F}_{id}\left[\rho^{(1)}\right] = \int \mathrm{d}\mathbf{r}\,\mathrm{d}\hat{\mathbf{n}}\,\rho^{(1)}(\mathbf{r},\hat{\mathbf{n}})\,\left(\ln\left(\lambda^3\rho^{(1)}(\mathbf{r},\hat{\mathbf{n}})\right) - 1\right) \tag{39}$$

is the entropic contribution for an ideal gas of non-interacting particles with λ the thermal de Broglie wave length.[72] We recall that energies are measured in units of k_BT throughout this work. Next, the excess free energy $\mathcal{F}_{exc}$ contains all particle interactions, i.e., contributions beyond the limit of an ideal gas. $\mathcal{F}_{exc}$ is generally not known analytically and must be approximated. The third term reads

$$\mathcal{F}_{ext}\left[\rho^{(1)}\right] = \int \mathrm{d}\mathbf{r}\,\mathrm{d}\hat{\mathbf{n}}\,\Phi_{ext}(\mathbf{r},\hat{\mathbf{n}})\rho^{(1)}(\mathbf{r},\hat{\mathbf{n}}), \tag{40}$$

where here we have included the effect of a chemical potential into $\Phi_{ext}(\mathbf{r},\hat{\mathbf{n}})$. In this form, DFT reduces to a variational problem to determine the equilibrium density,

$$\left.\frac{\delta\Omega}{\delta\rho^{(1)}(\mathbf{r},\hat{\mathbf{n}})}\right|_{\rho^{(1)}(\mathbf{r},\hat{\mathbf{n}})=\rho^{(1)}_{eq}(\mathbf{r},\hat{\mathbf{n}})} = 0. \tag{41}$$

Inserting Eq. (38) leads to

$$\ln\left(\lambda^3\rho^{(1)}_{eq}(\mathbf{r},\hat{\mathbf{n}})\right) + \Phi_{ext}(\mathbf{r},\hat{\mathbf{n}}) = -\left.\frac{\delta\mathcal{F}_{exc}}{\delta\rho^{(1)}(\mathbf{r},\hat{\mathbf{n}})}\right|_{\rho^{(1)}(\mathbf{r},\hat{\mathbf{n}})=\rho^{(1)}_{eq}(\mathbf{r},\hat{\mathbf{n}})}. \tag{42}$$

The central approximation of DDFT is to transfer equilibrium relations to the non-equilibrium case. For this purpose, at each time t and for the corresponding $\rho^{(1)}(\mathbf{r},\hat{\mathbf{n}},t)$, one assumes an instantaneous external potential $\Phi_{ext}(\mathbf{r},\hat{\mathbf{n}},t)$ that satisfies the above relations. In particular, we assume that Eq. (42) still holds with $\rho^{(1)}_{eq}(\mathbf{r},\hat{\mathbf{n}})$ and $\Phi_{ext}(\mathbf{r},\hat{\mathbf{n}})$ replaced by $\rho^{(1)}(\mathbf{r},\hat{\mathbf{n}},t)$ and $\Phi_{ext}(\mathbf{r},\hat{\mathbf{n}},t)$, respectively, i.e.,

$$\ln\left(\lambda^3\rho^{(1)}(\mathbf{r},\hat{\mathbf{n}},t)\right) + \Phi_{ext}(\mathbf{r},\hat{\mathbf{n}},t) = -\frac{\delta\mathcal{F}_{exc}}{\delta\rho^{(1)}(\mathbf{r},\hat{\mathbf{n}},t)}. \tag{43}$$

In combination with that, to close our dynamic equation for $\rho^{(1)}(\mathbf{r},\hat{\mathbf{n}},t)$, we use relations that would follow from Eqs. (32)–(37) in static equilibrium. In this case, $f = 0$ and $\mathcal{J}_3 = \mathcal{J}_6 = \mathbf{0}$. Moreover, our interaction potentials and the external potential u_{ext} do not depend on the swimmer orientations. Then, in equilibrium, it follows that $\hat{\mathbf{n}}\times\nabla_{\hat{\mathbf{n}}}\rho^{(n)} = \mathbf{0}$ for all n and therefore $\mathcal{J}_2 = \mathcal{J}_5 = \mathbf{0}$. The remaining translational and rotational currents $\mathcal{J}_1$ and $\mathcal{J}_4$ must vanish independently of each other in static equilibrium. From these conditions, and replacing in the resulting expressions $u_{ext}(\mathbf{r})$ by $\Phi_{ext}(\mathbf{r},\hat{\mathbf{n}},t)$, which manifests the central DDFT approximation, we obtain

$$\mathbf{0} = \nabla_{\mathbf{r}}\rho^{(1)}(\mathbf{r},\hat{\mathbf{n}},t) + \rho^{(1)}(\mathbf{r},\hat{\mathbf{n}},t)\nabla_{\mathbf{r}}\Phi_{ext}(\mathbf{r},\hat{\mathbf{n}},t) + \int \mathrm{d}\mathbf{r}'\mathrm{d}\hat{\mathbf{n}}'\rho^{(2)}(\mathbf{r},\mathbf{r}',\hat{\mathbf{n}},\hat{\mathbf{n}}',t)\nabla_{\mathbf{r}}u(\mathbf{r},\mathbf{r}') \tag{44}$$

and

$$\mathbf{0} = \nabla_{\mathbf{r}'}\rho^{(2)}(\mathbf{r},\mathbf{r}',\hat{\mathbf{n}},\hat{\mathbf{n}}',t) + \rho^{(2)}(\mathbf{r},\mathbf{r}',\hat{\mathbf{n}},\hat{\mathbf{n}}',t)\nabla_{\mathbf{r}'}\left(\Phi_{ext}(\mathbf{r}',\hat{\mathbf{n}}',t) + u(\mathbf{r},\mathbf{r}')\right) + \int \mathrm{d}\mathbf{r}''\mathrm{d}\hat{\mathbf{n}}''\rho^{(3)}(\mathbf{r},\mathbf{r}',\mathbf{r}'',\hat{\mathbf{n}},\hat{\mathbf{n}}',\hat{\mathbf{n}}'',t)\nabla_{\mathbf{r}'}u(\mathbf{r}',\mathbf{r}''). \tag{45}$$

Here, Eq. (45) was used to eliminate a major part in Eq. (44) that followed from the expression for $\mathcal{J}_1$. In fact, Eqs. (44) and (45) are the first two members of a series of hierarchical relations, the so-called Yvon-Born-Green (YBG) relations, that can be derived in static equilibrium.[100]

Now, inserting Eq. (43) into Eqs. (44) and (45) to eliminate the unknown potential $\Phi_{ext}(\mathbf{r},\hat{\mathbf{n}},t)$, we find

$$\int \mathrm{d}\mathbf{r}'\mathrm{d}\hat{\mathbf{n}}'\rho^{(2)}(\mathbf{r},\mathbf{r}',\hat{\mathbf{n}},\hat{\mathbf{n}}',t)\nabla_{\mathbf{r}}u(\mathbf{r},\mathbf{r}') = \rho^{(1)}(\mathbf{r},\hat{\mathbf{n}},t)\nabla_{\mathbf{r}}\frac{\delta\mathcal{F}_{exc}}{\delta\rho^{(1)}(\mathbf{r},\hat{\mathbf{n}},t)} \tag{46}$$

and

$$\begin{aligned}&\nabla_{\mathbf{r}'}\rho^{(2)}(\mathbf{r},\mathbf{r}',\hat{\mathbf{n}},\hat{\mathbf{n}}',t) + \rho^{(2)}(\mathbf{r},\mathbf{r}',\hat{\mathbf{n}},\hat{\mathbf{n}}',t)\nabla_{\mathbf{r}'}u(\mathbf{r},\mathbf{r}') + \int \mathrm{d}\mathbf{r}''\mathrm{d}\hat{\mathbf{n}}''\rho^{(3)}(\mathbf{r},\mathbf{r}',\mathbf{r}'',\hat{\mathbf{n}},\hat{\mathbf{n}}',\hat{\mathbf{n}}'',t)\nabla_{\mathbf{r}'}u(\mathbf{r}',\mathbf{r}'')\\ &= \rho^{(2)}(\mathbf{r},\mathbf{r}',\hat{\mathbf{n}},\hat{\mathbf{n}}',t)\left(\nabla_{\mathbf{r}'}\ln\left(\lambda^3\rho^{(1)}(\mathbf{r}',\hat{\mathbf{n}}',t)\right) + \nabla_{\mathbf{r}'}\frac{\delta\mathcal{F}_{exc}}{\delta\rho^{(1)}(\mathbf{r}',\hat{\mathbf{n}}',t)}\right).\end{aligned} \tag{47}$$

As a major benefit of this procedure, the three-swimmer density $\rho^{(3)}$ can be eliminated from the currents in Eqs. (32)–(37) by inserting Eq. (47). Moreover, one occurrence of $\rho^{(2)}$ is eliminated using Eq. (46). The currents then reduce to

$$\mathcal{J}_1 = -\mu^t \left(\nabla_{\mathbf{r}} \rho^{(1)}(\mathbf{r},\hat{\mathbf{n}},t) + \rho^{(1)}(\mathbf{r},\hat{\mathbf{n}},t)\nabla_{\mathbf{r}} u_{ext}(\mathbf{r}) + \rho^{(1)}(\mathbf{r},\hat{\mathbf{n}},t)\nabla_{\mathbf{r}} \frac{\delta \mathcal{F}_{exc}}{\delta \rho^{(1)}(\mathbf{r},\hat{\mathbf{n}},t)} \right)$$
$$- \int \mathrm{d}\mathbf{r}'\mathrm{d}\hat{\mathbf{n}}' \mu^{tt}_{\mathbf{r},\mathbf{r}'} \cdot \left(\rho^{(2)}(\mathbf{r},\mathbf{r}',\hat{\mathbf{n}},\hat{\mathbf{n}}',t) \left(\nabla_{\mathbf{r}'} \ln\left(\lambda^3 \rho^{(1)}(\mathbf{r}',\hat{\mathbf{n}}',t)\right) + \nabla_{\mathbf{r}'} u_{ext}(\mathbf{r}') + \nabla_{\mathbf{r}'} \frac{\delta \mathcal{F}_{exc}}{\delta \rho^{(1)}(\mathbf{r}',\hat{\mathbf{n}}',t)} \right) \right), \quad (48)$$

$$\mathcal{J}_2 = -\int \mathrm{d}\mathbf{r}'\mathrm{d}\hat{\mathbf{n}}'\, \mu^{tr}_{\mathbf{r},\mathbf{r}'} (\hat{\mathbf{n}}' \times \nabla_{\hat{\mathbf{n}}'}) \rho^{(2)}(\mathbf{r},\mathbf{r}',\hat{\mathbf{n}},\hat{\mathbf{n}}',t), \quad (49)$$

$$\mathcal{J}_3 = f \left(\Lambda^{tt}_{\mathbf{r},\mathbf{r}} \cdot \hat{\mathbf{n}} \rho^{(1)}(\mathbf{r},\hat{\mathbf{n}},t) + \int \mathrm{d}\mathbf{r}'\mathrm{d}\hat{\mathbf{n}}' \Lambda^{tt}_{\mathbf{r},\mathbf{r}'} \cdot \hat{\mathbf{n}}' \rho^{(2)}(\mathbf{r},\mathbf{r}',\hat{\mathbf{n}},\hat{\mathbf{n}}',t) \right), \quad (50)$$

$$\mathcal{J}_4 = -\int \mathrm{d}\mathbf{r}'\mathrm{d}\hat{\mathbf{n}}' \mu^{rt}_{\mathbf{r},\mathbf{r}'} \left(\rho^{(2)}(\mathbf{r},\mathbf{r}',\hat{\mathbf{n}},\hat{\mathbf{n}}',t) \left(\nabla_{\mathbf{r}'} \ln\left(\lambda^3 \rho^{(1)}(\mathbf{r}',\hat{\mathbf{n}}',t)\right) + \nabla_{\mathbf{r}'} u_{ext}(\mathbf{r}') + \nabla_{\mathbf{r}'} \frac{\delta \mathcal{F}_{exc}}{\delta \rho^{(1)}(\mathbf{r}',\hat{\mathbf{n}}',t)} \right) \right), \quad (51)$$

$$\mathcal{J}_5 = -\mu^r \hat{\mathbf{n}} \times \nabla_{\hat{\mathbf{n}}} \rho^{(1)}(\mathbf{r},\hat{\mathbf{n}},t) - \int \mathrm{d}\mathbf{r}'\mathrm{d}\hat{\mathbf{n}}'\, \mu^{rr}_{\mathbf{r},\mathbf{r}'} \cdot (\hat{\mathbf{n}}' \times \nabla_{\mathbf{n}'}) \rho^{(2)}(\mathbf{r},\mathbf{r}',\hat{\mathbf{n}},\hat{\mathbf{n}}',t), \quad (52)$$

$$\mathcal{J}_6 = f \int \mathrm{d}\mathbf{r}'\mathrm{d}\hat{\mathbf{n}}'\, \Lambda^{rt}_{\mathbf{r},\mathbf{r}'} \hat{\mathbf{n}}' \rho^{(2)}(\mathbf{r},\mathbf{r}',\hat{\mathbf{n}},\hat{\mathbf{n}}',t). \quad (53)$$

In effect, we have replaced $\rho^{(3)}(\mathbf{r},\mathbf{r}',\mathbf{r}'',\hat{\mathbf{n}},\hat{\mathbf{n}}',\hat{\mathbf{n}}'',t)$ and one instance of $\rho^{(2)}(\mathbf{r},\mathbf{r}',\hat{\mathbf{n}},\hat{\mathbf{n}}',t)$ by their equilibrium expressions that would apply, if the equilibrium one-swimmer density were given by $\rho^{(1)}(\mathbf{r},\hat{\mathbf{n}},t)$. This procedure works best when $\rho^{(3)}$ and $\rho^{(2)}$ relax significantly quicker than $\rho^{(1)}$. It is therefore referred to as adiabatic elimination.[105] In our case, the overdamped nature of the microswimmer dynamics supports this procedure.

Finally, we need to express $\mathcal{F}_{exc}$ and $\rho^{(2)}$ as functionals of $\rho^{(1)}$ to close the dynamical equation for $\rho^{(1)}(\mathbf{r},\hat{\mathbf{n}},t)$. For moderate interaction strengths $\epsilon_0 \lesssim 1$ in our soft GEM-4 interaction potential Eq. (22), the classical mean-field approximation provides a reasonable and simple closure scheme.[98] It is given by

$$\mathcal{F}_{exc} = \frac{1}{2} \int \mathrm{d}\mathbf{r}\, \mathrm{d}\mathbf{r}' \mathrm{d}\hat{\mathbf{n}}\, \mathrm{d}\hat{\mathbf{n}}' \rho^{(2)}(\mathbf{r},\mathbf{r}',\hat{\mathbf{n}},\hat{\mathbf{n}}',t) u(\mathbf{r},\mathbf{r}'), \quad (54)$$

for the excess free energy and the approximation

$$\rho^{(2)}(\mathbf{r},\mathbf{r}',\hat{\mathbf{n}},\hat{\mathbf{n}}',t) = \rho^{(1)}(\mathbf{r},\hat{\mathbf{n}},t)\, \rho^{(1)}(\mathbf{r}',\hat{\mathbf{n}}',t), \quad (55)$$

for the two-swimmer density.

Overall, Eqs. (31) and (48)–(53) together with Eqs. (54) and (55) complete our derivation of a DDFT for dilute to semi-dilute suspensions of active microswimmers. We included hydrodynamic and soft steric interactions. Inserting the mobility tensors listed in Eqs. (8)–(12), (15), (16), (18), (19), (28), and (29), it applies for a suspension of our model microswimmers within a bulk viscous fluid in three spatial dimensions.

IV. PLANAR TRAPPED MICROSWIMMER ARRANGEMENTS

As a first application of the above DDFT, we are interested in the effect that the self-propulsion forces have on a confined assembly of microswimmers. In particular, this concerns the time evolution towards a final steady state when self-propulsion is suddenly switched on in an initially equilibrated system. Such a behavior could, for instance, be realized in experiments using light-activated microswimmers.[35,36,106–110]

Here, we present numerical results for two-dimensional arrangements. That is, the density field $\rho^{(1)}(\mathbf{r},\hat{\mathbf{n}},t)$ is calculated in the Cartesian x-y plane, with the direction $\hat{\mathbf{n}}$ likewise confined to that plane and parameterized by one orientational angle. Concerning hydrodynamic interactions, the presence of a surrounding three-dimensional bulk fluid is still taken into account, as introduced in Sec. II. Such a system could be realized approximately, for example, by confining the microswimmers to a plane using external laser potentials. Another realization could be microswimmers confined to the liquid–liquid interface between two immiscible fluids of identical viscosity.

The partial differential equation resulting from our DDFT, i.e., Eq. (31) together with Eqs. (48)–(53), was discretized using a finite-difference scheme on a regular grid. The grid points were separated by distances $\Delta x = 0.1$ in the spatial and $\Delta\phi = \pi/10$ in the angular direction, where we measure all lengths in units of σ. In each spatial direction, the numerical box length was 8. $\rho^{(1)}(\mathbf{r},\hat{\mathbf{n}},t)$ was iterated forward in time by employing a second-order Runge-Kutta scheme with fixed time step $\Delta t = 10^{-5}$. Here, we measure all times in units of the Brownian time scale $\tau_B = 1/\mu^t$, where we recall that energies are given in units of $k_B T$ (and lengths in units of σ). For simplicity and for practical purposes, periodic boundary conditions were used and the long-ranged hydrodynamic interactions were truncated at a cut-off radius of $r_c = 1.875$.

Typically, self-propulsion is quantified by the Péclet number Pe. Here, Pe corresponds to the ratio between the strength of self-propulsion and the strength of thermal fluctuations. In our units, we have Pe $= |f|$. We choose fixed numerical values for all other system parameters, $a = L = 0.75$, $\alpha = 0.15$, $\epsilon_0 = 2$, and $k = 30$, unless stated otherwise.

To study the time evolution of the confined system after switching on self-propulsion, we adhere to the following numerical protocol. First, we initialize the system by a random density profile and let it equilibrate with self-propulsion being switched off, i.e., Pe $= f = 0$. After equilibration, we turn on the active forces to $f \neq 0$ and let the system find its new steady state, if existent, in non-equilibrium. Our results are presented in terms of the density profile

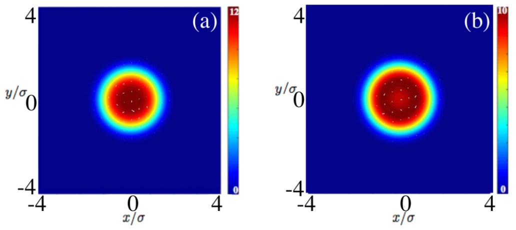

FIG. 2. Microswimmer density (color map) under confinement in equilibrium, i.e., for $\mathrm{Pe} = |f| = 0$. In this situation, the density profile is rotationally symmetric, while the orientations are completely disordered. (a) Steric swimmer interactions switched off, $\epsilon_0 = 0$, showing a maximum density in the center of the confinement. (b) Steric swimmer interactions turned on, $\epsilon_0 = 2$, leading to a depletion of the swimmer density in the center.

$$\rho(\mathbf{r},t) = \int \mathrm{d}\hat{\mathbf{n}}\, \rho^{(1)}(\mathbf{r},\hat{\mathbf{n}},t), \tag{56}$$

shown as color maps in the subsequent figures, as well as the orientational vector field

$$\langle\hat{\mathbf{n}}\rangle(\mathbf{r},t) = \int \mathrm{d}\hat{\mathbf{n}}\, \hat{\mathbf{n}}\, \rho^{(1)}(\mathbf{r},\hat{\mathbf{n}},t), \tag{57}$$

depicted as white arrows in the figures. In the following, we first describe our equilibrated initial state for $f = 0$. Then we switch on self-propulsion to moderate values setting $f \neq 0$, but we neglect hydrodynamic interactions between different swimmers. After that, we additionally include hydrodynamic interactions.

First, for $f = 0$, the system is in equilibrium. In our case, there are no orientation-dependent equilibrium interactions. Indeed, we find from Eqs. (31) and (48)–(53) that the swimmer orientations completely disorder. The equilibrium densities become independent of the swimmer orientations. Moreover, the system reaches a steady state, in which the entropic, steric inter-swimmer, and trapping forces balance each other. Hydrodynamic interactions do not affect these equilibrium states. As a result, the situation becomes rotationally symmetric in accordance with the rotational symmetry of the confinement. Fig. 2 shows two situations, one with the steric swimmer interactions switched off, $\epsilon_0 = 0$, see Fig. 2(a), where the maximum swimmer density is found in the center of the confinement; and one with the steric interactions switched on, $\epsilon_0 = 2$, see Fig. 2(b), which leads to a weak depletion of the density at the center point.

We now turn on the active drive, $f \neq 0$, yet to moderate magnitudes. Hydrodynamic interactions between different swimmers still remain switched off for the moment. Due to the active forces, the self-propelling microswimmers have an additional drive to work against the confining potential. In this way, they spread out and reach locations further separated from the center of the confinement. A time series is depicted in Figs. 3(a) and 3(b).

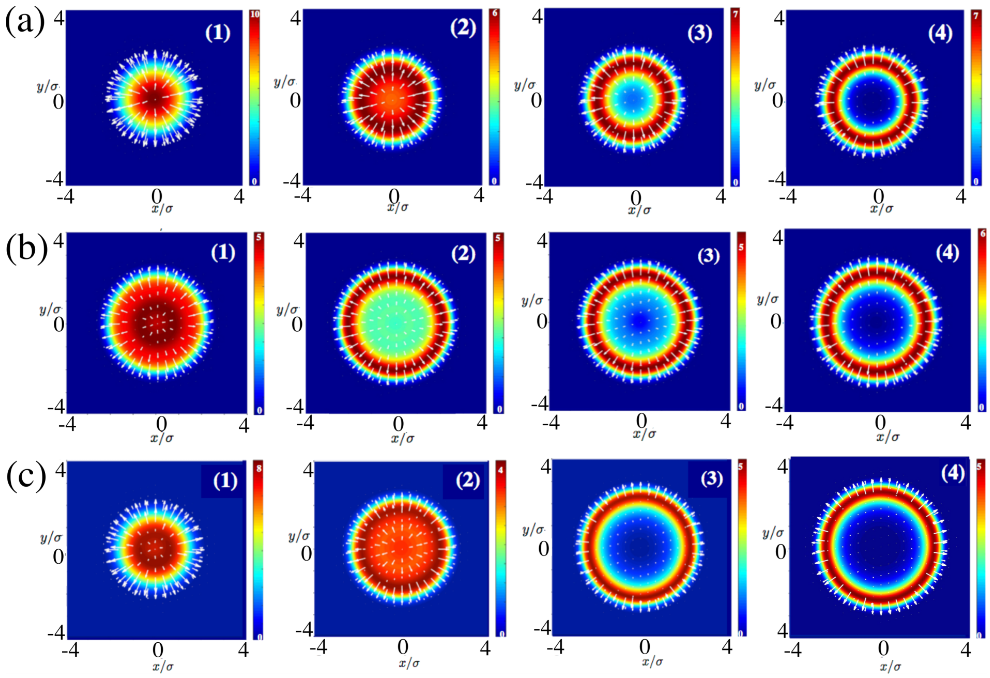

FIG. 3. Time evolution of the density profiles (color maps) and orientation profiles (white arrows) of our confined microswimmer systems starting from the equilibrated states of $f = 0$ depicted in Fig. 2. At time $t = 0$, the active force is switched on to $f = 8$. (a) Snapshots without any steric ($\epsilon_0 = 0$) and without any hydrodynamic interactions between the swimmers at times $t = 0.05$, $t = 0.1$, $t = 0.15$, and $t = 0.4$. (b) Snapshots with steric ($\epsilon_0 = 2$) but still without any hydrodynamic interactions between the swimmers at times $t = 0.02$, $t = 0.06$, $t = 0.08$, and $t = 0.4$. (c) Snapshots with both steric ($\epsilon_0 = 2$) and hydrodynamic interactions between the swimmers at times $t = 0.05$, $t = 0.15$, $t = 0.25$, and $t = 0.4$.

Still, the situation apparently remains rotationally symmetric and finally reaches a steady state. Yet, the density in the center is now depleted, while a density ring forms at finite distance from the center as has been observed before in statistical and in particle-based approaches.[81,110,111] From the white arrows in Fig. 3, we find that the active forces drive the swimmers outwards against the confining potential barrier. In this sense, the potential blocks the swimmer motion in the final steady state.[112] It takes a typical rotational diffusion time scale until a swimmer can reorient and leave the trapping location, before it propels towards another location on the high-density ring.[110,111]

The typical radius $\tilde{r}$ of the density ring in Fig. 3(a), where different swimmers do not interact with each other, can readily be estimated. In this case, the n-swimmer densities for $n \geq 2$ do not play a role. Consequently, in Eqs. (32)–(37) we find $\mathcal{J}_2 = \mathcal{J}_4 = \mathcal{J}_6 = 0$. The remaining orientational part in $\mathcal{J}_5$ decouples from the translational contributions and leads to free rotational diffusion. Finally, the remaining translational contributions in $\mathcal{J}_1$ and $\mathcal{J}_3$ must balance each other to allow for a steady state. This implies that the sum of the contributions from translational diffusion, confinement, and active forces must cancel. Assuming that at $r = \tilde{r}$ the density becomes maximum and exploiting the radial symmetry, we find

$$\tilde{r} \approx \left|\frac{3g(\alpha)}{8}\right|^{1/3} \left|\frac{f}{k}\right|^{1/3}, \tag{58}$$

where we have introduced the function

$$g(\alpha) = \left(\frac{1-2\alpha}{\alpha(1-\alpha)}\right)\left(1 - \frac{1-\alpha+\alpha^2}{3\alpha^2(1-\alpha)^2}\right), \tag{59}$$

for our special case of $a = L$. For harmonic confinement, this radius has been calculated in Refs. 81 and 111. It is conceivable that switching on an effective repulsion between the swimmers in the form of our soft steric interactions, $\epsilon_0 = 2$, adds to the spreading. This can be observed by the slightly larger diameter of the final density ring in Fig. 3(b) when compared to the diameter in Fig. 3(a).

In addition to the steric interactions between the microswimmers, we now also include the hydrodynamic interactions between them. At low to moderate magnitudes of the active forces, here $0 < \mathrm{Pe} = |f| \lesssim 10$, we still observe qualitatively the same scenario as described above in the absence of hydrodynamic interactions between the swimmers. At the end of our numerical simulation, see Fig. 3(c), we again observe a density ring and a radial orientation of the swimmer axes. Due to the hydrodynamic interactions, however, the diameter of this density ring increases when compared to the case without hydrodynamic interactions between the swimmers, see the final states in Figs. 3(b) and 3(c). Apparently, via the hydrodynamic interactions, the swimmers support each other in their collective propulsion against the confining potential. The presented snapshots were obtained for pushers ($f > 0$), yet the results are qualitatively the same for pullers ($f < 0$).

From now on, we include both steric and hydrodynamic interactions between the microswimmers. We next consider increased values of the Péclet number of $10 < \mathrm{Pe} = |f| \lesssim 50$. When switching on this active force, the swimmers initially propel outwards from the center of the confinement as before. Although the system still appears to reach a steady state, the latter is not rotationally symmetric any more. We depict corresponding time evolutions in Fig. 4 for $f = \pm 50$, i.e., for pushers and for pullers, respectively.

Pushers propel into the direction of the axis vector $\hat{\mathbf{n}}$, while pullers propel into the opposite direction, see Fig. 1. That is why the white arrows point outward in Fig. 4(a) and inward in Fig. 4(b). Since the rotational symmetry in the trapping plane is broken, a net fluid flow results in this plane. Therefore, the system can be viewed as a self-assembled

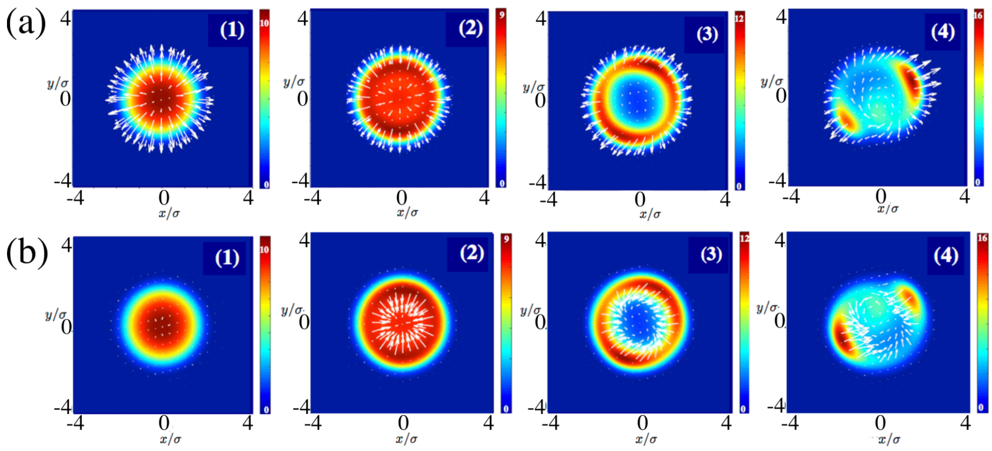

FIG. 4. Time evolution of the density profiles (color maps) and orientation profiles (white arrows) of our microswimmer systems at (a) $f = 50$ for pushers and (b) $f = -50$ for pullers. Both steric and hydrodynamic interactions between the swimmers are included. We observe rotational symmetry breaking within the plane. It corresponds to the formation of a "hydrodynamic fluid pump" consisting of self-assembled microswimmers. The snapshots were obtained at times $t = 0.05$, $t = 0.1$, $t = 0.2$, and $t = 0.8$.

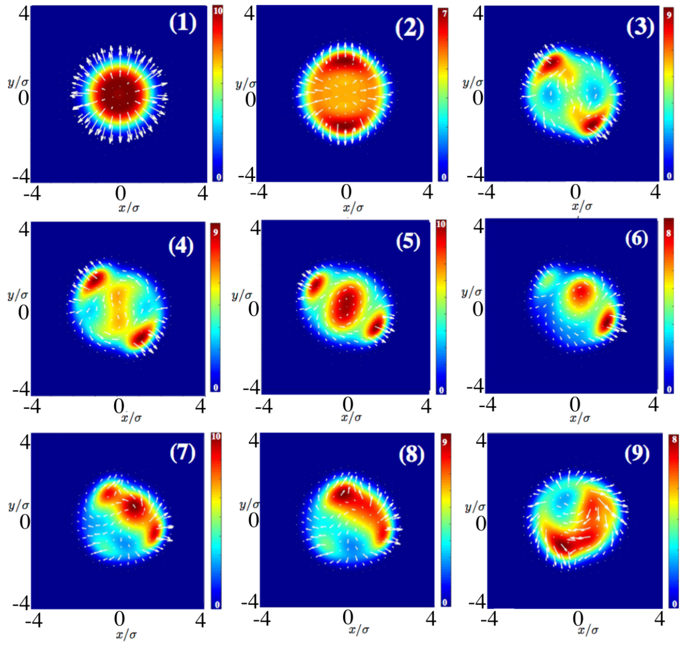

FIG. 5. Time evolution of the density profiles (color maps) and orientation profiles (white arrows) of pushers at $f = 100$. Both steric and hydrodynamic interactions between the swimmers are included. This system does not reach a steady state any more within our numerically observed time window. The snapshots are obtained at times $t = 0.02$, $t = 0.1$, $t = 0.25$, $t = 0.3$, $t = 1.25$, $t = 2.5$, $t = 2.7$, $t = 3.0$, and $t = 3.5$.

"hydrodynamic fluid pump," which has been observed and interpreted before using particle-based lattice Boltzmann and Brownian dynamics simulations.[80,81]

Upon further increase of Pe $= |f|$, the system does not enter a state of a steady hydrodynamic fluid pump any longer. Instead, the system becomes very dynamic. High density areas of localized orientational order of the swimmer axes form and continuously swap around within the spherical confinement. Examples for the time evolution are shown in Figs. 5 and 6 for pushers and pullers, respectively. As far as we could test numerically, the system for these strong active forces does not reach a steady state any more.

We briefly comment on the factors that lead to the observed destabilization effects. The first one breaks the

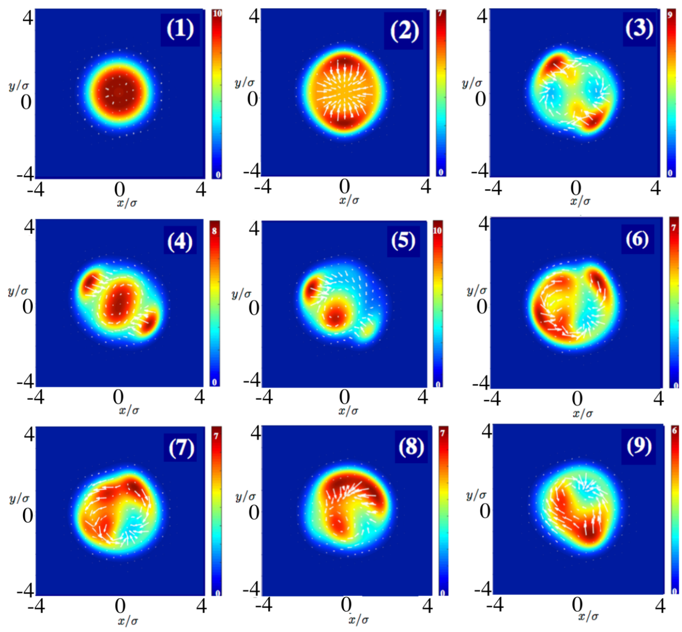

FIG. 6. Time evolution of the density profiles (color maps) and orientation profiles (white arrows) of pullers at $f = -100$. Both steric and hydrodynamic interactions between the swimmers are included. Again, this system does not reach a steady state any more within our numerically observed time window. The snapshots are obtained at times $t = 0.02$, $t = 0.1$, $t = 0.25$, $t = 0.3$, $t = 1.25$, $t = 2.5$, $t = 2.7$, $t = 3.0$, and $t = 3.5$.

initial rotational symmetry of Fig. 3. It induces the formation of the hydrodynamic fluid pump, see Fig. 4. In Refs. 80 and 81, it was explained that rotational diffusion stabilizes the rotationally symmetric states of Fig. 3. However, hydrodynamic interactions can lead to a destabilizing feedback mechanism that supports the rotational symmetry breaking. In brief, one has to realize that swimmers in the blocked state within the density ring transmit the confining forces to the surrounding fluid. As a consequence, fluid flows are induced. If a density fluctuation along the ring occurs, with a higher density at a certain spot, its induced fluid flow can reorient neighboring swimmers. The mechanism leads to positive feedback, i.e., the neighboring swimmers are reoriented such that they propel towards the high density region. In our formalism, a corresponding rotation–translation coupling to the influence of the confinement, introduced via u_{ext}, is contained in the current $\mathcal{J}_4$ in Eq. (51).

The second destabilization occurs when at very high $\mathrm{Pe} = |f|$ a persistent hydrodynamic fluid pump as in Fig. 4 cannot be observed any more and the system becomes truly dynamic, see Figs. 5 and 6. This effect can be traced back to the rotation–translation coupling between swimmer rotations and the active point forces. Aligned and concentrated active forces can induce rotations of neighboring swimmer bodies, which in turn can lead to rotational instabilities. This effect is proportional to the strength of the active forces $|f|$. At high $\mathrm{Pe} = |f|$, it apparently cannot be stabilized any longer. In our formalism, this contribution is represented by the current $\mathcal{J}_6$ in Eq. (53). We have numerically tested our assertion by deactivating this current.

V. CONCLUSIONS

In this work, we have derived a statistical characterization of dilute to semi-dilute suspensions of identical self-propelled microswimmers in the form of a DDFT. Our simple model microswimmers consist of a body that experiences hydrodynamic drag from the surrounding fluid, plus two separated active point-like force centers. Two antiparallel active point forces of equal magnitude are exerted by these force centers onto the surrounding fluid and set it into motion. Pushing and pulling swimming mechanisms can easily be distinguished. We include both hydrodynamic and steric interactions between the swimmers, as well as the effect of an external trapping potential. Hydrodynamic interactions result both from the active forces as well as from steric and external forces acting on the swimmer bodies. At this time, axially symmetric model microswimmers are considered, thus active torques do not arise. Moreover, only isotropic steric interactions are taken into account.

Our DDFT describes the overdamped time evolution of the microswimmer density, both concerning positions and orientations of the swimmers. As a first application and test of the theory, we consider a crowd of microswimmers restricted to planar motion within a three-dimensional bulk fluid. Such an arrangement could be achieved, for instance, using external trapping laser potentials, or by confining the swimmers to an interface between two immiscible fluids of equal viscosity. Moreover, an additional radially symmetric trapping potential was taken into account. Within this framework, the theory was evaluated numerically.

The numerical calculations started from an initial state in which a crowd of microswimmers is concentrated in the center of the spherical trap. At low Péclet numbers, which means low magnitude of the active forces, the microswimmers propel outwards, where in a final stationary state they form a ring-like density profile. This effect remains when hydrodynamic interactions are switched off in the numerical calculations as reported in different frameworks previously.[110,111,113] Increasing the Péclet number and including hydrodynamic interactions, the numerical evaluation of the DDFT shows a breaking of rotational symmetry. The ring-like density profile observed for lower Péclet numbers now is replaced by concentrated density spots. Likewise, this effect has been observed before by different approaches, both for lattice Boltzmann as well as for Brownian dynamics simulations.[80,81] Due to the polar order of the swimmers within the concentrated spots and the resulting fluid flows, this state was identified as a hydrodynamic fluid pump. Obviously, our DDFT reproduces these previously identified effects, which stresses its potential. Finally, upon further increase of the Péclet number, the numerical evaluation shows a persistently dynamic state of migrating density clouds.

As common for DDFT approaches, our description partially leans on equilibrium concepts. However, the situation under consideration is an intrinsically non-equilibrium one. For instance, we used a temperature variable to measure energies and to define the Péclet number. We identified this variable with a constant temperature of the background fluid. It might be stabilized by coupling to an external heat bath. Strictly speaking, the energy input due to self-propulsion can lead to local changes in the temperature. On one hand, this issue may become relevant for thermally driven artificial microswimmers in the form of externally heated Janus particles.[36,106–108] On the other hand, temperature changes only due to induced motion of the surrounding fluid are considered negligible. Effective temperatures were introduced to correctly describe deviations from equilibrium temperatures in driven systems.[114,115] The issue may be investigated in a profound analysis, but is not addressed here. As noted before, we only remark that the translational and rotational diffusion behaviors [represented by the terms containing $\ln P$ in Eqs. (20) and (24)] may need to be modified if local deviations from the heat bath temperature become perceptible. Our framework of hydrodynamic interactions remains basically unaffected, as long as local deviations of the viscosity or density remain approximately unaltered.

In the derivation of the statistical theory, conservation of the probability to find the particles somewhere in phase space [Eq. (25)] remains, of course, unaltered by the non-equilibrium nature of our system. Therefore, apart from the points mentioned above, no equilibrium approximations are involved in our initial statistical equations [Eqs. (25)–(37)]. The situation changes when formulae that were derived exactly in the context of equilibrium DFT are adapted [(38)–(53)] to close our hierarchy of non-equilibrium statistical equations. This crucial step is generic for DDFTs but needs to be tested by numerical evaluation of the full statistical equations or by particle-based simulations. In our case, we do reproduce corresponding results of previous particle-based simulations. This stresses the power of our newly derived DDFT in describing the complex behavior of microswimmer suspensions. As a side remark, we note that mainly the steric inter-particle interactions are directly concerned by the DFT approximation [see the presence of the $u(\mathbf{r},\mathbf{r}')$ terms on the left-hand sides of Eqs. (46) and (47)]. Further analysis may be necessary when such interactions form the central focus of a quantitative DDFT approach.

Naturally, future applications and extensions of our theory are manifold. It should be further compared to particle-based simulations and possible experiments to learn more about the range of its predictive power. As indicated above, an obvious next step is to extend the theory to include active torques and anisotropic steric interactions. Moreover, the influence of different effective steric interactions, for instance, hard-body interactions, may be investigated.[116] Other variations include, for example, the hydrodynamic effect of confining boundaries[2] or external magnetic alignment fields acting onto magnetic microswimmers.[117] In the longer term, an extension of the investigations to denser crystallized systems as well as three-dimensional numerical implementations are desirable.

ACKNOWLEDGMENTS

The authors thank the Deutsche Forschungsgemeinschaft for support of this work through the SPP 1726 on "Microswimmers."

[1]E. Lauga and T. R. Powers, Rep. Prog. Phys. **72**, 096601 (2009).
[2]S. E. Spagnolie and E. Lauga, J. Fluid Mech. **700**, 105 (2012).
[3]A. M. Menzel, Phys. Rep. **554**, 1 (2015).
[4]J. Elgeti, R. G. Winkler, and G. Gompper, Rep. Prog. Phys. **78**, 056601 (2015).
[5]M. Eisenbach and L. C. Giojalas, Nat. Rev. Mol. Cell Biol. **7**, 276 (2006).
[6]H. C. Berg and D. A. Brown, Nature **239**, 500 (1972).
[7]A. Walther and A. H. E. Müller, Chem. Rev. **113**, 5194 (2013).
[8]P. Romanczuk, M. Bär, W. Ebeling, B. Lindner, and L. Schimansky-Geier, Eur. Phys. J.: Spec. Top. **202**, 1 (2012).
[9]M. E. Cates, Rep. Prog. Phys. **75**, 042601 (2012).
[10]M. C. Marchetti, J. F. Joanny, S. Ramaswamy, T. B. Liverpool, J. Prost, M. Rao, and R. A. Simha, Rev. Mod. Phys. **85**, 1143 (2013).
[11]T. Vicsek, A. Czirók, E. Ben-Jacob, I. Cohen, and O. Shochet, Phys. Rev. Lett. **75**, 1226 (1995).
[12]J. Toner and Y. Tu, Phys. Rev. Lett. **75**, 4326 (1995).
[13]J. Toner and Y. Tu, Phys. Rev. E **58**, 4828 (1998).
[14]J. Toner, Y. Tu, and S. Ramaswamy, Ann. Phys. **318**, 170 (2005).
[15]E. Bertin, M. Droz, and G. Grégoire, Phys. Rev. E **74**, 022101 (2006).
[16]E. Bertin, M. Droz, and G. Grégoire, J. Phys. A: Math. Theor. **42**, 445001 (2009).
[17]M. Leoni and T. B. Liverpool, Phys. Rev. Lett. **105**, 238102 (2010).
[18]G. Grégoire and H. Chaté, Phys. Rev. Lett. **92**, 025702 (2004).
[19]S. Mishra, A. Baskaran, and M. C. Marchetti, Phys. Rev. E **81**, 061916 (2010).
[20]V. Schaller, C. Weber, C. Semmrich, E. Frey, and A. R. Bausch, Nature **467**, 73 (2010).
[21]A. M. Menzel, Phys. Rev. E **85**, 021912 (2012).
[22]T. Ihle, Phys. Rev. E **88**, 040303 (2013).
[23]J.-B. Caussin, A. Solon, A. Peshkov, H. Chaté, T. Dauxois, J. Tailleur, V. Vitelli, and D. Bartolo, Phys. Rev. Lett. **112**, 148102 (2014).
[24]T. Ohta and S. Yamanaka, Prog. Theor. Exp. Phys. **2014**, 011J01.
[25]H. H. Wensink, J. Dunkel, S. Heidenreich, K. Drescher, R. E. Goldstein, H. Löwen, and J. M. Yeomans, Proc. Natl. Acad. Sci. U. S. A. **109**, 14308 (2012).
[26]J. Słomka and J. Dunkel, Eur. Phys. J.: Spec. Top. **224**, 1349 (2015).
[27]A. Ordemann, G. Balazsi, and F. Moss, Physica A **325**, 260 (2003).
[28]F. Peruani, A. Deutsch, and M. Bär, Phys. Rev. E **74**, 030904 (2006).
[29]T. Ishikawa and T. J. Pedley, Phys. Rev. Lett. **100**, 088103 (2008).
[30]J. Tailleur and M. E. Cates, Phys. Rev. Lett. **100**, 218103 (2008).
[31]I. Theurkauff, C. Cottin-Bizonne, J. Palacci, C. Ybert, and L. Bocquet, Phys. Rev. Lett. **108**, 268303 (2012).
[32]Y. Fily and M. C. Marchetti, Phys. Rev. Lett. **108**, 235702 (2012).
[33]M. E. Cates and J. Tailleur, EPL **101**, 20010 (2013).
[34]G. S. Redner, M. F. Hagan, and A. Baskaran, Phys. Rev. Lett. **110**, 055701 (2013).
[35]J. Palacci, S. Sacanna, A. P. Steinberg, D. J. Pine, and P. M. Chaikin, Science **339**, 936 (2013).
[36]I. Buttinoni, J. Bialké, F. Kümmel, H. Löwen, C. Bechinger, and T. Speck, Phys. Rev. Lett. **110**, 238301 (2013).
[37]T. Speck, J. Bialké, A. M. Menzel, and H. Löwen, Phys. Rev. Lett. **112**, 218304 (2014).
[38]T. Speck, A. M. Menzel, J. Bialké, and H. Löwen, J. Chem. Phys. **142**, 224109 (2015).
[39]J. Bialké, T. Speck, and H. Löwen, Phys. Rev. Lett. **108**, 168301 (2012).
[40]A. M. Menzel and H. Löwen, Phys. Rev. Lett. **110**, 055702 (2013).
[41]A. M. Menzel, T. Ohta, and H. Löwen, Phys. Rev. E **89**, 022301 (2014).
[42]H. H. Wensink and H. Löwen, J. Phys.: Condens. Matter **24**, 464130 (2012).
[43]A. M. Menzel and T. Ohta, EPL **99**, 58001 (2012).
[44]S. R. McCandlish, A. Baskaran, and M. F. Hagan, Soft Matter **8**, 2527 (2012).
[45]A. M. Menzel, J. Phys.: Condens. Matter **25**, 505103 (2013).
[46]F. Kogler and S. H. L. Klapp, EPL **110**, 10004 (2015).
[47]M. Ballerini, N. Cabibbo, R. Candelier, A. Cavagna, E. Cisbani, I. Giardina, V. Lecomte, A. Orlandi, G. Parisi, A. Procaccini *et al.*, Proc. Natl. Acad. Sci. U. S. A. **105**, 1232 (2008).
[48]A. Sokolov, I. S. Aranson, J. O. Kessler, and R. E. Goldstein, Phys. Rev. Lett. **98**, 158102 (2007).
[49]I. S. Aranson and L. S. Tsimring, Rev. Mod. Phys. **78**, 641 (2006).
[50]J. Deseigne, O. Dauchot, and H. Chaté, Phys. Rev. Lett. **105**, 098001 (2010).
[51]A. Kudrolli, G. Lumay, D. Volfson, and L. S. Tsimring, Phys. Rev. Lett. **100**, 058001 (2008).
[52]W. F. Paxton, K. C. Kistler, C. C. Olmeda, A. Sen, S. K. St. Angelo, Y. Cao, T. E. Mallouk, P. E. Lammert, and V. H. Crespi, J. Am. Chem. Soc. **126**, 13424 (2004).
[53]P. Tierno, R. Albalat, and F. Sagués, Small **6**, 1749 (2010).
[54]B. ten Hagen, R. Wittkowski, D. Takagi, F. Kümmel, C. Bechinger, and H. Löwen, J. Phys.: Condens. Matter **27**, 194110 (2015).
[55]A. Baskaran and M. C. Marchetti, Phys. Rev. Lett. **101**, 268101 (2008).
[56]A. Baskaran and M. C. Marchetti, Proc. Natl. Acad. Sci. U. S. A. **106**, 15567 (2009).
[57]Y.-L. Chou, R. Wolfe, and T. Ihle, Phys. Rev. E **86**, 012120 (2012).
[58]R. Grossmann, P. Romanczuk, M. Bär, and L. Schimansky-Geier, Eur. Phys. J.: Spec. Top. **224**, 1325 (2015).
[59]S. Heidenreich, J. Dunkel, S. H. L. Klapp, and M. Bär, e-print arXiv:1509.08661 (2015).
[60]Y.-L. Chou and T. Ihle, Phys. Rev. E **91**, 022103 (2015).
[61]I. S. Aranson, A. Sokolov, J. O. Kessler, and R. E. Goldstein, Phys. Rev. E **75**, 040901 (2007).
[62]H. Pleiner, D. Svenšek, and H. R. Brand, Eur. Phys. J. E **36**, 1 (2013).
[63]H. R. Brand, H. Pleiner, and D. Svenšek, Eur. Phys. J. E **37**, 1 (2014).
[64]U. M. B. Marconi and P. Tarazona, J. Chem. Phys. **110**, 8032 (1999).
[65]U. M. B. Marconi and P. Tarazona, J. Phys.: Condens. Matter **12**, A413 (2000).
[66]A. J. Archer and R. Evans, J. Chem. Phys. **121**, 4246 (2004).
[67]A. J. Archer, J. Phys.: Condens. Matter **17**, 1405 (2005).
[68]S. van Teeffelen, C. N. Likos, and H. Löwen, Phys. Rev. Lett. **100**, 108302 (2008).
[69]F. Penna, J. Dzubiella, and P. Tarazona, Phys. Rev. E **68**, 061407 (2003).
[70]R. Wittkowski, H. Löwen, and H. R. Brand, J. Chem. Phys. **137**, 224904 (2012).
[71]A. J. Archer, M. J. Robbins, and U. Thiele, Phys. Rev. E **81**, 021602 (2010).
[72]R. Wittkowski, H. Löwen, and H. R. Brand, Phys. Rev. E **82**, 031708 (2010).
[73]A. A. Aerov and M. Krüger, J. Chem. Phys. **140**, 094701 (2014).
[74]A. A. Aerov and M. Krüger, Phys. Rev. E **92**, 042301 (2015).
[75]M. Rex and H. Löwen, Phys. Rev. Lett. **101**, 148302 (2008).
[76]M. Rex and H. Löwen, Eur. Phys. J. E **28**, 139 (2009).
[77]A. Donev and E. Vanden-Eijnden, J. Chem. Phys. **140**, 234115 (2014).
[78]H. H. Wensink and H. Löwen, Phys. Rev. E **78**, 031409 (2008).
[79]R. Wittkowski and H. Löwen, Mol. Phys. **109**, 2935 (2011).
[80]R. W. Nash, R. Adhikari, J. Tailleur, and M. E. Cates, Phys. Rev. Lett. **104**, 258101 (2010).

[81]M. Hennes, K. Wolff, and H. Stark, Phys. Rev. Lett. **112**, 238104 (2014).
[82]E. M. Purcell, Am. J. Phys. **45**, 3 (1977).
[83]R. Aditi Simha and S. Ramaswamy, Phys. Rev. Lett. **89**, 058101 (2002).
[84]Y. Hatwalne, S. Ramaswamy, M. Rao, and R. A. Simha, Phys. Rev. Lett. **92**, 118101 (2004).
[85]R. Golestanian, Eur. Phys. J. E **25**, 1 (2008).
[86]Y. Fily, A. Baskaran, and M. C. Marchetti, Soft Matter **8**, 3002 (2012).
[87]J. Happel and H. Brenner, *Low Reynolds Number Hydrodynamics* (Martinus Neijhoff Publishers, 1983).
[88]J. K. G. Dhont, *An Introduction to Dynamics of Colloids* (Elsevier, 1996).
[89]M. Reichert and H. Stark, Phys. Rev. E **69**, 031407 (2004).
[90]H. Brenner, Chem. Eng. Sci. **18**, 1 (1963).
[91]P. Mazur and W. Van Saarloos, Physica A **115**, 21 (1982).
[92]A. A. Evans, T. Ishikawa, T. Yamaguchi, and E. Lauga, Phys. Fluids **23**, 111702 (2011).
[93]F. Alarcon and I. Pagonabarraga, J. Mol. Liq. **185**, 56 (2013).
[94]A. Zöttl and H. Stark, Phys. Rev. Lett. **112**, 118101 (2014).
[95]R. M. Navarro and I. Pagonabarraga, Eur. Phys. J. E **33**, 27 (2010).
[96]B. M. Mladek, D. Gottwald, G. Kahl, M. Neumann, and C. N. Likos, Phys. Rev. Lett. **96**, 045701 (2006).
[97]H. H. Wensink, V. Kantsler, R. E. Goldstein, and J. Dunkel, Phys. Rev. E **89**, 010302 (2014).
[98]A. J. Archer, M. C. Walters, U. Thiele, and E. Knobloch, Phys. Rev. E **90**, 042404 (2014).
[99]M. Doi and S. F. Edwards, *The Theory of Polymer Dynamics* (Oxford University Press, 1988).
[100]J.-P. Hansen and I. R. McDonald, *Theory of Simple Liquids* (Elsevier, 1990).
[101]Y. Singh, Phys. Rep. **207**, 351 (1991).
[102]R. Evans, in *Fundamentals of Inhomogeneous Fluids*, edited by D. Henderson (Marcel Dekker, 1992), pp. 85–176.
[103]R. Evans, in *Lecture Notes 3rd Warsaw School of Statistical Physics*, edited by B. Cichocki, M. Napiórkowski, and J. Piasecki (Warsaw University Press, 2010), pp. 43–85.
[104]H. Löwen, in *Lecture Notes 3rd Warsaw School of Statistical Physics*, edited by B. Cichocki, M. Napiórkowski, and J. Piasecki (Warsaw University Press, 2010), pp. 87–121.
[105]H. Risken, *The Fokker-Planck Equation* (Springer, 1984).
[106]H.-R. Jiang, N. Yoshinaga, and M. Sano, Phys. Rev. Lett. **105**, 268302 (2010).
[107]G. Volpe, I. Buttinoni, D. Vogt, H.-J. Kümmerer, and C. Bechinger, Soft Matter **7**, 8810 (2011).
[108]I. Buttinoni, G. Volpe, F. Kümmel, G. Volpe, and C. Bechinger, J. Phys.: Condens. Matter **24**, 284129 (2012).
[109]S. Babel, B. ten Hagen, and H. Löwen, J. Stat. Mech. **2014**, P02011.
[110]A. M. Menzel, EPL **110**, 38005 (2015).
[111]J. Tailleur and M. E. Cates, EPL **86**, 60002 (2009).
[112]M. Enculescu and H. Stark, Phys. Rev. Lett. **107**, 058301 (2011).
[113]A. Pototsky and H. Stark, EPL **98**, 50004 (2012).
[114]I. K. Ono, C. S. O'Hern, D. J. Durian, S. A. Langer, A. J. Liu, and S. R. Nagel, Phys. Rev. Lett. **89**, 095703 (2002).
[115]U. Seifert, Rep. Prog. Phys. **75**, 126001 (2012).
[116]H. H. Wensink, H. Löwen, M. Marechal, A. Härtel, R. Wittkowski, U. Zimmermann, A. Kaiser, and A. M. Menzel, Eur. Phys. J.: Spec. Top. **222**, 3023 (2013).
[117]L. Baraban, D. Makarov, R. Streubel, I. Mönch, D. Grimm, S. Sanchez, and O. G. Schmidt, ACS Nano **6**, 3383 (2012).

P2 Dynamical density functional theory for circle swimmers

Reproduced from

C. Hoell, H. Löwen, and A. M. Menzel,
Dynamical density functional theory for circle swimmers,
New J. Phys. **19**, 125004 (2017),
published by *IOP Publishing Ltd* on behalf of *Deutsche Physikalische Gesellschaft.*

Digital Object Identifier (DOI): `https://doi.org/10.1088/1367-2630/aa942e`

Statement of contribution

AMM and HL supervised this work. All authors developed the theory, which included a new model microswimmer and adjustments in the statistical description when compared to a former study. I performed the numerical evaluations, prepared all figures, and implemented several order parameters to quantify parts of the results. I drafted the manuscript, which then AMM and I completed. All authors discussed and interpreted the results, edited the text, and finalized the manuscript.

Copyright and license notice

IOP Publishing New J. Phys. 19 (2017) 125004 https://doi.org/10.1088/1367-2630/aa942e

New Journal of Physics

The open access journal at the forefront of physics

Deutsche Physikalische Gesellschaft DPG
IOP Institute of Physics

Published in partnership with: Deutsche Physikalische Gesellschaft and the Institute of Physics

CrossMark

OPEN ACCESS

RECEIVED
13 July 2017

REVISED
21 September 2017

ACCEPTED FOR PUBLICATION
17 October 2017

PUBLISHED
5 December 2017

PAPER

Dynamical density functional theory for circle swimmers

Christian Hoell, Hartmut Löwen and Andreas M Menzel

Institut für Theoretische Physik II: Weiche Materie, Heinrich-Heine-Universität Düsseldorf, D-40225 Düsseldorf, Germany

E-mail: menzel@thphy.uni-duesseldorf.de

Keywords: microswimmer suspensions, circle swimmers, active matter, hydrodynamic interactions, dynamical density functional theory, statistical physics

Abstract

The majority of studies on self-propelled particles and microswimmers concentrates on objects that do not feature a deterministic bending of their trajectory. However, perfect axial symmetry is hardly found in reality, and shape-asymmetric active microswimmers tend to show a persistent curvature of their trajectories. Consequently, we here present a particle-scale statistical approach to circle-swimmer suspensions in terms of a dynamical density functional theory. It is based on a minimal microswimmer model and, particularly, includes hydrodynamic interactions between the swimmers. After deriving the theory, we numerically investigate a planar example situation of confining the swimmers in a circularly symmetric potential trap. There, we find that increasing curvature of the swimming trajectories can reverse the qualitative effect of active drive. More precisely, with increasing curvature, the swimmers less effectively push outwards against the confinement, but instead form high-density patches in the center of the trap. We conclude that the circular motion of the individual swimmers has a localizing effect, also in the presence of hydrodynamic interactions. Parts of our results could be confirmed experimentally, for instance, using suspensions of L-shaped circle swimmers of different aspect ratio.

1. Introduction

On the scales of active colloidal particles and self-propelled biological microswimmers [1–10], thermal fluctuations and other perturbations play a prominent role. They lead to continuous reorientation of the self-propelling objects and therefore to stochastically shaped trajectories [2, 3, 11]. Even more extreme events are given by stochastic run-and-tumble motions. For instance, certain bacteria or alga cells are observed to stop their migration, reorient basically on the spot, and then continue their propulsion [1, 12]. Such events lead to kinks on the trajectory. The statistics of both types of buckled motion has been studied in detail, both in experiment and in theory [1, 3, 11, 13–19]. Yet, in the absence of any noise, fluctuations, and perturbations, the self-propelling agents considered in most theoretical analyses would show a deterministic straight motion.

Here, we concentrate on active microswimmers that feature a different behavior. Their individual trajectories are systematically curved. Such a situation can arise only, if for each swimmer the axial symmetry around its propulsion direction is broken.

On the one hand, the symmetry breaking can be induced from outside. For instance, if microswimmers are exposed to local surrounding shear flows, the rotational component of the fluid flow can couple to the orientation of the suspended swimmer [15, 20–25]. Continuous reorientation of the propulsion direction leads to curved trajectories. Similarly, the symmetry is broken in the presence of a nearby surface. If during propulsion a swimmer shows rotations of its body around its axis, these rotations can on one side hydrodynamically interact with the surface. Via such hydrodynamic surface interactions the self-rotation couples to the propulsion direction and the trajectory bends. Also steric interactions can support or induce the effect. Thus circular trajectories are observed for many sperm cells and bacteria close to a substrate [26–30].

On the other hand, real swimmers often bring along a broken axial symmetry by themselves [31]. Hardly any object is really perfectly axially symmetric in shape. On purpose, L-shaped active microswimmers have been fabricated and their persistently curved trajectories were analyzed [32–35]. If the trajectories, including their persistent bending, are confined to a plane, then circular paths arise. This is what we understand by circle swimmers [36]. Apart from that, for deformable self-propelled particles and self-propelled nematic droplets, the symmetry breaking in shape or structure may also occur spontaneously [37–39]. Moreover, imperfections in the self-propulsion mechanism can lead to the symmetry breaking and thus to bent trajectories. An example are cells of the alga *Chlamydomonas reinhardtii*. If one of the two beating flagella generating self-propulsion is weaker or absent, the cellular paths curve [40, 41]. Apart from that, near surfaces bent self-propelled objects tend to follow circular trajectories [42, 43]. In modeling approaches, circle swimmers are often realized by simply imposing an effective torque or rotational drive in addition to the self-propulsion mechanism [15, 31, 35, 44–59].

We have mentioned above that studies on circle swimmers are relatively rarely encountered when compared to the numbers of works on objects propelling straight ahead. Even less frequent are studies on the collective behavior of circle swimmers [29, 43, 50, 52, 54]. Particularly, this applies when hydrodynamic interactions in crowds of suspended microswimmers are to be included.

When the collective properties of many interacting agents are investigated, such statistical approaches become important [60–66]. Recently, we have derived and evaluated a microscopic statistical description for straight-propelling microswimmers in terms of a classical dynamical density functional theory (DDFT) [66]. Microscopic here means that the description is based and operates on the length scales of the individual agents. Thus, for instance, when classical density functional theory (DFT) or its variants are used to describe the properties of crystalline structures [67–80], individual crystal peaks can be resolved in the statistical density field.

In equilibrium, i.e., for passive systems, DFT [81–85] is, in principle, an exact theory. It can be extended to overdamped relaxational dynamics in terms of DDFT [85–88] by assuming at each instant an effective equilibrium situation to evaluate the involved potential interactions. For example, solidification processes are addressed in this way [71, 72, 74, 78]. Since microswimmers by construction operate at low Reynolds numbers [89], their dynamics is overdamped. This makes DDFT a promising candidate to study their statistical behavior.

Extending DFT to intrinsically non-equilibrium systems, DDFTs for ‘dry’ self-propelling agents had already been developed before [90–92] and tested against agent-based simulations [90, 92]. Moreover, to characterize passive colloidal particles in suspensions, hydrodynamic interactions had been incorporated into DDFT [93–99] and agreement was found with explicit particle-based simulations [93, 94, 96, 97]. Our recently developed DDFT for microswimmers incorporates and combines all the central previous ingredients, i.e., self-propulsion, steric interactions between the swimmers, hydrodynamic interactions between the swimmers, as well as exposure to and confinement by external potentials [66]. As we have demonstrated and as further detailed below, this dynamical theory qualitatively reproduces previous simulation results [100, 101] in which combined action of all these ingredients determines the overall behavior.

Here, we proceed by an additional step forward. We extend our microscopic statistical characterization (DDFT) to circle swimmers. In this way, we can now characterize the collective behavior of such non-straight-propelling agents, including the effect of hydrodynamic interactions. Only then, for instance and as we will show below, can the symmetry breaking induced by hydrodynamic interactions in a radial confinement be described qualitatively correctly.

We first introduce our minimal model for circle swimmers in section 2. Next, in section 3, we list the extension of the theory. It is evaluated numerically in section 4 to study the behavior of circle swimmers under radial confinement as a function of the bending of their trajectory. A short summary and outlook are given in section 5.

2. Minimal model circle swimmer

As outlined above, our goal is to establish a microscopic DDFT of circle-swimmer suspensions. The term ‘microscopic’ here refers to the length scales of an individual microswimmer. To base our DDFT on such scales, we need to first introduce an explicit minimal model for a microscopic circle swimmer.

Our statistical theory will apply to (semi)dilute suspensions of microswimmers based on their far-field hydrodynamic interactions. Therefore, a minimal model microswimmer is needed that shows the correct leading-order far-field hydrodynamic fluid flows together with a self-consistent description of its self-propulsion. Yet, at the same time, it must be simple enough to still be efficiently included into the statistical description. Figure 1 represents our corresponding swimmer model. The unit vector $\hat{\mathbf{n}}$ identifies the principal swimmer axis and orientation.

Any active microswimmer exerts forces onto the surrounding fluid. Amongst them are the spatially distributed active forces that initiate self-propulsion. They are generated, for instance, by the rotation of flagella or beating of cilia [12, 14, 40, 41]. In our model, all these active forces are thought to be gathered and concentrated in one spot. In figure 1, this leads to the active point force $-\boldsymbol{f}$ acting on the surrounding fluid. Instantly, due to the nature of the considered low-Reynolds-number motion, see below [89], for a freely

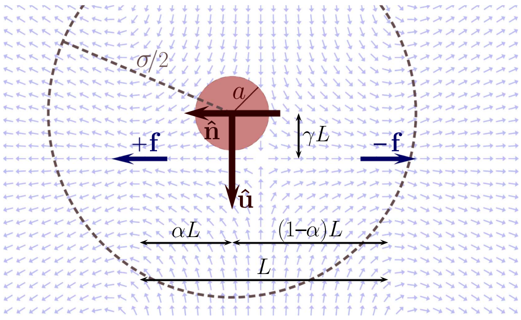

Figure 1. Minimal model of a circle microswimmer. Two active force centers separated by a distance L exert the active forces $\pm\boldsymbol{f} = \pm f\,\hat{\mathbf{n}}$ onto the fluid, where $\hat{\mathbf{n}}$ marks the direction of the principal swimmer axis. The resulting fluid flow is indicated by the small light arrows that are rescaled to identical length for visualization. A spherical swimmer body of effective hydrodynamic radius a is, in general, asymmetrically placed between the force centers. Its shift along $\hat{\mathbf{n}}$ out of the symmetry center, quantified by $\alpha \neq 1/2$, leads to forward (or backward) propulsion. An additional transversal shift, quantified by γ, implies circular trajectories for $\alpha \neq 1/2$ and $\gamma \neq 0$. This circle swimmer is biaxial, the secondary axis denoted by $\hat{\mathbf{u}}$. We impose spherically symmetric steric interactions between the swimmers, with an effective interaction radius $\sigma/2$.

suspended microswimmer all these active forces are balanced by frictional forces distributed over its body. We consider all these counteracting frictional forces to be concentrated in another spot, leading to the point force $+\boldsymbol{f}$ in figure 1. These two spots in general do not coincide, depending on the actual swimmer geometry. Here, they are separated by a distance L, see figure 1. However, since no net force nor torque may act on a freely suspended microswimmer, the two forces $\pm\boldsymbol{f}$ need to be of same magnitude but oppositely oriented, located and aligned along a common axis. We may thus parameterize them as $\pm\boldsymbol{f} = \pm f\,\hat{\mathbf{n}}$. They act onto the fluid and set it into motion as indicated by the small arrows in the background of figure 1. In analogy to straight-swimming terminology [4], for $f > 0$, i.e., the depicted case, we call the object a *pusher*. For $f < 0$, we term it a *puller*.

Next, we place a spherical swimmer body of effective hydrodynamic radius a nearby the two force centers. The whole construct is a rigid object, i.e., the force centers and forces have to rigidly translate and rotate together with the sphere, maintaining their mutual distances and orientations. The role of the sphere is purely to realize self-propulsion of the whole object. Since all forces exerted by the swimmer onto the fluid have already been concentrated into the two force centers (ignoring all forces that lead to higher-order contributions to the hydrodynamic far-field) the sphere is considered not to exert any remaining force onto the fluid any longer. Its sole role is to be convected by the self-induced fluid flow, leading to the overall self-propulsion. Unless it is positioned into the exact point of symmetry between the two force centers, a net transport of the swimmer results in the induced fluid flow. For a shift of the sphere along $\hat{\mathbf{n}}$ out of the symmetry plane between the two force centers, the whole object propels into the direction of one of the two forces. This shift is quantified by the parameter α, with $\alpha = 1/2$ marking the symmetric configuration.

In addition to our swimmer model in [66], we now consider an extra shift of the spherical swimmer body into a direction perpendicular to $\hat{\mathbf{n}}$. The parameter γ quantifies this shift, see figure 1, so that the axial symmetry is broken for $\gamma \neq 0$. Consequently, for $\alpha \neq 1/2$ and $\gamma \neq 0$, the swimmer in the absence of any fluctuations starts to circle, as quantified below. Moreover, it is now biaxial, with the additional axis marked as $\hat{\mathbf{u}}$, see figure 1.

Since we consider the hydrodynamic interactions at a far-field level, we need to hinder the microswimmers from coming too close to each other. Therefore, we consider spherically symmetric soft steric interactions between the swimmer bodies of effective radius $\sigma/2 > [(\max\{\alpha,\ 1-\alpha\})^2 + \gamma^2]^{1/2}\,L$ to maintain an effective distance between them. Altogether, the whole rigid swimmer object in figure 1 is force- and torque-free, as mandatory for a microswimmer suspended in a bulk fluid, see also the appendix.

2.1. Hydrodynamic interactions

We now consider N identical circle microswimmers suspended in the fluid and use indices $i = 1, \ldots, N$ to label them. As described above, for $f \neq 0$, each circle swimmer sets the surrounding fluid into motion due to its active forces exerted by the active force centers. In addition to that, the swimmer bodies may be subjects to forces $\boldsymbol{F}_i$ and torques $\boldsymbol{T}_i$. These may, for instance, be stochastic in nature, result from steric interactions between the circle swimmers, or be imposed from outside. Since the dynamics of microswimmers is usually determined by low Reynolds numbers [89], it is described by the linear Stokes equation [102]. That is, their dynamics is overdamped, and the forces $\boldsymbol{F}_i$ and torques $\boldsymbol{T}_i$ are directly transmitted to the surrounding fluid, setting it into motion. Moreover, since the swimmers are suspended in the fluid, they are translated and rotated by the induced fluid flows. The instantly resulting swimming velocities $\boldsymbol{v}_i$ and angular velocities $\boldsymbol{\omega}_i$ are calculated from a matrix equation as [66]

$$\begin{bmatrix} \boldsymbol{v}_i \\ \boldsymbol{\omega}_i \end{bmatrix} = \sum_{j=1}^{N} \left(\begin{bmatrix} \boldsymbol{\mu}_{ij}^{\mathrm{tt}} & \boldsymbol{\mu}_{ij}^{\mathrm{tr}} \\ \boldsymbol{\mu}_{ij}^{\mathrm{rt}} & \boldsymbol{\mu}_{ij}^{\mathrm{rr}} \end{bmatrix} \cdot \begin{bmatrix} \boldsymbol{F}_j \\ \boldsymbol{T}_j \end{bmatrix} + \begin{bmatrix} \boldsymbol{\Lambda}_{ij}^{\mathrm{tt}} & \mathbf{0} \\ \boldsymbol{\Lambda}_{ij}^{\mathrm{rt}} & \mathbf{0} \end{bmatrix} \cdot \begin{bmatrix} f\hat{\mathbf{n}}_j \\ \mathbf{0} \end{bmatrix} \right) \tag{1}$$

for $i = 1, \ldots, N$.

In (1), the first product on the right-hand side includes the influence of the passive swimmer bodies. $\boldsymbol{\mu}_{ij}^{\mathrm{tt}}$, $\boldsymbol{\mu}_{ij}^{\mathrm{tr}}$, $\boldsymbol{\mu}_{ij}^{\mathrm{rt}}$, and $\boldsymbol{\mu}_{ij}^{\mathrm{rr}}$ are the familiar mobility matrices that express how swimmer i is translated and rotated due to the forces and torques transmitted by the swimmer body j onto the fluid [66, 102–104]. These expressions are the same as for suspended passive colloidal particles and result from an expansion in the inverse separation distance between the swimmer bodies, where here we proceed up to the third order, i.e., the Rotne–Prager level.

Then, for $i = j$, we have [66, 102–104]

$$\boldsymbol{\mu}_{ii}^{\mathrm{tt}} = \mu^{\mathrm{t}}\mathbf{1}, \quad \boldsymbol{\mu}_{ii}^{\mathrm{rr}} = \mu^{\mathrm{r}}\mathbf{1}, \quad \boldsymbol{\mu}_{ii}^{\mathrm{tr}} = \boldsymbol{\mu}_{ii}^{\mathrm{rt}} = \mathbf{0}, \tag{2}$$

with

$$\mu^{\mathrm{t}} = \frac{1}{6\pi\eta a}, \qquad \mu^{\mathrm{r}} = \frac{1}{8\pi\eta a^3}. \tag{3}$$

Here, η is the viscosity of the fluid.

For $i \neq j$, the mobility matrices read [66, 102–104]

$$\boldsymbol{\mu}_{ij}^{\mathrm{tt}} = \mu^{\mathrm{t}} \left(\frac{3a}{4r_{ij}} (\mathbf{1} + \hat{\mathbf{r}}_{ij}\hat{\mathbf{r}}_{ij}) + \frac{1}{2} \left(\frac{a}{r_{ij}} \right)^3 (\mathbf{1} - 3\hat{\mathbf{r}}_{ij}\hat{\mathbf{r}}_{ij}) \right), \tag{4}$$

$$\boldsymbol{\mu}_{ij}^{\mathrm{rr}} = -\frac{1}{2} \mu^{\mathrm{r}} \left(\frac{a}{r_{ij}} \right)^3 (\mathbf{1} - 3\hat{\mathbf{r}}_{ij}\hat{\mathbf{r}}_{ij}), \tag{5}$$

$$\boldsymbol{\mu}_{ij}^{\mathrm{tr}} = \boldsymbol{\mu}_{ij}^{\mathrm{rt}} = \mu^{\mathrm{r}} \left(\frac{a}{r_{ij}} \right)^3 \boldsymbol{r}_{ij} \times , \tag{6}$$

where $\boldsymbol{r}_{ij} = \boldsymbol{r}_j - \boldsymbol{r}_i$, with $\boldsymbol{r}_i$ and $\boldsymbol{r}_j$ marking the swimmer positions, $r_{ij} = |\boldsymbol{r}_{ij}|$, $\hat{\mathbf{r}}_{ij} = \boldsymbol{r}_{ij}/r_{ij}$, and '$\times$' is the vector product.

The second product on the right-hand side of (1) arises because of the active forces that the swimmers exert onto the fluid. Naturally, these actively induced fluid flows likewise contribute to the velocities $\boldsymbol{v}_i$ and angular velocities $\boldsymbol{\omega}_i$ of all swimmer bodies. $\boldsymbol{\Lambda}_{ij}^{\mathrm{tt}}$ and $\boldsymbol{\Lambda}_{ij}^{\mathrm{rt}}$ are the corresponding mobility matrices. The entries $\mathbf{0}$ in these expressions arise because our swimmers do not exert active torques onto the suspending fluid.

More precisely, the mobility matrices $\boldsymbol{\Lambda}_{ij}^{\mathrm{tt}}$ and $\boldsymbol{\Lambda}_{ij}^{\mathrm{rt}}$ describe how the active forces exerted by the two force centers of swimmer j onto the fluid influence the velocity $\boldsymbol{v}_i$ and angular velocity $\boldsymbol{\omega}_i$ of swimmer i, respectively. Since swimmer j carries two active force centers exerting the two forces $\pm\boldsymbol{f}_j = \pm f\hat{\mathbf{n}}_j$, both $\boldsymbol{\Lambda}_{ij}^{\mathrm{tt}}$ and $\boldsymbol{\Lambda}_{ij}^{\mathrm{rt}}$ split into two contributions [66],

$$\boldsymbol{\Lambda}_{ij}^{\mathrm{tt}} = \boldsymbol{\mu}_{ij}^{\mathrm{tt}+} - \boldsymbol{\mu}_{ij}^{\mathrm{tt}-}, \tag{7}$$

$$\boldsymbol{\Lambda}_{ij}^{\mathrm{rt}} = \boldsymbol{\mu}_{ij}^{\mathrm{rt}+} - \boldsymbol{\mu}_{ij}^{\mathrm{rt}-}. \tag{8}$$

In contrast to the passive swimmer bodies, the active force centers are point-like. Therefore, the expressions for the four mobility matrices $\boldsymbol{\mu}_{ij}^{\mathrm{tt}\pm}$ and $\boldsymbol{\mu}_{ij}^{\mathrm{rt}\pm}$ are slightly modified when compared to the corresponding expressions for the hydrodynamic interactions between the passive swimmer bodies in (4) and (6) [66],

$$\boldsymbol{\mu}_{ij}^{\mathrm{tt}\pm} = \frac{1}{8\pi\eta r_{ij}^{\pm}} (\mathbf{1} + \hat{\mathbf{r}}_{ij}^{\pm}\hat{\mathbf{r}}_{ij}^{\pm}) + \frac{a^2}{24\pi\eta (r_{ij}^{\pm})^3} (\mathbf{1} - 3\hat{\mathbf{r}}_{ij}^{\pm}\hat{\mathbf{r}}_{ij}^{\pm}), \tag{9}$$

$$\boldsymbol{\mu}_{ij}^{\mathrm{rt}\pm} = \frac{1}{8\pi\eta (r_{ij}^{\pm})^3} \boldsymbol{r}_{ij}^{\pm} \times . \tag{10}$$

Here, $\boldsymbol{r}_{ij}^{\pm}$ are the distance vectors between the passive body of swimmer i and the active force centers of swimmer j, exerting the forces $\pm\boldsymbol{f}_j = \pm f\hat{\mathbf{n}}_j$ onto the fluid, respectively. Again, $r_{ij}^{\pm} = |\boldsymbol{r}_{ij}^{\pm}|$ and $\hat{\mathbf{r}}_{ij}^{\pm} = \boldsymbol{r}_{ij}^{\pm}/r_{ij}^{\pm}$. In contrast to [66], where straight-propelling microswimmers were investigated, we here must take into account the additional transversal shift of the active force centers with respect to the swimmer bodies, see figure 1. Therefore, we now obtain

$$\boldsymbol{r}_{ij}^{+} = \boldsymbol{r}_{ij} + \alpha L\hat{\mathbf{n}}_j + \gamma L\hat{\mathbf{u}}_j, \tag{11}$$

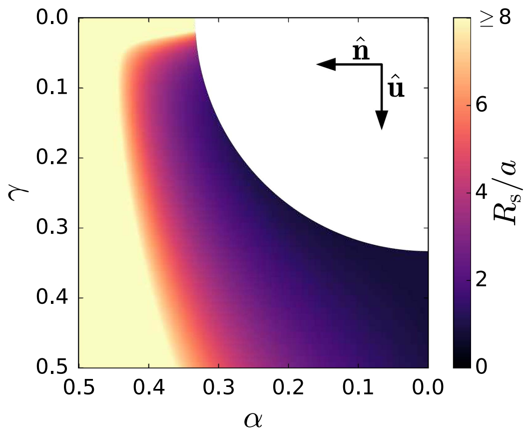

Figure 2. Radius R_s of the circular trajectory at vanishing fluctuations for one single isolated circle microswimmer as introduced in figure 1 ($L/a = 3$). The color map indicates R_s as a function of α and γ. For $\gamma \to 0$, $R_s/a \to \infty$ and the swimmer self-propels straight ahead. We do not allow a force center to be placed within the hydrodynamic radius a from the center of the swimmer body, reflected by the white area on the top right.

$$\boldsymbol{r}_{ij}^{-} = \boldsymbol{r}_{ij} - (1 - \alpha)L\hat{\mathbf{n}}_j + \gamma L\hat{\mathbf{u}}_j. \tag{12}$$

Naturally, the values of α and γ must assure that the force centers of each swimmer are located outside the hydrodynamic radius a of the swimmer body, i.e., $[(\min\{\alpha, 1 - \alpha\})^2 + \gamma^2]^{1/2} L > a$.

We consider our spherical swimmer body to exclusively act as a probe particle. Therefore our active mobility matrices for interactions between different swimmers ($i \neq j$) are given to lowest order in $(\alpha - 1/2)$ and/or a/L. In a next step, the distortion of the flow field by the rigid swimmer body could be included by considering the image system within a rigid sphere [105, 106].

Moreover, for $i = j$, (1) together with (7)–(12) describe the self-propelled motion of one individual circle swimmer. At the moment not considering any fluctuations, one such isolated microswimmer ($N = 1$) keeps self-propelling with constant translational speed v_s and constant angular speed ω_s along a closed circular trajectory of radius $R_s = v_s/\omega_s$ for all times. Since both v_s and ω_s depend on the position of the swimmer body relative to the two force centers, R_s can smoothly be tuned between almost zero and infinity by altering the parameters α and γ; see figure 2. Moreover, both $\boldsymbol{\Lambda}_{ii}^{\mathrm{tt}}$ and $\boldsymbol{\Lambda}_{ii}^{\mathrm{rt}}$ are independent of f. Thus, both v_s and ω_s scale linearly with f, see (7)–(12). Therefore, R_s is independent of the active force f. Swimming faster does not change the radius of the circle.

Technically, our mobility matrices represent the solutions to the underlying Stokes equation for the flow of the suspending fluid at low Reynolds number [102]. In this way, the role of the fluid is implicitly included in our description.

2.2. Stochastic forces, external forces, and steric interactions

Our remaining task is to specify the forces $\boldsymbol{F}_i$ and torques $\boldsymbol{T}_i$ acting on the swimmer bodies in (1). The forces are set to

$$\boldsymbol{F}_i = -k_B T\ \nabla_i \ln P - \nabla_i U. \tag{13}$$

Here, the first contribution represents the effective influence of the stochastic forces due to thermal fluctuations [107]. k_B is the Boltzmann constant, T the temperature, $\nabla_i = \partial/\partial\boldsymbol{r}_i$, and $P = P(\boldsymbol{r}_1, \hat{\mathbf{n}}_1, \hat{\mathbf{u}}_1, \ldots, \boldsymbol{r}_N, \hat{\mathbf{n}}_N, \hat{\mathbf{u}}_N, t)$ is the probability density to find at a certain time t the swimmers at positions $\boldsymbol{r}_i$ with orientations $\hat{\mathbf{n}}_i$ and $\hat{\mathbf{u}}_i$, $i = 1, \ldots, N$. From this form, the correct diffusional behavior is reproduced in the statistical approach, see below.

The overall potential in the second part of (13) reads

$$U = \frac{1}{2}\sum_{k,l=1;k\neq l}^{N} u(\boldsymbol{r}_k, \boldsymbol{r}_l) + \sum_{k=1}^{N} u_{\mathrm{ext}}(\boldsymbol{r}_k). \tag{14}$$

In this expression, the first term describes the steric interactions between the swimmer bodies. We here choose a soft GEM-4 potential of the form [78, 108]

$$u(\boldsymbol{r}_k, \boldsymbol{r}_l) = \epsilon_0 \exp\left(-\frac{r_{kl}^4}{\sigma^4}\right), \tag{15}$$

where ϵ_0 sets the strength of the interactions. u_{ext} is an external potential acting on each swimmer body and further addressed below.

Finally, the only torques that we consider to act on our spherically symmetric swimmer bodies are stochastic ones,

$$\boldsymbol{T}_i = -k_B T\ \nabla_i^{\text{or}} \ln P. \tag{16}$$

Here, the operator ∇_i^{or} contains the derivatives with respect to the particle orientations. If the swimmers and their orientations are confined to a flat plane, for instance, the xy plane in Cartesian coordinates, one angle φ_i is sufficient to characterize the orientation of each swimmer i. Then the operator reduces to $\nabla_i^{\text{or}} = \hat{\boldsymbol{z}}\, \partial/\partial\varphi_i$, where $\hat{\boldsymbol{z}}$ is the (oriented) Cartesian unit vector perpendicular to the xy plane in a three-dimensional Euclidean space. In three dimensions, explicit expressions using Eulerian angles exist [91, 109].

3. DDFT for circle swimmers

Based on our minimal microswimmer model, we can now derive a microscopic statistical description in terms of a DDFT for suspensions of identical circle swimmers. The derivation follows the same lines as in our previous work on straight-propelling microswimmers [66]. However, several changes result from the present biaxiality of the individual swimmers.

We start from the microscopic Smoluchowski equation

$$\frac{\partial P}{\partial t} = -\sum_{i=1}^{N}(\nabla_i \cdot (\boldsymbol{v}_i P) + \nabla_i^{\text{or}} \cdot (\boldsymbol{\omega}_i P)), \tag{17}$$

which states the conservation of the overall probability density. Here, we have to insert the swimmer velocities $\boldsymbol{v}_i$ and angular velocities $\boldsymbol{\omega}_i$ as given by (1)–(16). Although $\boldsymbol{v}_i$ and $\boldsymbol{\omega}_i$ depend on $\ln P$ via (13) and (16), it is important to stress that (17) is still linear in P. Using the chain rule in (13) leads to $\nabla_i \ln P = (\nabla_i P)/P$, which in combination with the factor P in (17) leads to the linear contribution $\nabla_i P$. The same argument applies to the term $\nabla_i^{\text{or}} \ln P$ in (16) when inserted into (17).

To obtain from (17) the n-swimmer density of finding n of the identical N circle swimmers at a certain time at certain positions with certain orientations, we must integrate out from (17) all but the degrees of freedom of n swimmers. We denote by $\boldsymbol{X}_i$ all degrees of freedom of the ith swimmer. Then, the n-swimmer density is obtained from the overall probability density P as

$$\rho^{(n)}(\boldsymbol{X}_1, \ldots, \boldsymbol{X}_n, t) = \frac{N!}{(N-n)!}\int \mathrm{d}\boldsymbol{X}_{n+1} \ldots \mathrm{d}\boldsymbol{X}_N\ P. \tag{18}$$

In the special case of all swimmers and their orientations being confined to a flat plane, $\boldsymbol{X}_i = (\boldsymbol{r}_i, \varphi_i)$ and $\mathrm{d}\boldsymbol{X}_i = \mathrm{d}\boldsymbol{r}_i \mathrm{d}\varphi_i$.

Our goal is to obtain an equation for the dynamics of the one-swimmer density $\rho^{(1)}(\boldsymbol{X}, t)$ to find a circle swimmer at time t with position and orientation $\boldsymbol{X}$. However, the integration scheme in (18) leads to a non-closed equation for the time derivative of $\rho^{(1)}$. Because of our pairwise hydrodynamic and steric interactions, $\rho^{(1)}$ couples to the pair density $\rho^{(2)}$, and, in combination of both interactions, also to $\rho^{(3)}$ [66, 93, 94]. This starts a whole hierarchy of coupled dynamical equations, called BBGKY hierarchy [81]. To close the dynamical equation for $\rho^{(1)}$, we need to express the densities $\rho^{(2)}$ and $\rho^{(3)}$ in this equation as a function of $\rho^{(1)}$. DDFT provides a strategy by mapping each state of the system instantaneously to a corresponding equilibrium situation [85–88].

For this purpose, we recall that an external potential enters the dynamical equation via (14). At each moment in time, DDFT assumes that the instant state of the system is caused by an effective external potential Φ_{ext}. This Φ_{ext} intermittently takes the place of our physical external potential u_{ext}.

In equilibrium, DFT implies that Φ_{ext} is uniquely determined by the density $\rho^{(1)}$ [81–88]. It follows by minimizing the grand canonical potential functional Ω

$$\Omega[\rho^{(1)}] = \mathcal{F}_{\text{id}}[\rho^{(1)}] + \mathcal{F}_{\text{exc}}[\rho^{(1)}] + \mathcal{F}_{\text{ext}}[\rho^{(1)}] \tag{19}$$

with respect to $\rho^{(1)}$. Here,

$$\mathcal{F}_{\text{id}}[\rho^{(1)}] = k_B T \int \mathrm{d}\boldsymbol{X}\ \rho^{(1)}(\boldsymbol{X})(\ln(\lambda^3 \rho^{(1)}(\boldsymbol{X})) - 1) \tag{20}$$

is the entropic free-energy functional for ideal non-interacting particles, with λ the thermal de Broglie wave length [110]. An exact expression for the excess free-energy functional $\mathcal{F}_{\text{exc}}[\rho^{(1)}]$, which contains all particle interactions beyond the idealized non-interacting limit, is typically not known and needs to be approximated.

The third functional

$$\mathcal{F}_{\text{ext}}[\rho^{(1)}] = \int \mathrm{d}\boldsymbol{X}\; \Phi_{\text{ext}}(\boldsymbol{X})\rho^{(1)}(\boldsymbol{X}), \tag{21}$$

describes the interactions with the external potential, where the effect of a chemical potential is implicitly included into Φ_{ext}. Minimizing Ω with respect to $\rho^{(1)}$ leads to the equilibrium relation

$$\Phi_{\text{ext}}(\boldsymbol{X}) = -k_{\text{B}}T\,\ln(\lambda^3\rho^{(1)}(\boldsymbol{X})) - \frac{\delta\mathcal{F}_{\text{exc}}}{\delta\rho^{(1)}(\boldsymbol{X})}. \tag{22}$$

In equilibrium the swimmers are inactive ($f = 0$). Then, we may further argue that the corresponding N-swimmer probability density P^{eq} solely depends on the overall potential $U = U(\boldsymbol{X}_1, \ldots, \boldsymbol{X}_N)$ as in (14), but with Φ_{ext} taking the place of u_{ext}. Thus, P^{eq} should follow the Boltzmann form

$$P^{\text{eq}} \propto \exp(-\beta U), \tag{23}$$

with $\beta = (k_{\text{B}}T)^{-1}$. Applying to this relation the positional gradient for the ith swimmer, we obtain

$$\nabla_{\boldsymbol{r}_i}P^{\text{eq}} = -\beta\, P^{\text{eq}}\left(\nabla_{\boldsymbol{r}_i}\Phi_{\text{ext}}(\boldsymbol{r}_i) + \nabla_{\boldsymbol{r}_i}\sum_{k\neq i}^{N} u(\boldsymbol{r}_k, \boldsymbol{r}_i)\right). \tag{24}$$

We then follow (18) and integrate out all coordinates from this relation except for those of the ith swimmer. Since all swimmers are identical, this leads to the so-called YGB relations of first order [81, 109],

$$k_{\text{B}}T\;\nabla_{\boldsymbol{r}}\rho^{(1)}(\boldsymbol{X}) = -\rho^{(1)}(\boldsymbol{X})\nabla_{\boldsymbol{r}}\Phi_{\text{ext}}(\boldsymbol{X}) - \int \mathrm{d}\boldsymbol{X}'\rho^{(2)}(\boldsymbol{X}, \boldsymbol{X}')\nabla_{\boldsymbol{r}}u(\boldsymbol{r}, \boldsymbol{r}'). \tag{25}$$

The YGB relations of second order are obtained by integrating out from (24) all coordinates but those of the ith and one other swimmer [81, 109], resulting in

$$\begin{aligned} k_{\text{B}}T\;\nabla_{\boldsymbol{r}'}\rho^{(2)}(\boldsymbol{X}, \boldsymbol{X}') = &-\rho^{(2)}(\boldsymbol{X}, \boldsymbol{X}')\nabla_{\boldsymbol{r}'}\Phi_{\text{ext}}(\boldsymbol{X}') - \rho^{(2)}(\boldsymbol{X}, \boldsymbol{X}')\nabla_{\boldsymbol{r}'}u(\boldsymbol{r}, \boldsymbol{r}') \\ &- \int \mathrm{d}\boldsymbol{X}''\rho^{(3)}(\boldsymbol{X}, \boldsymbol{X}', \boldsymbol{X}'')\nabla_{\boldsymbol{r}'}u(\boldsymbol{r}', \boldsymbol{r}''). \end{aligned} \tag{26}$$

We then eliminate Φ_{ext} from the last two equations by inserting (22). The resulting relations

$$\int \mathrm{d}\boldsymbol{X}'\;\rho^{(2)}(\boldsymbol{X}, \boldsymbol{X}')\nabla_{\boldsymbol{r}}u(\boldsymbol{r}, \boldsymbol{r}') = \rho^{(1)}(\boldsymbol{X})\nabla_{\boldsymbol{r}}\frac{\delta\mathcal{F}_{\text{exc}}}{\delta\rho^{(1)}(\boldsymbol{X})} \tag{27}$$

and

$$\begin{aligned} \int \mathrm{d}\boldsymbol{X}''\;\rho^{(3)}(\boldsymbol{X}, \boldsymbol{X}', \boldsymbol{X}'')\nabla_{\boldsymbol{r}'}u(\boldsymbol{r}', \boldsymbol{r}'') = &-k_{\text{B}}T\;\nabla_{\boldsymbol{r}'}\rho^{(2)}(\boldsymbol{X}, \boldsymbol{X}') - \rho^{(2)}(\boldsymbol{X}, \boldsymbol{X}')\nabla_{\boldsymbol{r}'}u(\boldsymbol{r}, \boldsymbol{r}') \\ &+ k_{\text{B}}T\rho^{(2)}(\boldsymbol{X}, \boldsymbol{X}')\;\nabla_{\boldsymbol{r}'}\ln(\lambda^3\rho^{(1)}(\boldsymbol{X}', t)) \\ &+ \rho^{(2)}(\boldsymbol{X}, \boldsymbol{X}')\nabla_{\boldsymbol{r}'}\frac{\delta\mathcal{F}_{\text{exc}}}{\delta\rho^{(1)}(\boldsymbol{X}')} \end{aligned} \tag{28}$$

have the same structure as the corresponding ones in [66].

DDFT assumes that these relations are still instantly satisfied in non-equilibrium at each moment in time. All contained quantities are then assumed to be dynamical and non-equilibrium ones. In this way, they are inserted into the dynamical equation for $\rho^{(1)}$, which eliminates the dependence on $\rho^{(3)}$. Our assumption implies that the higher-order swimmer densities relax quickly when compared to the lower-order ones [111]. Since our motion at low Reynolds numbers is overdamped, it is conceivable that this adiabatic approximation leads to reasonable results. Previous comparison with particle simulations has confirmed this assertion qualitatively [66].

Altogether, we obtain from this procedure

$$\frac{\partial\rho^{(1)}(\boldsymbol{X}, t)}{\partial t} = -\nabla_{\boldsymbol{r}}\cdot(\mathcal{J}_1 + \mathcal{J}_2 + \mathcal{J}_3) - \nabla^{\text{or}}\cdot(\mathcal{J}_4 + \mathcal{J}_5 + \mathcal{J}_6), \tag{29}$$

where $\mathcal{J}_1, \ldots, \mathcal{J}_6$ are current densities. Overall, they are of similar structure as the corresponding quantities in [66], but particularly the active current densities $\mathcal{J}_3$ and $\mathcal{J}_6$ differ in the present case because of the transversal shift of the active force centers, see figure 1,

$$\begin{aligned} \mathcal{J}_1 = &-\mu^{\text{t}}\left(k_{\text{B}}T\;\nabla_{\boldsymbol{r}}\rho^{(1)}(\boldsymbol{X}, t) + \rho^{(1)}(\boldsymbol{X}, t)\nabla_{\boldsymbol{r}}u_{\text{ext}}(\boldsymbol{r}) + \rho^{(1)}(\boldsymbol{X}, t)\nabla_{\boldsymbol{r}}\frac{\delta\mathcal{F}_{\text{exc}}}{\delta\rho^{(1)}(\boldsymbol{X}, t)}\right) \\ &- \int \mathrm{d}\boldsymbol{X}'\boldsymbol{\mu}^{\text{tt}}_{\boldsymbol{r},\boldsymbol{r}'}\cdot\left(\rho^{(2)}(\boldsymbol{X}, \boldsymbol{X}', t)\left(k_{\text{B}}T\;\nabla_{\boldsymbol{r}'}\ln(\lambda^3\rho^{(1)}(\boldsymbol{X}', t)) + \nabla_{\boldsymbol{r}'}u_{\text{ext}}(\boldsymbol{r}')\right.\right. \\ &\left.\left.+ \nabla_{\boldsymbol{r}'}\frac{\delta\mathcal{F}_{\text{exc}}}{\delta\rho^{(1)}(\boldsymbol{X}', t)}\right)\right), \end{aligned} \tag{30}$$

$$\mathcal{J}_2 = -\int \mathrm{d}\boldsymbol{X}'\, \boldsymbol{\mu}^{\mathrm{tr}}_{\boldsymbol{r},\boldsymbol{r}'}\, k_{\mathrm{B}}T\ \nabla^{\mathrm{or}'}\rho^{(2)}(\boldsymbol{X}, \boldsymbol{X}', t), \tag{31}$$

$$\mathcal{J}_3 = f\left(\boldsymbol{\Lambda}^{\mathrm{tt}}_{\boldsymbol{r},\boldsymbol{r}} \cdot \hat{\mathbf{n}}\rho^{(1)}(\boldsymbol{X}, t) + \int \mathrm{d}\boldsymbol{X}'\boldsymbol{\Lambda}^{\mathrm{tt}}_{\boldsymbol{r},\boldsymbol{r}'} \cdot \hat{\mathbf{n}}'\rho^{(2)}(\boldsymbol{X}, \boldsymbol{X}', t)\right), \tag{32}$$

$$\mathcal{J}_4 = -\int \mathrm{d}\boldsymbol{X}'\boldsymbol{\mu}^{\mathrm{rt}}_{\boldsymbol{r},\boldsymbol{r}'}\left(\rho^{(2)}(\boldsymbol{X}, \boldsymbol{X}', t)\left(k_{\mathrm{B}}T\ \nabla_{\boldsymbol{r}'}\ln(\lambda^3\rho^{(1)}(\boldsymbol{X}', t)) + \nabla_{\boldsymbol{r}'}u_{\mathrm{ext}}(\boldsymbol{r}') + \nabla_{\boldsymbol{r}'}\frac{\delta\mathcal{F}_{\mathrm{exc}}}{\delta\rho^{(1)}(\boldsymbol{X}', t)}\right)\right), \tag{33}$$

$$\mathcal{J}_5 = -\mu^{\mathrm{r}}k_{\mathrm{B}}T\ \nabla^{\mathrm{or}}\rho^{(1)}(\boldsymbol{X}, t) - \int \mathrm{d}\boldsymbol{X}'\, \boldsymbol{\mu}^{\mathrm{rr}}_{\boldsymbol{r},\boldsymbol{r}'} \cdot k_{\mathrm{B}}T\ \nabla^{\mathrm{or}'}\rho^{(2)}(\boldsymbol{X}, \boldsymbol{X}', t), \tag{34}$$

$$\mathcal{J}_6 = f\left(\boldsymbol{\Lambda}^{\mathrm{rt}}_{\boldsymbol{r},\boldsymbol{r}}\hat{\mathbf{n}}\rho^{(1)}(\boldsymbol{X}, t) + \int \mathrm{d}\boldsymbol{X}'\, \boldsymbol{\Lambda}^{\mathrm{rt}}_{\boldsymbol{r},\boldsymbol{r}'}\, \hat{\mathbf{n}}'\rho^{(2)}(\boldsymbol{X}, \boldsymbol{X}', t)\right). \tag{35}$$

We note that, in our case, $\mathcal{J}_2 = \mathbf{0}$ in (31), and also the integral containing $\rho^{(2)}$ in (34) vanishes. The reason is the spherical shape of our passive swimmer bodies, resulting in passive hydrodynamic interactions that do not depend on the swimmer orientations.

For the excess functional, we choose a mean-field approximation

$$\mathcal{F}_{\mathrm{exc}} = \frac{1}{2}\int \mathrm{d}\boldsymbol{X}\ \mathrm{d}\boldsymbol{X}'\rho^{(1)}(\boldsymbol{X}, t)\rho^{(1)}(\boldsymbol{X}', t)u(\boldsymbol{r}, \boldsymbol{r}'), \tag{36}$$

which is reasonable in our case of soft GEM-4 steric interaction potentials. Still, some pair densities $\rho^{(2)}$ remain in (30)–(35). They are expressed in terms of $\rho^{(1)}$ using a dilute-limit Onsager-like approximation [112]

$$\rho^{(2)}(\boldsymbol{X}, \boldsymbol{X}', t) = \rho^{(1)}(\boldsymbol{X}, t)\rho^{(1)}(\boldsymbol{X}', t)\exp(-\beta V(\boldsymbol{r}, \boldsymbol{r}')). \tag{37}$$

Here, $V(\boldsymbol{r}, \boldsymbol{r}') = u(\boldsymbol{r}, \boldsymbol{r}')$, if $\boldsymbol{r} \neq \boldsymbol{r}'$. For $\boldsymbol{r} - \boldsymbol{r}' \to \mathbf{0}$, we let $\beta V \to \infty$ to avoid the hydrodynamic divergence that appears in the unphysical situation of two swimmers being located at the same position. This corresponds to setting $\exp(-\beta\epsilon_0) \to 0$ for $\boldsymbol{r} - \boldsymbol{r}' \to \mathbf{0}$. (For our typical choice of parameters, we obtain $\exp(-\beta\epsilon_0) = \exp(-10)$. Thus the procedure represents a relatively small modification.)

In this way, our dynamical equation for $\rho^{(1)}$ is derived and finally closed. To demonstrate the power of our DDFT for circle swimmers, we now address the confinement in a spherically symmetric trap. In particular, we focus on the effect of an increasing curvature of the swimming paths.

4. Circle swimmers in a spherically symmetric trap

To address planar geometries, we confine the center of mass of each swimmer i as well as its two orientation vectors $\hat{\mathbf{n}}_i$ and $\hat{\mathbf{u}}_i$ to the Cartesian xy plane so that $\hat{\mathbf{n}}_i \times \hat{\mathbf{u}}_i = \hat{\mathbf{z}}$. Then, one angle φ_i is sufficient to parameterize the swimmer orientation, see our remarks below (16). We measure φ_i relatively to the x axis. Still, three-dimensional hydrodynamic interactions apply. One possible realization of this geometry are swimmers confined to the interface between two immiscible fluids of identical viscosity.

Next, we specify the spherically symmetric confining external potential in (14). As in [66], we use a quartic potential

$$u_{\mathrm{ext}}(\boldsymbol{r}_k) = V_0\left(\frac{r_k}{\sigma}\right)^4, \tag{38}$$

centered in the origin, where $r_k = |\boldsymbol{r}_k|$. This potential is more shallow around the center and then shows a steeper increase than a harmonic trap, which partially emphasizes the effects that we address in the following. Yet the precise functional form is not relevant for their qualitative nature.

To evaluate our DDFT numerically, the finite-volume-method partial-differential-equation solver FiPy [113] is employed. Our numerical grid is regular, quadratic in the xy space, and typically consists of $80 \times 80 \times 16$ grid points for the x, y, and φ coordinates, respectively. (Non-orthogonal meshes might produce significant numerical errors due to the assumption of orthogonality by the solver [114, 115]. We avoid this by using an orthogonal grid.)

We only analyze the behavior in one single isolated trap. Nevertheless, for the numerical solution, periodic boundary conditions are imposed in all directions for technical reasons to allow for fast Fourier transformation. To avoid unphysical feedback between particles through the walls of the box, long-ranged hydrodynamic interactions are cut at distances larger than half a box length. Care is taken that the extension of the density cloud, before it basically decays to zero due to the external potential, is smaller than half a box length. In this way, the density cloud does not interact with itself through the periodic box boundaries. However, the box is large enough to account for all hydrodynamic interactions within the effective confinement by the spherical trap. The steric interactions in (15) are not cut as they quickly decay with increasing distance. If, instead of one single

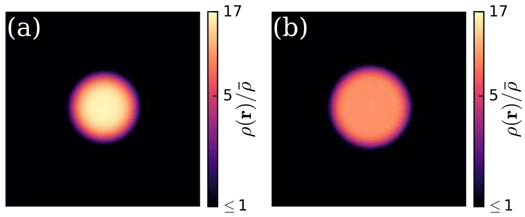

Figure 3. Equilibrated initial state for the numerical evaluation of our DDFT for microswimmer suspensions, with a trapping strength $V_0 = 0.1k_B T$. In this state, the active forces are still switched off, $f = 0$. (a) Steric interactions not included, $\epsilon_0 = 0$. (b) Steric interactions included with strength $\epsilon_0 = 10k_B T$. Brighter color reflects higher density as given by the scale bars, where we used a logarithmic scale for illustration. The local density $\rho(\boldsymbol{r})$ is normalized by the mean density $\bar{\rho} = 2.78 \times 10^{-2}\sigma^{-2}$ in the whole simulation box.

isolated trap, an array of periodically placed traps were to be regarded, one would have to account for the long-ranged hydrodynamic interactions between the individual traps including the periodic images of the system, e.g., via Ewald summation techniques [116–118].

To display our results, we extract the spatial swimmer density

$$\rho(\boldsymbol{r}, t) = \int \mathrm{d}\varphi\ \rho^{(1)}(\boldsymbol{r}, \varphi, t) \tag{39}$$

and the orientational vector field

$$\langle \hat{\mathbf{n}} \rangle (\boldsymbol{r}, t) = \int \mathrm{d}\varphi\ \hat{\mathbf{n}}(\varphi)\ \rho^{(1)}(\boldsymbol{r}, \varphi, t) \tag{40}$$

from our calculations. These two fields are indicated by color plots and by white arrows, respectively, in the figures referred to below. In these plots, the spatial density $\rho(\boldsymbol{r}, t)$ is normalized by the density $\bar{\rho}$ averaged over the whole simulation box.

As an initial condition, we start from randomized density distributions. The system is then equilibrated in the trap with self-propulsion switched off, $f = 0$. The density quickly relaxes into a radially decaying distribution with a small central dip stemming from steric repulsion, see figure 3. We measure time t in units of $\sigma^2/(\mu_t k_B T)$. At $t = 0$, self-propulsion is switched on. Such a process could be achieved in reality, for instance, using light-activated synthetic swimmers [11, 16, 34, 119–121]. If, for example, activation of self-propulsion is sensitive to the wavelength of the irradiated light [119], confinement might be achieved simultaneously by optical trapping using light of a different frequency.

To characterize the relative strength of self-propulsion, often the dimensionless Péclet number $\mathrm{Pe}_{\mathrm{tr}}$ is introduced [101]. In our context, it measures the ratio of active to diffusive passive motion on a relevant length scale, here set by σ. Therefore,

$$\mathrm{Pe}_{\mathrm{tr}} = \frac{v_s \sigma}{\mu^t k_B T}. \tag{41}$$

In the following, we concentrate on microswimmers of significant activity, $\mathrm{Pe}_{\mathrm{tr}} \gg 1$. Moreover, we may in the case of circle swimming analogously define a rotational Péclet number,

$$\mathrm{Pe}_{\mathrm{rot}} = \frac{\omega_s}{\mu^r k_B T} = \frac{4a^2}{3R_s \sigma} \mathrm{Pe}_{\mathrm{tr}}. \tag{42}$$

For $\mathrm{Pe}_{\mathrm{rot}} \approx 0$, the curvature of the swimmer trajectory is negligible. In our numerical scheme, we directly set the parameters determining the geometry of the swimmers in figure 1. The corresponding Péclet numbers can then be extracted by calculating v_s and ω_s from (1) and (7)–(12) for $i = j$.

It turns out that increasing the character of circle swimming, i.e., decreasing the radius of the unperturbed swimming path, see figure 2, has a qualitative effect on the appearance of the trapped swimmer suspension. To demonstrate this, we first further analyze some results of straight swimming [66] obtained by our modified simulation scheme and then compare with the results for circle swimming.

4.1. Straight swimming

Straight motion of the individual swimmers is enforced in our approach by setting $\gamma = 0$, see figure 1 [66]. For straight propelling objects under spherical confinement, the formation of a high-density ring has been reported several times [66, 100, 101, 122, 123]. In agreement with previous studies, the formation of a high-density ring can be reproduced after switching on the active drive in our simulations. This ring is particularly symmetric when we switch

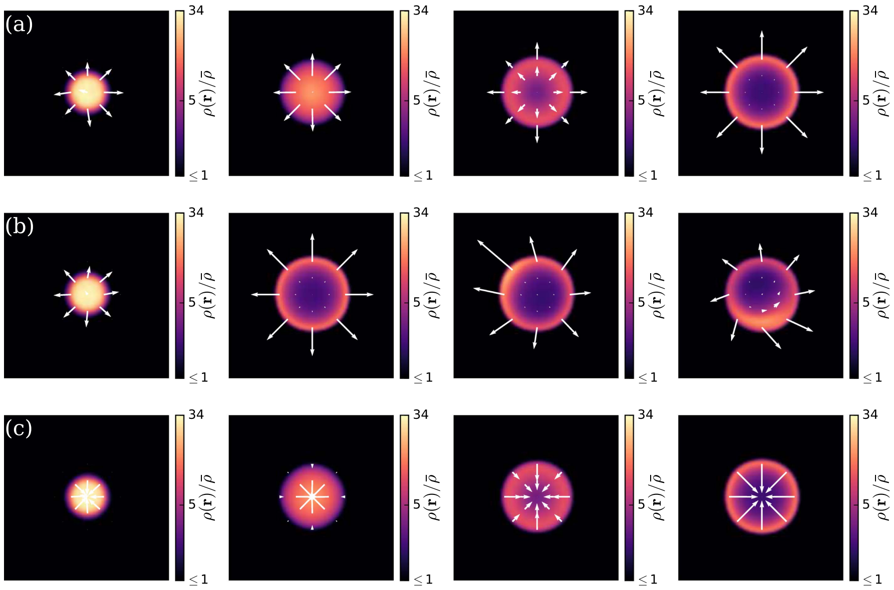

Figure 4. Each row represents a time series (from left to right) for a suspension of straight-propelling swimmers in a quartic external trapping potential for the spatial density $\rho(\mathbf{r})$ normalized by the mean density $\bar{\rho} = 7.56 \times 10^{-3}\sigma^{-2}$ in the simulation box (color plots, brighter color indicating higher density, logarithmic scale) and for the local swimmer orientation $\langle\hat{\mathbf{n}}\rangle(\boldsymbol{r})$ (white arrows). Our parameters are set to $a = 0.25\sigma$, $L = 3a = 0.75\sigma$, $\alpha = 0.4$, $\gamma = 0$, $N = 4$, $V_0 = 0.1k_BT$, and $\epsilon_0 = 10k_BT$. For each row, the system was pre-equilibrated with self-propulsion switched off, $f = 0$. Then, self-propulsion is turned on at time $t = 0$, with times measured in units of $\sigma^2/(\mu_t k_BT)$. (a) $f = 250k_BT/\sigma > 0$ for pushers, implying $\mathrm{Pe}_{tr} \approx 53$, with hydrodynamic interactions between the swimmers switched off. Snapshots provided for times $t = 0.01,\ 0.05,\ 0.1,\ 0.3$, where the last image already shows the steady state. (b) Same as in (a), now including hydrodynamic interactions. The latter destabilize the high-density ring and lead to the formation of a high-density spot. Over time, for the chosen parameters, the self-propulsion directions in this spot lean towards one side by another spontaneous symmetry breaking. The spot then starts to move along the ring contour, smearing out in the process. Times: $t = 0.01,\ 0.5,\ 1.4,\ 1.8$. (c) Same as in (b), but for pullers $f = -250k_BT/\sigma < 0$, which restricts the spot formation. Times: $t = 0.01,\ 0.05,\ 0.1,\ 0.3$. Inverting f makes the swimmers propel into the opposite direction $-\hat{\mathbf{n}}$, see figure 1, which makes the white arrows point inward in the case of pullers. As in (a), the last picture shows the steady state of the system.

off the hydrodynamic interactions between the swimmers, see figure 4(a). Its approximate radius is determined by balancing the active forward drive of the swimmers with the confining external potential force, leading to $R_{\mathrm{ring}} \sim \sigma(v_s\sigma/4\mu^t V_0)^{1/3} = \sigma(\mathrm{Pe}_{tr}k_BT/4V_0)^{1/3}$.

In the next two rows, figure 4 shows the behavior when hydrodynamic interactions between the swimmers are included as prescribed by our DDFT. They have a qualitative impact. The high-density ring at the investigated propulsion strengths develops a tangential instability and the circular symmetry is broken. Also this effect has been described before [66, 100, 101]. The swimmers tend to polarly order in the emerging high-density spot while propagating against the confining potential. Consequently, they collectively pump the surrounding fluid into the opposite direction. Thus the configuration was referred to as a 'hydrodynamic fluid pump' [66, 101]. Here, we observe that the effect is stronger in figure 4(b), which depicts the result for pushers, $f > 0$. In contrast to that, figure 4(c) was obtained with the sign of the active forces flipped to $f < 0$, describing a suspension of pullers, yet with all other parameters unchanged. Obviously, the tangential symmetry breaking is restricted in the latter case.

The cause of this spontaneous symmetry breaking was attributed in [101] to a positive feedback mechanism. If a spot of higher density appears on the ring, with the swimmers collectively pushing against the external potential, the resulting oppositely oriented fluid flow rotates nearby swimmers towards the high-density area. Consequently, they join the spot of higher concentration. In our DDFT, this effect is included by the contribution $\sim\boldsymbol{\mu}^{\mathrm{rt}}_{\mathbf{r},\mathbf{r}'}\nabla_{\mathbf{r}'}u_{\mathrm{ext}}(\mathbf{r}')$ to the current density $\mathcal{J}_4$ in (33). Additionally, pushers actively generate inward flows from their sides, see figure 1. When the swimmers are pointing outward on the ring, this further supports their lateral concentration, see the illustration in figure 5(a). Here, these active contributions are represented by the second term in the current density $\mathcal{J}_3$ in (32). In contrast to that, for pullers, the actively induced flow fields are inverted. This in effect repels outward pointing swimmers on the ring from each other, see also our schematic illustration in figure 5(b). The qualitative schematics in figures 5(c)–(f) indicate that also the curvature of the high-density ring may have a significant impact via the current density $\mathcal{J}_6$ and lead to differences between pushers and pullers. The relative magnitudes of all these different contributions basically involve all system

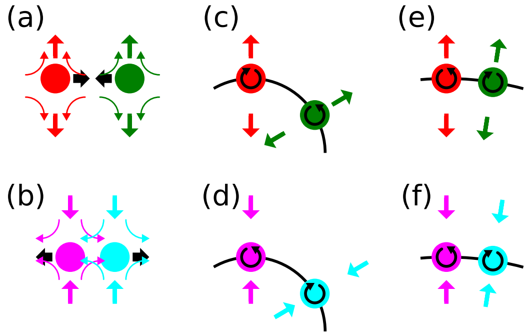

Figure 5. Effects that can contribute to the observed varying tendency of forming a high-density spot for pushers and pullers in figures 4(b) and (c), respectively. Large straight arrows of the same color as the swimmer bodies represent the active forces, while the thinner curved arrows of the same color indicate the corresponding flow fields. (a) Due to their actively induced transversal inflow of fluid, see figure 1, pushers laterally attract each other hydrodynamically. This supports spot formation in figure 4(b) when the swimmers are aligned next to each other on a high-density ring. (b) In contrast to that, pullers laterally repel each other hydrodynamically, which counteracts a spot formation, see figure 4(c). Both effects are described by the contribution $\sim\boldsymbol{\Lambda}^{\mathrm{tt}}_{\boldsymbol{r},\boldsymbol{r}'}$ to the current density $\mathcal{J}_3$ in (32). (c)–(f) Different effects are possible for the active rotation–translation coupling described by the contribution $\sim\boldsymbol{\Lambda}^{\mathrm{rt}}_{\boldsymbol{r},\boldsymbol{r}'}$ to the current density $\mathcal{J}_6$ in (35). (c) For pushers next to each other on a high-density ring of high curvature, the inward pointing force center of one swimmer is in close vicinity of the body of the other swimmer, and vice versa. This leads to actively induced rotations of the swimmers and their propulsion directions towards each other, supporting the formation of a high-density spot. (d) The situation is reversed for pullers, leading to effective rotations away from each other. (e) In contrast to the configuration in (c), for low curvature of the high-density ring, the outward pointing active force of one swimmer is closer to the body of the other swimmer, and vice versa. In this way, the swimmers tend to turn away from each other. (f) Along the same lines, pullers also for low curvature of the high-density ring turn away from each other, again counteracting the formation of a high-density spot.

parameters, i.e., temperature T, the viscosity η of the fluid, the strength of the active force f, the nature of the swimmer (pusher versus puller) together with the magnitudes of the parameters that determine the swimmer geometry, the strength and radius of the steric interactions, the overall density, and the strength of the confinement.

After the formation of the high-density spot, see figure 4(b), at strong enough active drive $f > 0$, we observe yet another spontaneous symmetry breaking. In the rightmost snapshot of figure 4(b), the averaged self-propulsion directions do not point radially outward any more. Instead, they have tilted to one side towards the tangent of the previous high-density ring. For straight swimming objects, the selection of one of the two tilting directions depends solely on small variations in the initialization of the system.

As a result of the tilting, the high-density spot starts to circle around the trap, smearing out the faded ring to some extent. Depending on the parameters, we may nearly recover a high-density ring, however, now with the swimmer orientations *not* pointing outward. Interestingly, for suspensions of pullers at elevated $|f|$, we so far have not observed this behavior. Instead, again a ring of radially oriented swimmers emerges, see figure 4(c). It appears approximately in the same way as for the case without hydrodynamic interactions in figure 4(a). This behavior is in line with our interpretation of the role of the current density $\mathcal{J}_3 \sim f$ of repelling pullers from each other.

We note that the active current density $\mathcal{J}_6$ in (35) has the potential to drive the secondary spontaneous symmetry breaking observed in the rightmost snapshot of figure 4(b). Comparing the strength of $\mathcal{J}_6$ with the one of $\mathcal{J}_4$ may also explain the initial formation of the high-density spot as a first instability and then the observed secondary instability. First, on the high-density ring, the swimmers on average feature a larger mutual separation, in the second snapshot of figure 4(b). Then, at these larger interswimmer distances r_{ij}, the contribution in the current density $\mathcal{J}_4$ driving the spot formation scales as $\sim|\boldsymbol{\mu}^{\mathrm{rt}}_{ij}| \sim r_{ij}^{-2}$. In contrast to that, in the active current density $\mathcal{J}_6$, we find a scaling $\sim r_{ij}^{-3}$ at large interswimmer distances (the two oppositely oriented active forces of each swimmer together appear as a force dipole at larger distances, which reduces the exponent in the scaling of $\boldsymbol{\Lambda}^{\mathrm{rt}}_{ij}$ to $\sim r_{ij}^{-3}$). Therefore $\mathcal{J}_4$ dominates and can drive the spot formation. At reduced separation in the high-density spot, the active forces are resolved individually and the influence of $\mathcal{J}_6$ can become substantial when comparing with $\mathcal{J}_4$. Now both scale as $\sim r_{ij}^{-2}$, but for elevated $|f|$ the importance of $\mathcal{J}_6$ grows.

4.2. Circle swimming

We now turn to increasingly biaxial swimmers for $\gamma \neq 0$, see figure 1. Depending on the values of both parameters α and γ, the unperturbed individual swimmers then show circular trajectories, see figure 2.

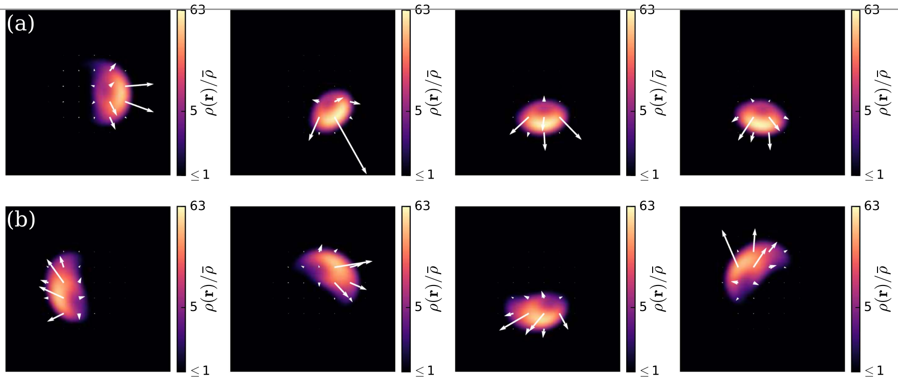

Figure 6. Influence of a (small) biaxiality, quantified by the parameter γ, on the motion of the high-density spot formed by pushers ($f > 0$). The type of presentation is identical to figure 4, but the parameters are given by $a = 0.5\sigma$, $L = 8a = 4\sigma$, $\alpha = 0.4$, $N = 4$, $V_0 = k_B T$, $\epsilon_0 = 5k_B T$, and $f = 100k_B T/\sigma$. In the plot, the local density $\rho(\mathbf{r})$ is normalized by the mean density $\bar{\rho} = 6.47 \times 10^{-2}\sigma^{-2}$ in the whole simulation box. Self-propulsion is switched on at $t = 0$, the snapshots in each row are taken at $t = 2,\ 2.3,\ 2.6,\ 2.9$. (a) For straight-swimming pushers ($\gamma = 0$, $\mathrm{Pe_{tr}} = 23$) the high-density spot only slowly migrates around the trap, the sense of motion resulting from spontaneous symmetry breaking. (b) For weak circle swimmers ($\gamma = 0.01$, $\mathrm{Pe_{tr}} = 23$, $\mathrm{Pe_{rot}} = 0.61$) the high-density spot persistently moves around the trap, with the sense of motion affected by the sense of circle swimming.

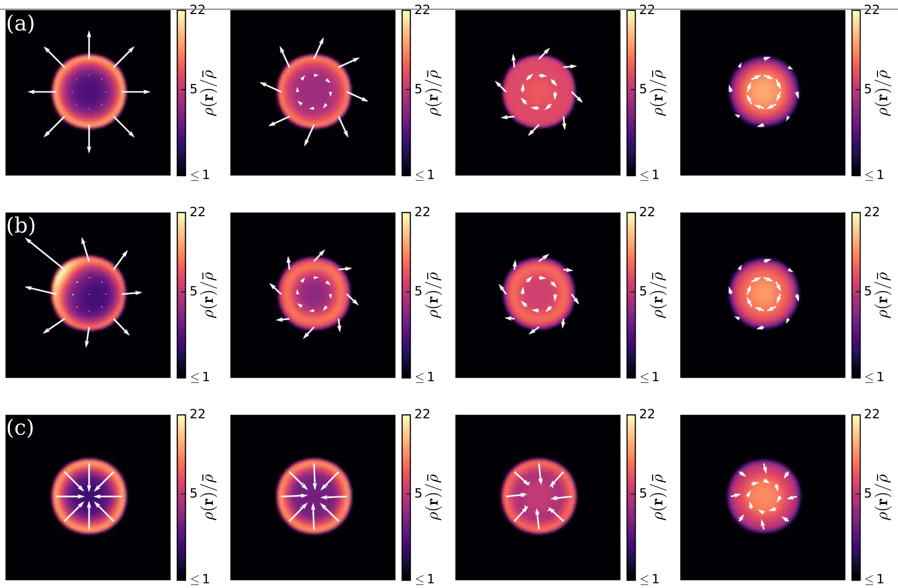

Figure 7. Long-term behavior for different strengths of circle swimming, namely $\gamma = 0,\ 0.01,\ 0.02,\ 0.04$ from left to right in each row. The other parameters and the type of presentation are the same as in figure 4. In all depicted cases, a *localizing* effect of circle swimming becomes obvious. Pronounced circle swimming leads to concentration of the swimmers around the center of the trap, see the rightmost column. (a) Switching off hydrodynamic interactions supports the localization around the center of the trap. (b) For pushers ($f > 0$), we observe with increasing γ that first the high-density spot smears out to a high-density ring that broadens and for high γ collapses towards the center. (c) For pullers ($f < 0$) the high-density ring appears a bit more stable at lower values of γ, but again a concentration around the center occurs at high γ.

Particularly, we analyze the changes in the behavior of the suspension when we stepwise increment γ. For each value of γ, we again start from an equilibrated passive initial system and then switch on self-propulsion at $t = 0$, as before.

By and large, we do not observe abrupt modifications in the overall behavior. Instead it changes rather gradually with increasing γ. For small $\gamma \neq 0$, the behavior of the straight swimming objects is reproduced

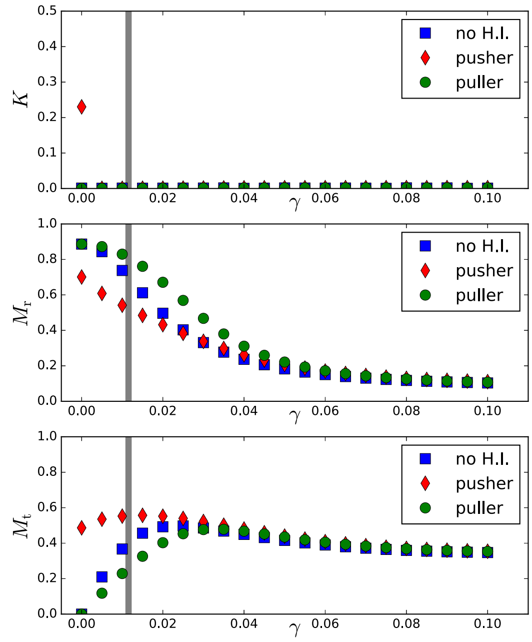

Figure 8. Order parameters K, measuring the degree of off-center density concentration in a high-density spot, as well as M_r and M_t, measuring the degrees of swimmer orientations along the radial and one of the tangential directions, respectively, for the systems in figure 7 with increasing biaxiality parameter γ. Again, the situation without hydrodynamic interactions between the swimmers ('no H.I.'), the case of $f > 0$ ('pusher'), and the case of $f < 0$ ('puller') are depicted. Generally, with increasing γ, off-center concentration in non-rotationally symmetric structures diminishes (drop of K) and the swimmers tilt away from the radial direction (decreasing M_r). We find smooth intermediate transitions for M_r and M_t around the value of γ that leads to $R_s = R_{ring}$, as indicated by the vertical gray lines. For the parameters chosen here, K drops to zero already at very low biaxiality. Other parameter combinations lead to less abrupt decrease in K, see, e.g., figure 6.

qualitatively. Only for pushers of stronger active drive $f > 0$, we note an illustrative alteration. While the sense of circling of the high-density spot around the trap as illustrated in the rightmost snapshot of figure 4(b) resulted from spontaneous symmetry breaking for $\gamma \neq 0$ and could be clockwise or counterclockwise, it is now increasingly dictated by the sense of the circular swimming trajectory. A comparison between straight swimmers and weak circle swimmers is included by figure 6.

Remarkably, the overall appearance of the suspension changes qualitatively when the nature of circle swimming becomes more pronounced. In our set of parameters we achieve this by increasing γ. The bending of the swimmer trajectories has a *localizing* effect, as illustrated in figure 7. There, all snapshots show the long-term behavior of the corresponding suspension. From left to right in each row, the strength of circle swimming grows. Due to their persistent self-rotation, the outward propagation of the swimmers against the confining trapping potential is restricted. As a consequence, the concentration of the swimmers in the center of the trap increases. At high enough γ, the density is again peaked around the center of the trap. Comparing figure 7(a), where hydrodynamic interactions have been switched off, to figures 7(b) and (c), we infer that hydrodynamic interactions significantly delay the localization around the center of the trap with increasing γ. Yet, at high enough values of γ (rightmost column in figure 7) the localization dominates in all cases. Comparing pushers and pullers in figures 7(b) and (c), respectively, we note the more persistent nature of the high-density ring in the case of pullers at smaller values of γ, before the collapse towards the center of the trap occurs.

To quantify the modified appearance of the suspension with increasing γ, we introduce the following order parameters. First, we evaluate

$$K(t) = \frac{1}{N} \left| \int \mathrm{d}\mathbf{r}\mathrm{d}\varphi \ \exp(\mathrm{i}\vartheta) \ \rho^{(1)}(\mathbf{r}, \varphi, t) \right|, \tag{43}$$

where in this expression spatial positions $\mathbf{r}$ are parameterized by polar coordinates $\mathbf{r} = (r, \vartheta)$. $K(t)$ becomes non-zero when a tangential instability occurs that breaks the circular symmetry of a high-density ring, leading to an off-center high-density spot.

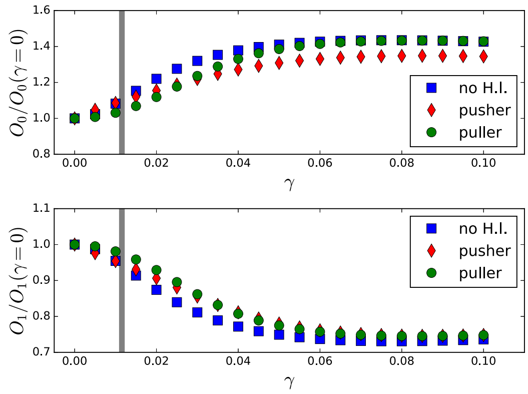

Figure 9. Same as in figure 8, but for the order parameters O_0 and O_1 that measure the degree of near-center and off-center concentration, respectively. At smaller values of the biaxiality parameter γ, O_0 is low and O_1 is high when a high-density ring or a high-density off-center spot has formed. In contrast to that, high O_0 and low O_1 signal a localization of the density around the center of the trap for pronounced circle swimming at high values of γ (see also the rightmost column in figure 7). Again, the vertical gray lines indicate the value of γ implying $R_s = R_{\text{ring}}$. Apparently, hydrodynamic interactions slightly counteract the concentration around the center. For strong circle swimming, pullers appear more concentrated around the center than pushers.

Next, we define

$$M_{\mathrm{r}}(t) = \frac{1}{N}\int \mathrm{d}\boldsymbol{r}\mathrm{d}\varphi\ (\hat{\mathbf{v}}_{\mathrm{s}}\cdot\hat{\mathbf{r}})\ \rho^{(1)}(\boldsymbol{r}, \varphi, t), \tag{44}$$

with $\hat{\mathbf{v}}_{\mathrm{s}}$ for each swimmer denoting the hypothetical instantaneous unperturbed direction of self-propulsion. For $\gamma = 0$, $\hat{\mathbf{v}}_{\mathrm{s}}$ points along $\pm\hat{\mathbf{n}}$ according to the sign of f, but it becomes slightly tilted towards $\hat{\mathbf{u}}$ for $\gamma \neq 0$. $M_{\mathrm{r}}(t)$ quantifies the overall degree of swimmer orientations along the radial direction.

In analogy to that, to quantify the ordering of the swimmer orientations along one of the two tangential directions, the order parameter

$$M_{\mathrm{t}}(t) = \frac{1}{N}\left|\int \mathrm{d}\boldsymbol{r}\mathrm{d}\varphi\ (\hat{\mathbf{v}}_{\mathrm{s}}\cdot(\hat{\mathbf{r}}\times\hat{\mathbf{z}}))\ \rho^{(1)}(\boldsymbol{r}, \varphi, t)\ \right| \tag{45}$$

is evaluated. In the absence of any local orientational order, both $M_{\mathrm{r}}(t)$ and $M_{\mathrm{t}}(t)$ vanish. For steady-state systems, all three of the above order parameters no longer depend on time in the long-term limit.

Figure 8 shows the long-term values of the order parameters K, M_{r}, and M_{t} with increasing biaxiality and degree of circle swimming γ. When hydrodynamic interactions are switched off, for $\gamma = 0$ a high-density ring is formed with the swimmers radially aligned, see figure 4(a). Therefore, K and M_{t} are low, while M_{r} is high.

Including hydrodynamic interactions, pullers ($f < 0$) here behave in a very similar way, see also figure 7(c). In contrast to that, pushers ($f > 0$) show a concentration in high-density spots for $\gamma = 0$, see figures 6 and 7(b), leading to an elevated value of K. Moreover, the self-propulsion directions in this high-density spot by spontaneous symmetry breaking can lean towards one of the two tangential directions, see figures 4(b) and 6. Therefore, M_{r} and M_{t} are reduced and elevated, respectively, when compared to the other systems in figure 8.

As the degree of circle swimming increases with γ and the swimmers tilt away from the radial outward direction, M_{r} generally decreases. M_{t} first increases as the orientational order shifts from radial to tangential. It then saturates and again slightly decays for high γ, i.e., for small swimming radii. The latter slow decay is supported by the increasing localization in the center of the trap where orientational order vanishes by the overall rotational symmetry. The smooth changes of M_{r} and M_{t} in figure 8 indicate that the transition from off-center high-density rings or spots to centrally localized distributions with increasing γ is rather continuous. This transition should occur when the radius R_{s} of the unperturbed swimmer trajectories and the characteristic radius of the trap R_{ring} become approximately identical. We have indicated the corresponding value of γ in figure 8 by the vertical gray lines.

To also quantify the depletion of the swimmer density in the center of the trap when high-density rings or off-center high-density spots occur, in contrast to the central accumulation when the localizing effect of circle swimming becomes strong, we introduce additional order parameters

$$O_\nu(t) = \int \mathrm{d}\boldsymbol{r}\mathrm{d}\varphi\ J_\nu(r/R_{\text{ring}})\ \rho^{(1)}(\boldsymbol{r}, \varphi, t) \tag{46}$$

for $\nu = 0$ and 1. Here, J_ν are the Bessel functions of first kind. By construction, $O_0(t)$ is large when the density is concentrated in the center of the trap, while $O_1(t)$ is elevated for off-center distributions.

As demonstrated by figure 9, the transitions as a function of the biaxiality parameter γ are again smooth. Yet, the increasing localization in the center of the trap for increasing γ is obvious. Particularly in the transitional regime, that is, for intermediate values of γ, hydrodynamic interactions apparently counteract localization in the center of the trap. Moreover, for our set of parameters and at large γ, the central concentration of pushers is slightly lower than the one for pullers, if only the sign of f is inverted and all other parameters are kept the same.

5. Conclusions

In summary, we have presented a microscopic statistical approach in the framework of DDFT for active circle swimmers. Hardly any real microswimmer is a perfectly symmetric straight swimmer. Therefore, investigations on the effect of bent migration trajectories are mandatory.

Our theory captures self-propulsion along swimming paths of different preferred curvature, steric and hydrodynamic interactions between the microswimmers, as well as confinement by an external potential. In contrast to many previous descriptions, the curved motion in our case is not directly imposed by an effective torque or angular frequency on the swimmer body. Here, it naturally follows from the geometric structure of our microscopic minimal swimmer model and resulting hydrodynamic effects.

Persistently bent swimming trajectories reduce the global mobility of the swimmers. To study this *localizing* effect, we analyzed the behavior of microswimmer suspensions in a circularly symmetric trapping potential for increasing degree of circle swimming. Moreover, we distinguished between pusher and puller circle swimmers, and also studied the effect of hydrodynamics by comparison with switched-off hydrodynamic interactions between the swimmers.

Straight swimming objects tend to spread out towards the confinement until their active drive is balanced by the confining potential [66, 100, 101, 122, 123]. This leads to high-density rings. Such rings may get unstable due to hydrodynamic interactions, particularly for pusher swimmers, leading to the formation of off-center high-density spots [66, 100, 101]. We have further investigated and quantified this scenario.

Circle swimming can qualitatively affect the behavior. Increasing the degree of circular self-propulsion supports a persistent circling motion of the high-density spots around the trap. At high degrees of circle swimming, the swimmers become localized around the center of the trap, while hydrodynamic interactions seem to slightly counteract this effective confinement. The transition from the off-center towards the centered density distributions appears to be smooth, and we quantified it by introducing several corresponding order parameters.

A long-term goal to extend the present theory would be the characterization of motility-induced phase separation into a dense clustered state and a surrounding low-density gas-like state [119, 120, 124–145]. This phenomenon was observed in particle-based simulations of active Brownian particles [120, 125, 127, 130, 133–136, 138, 142, 144, 145] and described by different statistical or continuum approaches [126, 128, 129, 131, 132, 136, 137, 141]. So far, the effect of hydrodynamic interactions on this scenario has only rarely been addressed [134, 138]. Our DDFT by construction contains self-propulsion driving the phase separation, steric interactions to avoid a collapse of the clustered state, and hydrodynamic interactions. In previous theoretical approaches, input for the density dependence of the swimming speed [128] or for the front-back imbalance of the pair-correlation function [126, 131, 141] was required to capture the phenomenon. An interesting question for statistical theories and DDFT is whether such an input will further be necessary in the future, or whether the theories will provide it in a self-consistent way, as encouraged by a recent theoretical study [146]. Moreover, one could then analyze how the clustering behavior is influenced by the circular swimming paths.

We note that, in a different context, the consequences of reorienting the swimming motion, e.g., by external fields, have been analyzed for the translational behavior as well as for the swim stress and pressure [147, 148]. Possibly, the latter quantities could also be extracted using our approach and explicit swimmer model. Apart from that, in the future also the dynamic behavior of pure active swimming rotors [149–151] could be considered in an analogous statistical approach, including the induced hydrodynamic interactions between the rotors. Another extension concerns the treatment of crystallization effects [78] for active microswimmers taking into account hydrodynamic interactions.

Acknowledgments

The authors thank Urs Zimmermann for helpful discussions on the simulation scheme and Gerhard Nägele for helpful comments. Support of this work by the Deutsche Forschungsgemeinschaft through the priority program SPP 1726 is gratefully acknowledged.

Appendix

In our model, each swimmer consists of two force centers in the fluid in the vicinity of the swimmer body as shown in figure 1. To constitute a realistic microswimmer, no net force and no net torque may be exerted on the fluid.

Since the two anti-parallel forces have the same magnitude f, the net force vanishes by construction. The individual torques $\boldsymbol{T}_{\pm} = \boldsymbol{r}^{\pm} \times (\pm f\,\hat{\mathbf{n}})$ caused by the two force centers of the swimmer can be calculated from the distance vectors $\boldsymbol{r}^{\pm}$ defined in (11) and (12). Thus, they read

$$\boldsymbol{T}_{+} = f(\alpha L\hat{\mathbf{n}} \times \hat{\mathbf{n}} + \gamma L\hat{\mathbf{u}} \times \hat{\mathbf{n}}) = f\gamma L\hat{\mathbf{u}} \times \hat{\mathbf{n}}, \tag{A.1}$$

$$\boldsymbol{T}_{-} = -f(-(1-\alpha)L\hat{\mathbf{n}} \times \hat{\mathbf{n}} + \gamma L\hat{\mathbf{u}} \times \hat{\mathbf{n}}) = -f\gamma L\hat{\mathbf{u}} \times \hat{\mathbf{n}}, \tag{A.2}$$

and cancel upon summation so that the net torque vanishes, as required.

ORCID iDs

Andreas M Menzel https://orcid.org/0000-0003-0713-4979

References

[1] Berg H C and Brown D A 1972 *Nature* **239** 500
[2] Paxton W F, Kistler K C, Olmeda C C, Sen A St, Angelo S K, Cao Y, Mallouk T E, Lammert P E and Crespi V H 2004 *J. Am. Chem. Soc.* **126** 13424
[3] Howse J R, Jones R A, Ryan A J, Gough T, Vafabakhsh R and Golestanian R 2007 *Phys. Rev. Lett.* **99** 048102
[4] Lauga E and Powers T R 2009 *Rep. Prog. Phys.* **72** 096601
[5] Romanczuk P, Bär M, Ebeling W, Lindner B and Schimansky-Geier L 2012 *Eur. Phys. J. Spec. Top.* **202** 1
[6] Cates M E 2012 *Rep. Prog. Phys.* **75** 042601
[7] Menzel A M 2015 *Phys. Rep.* **554** 1
[8] Elgeti J, Winkler R G and Gompper G 2015 *Rep. Prog. Phys.* **78** 056601
[9] Zöttl A and Stark H 2016 *J. Phys.: Condens. Matter* **28** 253001
[10] Bechinger C, Di Leonardo R, Löwen H, Reichhardt C, Volpe G and Volpe G 2016 *Rev. Mod. Phys.* **88** 045006
[11] Buttinoni I, Volpe G, Kümmel F, Volpe G and Bechinger C 2012 *J. Phys.: Condens. Matter* **24** 284129
[12] Polin M, Tuval I, Drescher K, Gollub J P and Goldstein R E 2009 *Science* **325** 487
[13] Tailleur J and Cates M E 2008 *Phys. Rev. Lett.* **100** 218103
[14] Min T L, Mears P J, Chubiz L M, Rao C V, Golding I and Chemla Y R 2009 *Nat. Methods* **6** 831
[15] ten Hagen B, Wittkowski R and Löwen H 2011 *Phys. Rev.* E **84** 031105
[16] Volpe G, Buttinoni I, Vogt D, Kümmerer H J and Bechinger C 2011 *Soft Matter* **7** 8810
[17] Bennett R R and Golestanian R 2013 *Phys. Rev. Lett.* **110** 148102
[18] Zheng X, ten Hagen B, Kaiser A, Wu M, Cui H, Silber-Li Z and Löwen H 2013 *Phys. Rev.* E **88** 032304
[19] Sevilla F J 2016 *Phys. Rev.* E **94** 062120
[20] Zöttl A and Stark H 2012 *Phys. Rev. Lett.* **108** 218104
[21] Tarama M, Menzel A M, ten Hagen B, Wittkowski R, Ohta T and Löwen H 2013 *J. Chem. Phys.* **139** 104906
[22] Tournus M, Kirshtein A, Berlyand L and Aranson I S 2015 *J. R. Soc. Interface* **12** 20140904
[23] Rusconi R and Stocker R 2015 *Curr. Opin. Microbiol.* **25** 1
[24] Mathijssen A J T M, Shendruk T N, Yeomans J M and Doostmohammadi A 2016 *Phys. Rev. Lett.* **116** 028104
[25] Mathijssen A J, Doostmohammadi A, Yeomans J M and Shendruk T N 2016 *J. R. Soc. Interface* **13** 20150936
[26] Ramia M, Tullock D L and Phan-Thien N 1993 *Biophys. J.* **65** 755
[27] Frymier P D, Ford R M, Berg H C and Cummings P T 1995 *Proc. Natl. Acad. Sci. USA* **92** 6195
[28] Lauga E, DiLuzio W R, Whitesides G M and Stone H A 2006 *Biophys. J.* **90** 400
[29] Riedel I H, Kruse K and Howard J 2005 *Science* **309** 300
[30] Elgeti J, Kaupp U B and Gompper G 2010 *Biophys. J.* **99** 1018
[31] Wittkowski R and Löwen H 2012 *Phys. Rev.* E **85** 021406
[32] Ledesma-Aguilar R, Löwen H and Yeomans J M 2012 *Eur. Phys. J.* E **35** 70
[33] Kümmel F, ten Hagen B, Wittkowski R, Buttinoni I, Eichhorn R, Volpe G, Löwen H and Bechinger C 2013 *Phys. Rev. Lett.* **110** 198302
[34] ten Hagen B, Kümmel F, Wittkowski R, Takagi D, Löwen H and Bechinger C 2014 *Nat. Commun.* **5** 4829
[35] ten Hagen B, Wittkowski R, Takagi D, Kümmel F, Bechinger C and Löwen H 2015 *J. Phys.: Condens. Matter* **27** 194110
[36] Löwen H 2016 *Eur. Phys. J. Spec. Top.* **225** 2319
[37] Ohta T and Ohkuma T 2009 *Phys. Rev. Lett.* **102** 154101
[38] Hiraiwa T, Shitara K and Ohta T 2011 *Soft Matter* **7** 3083
[39] Krüger C, Klös G, Bahr C and Maass C C 2016 *Phys. Rev. Lett.* **117** 048003
[40] Brokaw C J, Luck D J and Huang B 1982 *J. Cell Biol.* **92** 722
[41] Kamiya R and Witman G B 1984 *J. Cell Biol.* **98** 97
[42] Takagi D, Braunschweig A B, Zhang J and Shelley M J 2013 *Phys. Rev. Lett.* **110** 038301
[43] Denk J, Huber L, Reithmann E and Frey E 2016 *Phys. Rev. Lett.* **116** 178301
[44] van Teeffelen S and Löwen H 2008 *Phys. Rev.* E **78** 020101
[45] van Teeffelen S, Zimmermann U and Löwen H 2009 *Soft Matter* **5** 4510
[46] Weber C, Radtke P K, Schimansky-Geier L and Hänggi P 2011 *Phys. Rev.* E **84** 011132
[47] Fily Y, Baskaran A and Marchetti M C 2012 *Soft Matter* **8** 3002
[48] Radtke P K and Schimansky-Geier L 2012 *Phys. Rev.* E **85** 051110

[49] Weber C, Sokolov I M and Schimansky-Geier L 2012 *Phys. Rev.* E **85** 052101
[50] Kaiser A and Löwen H 2013 *Phys. Rev.* E **87** 032712
[51] Mijalkov M and Volpe G 2013 *Soft Matter* **9** 6376
[52] Reichhardt C and Reichhardt C J O 2013 *Phys. Rev.* E **88** 042306
[53] Marine N A, Wheat P M, Ault J and Posner J D 2013 *Phys. Rev.* E **87** 052305
[54] Yang Y, Qiu F and Gompper G 2014 *Phys. Rev.* E **89** 012720
[55] Chen Q and Ai B Q 2015 *J. Chem. Phys.* **143** 104113
[56] Nourhani A, Crespi V H and Lammert P E 2015 *Phys. Rev. Lett.* **115** 118101
[57] Ao X, Ghosh P K, Li Y, Schmid G, Hänggi P and Marchesoni F 2015 *Europhys. Lett.* **109** 10003
[58] Liebchen B and Levis D 2017 *Phys. Rev. Lett.* **119** 058002
[59] Jahanshahi S, Löwen H and ten Hagen B 2017 *Phys. Rev.* E **95** 022606
[60] Baskaran A and Marchetti M C 2009 *Proc. Natl. Acad. Sci. USA* **106** 15567
[61] Menzel A M 2012 *Phys. Rev.* E **85** 021912
[62] Chou Y L, Wolfe R and Ihle T 2012 *Phys. Rev.* E **86** 021120
[63] Großmann R, Romanczuk P, Bär M and Schimansky-Geier L 2015 *Eur. Phys. J.: Spec. Top.* **224** 1325
[64] Chou Y L and Ihle T 2015 *Phys. Rev.* E **91** 022103
[65] Heidenreich S, Dunkel J, Klapp S H L and Bär M 2016 *Phys. Rev.* E **94** 020601
[66] Menzel A M, Saha A, Hoell C and Löwen H 2016 *J. Chem. Phys.* **144** 024115
[67] Elder K R, Katakowski M, Haataja M and Grant M 2002 *Phys. Rev. Lett.* **88** 245701
[68] Elder K R and Grant M 2004 *Phys. Rev.* E **70** 051605
[69] Goldenfeld N, Athreya B P and Dantzig J A 2005 *Phys. Rev.* E **72** 020601
[70] Elder K R, Provatas N, Berry J, Stefanovic P and Grant M 2007 *Phys. Rev.* B **75** 064107
[71] van Teeffelen S, Likos C N and Löwen H 2008 *Phys. Rev. Lett.* **100** 108302
[72] van Teeffelen S, Backofen R, Voigt A and Löwen H 2009 *Phys. Rev.* E **79** 051404
[73] Tegze G, Tóth G I and Gránásy L 2011 *Phys. Rev. Lett.* **106** 195502
[74] Neuhaus T, Schmiedeberg M and Löwen H 2013 *New J. Phys.* **15** 073013
[75] Menzel A M and Löwen H 2013 *Phys. Rev. Lett.* **110** 055702
[76] van Teeffelen S, Achim C V and Löwen H 2013 *Phys. Rev.* E **87** 022306
[77] Menzel A M, Ohta T and Löwen H 2014 *Phys. Rev.* E **89** 022301
[78] Archer A J, Walters M, Thiele U and Knobloch E 2014 *Phys. Rev.* E **90** 042404
[79] Chervanyov A I, Gomez H and Thiele U 2016 *Europhys. Lett.* **115** 68001
[80] Zimmermann U, Smallenburg F and Löwen H 2016 *J. Phys.: Condens. Matter* **28** 244019
[81] Hansen J P and McDonald I R 1990 *Theory of Simple Liquids* (Amsterdam: Elsevier)
[82] Singh Y 1991 *Phys. Rep.* **207** 351
[83] Evans R 1992 Density functionals in the theory of nonuniform fluids *Fundamentals of Inhomogeneous Fluids* ed D Henderson (New York: Marcel Dekker) pp 85–176
[84] Evans R 2010 Density functional theory for inhomogeneous fluids: I. Simple fluids in equilibrium *Lecture Notes 3rd Warsaw School of Statistical Physics* ed B Cichocki *et al* (Warsaw: Warsaw University Press) pp 43–85
[85] Löwen H 2010 Density functional theory for inhomogeneous fluids: II. Statics, dynamics, and applications *Lecture Notes 3rd Warsaw School of Statistical Physics* ed B Cichocki *et al* (Warsaw: Warsaw University Press) pp 87–121
[86] Marconi U M B and Tarazona P 1999 *J. Chem. Phys.* **110** 8032
[87] Marconi U M B and Tarazona P 2000 *J. Phys.: Condens. Matter* **12** A413
[88] Archer A J and Evans R 2004 *J. Chem. Phys.* **121** 4246
[89] Purcell E M 1977 *Am. J. Phys* **45** 3
[90] Wensink H H and Löwen H 2008 *Phys. Rev.* E **78** 031409
[91] Wittkowski R and Löwen H 2011 *Mol. Phys.* **109** 2935
[92] Pototsky A and Stark H 2012 *Europhys. Lett.* **98** 50004
[93] Rex M and Löwen H 2008 *Phys. Rev. Lett.* **101** 148302
[94] Rex M and Löwen H 2009 *Eur. Phys. J.* E **28** 139
[95] Rauscher M 2010 *J. Phys.: Condens. Matter* **22** 364109
[96] Goddard B D, Nold A, Savva N, Pavliotis G A and Kalliadasis S 2012 *Phys. Rev. Lett.* **109** 120603
[97] Goddard B D, Nold A, Savva N, Yatsyshin P and Kalliadasis S 2012 *J. Phys.: Condens. Matter* **25** 035101
[98] Donev A and Vanden-Eijnden E 2014 *J. Chem. Phys.* **140** 234115
[99] Goddard B D, Nold A and Kalliadasis S 2016 *J. Chem. Phys.* **145** 214106
[100] Nash R W, Adhikari R, Tailleur J and Cates M E 2010 *Phys. Rev. Lett.* **104** 258101
[101] Hennes M, Wolff K and Stark H 2014 *Phys. Rev. Lett.* **112** 238104
[102] Dhont J K G 1996 *An Introduction to Dynamics of Colloids* (Amsterdam: Elsevier)
[103] Rotne J and Prager S 1969 *J. Chem. Phys.* **50** 4831
[104] Reichert M and Stark H 2004 *Phys. Rev.* E **69** 031407
[105] Kim S and Karrila S J 2013 *Microhydrodynamics: Principles and Selected Applications* (Mineola, NY: Dover)
[106] Adhyapak T C and Jabbari-Farouji S 2017 arXiv:1706.02752
[107] Doi M and Edwards S F 1988 *The Theory of Polymer Dynamics* (Oxford: Oxford University Press)
[108] Mladek B M, Gottwald D, Kahl G, Neumann M and Likos C N 2006 *Phys. Rev. Lett.* **96** 045701
[109] Gray C G and Gubbins K E 1984 *Theory of Molecular Fluids: I: Fundamentals* (*International Series of Monographs on Chemistry*) (Oxford: Oxford University Press)
[110] Wittkowski R, Löwen H and Brand H R 2010 *Phys. Rev.* E **82** 031708
[111] Español P and Löwen H 2009 *J. Chem. Phys.* **131** 244101
[112] Onsager L 1949 *Ann. NY Acad. Sci.* **51** 627
[113] Guyer J E, Wheeler D and Warren J A 2009 *Comput. Sci. Eng.* **11** 6
[114] Pavelka R 2012 *Numerical Solving of Anisotropic Elliptic Equation on Disconnected Mesh Using FiPy and Gmsh* (Prague: Czech Technical University)
[115] Guyer J E, Wheeler D and Warren J A 2017 *FiPy Manual, Release 3.1.3* (Gaithersburg, MD: National Institute of Standards and Technology)

[116] Ewald P P 1921 *Ann. Phys.* **369** 253
[117] Beenakker C W J 1986 *J. Chem. Phys.* **85** 1581
[118] Brady J F, Phillips R J, Lester J C and Bossis G 1988 *J. Fluid Mech.* **195** 257
[119] Palacci J, Sacanna S, Steinberg A P, Pine D J and Chaikin P M 2013 *Science* **339** 936
[120] Buttinoni I, Bialké J, Kümmel F, Löwen H, Bechinger C and Speck T 2013 *Phys. Rev. Lett.* **110** 238301
[121] Samin S and van Roij R 2015 *Phys. Rev. Lett.* **115** 188305
[122] Menzel A M 2015 *Europhys. Lett.* **110** 38005
[123] Yan W and Brady J F 2015 *J. Fluid Mech.* **785** R1
[124] Theurkauff I, Cottin-Bizonne C, Palacci J, Ybert C and Bocquet L 2012 *Phys. Rev. Lett.* **108** 268303
[125] Fily Y and Marchetti M C 2012 *Phys. Rev. Lett.* **108** 235702
[126] Bialké J, Löwen H and Speck T 2013 *Europhys. Lett.* **103** 30008
[127] Redner G S, Hagan M F and Baskaran A 2013 *Phys. Rev. Lett.* **110** 055701
[128] Cates M E and Tailleur J 2013 *Europhys. Lett.* **101** 20010
[129] Stenhammar J, Tiribocchi A, Allen R J, Marenduzzo D and Cates M E 2013 *Phys. Rev. Lett.* **111** 145702
[130] Suma A, Gonnella G, Marenduzzo D and Orlandini E 2014 *Europhys. Lett* **108** 56004
[131] Speck T, Bialké J, Menzel A M and Löwen H 2014 *Phys. Rev. Lett.* **112** 218304
[132] Takatori S C, Yan W and Brady J F 2014 *Phys. Rev. Lett.* **113** 028103
[133] Stenhammar J, Marenduzzo D, Allen R J and Cates M E 2014 *Soft Matter* **10** 1489
[134] Matas-Navarro R, Golestanian R, Liverpool T B and Fielding S M 2014 *Phys. Rev.* E **90** 032304
[135] Wysocki A, Winkler R G and Gompper G 2014 *Europhys. Lett.* **105** 48004
[136] Fily Y, Henkes S and Marchetti M C 2014 *Soft Matter* **10** 2132
[137] Wittkowski R, Tiribocchi A, Stenhammar J, Allen R J, Marenduzzo D and Cates M E 2014 *Nat. Commun.* **5** 4351
[138] Zöttl A and Stark H 2014 *Phys. Rev. Lett.* **112** 118101
[139] Cates M E and Tailleur J 2015 *Annu. Rev. Condens. Matter Phys.* **6** 219
[140] Bialké J, Speck T and Löwen H 2015 *J. Non-Cryst. Solids* **407** 367
[141] Speck T, Menzel A M, Bialké J and Löwen H 2015 *J. Chem. Phys.* **142** 224109
[142] Bialké J, Siebert J T, Löwen H and Speck T 2015 *Phys. Rev. Lett.* **115** 098301
[143] Speck T 2016 *Eur. Phys. J. Spec. Top.* **225** 2287
[144] Richard D, Löwen H and Speck T 2016 *Soft Matter* **12** 5257
[145] Siebert J T, Letz J, Speck T and Virnau P 2017 *Soft Matter* **13** 1020
[146] Härtel A, Richard D and Speck T 2017 arXiv:1708.01115
[147] Takatori S C and Brady J F 2014 *Soft Matter* **10** 9433
[148] Yan W and Brady J F 2015 *Soft Matter* **11** 6235
[149] Nguyen N H P, Klotsa D, Engel M and Glotzer S C 2014 *Phys. Rev. Lett.* **112** 075701
[150] van Zuiden B C, Paulose J, Irvine W T, Bartolo D and Vitelli V 2016 *Proc. Natl. Acad. Sci. USA* **113** 12919
[151] Wykes M S D, Palacci J, Adachi T, Ristroph L, Zhong X, Ward M D, Zhang J and Shelley M J 2016 *Soft Matter* **12** 4584

P3 Multi-species dynamical density functional theory for microswimmers: derivation, orientational ordering, trapping potential, and shear cells

C. Hoell, H. Löwen, and A. M. Menzel,
Multi-species dynamical density functional theory for microswimmers: derivation, orientational ordering, trapping potential, and shear cells,
J. Chem. Phys. **151**, 064902 (2019),
with the permission of *AIP Publishing.*

Digital Object Identifier (DOI): `https://doi.org/10.1063/1.5099554`

Statement of contribution

AMM and HL supervised this work. All authors developed the theory. I performed the numerical evaluations and the analytical calculations, prepared all figures, implemented the calculation of one order parameter, and drafted the manuscript, which then AMM and I completed. All authors discussed and interpreted the results, edited the text, and finalized the manuscript.

Copyright and license notice

The Journal of Chemical Physics ARTICLE scitation.org/journal/jcp

Multi-species dynamical density functional theory for microswimmers: Derivation, orientational ordering, trapping potentials, and shear cells

Cite as: J. Chem. Phys. 151, 064902 (2019); doi: 10.1063/1.5099554
Submitted: 11 April 2019 • Accepted: 19 July 2019 •
Published Online: 9 August 2019 • Corrected: 17 September 2019

View Online Export Citation CrossMark

Christian Hoell,[a] Hartmut Löwen, and Andreas M. Menzel[b]

AFFILIATIONS

Institut für Theoretische Physik II: Weiche Materie, Heinrich-Heine-Universität Düsseldorf, Universitätsstraße 1, D-40225 Düsseldorf, Germany

[a]Electronic mail: christian.hoell@uni-duesseldorf.de
[b]Electronic mail: menzel@hhu.de

ABSTRACT

Microswimmers typically operate in complex environments. In biological systems, often diverse species are simultaneously present and interact with each other. Here, we derive a (time-dependent) particle-scale statistical description, namely, a dynamical density functional theory, for such multispecies systems, extending existing works on one-component microswimmer suspensions. In particular, our theory incorporates not only the effect of external potentials but also steric and hydrodynamic interactions between swimmers. For the latter, a previously introduced force-dipole-based minimal (pusher or puller) microswimmer model is used. As a limiting case of our theory, mixtures of hydrodynamically interacting active and passive particles are captured as well. After deriving the theory, we apply it to different planar swimmer configurations. First, these are binary pusher–puller mixtures in external traps. In the considered situations, we find that the majority species imposes its behavior on the minority species. Second, for unconfined binary pusher–puller mixtures, the linear stability of an orientationally disordered state against the emergence of global polar orientational order (and thus emergent collective motion) is tested analytically. Our statistical approach predicts, qualitatively in line with previous particle-based computer simulations, a threshold for the fraction of pullers and for their propulsion strength that lets overall collective motion arise. Third, we let driven passive colloidal particles form the boundaries of a shear cell, with confined active microswimmers on their inside. Driving the passive particles then effectively imposes shear flows, which persistently acts on the inside microswimmers. Their resulting behavior reminds of the one of circle swimmers although with varying swimming radii.

I. INTRODUCTION

From a fundamental point of view, the study of active microswimmers[1–6]—i.e., micronsized self-propelling particles suspended in a fluid—is interesting already because of the inherent nonequilibrium nature of self-propelling particles.[7–10] Unusual collective behavior arises from this feature, e.g., motility-induced phase separation (MIPS)[11–17] and laning.[10,18–22] Moreover, on the applied side, natural biological microswimmers[1,23–30] occur in almost all locations on Earth, including the human body, and artificial microswimmers[31–36] may in the near future be used in medical and technical applications on the microscale, e.g., for precise drug delivery,[37–41] for noninvasive surgery,[39,42,43] when guiding sperm cells,[44] and to power microengines.[45–47]

Both biological and artificial microswimmers typically operate under complex conditions.[6] For example, the complexity can arise from steric confinement of the swimmers[48–53] or be induced by a complex dispersion medium.[54–59] Here, we consider the complementing case of complexity caused by interactions between different swimmer species as can occur in a diverse set of situations.

In medical contexts, active multispecies systems (including both active–active and active–passive mixtures) appear when active agents, e.g., pathogenic bacteria or cargo-delivering microrobots, interact with (similar-sized) human cells. Furthermore, real-world

The Journal of Chemical Physics ARTICLE scitation.org/journal/jcp

microorganisms can change between motile and nonmotile (i.e., active and passive in our notation) behavior during their life with the organization in many-particle biofilms[60,61] and active carpets[62,63] as examples for extreme cases. Also, different mutant lines of the same bacterial species can show different motility properties; see, e.g., motile and nonmotile strains of *E. coli* bacteria.[26] More in general, subgroups of swimmers may be identified if a strong polydispersity, e.g., of swimming speeds, is present inside a system. Finally, at least two species of swimmers are necessary to construct "heteronuclear" (i.e., composed of different building blocks) microswimmer molecules.[64–66]

Despite these manifold possible applications, studies on mixtures of microswimmers (and active particles, in general) are still relatively rare. The problems regarded thus far include predator–prey dynamics,[67,68] mixtures of active rotors with opposite senses of rotation[69,70] (see also the corresponding macroscale equivalent in Ref. 71), transport of passive V-shaped cargo particles by active rods in the bulk[72–75] and by circle swimmers in channels,[76] depletion interactions between passive particles induced by an active bath,[77,78] segregation effects in mixtures of Taylor-line swimmers propelling by self-deformation,[79] mixtures in which the activity is introduced by an effective colored noise,[80] mesoscale transport phenomena in multispecies microorganism systems,[81] and MIPS-like phase separation in active–passive mixtures.[82–86] Furthermore, collective behavior in mixtures of straight-propelling particles[87,88] and those migrating on circular trajectories[89,90] has been studied assuming Vicsek-type[91–93] effective alignment interactions between the swimmers. In addition to that, particle-based computer simulations of binary mixtures of microswimmers with different types of propulsion mechanisms, subject to mutual hydrodynamic interactions, have been performed to quantify the effect on the overall collective alignment behavior.[94]

In the present work, we cover multicomponent microswimmer suspensions subject to external potentials. Different species here are mutually interacting, both via steric interaction potentials and via (far-field) hydrodynamic interactions. The latter may, following classical statistical mechanics (for passive particles), affect the dynamic behavior but, in general, not the appearance of static equilibrium systems. Microswimmer suspensions, however, are inherently out of equilibrium so that even steady states may be significantly altered by hydrodynamic interactions, calling for their incorporation in the physical description. Additionally, interesting phenomena can appear when hydrodynamic effects interplay with, e.g., magnetic interactions.[64,95]

Generally, supplementing experiments and many-body particle-based simulations with statistical descriptions, e.g., density-field equations, allows for thorough theoretical analysis. Ideally, the observed phenomena are explained in this way and new types of behavior are predicted, leading to a better understanding of the underlying physical effects. A well-established way of finding such density-field equations in nonequilibrium colloidal systems is dynamical density functional theory (DDFT).[48,96–108] Accordingly, we successfully derived a DDFT for one-species microswimmer systems and applied it to several example situations in previous works.[106–108] In other contexts, DDFTs for mixtures of passive colloidal particles have been developed before.[109–113] Here, we combine these two approaches and explicitly allow for different species of active microswimmers (and/or passive particles). In addition to the applications listed above, such a DDFT might in the future help to find dynamic correlation functions in one-component systems via "test-particle" methods.[108,114,115] We remark that multispecies DDFT approaches can also be used to describe the dynamics of other kinds of active matter, e.g., the growth of tumors in cell tissues.[116]

Below, the employed microswimmer model—introduced in previous works[94,106–108]—and its implications for hydrodynamic interactions are overviewed in Sec. II. It is then used in Sec. III as an input to derive the statistical theory, namely, the multispecies dynamical density functional theory for microswimmers. Subsequently, several applications of the theory are discussed in Sec. IV, where we confine ourselves to planar arrangements within three-dimensional fluids. First, extending the one-component case analyzed previously,[106,107] we explore binary mixtures of microswimmers in an external trap and find additional steady states resulting from interspecies interactions. Second, the possibility of emergent overall orientational order due to hydrodynamic interactions in binary mixtures of microswimmers is discussed. Third, microswimmers confined inside an externally driven ring of passive colloidal particles are investigated. The passive particles induce a shear flow that the enclosed active swimmers are exposed to. Finally, a short summary and an outlook are given in Sec. V.

II. SWIMMER MODEL AND THE RESULTING HYDRODYNAMIC INTERACTIONS

Before a particle-scale statistical description can be developed in Sec. III, an appropriate discretized swimmer model must first be defined. In particular, the hydrodynamic interactions between individual swimmers are specified below. For this purpose, we briefly review the previously introduced minimal swimmer model.[94,106–108]

Since a microswimmer cannot exert a net force on the surrounding liquid,[1,117] the far-field fluid flow around a swimmer (to lowest order) can typically be described as if it were caused by a force dipole acting on the fluid. (Exceptions are "neutral-type" swimmers with a vanishing time-averaged force-dipole contribution,[118–121] which only feature higher-order multipole terms in the far-field flow caused, e.g., by an effective force quadrupole.) Here, we explicitly resolve the force dipole by two oppositely oriented forces of equal magnitude.

Depending on whether the forces push out or pull in the fluid along the axis of self-propulsion, one distinguishes between *pusher* (extensile) and *puller* (contractile) microswimmers.[122,123] Consequently, pushers draw in the fluid from the transverse directions, while pullers expel it along them. Our model can cover both cases, as detailed below.

Low Reynolds numbers—as are typical for microswimmers[1]—and incompressibility of the fluid are henceforth assumed. Particularly, this means that the response of the fluid to a force is linear, overdamped, and instantaneous. In the bulk, the analytically known Oseen tensor then explicitly connects the effect of a pointlike force center to the resulting fluid flow.[124–126] For finite-sized spherical particles subject to net forces and torques, the way to find (approximate) expressions for the induced hydrodynamic interactions between them is well-established.[125,126]

The Journal of Chemical Physics ARTICLE scitation.org/journal/jcp

This said, we now detail our minimal microswimmer model, see Fig. 1, referring to one swimmer labeled by i. In this model, a no-slip boundary encloses the spherical swimmer body, the latter being centered at position $\mathbf{r}_i$ and being of radius a_i. Below, $\mathbf{v}_i$ and $\boldsymbol{\omega}_i$ denote the velocity and angular velocity of the sphere, respectively.

Additionally, two oppositely oriented forces

$$\mathbf{f}_{i\pm} = \pm f_i\,\hat{\mathbf{n}}_i \tag{1}$$

of equal magnitude are exerted by the swimmer onto the surrounding fluid at positions

$$\mathbf{r}_{i+} = \mathbf{r}_i + \alpha_i\,L_i\,\hat{\mathbf{n}}_i, \tag{2}$$

$$\mathbf{r}_{i-} = \mathbf{r}_i - (1-\alpha_i)\,L_i\,\hat{\mathbf{n}}_i, \tag{3}$$

respectively, relative to its body center. They move and rotate along with the sphere and create the fluid flow that (self-)propels the swimmer. Here, $\hat{\mathbf{n}}_i$ is the unit vector describing the orientation of the axially symmetric swimmer, $L_i > 2a_i$ is the distance between the two force centers, and $|f_i|$ sets the magnitude of the forces. Depending on the sign of f_i, either pusher ($f_i > 0$) or puller ($f_i < 0$) microswimmers are constructed. Furthermore, the real number α_i (with $a_i/L_i < \alpha_i < 1/2$) is a geometric parameter, see Fig. 1, that quantifies the breaking of the front–rear symmetry, which implies self-propulsion. The swimmer self-propels in the direction of $\hat{\mathbf{n}}_i$ for pushers, see Fig. 1(a), and $-\hat{\mathbf{n}}_i$ for pullers, see Fig. 1(b).

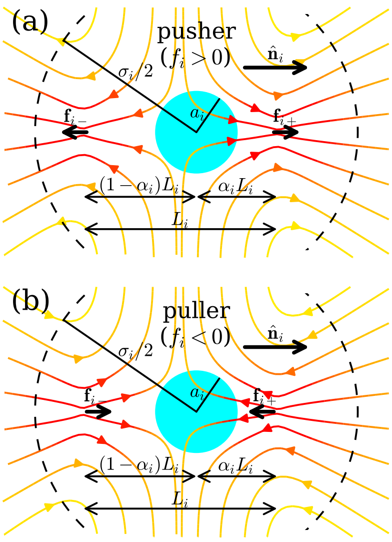

FIG. 1. Force-dipole-based minimal microswimmer model.[106] Around a central sphere of radius a_i, two antiparallel equal-magnitude forces $\mathbf{f}_{i\pm} = \pm f_i\hat{\mathbf{n}}_i$ are exerted asymmetrically onto the fluid. The sphere is transported by the resulting fluid flow [streamlines are shown, with dark (red) line segments corresponding to high magnitudes and light (yellow) ones to low magnitudes of the local fluid flow] for $\alpha_i \neq 1/2$. A dashed circle of diameter σ_i indicates the effective swimmer size due to steric interactions between the swimmers. (a) For $f_i > 0$, a pusher microswimmer is constructed, which expels fluid along its symmetry axis and draws fluid in from the sides. (b) For a puller microswimmer ($f_i < 0$), the directions of the fluid flow are inverted.

Moreover, an isotropic steric interaction between the swimmers is assumed that avoids unphysical overlap between force centers and bodies of different swimmers. As indicated in Fig. 1 and further detailed later, the effective center-to-center range of the steric interactions is denoted by σ_i.

Next, we specify the hydrodynamic interactions in a system of N potentially different such model swimmers, labeled by $i = 1, \ldots, N$. For shorter notation, we furthermore define the phase-space coordinate $\mathbf{X}_i = \{\mathbf{r}_i, \hat{\mathbf{n}}_i\}$ of each swimmer i. In our overdamped system of microswimmers in suspension, $\mathbf{v}_i$ and $\boldsymbol{\omega}_i$ follow instantaneously from the microstate $\mathbf{X}^N = \{\mathbf{X}_1, \ldots, \mathbf{X}_N\}$.

In principle, hydrodynamic interactions are many-body interactions.[124–126] Yet, already the lowest-order contributions beyond pairwise interactions are of fourth order in the ratio of body size to swimmer distance[125] and can be neglected when one is primarily interested in the effect of far-field hydrodynamic interactions, e.g., in semidilute suspensions.[127–131] This is further supported by our use of repulsive steric interactions between swimmers, as detailed below, that keep them at distances from each other that are significantly larger than their hydrodynamic radii a_i; see also Fig. 1. Thus, here we only account for pairwise interactions and restrict ourselves to an expansion up to (including) the third order, also known as the Rotne-Prager level.[132,133]

Following this idea, $\mathbf{v}_i$ and $\boldsymbol{\omega}_i$ are connected to the (nonhydrodynamic) forces $\mathbf{F}_j$ and torques $\mathbf{T}_j$ acting on the swimmer bodies $j = 1, \ldots, N$ and the self-propulsion forces that the swimmers exert via[106]

$$\begin{bmatrix}\mathbf{v}_i\\ \boldsymbol{\omega}_i\end{bmatrix} = \sum_{j=1}^{N}\left(\begin{bmatrix}\boldsymbol{\mu}_{ij}^{\mathrm{tt}} & \boldsymbol{\mu}_{ij}^{\mathrm{tr}}\\ \boldsymbol{\mu}_{ij}^{\mathrm{rt}} & \boldsymbol{\mu}_{ij}^{\mathrm{rr}}\end{bmatrix}\cdot\begin{bmatrix}\mathbf{F}_j\\ \mathbf{T}_j\end{bmatrix} + \begin{bmatrix}\boldsymbol{\Lambda}_{ij}^{\mathrm{tt}} & \mathbf{0}\\ \boldsymbol{\Lambda}_{ij}^{\mathrm{rt}} & \mathbf{0}\end{bmatrix}\cdot\begin{bmatrix}f\hat{\mathbf{n}}_j\\ \mathbf{0}\end{bmatrix}\right). \tag{4}$$

Here, the mobility tensors representing the passive hydrodynamic interactions between two swimmer bodies $i \neq j$ are given by[106,125,132,133]

$$\boldsymbol{\mu}_{ij}^{tt} = \frac{1}{6\pi\eta}\left(\frac{3}{4r_{ij}}\left(\mathbf{1} + \hat{\mathbf{r}}_{ij}\hat{\mathbf{r}}_{ij}\right) + \frac{a_i^2 + a_j^2}{4}\left(\frac{1}{r_{ij}}\right)^3\left(\mathbf{1} - 3\,\hat{\mathbf{r}}_{ij}\hat{\mathbf{r}}_{ij}\right)\right), \tag{5}$$

$$\boldsymbol{\mu}_{ij}^{rr} = -\frac{1}{8\pi\eta}\frac{1}{2}\left(\frac{1}{r_{ij}}\right)^3\left(\mathbf{1} - 3\,\hat{\mathbf{r}}_{ij}\hat{\mathbf{r}}_{ij}\right), \tag{6}$$

$$\boldsymbol{\mu}_{ij}^{tr} = \boldsymbol{\mu}_{ij}^{rt} = \frac{1}{8\pi\eta}\left(\frac{1}{r_{ij}}\right)^3\mathbf{r}_{ij}\times, \tag{7}$$

where η is the dynamic viscosity of the fluid, "×" denotes the outer vector product, $\mathbf{1}$ represents the identity matrix, $\mathbf{r}_{ij} = \mathbf{r}_j - \mathbf{r}_i$ is the distance vector, $r_{ij} = |\mathbf{r}_{ij}|$ denotes its absolute value, and $\hat{\mathbf{r}}_{ij} = \mathbf{r}_{ij}/r_{ij}$ is the corresponding unit vector. Additionally, the passive "self" (i.e., $i = j$) mobilities read (no summation over repeated indices in these expressions)

$$\boldsymbol{\mu}_{ii}^{\mathrm{tt}} = \mu_i^{\mathrm{t}}\,\mathbf{1}, \quad \boldsymbol{\mu}_{ii}^{\mathrm{rr}} = \mu_i^{\mathrm{r}}\,\mathbf{1}, \quad \boldsymbol{\mu}_{ii}^{\mathrm{tr}} = \boldsymbol{\mu}_{ii}^{\mathrm{rt}} = \mathbf{0}, \tag{8}$$

with

The Journal of Chemical Physics ARTICLE scitation.org/journal/jcp

$$\mu_i^{\mathrm{t}} = 1/(6\pi\eta a_i), \quad \mu_i^{\mathrm{r}} = 1/(8\pi\eta a_i^3). \tag{9}$$

Next, the active contribution to Eq. (4) is given by the tensors[106]

$$\boldsymbol{\Lambda}_{ij}^{\mathrm{tt}} = \boldsymbol{\mu}_{ij}^{\mathrm{tt}+} - \boldsymbol{\mu}_{ij}^{\mathrm{tt}-}, \tag{10}$$

$$\boldsymbol{\Lambda}_{ij}^{\mathrm{rt}} = \boldsymbol{\mu}_{ij}^{\mathrm{rt}+} - \boldsymbol{\mu}_{ij}^{\mathrm{rt}-}, \tag{11}$$

with

$$\boldsymbol{\mu}_{ij}^{\mathrm{tt}\pm} = \frac{1}{8\pi\eta r_{ij}^{\pm}}\left(\mathbf{1} + \hat{\mathbf{r}}_{ij}^{\pm}\hat{\mathbf{r}}_{ij}^{\pm}\right) + \frac{a_i^2}{24\pi\eta\left(r_{ij}^{\pm}\right)^3}\left(\mathbf{1} - 3\,\hat{\mathbf{r}}_{ij}^{\pm}\hat{\mathbf{r}}_{ij}^{\pm}\right), \tag{12}$$

$$\boldsymbol{\mu}_{ij}^{\mathrm{rt}\pm} = \frac{1}{8\pi\eta\left(r_{ij}^{\pm}\right)^3}\,\mathbf{r}_{ij}^{\pm}\times, \tag{13}$$

and

$$\mathbf{r}_{ij}^{+} = \mathbf{r}_{ij} + \alpha_j\, L_j\, \hat{\mathbf{n}}_j, \tag{14}$$

$$\mathbf{r}_{ij}^{-} = \mathbf{r}_{ij} - (1 - \alpha_j)\, L_j\, \hat{\mathbf{n}}_j. \tag{15}$$

As can be seen, there is only little change to the one-species case $(a_i = a_j \equiv a)$[106] at this order of the expansion in a_k/r_{ij}, $k = i, j$, namely, only in Eq. (5).

Setting $i = j$ in Eqs. (10) and (11), the velocity and angular velocity of a free swimmer i are obtained as[94]

$$\mathbf{v}_{0i} = \frac{a_i}{2L_i}\frac{1 - 2\alpha_i}{\alpha_i(1 - \alpha_i)}\left(3 - \frac{a_i^2}{L_i^2}\frac{1 - \alpha_i + \alpha_i^2}{\alpha_i^2(1 - \alpha_i)^2}\right)\mu_i^{\mathrm{t}}\, f_i\, \hat{\mathbf{n}}_i \tag{16}$$

and, respectively, $\boldsymbol{\omega}_{0i} = \mathbf{0}$. Thus, in the absence of thermal noise and outer influences, this kind of swimmer self-propels along a straight trajectory. Corresponding circle swimmers of axial asymmetry and a nonvanishing $\boldsymbol{\omega}_{0i}$ were considered in a previous work.[107]

We remark that, for simplicity, we here do not account for the distortions caused by the finite spherical swimmer bodies on the flow field induced by the active force centers.[126,134] That is, when discussing the active mobility tensors $\boldsymbol{\Lambda}_{ij}^{\mathrm{tt}}$ and $\boldsymbol{\Lambda}_{ij}^{\mathrm{rt}}$ for $i \neq j$, in effect, we only consider terms in a_j/L_j to the leading order.

Finally, the forces and torques in Eq. (4) remain to be defined. First, we set the overall potential in our system of N swimmers as

$$U(\mathbf{r}_1, \ldots, \mathbf{r}_N) = \sum_{k=1}^{N} u_{\mathrm{ext}}^{k}(\mathbf{r}_k) + \sum_{k,l=1;\,k<l}^{N} u^{kl}(|\mathbf{r}_k - \mathbf{r}_l|). \tag{17}$$

Here, the external potentials u_{ext}^{k} can differ for different particles k. Additionally, pairwise steric interactions are introduced via $u^{kl}(|\mathbf{r}_k - \mathbf{r}_l|)$, which we specify for the applications in Sec. IV as the GEM-4 potential[135,136]

$$u^{kl}(|\mathbf{r}_k - \mathbf{r}_l|) = \epsilon_0^{kl}\exp\left(-\left(\frac{|\mathbf{r}_k - \mathbf{r}_l|}{\sigma_{kl}}\right)^4\right), \tag{18}$$

with the potential strength ϵ_0^{kl} and the effective diameter $\sigma_{kl} = (\sigma_k + \sigma_l)/2$ being set for each pair k and l.

The forces $\mathbf{F}_j$ in Eq. (4) then read

$$\mathbf{F}_j = -k_B T\, \nabla_{\mathbf{r}_j} \ln P - \nabla_{\mathbf{r}_j} U(\mathbf{r}_1, \ldots, \mathbf{r}_N), \tag{19}$$

where the effect of thermal forces enters via the first term based on the effective entropic potential,[137] which involves the microstate probability density $P = P(\mathbf{X}^N, t)$, the Boltzmann factor k_B, and the temperature T of the system. This expression ensures that the correct (translational) diffusion terms eventually appear in the statistical description in Sec. III.

Similarly, the torques in Eq. (4) are given by

$$\mathbf{T}_j = -k_B T\, \hat{\mathbf{n}}_j \times \nabla_{\hat{\mathbf{n}}_j} \ln P. \tag{20}$$

Again, this expression correctly reproduces (rotational) diffusion in the statistical description; see Sec. III.

III. DERIVATION OF THE DYNAMICAL DENSITY FUNCTIONAL THEORY

In this section, we derive the partial differential equations describing the dynamical microscopic statistics of a multicomponent microswimmer system via dynamical density functional theory (DDFT), building on the derivations of the one-component case.[106,107] For this purpose, the hydrodynamic swimmer model overviewed in Sec. II is used as an input. The resulting theory covers, combines, and extends several previously considered theories for systems of, e.g., one-species microswimmer suspensions,[106] "dry"—i.e., not hydrodynamically interacting—self-propelled particles,[48,105] hydrodynamically interacting passive colloidal particles,[138] and binary mixtures of dry passive colloidal particles.[109]

First, we specify our system, which contains two different species of microswimmers suspended in a surrounding bulk fluid. For these species, the number of corresponding swimmers in the system is given by N_A and N_B, respectively, adding up to a total of $N = N_A + N_B$ swimmers. Here, we order the swimmers by species, such that swimmers 1, ..., N_A belong to the first species and swimmers $N_A + 1$, ..., N to the second species. Additionally, a constant temperature T of the fluid and a constant volume of the system are assumed. We adhere to the swimmer model introduced in Sec. II, with all swimmers of species $\nu \in \{A, B\}$ featuring the same parameters $a_\nu, f_\nu, \alpha_\nu, L_\nu$, and σ_ν. Setting $f_\nu = 0$, also passive particles can be described accordingly, i.e., active–passive mixtures are covered by our theory as well.

Our starting point to derive the statistical description is the many-body Smoluchowski equation[137]

$$\frac{\partial P}{\partial t} = -\sum_{i=1}^{N}\left(\nabla_{\mathbf{r}_i}\cdot(\mathbf{v}_i P) + (\hat{\mathbf{n}}_i \times \nabla_{\hat{\mathbf{n}}_i})\cdot(\boldsymbol{\omega}_i P)\right) \tag{21}$$

for the overdamped dynamics of our microswimmers. Here, $P = P(\mathbf{X}_1, \ldots, \mathbf{X}_N, t)$ denotes the microstate probability density of the corresponding configuration at time t. The velocities $\mathbf{v}_i$ and the angular velocities $\boldsymbol{\omega}_i$ are again related to the forces, torques, and the self-propulsion mechanisms via Eq. (4).

Next, we introduce $\mathbf{X}_A^m = \{\mathbf{X}_1, \ldots, \mathbf{X}_m\}$ and $\mathbf{X}_B^n = \{\mathbf{X}_{N_A+1}, \ldots, \mathbf{X}_{N_A+n}\}$ as short notations for the sets containing the phase-space coordinates of the first m swimmers of species A and, respectively, the first n swimmers of species B in the system. Since

The Journal of Chemical Physics ARTICLE scitation.org/journal/jcp

all swimmers are identical, we now define, for $m \le N_\mathrm{A}$ and $n \le N_\mathrm{B}$, the reduced (m, n)-swimmer density $\rho^{(m,n)}(\mathbf{X}_\mathrm{A}^m, \mathbf{X}_\mathrm{B}^n, t)$ of finding (any) m swimmers of species A and (any) n swimmers of species B at the coordinates indicated in the argument. It is obtained from the full probability distribution $P(\mathbf{X}_\mathrm{A}^{N_\mathrm{A}}, \mathbf{X}_\mathrm{B}^{N_\mathrm{B}}, t)$ by integrating out the degrees of freedom of $N_\mathrm{A} - m$ swimmers of species A and $N_\mathrm{B} - n$ swimmers of species B, reading

$$\rho^{(m,n)}(\mathbf{X}_\mathrm{A}^m, \mathbf{X}_\mathrm{B}^n, t) = \frac{N_\mathrm{A}!}{(N_\mathrm{A}-m)!}\frac{N_\mathrm{B}!}{(N_\mathrm{B}-n)!}\int \mathrm{d}\mathbf{X}_{m+1}\cdots\int \mathrm{d}\mathbf{X}_{N_\mathrm{A}} \times \int \mathrm{d}\mathbf{X}_{N_\mathrm{A}+n+1}\cdots\int \mathrm{d}\mathbf{X}_{N_\mathrm{A}+N_\mathrm{B}}\, P(\mathbf{X}_\mathrm{A}^{N_\mathrm{A}}, \mathbf{X}_\mathrm{B}^{N_\mathrm{B}}, t). \tag{22}$$

Here, the prefactors result from the considered indistinguishability between swimmers of the same species. Particularly, we define the one-swimmer densities $\rho_\mathrm{A}(\mathbf{X}, t) := \rho^{(1,0)}(\mathbf{X}, t)$ and $\rho_\mathrm{B}(\mathbf{X}, t) := \rho^{(0,1)}(\mathbf{X}, t)$. Instead of referring to one specific swimmer, the coordinates $\mathbf{X}$ now simply identify "a swimmer" of the corresponding species. Furthermore, reduced densities with $m + n = 2$ $(m + n = 3)$ will be referred to as two-swimmer (three-swimmer) densities below.

Our aim is to derive a physically well-grounded, closed set of coupled dynamical equations for the two one-swimmer densities. Thus, eventually, there shall be no remaining explicit dependence on the (generally unknown) higher-order densities. The starting point for our derivation is the many-body Smoluchowski equation given in Eq. (21). We first integrate out all swimmer coordinates except for those of one swimmer of species A. Second, we integrate out in the initial Eq. (21) all swimmer coordinates except for those of one swimmer of species B. As a result, we obtain one dynamical equation for $\rho_\mathrm{A}(\mathbf{X}, t)$ and one for $\rho_\mathrm{B}(\mathbf{X}, t)$, respectively. These equations (given below) form a coupled set but at this point still contain higher-order densities and thus require an additional closure, as will be addressed afterward via methods of dynamical density functional theory.

The corresponding equation for species A reads

$$\frac{\partial \rho_\mathrm{A}(\mathbf{X},t)}{\partial t} = -\nabla_\mathbf{r}\cdot\Big(\mathcal{J}_\mathrm{A}^\mathrm{tt} + \mathcal{J}_\mathrm{A}^\mathrm{tr} + \mathcal{J}_\mathrm{A}^\mathrm{ta} + \mathcal{K}_\mathrm{AA}^\mathrm{tt} + \mathcal{K}_\mathrm{AA}^\mathrm{tr} + \mathcal{K}_\mathrm{AA}^\mathrm{ta} + \mathcal{K}_\mathrm{AB}^\mathrm{tt} + \mathcal{K}_\mathrm{AB}^\mathrm{tr} + \mathcal{K}_\mathrm{AB}^\mathrm{ta}\Big) - (\hat{\mathbf{n}}\times\nabla_{\hat{\mathbf{n}}})\cdot\Big(\mathcal{J}_\mathrm{A}^\mathrm{rt} + \mathcal{J}_\mathrm{A}^\mathrm{rr} + \mathcal{J}_\mathrm{A}^\mathrm{ra} + \mathcal{K}_\mathrm{AA}^\mathrm{rt} + \mathcal{K}_\mathrm{AA}^\mathrm{rr} + \mathcal{K}_\mathrm{AA}^\mathrm{ra} + \mathcal{K}_\mathrm{AB}^\mathrm{rt} + \mathcal{K}_\mathrm{AB}^\mathrm{rr} + \mathcal{K}_\mathrm{AB}^\mathrm{ra}\Big). \tag{23}$$

In this expression, the current densities labeled as $\mathcal{J}^{\cdot\cdot}$ do not involve hydrodynamic interactions between swimmers. These current densities are given by

$$\mathcal{J}_\mathrm{A}^\mathrm{tt} = -\mu^{\mathrm{t,A}}\Big(k_\mathrm{B}T\,\nabla_\mathbf{r}\rho_\mathrm{A}(\mathbf{X},t) + \rho_\mathrm{A}(\mathbf{X},t)\nabla_\mathbf{r}u_\mathrm{ext}^\mathrm{A}(\mathbf{r}) + \int \mathrm{d}\mathbf{X}'\rho^{(2,0)}(\mathbf{X},\mathbf{X}',t)\nabla_\mathbf{r}u^\mathrm{AA}(|\mathbf{r}-\mathbf{r}'|) + \int \mathrm{d}\mathbf{X}'\rho^{(1,1)}(\mathbf{X},\mathbf{X}',t)\nabla_\mathbf{r}u^\mathrm{AB}(|\mathbf{r}-\mathbf{r}'|)\Big), \tag{24}$$

$$\mathcal{J}_\mathrm{A}^\mathrm{ta} = f_\mathrm{A}\boldsymbol{\Lambda}_{\mathbf{r},\mathbf{X}}^{\mathrm{tt,AA}}\cdot\hat{\mathbf{n}}\,\rho_\mathrm{A}(\mathbf{X},t), \tag{25}$$

$$\mathcal{J}_\mathrm{A}^\mathrm{rr} = -k_\mathrm{B}T\,\mu^{\mathrm{r,A}}\,\hat{\mathbf{n}}\times\nabla_{\hat{\mathbf{n}}}\rho_\mathrm{A}(\mathbf{X},t), \tag{26}$$

$$\mathcal{J}_\mathrm{A}^\mathrm{tr} = \mathcal{J}_\mathrm{A}^\mathrm{rt} = \mathcal{J}_\mathrm{A}^\mathrm{ra} = \mathbf{0}. \tag{27}$$

In contrast to that, the current densities involving hydrodynamic interactions between pairs of swimmers of species A follow as

$$\mathcal{K}_\mathrm{AA}^\mathrm{tt} = -\int \mathrm{d}\mathbf{X}'\,\boldsymbol{\mu}_{\mathbf{r},\mathbf{r}'}^{\mathrm{tt,AA}}\cdot\Big(k_\mathrm{B}T\,\nabla_{\mathbf{r}'}\rho^{(2,0)}(\mathbf{X},\mathbf{X}',t) + \rho^{(2,0)}(\mathbf{X},\mathbf{X}',t)\nabla_{\mathbf{r}'}\big(u_\mathrm{ext}^\mathrm{A}(\mathbf{r}') + u^\mathrm{AA}(|\mathbf{r}-\mathbf{r}'|)\big) + \int \mathrm{d}\mathbf{X}''\rho^{(2,1)}(\mathbf{X},\mathbf{X}',\mathbf{X}'',t)\nabla_{\mathbf{r}'}u^\mathrm{AB}(|\mathbf{r}'-\mathbf{r}''|) + \int \mathrm{d}\mathbf{X}''\rho^{(3,0)}(\mathbf{X},\mathbf{X}',\mathbf{X}'',t)\nabla_{\mathbf{r}'}u^\mathrm{AA}(|\mathbf{r}'-\mathbf{r}''|)\Big), \tag{28}$$

$$\mathcal{K}_\mathrm{AA}^\mathrm{tr} = -\int \mathrm{d}\mathbf{X}'\,k_\mathrm{B}T\,\boldsymbol{\mu}_{\mathbf{r},\mathbf{r}'}^{\mathrm{tr,AA}}(\hat{\mathbf{n}}'\times\nabla_{\hat{\mathbf{n}}'})\rho^{(2,0)}(\mathbf{X},\mathbf{X}',t) = \mathbf{0}, \tag{29}$$

$$\mathcal{K}_\mathrm{AA}^\mathrm{ta} = f_\mathrm{A}\int \mathrm{d}\mathbf{X}'\,\boldsymbol{\Lambda}_{\mathbf{r},\mathbf{X}'}^{\mathrm{tt,AA}}\cdot\hat{\mathbf{n}}'\rho^{(2,0)}(\mathbf{X},\mathbf{X}',t), \tag{30}$$

$$\mathcal{K}_\mathrm{AA}^\mathrm{rt} = -\int \mathrm{d}\mathbf{X}'\,\boldsymbol{\mu}_{\mathbf{r},\mathbf{r}'}^{\mathrm{rt,AA}}\Big(k_\mathrm{B}T\,\nabla_{\mathbf{r}'}\rho^{(2,0)}(\mathbf{X},\mathbf{X}',t) + \rho^{(2,0)}(\mathbf{X},\mathbf{X}',t)\nabla_{\mathbf{r}'}\big(u_\mathrm{ext}^\mathrm{A}(\mathbf{r}') + u^\mathrm{AA}(|\mathbf{r}-\mathbf{r}'|)\big) + \int \mathrm{d}\mathbf{X}''\rho^{(2,1)}(\mathbf{X},\mathbf{X}',\mathbf{X}'',t)\nabla_{\mathbf{r}'}u^\mathrm{AB}(|\mathbf{r}'-\mathbf{r}''|) + \int \mathrm{d}\mathbf{X}''\rho^{(3,0)}(\mathbf{X},\mathbf{X}',\mathbf{X}'',t)\nabla_{\mathbf{r}'}u^\mathrm{AA}(|\mathbf{r}'-\mathbf{r}''|)\Big), \tag{31}$$

$$\mathcal{K}_\mathrm{AA}^\mathrm{rr} = -\int \mathrm{d}\mathbf{X}'\,k_\mathrm{B}T\,\boldsymbol{\mu}_{\mathbf{r},\mathbf{r}'}^{\mathrm{rr,AA}}\cdot(\hat{\mathbf{n}}'\times\nabla_{\hat{\mathbf{n}}'})\rho^{(2,0)}(\mathbf{X},\mathbf{X}',t) = \mathbf{0}, \tag{32}$$

$$\mathcal{K}_\mathrm{AA}^\mathrm{ra} = f_\mathrm{A}\int \mathrm{d}\mathbf{X}'\,\boldsymbol{\Lambda}_{\mathbf{r},\mathbf{X}'}^{\mathrm{rt,AA}}\,\hat{\mathbf{n}}'\rho^{(2,0)}(\mathbf{X},\mathbf{X}',t). \tag{33}$$

Third, the current densities associated with hydrodynamic effects of swimmers of species B on swimmers of species A are

$$\mathcal{K}_\mathrm{AB}^\mathrm{tt} = -\int \mathrm{d}\mathbf{X}'\,\boldsymbol{\mu}_{\mathbf{r},\mathbf{r}'}^{\mathrm{tt,AB}}\cdot\Big(k_\mathrm{B}T\,\nabla_{\mathbf{r}'}\rho^{(1,1)}(\mathbf{X},\mathbf{X}',t) + \rho^{(1,1)}(\mathbf{X},\mathbf{X}',t)\nabla_{\mathbf{r}'}\big(u_\mathrm{ext}^\mathrm{B}(\mathbf{r}') + u^\mathrm{AB}(|\mathbf{r}-\mathbf{r}'|)\big) + \int \mathrm{d}\mathbf{X}''\rho^{(1,2)}(\mathbf{X},\mathbf{X}',\mathbf{X}'',t)\nabla_{\mathbf{r}'}u^\mathrm{BB}(|\mathbf{r}'-\mathbf{r}''|) + \int \mathrm{d}\mathbf{X}''\rho^{(2,1)}(\mathbf{X},\mathbf{X}'',\mathbf{X}',t)\nabla_{\mathbf{r}'}u^\mathrm{AB}(|\mathbf{r}'-\mathbf{r}''|)\Big), \tag{34}$$

$$\mathcal{K}_\mathrm{AB}^\mathrm{tr} = -\int \mathrm{d}\mathbf{X}'\,k_\mathrm{B}T\,\boldsymbol{\mu}_{\mathbf{r},\mathbf{r}'}^{\mathrm{tr,AB}}(\hat{\mathbf{n}}'\times\nabla_{\hat{\mathbf{n}}'})\rho^{(1,1)}(\mathbf{X},\mathbf{X}',t) = \mathbf{0}, \tag{35}$$

$$\mathcal{K}_\mathrm{AB}^\mathrm{ta} = f_\mathrm{B}\int \mathrm{d}\mathbf{X}'\,\boldsymbol{\Lambda}_{\mathbf{r},\mathbf{X}'}^{\mathrm{tt,AB}}\cdot\hat{\mathbf{n}}'\rho^{(1,1)}(\mathbf{X},\mathbf{X}',t), \tag{36}$$

$$\mathcal{K}_\mathrm{AB}^\mathrm{rt} = -\int \mathrm{d}\mathbf{X}'\,\boldsymbol{\mu}_{\mathbf{r},\mathbf{r}'}^{\mathrm{rt,AB}}\Big(k_\mathrm{B}T\,\nabla_{\mathbf{r}'}\rho^{(1,1)}(\mathbf{X},\mathbf{X}',t) + \rho^{(1,1)}(\mathbf{X},\mathbf{X}',t)\nabla_{\mathbf{r}'}\big(u_\mathrm{ext}^\mathrm{B}(\mathbf{r}') + u^\mathrm{AB}(|\mathbf{r}-\mathbf{r}'|)\big) + \int \mathrm{d}\mathbf{X}''\rho^{(1,2)}(\mathbf{X},\mathbf{X}',\mathbf{X}'',t)\nabla_{\mathbf{r}'}u^\mathrm{BB}(|\mathbf{r}'-\mathbf{r}''|) + \int \mathrm{d}\mathbf{X}''\rho^{(2,1)}(\mathbf{X},\mathbf{X}'',\mathbf{X}',t)\nabla_{\mathbf{r}'}u^\mathrm{AB}(|\mathbf{r}'-\mathbf{r}''|)\Big), \tag{37}$$

$$\mathcal{K}_\mathrm{AB}^\mathrm{rr} = -\int \mathrm{d}\mathbf{X}'\,k_\mathrm{B}T\,\boldsymbol{\mu}_{\mathbf{r},\mathbf{r}'}^{\mathrm{rr,AB}}\cdot(\hat{\mathbf{n}}'\times\nabla_{\hat{\mathbf{n}}'})\rho^{(1,1)}(\mathbf{X},\mathbf{X}',t) = \mathbf{0}, \tag{38}$$

$$\mathcal{K}_\mathrm{AB}^\mathrm{ra} = f_\mathrm{B}\int \mathrm{d}\mathbf{X}'\,\boldsymbol{\Lambda}_{\mathbf{r},\mathbf{X}'}^{\mathrm{rt,AB}}\,\hat{\mathbf{n}}'\rho^{(1,1)}(\mathbf{X},\mathbf{X}',t). \tag{39}$$

The Journal of Chemical Physics ARTICLE scitation.org/journal/jcp

Here, the tensors $\boldsymbol{\mu}_{\cdot\cdot}^{\cdot\cdot}$ and $\boldsymbol{\Lambda}_{\cdot\cdot}^{\cdot\cdot}$ follow from the definitions in Eqs. (5)–(15) by inserting the parameters corresponding to the (phase-space) coordinates given in the subscripts and the combination of species referred to in the superscripts. The current densities $\mathcal{K}_{AA}^{tr}$, $\mathcal{K}_{AA}^{rr}$, $\mathcal{K}_{AB}^{tr}$, and $\mathcal{K}_{AB}^{rr}$ vanish for spherical swimmer bodies because the corresponding mobility tensors are independent of $\hat{\mathbf{n}}'$; see Eqs. (6) and (7). Integrating the remaining gradient expressions over the closed surface of the unit sphere yields zero in each case. For nonspherical swimmer bodies, however, these current densities (as well as $\mathcal{J}_A^{tt}$, $\mathcal{J}_A^{rt}$, and $\mathcal{J}_A^{ra}$) could be nonzero. Moreover, we remark that all $\mathcal{K}$s become zero if hydrodynamic interactions are neglected.

An analogous dynamical equation for $\rho_B(\mathbf{X}, t)$ follows by replacing A → B, B → A, and $\rho^{(m,n)} \to \rho^{(n,m)}$. Moreover, because of our convention of ordering species coordinates by first A and then B, we need to replace

$$\begin{aligned}\rho^{(1,1)}(\mathbf{X},\mathbf{X}',t) &\to \rho^{(1,1)}(\mathbf{X}',\mathbf{X},t),\\ \rho^{(1,2)}(\mathbf{X},\mathbf{X}',\mathbf{X}'',t) &\to \rho^{(2,1)}(\mathbf{X}',\mathbf{X}'',\mathbf{X},t),\\ \rho^{(2,1)}(\mathbf{X},\mathbf{X}',\mathbf{X}'',t) &\to \rho^{(1,2)}(\mathbf{X}'',\mathbf{X},\mathbf{X}',t),\\ \rho^{(2,1)}(\mathbf{X},\mathbf{X}'',\mathbf{X}',t) &\to \rho^{(1,2)}(\mathbf{X}',\mathbf{X},\mathbf{X}'',t).\end{aligned}$$

Obviously, Eqs. (24)–(39) depend on unknown higher-order densities. In principle, one can now find dynamical equations for these quantities by applying corresponding integral operations on Eq. (21), but the resulting equations again contain unknown densities of even higher order. This escalating loop is typical for BBGKY-like hierarchies[139] and must be truncated and closed by appropriate approximations of the higher-order densities, e.g., as functions of the one-swimmer densities. In the following, DDFT methods will be employed for this purpose.

The main step in DDFT[96–105] is the *adiabatic approximation*. It transfers equilibrium closure relations established in (classical) density functional theory (DFT) to the nonequilibrium case. Particularly, DDFTs imply that the higher-order densities relax faster than the one-swimmer densities[102] as is conceivable for typical overdamped systems of colloidal particles (i.e., at low Reynolds numbers) and thus also for microswimmers.[106]

In equilibrium, DFT states that each observed density profile results from exactly one, uniquely specified external potential working on the corresponding particles.[97–101,104,140] We call these potentials $\Phi_{ext}^{\nu}(\mathbf{X})$, ν = A, B, for the two species in our case. DDFT assumes these relations to hold at any time t. Thus, the external DFT potentials become time-dependent, and we denote them by $\Phi_{ext}^{\nu}(\mathbf{X},t)$. We remark that the equilibrium relations strictly hold only for $f_\nu = 0$, ν = A, B, i.e., for passive particles. This limits the applicability of the theory when activity-induced correlation effects in the higher-order densities dominate the behavior of the system. Nevertheless, the overdamped nature of the systems favors the DDFT approach. Previously, bulk swimmer–swimmer pair distribution functions have been determined[108] by combining DDFT with a Percus-like[141] test-particle protocol.

We now discuss the above-introduced virtual external potentials, which may (and generally will) differ for the two species. In contrast to the "real" external potential introduced in Eq. (17), a dependence on the orientations of the swimmers here is allowed and indeed even needed when the distributions of the orientations become nonuniform.

It must be stressed that these virtual potentials do not need to be determined explicitly. Repeating usual steps in derivations of DDFTs, we will in the following show two different ways of expressing $\Phi_{ext}^{\nu}(\mathbf{X},t)$ so that they can be eliminated from the mathematical description. Accordingly, we obtain expressions that help us to close the above BBGKY-like set of equations.

We start from the equilibrium grand potential as a functional of the one-swimmer densities, which is minimal for the equilibrium density distributions. The general ansatz for this functional can be written as[109]

$$\Omega[\rho_A,\rho_B] = \sum_{\nu=A,B}\Big(\mathcal{F}_{ext}^{\nu}[\rho_\nu] + \mathcal{F}_{id}^{\nu}[\rho_\nu]\Big) + \mathcal{F}_{exc}[\rho_A,\rho_B]. \tag{40}$$

Here, all terms on the right-hand side except for the last one are known analytically. Namely,

$$\mathcal{F}_{id}^{\nu}[\rho_\nu] = k_BT\int d\mathbf{X}\,\rho_\nu(\mathbf{X})\Big(\ln\big(\lambda_\nu^3\rho_\nu(\mathbf{X})\big) - 1\Big), \tag{41}$$

ν = A, B, is the ideal gas part, with λ_ν being the corresponding thermal de Broglie wavelength λ_ν. The contributions due to the external DFT potentials read

$$\mathcal{F}_{ext}^{\nu}[\rho_\nu] = \int d\mathbf{X}\,\rho_\nu(\mathbf{X})\,\Phi_{ext}^{\nu}(\mathbf{X}), \tag{42}$$

ν = A, B. For our purposes, we may assume the chemical potentials to be combined with the external potentials.

Finally, the third contribution $\mathcal{F}_{exc}$ includes interactions between the particles and represents the excess free energy beyond the ideal gas part. In almost all situations, an exact expression for $\mathcal{F}_{exc}$ is not known analytically, and it must be approximated by an appropriate functional depending on the case at hand. Typically, this assumption needs to be carefully tested against experimental and simulational results. Nevertheless, the general theoretical framework up to this point applies to any interaction potential, here independent of the orientations of the swimmers (in principle, this restriction could be lifted, e.g., when describing rodlike active particles[48,142]).

In equilibrium, the actual magnitude of the grand potential is found by minimizing the grand potential functional over all possible density distributions. Thus, the equilibrium density fields $\rho_\nu^{eq}(\mathbf{X})$ satisfy

$$0 = \frac{\delta\Omega}{\delta\rho_\nu(\mathbf{X})}\bigg|_{\rho_\nu\equiv\rho_\nu^{eq}} \tag{43}$$

for ν = A, B. Inserting Eqs. (40)–(42) leads to

$$-\Phi_{ext}^{\nu}(\mathbf{X}) = k_BT\,\ln\big(\lambda_\nu^3\rho_\nu^{eq}(\mathbf{X})\big) + \frac{\delta\mathcal{F}_{exc}}{\delta\rho_\nu(\mathbf{X})}\bigg|_{\rho_\nu\equiv\rho_\nu^{eq}} \tag{44}$$

for ν = A, B.

Second, we employ standard equilibrium statistical mechanics.[143] In equilibrium, the static system properties are set completely by the temperature and the overall potential $U = U(\mathbf{X}_1, \ldots, \mathbf{X}_N)$

The Journal of Chemical Physics ARTICLE scitation.org/journal/jcp

as defined in Eq. (17), writing $\Phi^{\nu}_{\mathrm{ext}}(\mathbf{X})$ instead of $u^{\nu}_{\mathrm{ext}}(\mathbf{r})$. Thus, the microstate probability density is given by

$$P \equiv P^{\mathrm{eq}} \propto \exp(-\beta U), \tag{45}$$

where $\beta = (k_{\mathrm{B}}T)^{-1}$.

Applying the gradient with respect to the position of the first swimmer, which is of species A, leads to

$$\nabla_{\mathbf{r}_1} P^{\mathrm{eq}} = -\beta P^{\mathrm{eq}}\Bigg(\nabla_{\mathbf{r}_1}\Phi^{\mathrm{A}}_{\mathrm{ext}}(\mathbf{X}_1) + \nabla_{\mathbf{r}_1}\sum_{j=2}^{N_{\mathrm{A}}} u^{\mathrm{AA}}(|\mathbf{r}_1 - \mathbf{r}_j|) + \nabla_{\mathbf{r}_1}\sum_{j=N_{\mathrm{A}}+1}^{N_{\mathrm{A}}+N_{\mathrm{B}}} u^{\mathrm{AB}}(|\mathbf{r}_1 - \mathbf{r}_j|)\Bigg). \tag{46}$$

Since swimmers of the same species are considered to be identical and indistinguishable, we may write

$$\begin{aligned} k_{\mathrm{B}}T\,\nabla_{\mathbf{r}}\rho^{\mathrm{eq}}_{\mathrm{A}}(\mathbf{X}) = &-\rho^{\mathrm{eq}}_{\mathrm{A}}(\mathbf{X})\nabla_{\mathbf{r}}\Phi^{\mathrm{A}}_{\mathrm{ext}}(\mathbf{X}) \\ &- \int \mathrm{d}\mathbf{X}'\,\rho^{(2,0),\mathrm{eq}}(\mathbf{X},\mathbf{X}')\nabla_{\mathbf{r}}u^{\mathrm{AA}}(|\mathbf{r}-\mathbf{r}'|) \\ &- \int \mathrm{d}\mathbf{X}'\,\rho^{(1,1),\mathrm{eq}}(\mathbf{X},\mathbf{X}')\nabla_{\mathbf{r}}u^{\mathrm{AB}}(|\mathbf{r}-\mathbf{r}'|) \end{aligned} \tag{47}$$

after integrating over the coordinates of all but the first swimmer of species A and using Eq. (22). This constitutes a lowest-order member of the binary-mixture translational *Yvon-Born-Green* (*YBG*) *relations*.[139,143] Combining Eqs. (44) and (47), $\Phi^{\mathrm{A}}_{\mathrm{ext}}(\mathbf{X})$ is eliminated and

$$\begin{aligned} &\int \mathrm{d}\mathbf{X}'\,\rho^{(2,0)}(\mathbf{X},\mathbf{X}',t)\,\nabla_{\mathbf{r}}u^{\mathrm{AA}}(|\mathbf{r}-\mathbf{r}'|) \\ &\quad + \int \mathrm{d}\mathbf{X}'\,\rho^{(1,1)}(\mathbf{X},\mathbf{X}',t)\,\nabla_{\mathbf{r}}u^{\mathrm{AB}}(|\mathbf{r}-\mathbf{r}'|) \\ &= \rho_{\mathrm{A}}(\mathbf{X},t)\,\nabla_{\mathbf{r}}\frac{\delta\mathcal{F}_{\mathrm{exc}}}{\delta\rho_{\mathrm{A}}(\mathbf{X},t)} \end{aligned} \tag{48}$$

is obtained. Here, we now applied the adiabatic approximation and also switched to a time-dependent description. This equation is inserted into Eq. (24) on our way of closing our dynamical equations.

Based on Eqs. (22), (44), and (45), i.e., again applying the adiabatic approximation, we find two further helpful relations, namely,

$$\begin{aligned} &k_{\mathrm{B}}T\,\nabla_{\mathbf{r}'}\rho^{(2,0)}(\mathbf{X},\mathbf{X}',t) + \rho^{(2,0)}(\mathbf{X},\mathbf{X}',t)\nabla_{\mathbf{r}'}u^{\mathrm{AA}}(|\mathbf{r}-\mathbf{r}'|) \\ &\quad + \int \mathrm{d}\mathbf{X}''\rho^{(2,1)}(\mathbf{X},\mathbf{X}',\mathbf{X}'',t)\nabla_{\mathbf{r}'}u^{\mathrm{AB}}(|\mathbf{r}'-\mathbf{r}''|) \\ &\quad + \int \mathrm{d}\mathbf{X}''\rho^{(3,0)}(\mathbf{X},\mathbf{X}',\mathbf{X}'',t)\nabla_{\mathbf{r}'}u^{\mathrm{AA}}(|\mathbf{r}'-\mathbf{r}''|) \\ &= k_{\mathrm{B}}T\,\rho^{(2,0)}(\mathbf{X},\mathbf{X}',t)\nabla_{\mathbf{r}'}\ln\big(\lambda^3_{\mathrm{A}}\rho_{\mathrm{A}}(\mathbf{X}',t)\big) \\ &\quad + \rho^{(2,0)}(\mathbf{X},\mathbf{X}',t)\nabla_{\mathbf{r}'}\frac{\delta\mathcal{F}_{\mathrm{exc}}}{\delta\rho_{\mathrm{A}}(\mathbf{X}',t)} \end{aligned} \tag{49}$$

and

$$\begin{aligned} &k_{\mathrm{B}}T\,\nabla_{\mathbf{r}'}\rho^{(1,1)}(\mathbf{X},\mathbf{X}',t) + \rho^{(1,1)}(\mathbf{X},\mathbf{X}',t)\nabla_{\mathbf{r}'}u^{\mathrm{AB}}(|\mathbf{r}-\mathbf{r}'|) \\ &\quad + \int \mathrm{d}\mathbf{X}''\rho^{(1,2)}(\mathbf{X},\mathbf{X}',\mathbf{X}'',t)\nabla_{\mathbf{r}'}u^{\mathrm{BB}}(|\mathbf{r}'-\mathbf{r}''|) \\ &\quad + \int \mathrm{d}\mathbf{X}''\rho^{(2,1)}(\mathbf{X},\mathbf{X}'',\mathbf{X}',t)\nabla_{\mathbf{r}'}u^{\mathrm{AB}}(|\mathbf{r}'-\mathbf{r}''|) \\ &= k_{\mathrm{B}}T\,\rho^{(1,1)}(\mathbf{X},\mathbf{X}',t)\nabla_{\mathbf{r}'}\ln\big(\lambda^3_{\mathrm{B}}\rho_{\mathrm{B}}(\mathbf{X}',t)\big) \\ &\quad + \rho^{(1,1)}(\mathbf{X},\mathbf{X}',t)\nabla_{\mathbf{r}'}\frac{\delta\mathcal{F}_{\mathrm{exc}}}{\delta\rho_{\mathrm{B}}(\mathbf{X}',t)}. \end{aligned} \tag{50}$$

Analogs for species B follow after applying to Eqs. (48)–(50) the replacements listed below Eq. (39).

Inserting the above relations into Eqs. (24), (28), (31), (34), and (37) yields

$$\mathcal{J}^{\mathrm{tt}}_{\mathrm{A}} = -\mu^{\mathrm{t}}_{\mathrm{A}}\Bigg(k_{\mathrm{B}}T\,\nabla_{\mathbf{r}}\rho_{\mathrm{A}}(\mathbf{X},t) + \rho_{\mathrm{A}}(\mathbf{X},t)\,\nabla_{\mathbf{r}}u^{\mathrm{A}}_{\mathrm{ext}}(\mathbf{r}) + \rho_{\mathrm{A}}(\mathbf{X},t)\nabla_{\mathbf{r}}\frac{\delta\mathcal{F}_{\mathrm{exc}}}{\delta\rho_{\mathrm{A}}(\mathbf{X},t)}\Bigg), \tag{51}$$

$$\mathcal{K}^{\mathrm{tt}}_{\mathrm{AA}} = -\int \mathrm{d}\mathbf{X}'\,\rho^{(2,0)}(\mathbf{X},\mathbf{X}',t)\;\boldsymbol{\mu}^{\mathrm{tt,AA}}_{\mathbf{r},\mathbf{r}'}\cdot\mathbf{j}_{\mathrm{A}}(\mathbf{X}',t), \tag{52}$$

$$\mathcal{K}^{\mathrm{rt}}_{\mathrm{AA}} = -\int \mathrm{d}\mathbf{X}'\,\rho^{(2,0)}(\mathbf{X},\mathbf{X}',t)\;\boldsymbol{\mu}^{\mathrm{rt,AA}}_{\mathbf{r},\mathbf{r}'}\;\mathbf{j}_{\mathrm{A}}(\mathbf{X}',t), \tag{53}$$

$$\mathcal{K}^{\mathrm{tt}}_{\mathrm{AB}} = -\int \mathrm{d}\mathbf{X}'\,\rho^{(1,1)}(\mathbf{X},\mathbf{X}',t)\;\boldsymbol{\mu}^{\mathrm{tt,AB}}_{\mathbf{r},\mathbf{r}'}\cdot\mathbf{j}_{\mathrm{B}}(\mathbf{X}',t), \tag{54}$$

$$\mathcal{K}^{\mathrm{rt}}_{\mathrm{AB}} = -\int \mathrm{d}\mathbf{X}'\,\rho^{(1,1)}(\mathbf{X},\mathbf{X}',t)\;\boldsymbol{\mu}^{\mathrm{rt,AB}}_{\mathbf{r},\mathbf{r}'}\;\mathbf{j}_{\mathrm{B}}(\mathbf{X}',t), \tag{55}$$

respectively, where we defined the vector fields

$$\mathbf{j}_{\nu}(\mathbf{X}',t) = k_{\mathrm{B}}T\,\nabla_{\mathbf{r}'}\ln\big(\lambda^3_{\nu}\rho_{\nu}(\mathbf{X}',t)\big) + \nabla_{\mathbf{r}'}\Bigg(u^{\nu}_{\mathrm{ext}}(\mathbf{r}') + \frac{\delta\mathcal{F}_{\mathrm{exc}}}{\delta\rho_{\nu}(\mathbf{X}',t)}\Bigg). \tag{56}$$

This way, the two-swimmer density in Eq. (24) and all three-swimmer densities have been eliminated. Again, analogous relations apply to the dynamical equation for $\rho_{\mathrm{B}}(\mathbf{x}, t)$ and are obtained by considering the replacements introduced below Eq. (39).

Still, the remaining two-swimmer densities in the $\mathcal{K}^{\cdot\cdot}_{\cdot\cdot}$ current densities must be addressed. For this purpose, as in a previous work,[107] we employ the Onsager-type[144] approximations

$$\rho^{(2,0)}(\mathbf{X},\mathbf{X}',t) = \rho_{\mathrm{A}}(\mathbf{X},t)\,\rho_{\mathrm{A}}(\mathbf{X}',t)\exp\big(-\beta u^{\mathrm{AA}}(|\mathbf{r}-\mathbf{r}'|)\big), \tag{57}$$

$$\rho^{(1,1)}(\mathbf{X},\mathbf{X}',t) = \rho_{\mathrm{A}}(\mathbf{X},t)\,\rho_{\mathrm{B}}(\mathbf{X}',t)\exp\big(-\beta u^{\mathrm{AB}}(|\mathbf{r}-\mathbf{r}'|)\big), \tag{58}$$

$$\rho^{(0,2)}(\mathbf{X},\mathbf{X}',t) = \rho_{\mathrm{B}}(\mathbf{X},t)\,\rho_{\mathrm{B}}(\mathbf{X}',t)\exp\big(-\beta u^{\mathrm{BB}}(|\mathbf{r}-\mathbf{r}'|)\big). \tag{59}$$

Here, for $|\mathbf{r}-\mathbf{r}'|$ smaller than the sum of the radii of the involved swimmer bodies, we furthermore set the pair densities to zero to avoid the otherwise-appearing unphysical hydrodynamic divergences. Strictly speaking, this leads to a discontinuity, but typically the jump is vanishingly small, e.g., $\exp(-5\exp(-1/16)) \approx 0.009 \ll 1$ for $\epsilon^{\cdot\cdot}_0 = 5k_{\mathrm{B}}T$ and $a_{\cdot} = \sigma_{\cdot}/4$; see Eq. (18). This order of magnitude is sufficiently low to treat the function as basically "smooth" in the numerical evaluation.

The Journal of Chemical Physics ARTICLE scitation.org/journal/jcp

Equations (57)–(59) implicitly assume $g_{\mu\nu}(\mathbf{X},\mathbf{X}',t) \approx \exp\big(-\beta u^{\mu\nu}(|\mathbf{r}-\mathbf{r}'|)\big)$ for the pair distribution functions, with $\mu, \nu \in \{\mathrm{A}, \mathrm{B}\}$. Using these relations is exact for passive equilibrium systems in the low-density limit[139] as the expressions are based on the assumption that the two involved particles interact only with each other (and with no third particles). Adapting these relations to describe semidilute active suspensions thus constitutes a reasonable first-order approximation beyond assuming a constant pair distribution function. More generally, one could at this point also insert another reasonable approximation for the pair distribution function.

Similarly, our (pairwise) treatment of hydrodynamic interactions between the swimmers, see Eqs. (4)–(15), requires sufficiently large distances between the swimmer bodies. First, this is ensured by the steric interaction between the swimmers when half of its effective range, i.e., $\sigma_{\mu\nu}/2$ in Eq. (18), is larger than a_κ, $\alpha_\kappa L_\kappa$, and $(1-\alpha_\kappa)L_\kappa$, with $\mu, \nu \in \{\mathrm{A}, \mathrm{B}\}$ and $\kappa \in \{\mu, \nu\}$. The larger the mean distances are between the swimmers, the higher the accuracy of our description of hydrodynamic interactions will be. Together with the assumptions involved in Eqs. (57)–(59), we thus expect our DDFT for multispecies systems of microswimmers to perform best for (semi)dilute suspensions of swimmers, within which our steric interaction potentials maintain a significant distance between the swimmer bodies, even when they are heading for collisions.

Finally, the excess functional $\mathcal{F}_{\mathrm{exc}}$ involving the effective steric interactions between the swimmers needs to be specified. As appropriate for GEM potentials,[136] we from now on use a mean-field approximation, here for our case of binary mixtures, reading

$$\mathcal{F}_{\mathrm{exc}} = \frac{1}{2}\int \mathrm{d}\mathbf{X}\int \mathrm{d}\mathbf{X}'\,\rho_\mu(\mathbf{X},t)\,\rho_\nu(\mathbf{X}',t)\;u^{\mu\nu}\big(|\mathbf{r}-\mathbf{r}'|\big), \tag{60}$$

with $\mu, \nu \in \{\mathrm{A}, \mathrm{B}\}$ and summing over repeated indices. In this way, our set of coupled dynamical equations for $\rho_{\mathrm{A}}(\mathbf{X}, t)$ and $\rho_{\mathrm{B}}(\mathbf{X}, t)$ is closed. We remark that, along the same lines, a theory for more than two different species can be derived as well, leading to a correspondingly further increased number of terms. Here, we continue by applying the above theory to concrete example situations in Sec. IV.

IV. APPLICATIONS

In this section, the DDFT derived in Sec. III is applied to several illustrative cases. Specifically, for simplicity, these will be setups in which the positions and orientations of the swimmers are constricted to the xy-plane. Still, a surrounding bulk fluid is considered with the planar swimmer ensemble embedded therein, allowing for three-dimensional fluid flows. Possible methods to experimentally realize this situation could be the confinement of microswimmers to the interface between two immiscible fluids of identical viscosity η or the use of optical trapping fields.

In such a setup, the orientation of a swimmer is described by a single angle ϕ (measured from the x-axis) via $\hat{\mathbf{n}} = (\cos\phi, \sin\phi, 0)$. The orientational gradient operator then reduces to $\hat{\mathbf{n}} \times \nabla_{\hat{\mathbf{n}}} = \hat{\mathbf{z}}\partial_\phi$, where $\hat{\mathbf{z}}$ is the oriented Cartesian unit vector pointing (upwards) out of the xy-plane. Furthermore, the phase-space coordinate $\mathbf{X}$ in this situation becomes $\mathbf{X} = \{x, y, \phi\}$.

The numerical solution of the coupled set of partial differential equations derived in Sec. III is then performed on an equidistant $N_x \times N_y \times N_\phi$ grid using the finite-volume-method solver *FiPy*.[145] Formally, numerical periodic boundary conditions are imposed on all coordinates x, y, and ϕ, but hydrodynamic and steric interactions are cut at a distance chosen such that no (unphysical) interactions across the boundaries occur. As nevertheless all physical interactions inside the system should, of course, be accounted for, we further always set the length of the simulation box in both spatial directions to at least twice the largest relevant interparticle distance.

Since the orientation-dependent densities $\rho_\nu(\mathbf{X}, t)$ at time t are still a function of x, y, and ϕ, they cannot be easily plotted even for our planar configurations. For displaying our results, we thus further define the (orientation-integrated) spatial swimmer densities

$$\rho_\nu(\mathbf{r},t) = \int_0^{2\pi} \mathrm{d}\phi\;\rho_\nu(\mathbf{X},t) \tag{61}$$

and the orientational vector fields

$$\langle\hat{\mathbf{n}}\rangle_\nu(\mathbf{r},t) = \int_0^{2\pi} \mathrm{d}\phi\;\hat{\mathbf{n}}(\phi)\,\rho_\nu(\mathbf{X},t), \tag{62}$$

where $\nu \in \{\mathrm{A}, \mathrm{B}\}$. Moreover, the overall (average) one-species densities are described by $\bar{\rho}_\nu = A^{-1}\int_A \mathrm{d}\mathbf{r}\,\rho_\nu(\mathbf{r},t)$, where A is the area of the regarded system.

A. Trapped binary swimmer system

While restricting the binary microswimmer configuration to two spatial dimensions as detailed above, we now additionally introduce radially symmetric quartic trapping potentials given by

$$u^{\nu}_{\mathrm{ext}}(\mathbf{r}) = V_0^{\nu}\left(\frac{r}{\sigma}\right)^4, \tag{63}$$

with potential strengths V_0^ν, distance $r = |\mathbf{r}|$ to the center of the trap, and $\nu = \mathrm{A}, \mathrm{B}$. As in previous works,[106,107] we use a quartic potential—instead of, e.g., a harmonic one ($\propto r^2$)—to observe more pronounced differences between activity-induced off-center density distributions (see below) and center-heavy equilibrium distributions for passive particles. Previously reported results for harmonic traps[146,147] showed qualitative agreement with our results for a quartic potential.[106,107] For simplicity, we furthermore from now on assume that all species-related parameters are the same for both species, except for $f_{\mathrm{A}} = -f_{\mathrm{B}} > 0$. Thus, species A is formed by pushers and species B represents pullers (of the same strength).

In analogous one-component suspensions,[106,107] without any active drive, the external potential leads to center-heavy distributions following standard equilibrium statistics. When the active drive is switched on in the one-component systems, but hydrodynamic interactions are still neglected, the self-propelled particles start forming a radially symmetric high-density ring, along which the outward self-propulsion is balanced by the restoring trapping force.[106,148,149] With hydrodynamic interactions incorporated, this ring of microswimmers can become unstable against collapsing to one spot on this ring, which is induced by the hydrodynamic coupling through the resulting fluid flows.[106,107,146,147] In parts of the parameter space, pushers and pullers were observed to behave quite

The Journal of Chemical Physics ARTICLE scitation.org/journal/jcp

differently, with pushers showing a significantly more pronounced destabilization of the high-density ring and formation of a high-density spot, while pullers showed a much weaker density variation along the ring.[107]

We are now interested in pusher–puller mixtures. There is a crucial competition between hydrodynamic effects resulting from the external potential acting on the swimmer bodies and from the actively introduced forces exerted by the microswimmers themselves. We here concentrate on a parameter range for which the hydrodynamic interactions induced by the self-propulsion mechanism dominate those induced by the external potential force. Concerning our current densities, we thus always check that $|\mathcal{K}^{\mathrm{ra}}_{..}| > |\mathcal{K}^{\mathrm{rt}}_{..}|$, see, e.g., Eqs. (37) and (39), for our chosen parameters.

Numerical results for (steady-state) distributions of pusher–puller mixtures are shown in Fig. 2, for varying overall densities of the two species. In strong contrast to the corresponding one-component systems, for which the (steady-state) distributions strongly differed between pure pusher and pure puller systems,[107] we here frequently observe the same qualitative behavior when both species are present simultaneously. For instance, in Fig. 2(a), pushers transfer their "spot-forming" tendency onto the pullers, which in the absence of the pushers would show a ringlike arrangement instead of the spot. However, the plots in Fig. 2 indicate the rough relation $\rho_{\mathrm{A}}(\mathbf{r},\hat{\mathbf{n}},t)/\bar{\rho}_{\mathrm{A}} \approx \rho_{\mathrm{B}}(\mathbf{r},-\hat{\mathbf{n}},t)/\bar{\rho}_{\mathrm{B}}$. Choosing, e.g., $|f_{\mathrm{A}}| \neq |f_{\mathrm{B}}|$, this approximate relation breaks down as the two species aggregate at different distances from the origin, but for sufficiently small deviations, we still observe a qualitatively similar collective behavior for both species.

In Fig. 2, the overall density $\bar{\rho}_{\mathrm{B}}$ of pullers increases from left to right, while the overall density $\bar{\rho}_{\mathrm{A}}$ for pushers decreases from the top row to the bottom row. We observe clear spot formation in Figs. 2(a) and 2(b), while Fig. 2(c) shows less-pronounced instabilities of the high-density ring. Thus, we may conclude that the dominating species imposes its behavior onto the other species.

For Figs. 2(c) and 2(e), where $\bar{\rho}_{\mathrm{A}} = \bar{\rho}_{\mathrm{B}}$ and therefore $\rho_{\mathrm{A}}(\mathbf{r},\hat{\mathbf{n}},t) \approx \rho_{\mathrm{B}}(\mathbf{r},-\hat{\mathbf{n}},t)$ holds, the probability currents associated with the rotation due to the active forces approximately cancel each other by symmetry, e.g., $\mathcal{K}^{\mathrm{ra}}_{\mathrm{AA}} \approx -\mathcal{K}^{\mathrm{ra}}_{\mathrm{AB}}$, so that only the currents $\mathcal{K}^{\mathrm{rt}}_{..}$ can lead to spot formation. The latter starts to outperform the rotational diffusion for the case depicted in Fig. 2(c) but not for the lower overall densities in Fig. 2(e). The instability of the ring here seems to be a question of high-enough overall density because, e.g., $|\mathcal{K}^{\mathrm{rt}}_{\mathrm{AA}}| \propto \bar{\rho}_{\mathrm{A}}^2$ and $|\mathcal{J}^{\mathrm{rr}}_{\mathrm{A}}| \propto \bar{\rho}_{\mathrm{A}}$.

The bottom row of Fig. 2 shows the corresponding density distributions for a smaller $\bar{\rho}_{\mathrm{A}}$. Thus, a decreased density of pushers leads to an increased stability of the high-density ring against aggregation in one spot. When (significantly) more pullers than pushers are in the system, as in Fig. 2(f), they dominate the overall behavior and restabilize the high-density ring.

In summary, the majority species seems to dominate the overall behavior of the system. A similar conclusion has recently been drawn for the unconfined motion in pusher–puller mixtures,[94] which we will treat as the next example using our theoretical approach.

At this point, we include a short remark on the performance of our theory. We can remove the second species from our DDFT equations derived in Sec. III by setting $\rho_{\mathrm{B}}(\mathbf{X}, t) \equiv 0$. Then, the present set of equations reduces to the previous DDFT for monodisperse microswimmers.[106] In that case, likewise, the statistical theory was evaluated by exposing the system of swimmers to a radial external trapping potential, in analogy to the above consideration for a pusher–puller mixture. There, hydrodynamic interactions lead to the formation a high-density spot of aligned swimmers as well, resulting in overall flow fields.[106,107] This "hydrodynamic fluid pump" had previously been reported in particle-based computer simulations,[146,147] using different swimmer models. Thus, a qualitative comparison shows that our DDFT reproduces corresponding general phenomena. Adding another microswimmer

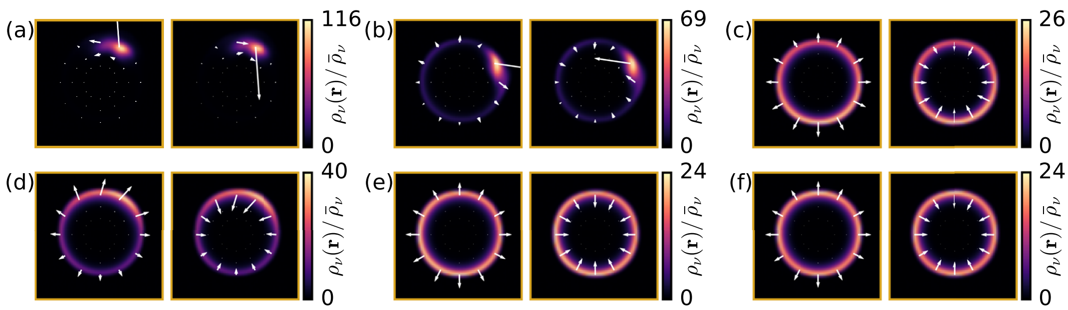

FIG. 2. Steady-state density distribution for binary mixtures of pusher (A) and puller (B) microswimmers in an external trapping potential, see Eq. (63), for varying overall densities $\bar{\rho}_{\mathrm{A}}$ (pushers) and $\bar{\rho}_{\mathrm{B}}$ (pullers). All other parameters are held constant at $a_{\mathrm{A}} = a_{\mathrm{B}} = 0.25\sigma$, $L_{\mathrm{A}} = L_{\mathrm{B}} = 0.75\sigma$, $\alpha_{\mathrm{A}} = \alpha_{\mathrm{B}} = 0.4$, $V_0^{\mathrm{A}} = V_0^{\mathrm{B}} = 0.5\,k_{\mathrm{B}}T$, $\epsilon_0^{\mathrm{A}} = \epsilon_0^{\mathrm{B}} = 10\,k_{\mathrm{B}}T$, and $f_{\mathrm{A}} = -f_{\mathrm{B}} = 600 k_{\mathrm{B}}T/\sigma$, with $\sigma_{\mathrm{A}} = \sigma_{\mathrm{B}} \equiv \sigma$. The simulation box is of size $18\sigma \times 18\sigma$ (only the inner $12\sigma \times 12\sigma$ are on display), and the numerical evaluations were performed on ($80 \times 80 \times 16$)-grids. Each pair of plots shows on the left-hand side the results for species A (pushers) and on the right-hand side the corresponding distribution for species B (pullers). In each plot, the color encodes the (reduced) spatial density profile $\rho_\nu(\mathbf{r},t)/\bar{\rho}_\nu$ (reduced by the average density $\bar{\rho}_\nu$), with brighter color corresponding to higher density, and white arrows indicate the orientational vector field $\langle\hat{\mathbf{n}}\rangle_\nu(\mathbf{r},t)$, as defined in Eqs. (61) and (62), respectively. The overall densities $(\bar{\rho}_{\mathrm{A}}, \bar{\rho}_{\mathrm{B}})$ are given (in units of σ^{-2}) by (a) (0.0123, 0.006 17), (b) (0.0123, 0.009 26), (c) (0.0123, 0.0123), (d) (0.009 26, 0.006 17), (e) (0.009 26, 0.009 26), and (f) (0.009 26, 0.0123). The systems in (a), (b), and (d) do not reach steady states in a strict sense as the spot formation there is unstable against (spontaneous) movement of the density profile along the rim of the trap.

The Journal of Chemical Physics ARTICLE scitation.org/journal/jcp

species to the same framework, we expect a similarly successful performance of the present theory. A direct quantitative comparison could be carried out in the future by implementing a suitable particle picture into many-swimmer computer simulations including hydrodynamic interactions and thermal fluctuations, e.g., via multiparticle collision dynamics[150–155]/stochastic rotation dynamics.[156,157] Then, also higher swimmer densities could be addressed numerically. Another way to explicitly take into account the induced hydrodynamic fluid flows in computer simulations could be Lattice-Boltzmann methods.[146,158–161]

B. Emergence of polar orientational order and collective motion in pusher–puller mixtures

In the absence of the spherical trapping potential considered in Sec. IV A, previous particle-based computer simulations of planar arrangements of microswimmers with periodic boundary conditions and using the same swimmer model have identified a tendency of puller microswimmers to develop (global) collective polar orientational order.[94] Related observations were made in simulations of analogous three-dimensional configurations of squirmer microswimmers.[159] Such order in the swimmer orientations naturally leads to collective motion, maintaining a common average propulsion direction. Moreover, we have performed a corresponding linear stability analysis of our DDFT for planar pure (one-species) pusher or puller systems, with spontaneous ordering identified beyond a threshold active drive for pullers,[108] in contrast to pushers. We now address the corresponding two-species situation. In related computer simulations for mixtures of pushers and pullers using the same swimmer model,[94] it was found that collective orientational order only develops if the fraction of pushers is sufficiently small. As we demonstrate, our DDFT reproduces these results and leads to a more quantitative insight.

For this purpose, the external potential in our planar arrangement is now set to $u_{\mathrm{ext}}(\mathbf{r}) \equiv 0$. For simplicity, we assume that the one-swimmer densities are spatially homogeneous, i.e., $\rho_\nu(\mathbf{X}, t) = \rho_\nu(\phi, t)/A$, with A denoting the area (considered to be large) of the periodic plane containing the swimmers and $\nu \in \{\mathrm{A, B}\}$. Then, integrating Eq. (23) over all positions $\mathbf{r}$ in the periodic box leads to

$$\frac{\partial \rho_{\mathrm{A}}(\phi,t)}{\partial t} = -\hat{\mathbf{z}}\cdot\int \mathrm{d}\mathbf{r}\,\frac{\partial}{\partial\phi}\Big(\mathcal{J}^{\mathrm{rr}}_{\mathrm{A}} + \sum_{\nu=\mathrm{A,B}}\big(\mathcal{K}^{\mathrm{rt}}_{\mathrm{A}\nu} + \mathcal{K}^{\mathrm{ra}}_{\mathrm{A}\nu}\big)\Big), \tag{64}$$

with the probability current densities defined in Eqs. (24)–(39). Following Ref. 108, the current densities $\mathcal{K}^{\mathrm{rt}}_{\cdot\cdot}$ are neglected for sufficiently dilute suspensions as all the contained nonvanishing terms scale with three-swimmer densities. Thus, Eq. (64) reduces to

$$\begin{aligned}\frac{\partial \rho_{\mathrm{A}}(\phi,t)}{\partial t} &= k_{\mathrm{B}}T\,\mu^{\mathrm{r,A}}\,\partial_\phi^2\rho_{\mathrm{A}}(\phi,t)\\ &\quad - f_{\mathrm{A}}\,\partial_\phi\int\mathrm{d}\mathbf{r}\int\mathrm{d}\mathbf{X}'\,\hat{\mathbf{z}}\cdot\big(\boldsymbol{\Lambda}^{\mathrm{rt,AA}}_{\mathbf{r},\mathbf{X}'}\,\hat{\mathbf{n}}'\big)\rho^{(2,0)}(\mathbf{X},\mathbf{X}',t)\\ &\quad - f_{\mathrm{B}}\,\partial_\phi\int\mathrm{d}\mathbf{r}\int\mathrm{d}\mathbf{X}'\,\hat{\mathbf{z}}\cdot\big(\boldsymbol{\Lambda}^{\mathrm{rt,AB}}_{\mathbf{r},\mathbf{X}'}\,\hat{\mathbf{n}}'\big)\rho^{(1,1)}(\mathbf{X},\mathbf{X}',t).\end{aligned} \tag{65}$$

Here, the two-swimmer densities are related to the pair distribution functions via

$$\rho^{(2,0)}(\mathbf{X},\mathbf{X}',t) = \frac{\rho_{\mathrm{A}}(\phi,t)\,\rho_{\mathrm{A}}(\phi',t)\,g_{\mathrm{AA}}(\mathbf{X},\mathbf{X}',t)}{A^2}, \tag{66}$$

$$\rho^{(1,1)}(\mathbf{X},\mathbf{X}',t) = \frac{\rho_{\mathrm{A}}(\phi,t)\,\rho_{\mathrm{B}}(\phi',t)\,g_{\mathrm{AB}}(\mathbf{X},\mathbf{X}',t)}{A^2}. \tag{67}$$

Thus, Eq. (65) becomes

$$\begin{aligned}\frac{\partial \rho_{\mathrm{A}}(\phi,t)}{\partial t} &= k_{\mathrm{B}}T\,\mu^{\mathrm{r,A}}\,\partial_\phi^2\rho_{\mathrm{A}}(\phi,t)\\ &\quad - f_{\mathrm{A}}\,\partial_\phi\Big[\rho_{\mathrm{A}}(\phi,t)\int\mathrm{d}\phi'\,\rho_{\mathrm{A}}(\phi',t)\,G_{\mathrm{AA}}(\phi-\phi',t)\Big]\\ &\quad - f_{\mathrm{B}}\,\partial_\phi\Big[\rho_{\mathrm{A}}(\phi,t)\int\mathrm{d}\phi'\,\rho_{\mathrm{B}}(\phi',t)\,G_{\mathrm{AB}}(\phi-\phi',t)\Big],\end{aligned} \tag{68}$$

where the hydrodynamic interactions are comprised by the coupling functions

$$G_{\mu\nu}(\phi-\phi',t) := \int\mathrm{d}\mathbf{r}\int\mathrm{d}\mathbf{r}'\,\frac{\hat{\mathbf{z}}\cdot\big(\boldsymbol{\Lambda}^{\mathrm{rt},\mu\nu}_{\mathbf{r},\mathbf{X}'}\,\hat{\mathbf{n}}'\big)\,g_{\mu\nu}(\mathbf{X},\mathbf{X}',t)}{A^2}, \tag{69}$$

with $\mu, \nu \in \{\mathrm{A, B}\}$. An analogous dynamical equation for species B is obtained by replacing A → B and B → A. In the following, species A again represents pushers, and species B represents pullers.

To allow for further analytical treatment, we include additional simplifying assumptions. Considering systems in which all active agents propel with the same amplitude of the active drive and further are identical in all other microscopic parameters, the coupling and pair distribution functions, see Eq. (69), were determined in Ref. 108 by a modified Percus test-particle method. For this purpose, hydrodynamic interactions were neglected and only the interplay of self-propulsion and steric interactions was evaluated. As a result, we had extracted and approximated the basic functional form as[108]

$$G_{\mu\nu}(\phi-\phi') = \tilde{C}_{\mu\nu}\sin(\phi-\phi'), \tag{70}$$

where $\tilde{C}_{\mathrm{AA}} = \tilde{C}_{\mathrm{BB}} = \tilde{C}/A > 0$ is positive for same-species coupling and $\tilde{C}_{\mathrm{AB}} = \tilde{C}_{\mathrm{BA}} = -\tilde{C}/A$. This distinction follows from the fact of our puller microswimmers propelling into the direction of $-\hat{\mathbf{n}}$ and/or $-\hat{\mathbf{n}}'$; see Fig. 1. Since ϕ and ϕ' parameterize the orientations of $\hat{\mathbf{n}}$ and $\hat{\mathbf{n}}'$, respectively, the swimming direction of a puller is shifted by an additional angle π relatively to ϕ and/or ϕ'. If only one of the angles ϕ and ϕ' refers to a puller, the additional shift of $\phi - \phi'$ by π requires a minus sign in the prefactor of $\sin(\phi - \phi')$ in Eq. (70).

The value of $\tilde{C} > 0$ generally depends on the overall density and the microscopic parameters. (Some further positive constant parameters are here incorporated by the coefficient $\tilde{C}$ when compared to the amplitude C in Ref. 108.) Since a similarly simple analytically treatable expression is still missing for hydrodynamic interactions included on the level of pair distribution functions, we use Eq. (70) as an input for our further calculations.

We assume that, if collective order arises, there is only one common direction of polar ordering, i.e., in this case, species A and B collectively propel along a common direction. This assumption is motivated by previous simulation results.[94] We now test the linear stability of the uniform distributions $\rho_\nu(\phi, t) \equiv N_\nu/(2\pi)$ against the emergence of collective orientational ordering. To this end, the

The Journal of Chemical Physics ARTICLE scitation.org/journal/jcp

ansatz $\rho_A(\phi, t) = N_A/(2\pi) + \epsilon_A(t)\cos(\phi - \phi_0)$ and $\rho_B(\phi, t) = N_B/(2\pi) + \epsilon_B(t)\cos(\phi - \phi_0 + \pi)$, with an arbitrary angle ϕ_0 and $|\epsilon_\nu(t)| \ll N_\nu$ for $\nu \in \{A, B\}$, is inserted into Eq. (68) and the equivalent equation for species B. This leads to the coupled ordinary differential equations

$$\frac{\mathrm{d}}{\mathrm{d}t}\begin{bmatrix}\epsilon_A(t)\\ \epsilon_B(t)\end{bmatrix} = \mathbf{M}\cdot\begin{bmatrix}\epsilon_A(t)\\ \epsilon_B(t)\end{bmatrix}, \tag{71}$$

with the coefficient matrix

$$\mathbf{M} = -\begin{bmatrix}k_B T\mu^{r,A} + m_{AA} & m_{AB}\\ m_{BA} & k_B T\mu^{r,B} + m_{BB}\end{bmatrix}, \tag{72}$$

where $m_{\mu\nu} := N_\mu f_\nu \tilde{C}/(2A)$.

We recall that species A (pushers) and species B (pullers) are considered to have the same amplitude of their active drive, i.e., $f_A = -f_B > 0$. Additionally, we keep $N_A + N_B = N$ constant, i.e., only the ratio of pushers to pullers is varied. Moreover, all other parameters are assumed to be identical for the two species. Then, the eigenvalues of $\mathbf{M}$ are determined as $(-k_B T\mu^{r,A}, -k_B T\mu^{r,A} + f_A\tilde{C}N(\chi_B - 1/2)/A)$. Here, the first eigenvalue is always negative, but the second one becomes positive if

$$k_B T\mu^{r,A} < f_A\tilde{C}\frac{N}{A}(\chi_B - 1/2), \tag{73}$$

with $\chi_B := N_B/N$ denoting the fraction of pullers. The corresponding eigenvector is (N_A, N_B).

Our system can thus be linearly unstable against polar orientational ordering only if the right-hand side of Eq. (73) is positive. Since $f_A > 0$, this implies that the pullers must outnumber the pushers ($\chi_B > 1/2$). If this condition is satisfied, the active drive additionally needs to be strong enough, i.e., Eq. (73) sets a threshold strength for $f_A = -f_B$. Particularly, the effect of the active drive and the hydrodynamic interactions need to outperform rotational diffusion. Furthermore, as indicated by the corresponding eigenvector (N_A, N_B), if orientational order arises, it does so simultaneously for both species.

Our results roughly agree with those in the previous simulation study.[94] We stress that our theory only tests linear instability with respect to polar orientational ordering and that the above approximations were involved. In particular, the influence of hydrodynamic interactions on the pair distribution function was neglected. To address this question, possibly the results of particle-based computer simulations could be used as an input to the theory in the future.[94,162] Since our previous theoretical analysis for single-species systems indicated polar orientational ordering for puller suspensions but not for pushers,[108] we again find that the majority species imposes its behavior onto the minority species as observed already for the confined (trapped) mixtures in Sec. IV A.

C. Shear cell

As a third example, we now address a planar circular configuration which effectively represents a shear cell. We compose this shear cell of passive colloidal particles forming an effective circular rim and active microswimmers trapped inside. The passive particles are continuously driven along the circular rim of the trap, inducing a shearlike circular fluid flow inside. In a very loose analogy, this geometry is similar to setups of Taylor-Couette flow[163] but, of course, here in the limit of low Reynolds numbers. In fact, driving passive colloidal particles along ringlike trajectories can be realized experimentally via optical trapping potentials.[164]

Considering the driven particles (that hydrodynamically interact with the interior microswimmers) as one component of a binary mixture naturally induces fluid flows to which the enclosed microswimmers are exposed. This avoids explicitly imposing such flows as an external flow field.[165–168] However, we do not account in the present work for possible effects of shear banding, which have been addressed in the context of DDFT as well.[166–168] Our one-body density, particularly for passive particles within the cell, remains basically unchanged by the translational effects of the shear flow as expected in the limits of our current theory regarding shear.[169,170] Instead, for active microswimmers within the cell, the induced rotation of the swimmer orientations, coupling to the directions of self-propulsion, can lead to changes in the spatial density.

In the context of our theory, the active microswimmers represent the first species A, while the driven colloidal particles are treated as species B. Consequently, $f_B = 0$, but we also define an effective potential of confinement

$$u^B_{ext}(\mathbf{r}) = V^B_0\left(\mathrm{erf}\left(\frac{r - R_0 - \frac{1}{2}\sigma_R}{\sigma_R}\right) - \mathrm{erf}\left(\frac{r - R_0 + \frac{1}{2}\sigma_R}{\sigma_R}\right)\right) \tag{74}$$

for the passive particles, based on the error function $\mathrm{erf}(s) = (2/\sqrt{\pi})\int_0^s \mathrm{d}u\,\exp(-u^2)$. For $V^B_0 \gg k_B T$ and $R_0 \gg \sigma_R$, this potential effectively anchors the particles on a (small-width) ring of radius R_0. Additionally, the nonconservative driving force

$$\mathbf{F}_d(\mathbf{r}) = \omega_d\,\frac{\hat{\mathbf{z}}\times\mathbf{r}}{\mu^{t,B}} \tag{75}$$

is taken into account to describe the continuous circular driving of the passive particles. Technically, we include it by adding $-\mathbf{F}_d(\mathbf{r})$ to $\nabla_\mathbf{r} u^B_{ext}(\mathbf{r})$ in the corresponding equations. Here, ω_d is the (signed) magnitude of the imposed (spatial) angular velocity with which the passive particles are driven along the ring.

For species A, we again choose the external trapping potential defined in Eq. (63) but take care when adjusting the potential strength that (even with $f_A \neq 0$) it at all times hinders the majority of the swimmers from reaching the passive particles on the outer ring. This way, species A and B mainly interact with each other hydrodynamically, as described by, e.g., the current densities in Eqs. (54) and (55).

The driven ring of passive colloidal particles of species B is shown in Fig. 3. For typical parameters, (a) the corresponding density profile and (b) the hydrodynamic influences on the microswimmers of species A are depicted. For the latter, we define for species A the contribution to the velocity resulting from the fluid flows induced by species B as

$$\mathbf{v}^{AB}(\mathbf{r}, t) = \frac{\mathcal{K}^{tt}_{AB}(\mathbf{X}, t)}{\rho_A(\mathbf{X}, t)}, \tag{76}$$

and the corresponding contribution to the z-component of the angular velocity as

The Journal of Chemical Physics ARTICLE scitation.org/journal/jcp

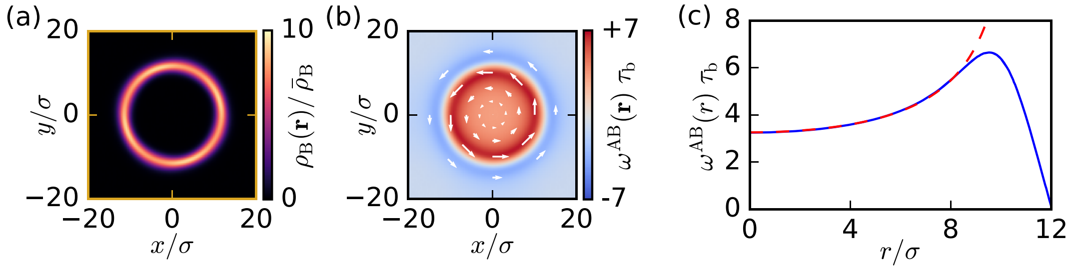

FIG. 3. Density ring of driven passive particles (species B) that impose a flow field on confined microswimmers (species A) on the inside (the density of the latter not explicitly shown here). The system parameters are $a_A = a_B = 0.25\sigma_B$, $\epsilon_0^{BB} = 10\,k_BT$, $R_0 = 11.5\sigma_B$, $\sigma_R = 3\sigma_B$, $V_0^B = 50\,k_BT$, $N_B = 10$, and $\omega_d\tau_b = 20$ [with Brownian time $\tau_b = \sigma_B^2/(\mu^{t,B}k_BT)$ and $\sigma_A = \sigma_B \equiv \sigma$]. Numerically, the evaluation is performed on a 256 × 256 grid (in x and y), for a simulation box of size $20\sigma \times 20\sigma$. (a) Ringlike density distribution of species B (passive particles), reduced by the average density $\bar{\rho}_B$. Brighter colors represent higher densities. (b) Illustration of the resulting steady hydrodynamic flows exerted on species A (microswimmers) by species B. White arrows indicate the magnitude and direction of $\mathbf{v}^{AB}(\mathbf{r})$ according to Eq. (76). The color code quantifies $\omega^{AB}(\mathbf{r})$ according to Eq. (77). (c) Radial distribution of $\omega^{AB}(r)$, as extracted from the full numerical evaluation [blue line, the same data as in (b)] and via the semianalytical approximation (red dashed line) given in Eq. (78).

$$\omega^{AB}(\mathbf{r},t) = \hat{\mathbf{z}}\cdot\frac{\mathcal{K}^{rt}_{AB}(\mathbf{X},t)}{\rho_A(\mathbf{X},t)}. \tag{77}$$

Here, the current densities, as defined in Eqs. (54) and (55) in combination with Eqs. (56) and (58), are proportional to $\rho_A(\mathbf{X},t)$ so that the above expressions do not diverge when the denominator vanishes.

The resulting density distribution of species B depicted in Fig. 3 is basically circularly symmetric and after initial equilibration does not vary over time any longer. Still, it represents the moving passive particles driven by the (tangential) external force defined in Eq. (75). The latter is the main source of the fluid flows induced by particles of species B. Resulting flow fields can be approximated inside the cell by evaluating the corresponding terms in Eqs. (76) and (77) under the assumption of $\rho_B(\mathbf{X}',t) \equiv N_B(2\pi)^{-2}R_0^{-1}\delta(r'-R_0)$. Considering the contribution of $\mathbf{F}_d(\mathbf{r}')$ as dominant, ignoring steric interactions between species A and B, and introducing $b = r/R_0 < 1$, we obtain from Eq. (77)

$$\begin{aligned}\omega^{AB}(\mathbf{r}) &\approx \frac{3}{4}\frac{a}{R_0}\,\omega_d N_B\,\frac{1}{2\pi}\int_{-\pi}^{\pi}\mathrm{d}\psi\,\frac{1-b\cos\psi}{(1-2b\cos\psi+b^2)^{3/2}}\\ &\approx \frac{3}{4}\frac{a}{R_0}\,\omega_d N_B\Big(1+\frac{3}{4}b^2+\frac{45}{64}b^4+\mathcal{O}(b^6)\Big)\end{aligned} \tag{78}$$

for the angular velocity. As shown in Fig. 3(c), there is good quantitative agreement between this approximation [the integral expression in Eq. (78) is plotted as the dashed line] and the full numerical solution (solid line). For positions close to the outer ring of the driven particles of species B, the curve drops, most likely because of the decreased probability of finding the swimmers and the driven particles within close distances from each other, formally introduced by the Onsager-like terms in Eqs. (57)–(59). To leading order in a, the flow field induced by the driven species B can be similarly obtained as

$$\begin{aligned}\mathbf{v}^{AB}(\mathbf{r}) &\approx \frac{3}{4}\,a\,\omega_d N_B(\hat{\mathbf{z}}\times\hat{\mathbf{r}})\frac{1}{\pi}\int_{-\pi}^{\pi}\mathrm{d}\psi\,\frac{\cos\psi}{(b^2-2b\cos\psi+1)^{1/2}}\\ &\approx \frac{3}{4}\,a\,\omega_d N_B(\hat{\mathbf{z}}\times\hat{\mathbf{r}})\Big(b+\frac{3}{8}b^3+\frac{15}{64}b^5+\mathcal{O}(b^7)\Big).\end{aligned} \tag{79}$$

We now concentrate on species A that is confined inside the shear cell. For $f_A = 0$, passive particles are recovered. As seen in the steady states shown in Figs. 4(a) and 4(b), the distribution of the inner passive particles remains virtually unaffected by the external driving of the outer passive particles, except for possible small deviations that cannot be resolved within the precision of our numerical discretization scheme. But when the enclosed swimmers are active ($f_A \neq 0$), see Figs. 4(c)–4(j), the effects of the induced shear flows become significant. Figures 4(c) and 4(d) show the situation of the enclosed swimmers for pushers and pullers without the external drive, i.e., $\omega_d = 0$. Here, for the chosen parameters, the microswimmers form high-density rings with average orientations tilted relatively to the outward direction for pushers (c)[107] and radially oriented for pullers (d). The directional sense of the tilt for pushers is spontaneously chosen by the system as either counterclockwise or clockwise (depicted here), depending on the initialization of our numerical evaluation. In contrast to these cases of vanishing external driving of species B, Figs. 4(e)–4(j) demonstrate that for $\omega_d \neq 0$, the externally induced shear flows can lead to a collapse of the steady-state density distributions toward the center of the confinement. Moreover, with increasing external driving ω_d, both pushers and pullers furthermore show an increasing tendency of their locally averaged swimming direction to be reoriented by the externally imposed fluid flow [see Fig. 3(b)]. This explains the different sense indicated by the white arrows for increased ω_d from Figs. 4(c)–4(e).

As a source of this behavior, the shear flow induced by the external driving of the outer ring persistently rotates the orientations of the internal swimmers so that the latter are hindered from efficiently swimming radially outwards against the trapping force.

The Journal of Chemical Physics ARTICLE scitation.org/journal/jcp

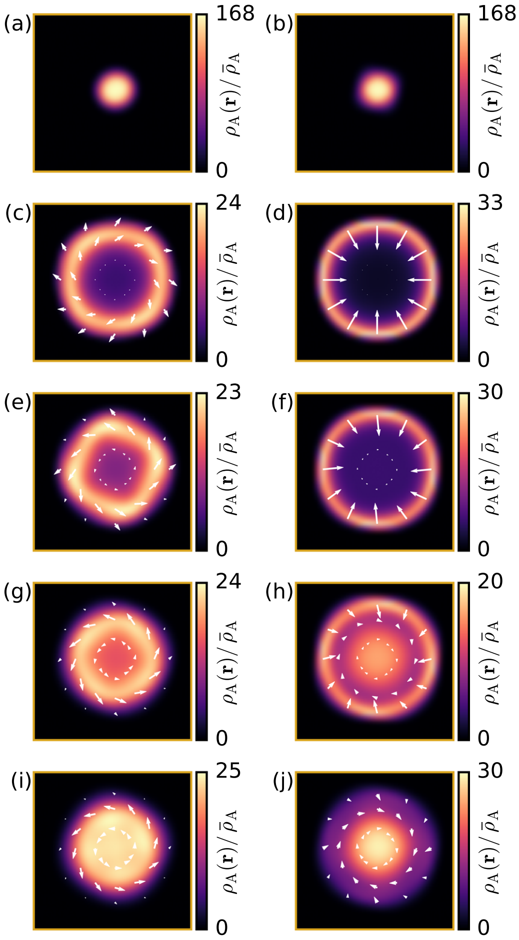

FIG. 4. Steady-state density distributions of species A inside the externally driven ring of passive particles (species B, not shown here). In addition to the parameters (for species B) given in Fig. 3, we have used $\bar{\rho}_A\sigma^2 = 0.001\,88$, $a_A = 0.25\sigma$, $L_A = 0.75\sigma$, $\alpha_A = 0.4$, $V_0^A = 0.1\,k_BT$, $\epsilon_0^{AA} = \epsilon_0^{AB} = 10\,k_BT$, with $\sigma_A = \sigma_B = \sigma$, and only the inner area of $16\sigma \times 16\sigma$ is shown. Again, brighter colors indicate higher spatial densities and white arrows reflect the average orientation vector fields, as defined in Eqs. (61) and (62), respectively. [(a) and (b)] Densities of internally confined passive particles ($f_A = 0$) at magnitudes of the external driving (a) $\omega_d = 0$ and (b) $\omega_d\tau_b = 80$ [with Brownian time $\tau_b = \sigma^2/(\mu^{t,B}k_BT)$]. Within the precision of our numerical discretization scheme, the distributions are identical. [(c)–(j)] Confined active microswimmers ($|f_A| = 400k_BT/\sigma$) subject to external driving strengths acting on the outer particles [(c) and (d)] $\omega_d\tau_b = 0$, [(e) and (f)] $\omega_d\tau_b = 40$, [(g) and (h)] $\omega_d\tau_b = 80$, and [(i) and (j)] $\omega_d\tau_b = 120$. Here, the cases of pushers are depicted on the left-hand side, while those for pullers are shown on the right-hand side. The induced shear flows lead to an increased localization toward the center of the cell, together with an induced tilting of the swimmer orientation, which is more pronounced for pushers than for pullers.

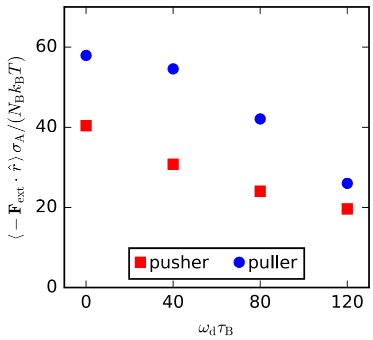

FIG. 5. Averaged radial component of the external force acting on the trapped microswimmers vs angular driving speed ω_d of the outer passive particles, for pushers (red squares) and pullers (blue circles), resulting from the steady-state density distributions displayed in Figs. 4(c)–4(j). Here, $\hat{\mathbf{r}} = \mathbf{r}/|\mathbf{r}|$ is the spatial unit vector pointing radially outward. With increasing ω_d, the swimmer orientations are rotated by the induced flow, which hinders the outward self-propulsion. This leads to increasingly centered density distributions, reducing the exposure to the external trapping in magnitude.

In this way, the behavior of species A becomes comparable to that of circle swimmers, i.e., self-propelled particles that additionally feature an active self-rotation.[171–175] Actually, we have observed a similar phenomenology as in Fig. 4 for increasing inherent curvature of the trajectories of circle swimmers in Ref. 107. In the present case, however, the (externally induced) rotation varies with the distance r from the origin so that the local radius of induced circle-swimming $R_{cs}(r) := |\mathbf{v}_{0A}/\omega_{AB}(r)|$, determined from the definitions in Eqs. (16) and (78), is nonconstant. It reaches a maximum at the origin and decreases with increasing r. For Figs. 4(e)–4(h), the length scale of $R_{cs}(r)$ is comparable to the radius of the effective trap so that a high-density ring is still visible. However, the average orientations are significantly tilted from the radial direction (especially for pusher microswimmers). Further increasing the external driving strength, see Figs. 4(i) and 4(j), leads to more localized density profiles and circling around the center of confinement.

The increasing localization can be quantified by the (negative) radial component of the averaged external trapping force experienced by the microswimmer ensemble, as given in Fig. 5 for the same (steady-state) data as in Figs. 4(c)–4(j). For vanishing angular driving speed ω_d of the outer passive particles, we find a higher value for pullers (blue circles) than for pushers (red squares), corresponding to the more off-center density distribution of pullers caused by their stronger tendency to show radial orientation. Both curves drop for increasing ω_d. The reason is again the induced shear flow increasingly hindering the swimmers from self-propelling efficiently against the radial external trapping potential. The drop is somewhat delayed for our pullers, in accordance with a similar effect previously seen for circle swimmers in an external trap, where the pullers also showed a stronger tendency of maintaining a ring of outward-oriented swimmers.[107]

In related works, rosettelike trajectories have been reported for (single) circle swimmers with explicitly time-dependent

The Journal of Chemical Physics ARTICLE scitation.org/journal/jcp

self-propulsion velocities.[176,177] Beyond the scope of the present work, when genuine circle swimmers are confined (as species A) in our setup, again high-density rings might be observed with average swimmer orientations along the local radial direction. For this purpose, the induced rotation ω^{AB} should balance the inherent self-rotation of the circle swimmers.

V. CONCLUSIONS

In this work, we have presented a dynamical density functional theory (DDFT) for multispecies suspensions of microswimmers. We have included (pairwise) hydrodynamic and effective steric interactions between swimmers. In this way, we conceptually extended the previous one-component equivalent.[106–108] The theory is based on a discrete force-dipole minimal microswimmer model, which has already been used successfully in several previous works.[58,94,106–108] We then applied our theory to three illustrative example situations of planar swimmer configurations inside a three-dimensional bulk fluid.

First, binary pusher–puller mixtures in external spherically symmetric trapping potentials have been discussed. For the two species only differing in their pusher/puller signature, we found that the majority species imposes its behavior on the minority species. For example, pushers at the considered propulsion strength on their own tend to form concentrated spots on the rim of the trap. Therefore, if pushers represent the majority species, this spot formation is conveyed to simultaneously present pullers. Conversely, pullers by themselves rather tend to form a roughly spherically symmetric high-density ring on the rim of the trap. Thus, if they represent the majority in a pusher–puller mixture, also pushers tend to organize themselves in a corresponding ring structure.

Second, in the absence of any external trapping potential, pusher–puller mixtures in large periodic boxes have been considered. In an analytical treatment analogous to the previously studied one-component case,[108] pullers are found to be able to establish the onset of the collective polar orientational order of the whole mixture. Accordingly, pullers can induce oriented collective motion. For this purpose, they need to represent the majority species and show a sufficiently large magnitude of their active drive. Our results are qualitatively in line with previous agent-based computer simulations.[94]

Third, a microswimmer species is confined inside a circular ring of externally driven passive particles. The induced shear flow persistently rotates the confined swimmers and thus can hinder them from forming the high-density rings that are typically observed for sufficiently quick self-propelled particles in radial trapping potentials. Instead, the swimmer densities tend to collapse toward the center of the confinement. Similar mechanisms have previously been found for circle swimmers (featuring an inherent self-rotation) without externally induced shear flows. One future task could be to focus further on the role of shear flows in our statistical theory.[169,170]

In the numerical examples, we have restricted our evaluations for hydrodynamically interacting microswimmers to small confined systems that suitably fit into the corresponding simulation box. Nevertheless, in the future, our set of partial differential equations could be solved numerically as well for (basically infinitely extended) bulk situations. For this purpose, (true) periodic boundary conditions are applied to a finite simulation box. Then, because of the long-range nature of the hydrodynamic interactions, the influence of all periodic images on the density distribution in the simulation box must be accounted for. Mathematically, this can be achieved by applying Ewald summation techniques[178] to the mobility tensors. Corresponding results have been derived for passive particles[179–181] but could, in principle, also be calculated for our active microswimmers, as has recently been demonstrated for a similar force-dipole-based microswimmer model.[182] For quantitative tests of our theory in the future and for extensions to higher densities, particle-based computer simulations (that include hydrodynamic flows of the surrounding fluid and thermal fluctuations explicitly) can be performed.

One very interesting question is whether our DDFT could be extended to describe the aforementioned motility-induced phase separation. In this context, existing statistical theories involved a density-dependent effective swimming speed and/or an anisotropic pair distribution function as additional inputs.[11,13,85,183,184] It would thus be interesting to study in the future the effect of at least one similar activity-induced term in our theory. Another promising statistical approach beyond the adiabatic approximation of DDFT is the power functional theory for “dry” self-propelled particles, which has recently been formulated and evaluated semianalytically.[185–187]

The present work derives the multispecies DDFT for the case of uniaxial straight-swimming microswimmers with spherical bodies. However, only a few changes transfer it to the case of (inherently biaxial) circle swimmers.[107] Even more generally, changes will allow to describe swimmers with less-symmetric body shapes, e.g., rodlike bodies. Nevertheless, we remark that more work is needed in the future regarding situations of still higher complexity. Examples are cases in which, for instance, additional phoretic chemical- or temperature-based interactions between swimmers become significant.[188] Moreover, effects of the fluctuations of the propulsion mechanism itself could be taken into account.[189]

Beyond the direct numerical evaluations performed in this work, DDFTs can serve as a foundation to derive corresponding phase-field-crystal models[86,190–193] and more macroscopic continuum theories[194–196] of microswimmer suspensions. The latter allow for connections toward still-larger length scales of theoretical descriptions. Altogether, we thus expect our DDFT to provide a powerful tool for the statistical characterization of dynamic multispecies systems of suspended microswimmers of future relevance both in fundamental physics and concerning the corresponding biological, technical, and medical applications.

ACKNOWLEDGMENTS

The authors thank Urs Zimmermann, Soudeh Jahanshahi, and Giorgio Pessot for helpful comments, as well as the Deutsche Forschungsgemeinschaft for support of this work through the SPP 1726 on microswimmers, Grant Nos. LO 418/17-2 and ME 3571/2-2.

REFERENCES

[1] E. M. Purcell, Am. J. Phys. **45**, 3 (1977).
[2] E. Lauga and T. R. Powers, Rep. Prog. Phys. **72**, 096601 (2009).
[3] J. Elgeti, R. G. Winkler, and G. Gompper, Rep. Prog. Phys. **78**, 056601 (2015).
[4] A. M. Menzel, Phys. Rep. **554**, 1 (2015).

The Journal of Chemical Physics ARTICLE scitation.org/journal/jcp

[5] A. Zöttl and H. Stark, J. Phys.: Condens. Matter **28**, 253001 (2016).
[6] C. Bechinger, R. Di Leonardo, H. Löwen, C. Reichhardt, G. Volpe, and G. Volpe, Rev. Mod. Phys. **88**, 045006 (2016).
[7] S. Ramaswamy, Annu. Rev. Condens. Matter Phys. **1**, 323 (2010).
[8] M. E. Cates, Rep. Prog. Phys. **75**, 042601 (2012).
[9] M. C. Marchetti, J.-F. Joanny, S. Ramaswamy, T. B. Liverpool, J. Prost, M. Rao, and R. A. Simha, Rev. Mod. Phys. **85**, 1143 (2013).
[10] A. M. Menzel, New J. Phys. **18**, 071001 (2016).
[11] M. E. Cates and J. Tailleur, Europhys. Lett. **101**, 20010 (2013).
[12] I. Buttinoni, J. Bialké, F. Kümmel, H. Löwen, C. Bechinger, and T. Speck, Phys. Rev. Lett. **110**, 238301 (2013).
[13] J. Bialké, H. Löwen, and T. Speck, Europhys. Lett. **103**, 30008 (2013).
[14] J. Bialké, T. Speck, and H. Löwen, J. Non-Cryst. Solids **407**, 367 (2015).
[15] M. E. Cates and J. Tailleur, Annu. Rev. Condens. Matter Phys. **6**, 219 (2015).
[16] A. Solon, J. Stenhammar, M. E. Cates, Y. Kafri, and J. Tailleur, New J. Phys. **20**, 075001 (2018).
[17] P. Digregorio, D. Levis, A. Suma, L. F. Cugliandolo, G. Gonnella, and I. Pagonabarraga, Phys. Rev. Lett. **121**, 098003 (2018).
[18] H. Wensink and H. Löwen, J. Phys.: Condens. Matter **24**, 464130 (2012).
[19] A. M. Menzel and T. Ohta, Europhys. Lett. **99**, 58001 (2012).
[20] A. M. Menzel, J. Phys.: Condens. Matter **25**, 505103 (2013).
[21] F. Kogler and S. H. L. Klapp, Europhys. Lett. **110**, 10004 (2015).
[22] P. Romanczuk, H. Chaté, L. Chen, S. Ngo, and J. Toner, New J. Phys. **18**, 063015 (2016).
[23] J. O. Kessler, Nature **313**, 218 (1985).
[24] M. Eisenbach and L. C. Giojalas, Nat. Rev. Mol. Cell Biol. **7**, 276 (2006).
[25] M. Engstler, T. Pfohl, S. Herminghaus, M. Boshart, G. Wiegertjes, N. Heddergott, and P. Overath, Cell **131**, 505 (2007).
[26] H. C. Berg, *E. Coli in Motion* (Springer Science & Business Media, New York, 2008).
[27] M. Polin, I. Tuval, K. Drescher, J. P. Gollub, and R. E. Goldstein, Science **325**, 487 (2009).
[28] W. M. Durham, J. O. Kessler, and R. Stocker, Science **323**, 1067 (2009).
[29] M. Mussler, S. Rafaï, P. Peyla, and C. Wagner, Europhys. Lett. **101**, 54004 (2013).
[30] R. E. Goldstein, Annu. Rev. Fluid Mech. **47**, 343 (2015).
[31] W. F. Paxton, K. C. Kistler, C. C. Olmeda, A. Sen, S. K. St. Angelo, Y. Cao, T. E. Mallouk, P. E. Lammert, and V. H. Crespi, J. Am. Chem. Soc. **126**, 13424 (2004).
[32] J. R. Howse, R. A. Jones, A. J. Ryan, T. Gough, R. Vafabakhsh, and R. Golestanian, Phys. Rev. Lett. **99**, 048102 (2007).
[33] I. Buttinoni, G. Volpe, F. Kümmel, G. Volpe, and C. Bechinger, J. Phys.: Condens. Matter **24**, 284129 (2012).
[34] A. Walther and A. H. Müller, Chem. Rev. **113**, 5194 (2013).
[35] S. Samin and R. van Roij, Phys. Rev. Lett. **115**, 188305 (2015).
[36] J. L. Moran and J. D. Posner, Annu. Rev. Fluid Mech. **49**, 511 (2017).
[37] J. Wang and W. Gao, ACS Nano **6**, 5745 (2012).
[38] D. Patra, S. Sengupta, W. Duan, H. Zhang, R. Pavlick, and A. Sen, Nanoscale **5**, 1273 (2013).
[39] L. K. Abdelmohsen, F. Peng, Y. Tu, and D. A. Wilson, J. Mater. Chem. B **2**, 2395 (2014).
[40] X. Ma, K. Hahn, and S. Sanchez, J. Am. Chem. Soc. **137**, 4976 (2015).
[41] A. F. Demirörs, M. T. Akan, E. Poloni, and A. R. Studart, Soft Matter **14**, 4741 (2018).
[42] B. J. Nelson, I. K. Kaliakatsos, and J. J. Abbott, Annu. Rev. Biomed. Eng. **12**, 55 (2010).
[43] W. Xi, A. A. Solovev, A. N. Ananth, D. H. Gracias, S. Sanchez, and O. G. Schmidt, Nanoscale **5**, 1294 (2013).
[44] V. Magdanz, S. Sanchez, and O. G. Schmidt, Adv. Mater. **25**, 6581 (2013).
[45] R. Di Leonardo, L. Angelani, D. Dell'Arciprete, G. Ruocco, V. Iebba, S. Schippa, M. P. Conte, F. Mecarini, F. De Angelis, and E. Di Fabrizio, Proc. Natl. Acad. Sci. U. S. A. **107**, 9541 (2010).
[46] A. Sokolov, M. M. Apodaca, B. A. Grzybowski, and I. S. Aranson, Proc. Natl. Acad. Sci. U. S. A. **107**, 969 (2010).
[47] C. Maggi, J. Simmchen, F. Saglimbeni, J. Katuri, M. Dipalo, F. De Angelis, S. Sanchez, and R. Di Leonardo, Small **12**, 446 (2016).
[48] H. H. Wensink and H. Löwen, Phys. Rev. E **78**, 031409 (2008).
[49] J. Elgeti and G. Gompper, Europhys. Lett. **85**, 38002 (2009).
[50] A. Kaiser, H. H. Wensink, and H. Löwen, Phys. Rev. Lett. **108**, 268307 (2012).
[51] N. A. Licata, B. Mohari, C. Fuqua, and S. Setayeshgar, Biophys. J. **110**, 247 (2016).
[52] L. M. C. Janssen, A. Kaiser, and H. Löwen, Sci. Rep. **7**, 5667 (2017).
[53] S. Praetorius, A. Voigt, R. Wittkowski, and H. Löwen, Phys. Rev. E **97**, 052615 (2018).
[54] J. R. Gomez-Solano, A. Blokhuis, and C. Bechinger, Phys. Rev. Lett. **116**, 138301 (2016).
[55] N. Narinder, C. Bechinger, and J. R. Gomez-Solano, Phys. Rev. Lett. **121**, 078003 (2018).
[56] B. Liebchen, P. Monderkamp, B. ten Hagen, and H. Löwen, Phys. Rev. Lett. **120**, 208002 (2018).
[57] C. Ferreiro-Córdova, J. Toner, H. Löwen, and H. H. Wensink, Phys. Rev. E **97**, 062606 (2018).
[58] A. Daddi-Moussa-Ider and A. M. Menzel, Phys. Rev. Fluids **3**, 094102 (2018).
[59] M. Puljiz and A. M. Menzel, Phys. Rev. E **99**, 012601 (2019).
[60] H.-C. Flemming, J. Wingender, U. Szewzyk, P. Steinberg, S. A. Rice, and S. Kjelleberg, Nat. Rev. Microbiol. **14**, 563 (2016).
[61] L. Vidakovic, P. K. Singh, R. Hartmann, C. D. Nadell, and K. Drescher, Nat. Microbiol. **3**, 26 (2018).
[62] A. P. Berke, L. Turner, H. C. Berg, and E. Lauga, Phys. Rev. Lett. **101**, 038102 (2008).
[63] A. J. Mathijssen, F. Guzmán-Lastra, A. Kaiser, and H. Löwen, Phys. Rev. Lett. **121**, 248101 (2018).
[64] S. Babel, H. Löwen, and A. M. Menzel, Europhys. Lett. **113**, 58003 (2016).
[65] N. Küchler, H. Löwen, and A. M. Menzel, Phys. Rev. E **93**, 022610 (2016).
[66] H. Löwen, Europhys. Lett. **121**, 58001 (2018).
[67] N. A. Mecholsky, E. Ott, and T. M. Antonsen, Jr., Physica D **239**, 988 (2010).
[68] A. Sengupta, T. Kruppa, and H. Löwen, Phys. Rev. E **83**, 031914 (2011).
[69] N. H. P. Nguyen, D. Klotsa, M. Engel, and S. C. Glotzer, Phys. Rev. Lett. **112**, 075701 (2014).
[70] K. Yeo, E. Lushi, and P. M. Vlahovska, Phys. Rev. Lett. **114**, 188301 (2015).
[71] C. Scholz, M. Engel, and T. Pöschel, Nat. Commun. **9**, 1497 (2018).
[72] L. Angelani and R. Di Leonardo, New J. Phys. **12**, 113017 (2010).
[73] A. Kaiser, A. Peshkov, A. Sokolov, B. ten Hagen, H. Löwen, and I. S. Aranson, Phys. Rev. Lett. **112**, 158101 (2014).
[74] A. Kaiser, A. Sokolov, I. S. Aranson, and H. Löwen, IEEE Trans. NanoBioscience **14**, 260 (2015).
[75] A. Kaiser, A. Sokolov, I. S. Aranson, and H. Löwen, Eur. Phys. J.: Spec. Top. **224**, 1275 (2015).
[76] J.-j. Liao, X.-q. Huang, and B.-q. Ai, J. Chem. Phys. **148**, 094902 (2018).
[77] D. Ray, C. Reichhardt, and C. J. O. Reichhardt, Phys. Rev. E **90**, 013019 (2014).
[78] R. Ni, M. A. C. Stuart, and P. G. Bolhuis, Phys. Rev. Lett. **114**, 018302 (2015).
[79] A. Agrawal and S. B. Babu, Phys. Rev. E **97**, 020401 (2018).
[80] R. Wittmann, J. M. Brader, A. Sharma, and U. M. B. Marconi, Phys. Rev. E **97**, 012601 (2018).
[81] E. Ben-Jacob, A. Finkelshtein, G. Ariel, and C. Ingham, Trends Microbiol. **24**, 257 (2016).
[82] J. Stenhammar, R. Wittkowski, D. Marenduzzo, and M. E. Cates, Phys. Rev. Lett. **114**, 018301 (2015).
[83] F. Kümmel, P. Shabestari, C. Lozano, G. Volpe, and C. Bechinger, Soft Matter **11**, 6187 (2015).
[84] A. Wysocki, R. G. Winkler, and G. Gompper, New J. Phys. **18**, 123030 (2016).
[85] R. Wittkowski, J. Stenhammar, and M. E. Cates, New J. Phys. **19**, 105003 (2017).
[86] F. Alaimo and A. Voigt, Phys. Rev. E **98**, 032605 (2018).
[87] A. M. Menzel, Phys. Rev. E **85**, 021912 (2012).
[88] L. Guisandez, G. Baglietto, and A. Rozenfeld, e-print arXiv:1711.11531 (2017).
[89] D. Levis, I. Pagonabarraga, and B. Liebchen, e-print arXiv:1802.02371 (2018).

The Journal of Chemical Physics ARTICLE scitation.org/journal/jcp

[90] D. Levis and B. Liebchen, Phys. Rev. E **100**, 012406 (2019).
[91] T. Vicsek, A. Czirók, E. Ben-Jacob, I. Cohen, and O. Shochet, Phys. Rev. Lett. **75**, 1226 (1995).
[92] J. Toner and Y. Tu, Phys. Rev. Lett. **75**, 4326 (1995).
[93] T. Ihle, Phys. Rev. E **83**, 030901 (2011).
[94] G. Pessot, H. Löwen, and A. M. Menzel, Mol. Phys. **116**, 3401 (2018).
[95] F. Guzmán-Lastra, A. Kaiser, and H. Löwen, Nat. Commun. **7**, 13519 (2016).
[96] R. Evans, Adv. Phys. **28**, 143 (1979).
[97] R. Evans, in *Fundamentals of Inhomogeneous Fluids*, edited by D. Henderson (Marcel Dekker, New York, 1992), pp. 85–176.
[98] U. M. B. Marconi and P. Tarazona, J. Chem. Phys. **110**, 8032 (1999).
[99] U. M. B. Marconi and P. Tarazona, J. Phys.: Condens. Matter **12**, A413 (2000).
[100] A. J. Archer and R. Evans, J. Chem. Phys. **121**, 4246 (2004).
[101] G. K.-L. Chan and R. Finken, Phys. Rev. Lett. **94**, 183001 (2005).
[102] P. Español and H. Löwen, J. Chem. Phys. **131**, 244101 (2009).
[103] R. Evans, in *Lecture Notes 3rd Warsaw School of Statistical Physics*, edited by B. Cichocki, M. Napiórkowski, and J. Piasecki (Warsaw University Press, Warsaw, 2010), pp. 43–85.
[104] H. Löwen, in *Lecture Notes 3rd Warsaw School of Statistical Physics*, edited by B. Cichocki, M. Napiórkowski, and J. Piasecki (Warsaw University Press, Warsaw, 2010), pp. 87–121.
[105] R. Wittkowski and H. Löwen, Mol. Phys. **109**, 2935 (2011).
[106] A. M. Menzel, A. Saha, C. Hoell, and H. Löwen, J. Chem. Phys. **144**, 024115 (2016).
[107] C. Hoell, H. Löwen, and A. M. Menzel, New J. Phys. **19**, 125004 (2017).
[108] C. Hoell, H. Löwen, and A. M. Menzel, J. Chem. Phys. **149**, 144902 (2018).
[109] A. J. Archer, J. Phys.: Condens. Matter **17**, 1405 (2005).
[110] B. D. Goddard, A. Nold, and S. Kalliadasis, J. Chem. Phys. **138**, 144904 (2013).
[111] A. Härtel, M. Kohl, and M. Schmiedeberg, Phys. Rev. E **92**, 042310 (2015).
[112] S. Babel, M. H. Eikerling, and H. Löwen, J. Phys. Chem. C **122**, 21724 (2018).
[113] W. R. C. Somerville, J. L. Stokes, A. M. Adawi, T. S. Horozov, A. J. Archer, and D. M. A. Buzza, J. Phys.: Condens. Matter **30**, 405102 (2018).
[114] A. J. Archer, P. Hopkins, and M. Schmidt, Phys. Rev. E **75**, 040501 (2007).
[115] P. Hopkins, A. Fortini, A. J. Archer, and M. Schmidt, J. Chem. Phys. **133**, 224505 (2010).
[116] H. M. Al-Saedi, A. J. Archer, and J. Ward, Phys. Rev. E **98**, 022407 (2018).
[117] B. ten Hagen, R. Wittkowski, D. Takagi, F. Kümmel, C. Bechinger, and H. Löwen, J. Phys.: Condens. Matter **27**, 194110 (2015).
[118] A. Najafi and R. Golestanian, Phys. Rev. E **69**, 062901 (2004).
[119] R. Zargar, A. Najafi, and M. Miri, Phys. Rev. E **80**, 026308 (2009).
[120] A. Daddi-Moussa-Ider, M. Lisicki, C. Hoell, and H. Löwen, J. Chem. Phys. **148**, 134904 (2018).
[121] A. Daddi-Moussa-Ider, M. Lisicki, A. J. Mathijssen, C. Hoell, S. Goh, J. Bławzdziewicz, A. M. Menzel, and H. Löwen, J. Phys.: Condens. Matter **30**, 254004 (2018).
[122] P. T. Underhill, J. P. Hernandez-Ortiz, and M. D. Graham, Phys. Rev. Lett. **100**, 248101 (2008).
[123] A. Baskaran and M. C. Marchetti, Proc. Natl. Acad. Sci. U. S. A. **106**, 15567 (2009).
[124] J. Happel and H. Brenner, *Low Reynolds Number Hydrodynamics: With Special Applications to Particulate Media* (Springer Netherlands, Dordrecht, 2012), Vol. 1.
[125] J. K. G. Dhont, *An Introduction to Dynamics of Colloids* (Elsevier, Amsterdam, 1996).
[126] S. Kim and S. J. Karrila, *Microhydrodynamics: Principles and Selected Applications* (Dover Publications, Mineola, 2013).
[127] C. W. J. Beenakker and P. Mazur, Physica A **120**, 388 (1983).
[128] C. W. J. Beenakker and P. Mazur, Physica A **126**, 349 (1984).
[129] G. Nägele, Phys. Rep. **272**, 215 (1996).
[130] G. Nägele and P. Baur, Physica A **245**, 297 (1997).
[131] A. J. Banchio, J. Gapinski, A. Patkowski, W. Häußler, A. Fluerasu, S. Sacanna, P. Holmqvist, G. Meier, M. P. Lettinga, and G. Nägele, Phys. Rev. Lett. **96**, 138303 (2006).
[132] J. Rotne and S. Prager, J. Chem. Phys. **50**, 4831 (1969).
[133] M. Reichert and H. Stark, Phys. Rev. E **69**, 031407 (2004).
[134] T. C. Adhyapak and S. Jabbari-Farouji, Phys. Rev. E **96**, 052608 (2017).
[135] B. M. Mladek, D. Gottwald, G. Kahl, M. Neumann, and C. N. Likos, Phys. Rev. Lett. **96**, 045701 (2006).
[136] A. J. Archer, M. Walters, U. Thiele, and E. Knobloch, Phys. Rev. E **90**, 042404 (2014).
[137] M. Doi and S. F. Edwards, *The Theory of Polymer Dynamics* (Oxford University Press, Oxford, 1988).
[138] M. Rex and H. Löwen, Eur. Phys. J. E **28**, 139 (2009).
[139] J.-P. Hansen and I. R. McDonald, *Theory of Simple Liquids* (Elsevier, Amsterdam, 1990).
[140] Y. Singh, Phys. Rep. **207**, 351 (1991).
[141] J. K. Percus, Phys. Rev. Lett. **8**, 462 (1962).
[142] M. Rex, H. H. Wensink, and H. Löwen, Phys. Rev. E **76**, 021403 (2007).
[143] C. G. Gray and K. E. Gubbins, *Theory of Molecular Fluids: I: Fundamentals*, International Series of Monographs on Chemistry (Oxford University Press, Oxford, 1984).
[144] L. Onsager, Ann. N. Y. Acad. Sci. **51**, 627 (1949).
[145] J. E. Guyer, D. Wheeler, and J. A. Warren, Comput. Sci. Eng. **11**, 6 (2009).
[146] R. W. Nash, R. Adhikari, J. Tailleur, and M. E. Cates, Phys. Rev. Lett. **104**, 258101 (2010).
[147] M. Hennes, K. Wolff, and H. Stark, Phys. Rev. Lett. **112**, 238104 (2014).
[148] A. M. Menzel, Europhys. Lett. **110**, 38005 (2015).
[149] W. Yan and J. F. Brady, J. Fluid Mech. **785**, R1 (2015).
[150] A. Malevanets and R. Kapral, J. Chem. Phys. **110**, 8605 (1999).
[151] R. Kapral, Adv. Chem. Phys. **140**, 89 (2008).
[152] G. Gompper, T. Ihle, D. M. Kroll, and R. G. Winkler, *Advanced Computer Simulation Approaches for Soft Matter Sciences III* (Springer, Berlin, Heidelberg, 2009), pp. 1–87.
[153] A. Zöttl and H. Stark, Phys. Rev. Lett. **108**, 218104 (2012).
[154] A. Zöttl and H. Stark, Phys. Rev. Lett. **112**, 118101 (2014).
[155] F. Rühle, J. Blaschke, J.-T. Kuhr, and H. Stark, New J. Phys. **20**, 025003 (2018).
[156] T. Ihle and D. M. Kroll, Phys. Rev. E **63**, 020201 (2001).
[157] M. T. Downton and H. Stark, J. Phys.: Condens. Matter **21**, 204101 (2009).
[158] G. R. McNamara and G. Zanetti, Phys. Rev. Lett. **61**, 2332 (1988).
[159] F. Alarcón and I. Pagonabarraga, J. Mol. Liq. **185**, 56 (2013).
[160] M. Kuron, P. Stärk, C. Burkard, J. de Graaf, and C. Holm, J. Chem. Phys. **150**, 144110 (2019).
[161] D. Bardfalvy, H. Nordanger, C. Nardini, A. Morozov, and J. Stenhammar, e-print arXiv:1904.03069 (2019).
[162] F. J. Schwarzendahl and M. G. Mazza, J. Chem. Phys. **150**, 184902 (2019).
[163] G. I. Taylor, Proc. R. Soc. London, Ser. A **223**, 289 (1923).
[164] I. Williams, E. C. Oğuz, T. Speck, P. Bartlett, H. Löwen, and C. P. Royall, Nat. Phys. **12**, 98 (2016).
[165] M. Rauscher, A. Domínguez, M. Krüger, and F. Penna, J. Chem. Phys. **127**, 244906 (2007).
[166] A. Scacchi, A. J. Archer, and J. M. Brader, Phys. Rev. E **96**, 062616 (2017).
[167] A. Scacchi and J. M. Brader, J. Phys.: Condens. Matter **30**, 095102 (2018).
[168] D. Stopper and R. Roth, Phys. Rev. E **97**, 062602 (2018).
[169] J. M. Brader and M. Krüger, Mol. Phys. **109**, 1029 (2011).
[170] A. A. Aerov and M. Krüger, J. Chem. Phys. **140**, 094701 (2014).
[171] S. van Teeffelen and H. Löwen, Phys. Rev. E **78**, 020101 (2008).
[172] Y. Fily, A. Baskaran, and M. C. Marchetti, Soft Matter **8**, 3002 (2012).
[173] F. Kümmel, B. ten Hagen, R. Wittkowski, I. Buttinoni, R. Eichhorn, G. Volpe, H. Löwen, and C. Bechinger, Phys. Rev. Lett. **110**, 198302 (2013).
[174] H. Löwen, Eur. Phys. J.: Spec. Top. **225**, 2319 (2016).
[175] F. J. Sevilla, Phys. Rev. E **94**, 062120 (2016).
[176] S. Babel, B. ten Hagen, and H. Löwen, J. Stat. Mech.: Theory Exp. **2014**, P02011.

The Journal of Chemical Physics ARTICLE scitation.org/journal/jcp

[177] S. Jahanshahi, H. Löwen, and B. ten Hagen, Phys. Rev. E **95**, 022606 (2017).
[178] P. P. Ewald, Ann. Phys. **369**, 253 (1921).
[179] C. W. J. Beenakker, J. Chem. Phys. **85**, 1581 (1986).
[180] J. F. Brady, R. J. Phillips, J. C. Lester, and G. Bossis, J. Fluid Mech. **195**, 257 (1988).
[181] M. Rex and H. Löwen, Eur. Phys. J. E **26**, 143 (2008).
[182] T. C. Adhyapak and S. Jabbari-Farouji, J. Chem. Phys. **149**, 144110 (2018).
[183] T. Speck, J. Bialké, A. M. Menzel, and H. Löwen, Phys. Rev. Lett. **112**, 218304 (2014).
[184] T. Speck, A. M. Menzel, J. Bialké, and H. Löwen, J. Chem. Phys. **142**, 224109 (2015).
[185] P. Krinninger, M. Schmidt, and J. M. Brader, Phys. Rev. Lett. **117**, 208003 (2016).
[186] P. Krinninger, M. Schmidt, and J. M. Brader, Phys. Rev. Lett. **119**, 029902 (2017).
[187] P. Krinninger and M. Schmidt, J. Chem. Phys. **150**, 074112 (2019).
[188] B. Liebchen and H. Löwen, J. Chem. Phys. **150**, 061102 (2019).
[189] P. Pietzonka and U. Seifert, J. Phys. A: Math. Theor. **51**, 01LT01 (2017).
[190] S. van Teeffelen, R. Backofen, A. Voigt, and H. Löwen, Phys. Rev. E **79**, 051404 (2009).
[191] A. M. Menzel and H. Löwen, Phys. Rev. Lett. **110**, 055702 (2013).
[192] A. M. Menzel, T. Ohta, and H. Löwen, Phys. Rev. E **89**, 022301 (2014).
[193] R. Wittkowski, A. Tiribocchi, J. Stenhammar, R. J. Allen, D. Marenduzzo, and M. E. Cates, Nat. Commun. **5**, 4351 (2014).
[194] S. Heidenreich, J. Dunkel, S. H. L. Klapp, and M. Bär, Phys. Rev. E **94**, 020601 (2016).
[195] H. Reinken, S. H. L. Klapp, M. Bär, and S. Heidenreich, Phys. Rev. E **97**, 022613 (2018).
[196] H. Reinken, S. Heidenreich, M. Bär, and S. H. L. Klapp, New J. Phys. **21**, 013037 (2019).

P4 Particle-scale statistical theory for hydrodynamically induced polar ordering in microswimmer suspensions

Reproduced from

C. Hoell, H. Löwen, and A. M. Menzel,
Particle-scale statistical theory for hydrodynamically induced polar ordering in microswimmer suspensions,
J. Chem. Phys. **149**, 144902 (2018),
with the permission of *AIP Publishing.*

Digital Object Identifier (DOI): `https://doi.org/10.1063/1.5048304`

Statement of contribution

AMM and HL supervised this work. All authors developed the theory. I conceived and implemented the adaptation of Percus' test-particle method to active systems, performed the numerical evaluations and the analytical calculations, prepared all figures, and drafted the manuscript, which then AMM and I completed. All authors discussed and interpreted the results, edited the text, and finalized the manuscript.

Copyright and license notice

THE JOURNAL OF CHEMICAL PHYSICS **149**, 144902 (2018)

Particle-scale statistical theory for hydrodynamically induced polar ordering in microswimmer suspensions

Christian Hoell,[a] Hartmut Löwen, and Andreas M. Menzel[b]
Institut für Theoretische Physik II: Weiche Materie, Heinrich-Heine-Universität Düsseldorf, 40225 Düsseldorf, Germany

(Received 12 July 2018; accepted 25 September 2018; published online 11 October 2018)

Previous particle-based computer simulations have revealed a significantly more pronounced tendency of spontaneous global polar ordering in puller (contractile) microswimmer suspensions than in pusher (extensile) suspensions. We here evaluate a microscopic statistical theory to investigate the emergence of such an order through a linear instability of the disordered state. For this purpose, input concerning the orientation-dependent pair-distribution function is needed, and we discuss the corresponding approaches, particularly a heuristic variant of the Percus test-particle method applied to active systems. Our theory identifies an inherent evolution of polar order in planar systems of puller microswimmers, if mutual alignment due to hydrodynamic interactions overcomes the thermal dealignment by rotational diffusion. In our theory, the cause of orientational ordering can be traced back to the actively induced hydrodynamic rotation–translation coupling between the swimmers. Conversely, disordered pusher suspensions remain linearly stable against homogeneous polar orientational ordering. We expect that our results can be confirmed in experiments on (semi-)dilute active microswimmer suspensions, based, for instance, on biological pusher- and puller-type swimmers. *Published by AIP Publishing.*
https://doi.org/10.1063/1.5048304

I. INTRODUCTION

Microswimmers[1–6]—both biological[7–11] and artificial[12–15]—have been studied widely and can be considered as an archetype of active soft matter.[16–18] Since these self-propelled particles are inherently in non-equilibrium with their surroundings, their study has led to rather unexpected findings, e.g., motility-induced phase separation,[19–26] laning,[27–31] various kinds of "taxes"[32] by implicit steering,[33–38] and bacterial turbulence.[27,39–43] Establishing a physical description of the observed collective phenomena calls for the development of new methods in statistical physics.[44–51] Furthermore, there is a huge amount of biological and medical problems for which the knowledge about microswimmers and their physical behavior is key,[33,34,52–57] warranting strong research interest in this topic.

Approaching the scientific field of microswimmers as an extension of the study of colloidal suspensions[58] allows both experimentalists and theoreticians to carry over methods and ideas. An important example is hydrodynamics: microswimmers typically operate in low-Reynolds-number regimes.[1] In this context, a whole apparatus of physical theory[58–60] is at hand as a toolkit for, e.g., the investigation of hydrodynamic interactions between swimmers and the influence of these interactions on the collective behavior of microswimmer suspensions.

As a consequence of the swimming at low Reynolds numbers, no net force may be exerted by a model microswimmer on its environment.[1,45] To the lowest order, the induced flow field of a typical swimmer in general can thus be described as generated by a force dipole (we here disregard "neutral-type" swimmers with a vanishing averaged force-dipole contribution to the flow field like, e.g., the famous Najafi-Golestanian three-sphere swimmer[61–64]). Depending on the orientation of the forces (outwards/inwards) of that dipole, one can distinguish "pusher" (also called extensile) microswimmers—for which fluid is pushed outwards along the axis of motion and sucked in from the transverse axes—and "puller" (also termed contractile) microswimmers—for which the inverse is true.[65,66] Since the direction of swimming is given by the orientation of the swimmer, interactions affecting the rotational degrees of freedom are of utmost interest.

A breakthrough in the study of orientational self-organization of self-propelled particles has been the Vicsek model, introducing simple effective local alignment rules. They can lead to emergent long-range orientational order in these active systems, even in two spatial dimensions.[67–72] Such an effective alignment mechanism can be interpreted either as being social in nature, e.g., when applied to flocks of birds,[67,68,70] or as a coarse-grained model representing underlying physical interactions, e.g., steric alignment interactions.[73] In the present work, we focus on the question, to which extent hydrodynamic interactions can provide sufficient alignment to result in polarly ordered collective motion.

Previously, corresponding computer simulations have found that indeed hydrodynamic interactions between microswimmers can lead to collective alignment in pure puller microswimmer suspensions,[74] also when doped with pusher

[a]Electronic mail: christian.hoell@uni-duesseldorf.de
[b]Electronic mail: menzel@hhu.de

microswimmers.[75] Typically, the degree of observed orientational order in pure pusher suspensions is notably lower.[74,75] In the current work, we analyze a microscopic statistical theory to understand reasons for these differences in polar ordering observed for pushers and pullers. For this purpose, we extend our previously developed dynamical density functional theory (DDFT) of microswimmers,[76,77] built on the force-dipole-based minimal swimmer model introduced in Refs. 75–77.

A brief recapitulation of the theoretical background follows in Sec. II. The theory is then applied to a (semi-)dilute swimmer configuration confined to a plane in Sec. III. Next, to theoretically analyze the emergence of collective polar alignment from hydrodynamic interactions, some microscopic details of the (orientation-dependent) pair distribution function are needed as an input. A reasonable approximation for this pair distribution function is discussed in Sec. IV. As the central step, a linear stability analysis probing the emergence of collective alignment out of the isotropic disordered state is performed in Sec. V. There, indeed we find that hydrodynamic interactions can induce polar ordering in (semi-)dilute suspensions of sufficiently strong puller microswimmers. In contrast to that, a linear stability of disorder is found for the corresponding spatially homogeneous pusher suspensions. Finally, a short conclusion and outlook are given in Sec. VI.

II. THEORY

As just mentioned, this section repeats the central parts of the statistical theory of microswimmers developed in our previous studies.[76,77] At the end of the section, a dynamical equation for the one-swimmer density (as defined below) is listed. It is the starting point for our investigation of possibly emerging polar ordering in planar (semi-)dilute microswimmer configurations in Secs. III–V.

We consider a suspension of N (identical) axially symmetric microswimmers in a volume V. Inertial effects are neglected in the investigated low-Reynolds-number regime. The state of each swimmer $i = 1, \ldots, N$ is characterized by a phase space coordinate $\mathbf{X}_i = (\mathbf{r}_i, \hat{\mathbf{n}}_i)$ that comprises its spatial position $\mathbf{r}_i$ and its orientation, described by the unit vector $\hat{\mathbf{n}}_i$. We recur to the minimal swimmer model introduced in Ref. 76, see Fig. 1.

There, two opposing force centers, exerting forces $\pm\mathbf{f} := \pm f\hat{\mathbf{n}}$ on the fluid, rigidly move and rotate together with a spherical swimmer body of hydrodynamic radius a. In terms of the swimmer coordinates, the force centers are located at positions $\mathbf{r}_i^+ := \mathbf{r}_i + \alpha L\hat{\mathbf{n}}$ and $\mathbf{r}_i^- := \mathbf{r}_i - (1-\alpha)L\hat{\mathbf{n}}$, respectively, with $a/L < \alpha \le 1/2$ a positive number and L the fixed distance between the two force centers. The rigid spherical swimmer body of no-slip surface condition is located at position $\mathbf{r}_i$ in the generated flow of the surrounding fluid. This configuration of the sphere and the two force centers is treated as a rigid entity that translates and rotates as one. For $\alpha \neq 1/2$, net self-propulsion in the direction of sign$(f)\hat{\mathbf{n}}$ results. Accordingly, a pusher (puller) microswimmer[66] is constructed for $f > 0$ ($f < 0$). Furthermore, a steric interaction potential between different swimmers with sufficiently large effective diameter σ is introduced to counteract unphysical overlap. By construction, no net force and no net torque are exerted by the swimmer on the fluid, a necessary condition for microswimmers.[1,45]

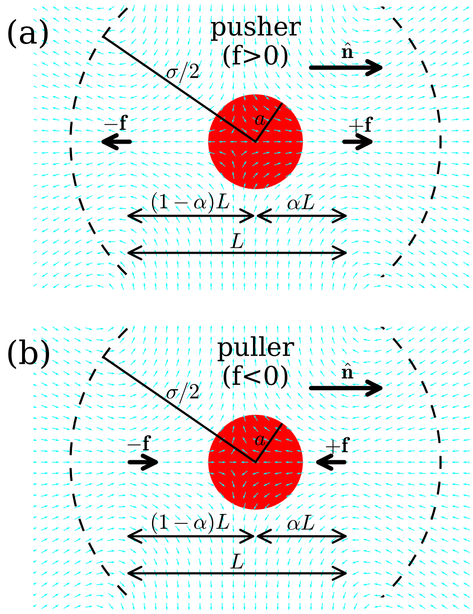

FIG. 1. Minimal microswimmer model, as introduced in Ref. 76. A sphere of radius a constitutes a no-slip boundary for the flow of the surrounding fluid and represents the hydrodynamic swimmer body. Two force centers exerting opposite forces $\pm\mathbf{f} = \pm f\hat{\mathbf{n}}$ of equal magnitude on the fluid are placed nearby in an axially symmetric configuration. They generate the flow indicated by the small arrows, which propels the swimmer. This force-sphere combination is rigidly kept in its internal (body-frame) configuration. (a) For $f > 0$, a pusher microswimmer is created, while (b) a puller microswimmer results for $f < 0$. Other swimmers are exposed to the flow, too, but are kept at a distance by a repulsive interaction potential of characteristic range σ. The resulting effective steric extension of the swimmer is indicated by the dashed line.

In the following, a statistical description of the microswimmer suspension is employed. We start our approach from the (time-dependent) microstate probability density $P = P(\mathbf{X}^N, t)$ to find the system in microstate $\mathbf{X}^N$ at time t, with $\mathbf{X}^N = \{\mathbf{X}_1, \ldots, \mathbf{X}_N\}$. For our overdamped low-Reynolds-number system,[1,58] the dynamical evolution of P is described by the many-body Smoluchowski equation

$$\frac{\partial P}{\partial t} = -\sum_{i=1}^{N}\Big[\nabla_{\mathbf{r}_i}\cdot(\mathbf{v}_i P) + (\hat{\mathbf{n}}_i \times \nabla_{\hat{\mathbf{n}}_i})\cdot(\boldsymbol{\omega}_i P)\Big], \tag{1}$$

where $\mathbf{v}_i$ is the velocity of swimmer i and $\boldsymbol{\omega}_i$ is its angular velocity, both of which generally depend on the configuration $\mathbf{X}^N$ of the system.

We only take into account pairwise additive hydrodynamic interactions between the swimmers on the Rotne-Prager level.[58] Neglecting many-body hydrodynamic interactions is a good approximation at low to intermediate densities[78–82] as regarded here. Thus, in the discrete particle picture, $\mathbf{v}_i$ and $\boldsymbol{\omega}_i$

of swimmer i follow from the forces $\mathbf{F}_j$ and torques $\mathbf{T}_j$ acting on all swimmers j via[76,77]

$$\begin{bmatrix}\mathbf{v}_i\\ \boldsymbol{\omega}_i\end{bmatrix} = \sum_{j=1}^{N}\left(\begin{bmatrix}\boldsymbol{\mu}_{ij}^{\mathrm{tt}} & \boldsymbol{\mu}_{ij}^{\mathrm{tr}}\\ \boldsymbol{\mu}_{ij}^{\mathrm{rt}} & \boldsymbol{\mu}_{ij}^{\mathrm{rr}}\end{bmatrix}\cdot\begin{bmatrix}\mathbf{F}_j\\ \mathbf{T}_j\end{bmatrix} + \begin{bmatrix}\boldsymbol{\Lambda}_{ij}^{\mathrm{tt}} & \mathbf{0}\\ \boldsymbol{\Lambda}_{ij}^{\mathrm{rt}} & \mathbf{0}\end{bmatrix}\cdot\begin{bmatrix}f\hat{\mathbf{n}}_j\\ \mathbf{0}\end{bmatrix}\right), \tag{2}$$

$i = 1, \ldots, N$, exploiting the linearity of the underlying Stokes equation in the low-Reynolds-number regime.[58] The viscosity η of the background fluid is assumed to be constant, and the well-known hydrodynamic mobility expressions for passive rigid spheres on the Rotne-Prager level[83,84] are used. This way, the self mobilities are given by

$$\boldsymbol{\mu}_{ii}^{\mathrm{tt}} = \mu^{\mathrm{t}}\mathbf{1}, \quad \boldsymbol{\mu}_{ii}^{\mathrm{rr}} = \mu^{\mathrm{r}}\mathbf{1}, \quad \boldsymbol{\mu}_{ii}^{\mathrm{tr}} = \boldsymbol{\mu}_{ii}^{\mathrm{rt}} = \mathbf{0}, \tag{3}$$

with $\mathbf{1}$ denoting the identity matrix and

$$\mu^{\mathrm{t}} = 1/(6\pi\eta a), \quad \mu^{\mathrm{r}} = 1/(8\pi\eta a^3), \tag{4}$$

while the pair mobilities ($j \neq i$) read

$$\boldsymbol{\mu}_{ij}^{\mathrm{tt}} = \mu^{\mathrm{t}}\left(\frac{3a}{4r_{ij}}\left(\mathbf{1} + \hat{\mathbf{r}}_{ij}\hat{\mathbf{r}}_{ij}\right) + \frac{1}{2}\left(\frac{a}{r_{ij}}\right)^3\left(\mathbf{1} - 3\hat{\mathbf{r}}_{ij}\hat{\mathbf{r}}_{ij}\right)\right), \tag{5}$$

$$\boldsymbol{\mu}_{ij}^{\mathrm{rr}} = -\mu^{\mathrm{r}}\frac{1}{2}\left(\frac{a}{r_{ij}}\right)^3\left(\mathbf{1} - 3\hat{\mathbf{r}}_{ij}\hat{\mathbf{r}}_{ij}\right), \tag{6}$$

$$\boldsymbol{\mu}_{ij}^{\mathrm{tr}} = \boldsymbol{\mu}_{ij}^{\mathrm{rt}} = \mu^{\mathrm{r}}\left(\frac{a}{r_{ij}}\right)^3\mathbf{r}_{ij}\times, \tag{7}$$

with the distance vector $\mathbf{r}_{ij} = \mathbf{r}_j - \mathbf{r}_i$, $r_{ij} = |\mathbf{r}_{ij}|$ its absolute value, and $\hat{\mathbf{r}}_{ij} = \mathbf{r}_{ij}/r_{ij}$. The additional contributions due to the presence of the active force centers (derived from the previously introduced minimal microswimmer model) are given by[76,77]

$$\boldsymbol{\Lambda}_{ij}^{\mathrm{tt}} = \boldsymbol{\mu}_{ij}^{\mathrm{tt}+} - \boldsymbol{\mu}_{ij}^{\mathrm{tt}-}, \tag{8}$$

$$\boldsymbol{\Lambda}_{ij}^{\mathrm{rt}} = \boldsymbol{\mu}_{ij}^{\mathrm{rt}+} - \boldsymbol{\mu}_{ij}^{\mathrm{rt}-}, \tag{9}$$

with

$$\boldsymbol{\mu}_{ij}^{\mathrm{tt}\pm} = \frac{1}{8\pi\eta r_{ij}^{\pm}}\left(\mathbf{1} + \hat{\mathbf{r}}_{ij}^{\pm}\hat{\mathbf{r}}_{ij}^{\pm}\right) + \frac{a^2}{24\pi\eta\left(r_{ij}^{\pm}\right)^3}\left(\mathbf{1} - 3\hat{\mathbf{r}}_{ij}^{\pm}\hat{\mathbf{r}}_{ij}^{\pm}\right), \tag{10}$$

$$\boldsymbol{\mu}_{ij}^{\mathrm{rt}\pm} = \frac{1}{8\pi\eta\left(r_{ij}^{\pm}\right)^3}\mathbf{r}_{ij}^{\pm}\times, \tag{11}$$

and

$$\mathbf{r}_{ij}^{+} = \mathbf{r}_{ij} + \alpha L\hat{\mathbf{n}}_j, \tag{12}$$

$$\mathbf{r}_{ij}^{-} = \mathbf{r}_{ij} - (1-\alpha)L\hat{\mathbf{n}}_j. \tag{13}$$

We neglect the distortion of the self-induced flow field that would result from the presence of the rigid spheres.[60,85,86]

Next, we specify the forces on the sphere representing the passive body of swimmer j as

$$\mathbf{F}_j = -\nabla_{\mathbf{r}_j}u_{\mathrm{ext}}(\mathbf{r}_j) - \nabla_{\mathbf{r}_j}\sum_{k\neq j}u(\mathbf{r}_j, \mathbf{r}_k) - k_{\mathrm{B}}T\,\nabla_{\mathbf{r}_j}\ln P, \tag{14}$$

where $u_{\mathrm{ext}}(\mathbf{r})$ may include the effect of an external potential, $u(\mathbf{r}_j, \mathbf{r}_k)$ is a pairwise additive interaction potential, and the last term constitutes an entropic force that eventually leads to the correct diffusional parts of our statistical description. As usual, k_{B} denotes the Boltzmann constant and T denotes the temperature. The corresponding passive torques read

$$\mathbf{T}_j = -k_{\mathrm{B}}T\,\hat{\mathbf{n}}_j\times\nabla_{\hat{\mathbf{n}}_j}\ln P, \tag{15}$$

consisting of only an entropic part, which likewise in the end correctly reproduces (rotational) diffusion.

To reduce the multi-dimensional nature of the probability density P containing all N swimmer coordinates $\mathbf{X}_i$, we intend to derive a dynamical equation only involving the reduced n-swimmer densities,

$$\rho^{(n)}(\mathbf{X}^n, t) = \frac{N!}{(N-n)!}\int \mathrm{d}\mathbf{X}_{n+1}\ldots\mathrm{d}\mathbf{X}_N P(\mathbf{X}^N, t). \tag{16}$$

Particularly, we are interested in a dynamical equation for the one-swimmer density $\rho^{(1)}(\mathbf{X}, t)$. As the swimmers are identical and, e.g., $\mathbf{X}$ in $\rho^{(1)}(\mathbf{X}, t)$ stands for the coordinate of "one swimmer" and not of "swimmer 1", the enumeration $\mathbf{X}, \mathbf{X}', \mathbf{X}'', \ldots$ is used throughout this work when discussing arguments of n-swimmer densities.

Integrating out the degrees of freedom $\mathbf{X}_i$ for all swimmers but one in Eq. (1), we obtain[76,77]

$$\frac{\partial\rho^{(1)}(\mathbf{X}, t)}{\partial t} = -\nabla_{\mathbf{r}}\cdot(\mathcal{J}^{\mathrm{tt}} + \mathcal{J}^{\mathrm{tr}} + \mathcal{J}^{\mathrm{ta}}) - (\hat{\mathbf{n}}\times\nabla_{\hat{\mathbf{n}}})\cdot(\mathcal{J}^{\mathrm{rt}} + \mathcal{J}^{\mathrm{rr}} + \mathcal{J}^{\mathrm{ra}}), \tag{17}$$

with current densities[76,77]

$$\begin{aligned}\mathcal{J}^{\mathrm{tt}} = &-\mu^{\mathrm{t}}\left(k_{\mathrm{B}}T\nabla_{\mathbf{r}}\,\rho^{(1)}(\mathbf{X}, t) + \rho^{(1)}(\mathbf{X}, t)\nabla_{\mathbf{r}}\,u_{\mathrm{ext}}(\mathbf{r}) + \int \mathrm{d}\mathbf{X}'\rho^{(2)}(\mathbf{X}, \mathbf{X}', t)\nabla_{\mathbf{r}}u(\mathbf{r}, \mathbf{r}')\right)\\ &-\int \mathrm{d}\mathbf{X}'\,\boldsymbol{\mu}_{\mathbf{r},\mathbf{r}'}^{\mathrm{tt}}\cdot\Big(k_{\mathrm{B}}T\nabla_{\mathbf{r}'}\rho^{(2)}(\mathbf{X}, \mathbf{X}', t) + \rho^{(2)}(\mathbf{X}, \mathbf{X}', t)\nabla_{\mathbf{r}'}u_{\mathrm{ext}}(\mathbf{r}')\\ &+\rho^{(2)}(\mathbf{X}, \mathbf{X}', t)\nabla_{\mathbf{r}'}u(\mathbf{r}, \mathbf{r}') + \int \mathrm{d}\mathbf{X}''\rho^{(3)}(\mathbf{X}, \mathbf{X}', \mathbf{X}'', t)\nabla_{\mathbf{r}'}u(\mathbf{r}', \mathbf{r}'')\Big),\end{aligned} \tag{18}$$

$$\mathcal{J}^{\mathrm{tr}} = -\int \mathrm{d}\mathbf{X}'\,k_{\mathrm{B}}T\boldsymbol{\mu}_{\mathbf{r},\mathbf{r}'}^{\mathrm{tr}}(\hat{\mathbf{n}}'\times\nabla_{\hat{\mathbf{n}}'})\rho^{(2)}(\mathbf{X}, \mathbf{X}', t), \tag{19}$$

$$\mathcal{J}^{\mathrm{ta}} = f\left(\mathbf{\Lambda}^{\mathrm{tt}}_{\mathbf{r},\mathbf{r}} \cdot \hat{\mathbf{n}}\rho^{(1)}(\mathbf{X},t) + \int \mathrm{d}\mathbf{X}'\, \mathbf{\Lambda}^{\mathrm{tt}}_{\mathbf{r},\mathbf{X}'} \cdot \hat{\mathbf{n}}'\rho^{(2)}(\mathbf{X},\mathbf{X}',t)\right), \tag{20}$$

$$\begin{aligned}\mathcal{J}^{\mathrm{rt}} = &-\int \mathrm{d}\mathbf{X}'\boldsymbol{\mu}^{\mathrm{rt}}_{\mathbf{r},\mathbf{r}'}\Big(k_{\mathrm{B}}T\nabla_{\mathbf{r}'}\rho^{(2)}(\mathbf{X},\mathbf{X}',t) + \rho^{(2)}(\mathbf{X},\mathbf{X}',t)\nabla_{\mathbf{r}'}u_{\mathrm{ext}}(\mathbf{r}')\\ &+ \rho^{(2)}(\mathbf{X},\mathbf{X}',t)\nabla_{\mathbf{r}'}u(\mathbf{r},\mathbf{r}') + \int \mathrm{d}\mathbf{X}''\rho^{(3)}(\mathbf{X},\mathbf{X}',\mathbf{X}'',t)\nabla_{\mathbf{r}'}u(\mathbf{r}',\mathbf{r}'')\Big),\end{aligned} \tag{21}$$

$$\mathcal{J}^{\mathrm{rr}} = -k_{\mathrm{B}}T\mu^{\mathrm{r}}\hat{\mathbf{n}}\times\nabla_{\hat{\mathbf{n}}}\rho^{(1)}(\mathbf{X},t) - \int \mathrm{d}\mathbf{X}'\,k_{\mathrm{B}}T\boldsymbol{\mu}^{\mathrm{rr}}_{\mathbf{r},\mathbf{r}'}\cdot(\hat{\mathbf{n}}'\times\nabla_{\mathbf{n}'})\rho^{(2)}(\mathbf{X},\mathbf{X}',t), \tag{22}$$

$$\mathcal{J}^{\mathrm{ra}} = f\int \mathrm{d}\mathbf{X}'\,\mathbf{\Lambda}^{\mathrm{rt}}_{\mathbf{r},\mathbf{X}'}\,\hat{\mathbf{n}}'\rho^{(2)}(\mathbf{X},\mathbf{X}',t). \tag{23}$$

It is important to keep in mind that Eqs. (17)–(23) form a non-closed set of equations, as the unknown higher order densities $\rho^{(2)}$ and $\rho^{(3)}$ are needed as an input. When a similar procedure is applied to Eq. (1) to find dynamical equations for, e.g., the two-swimmer density $\rho^{(2)}$, next-higher orders appear, constituting an escalating loop typical for BBGKY-like hierarchies of equations.[87] Therefore, a closure is needed by expressing the interaction terms in Eqs. (18)–(23) containing the two- and three-swimmer densities as functionals of only the one-swimmer density. Dynamical density functional theory (DDFT)[88–97] provides a well-established means for this purpose, where an approach for the present system was outlined in previous studies.[76,77]

Yet, our previous mean-field approach[76,77] seems not to be sufficient to address the question below, namely, the question under which circumstances the swimmers develop collective polar orientational order. Particularly, the interplay between the hydrodynamic interactions and the two-swimmer density in the equations above appears to be insufficiently resolved at the level of our previous mean-field- and Onsager-type formulation. Thus, a more refined version is needed, see below.

III. APPLICATION TO MICROSWIMMERS CONFINED TO A PLANE

In the following, we consider microswimmers in suspension, yet with their positions $\mathbf{r}_i$ and orientations $\hat{\mathbf{n}}_i$, $i = 1, \ldots, N$, confined to the flat xy-plane. The surrounding fluid is still treated as three-dimensional. Then, the orientation of each swimmer in Eqs. (17)–(23) can be fully described by one angle ϕ_i, and the orientational gradient operator becomes $\hat{\mathbf{n}}\times\nabla_{\hat{\mathbf{n}}} = \hat{\mathbf{z}}\partial_\phi$. Such a system could possibly be realized, e.g., by using optical trapping fields or by placing the swimmers at the interface between two immiscible fluids of identical viscosity.

Several further assumptions are introduced. First, the external potential shall vanish, i.e., $u_{\mathrm{ext}} = 0$. Next, the system is confined to a two-dimensional box of area A with periodic boundary conditions, containing our N identical microswimmers. We further assume that the one-swimmer density $\rho^{(1)}(\mathbf{X}, t)$, now with $\mathbf{X} = (\mathbf{r}, \phi)$, is spatially homogeneous.[98] Thus, only variations as a function of the orientation variable ϕ are considered, i.e., $\rho^{(1)}(\mathbf{X}, t) =: A^{-1}\rho^{(1)}(\phi, t)$, where the one-swimmer orientational density $\rho^{(1)}(\phi, t)$ has been defined.

Equation (17) is now integrated over all spatial positions $\mathbf{r}$ in the area A. Then the currents $\mathcal{J}^{\mathrm{tt}}$, $\mathcal{J}^{\mathrm{tr}}$, $\mathcal{J}^{\mathrm{ta}}$ disappear from the equation, and the set of Eqs. (17)–(23) is simplified to

$$\frac{\partial\rho^{(1)}(\phi,t)}{\partial t} = -\partial_\phi\int \mathrm{d}\mathbf{r}\,(\hat{\mathbf{z}}\cdot\mathcal{J}^{\mathrm{rt}} + \hat{\mathbf{z}}\cdot\mathcal{J}^{\mathrm{rr}} + \hat{\mathbf{z}}\cdot\mathcal{J}^{\mathrm{ra}}). \tag{24}$$

For spherical swimmer bodies, the integral term in Eq. (22) vanishes[77] so that only the direct rotational diffusional part remains. Thus, Eq. (24) can be rewritten as

$$\begin{aligned}\frac{\partial\rho^{(1)}(\phi,t)}{\partial t} = &D^{\mathrm{r}}\partial_\phi^2\rho^{(1)}(\phi,t) - f\partial_\phi\int \mathrm{d}\mathbf{r}\int \mathrm{d}\mathbf{X}'\,\hat{\mathbf{z}}\\ &\cdot\left(\mathbf{\Lambda}^{\mathrm{rt}}_{\mathbf{r},\mathbf{X}'}\,\hat{\mathbf{n}}'\right)\rho^{(2)}(\mathbf{X},\mathbf{X}',t) - \partial_\phi\int \mathrm{d}\mathbf{r}\,\hat{\mathbf{z}}\cdot\mathcal{J}^{\mathrm{rt}},\end{aligned} \tag{25}$$

where the last term approximately vanishes as detailed in Appendix A and $D^{\mathrm{r}} = k_{\mathrm{B}}T\mu^{\mathrm{r}}$ is the rotational diffusion constant for passive particles.

The remaining task is to find a reasonable approximation for $\rho^{(2)}(\mathbf{X}, \mathbf{X}', t)$. Generally, the two-swimmer density is related to the one-swimmer density via $\rho^{(2)}(\mathbf{X}, \mathbf{X}', t) = \rho^{(1)}(\mathbf{X}, t)\,\rho^{(1)}(\mathbf{X}', t)\,g^{(2)}(\mathbf{X}, \mathbf{X}', t)$, where $g^{(2)}(\mathbf{X}, \mathbf{X}', t)$ is the pair distribution function. Since we assume that the one-swimmer density does not depend on the spatial position, this simplifies to $\rho^{(2)}(\mathbf{X}, \mathbf{X}', t) = A^{-2}\rho^{(1)}(\phi, t)\,\rho^{(1)}(\phi', t)\,g^{(2)}(\mathbf{X}, \mathbf{X}', t)$. Furthermore, the pair distribution function in a spatially homogeneous system depends on only the *relative* distance vector between the two particles, so that $g^{(2)}(\mathbf{X}, \mathbf{X}', t) = g^{(2)}(\mathbf{R}, \phi, \phi', t)$ holds, with $\mathbf{R} := \mathbf{r}' - \mathbf{r}$ denoting the distance vector. Thus, the second term on the right-hand side of Eq. (25) becomes

$$\begin{aligned}I_1 &:= -f\partial_\phi\int \mathrm{d}\mathbf{r}\int \mathrm{d}\mathbf{r}'\int \mathrm{d}\phi'\,\hat{\mathbf{z}}\cdot\left(\mathbf{\Lambda}^{\mathrm{rt}}_{\mathbf{r},\mathbf{X}'}\,\hat{\mathbf{n}}'\right)\rho^{(2)}(\mathbf{X},\mathbf{X}',t)\\ &= -A^{-2}f\partial_\phi\Big(\rho^{(1)}(\phi,t)\int \mathrm{d}\phi'\,\rho^{(1)}(\phi',t)\int \mathrm{d}\mathbf{r}\int \mathrm{d}\mathbf{R}\,\hat{\mathbf{z}}\\ &\quad\cdot\left(\mathbf{\Lambda}^{\mathrm{rt}}_{\mathbf{r},\mathbf{X}'}\,\hat{\mathbf{n}}'\right)g^{(2)}(\mathbf{R},\phi,\phi',t)\Big),\end{aligned} \tag{26}$$

where the spatial integral over $\mathbf{r}'$ has been shifted to $\mathbf{R}$.

To leading order in R^{-1}, with $R = |\mathbf{R}|$ denoting the absolute value of the distance vector, the approximation

$$\hat{\mathbf{z}}\cdot\left(\mathbf{\Lambda}^{\mathrm{rt}}_{\mathbf{r},\mathbf{X}'}\,\hat{\mathbf{n}}'\right) \approx -3\mu^{\mathrm{r}}a^3L\cos(\phi'-\theta)\sin(\phi'-\theta)R^{-3} \tag{27}$$

holds, where θ is the angle between $\mathbf{R}$ and $\hat{\mathbf{x}}$, i.e., $\mathbf{R} = R(\cos\theta, \sin\theta)$. The orientation-dependent pair distribution function in the isotropic disordered state features a global rotational symmetry; i.e., it stays the same when we rotate the system by subtracting a common angle from all angles θ, ϕ, and ϕ'. We select ϕ as that angle. In other words, following standard arguments, we may address the function in one particular frame of reference,[99] for which we now choose the frame of $\phi = 0$. In the following, $\bar{g}^{(2)}(R, \theta - \phi, \phi' - \phi)$ denotes the pair distribution function in this frame. Moreover, the integral over $\mathbf{r}$ is now trivial, yielding the area A. In combination, this leads to

$$I_1 \approx \frac{3\mu^{\mathrm{r}} a^3 Lf}{A}\partial_\phi\Big(\rho^{(1)}(\phi,t)\int \mathrm{d}\phi'\,\rho^{(1)}(\phi',t)\int \mathrm{d}R\int \mathrm{d}\theta \times \frac{\cos(\phi'-\theta)\sin(\phi'-\theta)}{R^2}\,\bar{g}^{(2)}(R,\theta-\phi,\phi'-\phi,t)\Big). \quad (28)$$

The starting point for all the following considerations is thus the equation

$$\begin{aligned}\frac{\partial\rho^{(1)}(\phi,t)}{\partial t} &= D^{\mathrm{r}}\partial_\phi^2\rho^{(1)}(\phi,t) + \frac{3\mu^{\mathrm{r}} a^3 Lf}{A}\partial_\phi\Big(\rho^{(1)}(\phi,t)\int \mathrm{d}\phi'\,\rho^{(1)}(\phi',t) \\ &\quad\times\int \mathrm{d}R\int \mathrm{d}\theta\,\frac{\cos(\phi'-\theta)\sin(\phi'-\theta)}{R^2}\,\bar{g}^{(2)}(R,\theta-\phi,\phi'-\phi,t)\Big) \\ &=: D^{\mathrm{r}}\partial_\phi^2\rho^{(1)}(\phi,t) - 3\mu^{\mathrm{r}} a^3 Lf\frac{\rho_0}{N}\partial_\phi\Big(\rho^{(1)}(\phi,t)\int \mathrm{d}\phi'\,\rho^{(1)}(\phi',t)K(\phi-\phi',t)\Big),\end{aligned} \quad (29)$$

where we have introduced the global density $\rho_0 = N/A$ and further defined the function

$$K(\phi-\phi',t) := -\int \mathrm{d}R\int \mathrm{d}\theta\,\frac{\cos(\phi'-\theta)\sin(\phi'-\theta)}{R^2} \times \bar{g}^{(2)}(R,\theta-\phi,\phi'-\phi,t), \quad (30)$$

which represents a weighted integral of the pair distribution function over the distance vector. If $\bar{g}^{(2)}(R,\theta-\phi,\phi'-\phi,t)$ is known, $K(\phi - \phi', t)$ can be calculated. In case this input is available, Eq. (29) can serve as the starting point of a stability analysis of the isotropic disordered state, see Sec. V below.

From symmetry, it follows that the simplest guess $g^{(2)} \equiv 1$ lets the second term on the right-hand side of Eq. (29) vanish and is thus not sufficient to study the possible development of alignment. As shown later, an ansatz only featuring a spatial front–rear asymmetry, as previously used for a minimal mathematical description of motility-induced phase separation,[21] also leads to a decay of any weak initial orientational order in a linear stability analysis of the isotropic disordered state. Thus, our next step is to address more carefully the pair distribution and to find approximate expressions in order to investigate the emergence of possible alignment.

IV. APPROXIMATION OF THE PAIR DISTRIBUTION FUNCTION IN THE ISOTROPIC DISORDERED STATE: DDFT AND THE PERCUS METHOD

Our goal in this section is to identify a reasonable approximation for the pair distribution function of microswimmers in an isotropic disordered suspension to enable our subsequent study of the linear stability of the disordered state in Sec. V. For this purpose, we here adapt the Percus method,[100] which is exact in equilibrium isotropic systems. Yet, it should at least qualitatively hint at the basic shape of the pair distribution in our inherently non-equilibrium system of self-propelled microswimmers. Since a coarse knowledge of the general shape is sufficient for our objective, as well as for technical reasons detailed below, hydrodynamic interactions are neglected throughout the present section for simplicity. That is, approximations for the pair distribution function of "dry" self-propelled particles are determined. For strong force dipoles and in aligned systems, deviations from these reduced expressions will occur.[75]

A. The Percus method

In the Percus method for fluids in equilibrium,[100] one particle is declared a test particle and fixed in (phase) space, e.g., at position $\mathbf{r}$. Then its effect on the remaining particles is effectively described as an external potential. Percus showed that in a homogeneous fluid the resulting inhomogeneous density distribution of the other particles at positions $\mathbf{r}'$ around the first particle is connected to the pair distribution function via the exact relation $\rho(\mathbf{r}' - \mathbf{r}) = \rho_0 g^{(2)}(\mathbf{r}' - \mathbf{r})$, where ρ_0 is the (constant) overall density of the bulk fluid. This way, the pair distribution function of a liquid equilibrium system can be obtained.

A recent equilibrium classical density functional theory study shows that employing the Percus method can lead to good approximations of pair distribution functions, even if using a simple mean-field approximation for the excess functional.[101] In the past, some studies have addressed dynamical test-particle methods for passive particles.[102,103] Nevertheless, it is still an open question how good of an approximation this method is for an active non-equilibrium system (as ours). This should be examined in detail in future work and compared to other approaches.[104,105]

For a reasonable description of the pair distribution function, we additionally need to account for the orientational degree(s) of freedom and the self-propulsion of the test particle. The latter can be achieved by switching to the body frame of the test particle and "streaming" all other particles oppositely to the (fixed) swimming direction of the test particle with its effective swimming speed v_s. In a non-dilute system, interactions between the "non-test" particles can be included via DDFT.[76,88–97] By definition, $0 < v_s \leq v_0$ holds in our "dry" system, with v_0 denoting the free swimming speed of an unconstricted single swimmer. In very dense cases of swimming being blocked by the presence of other particles, $v_s \to 0$ is also possible (over a certain interval, v_s will decline approximately linearly with increasing local density[21,106]).

We select the orientation of the fixed particle as $\phi = 0$. The sign of f then determines the angle ψ of swimming given by $\psi = \phi$ for pushers and $\psi = \phi + \pi$ for pullers. Thus, $\mathbf{v}_{\mathrm{st}} := -\,\mathrm{sign}(f) v_s \hat{\mathbf{x}}$ is the additional velocity with which the other particles are streamed against the first, fixed particle. Here, we choose $v_s = v_0$, which is appropriate for dilute systems.

B. Evaluation using DDFT

Now we follow our previous studies[76,77] for (numerically) implementing the DDFT (neglecting hydrodynamic interactions as mentioned above).[107] Formally, this means that the tensors $\boldsymbol{\mu}^{\mathrm{tt}}_{\mathbf{r},\mathbf{r}'}$, $\boldsymbol{\mu}^{\mathrm{tr}}_{\mathbf{r},\mathbf{r}'}$, $\boldsymbol{\Lambda}^{\mathrm{tt}}_{\mathbf{r},\mathbf{X}'}$, $\boldsymbol{\mu}^{\mathrm{rt}}_{\mathbf{r},\mathbf{r}'}$, $\boldsymbol{\mu}^{\mathrm{rr}}_{\mathbf{r},\mathbf{r}'}$, and $\boldsymbol{\Lambda}^{\mathrm{rt}}_{\mathbf{r},\mathbf{X}'}$ in Eqs. (18)–(23) are all set to zero. Without hydrodynamic interactions, the only difference between pusher and puller microswimmers is that a corresponding swimmer propels into the direction of $\hat{\mathbf{n}}$ or, respectively, $-\hat{\mathbf{n}}$, see Fig. 1. The steric interaction potential between swimmers i and j is now specified as the GEM-4 potential[108,109] with

$$u(\mathbf{r}_i, \mathbf{r}_j) = V_0 \exp\left(-\left(\frac{r_{ij}}{\sigma}\right)^4\right), \tag{31}$$

where V_0 describes the strength of the potential.

Consequently, the potential $u(\mathbf{0}, \mathbf{r})$ following from Eq. (31) is used as the external potential $u_{\mathrm{ext}}(\mathbf{r})$ in Eq. (18) when evaluating our DDFT. It represents the fixed particle at the origin used in the Percus method. Furthermore, the streaming of all other swimmers, as described above, is enforced by applying an additional constant force $\nabla_{\mathbf{r}} u_{\mathrm{ext}}(\mathbf{r}) = -\mathbf{v}_{\mathrm{st}}/\mu^{\mathrm{t}}$ in Eq. (18), which continuously drives the particle density against the test particle and across the periodic boundaries. At this point, it also becomes obvious why including the hydrodynamic interactions in this method would lead to challenging problems. If hydrodynamic interactions were present, simply including the streaming velocity $\mathbf{v}_{\mathrm{st}}$ as indicated above would neglect the hydrodynamic interactions resulting from the flow fields that the test swimmer and the other swimmers generate during their active motion. Moreover, driving swimmers toward each other by net forces to mimic their mutual approach during self-propulsion would induce unphysical fluid flows. The hydrodynamic interactions resulting from such net forces (force monopoles) are different from the actual ones resulting from force dipoles. Clearly, this opens the way for additional studies in the future to address these issues. At our present level of searching for the leading-order angular dependence of the pair distribution function, neglecting the hydrodynamic interactions appears viable, see below.

For consistency, the interaction strength V_0 must be sufficiently high to hinder other particles from swimming or being streamed through the fixed particle. Repeating the choice of our previous studies, again the mean-field functional is employed to specify the corresponding excess free energy in the DDFT. Then, the DDFT equations are solved numerically using a finite-volume method solver[110] until a steady state is reached. This steady state describes the orientation-dependent particle distribution function (with $\phi = 0$) that we searched for.

C. Resulting functional form

Figure 2(a) shows a typical pair distribution function obtained in this way for non-hydrodynamically interacting pushers in the isotropic disordered state. We find qualitative agreement with previous (orientationally averaged) pair distribution functions of self-propelled agents determined by particle-based computer simulations,[21,75] e.g., concerning the

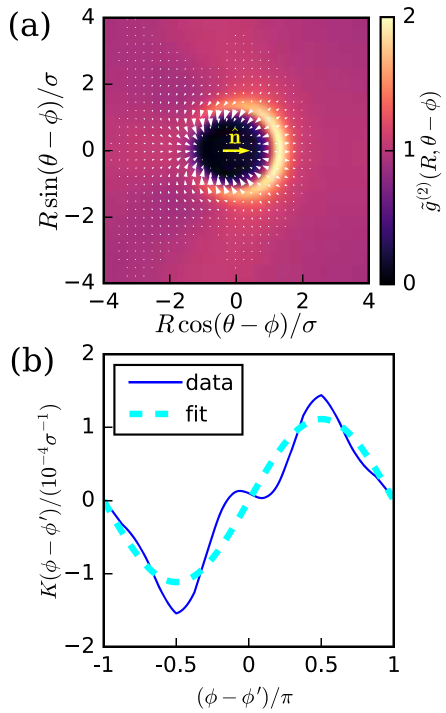

FIG. 2. (a) Swimmer–swimmer orientation-dependent pair distribution function, obtained via DDFT in combination with our adapted Percus test-particle method for active agents as described in the main text. Brighter colors indicate a higher magnitude of the pair distribution function integrated over all orientations; i.e., we define $\bar{g}^{(2)}(R, \theta - \phi) := \int d\phi' \bar{g}^{(2)}(R, \theta - \phi, \phi' - \phi)$. Thus, brighter colors imply a higher probability to find a nearby swimmer. White arrows mark the average orientations of nearby swimmers, calculated from $\int d\phi' \hat{\mathbf{n}}'(\phi' - \phi)\bar{g}^{(2)}(R, \theta - \phi, \phi' - \phi)$. The large arrow at the center displays the orientation $\hat{\mathbf{n}}(\phi = 0)$ of the fixed particle. Parameter values are set to $\rho_0 = 0.0313\sigma^{-2}$, $L = 1.5\sigma$, $a = 0.5\sigma$, $\alpha = 0.4$, $V_0 = 20k_{\mathrm{B}}T$, and $f = 50k_{\mathrm{B}}T/\sigma$. The dimension of the square simulation box here is $8\sigma \times 8\sigma$, and the DDFT equations are solved on a $128 \times 128 \times 16$ numerical grid for the discretization of x, y, and ϕ coordinates, respectively. Periodic boundary conditions were applied in all directions. (b) Extracted function $K(\phi - \phi')$, defined in Eq. (30), for the same parameters as in (a). Fitting with the function $C \sin(\phi - \phi')$ (dashed line) here leads to $C \approx 1.11 \times 10^{-4}\sigma^{-1}$.

front–rear asymmetry. The extracted function $K(\phi - \phi')$ is displayed in Fig. 2(b). For pullers of identical $|f|$, an analogous picture is found (as mentioned above, hydrodynamic interactions are not taken into account at the moment). In the end, an identical $K(\phi - \phi')$ is obtained.

Figure 2(b), determined in this way, demonstrates a dominant sinusoidal first-harmonic contribution in $K(\phi - \phi')$. We thus approximate $K(\phi - \phi')$ to lowest order as

$$K(\phi - \phi') \approx C \sin(\phi - \phi'), \text{ with } C > 0. \tag{32}$$

The amplitude C has the dimension of inverse length and depends in a non-trivial way on v_s, ρ_0, and the microscopic parameters in the swimmer model.

Since the anisotropy of the pair distribution function is most pronounced near the surface of the fixed particle, see Fig. 2(a), this angular dependence of $K(\phi - \phi')$ seems to be effectively caused by the short-range steric interaction. Thus, point particles may not show the type of behavior identified in Sec. V below.[111] A corresponding dominance of the steric interactions at least supports neglecting the hydrodynamic interactions in the treatment above to lowest order.

Moreover, the functional form of $K(\phi - \phi')$ in Eq. (32) can also be motivated in a different way for dilute systems as ours, see Appendix B. Accordingly, our result above is supported by an independent approach. A further confirmation of the form in Eq. (32) is given in Appendix C.

V. LINEAR STABILITY ANALYSIS

Finally, we now test for the linear instability of the isotropic disordered microswimmer system. For this purpose, we turn back to Eqs. (17)–(29) that explicitly include hydrodynamic interactions via the hydrodynamic mobility tensors. Nevertheless, in the absence of a more sophisticated approximation, we assume the functional form in Eq. (32) found for neglected hydrodynamic interactions and use it as an input to these equations to check whether collective orientational order spontaneously arises from a linear instability of the state of absent orientational order.

As further elucidated in Appendix D, the static uniform distribution $\rho(\phi, t) = N(2\pi)^{-1}$ is always a solution of Eq. (29). However, as shown in the following, it is either linearly stable or unstable, depending on the system parameters. If it is linearly stable, the system remains in the isotropic disordered state for that set of parameter values, at least in the absence of larger fluctuations, perturbations, and spatial inhomogeneities. If it is linearly unstable, it will develop a different state, e.g., one of collective polar order. To test for linear stability, a small harmonic fluctuation is superimposed onto the uniform distribution, i.e., $\rho(\phi, t) = N(2\pi)^{-1} + \epsilon(t)\cos(\phi - \phi_0)$, with small $\epsilon(t) \ll N(2\pi)^{-1}$ and arbitrary ϕ_0.

This ansatz is inserted into Eq. (29). Through Eq. (32), two terms vanish due to symmetry upon performing the integration, one term can be neglected via $\epsilon^2(t) \ll \epsilon(t)$, and we arrive at

$$\dot{\epsilon}(t)\cos(\phi - \phi_0) = -D^{\mathrm{r}}\epsilon(t)\cos(\phi - \phi_0) + \tilde{I}_1\epsilon(t) \tag{33}$$

with a dot denoting a time derivative and

$$\tilde{I}_1 := -\frac{3\mu^{\mathrm{r}}a^3 Lf\rho_0}{2\pi}\,\partial_\phi\left(\int \mathrm{d}\phi'\,\cos(\phi' - \phi_0)K(\phi - \phi')\right). \tag{34}$$

Using Eq. (32), this simplifies to

$$\tilde{I}_1 = -\frac{3}{2}\mu^{\mathrm{r}}a^3 LCf\rho_0\cos(\phi - \phi_0). \tag{35}$$

Combining Eqs. (33) and (35) leads to the ordinary differential equation

$$\dot{\epsilon}(t) = \left(-D^{\mathrm{r}} - \frac{3}{2}\mu^{\mathrm{r}}a^3 LC\rho_0 f\right)\epsilon(t). \tag{36}$$

Its solution for the amplitude $\epsilon(t)$ of the perturbation is an exponential function that decays in time when the bracketed term is negative, and grows otherwise. For pushers ($f > 0$), the fluctuation thus always decays ($\mu^{\mathrm{r}}, a, L, C, \rho_0$ are all positive). In contrast to that, strong pullers with

$$fL < -\frac{2}{3}\frac{D^{\mathrm{r}}}{\mu^{\mathrm{r}}a^3\rho_0 C} = -\frac{2}{3}\frac{k_{\mathrm{B}}T}{a^3\rho_0 C} \tag{37}$$

show exponential growth of fluctuations involving polar orientational order; i.e., the isotropic disordered state is linearly unstable against initial polar ordering.

We remark that, while an increased density ρ_0 in Eq. (37) seems to support the emergence of orientational order, it is to be noted that C heavily depends on the system parameters, including ρ_0, and can overshadow that effect. For instance, at high densities, the swimmers may mutually disturb and block their motion. Then, the global orientational dependence of the pair distribution function should change, possibly implying $C \to 0$. This would counteract the emergence of a global polar ordering via the mechanism described in this work. However, spatial variations would then certainly become important and should be included into the theoretical consideration as a possible future extension.

VI. CONCLUSIONS

In summary, we have presented a microscopic statistical approach to describing and predicting the emergence of collective polar ordering in (semi-)dilute suspensions of active force-dipole microswimmers. We found that such a polar order can arise in systems of pullers of strong enough activity to overcome thermal dealignment caused by rotational diffusion. Our statistical approach traces back the self-ordering of the system to the actively induced hydrodynamic rotation–translation coupling between the swimmers. To find a reasonable approximation for the involved pair distribution function, a technique combining DDFT and the Percus method (pinning one swimmer and treating it as an obstacle for the other swimmers) for an active system has been proposed, as well as intuitive arguments of broken symmetry. As the central result, disordered suspensions of pushers in our approach were always found to be linearly stable against initial development of collective polar orientational order. In contrast to that, suspensions of strong pullers were observed to be linearly unstable against polar orientational ordering. It will be interesting to further challenge our adapted test-particle method by quantitative comparison with simulations or other theoretical methods[21,75,104,105,112] in the future. Additionally, it would be intriguing to test the applicability of our approach and results as an input for further studies on the mesoscale hydrodynamic behavior of microswimmer suspensions, possibly even concerning mesoscale turbulence.[113,114]

We wish to remark that our system when taken to the thermodynamic limit ($N \to \infty$ and $A \to \infty$, while the average density is kept constant) might still develop overall orientational order, against the Mermin-Wagner theorem.[115] This is because of its inherently non-equilibrium nature.[68,116] Nevertheless, additional spatially resolved investigations would be very interesting as they could be able to discern between local and global ordering and show their interplay.

Furthermore, the theory can also be generalized to binary mixtures of different swimmer species, resulting in two coupled equations similar to Eq. (29). Each of them contains an additional coupling term including the one-swimmer density of the other swimmer species. The results could then be compared with previous particle-based computer simulations of binary pusher–puller mixtures.[75] Apart from that, an extension to systems of hydrodynamically interacting self-propelled rods[117] is conceivable as well.

ACKNOWLEDGMENTS

The authors thank Giorgio Pessot for helpful discussions. Support of this work by the Deutsche Forschungsgemeinschaft through the priority program SPP 1726 on microswimmers, Grant Nos. LO 418/17-2 and ME 3571/2-2, is gratefully acknowledged.

APPENDIX A: FURTHER DETAILS ON EVALUATING THE LAST TERM IN EQ. (25)

In this appendix, we briefly demonstrate that the last term in Eq. (25) vanishes approximately. Regarding the current density $\mathcal{J}^{\mathrm{rt}}$ defined in Eq. (21), the second contribution drops out because we here set $u_{\mathrm{ext}} = 0$. The third contribution vanishes for all isotropic central-force interaction potentials $u(\mathbf{r}, \mathbf{r}') = u(|\mathbf{r}' - \mathbf{r}|)$ because the gradient of such a potential is parallel to the distance vector. However, $\boldsymbol{\mu}^{\mathrm{rt}}_{\mathbf{r},\mathbf{r}'}$ in Eq. (21) introduces the vector product with this distance vector, see Eq. (7), which then vanishes. Finally, the contribution containing $\rho^{(3)}(\mathbf{X}, \mathbf{X}', \mathbf{X}'', t)$ in Eq. (21) is neglected for sufficiently dilute systems as it scales with a higher order in ρ_0 than the other contributions. Together, this reduces the last term of Eq. (25) to

$$I_2 := -\partial_\phi \int \mathrm{d}\mathbf{r}\, \hat{\mathbf{z}} \cdot \mathcal{J}^{\mathrm{rt}} \approx k_{\mathrm{B}} T \partial_\phi \int \mathrm{d}\mathbf{r} \int \mathrm{d}\mathbf{X}'\, \hat{\mathbf{z}} \cdot \Big(\boldsymbol{\mu}^{\mathrm{rt}}_{\mathbf{r},\mathbf{r}'} \nabla_{\mathbf{r}'} \rho^{(2)}(\mathbf{X}, \mathbf{X}', t)\Big), \tag{A1}$$

which vanishes as is shown in the following.

Using $\rho^{(2)}(\mathbf{X}, \mathbf{X}', t) = \rho^{(1)}(\mathbf{X}, t)\, \rho^{(1)}(\mathbf{X}', t)\, g^{(2)}(\mathbf{X}, \mathbf{X}', t)$ and $\rho^{(1)}(\mathbf{X}, t) = A^{-1} \rho^{(1)}(\phi, t)$ as before, Eq. (A1) can be rewritten as

$$I_2 \approx \frac{k_{\mathrm{B}} T}{A^2} \partial_\phi \bigg(\rho^{(1)}(\phi, t) \int \mathrm{d}\mathbf{r} \int \mathrm{d}\phi' \rho^{(1)}(\phi', t) \times \int \mathrm{d}\mathbf{r}' \mu^{\mathrm{r}} a^3 |\mathbf{r}' - \mathbf{r}|^{-3}\, \hat{\mathbf{z}} \cdot \Big((\mathbf{r}' - \mathbf{r}) \times \nabla_{\mathbf{r}' - \mathbf{r}}\, g^{(2)}(\mathbf{r}' - \mathbf{r}, \phi, \phi', t)\Big)\bigg). \tag{A2}$$

The inner spatial integral is then transformed into the polar coordinates (R, θ), with $\mathbf{R} = \mathbf{r}' - \mathbf{r} =: R(\cos\theta, \sin\theta)$, yielding

$$I_2 \approx \frac{D^{\mathrm{r}} a^3}{A^2} \partial_\phi \bigg(\rho^{(1)}(\phi, t) \int \mathrm{d}\mathbf{r} \int \mathrm{d}\phi' \rho^{(1)}(\phi', t) \int \mathrm{d}R\, R^{-2} \times \int \mathrm{d}\theta\, \hat{\mathbf{z}} \cdot \Big(\mathbf{R} \times \nabla_{\mathbf{R}}\, g^{(2)}(R, \theta, \phi, \phi', t)\Big)\bigg). \tag{A3}$$

Through the relation $\hat{\mathbf{z}} \cdot (\mathbf{R} \times \nabla_{\mathbf{R}}) = \partial_\theta$ and the inherent periodicity of the pair distribution function with respect to the angular variables, the integral over θ leads to $I_2 \approx 0$.

APPENDIX B: WEAK SCATTERING

Equation (32) can further be motivated for dilute systems as ours via a "weak scattering" approach, effectively including hydrodynamic interactions to an approximate extent. Here, we suppose that two microswimmers are located at arbitrary phase space positions $\mathbf{X}$ and $\mathbf{X}'$. We disregard all diffusional processes and any disturbing hydrodynamic interactions for almost all times so that the swimmers move along straight paths, with initial orientations $\hat{\mathbf{n}}$ and $\hat{\mathbf{n}}'$. In effect, their hydrodynamic interactions are considered to occur only once in time, at the moment when they come closest to each other. Furthermore, we use the leading-order expansion of $\hat{\mathbf{z}} \cdot \big(\boldsymbol{\Lambda}^{\mathrm{rt}}_{\mathbf{r},\mathbf{X}'}\, \hat{\mathbf{n}}'\big)$ as given in Eq. (27). Then, the effective angular shift of the first swimmer due to the mutual hydrodynamic interaction between the swimmers is approximated as

$$\delta\phi := -3\mu^{\mathrm{r}} a^3 L f\, |\mathbf{R}_0|^{-3} \delta t \cos(\phi' - \theta_0) \sin(\phi' - \theta_0), \tag{B1}$$

with a typical interaction time δt assumed to be the same for all configurations. Additionally, $\mathbf{R}_0$ is the closest distance vector, with $\mathbf{R}_0 =: |\mathbf{R}_0|(\cos\theta_0, \sin\theta_0)$.

For this vector, $\mathbf{R}_0 \cdot (\hat{\mathbf{n}}' - \hat{\mathbf{n}}) = 0$ applies, which leads to $\theta_0 = (\phi + \phi')/2$. Inserting this relation into Eq. (B1) leads to

$$\delta\phi = \frac{3}{2} \mu^{\mathrm{r}} a^3 L f\, \delta t\, |\mathbf{R}_0|^{-3} \sin(\phi - \phi'), \tag{B2}$$

which again implies mutual dealignment for pushers ($f > 0$) and mutual alignment for pullers ($f < 0$). We remark that Eq. (B2) is compatible with Eq. (32), i.e., with $K(\phi - \phi') \approx C \sin(\phi - \phi')$, $C > 0$.

APPENDIX C: ADDITIONAL COMMENTS ON APPROXIMATING THE PAIR DISTRIBUTION FUNCTION

In the following, we consider some more aspects concerning the angular dependence of the pair distribution function $\bar{g}^{(2)}(R, \theta - \phi, \phi' - \phi)$ in the regarded isotropic disordered state, leading to Eq. (32). From Eq. (30), it is obvious that homogeneous terms in $\bar{g}^{(2)}(R, \theta - \phi, \phi' - \phi)$ do not contribute to $K(\phi - \phi')$. Moreover, since the hydrodynamic interactions decrease with increasing swimmer–swimmer distance, attention is now focused on the high-density ring the radius of which is approximately equal to the effective particle diameter σ, see Fig. 2(a).

The pair distribution function shown in Fig. 2(a) features a front–rear asymmetry in the spatial distribution, which can be phenomenologically addressed to lowest order by a term $\sim\cos(\theta - \psi)$, where ψ denotes the angle of the swimming direction as before. Furthermore, the orientational distribution of nearby swimmers around the central swimmer seems to point inward, see the innermost white arrows in Fig. 2(a). An orientational distribution peaked at $\psi' = \theta + \pi$ would reflect this and can be modeled by a contribution $\sim -\cos(\psi' - \theta)$. Eventually, we notice that in the high-density area at the front of the central swimmer in Fig. 2(a), the surrounding swimmers are preferably oriented in the propulsion direction of the central swimmer. This can be represented by a term $\sim\cos(\theta - \psi)\cos(\psi' - \theta)$. At the rear of the central swimmer, this term still maintains the preferred inward orientation of the surrounding swimmers in Fig. 2(a).

Taking into account the different terms described above, we investigate the ansatz

$$\bar{g}^{(2)}(R, \theta - \phi, \phi' - \phi) \approx 1 + \delta(R - \sigma)\Big(c_1 + c_2\cos(\theta - \psi) - c_3\cos(\psi' - \theta) + c_4\cos(\theta - \psi)\cos(\psi' - \theta)\Big), \tag{C1}$$

with c_1, c_2, c_3, $c_4 > 0$. Inserting it into Eq. (30), only the contribution $\sim c_4$ does not vanish but indeed is in agreement with Eq. (32) for $K(\phi - \phi')$.

APPENDIX D: THE UNIFORM DISTRIBUTION AS A SOLUTION OF EQ. (29)

We here argue that the uniform distribution $\rho^{(1)}(\phi, t) = N/(2\pi)$ is indeed an exact solution of Eq. (29). For $f = 0$, the equilibrium case of passive spherical particles is recovered. It is readily seen that in this case $\rho^{(1)}(\phi, t) = N/(2\pi)$ solves Eq. (29). Otherwise, for $f \neq 0$, the only remaining term in Eq. (29) is the activity-induced one stemming from $\mathcal{J}^{\mathrm{ra}}$ in Eq. (23).

Evaluating this term in Eq. (29) for $\rho^{(1)}(\phi, t) = \rho^{(1)}(\phi', t) = N(2\pi)^{-1}$ and disregarding all constants reduce our task to show that

$$W := \partial_\phi\Big(\int \mathrm{d}\phi' \int \mathrm{d}R \int \mathrm{d}\theta\, \frac{\cos(\phi' - \theta)\sin(\phi' - \theta)}{R^2} \times \bar{g}^{(2)}(R, \theta - \phi, \phi' - \phi)\Big) \tag{D1}$$

vanishes. If the integrals over the angles ϕ' and θ are now shifted to the angles $\phi' - \phi$ and $\theta - \phi$, respectively, no formal dependence on ϕ remains after integration. Thus, W indeed vanishes. We remark that this result still holds when taking into account all orders in R^{-1}, e.g., starting from Eq. (26).

[1] E. M. Purcell, Am. J. Phys. **45**, 3 (1977).
[2] J. R. Howse, R. A. Jones, A. J. Ryan, T. Gough, R. Vafabakhsh, and R. Golestanian, Phys. Rev. Lett. **99**, 048102 (2007).
[3] E. Lauga and T. R. Powers, Rep. Prog. Phys. **72**, 096601 (2009).
[4] J. Elgeti, R. G. Winkler, and G. Gompper, Rep. Prog. Phys. **78**, 056601 (2015).
[5] A. Zöttl and H. Stark, J. Phys.: Condens. Matter **28**, 253001 (2016).
[6] C. Bechinger, R. Di Leonardo, H. Löwen, C. Reichhardt, G. Volpe, and G. Volpe, Rev. Mod. Phys. **88**, 045006 (2016).
[7] M. Eisenbach and L. C. Giojalas, Nat. Rev. Mol. Cell Biol. **7**, 276 (2006).
[8] H. C. Berg, *E. coli in Motion* (Springer Science & Business Media, New York, 2008).
[9] M. Polin, I. Tuval, K. Drescher, J. P. Gollub, and R. E. Goldstein, Science **325**, 487 (2009).
[10] M. Mussler, S. Rafaï, P. Peyla, and C. Wagner, Europhys. Lett. **101**, 54004 (2013).
[11] R. E. Goldstein, Annu. Rev. Fluid Mech. **47**, 343 (2015).
[12] W. F. Paxton, K. C. Kistler, C. C. Olmeda, A. Sen, S. K. St. Angelo, Y. Cao, T. E. Mallouk, P. E. Lammert, and V. H. Crespi, J. Am. Chem. Soc. **126**, 13424 (2004).
[13] I. Buttinoni, G. Volpe, F. Kümmel, G. Volpe, and C. Bechinger, J. Phys.: Condens. Matter **24**, 284129 (2012).
[14] A. Walther and A. H. Müller, Chem. Rev. **113**, 5194 (2013).
[15] S. Samin and R. van Roij, Phys. Rev. Lett. **115**, 188305 (2015).
[16] S. Ramaswamy, Annu. Rev. Condens. Matter Phys. **1**, 323 (2010).
[17] M. C. Marchetti, J.-F. Joanny, S. Ramaswamy, T. B. Liverpool, J. Prost, M. Rao, and R. A. Simha, Rev. Mod. Phys. **85**, 1143 (2013).
[18] A. M. Menzel, Phys. Rep. **554**, 1 (2015).
[19] M. E. Cates and J. Tailleur, Europhys. Lett. **101**, 20010 (2013).
[20] I. Buttinoni, J. Bialké, F. Kümmel, H. Löwen, C. Bechinger, and T. Speck, Phys. Rev. Lett. **110**, 238301 (2013).
[21] J. Bialké, H. Löwen, and T. Speck, Europhys. Lett. **103**, 30008 (2013).
[22] J. Bialké, T. Speck, and H. Löwen, J. Non-Cryst. Solids **407**, 367 (2015).
[23] M. E. Cates and J. Tailleur, Annu. Rev. Condens. Matter Phys. **6**, 219 (2015).
[24] R. Wittkowski, J. Stenhammar, and M. E. Cates, New J. Phys. **19**, 105003 (2017).
[25] A. Solon, J. Stenhammar, M. E. Cates, Y. Kafri, and J. Tailleur, New J. Phys. **20**, 075001 (2018).
[26] P. Digregorio, D. Levis, A. Suma, L. F. Cugliandolo, G. Gonnella, and I. Pagonabarraga, Phys. Rev. Lett. **121**, 098003 (2018).
[27] H. Wensink and H. Löwen, J. Phys.: Condens. Matter **24**, 464130 (2012).
[28] A. M. Menzel, J. Phys.: Condens. Matter **25**, 505103 (2013).
[29] F. Kogler and S. H. L. Klapp, Europhys. Lett. **110**, 10004 (2015).
[30] P. Romanczuk, H. Chaté, L. Chen, S. Ngo, and J. Toner, New J. Phys. **18**, 063015 (2016).
[31] A. M. Menzel, New J. Phys. **18**, 071001 (2016).
[32] D. B. Dusenbery, *Living at Micro Scale: The Unexpected Physics of Being Small* (Harvard University Press, Cambridge, 2009).
[33] J. O. Kessler, Nature **313**, 218 (1985).
[34] W. M. Durham, J. O. Kessler, and R. Stocker, Science **323**, 1067 (2009).
[35] B. ten Hagen, F. Kümmel, R. Wittkowski, D. Takagi, H. Löwen, and C. Bechinger, Nat. Commun. **5**, 4829 (2014).
[36] C. Lozano, B. ten Hagen, H. Löwen, and C. Bechinger, Nat. Commun. **7**, 12828 (2016).
[37] A. I. Campbell, R. Wittkowski, B. ten Hagen, H. Löwen, and S. J. Ebbens, J. Chem. Phys. **147**, 084905 (2017).
[38] B. Liebchen, P. Monderkamp, B. ten Hagen, and H. Löwen, Phys. Rev. Lett. **120**, 208002 (2018).
[39] H. H. Wensink, J. Dunkel, S. Heidenreich, K. Drescher, R. E. Goldstein, H. Löwen, and J. M. Yeomans, Proc. Natl. Acad. Sci. U. S. A. **109**, 14308 (2012).
[40] A. Sokolov and I. S. Aranson, Phys. Rev. Lett. **109**, 248109 (2012).
[41] J. Dunkel, S. Heidenreich, K. Drescher, H. H. Wensink, M. Bär, and R. E. Goldstein, Phys. Rev. Lett. **110**, 228102 (2013).
[42] A. Kaiser, A. Peshkov, A. Sokolov, B. ten Hagen, H. Löwen, and I. S. Aranson, Phys. Rev. Lett. **112**, 158101 (2014).
[43] J. Słomka and J. Dunkel, Eur. Phys. J.: Spec. Top. **224**, 1349 (2015).
[44] M. E. Cates, Rep. Prog. Phys. **75**, 042601 (2012).
[45] B. ten Hagen, R. Wittkowski, D. Takagi, F. Kümmel, C. Bechinger, and H. Löwen, J. Phys.: Condens. Matter **27**, 194110 (2015).
[46] W. Yan and J. F. Brady, J. Fluid Mech. **785**, R1 (2015).
[47] W. Yan and J. F. Brady, Soft Matter **11**, 6235 (2015).

[48]S. C. Takatori, W. Yan, and J. F. Brady, Phys. Rev. Lett. **113**, 028103 (2014).
[49]A. P. Solon, Y. Fily, A. Baskaran, M. E. Cates, Y. Kafri, M. Kardar, and J. Tailleur, Nat. Phys. **11**, 673 (2015).
[50]F. Smallenburg and H. Löwen, Phys. Rev. E **92**, 032304 (2015).
[51]A. Liluashvili, J. Ónody, and T. Voigtmann, Phys. Rev. E **96**, 062608 (2017).
[52]M. Engstler, T. Pfohl, S. Herminghaus, M. Boshart, G. Wiegertjes, N. Heddergott, and P. Overath, Cell **131**, 505 (2007).
[53]B. J. Nelson, I. K. Kaliakatsos, and J. J. Abbott, Annu. Rev. Biomed. Eng. **12**, 55 (2010).
[54]J. Wang and W. Gao, ACS Nano **6**, 5745 (2012).
[55]D. Patra, S. Sengupta, W. Duan, H. Zhang, R. Pavlick, and A. Sen, Nanoscale **5**, 1273 (2013).
[56]W. Xi, A. A. Solovev, A. N. Ananth, D. H. Gracias, S. Sanchez, and O. G. Schmidt, Nanoscale **5**, 1294 (2013).
[57]L. K. Abdelmohsen, F. Peng, Y. Tu, and D. A. Wilson, J. Mater. Chem. B **2**, 2395 (2014).
[58]J. K. G. Dhont, *An Introduction to Dynamics of Colloids* (Elsevier, Amsterdam, 1996).
[59]J. Happel and H. Brenner, *Low Reynolds Number Hydrodynamics: With Special Applications to Particulate Media* (Springer Science & Business Media, New York, 2012), Vol. 1.
[60]S. Kim and S. J. Karrila, *Microhydrodynamics: Principles and Selected Applications* (Dover Publications, Mineola, 2013).
[61]A. Najafi and R. Golestanian, Phys. Rev. E **69**, 062901 (2004).
[62]R. Zargar, A. Najafi, and M. Miri, Phys. Rev. E **80**, 026308 (2009).
[63]A. Daddi-Moussa-Ider, M. Lisicki, C. Hoell, and H. Löwen, J. Chem. Phys. **148**, 134904 (2018).
[64]A. Daddi-Moussa-Ider, M. Lisicki, A. J. Mathijssen, C. Hoell, S. Goh, J. Bławzdziewicz, A. M. Menzel, and H. Löwen, J. Phys.: Condens. Matter **30**, 254004 (2018).
[65]P. T. Underhill, J. P. Hernandez-Ortiz, and M. D. Graham, Phys. Rev. Lett. **100**, 248101 (2008).
[66]A. Baskaran and M. C. Marchetti, Proc. Natl. Acad. Sci. U. S. A. **106**, 15567 (2009).
[67]T. Vicsek, A. Czirók, E. Ben-Jacob, I. Cohen, and O. Shochet, Phys. Rev. Lett. **75**, 1226 (1995).
[68]J. Toner and Y. Tu, Phys. Rev. Lett. **75**, 4326 (1995).
[69]F. D. C. Farrell, M. C. Marchetti, D. Marenduzzo, and J. Tailleur, Phys. Rev. Lett. **108**, 248101 (2012).
[70]T. Vicsek and A. Zafeiris, Phys. Rep. **517**, 71 (2012).
[71]B. Liebchen and D. Levis, Phys. Rev. Lett. **119**, 058002 (2017).
[72]D. Levis and B. Liebchen, J. Phys.: Condens. Matter **30**, 084001 (2018).
[73]F. Ginelli, F. Peruani, M. Bär, and H. Chaté, Phys. Rev. Lett. **104**, 184502 (2010).
[74]F. Alarcón and I. Pagonabarraga, J. Mol. Liq. **185**, 56 (2013).
[75]G. Pessot, H. Löwen, and A. M. Menzel, Mol. Phys. **116**, 3401 (2018).
[76]A. M. Menzel, A. Saha, C. Hoell, and H. Löwen, J. Chem. Phys. **144**, 024115 (2016).
[77]C. Hoell, H. Löwen, and A. M. Menzel, New J. Phys. **19**, 125004 (2017).
[78]C. W. J. Beenakker and P. Mazur, Physica A **120**, 388 (1983).
[79]C. W. J. Beenakker and P. Mazur, Physica A **126**, 349 (1984).
[80]G. Nägele, Phys. Rep. **272**, 215 (1996).
[81]G. Nägele and P. Baur, Physica A **245**, 297 (1997).
[82]A. J. Banchio, J. Gapinski, A. Patkowski, W. Häußler, A. Fluerasu, S. Sacanna, P. Holmqvist, G. Meier, M. P. Lettinga, and G. Nägele, Phys. Rev. Lett. **96**, 138303 (2006).
[83]J. Rotne and S. Prager, J. Chem. Phys. **50**, 4831 (1969).
[84]M. Reichert and H. Stark, Phys. Rev. E **69**, 031407 (2004).
[85]T. C. Adhyapak and S. Jabbari-Farouji, Phys. Rev. E **96**, 052608 (2017).
[86]Strictly speaking, only the lowest-order terms in an expansion around $a/L = 0$ are included for $j \neq i$ in Eqs. (10) and (11). We neglect higher order corrections[60,85] in favor of simplicity and more traceable analytical expressions.
[87]J.-P. Hansen and I. R. McDonald, *Theory of Simple Liquids* (Elsevier, Amsterdam, 1990).
[88]R. Evans, Adv. Phys. **28**, 143 (1979).
[89]R. Evans, in *Fundamentals of Inhomogeneous Fluids*, edited by D. Henderson (Marcel Dekker, New York, 1992), pp. 85–176.
[90]U. M. B. Marconi and P. Tarazona, J. Chem. Phys. **110**, 8032 (1999).
[91]U. M. B. Marconi and P. Tarazona, J. Phys.: Condens. Matter **12**, A413 (2000).
[92]A. J. Archer and R. Evans, J. Chem. Phys. **121**, 4246 (2004).
[93]G. K.-L. Chan and R. Finken, Phys. Rev. Lett. **94**, 183001 (2005).
[94]P. Español and H. Löwen, J. Chem. Phys. **131**, 244101 (2009).
[95]R. Evans, in *Lecture Notes 3rd Warsaw School of Statistical Physics*, edited by B. Cichocki, M. Napiórkowski, and J. Piasecki (Warsaw University Press, Warsaw, 2010), pp. 43–85.
[96]H. Löwen, in *Lecture Notes 3rd Warsaw School of Statistical Physics*, edited by B. Cichocki, M. Napiórkowski, and J. Piasecki (Warsaw University Press, Warsaw, 2010), pp. 87–121.
[97]R. Wittkowski and H. Löwen, Mol. Phys. **109**, 2935 (2011).
[98]R. Lugo-Frías and S. H. Klapp, J. Phys.: Condens. Matter **28**, 244022 (2016).
[99]C. G. Gray and K. E. Gubbins, *Theory of Molecular Fluids. I: Fundamentals*, International Series of Monographs on Chemistry (Oxford University Press, Oxford, 1984).
[100]J. K. Percus, Phys. Rev. Lett. **8**, 462 (1962).
[101]A. J. Archer, B. Chacko, and R. Evans, J. Chem. Phys. **147**, 034501 (2017).
[102]P. Hopkins, A. Fortini, A. J. Archer, and M. Schmidt, J. Chem. Phys. **133**, 224505 (2010).
[103]J. M. Brader and M. Schmidt, J. Phys.: Condens. Matter **27**, 194106 (2015).
[104]M. Rein and T. Speck, Eur. Phys. J. E **39**, 84 (2016).
[105]A. Härtel, D. Richard, and T. Speck, Phys. Rev. E **97**, 012606 (2018).
[106]J. Stenhammar, A. Tiribocchi, R. J. Allen, D. Marenduzzo, and M. E. Cates, Phys. Rev. Lett. **111**, 145702 (2013).
[107]H. H. Wensink and H. Löwen, Phys. Rev. E **78**, 031409 (2008).
[108]B. M. Mladek, D. Gottwald, G. Kahl, M. Neumann, and C. N. Likos, Phys. Rev. Lett. **96**, 045701 (2006).
[109]A. J. Archer, M. Walters, U. Thiele, and E. Knobloch, Phys. Rev. E **90**, 042404 (2014).
[110]J. E. Guyer, D. Wheeler, and J. A. Warren, Comput. Sci. Eng. **11**, 6 (2009).
[111]J. Stenhammar, C. Nardini, R. W. Nash, D. Marenduzzo, and A. Morozov, Phys. Rev. Lett. **119**, 028005 (2017).
[112]N. de Macedo Biniossek, H. Löwen, T. Voigtmann, and F. Smallenburg, J. Phys.: Condens. Matter **30**, 074001 (2018).
[113]S. Heidenreich, J. Dunkel, S. H. L. Klapp, and M. Bär, Phys. Rev. E **94**, 020601 (2016).
[114]H. Reinken, S. H. L. Klapp, M. Bär, and S. Heidenreich, Phys. Rev. E **97**, 022613 (2018).
[115]N. D. Mermin and H. Wagner, Phys. Rev. Lett. **17**, 1133 (1966).
[116]J. Toner, Y. Tu, and S. Ramaswamy, Ann. Phys. **318**, 170 (2005).
[117]D. Saintillan and M. J. Shelley, Phys. Rev. Lett. **99**, 058102 (2007).

P5 Swimming trajectories of a three-sphere microswimmer near a wall

Reproduced from

A. Daddi-Moussa-Ider, M. Lisicki, C. Hoell, and H. Löwen,
Swimming trajectories of a three-sphere microswimmer near a wall,
J. Chem. Phys. **148**, 134904 (2018),
with the permission of *AIP Publishing.*

Digital Object Identifier (DOI): `https://doi.org/10.1063/1.5021027`

Statement of contribution

I contributed to the theoretical description, including the mobility tensor formulation derived from the Blake tensor, the self-propulsion mechanism of the three-sphere swimmer, and the introduction of an additional relative rotation between the spheres constituting the swimmer. I participated in the discussion and interpretation of the results, including the obtained swimming trajectories of a three-sphere swimmer near a rigid wall and the corresponding state diagram. Moreover, I contributed to drafting the manuscript, editing the text, and finalizing the manuscript. My work concerning this paper was supervised by ADMI and HL.

Copyright and license notice

Supplemented Material

Supplemental material concerning this work is found at `https://aip.scitation.org/doi/suppl/10.1063/1.5021027` and features supporting information and several movies of swimmer trajectories, as indicated in the main text.

THE JOURNAL OF CHEMICAL PHYSICS **148**, 134904 (2018)

Swimming trajectories of a three-sphere microswimmer near a wall

Abdallah Daddi-Moussa-Ider,[1,a)] Maciej Lisicki,[2,3] Christian Hoell,[1] and Hartmut Löwen[1,b)]
[1]*Institut für Theoretische Physik II: Weiche Materie, Heinrich-Heine-Universität Düsseldorf, Universitätsstraße 1, 40225 Düsseldorf, Germany*
[2]*Department of Applied Mathematics and Theoretical Physics, University of Cambridge, Wilberforce Rd., Cambridge CB3 0WA, United Kingdom*
[3]*Institute of Theoretical Physics, Faculty of Physics, University of Warsaw, Pasteura 5, 02-093 Warsaw, Poland*

(Received 30 December 2017; accepted 14 March 2018; published online 3 April 2018)

The hydrodynamic flow field generated by self-propelled active particles and swimming microorganisms is strongly altered by the presence of nearby boundaries in a viscous flow. Using a simple model three-linked sphere swimmer, we show that the swimming trajectories near a no-slip wall reveal various scenarios of motion depending on the initial orientation and the distance separating the swimmer from the wall. We find that the swimmer can either be trapped by the wall, completely escape, or perform an oscillatory gliding motion at a constant mean height above the wall. Using a far-field approximation, we find that, at leading order, the wall-induced correction has a source-dipolar or quadrupolar flow structure where the translational and angular velocities of the swimmer decay as inverse third and fourth powers with distance from the wall, respectively. The resulting equations of motion for the trajectories and the relevant order parameters fully characterize the transition between the states and allow for an accurate description of the swimming behavior near a wall. We demonstrate that the transition between the trapping and oscillatory gliding states is first order discontinuous, whereas the transition between the trapping and escaping states is continuous, characterized by non-trivial scaling exponents of the order parameters. In order to model the circular motion of flagellated bacteria near solid interfaces, we further assume that the spheres can undergo rotational motion around the swimming axis. We show that the general three-dimensional motion can be mapped onto a quasi-two-dimensional representational model by an appropriate redefinition of the order parameters governing the transition between the swimming states. *Published by AIP Publishing.*
https://doi.org/10.1063/1.5021027

I. INTRODUCTION

Swimming microorganisms use a variety of strategies to achieve propulsion or stir the suspending fluid.[1] To circumvent the constraint of time reversibility of the Stokes equation governing the small-scale motion of a viscous fluid, known as Purcell's scallop theorem,[2] many of them rely on the non-reciprocal motion of their bodies. To understand the nature of this process, a number of artificial designs have been proposed to construct and fabricate model swimmers capable of propelling themselves in a viscous fluid by internal actuation. Among these, a particular class is simplistic systems with only few degrees of freedom necessary to break kinematic reversibility, as opposed to continuous irreversible deformations or chemically powered locomotion.[3–8] A famous example of such a design is the swimmer of Najafi and Golestanian[9] encompassing three aligned spheres; their distances vary in time periodically with phase differences, thus leading to locomotion along straight trajectories.[10–13] This system has been also realized experimentally using optical tweezers.[14,15] Notably, a number of similar designs have been proposed: with one of the arms being passive and elastic,[16] both arms being muscle-like[17] or using a bead-spring swimmer model.[18–20] Variations of this idea leading to rotational motion have been proposed: a circle swimmer in the form of three spheres joined by two links crossing at an angle,[21] linked like spokes on a wheel,[22] or connected in an equilateral triangular fashion.[23] An extension to a collection of $N > 3$ spheres has also been considered.[24] Further investigations include the effect of fluid viscoelasticity,[25–31] swimming near a fluid interface[32–34] or inside a channel,[35–39] and the hydrodynamic interactions between two neighboring microswimmers near a wall.[40] Intriguing collective behavior and spatiotemporal patterns may arise from the interaction of many swimmers, including the onset of propagating density waves[41–48] and laning,[49–52] the motility-induced phase separation,[53–57] and the emergence of active turbulence.[58–64] Boundaries have also been shown to induce order in collective flows of bacterial suspensions,[65–67] leading to potential applications in autonomous microfluidic systems.[68] A step towards understanding these collective phenomena is to explore the dynamics of a single model swimmer interacting with a boundary.

The long-range nature of hydrodynamic interactions in low Reynolds number flows results in geometrical confinement significantly influencing the dynamics of suspended particles or organisms.[69] Interfacial effects govern the design of microfluidic systems,[70–72] they hinder translational and rotational diffusion of colloidal particles[73–81] and play an

[a)]Electronic mail: ider@thphy.uni-duesseldorf.de
[b)]Electronic mail: hlowen@hhu.de

important role in living systems, where walls have been shown to qualitatively modify the trajectories of swimming *E. coli* bacteria[82–87] or microalgae.[88,89] Simplistic two-sphere near-wall models of bacterial motion have revealed that the dynamics of a bead swimmer can be surprisingly rich, including circular motion in contact with the wall, swimming away from the wall, and a non-trivial steady circulation at a finite distance from the interface.[90] This diverse phase behavior has also been corroborated in systems of chemically powered autophoretic particles,[91–98] leading to a phase diagram also includes trapping, escape, and a steady hovering state. Swimming near a boundary has been addressed using a two-dimensional singularity model combined with a complex variable approach,[99] a resistive force theory,[100] and a multipole expansion technique.[101] It has further been demonstrated that geometric confinement can conveniently be utilized to steer active colloids along arbitrary trajectories.[102] The detention times of microswimmers trapped at solid surfaces have been studied theoretically, elucidating the interplay between hydrodynamic interactions and rotational noise.[103] Trapping in more complex geometries has particularly been analyzed in the context of collisions of swimming microorganisms with large spherical obstacles[104,105] and scattering on colloidal particles.[106] The generic underlying mechanism is thought to play a role in a number of biological processes, such as the formation of biofilms.[107,108]

In order to analyze the dynamics of a neutral three-sphere model swimmer near a no-slip wall, Zargar *et al.*[109] calculated the phase diagram, finding that the swimmer always orients itself parallel to the wall. In their calculation, they expand the hydrodynamic forces in the small parameter $\epsilon = L/z$, where L is the length of the swimmer and z is the wall-swimmer distance, arriving at the conclusion that the dominant term is proportional to z^{-2}. In this contribution, we revisit this problem and demonstrate that the dominant term in the swimming velocities scales rather as z^{-3}. This allows us to calculate the full phase diagram that shares qualitative features seen in the aforementioned artificial microswimmers, that is, steady gliding, trapping, and escaping trajectories, based on the initial conditions of the swimmer.

The paper is organized as follows. In Sec. II, we introduce a theoretical model for the swimmer and derive the governing equations of motion in the low-Reynolds-number regime. We then present in Sec. III a state diagram of swimming near a hard wall and introduce suitable order parameters governing the transitions between the states. In Sec. IV, we present a far-field theory that describes the swimming dynamics in the limit far away from the wall. We then discuss in Sec. V the effect of the rotation of the spheres on the swimming trajectories and show that the general 3D motion can be mapped onto a 2D generic model by properly redefining the order parameters. Finally, concluding remarks are contained in Sec. VI.

II. THEORETICAL MODEL

A. Stokes hydrodynamics

We consider the (sufficiently slow) motion of a swimmer moving in the vicinity of an infinitely extended planar hard wall. Since systems of biological or microfluidic relevance are typically micrometer-sized, the Reynolds number is low, and the dynamics are dominated by viscosity. For small amplitude and frequency of motion, the fluid flow surrounding the swimmer is governed by the steady incompressible Stokes equations,[110] which for a point force acting on the fluid at position $\boldsymbol{r}_0$ relate the velocity $\boldsymbol{v}$ and pressure field, p, by

$$\eta \boldsymbol{\nabla}^2 \boldsymbol{v}(\boldsymbol{r}) - \boldsymbol{\nabla} p(\boldsymbol{r}) + \boldsymbol{F}\delta(\boldsymbol{r}-\boldsymbol{r}_0) = 0, \tag{1}$$

$$\boldsymbol{\nabla}\cdot\boldsymbol{v}(\boldsymbol{r}) = 0, \tag{2}$$

where η denotes the dynamic viscosity of the fluid.

In an unbounded fluid, the solution of this set of equations for the velocity field is expressed in terms of Green's function

$$v_\alpha(\boldsymbol{r}) = \mathcal{G}_{\alpha\beta}(\boldsymbol{r},\boldsymbol{r}_0)F_\beta, \tag{3}$$

for $\alpha, \beta \in \{x, y, z\}$, referred to as the Oseen tensor, and given by

$$\mathcal{G}^{\mathrm{O}}_{\alpha\beta}(\boldsymbol{r},\boldsymbol{r}_0) = \frac{1}{8\pi\eta}\left(\frac{\delta_{\alpha\beta}}{s} + \frac{s_\alpha s_\beta}{s^3}\right), \tag{4}$$

where summation over repeated indices is assumed following Einstein's convention. Moreover $\boldsymbol{s} := \boldsymbol{r} - \boldsymbol{r}_0$ and $s := |\boldsymbol{s}|$. The flow due to a point force, called a Stokeslet, decays with the distance like $1/s$.

The solution of the forced Stokes equations in the presence of an infinitely extended hard wall can conveniently be determined using the image solution technique[111] and contains Stokeslets and higher-order flow singularities—force dipoles and source dipoles. The corresponding Green's function satisfying the no-slip boundary conditions at the wall is given in terms of the Blake tensor and can be presented as a sum of four contributions[110,111]

$$\boldsymbol{\mathcal{G}}(\boldsymbol{r}) = \boldsymbol{\mathcal{G}}^{\mathrm{O}}(\boldsymbol{s}) - \boldsymbol{\mathcal{G}}^{\mathrm{O}}(\boldsymbol{R}) + 2z_0^2\boldsymbol{\mathcal{G}}^{\mathrm{D}}(\boldsymbol{R}) - 2z_0\boldsymbol{\mathcal{G}}^{\mathrm{SD}}(\boldsymbol{R}), \tag{5}$$

wherein $\boldsymbol{r}_0 = (0, 0, z_0)$ is the point force position, $\boldsymbol{R} := \boldsymbol{r} - \overline{\boldsymbol{r}_0}$ with $\overline{\boldsymbol{r}_0} = (0, 0, -z_0)$ is the position of the Stokeslet image with respect to the wall. Moreover, $r := |\boldsymbol{r}|$ and $R := |\boldsymbol{R}|$. Here $\boldsymbol{\mathcal{G}}^{\mathrm{D}}$ is the force dipole given by

$$\mathcal{G}^{\mathrm{D}}_{\alpha\beta}(\boldsymbol{R}) = \frac{(1-2\delta_{\beta z})}{8\pi\eta}\left(\frac{\delta_{\alpha\beta}}{R^3} - \frac{3R_\alpha R_\beta}{R^5}\right), \tag{6}$$

and $\boldsymbol{\mathcal{G}}^{\mathrm{SD}}$ denotes the source dipole given by

$$\mathcal{G}^{\mathrm{SD}}_{\alpha\beta}(\boldsymbol{R}) = \frac{(1-2\delta_{\beta z})}{8\pi\eta}\left(\frac{\delta_{\alpha\beta}R_z}{R^3} - \frac{\delta_{\alpha z}R_\beta}{R^3} + \frac{\delta_{\beta z}R_\alpha}{R^3} - \frac{3R_\alpha R_\beta R_z}{R^5}\right). \tag{7}$$

The translational and rotational motion of the particles is related to the forces $\boldsymbol{F}$ and torques $\boldsymbol{L}$ acting upon them via the hydrodynamic mobility tensor. In the presence of a background flow with velocity v_0 and vorticity $2\omega_0$, this relation takes the form

$$\begin{pmatrix} \boldsymbol{V} - \boldsymbol{v}_0 \\ \boldsymbol{\Omega} - \omega_0 \end{pmatrix} = \begin{pmatrix} \boldsymbol{\mu}^{tt} & \boldsymbol{\mu}^{tr} \\ \boldsymbol{\mu}^{rt} & \boldsymbol{\mu}^{rr} \end{pmatrix} \begin{pmatrix} \boldsymbol{F} \\ \boldsymbol{L} \end{pmatrix}. \tag{8}$$

The indices indicate the translational (tt), rotational (rr), and translation-rotation coupling (tr, rt) parts of the mobility tensor. The mobility tensor contains contributions relative to a single particle (self-mobilities), in addition to contributions due to interactions between the particles (hereafter approximated by pair mobilities). Owing to the linearity of the Stokes equations and the reciprocal theorem, the hydrodynamic mobility tensor is always symmetric and positive definite.[112–114]

B. Swimmer model

In low-Reynolds-number hydrodynamics, swimming objects have to undergo non-reciprocal motion in order to achieve propulsion. In the present work, we use a simple model swimmer, originally proposed by Najafi and Golestanian,[9] which is made of three aligned spheres. The spheres are connected by rod-like elements of negligible hydrodynamic effects in order to ensure their alignment. This system is capable of swimming forward when the mutual distances between the spheres are varied periodically in such a way that the time-reversal symmetry is broken (see Fig. 1 for an illustration of the linear swimmer model). In the present article, we focus our attention on the behavior of a neutral swimmer for which the three spheres have equal size. The behavior of a general three-sphere microswimmer with different sphere radii

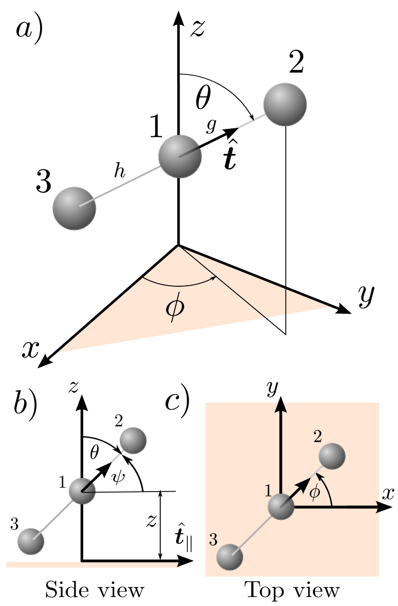

FIG. 1. (a) The frame of reference associated with a neutral three-linked sphere low-Reynolds-number microswimmer, relative to the laboratory frame. The swimmer is oriented along the unit vector $\hat{\boldsymbol{t}}$ defined by the azimuthal angle ϕ and polar angle θ. The spheres are connected to each other by dragless rods where the instantaneous distances between the spheres 2 and 3 relative to the sphere 1 are denoted g and h, respectively. The side and top views are shown in the subfigures (b) and (c), respectively, where $\hat{\boldsymbol{t}}_{\parallel}$ stands for the projection of orientation vector $\hat{\boldsymbol{t}}$ on the plane $z = 0$. Here $\psi := \theta - \pi/2$.

to discriminate between pushers and pullers will be reported elsewhere.[115]

1. Mathematical formulation

Assuming that the fluid surrounding the swimmer is at rest, the translational velocity of each sphere relative to the laboratory (LAB) frame of reference is related to the internal forces $\boldsymbol{F}_\lambda$ and torques $\boldsymbol{L}_\lambda$ via the hydrodynamic mobility tensor as [c.f. Eq. (8)]

$$\boldsymbol{V}_\gamma = \frac{\mathrm{d}\boldsymbol{r}_\gamma}{\mathrm{d}t} = \sum_{\lambda=1}^{3} \left(\boldsymbol{\mu}^{tt}_{\gamma\lambda} \cdot \boldsymbol{F}_\lambda + \boldsymbol{\mu}^{tr}_{\gamma\lambda} \cdot \boldsymbol{L}_\lambda \right), \tag{9}$$

for $\gamma \in \{1, 2, 3\}$. These internal forces and torques can be actuated, e.g., by imaginary motors embedded between the spheres along the swimmer axis. Analogously, the angular velocity of each sphere with respect to the LAB frame is

$$\boldsymbol{\Omega}_\gamma = \sum_{\lambda=1}^{3} \left(\boldsymbol{\mu}^{rt}_{\gamma\lambda} \cdot \boldsymbol{F}_\lambda + \boldsymbol{\mu}^{rr}_{\gamma\lambda} \cdot \boldsymbol{L}_\lambda \right). \tag{10}$$

We note that $\boldsymbol{\mu}^{tr}_{\gamma\lambda} = \boldsymbol{\mu}^{rt}_{\lambda\gamma}$ as required by the symmetry of the mobility tensor.

Since the swimmer has to undergo autonomous motion, its body has to be both force-free and torque-free in total. Accordingly,

$$\sum_{\lambda=1}^{3} \boldsymbol{F}_\lambda = 0, \qquad \sum_{\lambda=1}^{3} \left((\boldsymbol{r}_\lambda - \boldsymbol{r}_\mathrm{R}) \times \boldsymbol{F}_\lambda + \boldsymbol{L}_\lambda \right) = 0, \tag{11}$$

where $\times$ denotes the cross product. The moments of the internal forces can be taken with respect to any reference point, $\boldsymbol{r}_\mathrm{R}$, that we chose here for convenience as the position of the central sphere.

We now assume that the instantaneous relative distance vectors between the spheres are prescribed at each time as

$$\boldsymbol{r}_1 - \boldsymbol{r}_3 = h(t)\hat{\boldsymbol{t}}, \tag{12a}$$

$$\boldsymbol{r}_2 - \boldsymbol{r}_1 = g(t)\hat{\boldsymbol{t}}, \tag{12b}$$

where $\hat{\boldsymbol{t}}$ is the unit vector pointing along the swimming direction such that $\hat{\boldsymbol{t}} = \sin\theta\cos\phi\,\hat{\boldsymbol{e}}_x + \sin\theta\sin\phi\,\hat{\boldsymbol{e}}_y + \cos\theta\,\hat{\boldsymbol{e}}_z$ (c.f. Fig. 1). Here ϕ and θ stand for the azimuthal and polar angles, respectively, in the spherical coordinate system associated with the swimmer. We further define the unit vectors $\hat{\boldsymbol{\theta}} = \cos\phi\cos\theta\,\hat{\boldsymbol{e}}_x + \sin\phi\cos\theta\,\hat{\boldsymbol{e}}_y - \sin\theta\,\hat{\boldsymbol{e}}_z$ and $\hat{\boldsymbol{\phi}} = -\sin\phi\,\hat{\boldsymbol{e}}_x + \cos\phi\,\hat{\boldsymbol{e}}_y$. We note that the set of vectors $(\hat{\boldsymbol{t}}, \hat{\boldsymbol{\theta}}, \hat{\boldsymbol{\phi}})$ forms a direct orthonormal basis satisfying the relation $\hat{\boldsymbol{\theta}} \times \hat{\boldsymbol{\phi}} = \hat{\boldsymbol{t}}$. Throughout this work, we assume that the lengths of the rods change periodically in time relative to a mean value L,

$$g(t) = L + u_{10}\cos(\omega t), \tag{13a}$$

$$h(t) = L + u_{20}\cos(\omega t + \delta), \tag{13b}$$

where ω is the frequency of motion, $\delta \in [0, 2\pi)$ is the phase shift, and u_{10} and u_{20} are the amplitudes of the length change such that $|u_{10}| \ll L$ and $|u_{20}| \ll L$. For $\delta \notin \{0, \pi\}$ and non-vanishing u_{10} and u_{20}, this constitutes a non-reciprocal motion, which—as noted before—is needed for self-propulsion at low Reynolds numbers.

By combining Eqs. (9), providing the instantaneous velocities of the spheres with Eq. (12), we readily obtain

$$\sum_{\lambda=1}^{3}\left(\boldsymbol{G}_{\lambda}^{tt}\cdot\boldsymbol{F}_{\lambda}+\boldsymbol{G}_{\lambda}^{tr}\cdot\boldsymbol{L}_{\lambda}\right)=\dot{g}\,\hat{\boldsymbol{t}}+g\,\frac{\mathrm{d}\hat{\boldsymbol{t}}}{\mathrm{d}t}, \tag{14a}$$

$$\sum_{\lambda=1}^{3}\left(\boldsymbol{H}_{\lambda}^{tt}\cdot\boldsymbol{F}_{\lambda}+\boldsymbol{H}_{\lambda}^{tr}\cdot\boldsymbol{L}_{\lambda}\right)=\dot{h}\,\hat{\boldsymbol{t}}+h\,\frac{\mathrm{d}\hat{\boldsymbol{t}}}{\mathrm{d}t}, \tag{14b}$$

where, for convenience, we have defined the tensors

$$\boldsymbol{G}_{\lambda}^{\alpha\beta}:=\boldsymbol{\mu}_{2\lambda}^{\alpha\beta}-\boldsymbol{\mu}_{1\lambda}^{\alpha\beta}, \tag{15a}$$

$$\boldsymbol{H}_{\lambda}^{\alpha\beta}:=\boldsymbol{\mu}_{1\lambda}^{\alpha\beta}-\boldsymbol{\mu}_{3\lambda}^{\alpha\beta}, \tag{15b}$$

with $\alpha\beta\in\{tt,\ tr,\ rt,\ rr\}$. The time derivative of the unit orientation vector $\hat{\boldsymbol{t}}$ relative to the LAB frame is

$$\frac{\mathrm{d}\hat{\boldsymbol{t}}}{\mathrm{d}t}=\dot{\theta}\,\hat{\boldsymbol{\theta}}+\dot{\phi}\,\sin\theta\,\hat{\boldsymbol{\phi}}. \tag{16}$$

In order to model the circular trajectories observed in swimming bacteria near surfaces, we further assume that the spheres can freely rotate around the swimming axis at rotation rates $\dot{\varphi}_\gamma$. The frame of reference associated with the swimmer can be obtained by Euler transformations,[116] consisting of three successive rotations. Accordingly, the Euler angles, ϕ, θ, and φ_γ represent the precession, nutation, and intrinsic rotation along the swimming axis, respectively. The angular velocity vector of a sphere γ relative to the LAB frame reads

$$\boldsymbol{\Omega}_\gamma=-\dot{\phi}\sin\theta\,\hat{\boldsymbol{\theta}}+\dot{\theta}\,\hat{\boldsymbol{\phi}}+(\dot{\phi}\cos\theta+\dot{\varphi}_\gamma)\,\hat{\boldsymbol{t}}. \tag{17}$$

The dynamics of the swimmer are fully characterized by the instantaneous velocity of the central sphere in addition to the rotation rates $\dot{\theta}$ and $\dot{\phi}$. For their calculation, we require the knowledge of the internal forces and torques acting between the spheres.

By projecting Eqs. (14) onto the spherical coordinate basis vectors and eliminating the rotation rates $\dot{\theta}$ and $\dot{\phi}$, four scalar equations are obtained. The force- and torque-free conditions stated by Eq. (11) provide us with six additional equations. Moreover, the projection of the angular velocities (17) along the $\hat{\boldsymbol{\theta}}$ and $\hat{\boldsymbol{\phi}}$ directions yields

$$\boldsymbol{\Omega}_\gamma\cdot\hat{\boldsymbol{\theta}}=-\dot{\phi}\sin\theta, \tag{18a}$$

$$\boldsymbol{\Omega}_\gamma\cdot\hat{\boldsymbol{\phi}}=\dot{\theta}, \tag{18b}$$

for $\gamma\in\{1,2,3\}$, providing six further equations. For a closure of the system of equations, we prescribe the relative angular velocities between the adjacent spheres as

$$(\boldsymbol{\Omega}_1-\boldsymbol{\Omega}_3)\cdot\hat{\boldsymbol{t}}=\dot{\varphi}_1-\dot{\varphi}_3=:\omega_{13}, \tag{19a}$$

$$(\boldsymbol{\Omega}_2-\boldsymbol{\Omega}_1)\cdot\hat{\boldsymbol{t}}=\dot{\varphi}_2-\dot{\varphi}_1=:\omega_{21}. \tag{19b}$$

The determination of the internal forces and torques acting on each sphere is readily achievable by solving the resulting linear system composed of 18 independent equations given by (11), (14), (18), and (19), using the standard substitution method. In the remainder of this paper, all the lengths will be scaled by the mean length of the arms L and the times by the inverse frequency ω^{-1}. Finally, the swimming velocity can be calculated as

$$\boldsymbol{V}:=\boldsymbol{V}_1=\sum_{\lambda=1}^{3}\left(\boldsymbol{\mu}_{1\lambda}^{tt}\cdot\boldsymbol{F}_\lambda+\boldsymbol{\mu}_{1\lambda}^{tr}\cdot\boldsymbol{L}_\lambda\right) \tag{20}$$

and the rotation rates as

$$\dot{\theta}=\frac{1}{h}\sum_{\lambda=1}^{3}\left(\boldsymbol{H}_{\lambda}^{tt}\cdot\boldsymbol{F}_{\lambda}+\boldsymbol{H}_{\lambda}^{tr}\cdot\boldsymbol{L}_{\lambda}\right)\cdot\hat{\boldsymbol{\theta}}, \tag{21}$$

$$\dot{\phi}=\frac{1}{h\,\sin\theta}\sum_{\lambda=1}^{3}\left(\boldsymbol{H}_{\lambda}^{tt}\cdot\boldsymbol{F}_{\lambda}+\boldsymbol{H}_{\lambda}^{tr}\cdot\boldsymbol{L}_{\lambda}\right)\cdot\hat{\boldsymbol{\phi}}. \tag{22}$$

The swimming trajectories can thus be determined by integrating Eqs. (20)–(22) for a given set of initial conditions ($\boldsymbol{r}_0$, θ_0, ϕ_0).

2. Swimming in an unbounded domain

In an unbounded fluid domain, i.e., in the absence of the wall, the swimmer undergoes purely translational motion along its swimming axis without changing its orientation. In order to proceed analytically, we assume that the radius of the spheres a is much smaller than the arm lengths. The internal forces acting on the spheres averaged over one swimming period are

$$\boldsymbol{F}_1=\frac{a^2}{4}\left(5+\frac{11}{2}\,a\right)\pi\eta K\,\hat{\boldsymbol{t}},\qquad \boldsymbol{F}_2=\boldsymbol{F}_3=-\frac{\boldsymbol{F}_1}{2}, \tag{23}$$

wherein

$$K:=\langle g\dot{h}-h\dot{g}\rangle=-u_{10}u_{20}\sin\delta, \tag{24}$$

and $\langle\cdot\rangle$ denotes the time-averaging operator over one complete swimming cycle, defined by

$$\langle\cdot\rangle:=\frac{1}{2\pi}\int_0^{2\pi}(\cdot)\,\mathrm{d}t. \tag{25}$$

Clearly, no net swimming motion is achieved if $\delta=0$ or π. Moreover, the swimming speed is maximal when $\delta=\pi/2$, a value we consider in the subsequent analysis. The internal torques exerted on the rotating spheres read

$$\boldsymbol{L}_1=\frac{8\pi}{3}\,a^3\,(\omega_{13}-\omega_{21})\,\hat{\boldsymbol{t}}, \tag{26a}$$

$$\boldsymbol{L}_2=\frac{8\pi}{3}\,a^3\,(2\omega_{21}+\omega_{13})\,\hat{\boldsymbol{t}}, \tag{26b}$$

$$\boldsymbol{L}_3=-\frac{8\pi}{3}\,a^3\,(\omega_{21}+2\omega_{13})\,\hat{\boldsymbol{t}}. \tag{26c}$$

By making use of Eq. (20) and averaging over a swimming cycle, the translational velocity up to the second order in a reads

$$\boldsymbol{V}_1=V_0\,\hat{\boldsymbol{t}},\qquad V_0:=-\frac{a}{24}\,(7+5a)\,K, \tag{27}$$

while $\dot{\theta}=0$ and $\dot{\phi}=0$ so that the swimmer's orientation remains constant. Evidently, the averaged swimming speed is a function of just the swimmer's properties and does not depend on the fluid viscosity.[9] The fluid viscosity would nevertheless have to be accounted for to calculate the power needed to perform the prescribed motions of the three spheres. In the following, we will address the swimming behavior near a hard wall and investigate the possible scenarios of motion.

III. SWIMMING NEAR A WALL

A. State diagram

We now consider the swimming kinematics in the vicinity of a hard wall and examine in details the resulting swimming trajectories. For that aim, we solve numerically the linear system of equations described in Sec. II to determine the internal forces and torques acting between the spheres. The time-dependent position and orientation of the swimmer are then calculated by numerically integrating Eqs. (20)–(22) using a fourth-order Runge-Kutta scheme with adaptive time stepping.[117] For the particle hydrodynamic mobility functions, we employ the values obtained using the multipole method for Stokes flows.[118,119] This method is widely used and has the advantage of providing precise and accurate predictions of the self-mobilities, which are reasonable even at distances very close to the wall. The time-averaged positions and inclinations are determined numerically using the standard trapezoidal integration method. As the vertical position of one of the spheres gets closer to the wall such that $z \sim a$, an additional soft repulsive force $F_z = \kappa(z - a)^{-n}$ is introduced, where $\kappa = 10^{-5}\eta|K|$ and $n = 2$ are taken as typical values. We have checked that changing these values within moderate ranges results in qualitatively similar outcomes. Moreover, we take $a = u_{10} = u_{20} = 1/10$.

We begin with the relatively simple situation in which the spheres do not rotate around the swimming axis, so we take $\omega_{21} = \omega_{13} = 0$. In this particular case, the problem becomes two dimensional as the swimmer is constrained to move in the plane defined by its initial azimuthal orientation ϕ_0. Without loss of generality, we take $\phi_0 = 0$ for which the swimmer moves in the (x, z) plane.

In Fig. 2, we show the swimming state diagram constructed in the (z_0, ψ_0) space, where $\psi := \theta - \pi/2$ defines the angle relative to the horizontal direction. Hence, the swimmer is initially pointing towards (away from) the wall for $\psi_0 > 0$ ($\psi_0 < 0$). We observe that three different possible scenarios of motion emerge depending upon the initial distance from the wall and orientation. The swimmer may be trapped by the wall, totally escape from the wall, or undergo a nontrivial oscillatory gliding motion. In the trapping state (shown as red circles in Fig. 2), the swimmer moves towards the wall following a parabolic-like trajectory to progressively align perpendicular to the wall as $\psi \to \pi/2$. In the final stage, the swimmer reaches a stable state and hovers at a constant height above the wall. This behavior occurs for large initial inclinations when $\psi_0 > 0.3$ and that regardless of the initial distance that separates the swimmer from the wall. However, trapping can also take place for $\psi_0 \sim 0$ if the swimmer is initially located far enough from the wall, at distances larger than $z_0 = 1.5$. Notably, the swimmer is trapped by the wall if it is released from distances $z_0 < 0.25$ with a vanishing initial inclination $\psi_0 = 0$.

The escaping state (green triangles in Fig. 2) is observed if the swimmer is directed away from the wall with $\psi_0 < -0.5$. In this state, the swimmer moves straight away from the wall beyond a certain height at which the wall-induced hydrodynamic interactions die away completely. In the oscillatory gliding state (blue rectangles in Fig. 2), the swimmer undergoes a sinusoidal-like motion around a mean height above the wall. This state occurs in a bounded region of initial states when $z_0 \sim 1$ and $\psi_0 \sim 0$.

In Fig. 3, we show the transition from the trapping to the escaping states upon variation of the initial inclination for a swimmer initially positioned a distance $z_0 = 1$ above the wall. For initial inclinations $\psi_0 > -0.39$, the swimmer moves along a curved path following a projectile-like trajectory before ending up hovering at a steady height $z \simeq 1.12$ above the wall. Accordingly, the swimmer velocity normal to the wall vanishes and

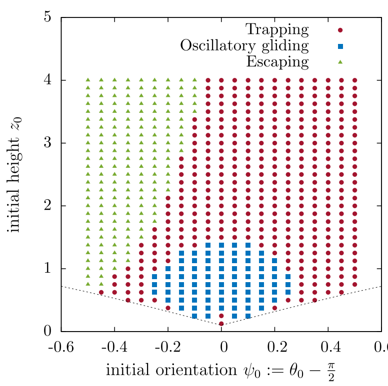

FIG. 2. State diagram illustrating the possible swimming scenarios in the presence of a hard wall for the 2D motion, i.e., for $\omega_{21} = \omega_{13} = 0$. The dashed line corresponds to impermissible situations in which one of the spheres is in contact with the wall. Here $a = u_{10} = u_{20} = 1/10$.

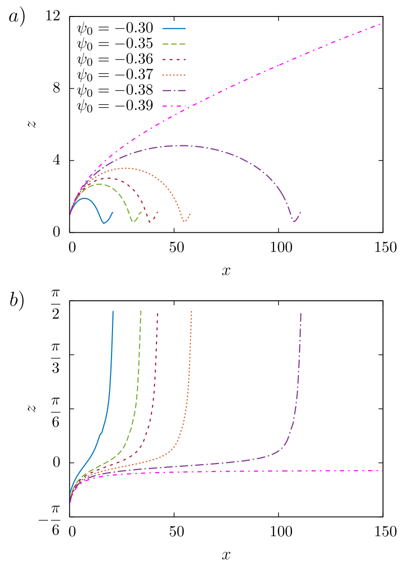

FIG. 3. Transition from the trapping to the escaping states upon variation of the initial inclination angle ψ_0 while keeping the initial distance from the wall constant at $z_0 = 1$. (a) shows the averaged swimming trajectories for the 2D motion in the plane (x, z) and (b) shows the inclination angle ψ as a function of x.

the inclination angle approaches the steady value corresponding to $\psi \simeq \pi/2$. Indeed, this final state is stable and is found to be independent of the initial orientation of the swimmer with respect to the wall. For $\psi_0 = -0.39$, the swimmer manages to escape from the attraction of the wall and moves along a straight line maintaining a constant orientation, i.e., just as it would be the case in an unbounded fluid.

Figure 4 illustrates the swimming trajectories in the oscillatory gliding state for (a) $\psi_0 = 0$ and (b) $\psi_0 = 0.2$ and various initial heights ranging from $z_0 = 0.5$ to 1.25. We observe that the amplitude of oscillations is strongly dependent on z_0 and eventually vanishes for $\psi_0 = 0$ and $z_0 \simeq 0.75$ giving rise to a steady sliding motion at a constant velocity. The mean inclination angle over one oscillation period amounts to zero and thus the swimmer undergoes motion at a constant mean height above the wall. We further note that the frequency of oscillations has nothing to do with ω which is several orders of magnitude larger.

For future reference, we denote by μ the magnitude of the scaled swimming velocity parallel to the wall averaged over one oscillation period, $\mu := \overline{V_\parallel}/V_0$ where $V_\parallel := \left(V_x^2 + V_y^2\right)^{1/2}$ and V_0 is the magnitude of the bulk swimming velocity given by Eq. (27).

B. Transition between states

We now investigate the swimming behavior more quantitatively and analyze the evolution of relevant order parameters around the transition points between the states.

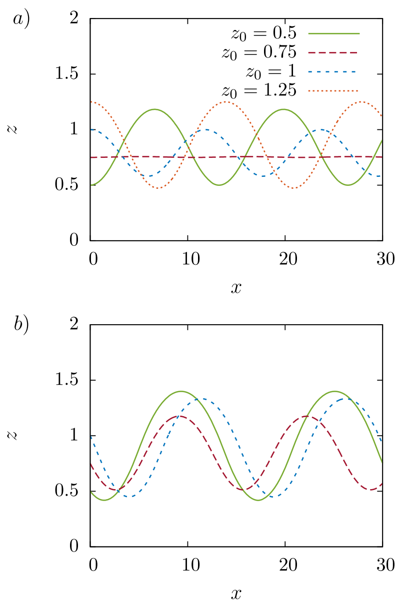

FIG. 4. Typical swimming trajectories in the oscillatory gliding state for different initial distances from the wall where (a) $\psi_0 = 0$ and (b) $\psi_0 = 0.2$. For $z_0 = 1.25$ and $\psi_0 = 0.2$, the swimmer is trapped by the wall and thus the trajectory has not been shown here. The swimmer inclination angle shows a similar oscillatory behavior around a mean angle $\psi = 0$.

1. *Transition between the trapping and escaping states*

In order to probe the transition between the trapping and escaping states, we define an order parameter z_P^{-1} as the inverse of the peak height achieved by the swimmer before it is trapped by the wall [c.f. Fig. 3(a)]. Additionally, we define a second order parameter δ^{-1} as the inverse of the distance along the x direction at which the peak height occurs. Clearly, both z_P^{-1} and δ^{-1} amount to zero for the escaping state and thus can serve as relevant order parameters to characterize the transition between the trapping and escaping states.

In Fig. 5, we present the evolution of the order parameters z_P^{-1} and δ^{-1} around the transition point between the trapping and escaping states along three different horizontal [subfigures (a)–(c)] and vertical [subfigures (d)–(f)] paths in the state diagram presented in Fig. 2. We observe that the inverse peak height z_P^{-1} exhibits a scaling behavior around the transition points with an exponent of 1/3. Similar behavior is displayed by the inverse peak position around the transition points with a scaling exponent of 5/6. We will show in Sec. IV B that these scaling laws can indeed be predicted theoretically by considering a simplified model based on the far-field approximation. It can clearly be seen that even beyond $\psi - \psi_0 = 0.1$ from the transition points, the scaling law is still approximatively obeyed. Despite its simplicity, the presented far-field model leads to a good prediction of the scaling behavior of these two order parameters around the transition points.

2. *Transition between the trapping and oscillatory-gliding states*

In the oscillatory-gliding state, the swimmer remains on average at the same height above the wall such that $\overline{V_z} = 0$ and translates at a constant velocity parallel to the wall. In order to study the transition between the trapping and oscillatory-gliding states, we utilize the scaled mean swimming velocity parallel to the wall, averaged over one oscillation period as a relevant order parameter, $\mu = \overline{V_x}/V_0$, where again V_0 is the magnitude of the swimming velocity in an unbounded fluid domain. Additionally, we define a second order parameter A as the amplitude of oscillations.

In Fig. 6, we present the evolution of the order parameters μ and A at the transition points between the oscillatory-gliding and trapping states along three different horizontal paths in the state diagram. The mean swimming velocity [Fig. 6(a)] is found to be about 5% lower than the bulk velocity and is weakly dependent on the initial orientation or distance from the wall. In the trapping state, the swimmer points toward the wall and remains at a constant height above the wall to attain a stable hovering state. Therefore, in this situation, both of the two order parameters μ and A vanish. The transition from the oscillatory-gliding and trapping states is thus first order, characterized by a discontinuity in the relevant order parameters. We further remark that the amplitudes of oscillations [Fig. 6(b)] reach a maximum value of about 1.2 around the transition points between the oscillatory-gliding and trapping states. Moreover, for $\psi_0 = 0$, the amplitude of oscillations is minimal and eventually vanishes for

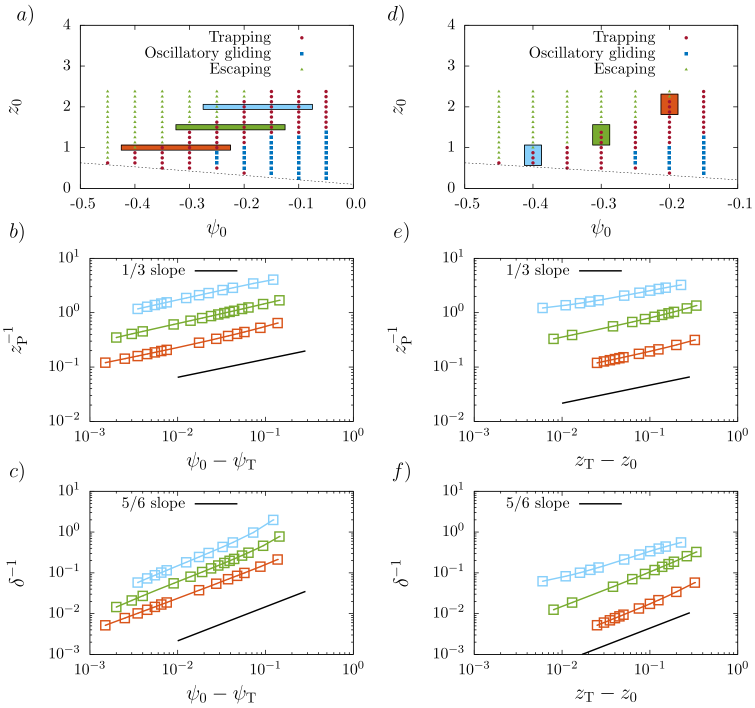

FIG. 5. Log-log plots of order parameters z_P^{-1} and δ^{-1} at the transition point between the trapping and escaping states in the 2D case for $\omega_{13} = \omega_{21} = 0$, as obtained from the numerical simulations. Here z_T and ψ_T denote, respectively, the swimmer height and inclination at the transition point between the trapping and escaping states. For the sake of readability, the curves associated with the green and blue paths are shifted on the vertical scale by factors of 3 and 9, respectively. The solid lines are a guide for the eye.

$z_0 \simeq 0.75$, leading to a pure gliding motion of vanishing amplitude, parallel to the wall. Both order parameters are found to be symmetric with respect to $\psi_0 = 0$, and thus (z_0, ψ_0) and $(z_0, -\psi_0)$ represent identical dynamical states along these considered paths.

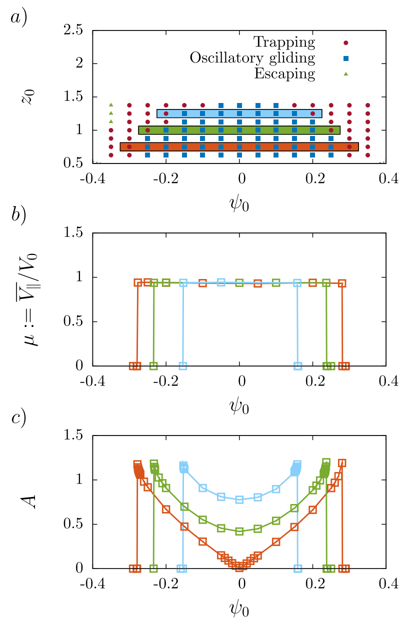

FIG. 6. Evolution of the order parameters (b) μ and (c) A versus the initial inclination angle ψ_0 at the transition between the trapping and oscillatory gliding states for various horizontal paths along the state diagram. (a) displays a part of the state diagram shown in Fig. 2.

In Sec. IV, we will present a far-field model for the near-wall swimming and provide theoretical arguments for the scaling behavior observed at the transition between the trapping and escaping states.

IV. FAR-FIELD MODEL

In order to address the swimming behavior in the far-field limit, we expand the averaged translational velocity and rotation rate of the swimmer as power series in the ratio $1/z$. We further employ the far-field expressions of the hydrodynamic mobility functions which can adequately be expressed as power series in the ratio a/z. Up to the second order in a, and by accounting for the leading order in $1/z$ only, the differential equations governing the averaged dynamics of the swimmer far away from the wall read

$$\frac{\mathrm{d}x}{\mathrm{d}t} = -aK\cos\psi\left(\frac{7}{24} + \frac{3\sin^2\psi\left(12-\cos^2\psi\right)}{64z^3} + a\left(\frac{5}{24} + \frac{620 - 453\cos^2\psi + 120\cos^4\psi}{1024z^3}\right)\right), \tag{28a}$$

$$\frac{\mathrm{d}z}{\mathrm{d}t} = aK\sin\psi\left(\frac{7}{24} + \frac{3\left(8 - 16\cos^2\psi + \cos^4\psi\right)}{64z^3} + a\left(\frac{5}{24} + \frac{158 - 111\cos^2\psi + 30\cos^4\psi}{256z^3}\right)\right), \tag{28b}$$

$$\frac{d\psi}{dt} = -\frac{9aK}{512z^4}\cos\psi\left(56 - 52\cos^2\psi + 11\cos^4\psi + \frac{a}{2}\left(68 - 31\cos^2\psi + 8\cos^4\psi\right)\right). \tag{28c}$$

The wall-induced correction to the swimmer translational velocities decays in the far field as z^{-3}, whereas its angular velocity undergoes a decay as z^{-4}. Therefore, the flow field induced by a neutral three-linked sphere swimmer near a wall resembles that of a microorganism whose flow field is modeled as a force quadrupole or a source dipole.

We recall that the swimming trajectories resulting from quadrupolar hydrodynamic interactions as derived from Faxén's law for a prolate ellipsoid of aspect ratio γ tilted an angle ψ and located a distance z above a rigid wall read[120]

$$\frac{dx}{dt} = \cos\psi\left(V_0 + \frac{\sigma}{16z^3}\left(27\cos^2\psi - 20\right)\right), \tag{29a}$$

$$\frac{dz}{dt} = -\sin\psi\left(V_0 + \frac{\sigma}{4z^3}\left(9\cos^2\psi - 2\right)\right), \tag{29b}$$

$$\frac{d\psi}{dt} = \frac{3\sigma\cos\psi}{32z^4}\left(8(\Gamma-1) + 6(\Gamma+2)\cos^2\psi - 3\Gamma\cos^4\psi\right), \tag{29c}$$

where V_0 is the propulsion velocity in a bulk fluid, i.e., far away from boundaries and $\Gamma := (\gamma^2 - 1)/(\gamma^2 + 1)$ is the shape factor. In addition, σ is the quadrupole strength (has the dimension of velocity $\times$ length^3) where $\sigma > 0$ for swimmers with small bodies and elongated flagella and $\sigma < 0$ in the opposite situation.[3,121] The equations governing the dynamics of a swimming microorganism near a wall, whose generated flow field is modeled as a source dipole, read[120]

$$\frac{dx}{dt} = \cos\psi\left(V_0 - \frac{\alpha}{4z^3}\right), \tag{30a}$$

$$\frac{dz}{dt} = -\sin\psi\left(V_0 - \frac{\alpha}{z^3}\right), \tag{30b}$$

$$\frac{d\psi}{dt} = -\frac{3\alpha\cos\psi}{16z^4}\left(2 + 3\Gamma(2 - \cos^2\psi)\right), \tag{30c}$$

where α is the source dipole strength (has the dimension of velocity $\times$ length^3) such that $\alpha > 0$ for ciliated swimming organisms which rely on local surface deformation to propel themselves through the fluid[3] and $\alpha < 0$ for non-ciliated microorganisms with helical flagella. Therefore, the effect of the wall on the dynamics of a three-linked sphere swimmer can conveniently be modeled as a superposition of a quadrupole of strength $\sigma > 0$ and a source dipole of strength $\alpha < 0$.

Notably, in the limit $z \to \infty$, Eqs. (28a) and (28b) reduce to Eq. (27) providing the swimming velocity in an unbounded bulk fluid. We further note that the asymptotic results derived in Ref. 109 have been reported with an erroneous far field decay that we correct here.

A. Approximate swimming trajectories

For small inclination angles relative to the horizontal plane such that $\psi \ll 1$, the sine and cosine functions can be approximated using Taylor series expansions around $\psi = 0$ where $\sin\psi \sim \psi$ and $\cos\psi \sim 1$. We have checked that accounting for the term with ψ^2 in the series expansion of cos ψ has a negligible effect on the swimming trajectories and thus has been discarded here for simplicity. Further, restricting to the leading order in a, Eqs. (28) can thus be approximated as

$$\frac{dx}{dt} = -\frac{7}{24}aK, \tag{31a}$$

$$\frac{dz}{dt} = aK\left(\frac{7}{24} - \frac{21}{64}\frac{1}{z^3}\right)\psi, \tag{31b}$$

$$\frac{d\psi}{dt} = -\frac{135}{512}\frac{aK}{z^4}. \tag{31c}$$

Based on these equations, we now derive approximate swimming trajectories analytically. By combining Eqs. (31b) and (31c) and eliminating the time differential dt, the equation relating the swimmer inclination to its vertical position reads

$$\psi\, d\psi = -\frac{405}{56}\frac{dz}{z(8z^3 - 9)}, \tag{32}$$

which can readily be solved subject to the initial condition of inclination and distance from the wall (ψ_0, z_0) to obtain

$$\exp\left(\frac{28}{15}\left(\psi^2 - \psi_0^2\right)\right) = \frac{z^3}{z_0^3}\frac{8z_0^3 - 9}{8z^3 - 9}. \tag{33}$$

When the swimmer reaches its peak position, the inclination angle necessarily vanishes (provided that the swimmer is initially pointing away from the wall such that $\psi_0 < 0$). Solving Eq. (33) for $\psi = 0$, the peak height can thus be estimated as

$$z_P = \frac{z_0}{\left(H + \frac{8}{9}(1 - H)z_0^3\right)^{1/3}}, \tag{34}$$

where we have defined the parameter $H \simeq 1 + \beta\psi_0^2$ with $\beta = 28/15$.

B. Order parameters

1. Inverse peak height z_P^{-1}

We now calculate the first order parameter z_P^{-1} governing the transition between the trapping and the escaping states, defined in Sec. III B as the inverse of the peak height,

$$z_P^{-1} = \frac{1}{z_0}\left(H + \frac{8}{9}(1 - H)z_0^3\right)^{1/3}. \tag{35}$$

At the transition to the escaping state, the order parameter z_P^{-1} amounts to zero. For a given initial inclination ψ_0, the transition height is estimated as

$$z_T = \frac{1}{2}\left(\frac{9H}{H - 1}\right)^{1/3}. \tag{36}$$

Similarly, the inclination angle at the transition point between the trapping and the escaping states for a given initial vertical distance z_0 reads

$$\psi_\mathrm{T} = -\frac{1}{14}\left(\frac{105}{\frac{8}{9}z_0^3 - 1}\right)^{1/2}. \tag{37}$$

The scaling behavior of the order parameter z_P^{-1} around the transition point can readily be obtained by performing a Taylor series expansion around $\psi_0 = \psi_\mathrm{T}$ and $z_0 = z_\mathrm{T}$ to obtain

$$z_\mathrm{P}^{-1} = \frac{1}{z_0}\left(\frac{2}{-\psi_\mathrm{T}}\right)^{1/3} (\psi_0 - \psi_\mathrm{T})^{1/3} + \mathcal{O}\left((\psi_0 - \psi_\mathrm{T})^{4/3}\right), \tag{38a}$$

$$z_\mathrm{P}^{-1} = \frac{(3H)^{1/3}}{z_\mathrm{T}^{4/3}} (z_\mathrm{T} - z_0)^{1/3} + \mathcal{O}\left((z_\mathrm{T} - z_0)^{4/3}\right). \tag{38b}$$

Therefore, the transition between the trapping and escaping states is continuous and characterized by a scaling exponent 1/3 of the order parameter.

2. *Inverse peak position δ^{-1}*

We next calculate the second order parameter δ^{-1}, defined earlier as the inverse of the horizontal position δ corresponding to the occurrence of the peak, i.e., $z(x = \delta) = z_\mathrm{P}$. Combining Eqs. (31a) and (31c) together, we obtain

$$\frac{\mathrm{d}x}{\mathrm{d}\psi} = \frac{448}{405} z^4, \tag{39}$$

where the ψ-dependence of the variable z can readily be obtained from Eq. (33) and is expressed as

$$z = \frac{r^{1/3} z_0}{\left(1 + \frac{8}{9}(r-1)z_0^3\right)^{1/3}}, \tag{40}$$

where we have defined

$$r \simeq 1 + \beta\left(\psi^2 - \psi_0^2\right). \tag{41}$$

By inserting Eq. (40) into Eq. (39), making the change of variable $r = 1 - \beta\psi_0^2 v$, and noting the relation between the differentials,

$$\mathrm{d}\psi = -\frac{1}{2\beta}\frac{\mathrm{d}r}{\left(\psi_0^2 + \beta^{-1}(r-1)\right)^{1/2}}, \tag{42}$$

the x-position corresponding to the occurrence of the peak follows forthwith upon integration of both sides of the resulting differential equation to obtain

$$\delta = -\frac{224}{405} z_0^4 \psi_0 \int_0^1 \left(\frac{1 - \beta\psi_0^2 v}{1 - \frac{8}{9}\beta\psi_0^2 z_0^3 v}\right)^{4/3} \frac{\mathrm{d}v}{(1-v)^{1/2}}. \tag{43}$$

Unfortunately, the latter integral cannot be solved analytically for arbitrary values of ψ_0 and z_0. In order to overcome this difficulty, we may have recourse to approximate analytical tools. Clearly, there are no issues coming from the factor $\left(1 - \beta\psi_0^2 v\right)^{4/3}(1-v)^{-1/2}$ since it is well behaved and integrable in the interval [0, 1]. However, difficulties arise from the factor $\left(1 - \frac{8}{9}\beta\psi_0^2 z_0^3 v\right)^{-4/3}$, in which, for $\psi_0^2 z_0^3 = 9/(8\beta)$, the denominator vanishes leading to a singularity of order −4/3 in addition to −1/2 coming from the $(1-v)^{-1/2}$ factor.

In order to proceed further and probe the behavior near the transition points, we approximate a factor which is well behaved at the singular point and put $\left(1 - \beta\psi_0^2 v\right)^{4/3} \simeq \left(1 - \beta\psi_0^2\right)^{4/3}$ since the singularity would be located at $v = 1$. Accordingly, the integral in Eq. (43) can be evaluated analytically, leading to

$$\delta \simeq -\frac{448}{405} z_0^4 \psi_0 \left(1 - \beta\psi_0^2\right)^{4/3} {}_2F_1\left(1, \frac{4}{3}; \frac{3}{2}; \frac{8}{9}\beta\psi_0^2 z_0^3\right),$$

where ${}_2F_1$ denotes the hypergeometric function[122] which for $x \to 1$ can conveniently be approximated as

$${}_2F_1\left(1, \frac{4}{3}; \frac{3}{2}; x\right) \sim \frac{\pi^{3/2}}{\Gamma(1/6)\,\Gamma(4/3)} (1-x)^{-5/6}, \tag{44}$$

where Γ denotes the Gamma function.[122]

The evolution of the second order parameter δ^{-1} around the transition points reads

$$\delta^{-1} \sim -\frac{\Lambda}{z_0^4 \psi_0}\left(1 - \beta\psi_0^2\right)^{-4/3}\left(1 - \frac{8}{9}\beta\psi_0^2 z_0^3\right)^{5/6}, \tag{45}$$

with the prefactor

$$\Lambda := \frac{405}{448}\frac{\Gamma(1/6)\,\Gamma(4/3)}{\pi^{3/2}}. \tag{46}$$

For a given initial distance from the wall, the transition angle is estimated as $\psi_\mathrm{T} = -3/\left(8\beta z_0^3\right)^{1/2}$ and thus

$$\delta^{-1} \sim (\psi_0 - \psi_\mathrm{T})^{5/6}, \tag{47}$$

around the transition point, bearing in mind that ψ_0 and ψ_T are both negative quantities. Similarly, by considering a given initial inclination ψ_0, the transition is expected to occur at a height $z_\mathrm{T} = \frac{1}{2}\left(9/(\beta\psi_0^2)\right)^{1/3}$ and thus

$$\delta^{-1} \sim (z_\mathrm{T} - z_0)^{5/6}, \tag{48}$$

around the transition point. Indeed, these scaling behaviors of the order parameters as derived from the far-field model are in a good agreement with the numerical results presented in Fig. 5.

Even though the far-field model is found to be able to capture the scaling behavior around the transition point between the escaping and trapping states, it is worth mentioning that this model nonetheless is not viable for predicting the swimming trajectories accurately. As the swimmer gets to a finite distance close to the wall, the far-field approximation is not strictly valid. An accurate analytical prediction of the swimming trajectories would thus require to account for the general z-dependence of the averaged swimming velocities and inclination.

V. EFFECT OF ROTATION

A. State diagram

Having investigated the state diagram of swimming near a wall in the absence of rotation, and provided an analytical theory rationalizing our findings on the basis of a far-field model, we next consider the situation where the spheres are allowed to rotate around the swimming axis. For flagellated bacteria, e.g., *E. coli*, which swim by the action of molecular rotary motors, the flagellum undergoes counterclockwise rotation (when viewed from behind the swimmer) at speeds of ∼100 Hz,[123,124] whereas the cell body rotates in the clockwise direction for the bacterium to remain torque-free, at speeds of ∼10 Hz.[125,126] Based on these observations, we assume that the spheres 1 and 3 rotate at the same rotation rate to mimic the rotating flagellum such that $\omega_{13} = 0$, whereas the sphere 2 represents the cell body that rotates in the opposite direction. Accordingly, $\omega_1 = \omega_3 < 0$ and $\omega_2 > 0$, and thus the relative rotation rate $\omega_{21} \equiv \omega_2 - \omega_1$ has to be positive.

In Fig. 7, we present the state diagram of the swimming behavior near a wall for two different values of the relative rotation rate ω_{21}. We observe that the state diagram is qualitatively similar to that obtained in the 2D case, shown in Fig. 2, where three distinct states of motion occur depending on the initial orientation and distance from the wall. The main difference is that the oscillatory-gliding state found earlier is substituted by an oscillatory circling in the clockwise direction, at a constant mean height above the wall. Indeed, the clockwise motion in circles has been observed experimentally for swimming *E. coli* bacteria near surfaces[83] and is a natural consequence of the fluid-mediated hydrodynamics interactions with the neighboring interface and the force- and torque-free constraints imposed on the swimmer.[126]

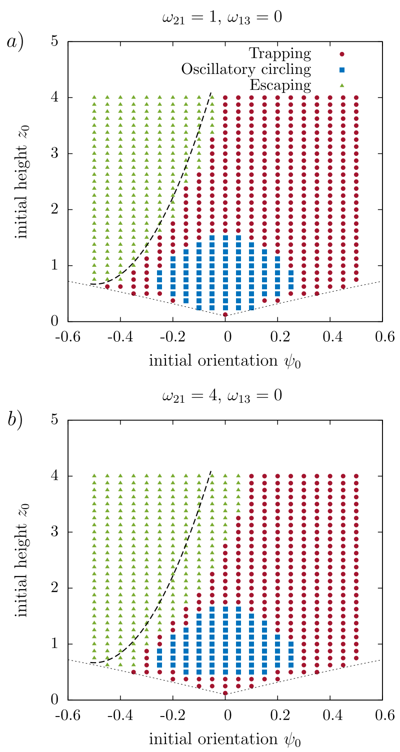

FIG. 7. State diagram of swimming near a hard wall for a non-vanishing angular velocity along the swimming axis where (a) $\omega_{21} = 1$ and (b) $\omega_{21} = 4$. Here $\omega_{13} = 0$. The dashed line displays the boundary at the transition between the trapping and escaping states for the non-rotating system ($\omega_{21} = \omega_{13} = 0$). The other parameters are the same as in Fig. 2.

Upon increasing the rotation rate, we observe that the escaping state is enhanced to the detriment of the trapping state. For instance, for $\omega_{13} = 4$ [Fig. 7(b)], even though the swimmer is initially pointing toward the wall at an angle $\psi_0 = 0.05$, it can surprisingly escape the wall trapping if $z_0 \geq 3.5$. This behavior is most probably attributed to the wall-induced hydrodynamic coupling between the translational and rotational motions, which tends to align the swimmer away from the wall. We further observe that increasing the rotation rate favors the trapping of the swimmer if it is initially released from distance close to the wall, for $z_0 < 0.5$.

B. Transition between states

1. Transition between the trapping and escaping states

As in the 2D case, we define two relevant order parameters z_P^{-1} and δ^{-1} quantifying the state transition between the trapping and escaping states. We keep the definition of the first order parameter z_P^{-1} as the inverse of the peak height. By considering the 2D projection of the trajectory on the (xy) plane, we define the second order parameter δ^{-1} for the 3D motion as the inverse of the curvilinear distance along the projected path, corresponding to the occurrence of the peak.

In Fig. 8, we present a log-log plot of the order parameters z_P^{-1} and δ^{-1} versus $\psi_0 - \psi_T$ [subfigures (a)–(c)], and versus $z_T - z_0$ [subfigures (d)–(f)] along example paths on the state diagram shown in Fig. 7(a), for $\omega_{21} = 1$. We observe that both order parameters exhibit analogous scaling behavior around the transition point as in the 2D case. We will show that the general 3D case can approximatively be mapped into a 2D representational model by considering the local reference frame along the curvilinear coordinate line. Nevertheless, the power laws predicted analytically may not be strictly obeyed as the scaling exponents 1/3 and 5/6 derived above may not be displayed properly, notably along the vertical paths in the state diagram [Figs. 8(e) and 8(f)]. This mismatch is most probably a drawback of the simplistic approximations involved in the analytical theory proposed here for the rotating system whose derivation is outlined in Sec. V C 2.

2. Transition between the trapping and oscillatory-circling states

We next consider the transition between the trapping and oscillatory-gliding states and define in a similar way, as in the 2D case, two relevant order parameters controlling the state transition. As before, we define the first order parameter as the magnitude of the scaled swimming velocity parallel to the wall averaged over one oscillation period, $\mu := \overline{V_\parallel}/V_0$. The second order parameter A is defined in an analogous way as the amplitude of the oscillations. The evolution of the order parameters has basically a similar behavior to that shown in Fig. 6 where the transition between the oscillatory-circling

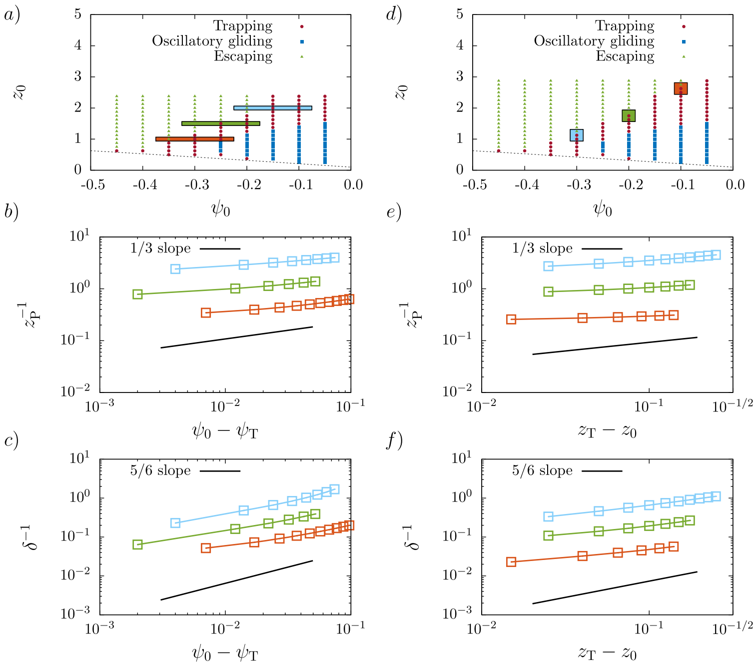

FIG. 8. Log-log plots of the first and second order parameters at the transition point between the trapping and escaping states in the 3D case for $\omega_{21} = 1$ and $\omega_{13} = 0$, as obtained from the numerical simulations. The curves associated with the green and blue paths are, respectively, shifted for the sake of readability on the vertical scale by factors of 3 and 9. The solid lines are a guide for the eye.

and trapping states is found also to be first order discontinuous (see Fig. 1 in the supplementary material for further details).

In the following, we present an extension of the far-field model presented in Sec. IV in order to assess the effect of the rotational motion of the spheres on the swimmer dynamics.

C. Far-field model

1. Pure rotational motion

We first consider the situation where $K = 0$ and confine ourselves for simplicity to the case where the swimmer is aligned parallel to the wall for which $\psi = 0$. The system of equations governing the swimmer dynamics at leading order in a reads

$$\frac{\mathrm{d}x}{\mathrm{d}t} = -a^5 M(z)\sin\phi, \tag{49a}$$

$$\frac{\mathrm{d}y}{\mathrm{d}t} = a^5 M(z)\cos\phi, \tag{49b}$$

$$\frac{\mathrm{d}\phi}{\mathrm{d}t} = -a^5 Q(z), \tag{49c}$$

$$\frac{\mathrm{d}\theta}{\mathrm{d}t} = 0, \tag{49d}$$

where we have defined

$$Q(z) := \frac{\omega_{13} + 2\omega_{21}}{24}\left(\frac{1}{z^4} - \frac{z}{\xi^5}\right) + 2M(z) \tag{50}$$

and

$$M(z) := \left(\frac{1}{24z^4} - \frac{4z}{3\zeta^5}\right)(\omega_{13} - \omega_{21}), \tag{51}$$

wherein $\zeta := \left(1 + 4z^2\right)^{1/2}$ and $\xi := \left(1 + z^2\right)^{1/2}$. It can be seen that if $\omega_{13} = \omega_{21}$, for which the rotation rate of the central sphere is the average of the rotation rates of the spheres 2 and 3, the translational velocity vanishes and thus the swimmer undergoes a pure rotational motion around the central sphere. For $\omega_{13} = 0$, the rotation rate $\dot{\phi}$ has a maximum value for $z \approx 0.2448$ and exhibits a decay as z^{-6} in the far-field limit.

2. Combined translation and rotation

We next combine the translational and rotational motions and write approximate equations governing the dynamics of the swimmer. As can be inferred from Eqs. (49), the leading-order terms in the swimming velocities for a pure rotational motion scale as a.[5] For the translational motion ($K \neq 0$), we have shown that at leading order, these velocities scale linearly with a [c.f. Eqs. (31)]. Therefore, the approximated governing equations about $\psi = 0$ for the combined translational and rotational motions are given by

$$\frac{\mathrm{d}x}{\mathrm{d}t} = -\frac{7}{24}aK\cos\phi, \tag{52a}$$

$$\frac{\mathrm{d}y}{\mathrm{d}t} = -\frac{7}{24}aK\sin\phi, \tag{52b}$$

$$\frac{\mathrm{d}z}{\mathrm{d}t} = aK\left(\frac{7}{24} - \frac{21}{64}\frac{1}{z^3}\right)\psi, \tag{52c}$$

$$\frac{\mathrm{d}\psi}{\mathrm{d}t} = -\frac{135}{512}\frac{aK}{z^4}, \tag{52d}$$

$$\frac{\mathrm{d}\phi}{\mathrm{d}t} = -a^5 Q(z). \tag{52e}$$

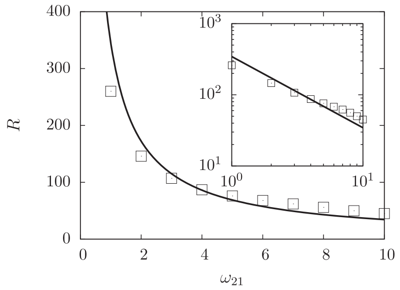

FIG. 9. Radius of curvature versus the scaled relative rotation rate ω_{21}. Solid line is the analytical prediction stated by Eq. (54) and symbols are the numerical simulations. The inset shows the same plot in a log-log scale.

Defining the curvilinear coordinate s along the projection of the particle trajectory on the (xy) plane such that $\mathrm{d}s^2 = \mathrm{d}x^2 + \mathrm{d}y^2$, Eqs. (52a) and (52b) yield

$$\frac{\mathrm{d}s}{\mathrm{d}t} = -\frac{7}{24}\, aK. \tag{53}$$

The system of equations composed of (52c), (52d), and (53) is mathematically equivalent to that earlier derived in the 2D case and stated by Eqs. (31). In the far-field limit, the effect of the rotation of the spheres along the swimmer axis intervenes only through Eq. (52e) describing the temporal change of the azimuthal angle ϕ. Therefore, by appropriately redefining the second order parameter δ^{-1} as the curvilinear coordinate corresponding to the peak height, the order parameters z_P^{-1} and δ^{-1} are expected to exhibit the same scaling behavior as in the 2D case.

Finally, we calculate the radius of curvature of the swimming trajectory in the special case when $\psi_0 = 0$ and $z_0 = 0.75$ for which the swimmer remains typically at a constant height above the wall. According to Eq. (52e), the azimuthal angle changes linearly with time, and thus the swimmer performs a circular trajectory of radius

$$R = \frac{7}{24}\frac{|K|}{a^4 Q(z_0)} \sim \omega_{21}^{-1}, \tag{54}$$

for $\omega_{13} = 0$. Interestingly, the radius of curvature decays as a fourth power with a, while it decreases linearly with the relative angular velocity ω_{21}. Figure 9 shows a quantitative comparison between analytical predictions and numerical simulations over a wide range of relative rotation rates. While the numerical results show a slightly slower decay with ω_{21}, the agreement is reasonable considering the approximations involved in the analytical theory.

VI. CONCLUSIONS

Inspired by the role of near-wall hydrodynamic interactions on the dynamics of living systems, particularly swimming bacteria[127] and the formation of biofilms,[107] we have explored the behavior of a simple model three-sphere swimmer proposed by Najafi and Golestanian[9] in the presence of a wall. Modeling the swimmer by three aligned spherical beads with periodically time-varying mutual distances, we have analyzed the long-time asymptotic behavior of the swimmer depending on its initial distance and orientation with respect to the wall. We have found that there are three regimes of motion, leading to either trapping of the swimmer at the wall, escape from the wall, or a non-trivial oscillatory gliding motion at a finite distance above the wall. We have found that these three states persist also when we allow the beads to rotate. The rotational motion of the beads, introduced to mimic to the rotation of a cell flagellum and a counter-rotation of its body, renders the near-wall motion of the swimmer fully three-dimensional, as opposed to the quasi-two-dimensional motion in the classic Najafi and Golestanian design.

Having classified the swimming behavior, we have quantified the transition between different states by introducing the appropriate order parameters and measuring their scaling with the initial height and orientation. Using the far-field analytical calculations, we have shown that the scaling exponents obtained from numerical solutions of the equations of motion of the swimmer can be found exactly from the dominant asymptotic behavior of the flow field. Moreover, we have demonstrated that in the presence of internal rotation, the three-dimensional dynamics in the far-field approach can be mapped onto a quasi-two-dimensional model and thus the scalings found in both cases remain the same. We have verified the analytical predictions with numerical solutions, finding very good agreement. This suggests that in order to grasp the general complex dynamics of the swimmer near an interface, it is sufficient to include the dominant flow field.

In view of recent experimental realizations of the three-sphere swimmer using optical tweezers,[14,15] we hope that the findings of this paper may be verified experimentally. On one hand, it would be interesting to see the purely translational case, varying only the distances between spheres. It might prove more challenging to construct a swimmer that would actually be capable of performing an internal rotation, yet it is an exciting perspective due to the relevance of this simple model to the widely used singularity representations for swimming microorganisms near interfaces.[101]

SUPPLEMENTARY MATERIAL

See supplementary material for the elements of the matrix resulting from the linear system of equations governing the generalized motion of a three-sphere swimmer near a wall given by (11), (14), (18), and (19). In addition, we provide the far-field expressions of the mobility functions used in the analytical model. Finally, we present the evolution of the order parameters A and μ in the oscillatory circling state associated with the 3D system.

The movies 1 and 2 illustrate a swimmer initially released from $z_0 = 1$ at $\psi_0 = -0.38$ (trapping) and $\psi_0 = -0.39$ (escaping). The movies 3 and 4 illustrate the oscillatory-gliding state for $\psi_0 = 0$, for a swimmer initially released from $z_0 = 0.75$ and $z_0 = 1$. The movie 5 shows the oscillatory circling state of a swimmer initially located at $z_0 = 1$ above the wall, released at an angle $\psi_0 = 0$ for $\omega_{21} = 2$ and $\omega_{13} = 0$.

ACKNOWLEDGMENTS

The authors gratefully acknowledge support from the DFG (Deutsche Forschungsgemeinschaft)–SPP 1726. This work has been supported by the Ministry of Science and Higher Education of Poland via the Mobility Plus Fellowship awarded to M.L. M.L. acknowledges funding from the Foundation for Polish Science within the START programme. This article is based upon work from COST Action MP1305, supported by COST (European Cooperation in Science and Technology).

[1] C. Brennen and H. Winet, "Fluid mechanics of propulsion by cilia and flagella," Annu. Rev. Fluid Mech. **9**, 339–398 (1977).
[2] E. M. Purcell, "Life at low Reynolds number," Am. J. Phys. **45**, 3–11 (1977).
[3] E. Lauga and T. R. Powers, "The hydrodynamics of swimming microorganisms," Rep. Prog. Phys. **72**, 096601 (2009).
[4] M. C. Marchetti, J. F. Joanny, S. Ramaswamy, T. B. Liverpool, J. Prost, M. Rao, and R. A. Simha, "Hydrodynamics of soft active matter," Rev. Mod. Phys. **85**, 1143 (2013).
[5] J. Elgeti, R. G. Winkler, and G. Gompper, "Physics of microswimmers—single particle motion and collective behavior: A review," Rep. Prog. Phys. **78**, 056601 (2015).
[6] C. Bechinger, R. Di Leonardo, H. Löwen, C. Reichhardt, G. Volpe, and G. Volpe, "Active particles in complex and crowded environments," Rev. Mod. Phys. **88**, 045006 (2016).
[7] A. Zöttl and H. Stark, "Emergent behavior in active colloids," J. Phys.: Condens. Matter **28**, 253001 (2016).
[8] E. Lauga, "Bacterial hydrodynamics," Annu. Rev. Fluid Mech. **48**, 105–130 (2016).
[9] A. Najafi and R. Golestanian, "Simple swimmer at low Reynolds number: Three linked spheres," Phys. Rev. E **69**, 062901 (2004).
[10] A. Najafi and R. Golestanian, "Propulsion at low Reynolds number," J. Phys.: Condens. Matter **17**, S1203 (2005).
[11] R. Golestanian and A. Ajdari, "Analytic results for the three-sphere swimmer at low Reynolds number," Phys. Rev. E **77**, 036308 (2008).
[12] R. Golestanian and A. Ajdari, "Mechanical response of a small swimmer driven by conformational transitions," Phys. Rev. Lett. **100**, 038101 (2008).
[13] G. P. Alexander, C. M. Pooley, and J. M. Yeomans, "Hydrodynamics of linked sphere model swimmers," J. Phys.: Condens. Matter **21**, 204108 (2009).
[14] M. Leoni, J. Kotar, B. Bassetti, P. Cicuta, and M. C. Lagomarsino, "A basic swimmer at low Reynolds number," Soft Matter **5**, 472–476 (2009).
[15] G. Grosjean, M. Hubert, G. Lagubeau, and N. Vandewalle, "Realization of the Najafi-Golestanian microswimmer," Phys. Rev. E **94**, 021101 (2016).
[16] A. Montino and A. DeSimone, "Three-sphere low-Reynolds-number swimmer with a passive elastic arm," Eur. Phys. J. E **38**, 42 (2015).
[17] A. Montino and A. DeSimone, "Dynamics and optimal actuation of a three-sphere low-Reynolds-number swimmer with muscle-like arms," Acta Appl. Math. **149**, 53–86 (2017).
[18] J. Pande and A.-S. Smith, "Forces and shapes as determinants of micro-swimming: Effect on synchronisation and the utilisation of drag," Soft Matter **11**, 2364–2371 (2015).
[19] J. Pande, L. Merchant, T. Krüger, J. Harting, and A.-S. Smith, "Effect of body deformability on microswimming," Soft Matter **13**, 3984–3993 (2017).
[20] S. Babel, H. Löwen, and A. M. Menzel, "Dynamics of a linear magnetic 'microswimmer molecule'," Europhys. Lett. **113**, 58003 (2016).
[21] R. Ledesma-Aguilar, H. Löwen, and J. M. Yeomans, "A circle swimmer at low Reynolds number," Eur. Phys. J. E **35**, 70 (2012).
[22] R. Dreyfus, J. Baudry, and H. A. Stone, "Purcell's 'rotator': Mechanical rotation at low Reynolds number," Eur. Phys. J. B **47**, 161–164 (2005).
[23] M. S. Rizvi, A. Farutin, and C. Misbah, "Three-bead steering microswimmers," Phys. Rev. E **97**, 023102 (2018).
[24] B. U. Felderhof, "The swimming of animalcules," Phys. Fluids **18**, 063101 (2006).
[25] O. S. Pak, L. Zhu, L. Brandt, and E. Lauga, "Micropropulsion and microrheology in complex fluids via symmetry breaking," Phys. Fluids **24**, 103102 (2012).
[26] L. Zhu, E. Lauga, and L. Brandt, "Self-propulsion in viscoelastic fluids: Pushers vs. pullers," Phys. Fluids **24**, 051902 (2012).
[27] M. P. Curtis and E. A. Gaffney, "Three-sphere swimmer in a nonlinear viscoelastic medium," Phys. Rev. E **87**, 043006 (2013).
[28] S. Yazdi, A. M. Ardekani, and A. Borhan, "Locomotion of microorganisms near a no-slip boundary in a viscoelastic fluid," Phys. Rev. E **90**, 043002 (2014).
[29] S. Yazdi, A. M. Ardekani, and A. Borhan, "Swimming dynamics near a wall in a weakly elastic fluid," J. Nonlinear Sci. **25**, 1153–1167 (2015).
[30] C. Datt, L. Zhu, G. J. Elfring, and O. S. Pak, "Squirming through shear-thinning fluids," J. Fluid Mech. **784**, R1 (2015).
[31] S. Yazdi and A. Borhan, "Effect of a planar interface on time-averaged locomotion of a spherical squirmer in a viscoelastic fluid," Phys. Fluids **29**, 093104 (2017).
[32] D. Pimponi, M. Chinappi, P. Gualtieri, and C. M. Casciola, "Hydrodynamics of flagellated microswimmers near free-slip interfaces," J. Fluid Mech. **789**, 514–533 (2016).
[33] A. Domínguez, P. Malgaretti, M. N. Popescu, and S. Dietrich, "Effective interaction between active colloids and fluid interfaces induced by Marangoni flows," Phys. Rev. Lett. **116**, 078301 (2016).
[34] K. Dietrich, D. Renggli, M. Zanini, G. Volpe, I. Buttinoni, and L. Isa, "Two-dimensional nature of the active Brownian motion of catalytic microswimmers at solid and liquid interfaces," New J. Phys. **19**, 065008 (2017).
[35] J. Elgeti and G. Gompper, "Self-propelled rods near surfaces," Europhys. Lett. **85**, 38002 (2009).
[36] L. Zhu, E. Lauga, and L. Brandt, "Low-Reynolds-number swimming in a capillary tube," J. Fluid Mech. **726**, 285–311 (2013).
[37] F. Yang, S. Qian, Y. Zhao, and R. Qiao, "Self-diffusiophoresis of Janus catalytic micromotors in confined geometries," Langmuir **32**, 5580–5592 (2016).
[38] J. Elgeti and G. Gompper, "Microswimmers near surfaces," Eur. Phys. J.: Spec. Top. **225**, 2333–2352 (2016).
[39] C. Liu, C. Zhou, W. Wang, and H. P. Zhang, "Bimetallic microswimmers speed up in confining channels," Phys. Rev. Lett. **117**, 198001 (2016).
[40] G.-J. Li and A. M. Ardekani, "Hydrodynamic interaction of microswimmers near a wall," Phys. Rev. E **90**, 013010 (2014).
[41] G. Grégoire and H. Chaté, "Onset of collective and cohesive motion," Phys. Rev. Lett. **92**, 025702 (2004).
[42] S. Mishra, A. Baskaran, and M. C. Marchetti, "Fluctuations and pattern formation in self-propelled particles," Phys. Rev. E **81**, 061916 (2010).
[43] S. Heidenreich, S. Hess, and S. H. L. Klapp, "Nonlinear rheology of active particle suspensions: Insights from an analytical approach," Phys. Rev. E **83**, 011907 (2011).
[44] A. M. Menzel, "Collective motion of binary self-propelled particle mixtures," Phys. Rev. E **85**, 021912 (2012).
[45] B. Liebchen, M. E. Cates, and D. Marenduzzo, "Pattern formation in chemically interacting active rotors with self-propulsion," Soft Matter **12**, 7259–7264 (2016).
[46] T. Le Goff, B. Liebchen, and D. Marenduzzo, "Pattern formation in polymerizing actin flocks: Spirals, spots, and waves without nonlinear chemistry," Phys. Rev. Lett. **117**, 238002 (2016).
[47] B. Liebchen and D. Levis, "Collective behavior of chiral active matter: Pattern formation and enhanced flocking," Phys. Rev. Lett. **119**, 058002 (2017).
[48] B. Liebchen, D. Marenduzzo, and M. E. Cates, "Phoretic interactions generically induce dynamic clusters and wave patterns in active colloids," Phys. Rev. Lett. **118**, 268001 (2017).
[49] A. M. Menzel, "Unidirectional laning and migrating cluster crystals in confined self-propelled particle systems," J. Phys.: Condens. Matter **25**, 505103 (2013).
[50] F. Kogler and S. H. L. Klapp, "Lane formation in a system of dipolar microswimmers," Europhys. Lett. **110**, 10004 (2015).
[51] P. Romanczuk, H. Chaté, L. Chen, S. Ngo, and J. Toner, "Emergent smectic order in simple active particle models," New J. Phys. **18**, 063015 (2016).
[52] A. M. Menzel, A. Saha, C. Hoell, and H. Löwen, "Dynamical density functional theory for microswimmers," J. Chem. Phys. **144**, 024115 (2016).
[53] J. Tailleur and M. E. Cates, "Statistical mechanics of interacting run-and-tumble bacteria," Phys. Rev. Lett. **100**, 218103 (2008).
[54] J. Palacci, S. Sacanna, A. P. Steinberg, D. J. Pine, and P. M. Chaikin, "Living crystals of light-activated colloidal surfers," Science **339**, 936–940 (2013).
[55] I. Buttinoni, J. Bialké, F. Kümmel, H. Löwen, C. Bechinger, and T. Speck, "Dynamical clustering and phase separation in suspensions of self-propelled colloidal particles," Phys. Rev. Lett. **110**, 238301 (2013).

[56] T. Speck, J. Bialké, A. M. Menzel, and H. Löwen, "Effective Cahn-Hilliard equation for the phase separation of active Brownian particles," Phys. Rev. Lett. **112**, 218304 (2014).

[57] T. Speck, A. M. Menzel, J. Bialké, and H. Löwen, "Dynamical mean-field theory and weakly non-linear analysis for the phase separation of active Brownian particles," J. Chem. Phys. **142**, 224109 (2015).

[58] H. H. Wensink, J. Dunkel, S. Heidenreich, K. Drescher, R. E. Goldstein, H. Löwen, and J. M. Yeomans, "Meso-scale turbulence in living fluids," Proc. Natl. Acad. Sci. U. S. A. **109**, 14308–14313 (2012).

[59] H. H. Wensink and H. Löwen, "Emergent states in dense systems of active rods: From swarming to turbulence," J. Phys.: Condens. Matter **24**, 464130 (2012).

[60] J. Dunkel, S. Heidenreich, K. Drescher, H. H. Wensink, M. Bär, and R. E. Goldstein, "Fluid dynamics of bacterial turbulence," Phys. Rev. Lett. **110**, 228102 (2013).

[61] S. Heidenreich, S. H. L. Klapp, and M. Bär, "Numerical simulations of a minimal model for the fluid dynamics of dense bacterial suspensions," J. Phys.: Conf. Ser. **490**, 012126 (2014).

[62] A. Kaiser, A. Peshkov, A. Sokolov, B. ten Hagen, H. Löwen, and I. S. Aranson, "Transport powered by bacterial turbulence," Phys. Rev. Lett. **112**, 158101 (2014).

[63] S. Heidenreich, J. Dunkel, S. H. L. Klapp, and M. Bär, "Hydrodynamic length-scale selection in microswimmer suspensions," Phys. Rev. E **94**, 020601 (2016).

[64] H. Löwen, "Chirality in microswimmer motion: From circle swimmers to active turbulence," Eur. Phys. J.: Spec. Top. **225**, 2319–2331 (2016).

[65] F. G. Woodhouse and R. E. Goldstein, "Spontaneous circulation of confined active suspensions," Phys. Rev. Lett. **109**, 168105 (2012).

[66] H. Wioland, F. G. Woodhouse, J. Dunkel, J. O. Kessler, and R. E. Goldstein, "Confinement stabilizes a bacterial suspension into a spiral vortex," Phys. Rev. Lett. **110**, 268102 (2013).

[67] H. Wioland, F. G. Woodhouse, J. Dunkel, and R. E. Goldstein, "Ferromagnetic and antiferromagnetic order in bacterial vortex lattices," Nat. Phys. **12**, 341–345 (2016).

[68] F. G. Woodhouse and J. Dunkel, "Active matter logic for autonomous microfluidics," Nat. Commun. **8**, 15169 (2017).

[69] J. Happel and B. J. Bryne, "Viscous flow in multiparticle systems. Motion of a sphere in a cylindrical tube," Ind. Eng. Chem. **46**, 1181–1186 (1954).

[70] H. A. Stone, A. D. Stroock, and A. Ajdari, "Engineering flows in small devices: Microfluidics toward a lab-on-a-chip," Annu. Rev. Fluid Mech. **36**, 381–411 (2004).

[71] T. Squires and S. Quake, "Microfluidics: Fluid physics at the nanoliter scale," Rev. Mod. Phys. **77**, 977 (2005).

[72] E. Lauga, M. Brenner, and H. Stone, "Microfluidics: The no-slip boundary condition," in *Springer handbook of Experimental Fluid Mechanics* (Springer, 2007), pp. 1219–1240.

[73] M. Lisicki, B. Cichocki, S. A. Rogers, J. K. G. Dhont, and P. R. Lang, "Translational and rotational near-wall diffusion of spherical colloids studied by evanescent wave scattering," Soft Matter **10**, 4312–4323 (2014).

[74] M. Lisicki, B. Cichocki, and E. Wajnryb, "Near-wall diffusion tensor of an axisymmetric colloidal particle," J. Chem. Phys. **145**, 034904 (2016).

[75] A. Daddi-Moussa-Ider and S. Gekle, "Hydrodynamic interaction between particles near elastic interfaces," J. Chem. Phys. **145**, 014905 (2016).

[76] B. Rallabandi, B. Saintyves, T. Jules, T. Salez, C. Schönecker, L. Mahadevan, and H. A. Stone, "Rotation of an immersed cylinder sliding near a thin elastic coating," Phys. Rev. Fluids **2**, 074102 (2017).

[77] B. Rallabandi, S. Hilgenfeldt, and H. A. Stone, "Hydrodynamic force on a sphere normal to an obstacle due to a non-uniform flow," J. Fluid Mech. **818**, 407–434 (2017).

[78] A. Daddi-Moussa-Ider, M. Lisicki, and S. Gekle, "Mobility of an axisymmetric particle near an elastic interface," J. Fluid Mech. **811**, 210–233 (2017).

[79] A. Daddi-Moussa-Ider and S. Gekle, "Hydrodynamic mobility of a solid particle near a spherical elastic membrane: Axisymmetric motion," Phys. Rev. E **95**, 013108 (2017).

[80] A. Daddi-Moussa-Ider, M. Lisicki, and S. Gekle, "Hydrodynamic mobility of a solid particle near a spherical elastic membrane. II. Asymmetric motion," Phys. Rev. E **95**, 053117 (2017).

[81] A. Daddi-Moussa-Ider, M. Lisicki, and S. Gekle, "Hydrodynamic mobility of a sphere moving on the centerline of an elastic tube," Phys. Fluids **29**, 111901 (2017).

[82] P. D. Frymier, R. M. Ford, H. C. Berg, and P. T. Cummings, "Three-dimensional tracking of motile bacteria near a solid planar surface," Proc. Natl. Acad. Sci. U. S. A. **92**, 6195–6199 (1995).

[83] W. R. DiLuzio, L. Turner, M. Mayer, P. Garstecki, D. B. Weibel, H. C. Berg, and G. M. Whitesides, "*Escherichia coli* swim on the right-hand side," Nature **435**, 1271–1274 (2005).

[84] A. P. Berke, L. Turner, H. C. Berg, and E. Lauga, "Hydrodynamic attraction of swimming microorganisms by surfaces," Phys. Rev. Lett. **101**, 038102 (2008).

[85] K. Drescher, J. Dunkel, L. H. Cisneros, S. Ganguly, and R. E. Goldstein, "Fluid dynamics and noise in bacterial cell–cell and cell–surface scattering," Proc. Natl. Acad. Sci. U. S. A. **108**, 10940–10945 (2011).

[86] G. Miño, T. E. Mallouk, T. Darnige, M. Hoyos, J. Dauchet, J. Dunstan, R. Soto, Y. Wang, A. Rousselet, and E. Clement, "Enhanced diffusion due to active swimmers at a solid surface," Phys. Rev. Lett. **106**, 048102 (2011).

[87] E. Lushi, V. Kantsler, and R. E. Goldstein, "Scattering of biflagellate microswimmers from surfaces," Phys. Rev. E **96**, 023102 (2017).

[88] K. Ishimoto and E. A. Gaffney, "Squirmer dynamics near a boundary," Phys. Rev. E **88**, 062702 (2013).

[89] M. Contino, E. Lushi, I. Tuval, V. Kantsler, and M. Polin, "Microalgae scatter off solid surfaces by hydrodynamic and contact forces," Phys. Rev. Lett. **115**, 258102 (2015).

[90] J. Dunstan, G. Miño, E. Clement, and S. Soto, "A two-sphere model for bacteria swimming near solid surfaces," Phys. Fluids **24**, 011901 (2012).

[91] W. E. Uspal, M. N. Popescu, S. Dietrich, and M. Tasinkevych, "Rheotaxis of spherical active particles near a planar wall," Soft Matter **11**, 6613–6632 (2015).

[92] W. E. Uspal, M. N. Popescu, S. Dietrich, and M. Tasinkevych, "Self-propulsion of a catalytically active particle near a planar wall: From reflection to sliding and hovering," Soft Matter **11**, 434–438 (2015).

[93] J. Simmchen, J. Katuri, W. E. Uspal, M. N. Popescu, M. Tasinkevych, and S. Sánchez, "Topographical pathways guide chemical microswimmers," Nat. Commun. **7**, 10598 (2016).

[94] Y. Ibrahim and T. B. Liverpool, "The dynamics of a self-phoretic Janus swimmer near a wall," Europhys. Lett. **111**, 48008 (2015).

[95] A. Mozaffari, N. Sharifi-Mood, J. Koplik, and C. Maldarelli, "Self-diffusiophoretic colloidal propulsion near a solid boundary," Phys. Fluids **28**, 053107 (2016).

[96] M. N. Popescu, W. E. Uspal, and S. Dietrich, "Self-diffusiophoresis of chemically active colloids," Eur. Phys. J.: Spec. Top. **225**, 2189–2206 (2016).

[97] F. Rühle, J. Blaschke, J.-T. Kuhr, and H. Stark, "Gravity-induced dynamics of a squirmer microswimmer in wall proximity," New J. Phys. **20**, 025003 (2018).

[98] A. Mozaffari, N. Sharifi-Mood, J. Koplik, and C. Maldarelli, "Self-propelled colloidal particle near a planar wall: A Brownian dynamics study," Phys. Rev. Fluids **3**, 014104 (2018).

[99] D. Crowdy, S. Lee, O. Samson, E. Lauga, and A. E. Hosoi, "A two-dimensional model of low-Reynolds number swimming beneath a free surface," J. Fluid Mech. **681**, 24–47 (2011).

[100] R. Di Leonardo, D. Dell'Arciprete, L. Angelani, and V. Iebba, "Swimming with an image," Phys. Rev. Lett. **106**, 038101 (2011).

[101] D. Lopez and E. Lauga, "Dynamics of swimming bacteria at complex interfaces," Phys. Fluids **26**, 071902 (2014).

[102] S. Das, A. Garg, A. I. Campbell, J. Howse, A. Sen, D. Velegol, R. Golestanian, and S. J. Ebbens, "Boundaries can steer active Janus spheres," Nat. Commun. **6**, 8999 (2015).

[103] K. Schaar, A. Zöttl, and H. Stark, "Detention times of microswimmers close to surfaces: Influence of hydrodynamic interactions and noise," Phys. Rev. Lett. **115**, 038101 (2015).

[104] S. E. Spagnolie, G. R. Moreno-Flores, D. Bartolo, and E. Lauga, "Geometric capture and escape of a microswimmer colliding with an obstacle," Soft Matter **11**, 3396–3411 (2015).

[105] N. Desai, V. A. Shaik, and A. M. Ardekani, "Hydrodynamics-mediated trapping of micro-swimmers near drops," Soft Matter **14**, 264 (2018).

[106] H. Shum and J. M. Yeomans, "Entrainment and scattering in microswimmer-colloid interactions," Phys. Rev. Fluids **2**, 113101 (2017).

[107] M. C. van Loosdrecht, J. Lyklema, W. Norde, and A. J. Zehnder, "Influence of interfaces on microbial activity," Microbiol. Rev. **54**(1), 75–87 (1990).

[108] K. Drescher, Y. Shen, B. L. Bassler, and H. A. Stone, "Biofilm streamers cause catastrophic disruption of flow with consequences for environmental and medical systems," Proc. Natl. Acad. Sci. U. S. A. **110**, 4345–4350 (2013).

[109] R. Zargar, A. Najafi, and M. Miri, "Three-sphere low-Reynolds-number swimmer near a wall," Phys. Rev. E **80**, 026308 (2009).

[110] S. Kim and S. J. Karrila, *Microhydrodynamics: Principles and Selected Applications* (Courier Corporation, 2013).

[111]J. R. Blake, "A note on the image system for a stokeslet in a no-slip boundary," Math. Proc. Cambridge Philos. Soc. **70**, 303–310 (1971).

[112]J. W. Swan and J. F. Brady, "Simulation of hydrodynamically interacting particles near a no-slip boundary," Phys. Fluids **19**, 113306 (2007).

[113]Y. Su, J. W. Swan, and R. N. Zia, "Pair mobility functions for rigid spheres in concentrated colloidal dispersions: Stresslet and straining motion couplings," J. Chem. Phys. **146**, 124903 (2017).

[114]A. M. Fiore, F. Balboa Usabiaga, A. Donev, and J. W. Swan, "Rapid sampling of stochastic displacements in Brownian dynamics simulations," J. Chem. Phys. **146**, 124116 (2017).

[115]A. Daddi-Moussa-Ider, M. Lisicki, A. J. T. M. Mathijssen, C. Hoell, S. Goh, J. Bławzdziewicz, A. M. Menzel, and H. Löwen, "State diagram of a three-sphere microswimmer in a channel," (unpublished); preprint arXiv:1803.02345 [physics.flu-dyn].

[116]T. I. Fossen, *Handbook of Marine Craft Hydrodynamics and Motion Control* (John Wiley & Sons, 2011).

[117]W. H. Press, *The Art of Scientific Computing* (Cambridge University Press, 1992).

[118]B. Cichocki, R. B. Jones, R. Kutteh, and E. Wajnryb, "Friction and mobility for colloidal spheres in Stokes flow near a boundary: The multipole method and applications," J. Chem. Phys. **112**, 2548–2561 (2000).

[119]M. Kedzierski and E. Wajnryb, "Precise multipole method for calculating many-body hydrodynamic interactions in a microchannel," J. Chem. Phys. **133**, 154105 (2010).

[120]S. E. Spagnolie and E. Lauga, "Hydrodynamics of self-propulsion near a boundary: Predictions and accuracy of far-field approximations," J. Fluid Mech. **700**, 105–147 (2012).

[121]A. J. T. M. Mathijssen, A. Doostmohammadi, J. M. Yeomans, and T. N. Shendruk, "Hotspots of boundary accumulation: Dynamics and statistics of micro-swimmers in flowing films," J. R. Soc. Interface **13**, 20150936 (2016).

[122]M. Abramowitz and I. A. Stegun, *Handbook of Mathematical Functions* (Dover New York, 1972), Vol. 1.

[123]G. Lowe, M. Meister, and H. C. Berg, "Rapid rotation of flagellar bundles in swimming bacteria," Nature **325**, 637–640 (1987).

[124]Y. Magariyama, S. Sugiyama, and S. Kudo, "Bacterial swimming speed and rotation rate of bundled flagella," FEMS Microbiol. Lett. **199**, 125–129 (2001).

[125]R. M. Macnab, "Bacterial flagella rotating in bundles: A study in helical geometry," Proc. Nat. Acad. Sci. U. S. A. **74**, 221–225 (1977).

[126]E. Lauga, W. R. DiLuzio, G. M. Whitesides, and H. A. Stone, "Swimming in circles: Motion of bacteria near solid boundaries," Biophys. J. **90**, 400–412 (2006).

[127]E. Lauga and T. M. Squires, "Brownian motion near a partial-slip boundary: A local probe of the no-slip condition," Phys. Fluids **17**, 103102 (2005).

P6 State diagram of a three-sphere microswimmer in a channel

Reproduced from

A. Daddi-Moussa-Ider, M. Lisicki, A. J. T. M. Mathijssen, C. Hoell, S. Goh,
J. Bławzdziewicz, A. M. Menzel, and H. Löwen,
State diagram of a three-sphere microswimmer in a channel,
J. Phys.: Condens. Matter **30**, 254004 (2018),
IOP Publishing Ltd.

Digital Object Identifier (DOI): `https://doi.org/10.1088/1361-648X/aac470`

Statement of contribution

I contributed to the theoretical description, concerning the self-propulsion mechanism of a three-sphere swimmer between two parallel rigid walls, and to the discussion and interpretation of the results, including the swimming trajectories of a three-sphere swimmer in a channel and the corresponding state diagrams. I contributed to drafting the parts of the manuscript concerning these trajectories and state diagrams. Moreover, I participated in editing the text and finalizing the manuscript. My work concerning this paper was supervised by ADMI, AMM, and HL.

Copyright and license notice

IOP Publishing Journal of Physics: Condensed Matter
J. Phys.: Condens. Matter **30** (2018) 254004 (21pp) https://doi.org/10.1088/1361-648X/aac470

State diagram of a three-sphere microswimmer in a channel

Abdallah Daddi-Moussa-Ider[1], Maciej Lisicki[2,3], Arnold J T M Mathijssen[4], Christian Hoell[1], Segun Goh[1], Jerzy Bławzdziewicz[5], Andreas M Menzel[1] and Hartmut Löwen[1]

[1] Institut für Theoretische Physik II: Weiche Materie, Heinrich-Heine-Universität Düsseldorf, Universitätsstraße 1, 40225 Düsseldorf, Germany
[2] Department of Applied Mathematics and Theoretical Physics, University of Cambridge, Wilberforce Rd, Cambridge CB3 0WA, United Kingdom
[3] Institute of Theoretical Physics, Faculty of Physics, University of Warsaw, Pasteura 5, 02-093 Warsaw, Poland
[4] Department of Bioengineering, Stanford University, 443 Via Ortega, Stanford, CA 94305, United States of America
[5] Department of Mechanical Engineering, Texas Tech University, Lubbock, TX 79409, United States of America

E-mail: ider@thphy.uni-duesseldorf.de and hlowen@hhu.de

Received 6 March 2018, revised 3 May 2018
Accepted for publication 14 May 2018
Published 1 June 2018

Abstract
Geometric confinements are frequently encountered in soft matter systems and in particular significantly alter the dynamics of swimming microorganisms in viscous media. Surface-related effects on the motility of microswimmers can lead to important consequences in a large number of biological systems, such as biofilm formation, bacterial adhesion and microbial activity. On the basis of low-Reynolds-number hydrodynamics, we explore the state diagram of a three-sphere microswimmer under channel confinement in a slit geometry and fully characterize the swimming behavior and trajectories for neutral swimmers, puller- and pusher-type swimmers. While pushers always end up trapped at the channel walls, neutral swimmers and pullers may further perform a gliding motion and maintain a stable navigation along the channel. We find that the resulting dynamical system exhibits a supercritical pitchfork bifurcation in which swimming in the mid-plane becomes unstable beyond a transition channel height while two new stable limit cycles or fixed points that are symmetrically disposed with respect to the channel mid-height emerge. Additionally, we show that an accurate description of the averaged swimming velocity and rotation rate in a channel can be captured analytically using the method of hydrodynamic images, provided that the swimmer size is much smaller than the channel height.

Keywords: microswimmer, biological fluid dynamics, low-Reynolds-number hydrodynamics, swimming

S Supplementary material for this article is available online

(Some figures may appear in colour only in the online journal)

1. Introduction

Microorganisms, particularly bacteria, constitute the bulk of the biomass on Earth and outnumber any other creatures. Despite their vast biological diversity and specific interaction with their environment, the physics of microscale fluid dynamics provides a unifying framework of the understanding of some aspects of their behavior [1–4]. Swimming on the microscale is conceptually very different from the everyday macroscale experience [5–7]. Since the typical sizes and velocities of microswimmers are of the order of microns and microns per second, the Reynolds number characterizing the flow is $\mathrm{Re} \ll 1$. In this case, inertial effects can be disregarded compared to viscous effects in flow, and the motion of the fluid is described by linear Stokes hydrodynamics [8, 9]. This has a pronounced effect on the physiology and swimming strategies of microswimmers [10, 11] which have to comply to the limitations imposed by the time reversibility of Stokes flows, termed the scallop theorem by Purcell [1].

One of the ways to overcome this barrier is to perform non-reciprocal swimming strokes. This can be achieved in systems of artificial biomimetic swimmers by introducing only few degrees of freedom, sufficient to gain propulsion but simplistic enough to remain analytically tractable. A well-known model example is the three-sphere swimmer designed by Najafi and Golestanian [12]. It encompasses three aligned spheres the mutual distance of which can be varied periodically in a controlled way. This guarantees the breaking of kinematic reversibility and leads to net translation along the axis of the body [13–17]. The strength of this design lies in the possible experimental realizations involving colloids trapped in optical tweezers [18, 19]. Similar bead-model designs have been proposed involving elastic deformations of one or both of the arms [20–27], non-collinear conformations leading to rotational motion [28–32], or new models with complex swimmer bodies and external propulsion forces [33, 34]. A simple model for free-swimming animalcules composed of beads, subject to periodic forces has further been considered [20, 35]. Fascinating spatiotemporal patterns and unusual macroscopic rheological signatures arise from the interaction of numerous microswimmers, including the onset of collective and cohesive motion [36–40], emergence of dynamic clusters [41, 42], laning [43–46] and wave patterns [47–50], motility-induced phase separation [51–55] and active turbulence [56–62].

One of the main challenges of microfluidics has been to design and control the motion of fluids in microchannels, where the effects of confinement dominate the dynamics [63, 64]. The long-ranged nature of hydrodynamic interactions in low-Reynolds-number flows under geometrical confinement significantly influences the dynamics of suspended particles or organisms [65]. Close confinement, e.g. in channels, can lead to a drastic increase in the range of interactions [66, 67]. Thus surface effects have to be accounted for when designing microfluidic systems [68, 69] and affect translational and rotational mobilities of colloidal particles diffusing near boundaries [70–77]. In living systems, walls have been demonstrated to drastically change the trajectories of swimming bacteria, such as *E. coli* [78–87], or algae [88, 89]. As seen already in simplistic models involving two linked spheres near a wall [90], a surprisingly rich behavior emerges, with the presence of trapping states, escape from the wall and non-trivial steady trajectories above the surface. This behavior has also been seen in an analogous system of self-phoretic active Janus particles [91–99], where a complex phase diagram has been found, based on the initial orientation and the distance separating the swimmer from the wall. Additional investigations have considered the hydrodynamic interactions between two squirmers near a boundary [100], the dynamics of active particles near a fluid interface [101–103], swimming in a confining microchannel [104–115], inside a spherical cavity [116–118], near a curved obstacle [119, 120] and in a liquid film [121–123]. Meanwhile, other studies have considered the low-Reynolds-number locomotion in non-Newtonian fluids [124–132] where boundaries have been found to drastically alter the swimming trajectories of microswimmers [133–135].

The analysis of dynamics of a single model swimmer interacting with a boundary is a crucial first step towards the understanding of complex collective processes involving living systems close to boundaries. In this paper, we address theoretically and numerically the low-Reynolds-number locomotion of a linear three-sphere microswimmer in a channel between two parallel walls. We show that the swimmer flow signature (pusher, puller, neutral swimmer) determines its general behavior and explore the resulting phase diagrams discerning between the gliding, sliding and trapping modes of motion.

The remainder of the paper is organized as follows. In section 2, we introduce the model microswimmer and derive the swimming kinematics in a channel between two planar walls in the framework of low-Reynolds-number hydrodynamics. We then present in section 3 a state diagram representing the various swimming scenarios for a neutral three-sphere swimmer and introduce a simplified analytical model valid in the limit where the swimmer length is small compared to the channel height. We discuss in section 4 the behavior of puller- and pusher-type swimmers, finding that the former can maintain a stable navigation along the channel, while the latter inevitably ends up trapped at the channel walls. We then examine the swimming stability about the mid-plane and show that a supercritical pitchfork bifurcation occurs beyond a certain transition channel height at which swimming at the centerline becomes unstable. Concluding remarks and summary are provided in section 5 and technical details are contained in appendices A through D.

2. Theoretical model

2.1. Hydrodynamics background

In low-Reynolds-number hydrodynamics, the flow is viscosity-dominated and the fluid motion is governed by the steady Stokes equations [8]

$$\eta \boldsymbol{\nabla}^2 \boldsymbol{v}(\boldsymbol{r}) - \boldsymbol{\nabla} P(\boldsymbol{r}) + \boldsymbol{f}_\mathrm{B}(\boldsymbol{r}) = 0\,, \tag{1a}$$

$$\boldsymbol{\nabla} \cdot \boldsymbol{v}(\boldsymbol{r}) = 0\,, \tag{1b}$$

where η denotes the fluid dynamic viscosity, and $\boldsymbol{v}(\boldsymbol{r})$ and $P(\boldsymbol{r})$ are respectively the fluid velocity and pressure fields at position $\boldsymbol{r} = (x, y, z)$ due to a bulk force density $\boldsymbol{f}_\mathrm{B}(\boldsymbol{r})$ acting on the fluid by the immersed objects.

For a point-force singularity $\boldsymbol{f}_\mathrm{B}(\boldsymbol{r}) = \boldsymbol{f}\delta(\boldsymbol{r} - \boldsymbol{r}_0)$ acting at position $\boldsymbol{r}_0$ in an otherwise quiescent fluid, the solution for the induced velocity field and pressure is expressed in terms of the Green's functions

$$v_i(\boldsymbol{r}) = \mathcal{F}_{ij}(\boldsymbol{r}, \boldsymbol{r}_0) f_j \, , \quad P(\boldsymbol{r}) = \mathcal{P}_j(\boldsymbol{r}, \boldsymbol{r}_0) f_j \, , \tag{2}$$

where repeated indices are summed over following Einstein's convention. In the absence of confining boundaries, the fundamental solution is the Oseen tensor, $\boldsymbol{\mathcal{F}} = (8\pi\eta s)^{-1}(\boldsymbol{I} + \boldsymbol{ss}/s^2)$ with $\boldsymbol{s} = \boldsymbol{r} - \boldsymbol{r}_0$ and $s = |\boldsymbol{s}|$. The solution for an arbitrary force distribution can then be constructed by linear superposition.

The Green's functions in a channel between two parallel planar walls was first derived by Liron and Mochon [136] using the image technique and a Fourier transform. In appendix A, we present a modified approach based on decomposing the Fourier-transformed vector fields into their longitudinal, transverse, and normal components. Upon inverse Fourier transformation, the Green's functions can then be expressed in terms of Bessel integrals of the first kind. Alternatively, following the method by Mathijssen *et al* [121], the Green's function may be expressed as an infinite series of image reflections. In appendix B we derive the recursion relations that yield the successive image systems, and provide explicit expressions for these. Truncation of this series can be computationally advantageous, provided a suitable number of images is chosen. In the limiting case of an infinitely wide channel, both Green's functions reduce to the familiar Oseen expressions. The image reflection method has previously been employed to address the behavior of swimming bacteria near a hard surface [81] or an air-fluid interface [137].

2.2. Swimmer dynamics

In the following, we consider the motion of a neutrally buoyant swimmer in a fluid bounded by two parallel planar walls infinitely extended in the planes $z = 0$ and $z = H$. As a model swimmer, we employ the linear three-sphere microswimmer originally proposed by Najafi and Golestanian [12]. The simplicity of the model provides a handy framework that allows a direct investigation of many aspects in low-Reynolds-number locomotion. The swimmer is composed of three spheres of radii a_1 (central), a_2 (front), and a_3 (rear) arranged colinearly via dragless rods. The periodic changes in the mutual distances between the spheres are set to perform a non-reversible sequence leading to propulsive motion (see figure 1 for an illustration of the model swimmer moving in a channel between two walls.)

The instantaneous orientation of the swimmer relative to the channel walls is described by the two-dimensional unit vector $\hat{\boldsymbol{t}} = \cos\theta\,\hat{\boldsymbol{e}}_x + \sin\theta\,\hat{\boldsymbol{e}}_z$ directed along the swimming axis. Under the action of the internal forces acting between the spheres, actuated, e.g. by embedded motors, the lengths of the rods connecting the spheres change periodically around mean values. Specifically,

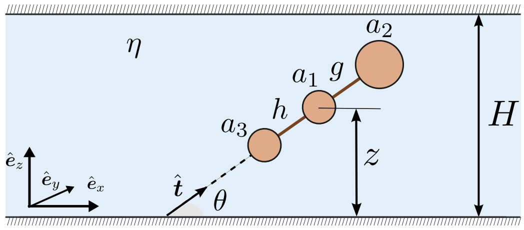

Figure 1. Illustration of a linear three-sphere microswimmer moving in a channel of constant height H. The swimmer is directed along the unit vector $\hat{\boldsymbol{t}}$ forming an angle θ relative to the horizontal direction. The central, front, and aft spheres composing the swimmer have different radii a_1, a_2, and a_3, respectively. The instantaneous positions of the front and aft spheres relative to the central sphere are denoted by g and h, respectively. The vertical position of the swimmer is defined by the height of the central sphere z above the bottom wall. The fluid filling the channel is quiescent and characterized by a dynamic viscosity η.

$$\boldsymbol{r}_1 - \boldsymbol{r}_3 = h(t)\hat{\boldsymbol{t}} \, , \quad \boldsymbol{r}_2 - \boldsymbol{r}_1 = g(t)\hat{\boldsymbol{t}} \, , \tag{3}$$

where $h(t)$ and $g(t)$ are periodic functions prescribing the instantaneous mutual distances between adjacent spheres, which we choose to be harmonic,

$$g(t) = L_1 + u_{10}\cos(\omega t) \, , \tag{4a}$$

$$h(t) = L_2 + u_{20}\cos(\omega t + \delta) \, , \tag{4b}$$

where ω is the oscillation frequency of motion and $\delta \in [0, 2\pi)$ is a phase shift necessary for the symmetry breaking. Here, L_1 and L_2 stand for the mean arm length connecting the central sphere to the front and rear spheres, respectively. In addition, u_{10} and u_{20} are the corresponding amplitudes of oscillation. Unless otherwise stated, we will consider consistently throughout this manuscript that $L_1 = L_2 =: L$ and $u_{10} = u_{20} =: u_0$. We further mention that the sphere radii and the oscillation amplitudes should be chosen small enough in such a way that the inequalities $a_1 + a_2 + 2|u_0| \ll L$ and $a_1 + a_3 + 2|u_0| \ll L$ remain satisfied. Moreover, we scale from now on all the lengths by L and the times by ω^{-1}.

We now briefly outline the main steps involved in the derivation of the swimming velocity and inclination. In Stokes hydrodynamics, the suspended particles take instantaneously on the velocity of the embedding flow since inertial effects are negligible. Additionally, the translational velocities of the three spheres are linearly related to the internal forces acting on them via

$$\boldsymbol{V}_\gamma = \frac{\mathrm{d}\boldsymbol{r}}{\mathrm{d}t} = \sum_{\lambda=1}^{3} \boldsymbol{\mu}^{\gamma\lambda} \cdot \boldsymbol{f}_\lambda \, , \tag{5}$$

where $\boldsymbol{\mu}^{\gamma\lambda}$ denotes the hydrodynamic mobility tensor bridging between the translational velocity of sphere γ and the force exerted on sphere λ. The mobility tensor is symmetric positive definite [138] and encompasses the effect of many-body hydrodynamics interactions. In this work, however, for the sake of simplicity we consider only contributions stemming from the hydrodynamic interaction between pairs of particles

($\gamma \neq \lambda$), in addition to contributions relative to the same particle ($\gamma = \lambda$) designated as self-mobility functions [9].

Taking the time derivative with respect to the laboratory frame on both sides of equation (3) yields

$$\boldsymbol{V}_2 = \boldsymbol{V}_1 + \dot{g}\,\hat{\boldsymbol{t}} + g\dot{\theta}\,\hat{\boldsymbol{n}}\,, \tag{6a}$$

$$\boldsymbol{V}_3 = \boldsymbol{V}_1 - \dot{h}\,\hat{\boldsymbol{t}} - h\dot{\theta}\,\hat{\boldsymbol{n}}\,, \tag{6b}$$

wherein dot stands for a derivative with respect to time. Moreover, $\hat{\boldsymbol{n}} = -\sin\theta\,\hat{\boldsymbol{e}}_x + \cos\theta\,\hat{\boldsymbol{e}}_z$ is a unit vector perpendicular (rotated 90 degrees anticlockwise) to the unit vector $\hat{\boldsymbol{t}}$. Accordingly, the triplet $(\hat{\boldsymbol{e}}_y, \hat{\boldsymbol{n}}, \hat{\boldsymbol{t}})$ forms a direct orthonormal basis in the frame of reference associated with the swimmer.

For the determination of the unknown internal forces acting between the spheres, a total of six equations is required. By projecting equation (6) onto the orientation vector $\hat{\boldsymbol{t}}$, two scalar equations are readily obtained. Projecting these equations onto the normal direction $\hat{\boldsymbol{n}}$ and eliminating the rotation rate yields an additional equation. Three further scalar equations are obtained by enforcing the physical constraint that the swimmer does not exert a net force or torque on the surrounding fluid. Specifically

$$\sum_{\lambda=1}^{3} \boldsymbol{f}_\lambda = 0\,, \qquad \sum_{\lambda=1}^{3} (\boldsymbol{r}_\lambda - \boldsymbol{r}_0) \times \boldsymbol{f}_\lambda = 0\,, \tag{7}$$

where $\times$ stands for the cross (outer) product and $\boldsymbol{r}_0$ denotes an arbitrary reference point, which we choose to be the position of the central sphere $\boldsymbol{r}_1$. The internal forces acting between the spheres follow from solving the resulting system of six linearly independent equations using the standard substitution technique.

In order to investigate the swimming behavior, we choose to follow the trajectory of the central sphere whose velocity can readily be determined from (5) upon knowledge of the internal forces. The instantaneous rotation rate of the swimmer can then be calculated from

$$\dot{\theta} = \frac{1}{g} (\boldsymbol{V}_2 - \boldsymbol{V}_1) \cdot \hat{\boldsymbol{n}} = \frac{1}{h} (\boldsymbol{V}_1 - \boldsymbol{V}_3) \cdot \hat{\boldsymbol{n}}\,. \tag{8}$$

3. Swimming state diagram

3.1. Behavior near a single wall

Having outlined the general procedure for the determination of the equations governing the swimmer dynamics, we next derive approximate expressions for the swimming translational and rotational velocities. We firstly consider the limiting case of an infinitely wide channel $H \to \infty$ and derive the averaged equations of motion for a swimmer located at a finite distance above a single wall infinitely extended in the plane $z = 0$. In addition, we restrict our attention to the particular case where the spheres have the same radius a as originally proposed in the Najafi and Golestanian design [12]. The general case for arbitrary particle radius will be discussed in the following section.

The Green's functions satisfying the no-slip boundary condition at an infinitely extended hard wall are expressed in the form of the Blake tensor [142] providing the leading-order terms in the pair hydrodynamic interactions. Restricting ourselves for simplicity to the point-particle framework, the scaled self-mobility functions for a sphere located at height z above a rigid wall are given up to $\mathcal{O}\left((a/z)^3\right)$ by [8]

$$\frac{\mu_\parallel}{\mu_0} = 1 - \frac{9}{16}\frac{a}{z}\,, \qquad \frac{\mu_\perp}{\mu_0} = 1 - \frac{9}{8}\frac{a}{z}\,, \tag{9}$$

for the translational motion parallel and perpendicular to the wall, respectively. Here $\mu_0 = (6\pi\eta a)^{-1}$ denotes the usual bulk mobility given by the Stokes law. (In our simulations, however, we use more detailed predictions obtained by the method of reflections incorporating nine images, and described in detail in appendix B.)

By performing a Taylor series expansion up to $\mathcal{O}(a^3)$ of the swimming velocity and rotation rate, the approximate differential equations governing the swimming dynamics above a single wall, averaged over one oscillation period, can be presented in the form

$$\frac{\mathrm{d}x}{\mathrm{d}t} = V_0 + KA(z)\,, \tag{10a}$$

$$\frac{\mathrm{d}z}{\mathrm{d}t} = \big(V_0 + KB(z)\big)\theta\,, \tag{10b}$$

$$\frac{\mathrm{d}\theta}{\mathrm{d}t} = KC(z)\,, \tag{10c}$$

where we have assumed small inclination angles relative to the horizontal direction such that $\sin\theta \sim \theta$ and $\cos\theta \sim 1$. Moreover,

$$V_0 = -\frac{aK}{24}(7 + 5a) \tag{11}$$

is the bulk swimming speed in the absence of a boundary, and

$$K := \langle g\dot{h} - h\dot{g} \rangle = -u_{10}u_{20}\sin\delta = -u_0^2 \sin\delta\,. \tag{12}$$

Here $\langle\cdot\rangle$ stands for the time-averaging operator over one full swimming cycle, defined by

$$\langle\cdot\rangle := \frac{1}{2\pi}\int_0^{2\pi} (\cdot)\,\mathrm{d}t\,. \tag{13}$$

Evidently, a net motion over one swimming cycle occurs only if the phase shift $\delta \notin \{0, \pi\}$. In the remainder of this article, we take $\delta = \pi/2$ for which the swimming speed is maximized.

In addition, A, B, and C are highly nonlinear functions of z which are explicitly provided to leading order in a in appendix D. In the far-field limit, in which the distance separating the swimmer from the wall is very large compared to the swimmer size ($z \gg 1$), these functions up to $\mathcal{O}\left(z^{-5}\right)$ read

$$A(z) = -\frac{287}{1024}\frac{a^2}{z^3}\,, \tag{14a}$$

$$B(z) = \left(\frac{21}{64} - \frac{77a}{256}\right)\frac{a}{z^3}\,, \tag{14b}$$

$$C(z) = \frac{135}{1024} \frac{a(2+3a)}{z^4} \,. \tag{14c}$$

Remarkably, the leading-order term in the wall-induced correction to the swimming velocity decays in the far field as z^{-3}. Not surprisingly, the dipolar contribution (decaying as z^{-2}) induced by a three-sphere microswimmer vanishes if the front and rear spheres have equal radii (see appendix C). As a result, the leading order in the velocity flow field possesses a quadrupolar flow structure that decays as inverse cube of distance. Approximate swimming trajectories are readily obtained by integrating equation (10) for given initial orientation and distance from the wall.

3.2. Approximate swimming trajectories in a channel

We next shift our attention to the swimming motion in a channel bounded by two parallel infinitely extended walls. As already pointed out, an accurate description of the channel-mediated hydrodynamic interactions requires the use of the Green's functions that satisfy the no-slip boundary conditions at both walls simultaneously. This approach, however, involves improper (infinite) integrals whose numerical evaluation at every time step is computationally expensive. In order to overcome this difficulty, we use as an alternative framework the successive image reflection technique. The latter consists of generating an infinite series of images containing Stokeslets and higher-order derivatives that satisfy the no-slip boundary conditions on both walls asymptotically. Further technical details on the derivation of the flow field using multiple reflections are provided in appendix B. Throughout this work, a total of eight reflections is consistently employed for the numerical evaluation of the Green's functions.

In order to proceed analytically, we restrict ourselves for simplicity to the first two image systems following Oseen's classical approximation [143]. This approach suggests that the wall-induced corrections to the hydrodynamic interactions between two planar parallel rigid walls could conveniently be approximated by superposition of the contributions stemming from each single wall independently. Accordingly, it follows from equation (10) that the averaged swimming velocities in a channel between two walls can adequately be approximated as

$$\frac{\mathrm{d}x}{\mathrm{d}t} = V_0 + K\left(A(z) + A(H-z)\right) , \tag{15a}$$

$$\frac{\mathrm{d}z}{\mathrm{d}t} = \big(V_0 + K\left(B(z) + B(H-z)\right)\big)\theta \,, \tag{15b}$$

$$\frac{\mathrm{d}\theta}{\mathrm{d}t} = K\big(C(z) - C(H-z)\big) \,, \tag{15c}$$

where again the inclination angle is assumed to vary within a narrow range relative to the horizontal direction.

In figure 2, we show the channel-induced corrections to the swimming velocities and rotation rate as functions of the vertical distance z for a neutral swimmer of equal sphere radii $a = 0.1$. The simplistic superposition approximation given by equation (15) is shown as dashed and solid lines for channel heights $H = 2$ and $H = 4$, respectively. The corresponding numerical solutions obtained using a total of eight reflections are shown as symbols, where diamonds and squares correspond to $H = 2$ and $H = 4$, respectively. Here we consider a small amplitude of oscillations $u_0 = 0.1$.

We observe that the corrections to the swimming velocities (figure 2(*a*) and (*b*)) tend to remain about constant around the channel mid-height and mostly monotonically increase in magnitude in the proximity of the walls due to the increased drag exerted on the swimmer. Upon decreasing the channel height, the drag force resulting from the resistance of the channel walls and opposing the motion through the fluid becomes more pronounced. For instance, swimming in the

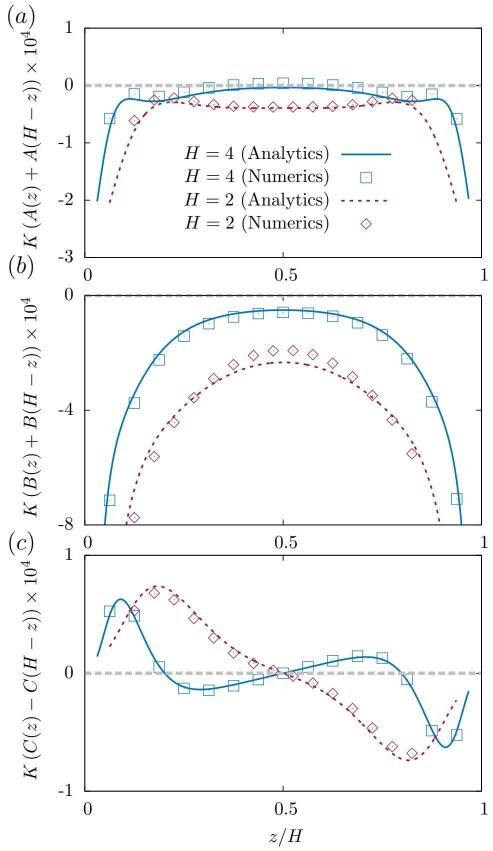

Figure 2. (*a*) and (*b*) Channel-induced corrections to the translational swimming velocities along the x and z directions, respectively, and (*c*) rotation rate versus the vertical distance z about $\theta \sim 0$. The analytical expressions based on the superposition approximation given by equation (15) derived up to $\mathcal{O}(a^3)$ are shown as dashed and solid lines for $H = 2$ and $H = 4$, respectively. Symbols are the numerically exact results obtained using a total of eight reflections for $H = 2$ (diamonds) and $H = 4$ (squares). Horizontal (gray) dashed lines are the corresponding bulk values. Here we consider a neutral swimmer with equal sphere radii $a = 0.1$ and an amplitude of arm oscillations $u_0 = 0.1$.

mid-plane of a channel of height $H = 2$ leads to increased drag of about 13% relative to the bulk value, while this increase is found to be about 2% for $H = 4$. The increase in the drag force for motion of arbitrary direction is mostly larger in the z direction than in the x direction since it is easier to move the fluid aside than to push it into or to squeeze it out of the gap between the swimmer and the channel walls.

Since the vertical velocity scales linearly with the inclination angle (see equation (15*b*)), a swimmer that is initially aligned parallel to the walls and released from a height of vanishing rotation rate will undergo a purely gliding motion along the channel. By examining the variations of the rotation rate (figure 2 (*c*)) we observe that the evolution equations for the swimming trajectories display either one or three fixed points in the comoving frame translating parallel to the channel walls. The first fixed point is trivial and occurs at the channel mid-height ($z/H = 1/2$) where both walls have the same effect on the orientation of the swimmer. For $H = 4$, two nontrivial fixed points symmetrically placed with respect to the channel mid-height are reached at $z/H \simeq 0.2$ and $z/H \simeq 0.8$.

The superposition approximation is found to be in a good agreement with the full numerical solution along the channel. A small mismatch, notably for $H = 2$ in the normal velocity (figure 2 (*b*)), is a drawback of the approximations proposed here. A good estimate of the swimming trajectories in a channel can therefore be made using the first two reflections provided that the swimmer size is much smaller than the channel height.

Figure 3 shows the state diagram displayed by a neutral three-sphere microswimmer of equal sphere radii, swimming in a channel for two different wall separations (*a*) $H = 2$ and (*b*) $H = 4$. The state diagram is obtained by integrating the full nonlinear equations governing the swimmer dynamics numerically using a fourth-order Runge–Kutta scheme with adaptive time stepping [144]. The hydrodynamic mobility functions employed in the simulations are obtained using the method of reflections with a total of nine images, providing a good accuracy even at small sphere–wall distances, as compared to far-field representation. A systematic comparison between the expressions of the self mobilities as obtained from the method of reflections and the exact multipole method [139–141] is provided in the supporting information[6]. Depending on the initial orientation and distance along the channel, the swimmer may be trapped by either walls (downward and upward pointing triangles) or undergoes a nontrivial oscillatory gliding motion at a constant mean height either at the channel centerline (squares in figure 3 (*a*)) or at a moderate distance near the channel wall (half-filled blue boxes in figure 3 (*b*)).

A swimmer that is initially aligned parallel to the walls ($\theta_0 = 0$) and released from the trivial fixed point at the channel mid-height ($z_0 = H/2$) (blue diamond) undergoes a purely gliding motion without oscillations. In the trapped state, the swimmer moves along a curved trajectory before it attains a

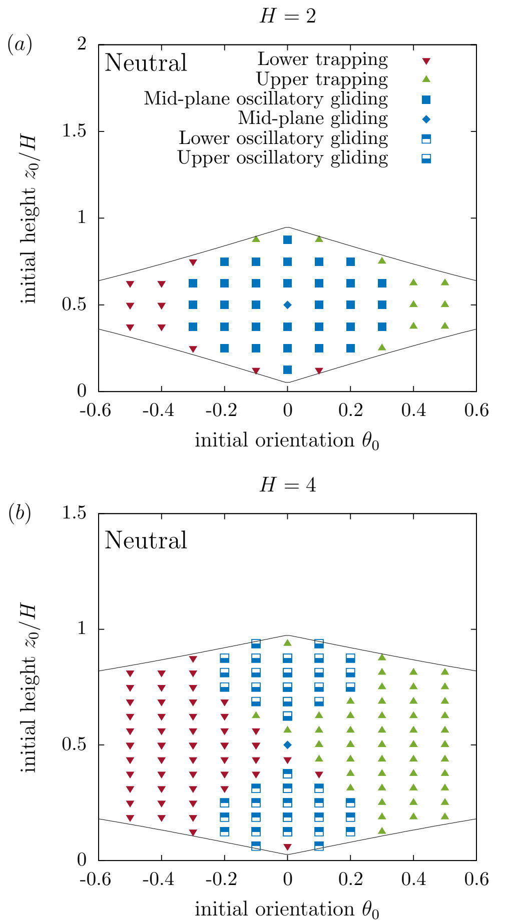

Figure 3. State diagram illustrating the swimming scenarios displayed by a neutral three-sphere swimmer of equal sphere radii $a = 0.1$ confined in a channel between two parallel planar walls for (*a*) $H = 2$ and (*b*) $H = 4$. Symbols represent the final swimming states for a given initial orientation and distance along the channel. Downward pointing triangles (red) indicate trapping near the lower wall whereas upward pointing triangles (green) stand for trapping near the upper wall. Filled boxes (blue) represent the oscillatory gliding state at the channel centerline while half-filled (blue) boxes correspond to the oscillatory gliding states near the corresponding wall. A (blue) diamond marks the trivial perpetual motion along the exact centerline of the channel. Solid lines correspond to forbidden situations in which one of the spheres is initially in contact with the channel walls. Here we take an amplitude of oscillations $u_0 = 0.1$.

hovering state during which the inclination angle approaches $\theta = -\pi/2$ for the lower trapping and $\theta = \pi/2$ for the upper trapping. Only trapping occurs if initially the swimmer is sufficiently oriented away from the horizontal direction at varying extent depending upon the channel height. Figure 4 shows exemplary trajectories displayed by a neutral swimmer released from various initial heights with orientations $\theta_0 = -0.3$ (for the lower trapping states) and $\theta_0 = 0.3$ (for the upper trapping

[6] See supporting information at (stacks.iop.org/JPhysCM/30/254004/mmedia) for approximate expressions of the self mobilities as obtained from the method of reflections in addition to a direct comparison with other approaches.

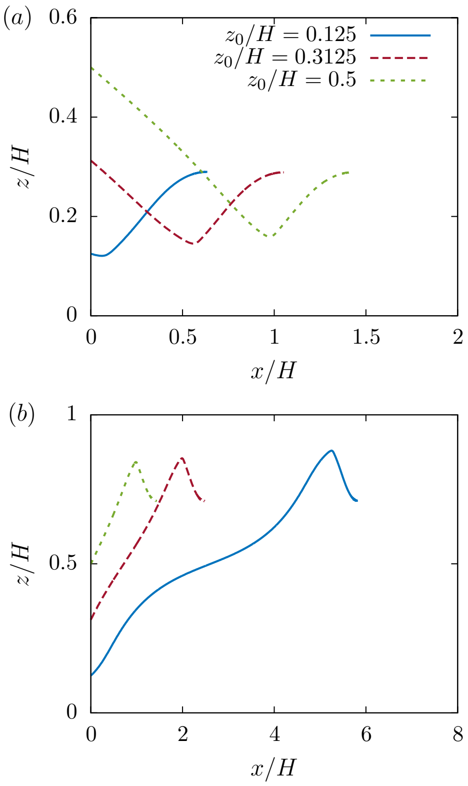

Figure 4. Typical swimming trajectories showing in (*a*) the lower trapping for $\theta_0 = -0.3$ and in (*b*) the upper trapping states for $\theta_0 = 0.3$ for various initial distances z_0 in a channel of height $H = 4$. In the steady state, the swimmer ends up trapped by a wall and attains a stable hovering state at a constant height close to that wall. This is why the trajectories end at a certain point.

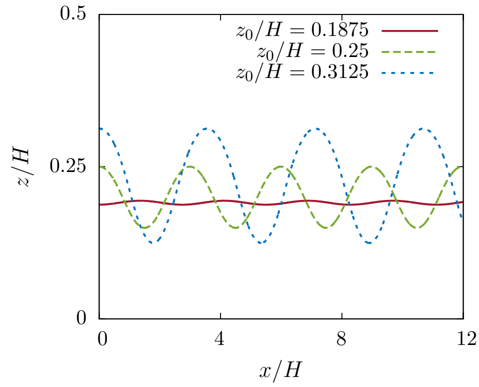

Figure 5. Exemplary swimming trajectories in the lower oscillatory gliding state for a separation $H = 4$ between the walls. The swimmer is initially aligned parallel to the walls ($\theta_0 = 0$) and released from various initial distances z_0. The amplitude of oscillations and frequency are strongly sensitive to the initial conditions. A nearly vanishing amplitude is observed for $z_0/H \simeq 0.1875$ close to the stable fixed point in figure 2 (*c*). The inclination angles show an analogous oscillatory behavior around a zero mean value. Here we set $a = 0.1$ and an amplitude of arm oscillation $u_0 = 0.1$.

states). After a transient evolution, the swimmer reorients itself perpendicular to the nearest wall and reaches a stable hovering state at a separation distance of about $z \simeq 1.12$. The final height is found to be independent of the initial inclination or distance from the wall in a way similar to that previously observed near a single boundary [145]. Physically, the hovering state corresponds to the situation in which the propulsion forces are equilibrated by the resistive viscous forces pushing the swimmer away from the nearest boundary.

We show in figure 5 typical swimming trajectories in the lower oscillatory gliding state for a swimmer that is released from different initial heights along the parallel direction ($\theta_0 = 0$) in a channel of height $H = 4$. In particular, the amplitude of oscillations almost vanishes when $z_0/H \simeq 0.1875$ for which the swimmer undergoes a purely gliding motion at a constant height. Not surprisingly, we have previously shown in figure 2 (*c*) that there exist in the comoving frame two nontrivial fixed points symmetrically placed relative to the channel centerline at $z/H \simeq 0.2$ and $z/H \simeq 0.8$ in addition to the trivial fixed point at the middle of the channel. As the initial swimming location is shifted far away from the fixed points, the amplitude of oscillations grows gradually before the swimmer ends up trapped by the nearest wall. The swimmer shows an analogous behavior in the upper oscillatory state upon making the transformation $z \to H - z$ due to the system reflectional symmetry with respect to the channel mid-plane[7].

4. Swimming puller versus pusher

Having analyzed in detail the swimming behavior of a neutral three-sphere swimmer of equal sphere radii, we next consider the more general situation and allow for differently sized spheres for which the swimming stroke is not time-reversal covariant [17]. For that purpose, we introduce the radii ratios $r_2 := a_2/a_1$ and $r_3 := a_3/a_1$ and use a to denote the radius of the central sphere a_1. It should be noted that r_2 and r_3 must vary only in such a way that the inequalities $(1 + r_2)a + 2|u_0| \ll L$ and $(1 + r_3)a + 2|u_0| \ll L$ remain satisfied during a full swimming cycle for the above-mentioned approximations to be valid.

In a bulk fluid, the flow field induced by a general three-sphere swimmer can conveniently be written in the far-field limit as a superposition of dipolar and quadrupolar flow fields (see appendix C), whose coefficients are respectively given by

[7] See supporting information at (stacks.iop.org/JPhysCM/30/254004/mmedia) for illustrative movies showing the swimming behaviors of a neutral three-sphere swimmer in a channel. Movie 1 illustrates the lower trapping state ($z_0/H = 0.125, \theta_0 = -0.3$) shown in figure 4(*a*) (solid blue line). Movie 2 illustrates the upper trapping state ($z_0/H = 0.125, \theta_0 = 0.3$) shown in figure 4(*b*) (solid blue line). Movie 3 shows the lower oscillatory gliding ($z_0 = 0.3125, \theta_0 = 0$) presented in figure 5 (short-dashed blue line). For illustrative purposes, the sizes of the spheres are not shown in real scale in the movies.

$$\alpha = \frac{3}{4}\frac{r_2 - r_3}{a}, \qquad \sigma = \frac{3}{56}\frac{4(r_2+r_3)-3}{a^2}, \tag{16}$$

where the swimmer is termed as pusher (extensile) if $\alpha > 0$ as it then pushes out the fluid along its swimming axis, and as puller (contractile) if $\alpha < 0$ as in that case it pulls in the fluid along its swimming path [2]. The swimmer studied in the previous section is a neutral swimmer, because $\alpha = 0$, and the dominant contribution to the flow-far-field thus is a quadrupole.

Keeping for convenience the same notation for the approximated swimming velocities and rotation rate as before, the averaged equations of motion of a general three-sphere swimmer near a single wall about the horizontal direction, can be presented up to $\mathcal{O}(a^3)$ as

$$\frac{\mathrm{d}x}{\mathrm{d}t} = V_0 + KA(z), \tag{17a}$$

$$\frac{\mathrm{d}z}{\mathrm{d}t} = \big(V_0 + KB(z)\big)\theta + KD(z), \tag{17b}$$

$$\frac{\mathrm{d}\theta}{\mathrm{d}t} = KC(z), \tag{17c}$$

where the bulk swimming velocity is now given by

$$V_0 = a\,(V_{10} + aV_{20})\,. \tag{18}$$

The coefficients V_{10} and V_{20} are functions of r_2 and r_3 only. They are explicitly given in appendix D. In particular, $V_{10} = -\frac{7K}{24}$ and $V_{20} = -\frac{5K}{24}$ when $r_2 = r_3$ directly leading to equation (11).

In the far-field limit, the generalized expressions for the functions $A(z)$, $B(z)$, and $C(z)$ are

$$A(z) = \frac{a^2 A_{23}}{z^3}, \tag{19a}$$

$$B(z) = a\left(\frac{B_{13}}{z^3} + \frac{aB_{23}}{z^3}\right), \tag{19b}$$

$$C(z) = a\,(C_{14} + aC_{24})\,\frac{1}{z^4}\,. \tag{19c}$$

In addition,

$$D(z) = a(r_3 - r_2)\left(\frac{D_{14}}{z^4} + \frac{a}{z^2}\left(D_{22} + \frac{D_{24}}{z^2}\right)\right). \tag{20}$$

The coefficients A_{ij}, B_{ij}, C_{ij}, and D_{ij} are provided in appendix D. The far-field equations (19) reduce to (14) in the particular case of $r_2 = r_3$.

By accounting only for the leading order in $1/z$, the normal velocity in the flow-far field reads $\mathrm{d}z/\mathrm{d}t = a^2K(r_3 - r_2)D_{22}z^{-2}$. For a pusher-like swimmer ($r_2 > r_3$), it follows that $\mathrm{d}z/\mathrm{d}t < 0$, and thus the swimmer is expected to be trapped by the bottom wall by noting that $D_{22} < 0$ and bearing in mind that $K < 0$. For a puller-like swimmer, however, $\mathrm{d}z/\mathrm{d}t > 0$ leading to an escape from the wall. These observations are in agreement with previous studies indicating that a noiseless pusher swimming parallel to a wall will be attracted whereas a puller will be repelled [146, 147]. It is worth mentioning that the dipolar flow signature neither emerges in the x-component of the swimming velocity nor in the rotation rate.

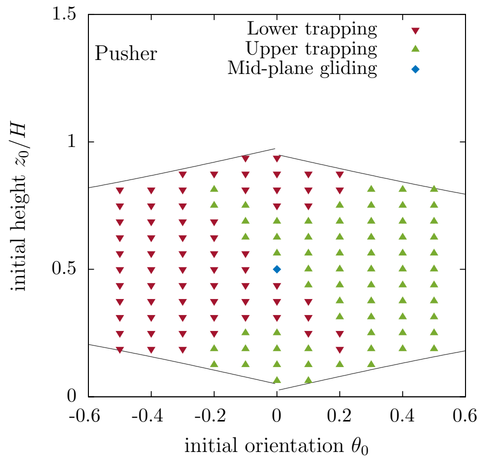

Figure 6. State diagram of swimming behavior in a channel of height $H = 4$, for a pusher-like swimmer with $a = 0.1$ and radius ratios $r_2 = 2, r_3 = 1$, using the same symbols as in figure 3. The pusher force-dipole hydrodynamics here lead to an amplification of the oscillations seen for neutral swimmers, which then moves the swimmer towards trapped states, as can be seen in the exemplary trajectories in figure 8 (*a*). The influence of the front-aft asymmetry was tested systematically by also varying the size of the larger front bead to $r_2 = 1.2$, but the corresponding state diagram does not differ qualitatively from the one shown here. Due to the front-aft asymmetry of this three-sphere swimmer, the solid lines indicating forbidden configurations here are asymmetric.

By considering only the first two image systems (superposition approximation), the generalized swimming velocities in a channel bounded by two walls can conveniently be approximated by

$$\frac{\mathrm{d}x}{\mathrm{d}t} = V_0 + K\,(A(z) + A(H-z))\,, \tag{21a}$$

$$\begin{aligned}\frac{\mathrm{d}z}{\mathrm{d}t} = {}& \Big(V_0 + K\,(B(z) + B(H-z))\Big)\theta \\ & + K\,(D(z) - D(H-z))\,,\end{aligned} \tag{21b}$$

$$\frac{\mathrm{d}\theta}{\mathrm{d}t} = K\big(C(z) - C(H-z)\big)\,. \tag{21c}$$

Explicit analytical expressions for the functions A, B, C, and D for a general three-sphere swimmer are rather complex and lengthy, and thus have not been listed here.

4.1. State diagram in a channel

Exemplary state diagrams for a general three-sphere swimmer in a channel of a height $H = 4$ are shown in figure 6 for a pusher-like swimmer and in figure 7 for a puller-like swimmer. For the former case, we observed one general behavior for a large range of parameters, while we found in the latter case that the behavior changes qualitatively when the radius of the

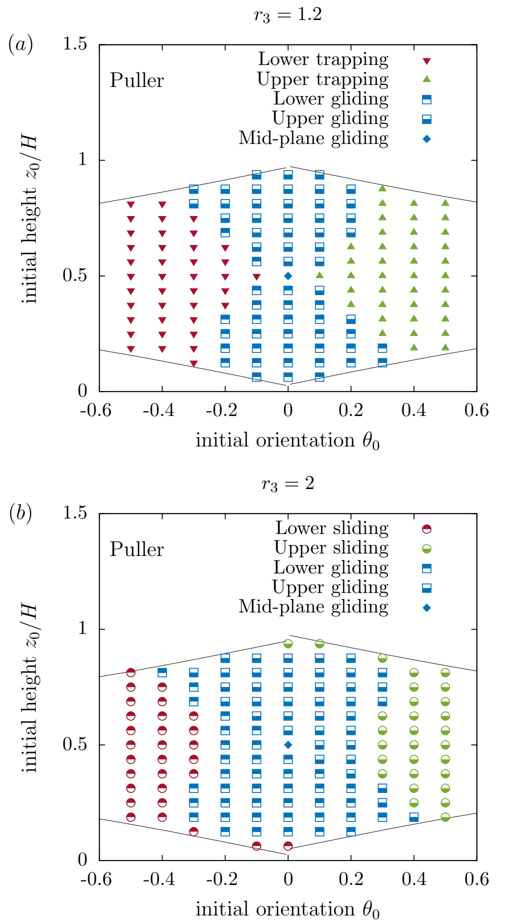

Figure 7. Swimming state diagram of a puller-like swimmer in a channel of height $H = 4$, for (*a*) $r_3 = 1.2$ and (*b*) $r_3 = 2$, while the other radius ratio $r_2 = 1$ is held constant. Symbols indicate the final state of the swimmer started at the corresponding initial phase space position. Here half-filled (blue) boxes stand for gliding states near the corresponding wall, and half-filled circles stand for states in which the swimmer slides along one of the walls. The positions of the filled sides (and the corresponding colors given in the legend) then indicate which wall the respective final swimming state is nearer to. Due to the front-aft asymmetry of the regarded three-sphere swimmers, the unaccessible phase space areas here are again asymmetric. (*a*) For small r_3, the swimmer either becomes trapped above one of the walls or glides well above/below it. (*b*) For larger r_3, a swimmer can either glide or start sliding along the corresponding wall, thereby maintaining a constant orientation, but is never trapped.

enlarged sphere is increased. As detailed below, both these types of non-neutral swimmers show qualitative differences to the state diagram for equal-sized spheres previously discussed in section 3.

For pusher-like swimmers, the oscillatory gliding state observed for neutral swimmers is destabilized (see figure 6, where $r_2 = 2, r_3 = 1$). The amplitude of any initial oscillation grows rapidly with time until the swimmer ceases oscillating to reach one of two phase-space fixed points which are symmetrically positioned with respect to the channel mid-height. After transient oscillations, the swimmer reorients itself towards the nearest wall and remains in a hovering state, as can be seen in the exemplary trajectories shown in figure 8 (*a*) for various initial heights with $\theta_0 = 0.2$.

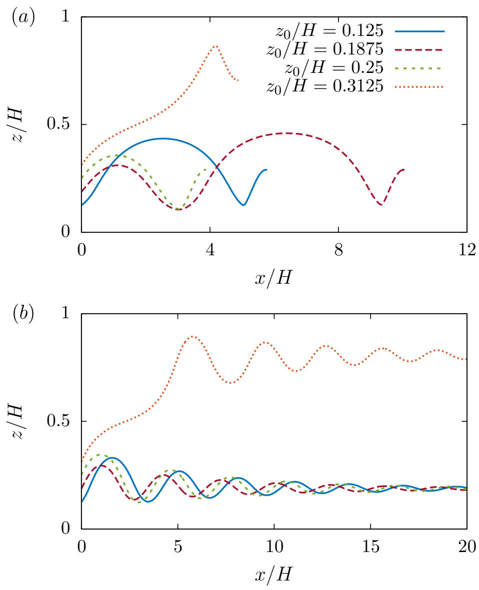

Figure 8. Typical swimming trajectories of three-sphere swimmers released at $\theta_0 = 0.2$ from different initial heights for (*a*) a pusher-like swimmer with $r_2 = 1.2$ and (*b*) for a puller-like swimmer with $r_3 = 1.2$. The respective other radius ratios are all set to one. (*a*) Pusher-like-front-heavy swimmers can no longer perform perpetual gliding motions as any oscillation is amplified until a trapped state is reached. The end of the trajectories marks the final position in the trapped state. (*b*) Puller-like, aft-heavy swimmers undergo damping of their oscillations so that a straight motion parallel to the wall channels is approached in the steady state. In both cases, the initial configuration determines which of two symmetric phase-space fixed points a swimmer will approach. Here we set $a = u_0 = 0.1$.

Consequently, a pusher-like swimmer always ends up trapped by the channel walls with the only exception of the exactly symmetric perpetual motion along the centerline. Depending on the initial configuration, the swimmer moves towards either the lower or the upper phase-space fixed points. As before, the state diagram is symmetric with respect to $(z_0, \theta_0) = (H/2, 0)$, when 'upper' becomes 'lower' upon the corresponding point reflection and vice versa. We have tested the qualitative robustness of this state diagram by varying the radius of the front sphere such that $r_2 = 1.2$, while keeping $r_3 = 1$ and have found no qualitative difference between both cases.

For puller-like swimmers, however, the behavior depends strongly on the size of the enlarged aft sphere. Figure 7 (*a*) shows the swimming state diagram for $r_3 = 1.2$ and $r_2 = 1$

resulting in a small dipolar contribution to the hydrodynamic flow field. In contrast to pusher-like swimmers, gliding states are here found to be generally compatible with puller hydrodynamics. As can be seen from typical trajectories depicted in figure 8 (b) for various initial heights with $\theta_0 = 0.2$, the oscillations in the gliding states seem to dampen out apparently. A strictly horizontal motion near either the upper or bottom wall is approached, termed as lower gliding and upper gliding, respectively. As shown before for neutral swimmers, other configurations can lead to trapped states for relatively small dipolar coefficient. However, when r_3 is further increased, e.g. $r_3 = 2$ as shown in figure 7 (b), the non-oscillatory gliding persists, but additionally trapped states cease to exist and new sliding states emerge. In these latter states, the swimmer maintains a constant non-zero orientation and undergoes a translational motion along the horizontal direction at a constant height. The sliding behavior emerges following a state in which the propulsive forces and the viscous forces balance each other. For a strong front-aft asymmetry, the swimmer reaches a fixed point in the comoving frame for an angle strictly less that $\pi/2$ in magnitude and undergoes a purely translational motion without oscillations parallel to the nearest wall.

As pointed out by de Graaf *et al* [114], the onset of the oscillatory behavior observed in neutral swimmers shown in figure 5 is attributed to the hydrodynamic quadrupole moment which tends to rotate the swimmer away from the nearest wall. Analogous persistent oscillations have been observed by Zhu *et al* [105] for a neutral squirmer moving in a capillary tube. In contrast, the dipolar contribution tends to attract a pusher toward the wall and retain a puller on the mid-channel plane. By combining both the quadrupolar and dipolar contributions, the swimmer undergoes an oscillatory motion characterized by growing and decaying amplitudes for a pusher- and puller-type swimmer[8].

4.2. Swimming stability in the mid-plane

In the previous section, we have shown that pusher-type swimmers are trapped at the walls while puller-type swimmers undergo a gliding or sliding motion along the channel after a rapid decay of their oscillations. An oscillatory gliding of non-varying amplitude at a constant mean height is displayed by neutral three-sphere swimmers. For symmetry considerations, however, all three types undergo a trivial gliding motion along the channel centerline for $z_0 = H/2$ and $\theta_0 = 0$.

We now address the question of whether or not swimming on the channel centerline is a stable dynamical state. In order to proceed analytically, we restrict ourselves to the neutral swimmer case and assume for simplicity a zero initial

[8] See supporting information at (stacks.iop.org/JPhysCM/30/254004/mmedia) for illustrative movies showing the additional swimming states observed for puller-type swimmers with $r_2 = 1$. Movie 4 illustrates the lower gliding state ($z_0/H = 0.125, \theta_0 = 0.2$) shown in figure 8($b$) for $r_3 = 1.2$ (solid blue line). Movie 5 illustrates the upper gliding state ($z_0/H = 0.3125, \theta_0 = 0.2$) shown in figure 8($b$) for $r_3 = 1.2$ (dotted orange line). Movie 6 illustrates the lower sliding ($z_0/H = 0.5, \theta_0 = -0.3$) for $r_3 = 2$. Movie 7 illustrates the upper sliding ($z_0/H = 0.5, \theta_0 = 0.3$) for $r_3 = 2$. For illustrative purposes, the sizes of the spheres are not shown in real scale.

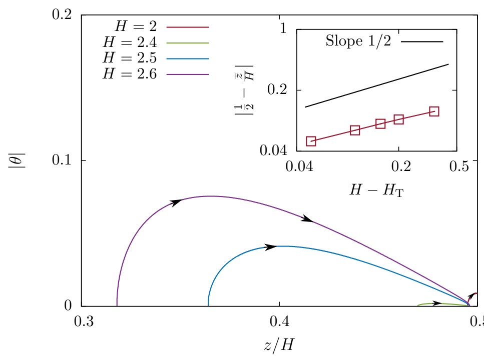

Figure 9. Trajectory of a neutral three-sphere swimmer in phase space, derived from equation (22) for $\theta_0 = 0$ and $z_0 = H/2 - \epsilon$ where $\epsilon = 0.01$. The inset shows a log–log plot of the scaled mean height relative to the channel centerline at the transition point. Arrow heads show the clockwise trajectories of the swimmer in the upper phase space.

orientation of the swimmer relative to the horizontal direction. By combining equations (15b) and (15c), eliminating the time variable and integrating both sides of the resulting equation, the orientation of the swimmer is related to the distance along the channel via

$$\theta^2 = \theta_0^2 + Q(z, z_0)\,, \tag{22}$$

where the integral function $Q(z,z_0)$ is given by

$$Q(z, z_0) = \int_{z_0}^{z} \frac{2K\,(C(u) - C(H-u))}{V_0 + K\,(B(u) + B(H-u))}\,\mathrm{d}u\,. \tag{23}$$

By evaluating the integral in equation (23) numerically and substituting the result into equation (22), we obtain trajectories in the (θ, z) phase space as plotted in figure 9 for $z_0 = H/2 - \epsilon$ where ϵ is an arbitrary small distance taken here as 0.01. As expected from the state diagram shown in figure 3, the trajectory for $H = 2$ corresponds to a limit cycle around the point with $z/H = 1/2$ and $\theta = 0$, indicating the central oscillatory gliding motion of the swimmer. In contrast, the trajectories are not centered at $z/H = 1/2$ anymore if values of H are larger than a transition value of about $H_\mathrm{T} \simeq 2.4$.

It is appropriate to denote by $\bar{z}$ the average value of the two points intersecting with the horizontal axis z/H. Around the channel centerline, the integrand on the right-hand side of equation (23) can be Taylor-expanded around $z = H/2$. Integrating the resulting equation between $H/2$ and $H/2 \pm \lambda$ yields

$$\theta^2 = c_2\lambda^2 + c_4\lambda^4 + \mathcal{O}(\lambda^6)\,, \tag{24}$$

where c_2 and c_4 are functions of H such that $c_4 < 0$ and c_2 changes sign from negative to positive as the channel height H increases beyond the transition height H_T. For $H > H_\mathrm{T}$, it undergoes an oscillatory motion around a mean height

$$\bar{z} = \frac{H}{2} \pm \frac{1}{2}\sqrt{-\frac{c_2}{c_4}}\,. \tag{25}$$

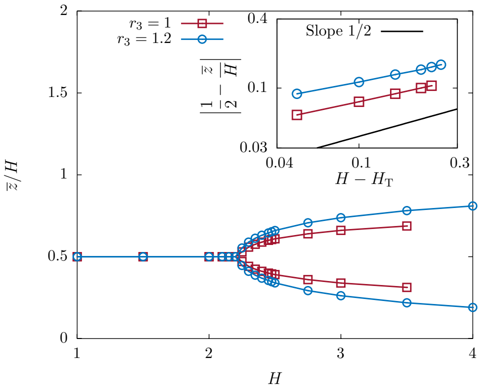

Figure 10. The scaled mean vertical position versus the channel height H for a neutral ($r_3 = 1$) and puller-type swimmer ($r_3 = 1.2$). The system undergoes a supercritical pitchfork bifurcation at $H_\mathrm{T} = 2.25$. Here $r_2 = 1$ and the swimmer is initially released from $\theta_0 = 0$ and $z_0 = H/2 \pm \epsilon$ where $\epsilon = 0.01$. Inset: Log–log plot of the mean oscillation height (for $r_3 = 1$) and steady gliding height (for $r_3 = 1.2$) around the transition point.

The scaling exponent of the scaled mean height relative to the channel centerline about the transition point is readily calculated from the logarithmic derivative,

$$\frac{\mathrm{d}\ln\left|\frac{\bar{z}}{H} - \frac{1}{2}\right|}{\mathrm{d}\ln\left(H - H_\mathrm{T}\right)} = \frac{1}{2}\frac{\mathrm{d}\ln\left(\frac{1}{H}\sqrt{-\frac{c_2}{c_4}}\right)}{\mathrm{d}\ln\left(H - H_\mathrm{T}\right)} \xrightarrow{H \to H_\mathrm{T}} \frac{1}{2}. \qquad (26)$$

Thus, the bifurcation is of a supercritical pitchfork-type. In the inset of figure 9, we show the evolution of $\left|\frac{1}{2} - \frac{\bar{z}}{H}\right|$ as a function of $H - H_T$ to verify the scaling behavior derived above around the transition height. An agreement between the theoretical value 1/2 and the numerical results is clearly manifested.

If the channel height H is further increased, the curve in figure 9 will finally intersect with the line $z = 0$, indicating the trapping of the swimmer. Such a behavior is in accord with the emergence of upper/lower trapping scenarios just above/below the central point corresponding to the central gliding motion in figure 3(*b*). Nevertheless, we note that a quantitative analysis is not available as the inclination angle may be large in this case, a situation that is beyond the simplified analytical theory proposed here.

We further elucidate the validity and reliability of our prediction by direct comparison with the numerical solution for a neutral swimmer as well as for a puller-type swimmer. As above, we also extract $\bar{z}$ values and observe a bifurcation behavior near $H \simeq 2.25$, as shown in figure 10. For a puller-type swimmer, $\bar{z}$ denotes the final height reached by the swimmer after the decay of oscillations. Clearly, the bifurcation is of a pitchfork-like type as swimming in the mid-channel in the $H < H_T$ regime (see figure 3(a)) becomes unstable for $H > H_T$. This corresponds to the appearance of the isolated points of central gliding at $z_0 = 0$ and $\theta_0 = 0$ in figure 3(*b*) and in figure 7(*a*). Instead, two new limit cycles emerge for a neutral swimmer, indicating the lower/upper oscillatory gliding modes of motion. For a puller swimmer, however, these new states represent stable fixed points since the oscillations are damped out in the steady limit. We also note that, in the case of the three-sphere swimmer of equal sphere radii with $H > 3.5$, a small perturbation leads to the trapping dynamics of the swimmer, as already discussed above. For the value of the exponent, however, a slight deviation from the theoretical prediction is observed (see the inset). We presume that this is most probably due to the approximations involved in our simplistic analytical theory.

5. Conclusions

The dynamics of microswimmers in confined geometries reveals qualitatively new behavior due to the anisotropic nature of hydrodynamic interactions with boundaries. In this work, we characterize the motion of a swimmer in the parallel-wall channel geometry, relevant to microfluidic and Hele-Shaw cell geometries. As a model swimmer, we choose the well known three-sphere model by Najafi and Golestanian [12]. By considering spheres of different radii, we are able to explore the relation between the flow signature of the swimmer (pusher, puller, or neutral swimmer) and the observed behavior. For each type we determine the phase diagram of possible final states as a function of the initial position and orientation of the swimmer in the channel. To account for the hydrodynamic interactions with the walls, we use the method of reflections [114, 121], which leads to good-quality approximations of the near-wall self and pair mobility for spheres.

In accord with the previously analyzed dynamics of the model swimmer close to a single planar no-slip boundary [145], for a neutral swimmer (corresponding to the classical design with three identical spheres) we observe three distinct types of behavior, namely trapping at the wall, escape from the wall, and gliding at a specific distance separated from the wall, determined by the size of the swimmer and in relation to the channel width. Here, we find that the oscillatory gliding state can occur both in the central area of the channel and closer to one of the walls. We then characterize the differences between puller- and pusher-type swimmer. For pusher-like swimmers, the oscillatory gliding state is unstable, and the evolution involves transient oscillations of growing amplitude, finally crossing into trapping in a hovering state at one of the walls. This observation within our numerical tests seems to be robust with respect to the changing properties of the swimmer. Puller-like swimmers, in contrast to that, exhibit a strong dependence of their modes of motion on their geometric characteristics. We find persistent gliding states compatible with the general puller hydrodynamics, with initial oscillations apparently dying out in favor of a steady solution at a fixed swimmer-to-wall distance. As the parameters of the swimmer are varied, the trapping states can vanish and sliding states appear, in which the swimmers translate at a constant height with a fixed orientation. We have also investigated analytically the stability of swimming along the centerline of the channel by considering small perturbations around the symmetric state. We find that above a critical channel width there is a pitchfork bifurcation for the motion closer to one of the two walls to appear, and we characterized it analytically.

We believe that our findings can be useful for the design and understanding of the motion of swimming microrobots in confined geometries. Relating the initial position in the channel to the final dynamical states is particularly important for engineering microfluidic devices to sort or accumulate swimmers. The presence of boundaries leads to a variety of complex behaviors emerging for the swimmers. Our work demonstrates, however, that simple analytical approximations can still be profitably used to characterize the dynamics in many cases.

Acknowledgments

The authors gratefully acknowledge support from the DFG (Deutsche Forschungsgemeinschaft) through the projects LO 418/17-2, ME 3571/2-2, and DA 2107/1-1. This work has been supported by the Ministry of Science and Higher Education of Poland via the Mobility Plus Fellowship awarded to ML. ML acknowledges funding from the Foundation for Polish Science within the START programme. The work of AJTMM was supported by a cross-disciplinary fellowship from the Human Frontier Science Program Organization (HFSPO - LT001670/2017). SG gratefully acknowledges funding from the Alexander von Humboldt Foundation. JB would like to acknowledge financial support from NSF Grant CBET 1603627. This article is based upon work from COST Action MP1305, supported by COST (European Cooperation in Science and Technology).

Appendices

In appendix A, we derive the Green's functions in a channel between two no-slip walls using a two-dimensional Fourier transform technique. We then describe in appendix B the method of reflections and express the Green's functions in the channel in terms of an infinite series of images. In appendix C, we provide an overview on the dynamics of a general three-sphere swimmer in an unbounded fluid domain and show that the induced flow far-field can conveniently be described by a combination of dipolar and quadrupolar flows. Further mathematical details are contained in appendix D.

Appendix A. Green's functions

In this appendix, we use a two-dimensional Fourier transform technique to derive the Green's functions in a channel between two no-slip walls. The solution method consists of reducing the partial differential equations (1) into ordinary differential equations in the direction perpendicular to the walls, whereas the spatial dependence of the hydrodynamic fields in the plane parallel to the wall are Fourier transformed into the wavenumber domain. Upon inverse Fourier transformation, the Green's functions can conveniently be expressed in terms of Bessel integrals of the first kind.

We define the two-dimensional Fourier transform

$$\mathscr{F}\{f(\boldsymbol{\rho})\} =: \tilde{f}(\boldsymbol{q}) = \int_{\mathbb{R}^2} f(\boldsymbol{\rho}) \mathrm{e}^{-\mathrm{i}\boldsymbol{q}\cdot\boldsymbol{\rho}} \, \mathrm{d}\boldsymbol{\rho} \,, \tag{A.1}$$

together with its inverse transform

$$\mathscr{F}^{-1}\{\tilde{f}(\boldsymbol{q})\} =: f(\boldsymbol{\rho}) = \frac{1}{(2\pi)^2} \int_{\mathbb{R}^2} \tilde{f}(\boldsymbol{q}) \mathrm{e}^{\mathrm{i}\boldsymbol{q}\cdot\boldsymbol{\rho}} \, \mathrm{d}\boldsymbol{q} \,, \tag{A.2}$$

where $\boldsymbol{\rho} = (x, y)$ is the projection of the vector $\boldsymbol{r}$ onto the plane $z = 0$, and $\boldsymbol{q} = (q_x, q_y)$ sets the coordinates in Fourier space.

It is more convenient to make use of the orthogonal basis introduced previously by Bickel [148, 149], in which the velocity vector field is decomposed into transverse, longitudinal, and normal components. Accordingly, the Fourier-transformed components of the velocity field in the Cartesian coordinate basis $\tilde{v}_x$ and $\tilde{v}_y$ are related to the longitudinal and transverse components in the new basis $\tilde{v}_l$ and $\tilde{v}_t$ via the orthogonal transformation

$$\begin{pmatrix} \tilde{v}_x \\ \tilde{v}_y \end{pmatrix} = \frac{1}{q} \begin{pmatrix} q_x & q_y \\ q_y & -q_x \end{pmatrix} \begin{pmatrix} \tilde{v}_l \\ \tilde{v}_t \end{pmatrix} , \tag{A.3}$$

wherein $q := |\boldsymbol{q}|$ is the wavenumber. The longitudinal and transverse components of the force f_l and f_t follow forthwith using an analogous transformation matrix.

We now assume that the point force is acting inside the channel at location $\boldsymbol{r}_0 = (0, 0, h)$, where $0 < h < H$. Upon two-dimensional Fourier transform, equations (1) governing the fluid motion yield ordinary differential equations in the variable z. Specifically [150]

$$\eta(-q^2\tilde{v}_l + \tilde{v}_{l,zz}) - \mathrm{i}q\tilde{p} + f_l \, \delta(z-h) = 0 \,, \tag{A.4}$$

$$\eta(-q^2\tilde{v}_t + \tilde{v}_{t,zz}) + f_t \, \delta(z-h) = 0 \,, \tag{A.5}$$

$$\eta(-q^2\tilde{v}_z + \tilde{v}_{z,zz}) - \tilde{p}_{,z} + f_z \, \delta(z-h) = 0 \,, \tag{A.6}$$

$$\mathrm{i}q\tilde{v}_l + \tilde{v}_{z,z} = 0 \,, \tag{A.7}$$

where a comma in a subscript stands for a partial derivative.

The velocity transverse component $\tilde{v}_t$ can directly be obtained by solving equation (A.5). By combining equations (A.6) and (A.4), the pressure field can readily be eliminated. As the continuity equation (A.7) provides a direct relation between the longitudinal and normal components, a fourth-order ordinary differential equation for $\tilde{v}_z$ is obtained, namely [148]

$$\tilde{v}_{z,zzzz} - 2q^2\tilde{v}_{z,zz} + q^4\tilde{v}_z = \frac{q^2}{\eta} f_z \, \delta(z-h) + \frac{\mathrm{i}q}{\eta} f_l \, \delta'(z-h) \,, \tag{A.8}$$

wherein δ' is the derivative of the Dirac delta function.

The Green's functions in 2D Fourier space can thus be identified from

$$\begin{pmatrix} \tilde{v}_t \\ \tilde{v}_l \\ \tilde{v}_z \end{pmatrix} = \begin{pmatrix} \tilde{\mathcal{G}}_{tt} & 0 & 0 \\ 0 & \tilde{\mathcal{G}}_{ll} & \tilde{\mathcal{G}}_{lz} \\ 0 & \tilde{\mathcal{G}}_{zl} & \tilde{\mathcal{G}}_{zz} \end{pmatrix} \begin{pmatrix} f_t \\ f_l \\ f_z \end{pmatrix} . \tag{A.9}$$

In the following, we present an analytical solution for the fluid velocity field in the channel by considering the solutions for the transverse and normal components independently.

A.1. Transverse velocity

The general solution of equation (A.5) inside a channel of width H can be written as

$$\tilde{v}_t = A_1 \mathrm{e}^{qz} + B_1 \mathrm{e}^{-qz} , \tag{A.10}$$

for $0 \leqslant z \leqslant h$, and

$$\tilde{v}_t = A_2 \mathrm{e}^{q(H-z)} + B_2 \mathrm{e}^{-q(H-z)} , \tag{A.11}$$

for $h \leqslant z \leqslant H$, wherein A_α and B_α, for $\alpha \in \{1, 2\}$, are wavenumber-dependent quantities to be determined from the underlying boundary conditions. The no-slip condition at the walls yields $\tilde{v}_t(z = 0) = \tilde{v}_t(z = H) = 0$. Additionally, the Dirac delta function implies the discontinuity of the first derivative at the point-force position. Specifically

$$\tilde{v}_{t,z}\big|_{z=h^+} - \tilde{v}_{t,z}\big|_{z=h^-} = -\frac{f_t}{\eta} , \tag{A.12}$$

by requiring the natural continuity of the transverse velocity at $z = h$.

Solving for the four unknown quantities yields

$$A_1 = \frac{f_t}{2q\eta} \frac{\sinh\left(q(H-h)\right)}{\sinh(qH)} , \tag{A.13}$$

$$A_2 = \frac{f_t}{2q\eta} \frac{\sinh(qh)}{\sinh(qH)} , \tag{A.14}$$

with $B_1 = -A_1$ and $B_2 = -A_2$.

A.2. Normal velocity

The general solution of equation (A.8) for the normal velocity is given by

$$\tilde{v}_z = (C_1 + D_1 z)\mathrm{e}^{qz} + (E_1 + F_1 z)\mathrm{e}^{-qz} , \tag{A.15}$$

for $0 \leqslant z \leqslant h$, and

$$\tilde{v}_z = \big(C_2 + D_2(H-z)\big)\mathrm{e}^{q(H-z)} + \big(E_2 + F_2(H-z)\big)\mathrm{e}^{-q(H-z)} \tag{A.16}$$

for $h \leqslant z \leqslant H$. Here $C_\alpha, D_\alpha, E_\alpha$, and F_α, $\alpha \in \{1, 2\}$, are unknown wavenumber-dependent functions to be determined from the boundary conditions. The no-slip condition at the channel walls yields $\tilde{v}_z(z = 0) = \tilde{v}_z(z = H) = 0$. In addition, since

$$\tilde{v}_l = \frac{\mathrm{i}}{q} \tilde{v}_{z,z} \tag{A.17}$$

as can be inferred from the continuity equation (A.7), we further require that $\tilde{v}_{z,z}(z = 0) = \tilde{v}_{z,z}(z = H) = 0$. Moreover, the Dirac delta function implies the discontinuity of the third derivative of the normal velocity,

$$\tilde{v}_{z,zzz}\big|_{z=h^+} - \tilde{v}_{z,zzz}\big|_{z=h^-} = \frac{q^2 f_z}{\eta} , \tag{A.18}$$

while the derivative of the delta function implies the discontinuity of the second derivative,

$$\tilde{v}_{z,zz}\big|_{z=h^+} - \tilde{v}_{z,zz}\big|_{z=h^-} = \frac{\mathrm{i}qf_l}{\eta} . \tag{A.19}$$

By requiring the continuity of the normal and longitudinal velocities at the point-force position, making use of (A.17), and solving the resulting system of eight equations for the unknown quantities, we readily obtain

$$C_1 = \frac{\mathrm{i}f_l}{8\eta q b_0}\Big(S_-(-u,-U) - S_+(u,U)\Big) - \frac{f_z}{8\eta q b_0}\Big(S_-(u,U) + S_+(-u,-U)\Big) ,$$
$$D_1 = \frac{1}{4\eta b_0}\Big(S_-(u,U) f_z + \mathrm{i}S_+(u,U) f_l\Big) ,$$
$$E_1 = -C_1 ,$$
$$F_1 = \frac{1}{4\eta b_0}\Big(S_+(-u,-U) f_z - \mathrm{i}S_-(-u,-U) f_l\Big) ,$$

where we have defined the dimensionless quantities

$$u = qh , \quad U = qH , \quad b_0 = 2 + 4U^2 - 2\cosh(2U) ,$$

in addition to

$$S_\pm(x_1, x_2) = b_1(x_1, x_2) \pm b_2(x_1, x_2) , \tag{A.20}$$

where

$$b_1(x_1, x_2) = 2\big(\cosh(x_1 - 2x_2) - \cosh(x_1) + 2U(u-U)\exp(-x_1)\big) ,$$
$$b_2(x_1, x_2) = 4\left(U\sinh(x_1) - u\exp(x_1 - x_2)\sinh x_2\right) .$$

The wavenumber-dependent functions for the fluid domain $h \leqslant z < H$ are obtained as

$$C_2 = -C_1|_{h \to H-h} , \tag{A.21}$$

and analogously for D_2, E_2, and F_2.

Upon inverse Fourier transformation, the Green's functions can conveniently be written in terms of convergent infinite integrals over the wavenumber q, as [151]

$$\mathcal{G}_{xx}(\boldsymbol{r}, z_0) = \frac{1}{4\pi}\int_0^\infty \Big(\tilde{\mathcal{G}}_+(q,z,z_0)J_0(\rho q) + \tilde{\mathcal{G}}_-(q,z,z_0)J_2(\rho q)\cos(2\theta)\Big) q \,\mathrm{d}q , \tag{A.22a}$$

$$\mathcal{G}_{yy}(\boldsymbol{r}, z_0) = \frac{1}{4\pi}\int_0^\infty \Big(\tilde{\mathcal{G}}_+(q,z,z_0)J_0(\rho q) - \tilde{\mathcal{G}}_-(q,z,z_0)J_2(\rho q)\cos(2\theta)\Big) q \,\mathrm{d}q , \tag{A.22b}$$

$$\mathcal{G}_{zz}(\boldsymbol{r}, z_0) = \frac{1}{2\pi}\int_0^\infty \tilde{\mathcal{G}}_{zz}(q,z,z_0)J_0(\rho q) q \,\mathrm{d}q \tag{A.22c}$$

for the diagonal components, and

$$\mathcal{G}_{xy}(\boldsymbol{r}, z_0) = \frac{\sin(2\theta)}{4\pi}\int_0^\infty \tilde{\mathcal{G}}_-(q,z,z_0)J_2(\rho q) q \,\mathrm{d}q , \tag{A.23a}$$

J. Phys.: Condens. Matter **30** (2018) 254004 A Daddi-Moussa-Ider *et al*

$$\mathcal{G}_{rz}(\boldsymbol{r}, z_0) = \frac{\mathrm{i}}{2\pi} \int_0^\infty \tilde{\mathcal{G}}_{lz}(q, z, z_0) J_1(\rho q) q \, \mathrm{d}q \,, \tag{A.23b}$$

$$\mathcal{G}_{zr}(\boldsymbol{r}, z_0) = \frac{\mathrm{i}}{2\pi} \int_0^\infty \tilde{\mathcal{G}}_{zl}(q, z, z_0) J_1(\rho q) q \, \mathrm{d}q \tag{A.23c}$$

for the off-diagonal components. Here $\rho^2 := x^2 + y^2$ and $\theta := \arctan(y/x)$ is the polar angle. In addition, J_n denotes the Bessel function [152] of the first kind of order n. Moreover,

$$\tilde{\mathcal{G}}_{\pm}(q, z) := \tilde{\mathcal{G}}_{tt}(q, z) \pm \tilde{\mathcal{G}}_{ll}(q, z) \,.$$

The components in Cartesian coordinates can be obtained from the usual transformation $\mathcal{G}_{xz} = \mathcal{G}_{rz} \cos\theta$, $\mathcal{G}_{yz} = \mathcal{G}_{rz} \sin\theta$, $\mathcal{G}_{zx} = \mathcal{G}_{zr} \cos\theta$, and $\mathcal{G}_{zy} = \mathcal{G}_{zr} \sin\theta$. Moreover, note that $\mathcal{G}_{yx} = \mathcal{G}_{xy}$.

Appendix B. Images of a Stokeslet between parallel no-slip walls

Here we describe the flow due to a point force in a Stokesian liquid between two parallel no-slip boundaries, in terms of an infinite series of image reflections. This method is complementary to the one developed by Liron and Mochon [136], who first gave the Green's function solution in terms of a Hankel transformation. A detailed comparison between these two methods is given by Mathijssen *et al* [121] for Stokeslets and higher order multipoles between a no-slip wall and a free surface. Previous studies have also used the reflection method to investigate the flow produced by mobile colloids [153]. To connect with previous notations in [121], we rewrite the Stokes equation (1) into the form

$$\boldsymbol{\nabla} P(\boldsymbol{x}) - \eta \nabla^2 \boldsymbol{v}(\boldsymbol{x}) = \boldsymbol{f}\, \delta(\boldsymbol{x} - \boldsymbol{y}), \tag{B.1}$$

$$\boldsymbol{\nabla} \cdot \boldsymbol{v}(\boldsymbol{x}) = 0, \tag{B.2}$$

where the fluid velocity is $\boldsymbol{v}(\boldsymbol{x}, t)$, the pressure field is $P(\boldsymbol{x}, t)$, the fluid position is $\boldsymbol{x} = (x_1, x_2, x_3)$ at time t, and the point force density is $\boldsymbol{f}\, \delta(\boldsymbol{x} - \boldsymbol{y})$ (Stokeslet) that acts on the liquid at position $\boldsymbol{y} = (y_1, y_2, y_3 = h)$. The velocity field must satisfy the no-slip boundary condition, $\boldsymbol{v}(\boldsymbol{x}) = \boldsymbol{0}$ at the channel walls $x_3 = 0, H$.

In the absence of boundaries, the flow is given by the Oseen tensor,

$$v_i^{\mathrm{S}}(\boldsymbol{x}, \boldsymbol{y}, \boldsymbol{f}) = \mathcal{J}_{ij}(\boldsymbol{x}, \boldsymbol{y}) f_j, \tag{B.3}$$

$$\mathcal{J}_{ij}(\boldsymbol{x}, \boldsymbol{y}) = \frac{1}{8\pi\eta} \left(\frac{\delta_{ij}}{r} + \frac{r_i r_j}{r^3} \right), \quad i, j \in \{1, 2, 3\}, \tag{B.4}$$

where $\boldsymbol{r} = \boldsymbol{x} - \boldsymbol{y}$, $r = |\boldsymbol{r}|$, δ_{ij} is the Kronecker delta, and repeated indices are summed over. The pressure that completes this solution is $P(\boldsymbol{x}, \boldsymbol{y}, \boldsymbol{f}) = \mathcal{P}_j f_j$ with $\mathcal{P}_j = r_j / 4\pi r^3$. We now aim to solve the flow in a channel in terms of this Oseen tensor and derivatives thereof only, using the method reflections.

On the one hand, for the case of only a single boundary being present, i.e. $H \to \infty$ in our system, Blake [142] first derived the Stokeslet flow in terms of an image system. The image is located at the position $\boldsymbol{Y}^{(0)} = (y_1, y_2, -y_3) = \mathrm{M} \cdot \boldsymbol{y}$, where the diagonal mirror matrix is $\mathrm{M} = \mathrm{diag}(1, 1, -1)$. The image tensor is found by applying the reflection operator, B, of the 'Bottom' wall to the Stokeslet. This operator $\mathrm{B}(\lambda)$ is a function of the distance from the wall to the Stokeslet, which is $\lambda = y_3$ here. Hence, we have

$$\mathcal{B}_{ij}(\boldsymbol{x}, \boldsymbol{Y}^{(0)}) = \mathrm{B} \;\; \mathcal{J}_{ij}(\boldsymbol{x}, \boldsymbol{y}^{(0)}) \,, \tag{B.5}$$

where the Blake solution can then be written in terms of the Oseen tensor as

$$\begin{aligned} &\mathcal{B}_{ij}(\boldsymbol{x}, \boldsymbol{Y}^{(0)}) \\ &\quad = (-\delta_{jk} + 2\lambda \delta_{k3} \tilde{\partial}_j + \lambda^2 \, \mathrm{M}_{jk} \tilde{\nabla}^2) \mathcal{J}_{ik}(\boldsymbol{x}, \boldsymbol{Y}^{(0)}) \\ &\quad = (-\delta_{jk} + 2 y_3 \delta_{k3} \tilde{\partial}_j + y_3^2 \, \mathrm{M}_{jk} \tilde{\nabla}^2) \mathcal{J}_{ik}(\boldsymbol{x}, \boldsymbol{Y}^{(0)}) \,, \end{aligned} \tag{B.6}$$

where the derivatives $\tilde{\partial}_j = \frac{\partial}{\partial y_j} = \mathrm{M}_{jl} \frac{\partial}{\partial Y_l^{(0)}}$ and $\tilde{\nabla}^2 = \tilde{\partial}_l \tilde{\partial}_l$ are with respect to the force position $\boldsymbol{y}$. The first row of table B1 lists this tensor $\mathcal{B}_{ij}(\boldsymbol{x}, \boldsymbol{Y}^{(0)})$ as the first 'Bottom' reflection. The overall flow field is then given by

$$v_i^{\mathrm{B}}(\boldsymbol{x}, \boldsymbol{y}) = \left[\mathcal{J}_{ij}(\boldsymbol{x}, \boldsymbol{y}^{(0)}) + \mathcal{B}_{ij}(\boldsymbol{x}, \boldsymbol{Y}^{(0)}) \right] f_j. \tag{B.7}$$

On the other hand, if only the top wall is present at $x_3 = H$, the distance from the wall to the Stokeslet is $\lambda = y_3 - H$ and the reflection is located at $\boldsymbol{Y}^{(-1)} = (y_1, y_2, 2H - y_3)$. The image tensor is then given by applying the reflection operator, $\mathrm{T}(\lambda)$, of the 'Top' wall to the Stokeslet,

$$\begin{aligned} &\mathcal{T}_{ij}(\boldsymbol{x}, \boldsymbol{Y}^{(-1)}) \\ &\quad = \mathrm{T} \;\; \mathcal{J}_{ij}(\boldsymbol{x}, \boldsymbol{y}^{(0)}) \\ &\quad = (-\delta_{jk} + 2\lambda \delta_{k3} \tilde{\partial}_j + \lambda^2 \, \mathrm{M}_{jk} \tilde{\nabla}^2) \mathcal{J}_{ik}(\boldsymbol{x}, \boldsymbol{Y}^{(-1)}) \\ &\quad = (-\delta_{jk} - 2\{H - y_3\} \delta_{k3} \tilde{\partial}_j \\ &\qquad + \{H - y_3\}^2 \, \mathrm{M}_{jk} \tilde{\nabla}^2) \mathcal{J}_{ik}(\boldsymbol{x}, \boldsymbol{Y}^{(-1)}) \,. \end{aligned} \tag{B.8}$$

The second row of table B1 lists this result as the first 'Top' reflection. The overall flow, given by adding (B.4) and (B.8), satisfies the no-slip condition exactly on the top surface.

Next, when there are two parallel plates, one can continue using the method of images by computing the reflections of the reflections, and again the reflections of those, in order to generate an infinite series of images. Each image system consists of Stokeslets and derivatives thereof, thus satisfies the Stokes equations, and by adding more reflections the boundary conditions on both surfaces will be satisfied asymptotically. We first determine the positions of the image systems,

$$\boldsymbol{y}^{(m)} = (y_1, y_2, y_3 - 2mH), \quad m = 0, \pm 1, \pm 2, \ldots, \tag{B.9}$$

$$\boldsymbol{Y}^{(m)} = (y_1, y_2, -y_3 - 2mH), \quad m = 0, \pm 1, \pm 2, \ldots, \tag{B.10}$$

Table B1. Recursion relations for the successive image systems of a Stokeslet between two parallel no-slip walls. The first image system of the Oseen tensor from reflection at the bottom wall is the Blake tensor, and the second image from reflection at the top interface is the mirrored Blake tensor. Subsequent image systems are obtained from further reflection operations with B denoting the 'bottom' wall and T the 'top' wall, that operate linearly on all the Oseen tensor terms $\mathcal{J}_{ij}$ of the image system tensor $\mathcal{G}_{ij}$.

(n)	Position	Replace	With
(0)	$\boldsymbol{y}^{(0)}$	—	$\mathcal{J}_{ij}(\boldsymbol{x},\boldsymbol{y}^{(0)})$
(1)	$\boldsymbol{Y}^{(0)}$	B $\mathcal{J}_{ij}(\boldsymbol{x},\boldsymbol{y}^{(0)})$	$(-\delta_{jk}+2y_3\delta_{k3}\tilde{\partial}_j+y_3^2\,\mathrm{M}_{jk}\tilde{\nabla}^2)\mathcal{J}_{ik}(\boldsymbol{x},\boldsymbol{Y}^{(0)})$
(2)	$\boldsymbol{Y}^{(-1)}$	T $\mathcal{J}_{ij}(\boldsymbol{x},\boldsymbol{y}^{(0)})$	$(-\delta_{jk}-2(H-y_3)\delta_{k3}\tilde{\partial}_j+(H-y_3)^2\,\mathrm{M}_{jk}\tilde{\nabla}^2)\mathcal{J}_{ik}(\boldsymbol{x},\boldsymbol{Y}^{(-1)})$
(3)	$\boldsymbol{y}^{(-1)}$	T $\mathcal{J}_{ij}(\boldsymbol{x},\boldsymbol{Y}^{(0)})$	$(-\delta_{jk}-2(H+y_3)\delta_{k3}\,\mathrm{M}_{jl}\tilde{\partial}_l+(H+y_3)^2\,\mathrm{M}_{jk}\tilde{\nabla}^2)\mathcal{J}_{ik}(\boldsymbol{x},\boldsymbol{y}^{(-1)})$
(4)	$\boldsymbol{y}^{(1)}$	B $\mathcal{J}_{ij}(\boldsymbol{x},\boldsymbol{Y}^{(-1)})$	$(-\delta_{jk}+2(2H-y_3)\delta_{k3}\,\mathrm{M}_{jl}\tilde{\partial}_l+(2H-y_3)^2\,\mathrm{M}_{jk}\tilde{\nabla}^2)\mathcal{J}_{ik}(\boldsymbol{x},\boldsymbol{y}^{(1)})$
(5)	$\boldsymbol{Y}^{(1)}$	B $\mathcal{J}_{ij}(\boldsymbol{x},\boldsymbol{y}^{(-1)})$	$(-\delta_{jk}+2(2H+y_3)\delta_{k3}\tilde{\partial}_j+(2H+y_3)^2\,\mathrm{M}_{jk}\tilde{\nabla}^2)\mathcal{J}_{ik}(\boldsymbol{x},\boldsymbol{Y}^{(1)})$
(6)	$\boldsymbol{Y}^{(-2)}$	T $\mathcal{J}_{ij}(\boldsymbol{x},\boldsymbol{y}^{(1)})$	$(-\delta_{jk}-2(3H-y_3)\delta_{k3}\tilde{\partial}_j+(3H-y_3)^2\,\mathrm{M}_{jk}\tilde{\nabla}^2)\mathcal{J}_{ik}(\boldsymbol{x},\boldsymbol{Y}^{(-2)})$
(7)	$\boldsymbol{y}^{(-2)}$	T $\mathcal{J}_{ij}(\boldsymbol{x},\boldsymbol{Y}^{(1)})$	$(-\delta_{jk}-2(3H+y_3)\delta_{k3}\,\mathrm{M}_{jl}\tilde{\partial}_l+(3H+y_3)^2\,\mathrm{M}_{jk}\tilde{\nabla}^2)\mathcal{J}_{ik}(\boldsymbol{x},\boldsymbol{y}^{(-2)})$
(8)	$\boldsymbol{y}^{(2)}$	B $\mathcal{J}_{ij}(\boldsymbol{x},\boldsymbol{Y}^{(-2)})$	$(-\delta_{jk}+2(4H-y_3)\delta_{k3}\,\mathrm{M}_{jl}\tilde{\partial}_l+(4H-y_3)^2\,\mathrm{M}_{jk}\tilde{\nabla}^2)\mathcal{J}_{ik}(\boldsymbol{x},\boldsymbol{y}^{(2)})$
(9)	$\boldsymbol{Y}^{(2)}$	B $\mathcal{J}_{ij}(\boldsymbol{x},\boldsymbol{y}^{(-2)})$	$(-\delta_{jk}+2(4H+y_3)\delta_{k3}\tilde{\partial}_j+(4H+y_3)^2\,\mathrm{M}_{jk}\tilde{\nabla}^2)\mathcal{J}_{ik}(\boldsymbol{x},\boldsymbol{Y}^{(2)})$
(10)	$\boldsymbol{Y}^{(-3)}$	T $\mathcal{J}_{ij}(\boldsymbol{x},\boldsymbol{y}^{(2)})$	$(-\delta_{jk}-2(5H-y_3)\delta_{k3}\tilde{\partial}_j+(5H-y_3)^2\,\mathrm{M}_{jk}\tilde{\nabla}^2)\mathcal{J}_{ik}(\boldsymbol{x},\boldsymbol{Y}^{(-3)})$
(11)	$\boldsymbol{y}^{(-3)}$	T $\mathcal{J}_{ij}(\boldsymbol{x},\boldsymbol{Y}^{(2)})$	$(-\delta_{jk}-2(5H+y_3)\delta_{k3}\,\mathrm{M}_{jl}\tilde{\partial}_l+(5H+y_3)^2\,\mathrm{M}_{jk}\tilde{\nabla}^2)\mathcal{J}_{ik}(\boldsymbol{x},\boldsymbol{y}^{(-3)})$
(12)	$\boldsymbol{y}^{(3)}$	B $\mathcal{J}_{ij}(\boldsymbol{x},\boldsymbol{Y}^{(-3)})$	$(-\delta_{jk}+2(6H-y_3)\delta_{k3}\,\mathrm{M}_{jl}\tilde{\partial}_l+(6H-y_3)^2\,\mathrm{M}_{jk}\tilde{\nabla}^2)\mathcal{J}_{ik}(\boldsymbol{x},\boldsymbol{y}^{(3)})$
(13)	$\boldsymbol{Y}^{(3)}$	B $\mathcal{J}_{ij}(\boldsymbol{x},\boldsymbol{y}^{(-3)})$	$(-\delta_{jk}+2(6H+y_3)\delta_{k3}\tilde{\partial}_j+(6H+y_3)^2\,\mathrm{M}_{jk}\tilde{\nabla}^2)\mathcal{J}_{ik}(\boldsymbol{x},\boldsymbol{Y}^{(3)})$
$\vdots$	$\vdots$	$\vdots$	$\vdots$

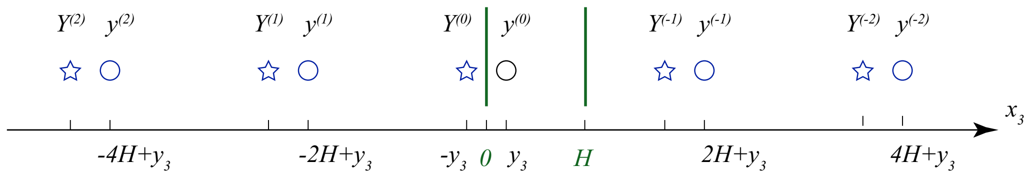

Figure B1. Diagram showing the image reflections of a Stokeslet, located at y_3, between two parallel no-slip walls, located at $x_3 = 0, H$. The images reflected an even number of times (circles) are located at $y_3^{(m)} = y_3 - 2mH$ and those reflected an odd number of times (stars) are located at $Y_3^{(m)} = -y_3 - 2mH$.

where the images at $\boldsymbol{Y}^{(m)}$ are reflected an odd number of times and the images at $\boldsymbol{y}^{(m)}$ an even number of times. The original Stokeslet is also included here at position $\boldsymbol{y} = \boldsymbol{y}^{(0)}$. The resulting series of images is shown in figure B1. Then we must determine the functional form of the image tensors, $\mathcal{G}_{ij}(\boldsymbol{x},\boldsymbol{y}^{(m)})$ and $\mathcal{G}_{ij}(\boldsymbol{x},\boldsymbol{Y}^{(m)})$. For a given image, this is done by replacing all the Oseen tensors $\mathcal{J}_{ij}$ in the previous image system by the appropriate Blake tensor. The key idea is that the newly obtained reflection is again an expression in terms of Oseen tensors, and derivatives thereof, which can then be replaced again for the next reflection.

To see this, we explicitly consider the second (T) reflection of the first (B) image (B.6). This upward reflection of the image at position $Y_3^{(0)} = -y_3$, located a distance $\lambda = -(H + y_3)$ from the top surface, creates a new image at position $y_3^{(-1)} = 2H + y_3$. Its image tensor is given by applying the T operator linearly to all Stokeslets in the image,

$$\begin{aligned}
&\mathcal{G}_{ij}(\boldsymbol{x},\boldsymbol{y}^{(-1)}) \\
&\quad= \mathrm{T}\ \mathcal{B}_{ij}(\boldsymbol{x},\boldsymbol{Y}^{(0)}) \\
&\quad= \mathrm{T}\ \left((-\delta_{jk}+2y_3\delta_{k3}\tilde{\partial}_j+y_3^2\,\mathrm{M}_{jk}\tilde{\nabla}^2)\mathcal{J}_{ik}(\boldsymbol{x},\boldsymbol{Y}^{(0)})\right) \\
&\quad= (-\delta_{jk}+2y_3\delta_{k3}\tilde{\partial}_j+y_3^2\,\mathrm{M}_{jk}\tilde{\nabla}^2)\left(\mathrm{T}\ \mathcal{J}_{ik}(\boldsymbol{x},\boldsymbol{Y}^{(0)})\right) \\
&\quad= (-\delta_{jk}+2y_3\delta_{k3}\tilde{\partial}_j+y_3^2\,\mathrm{M}_{jk}\tilde{\nabla}^2) \\
&\qquad\left((-\delta_{kl}-2(H+y_3)\delta_{l3}\,\mathrm{M}_{ku}\tilde{\partial}_u\right. \\
&\qquad\left.+(H+y_3)^2\,\mathrm{M}_{kl}\tilde{\nabla}^2)\mathcal{J}_{il}(\boldsymbol{x},\boldsymbol{y}^{(-1)})\right).
\end{aligned} \tag{B.11}$$

The replacement rule is listed as the 3rd entry in table B1 and the final expression as the 3rd entry in table B2. This

Table B2. Explicit expressions of the image system tensors $\mathcal{G}_{ij}$ of the first few image systems of a Stokeslet between two parallel no-slip walls. The indices $i, j, k, l, o, p, u, v \in \{1, 2, 3\}$, and repeated indices are summed over. Added together, these tensors yield the Green's function of flow between two parallel no-slip walls.

(n)	Image system tensor $\mathcal{G}_{ij}(\boldsymbol{x}, \boldsymbol{y}^{(m)}$ or $\boldsymbol{Y}^{(m)}) =$
(0)	$\mathcal{J}_{ij}(\boldsymbol{x}, \boldsymbol{y}^{(0)})$
(1)	$(-\delta_{jk} + 2y_3\delta_{k3}\tilde{\partial}_j + y_3^2\, \mathrm{M}_{jk}\tilde{\nabla}^2)\mathcal{J}_{ik}(\boldsymbol{x}, \boldsymbol{Y}^{(0)})$
(2)	$(-\delta_{jk} - 2(H - y_3)\delta_{k3}\tilde{\partial}_j + (H - y_3)^2\, \mathrm{M}_{jk}\tilde{\nabla}^2)\mathcal{J}_{ik}(\boldsymbol{x}, \boldsymbol{Y}^{(-1)})$
(3)	$(-\delta_{jk} + 2y_3\delta_{k3}\tilde{\partial}_j + y_3^2\, \mathrm{M}_{jk}\tilde{\nabla}^2)\,(-\delta_{kl} - 2(H + y_3)\delta_{l3}\, \mathrm{M}_{ku}\tilde{\partial}_u + (H + y_3)^2\, \mathrm{M}_{kl}\tilde{\nabla}^2)\mathcal{J}_{il}(\boldsymbol{x}, \boldsymbol{y}^{(-1)})$
(4)	$(-\delta_{jk} - 2(H - y_3)\delta_{k3}\tilde{\partial}_j + (H - y_3)^2\, \mathrm{M}_{jk}\tilde{\nabla}^2)\,(-\delta_{kl} + 2(2H - y_3)\delta_{l3}\, \mathrm{M}_{ku}\tilde{\partial}_u + (2H - y_3)^2\, \mathrm{M}_{kl}\tilde{\nabla}^2)\mathcal{J}_{il}(\boldsymbol{x}, \boldsymbol{y}^{(1)})$
(5)	$(-\delta_{jk} + 2y_3\delta_{k3}\tilde{\partial}_j + y_3^2\, \mathrm{M}_{jk}\tilde{\nabla}^2)\,(-\delta_{kl} - 2(H + y_3)\delta_{l3}\, \mathrm{M}_{ku}\tilde{\partial}_u + (H + y_3)^2\, \mathrm{M}_{kl}\tilde{\nabla}^2)$ $(-\delta_{lo} + 2(2H + y_3)\delta_{o3}\tilde{\partial}_l + (2H + y_3)^2\, \mathrm{M}_{lo}\tilde{\nabla}^2)\mathcal{J}_{io}(\boldsymbol{x}, \boldsymbol{Y}^{(1)})$
(6)	$(-\delta_{jk} - 2(H - y_3)\delta_{k3}\tilde{\partial}_j + (H - y_3)^2\, \mathrm{M}_{jk}\tilde{\nabla}^2)\,(-\delta_{kl} + 2(2H - y_3)\delta_{l3}\, \mathrm{M}_{ku}\tilde{\partial}_u + (2H - y_3)^2\, \mathrm{M}_{kl}\tilde{\nabla}^2)$ $(-\delta_{lo} - 2(3H - y_3)\delta_{o3}\tilde{\partial}_l + (3H - y_3)^2\, \mathrm{M}_{lo}\tilde{\nabla}^2)\mathcal{J}_{io}(\boldsymbol{x}, \boldsymbol{Y}^{(-2)})$
(7)	$(-\delta_{jk} + 2y_3\delta_{k3}\tilde{\partial}_j + y_3^2\, \mathrm{M}_{jk}\tilde{\nabla}^2)\,(-\delta_{kl} - 2(H + y_3)\delta_{l3}\, \mathrm{M}_{ku}\tilde{\partial}_u + (H + y_3)^2\, \mathrm{M}_{kl}\tilde{\nabla}^2)$ $(-\delta_{lo} + 2(2H + y_3)\delta_{o3}\tilde{\partial}_l + (2H + y_3)^2\, \mathrm{M}_{lo}\tilde{\nabla}^2)$ $(-\delta_{op} - 2(3H + y_3)\delta_{p3}\, \mathrm{M}_{ov}\tilde{\partial}_v + (3H + y_3)^2\, \mathrm{M}_{op}\tilde{\nabla}^2)\mathcal{J}_{ip}(\boldsymbol{x}, \boldsymbol{y}^{(-2)})$
(8)	$(-\delta_{jk} - 2(H - y_3)\delta_{k3}\tilde{\partial}_j + (H - y_3)^2\, \mathrm{M}_{jk}\tilde{\nabla}^2)\,(-\delta_{kl} + 2(2H - y_3)\delta_{l3}\, \mathrm{M}_{ku}\tilde{\partial}_u + (2H - y_3)^2\, \mathrm{M}_{kl}\tilde{\nabla}^2)$ $(-\delta_{lo} - 2(3H - y_3)\delta_{o3}\tilde{\partial}_l + (3H - y_3)^2\, \mathrm{M}_{lo}\tilde{\nabla}^2)$ $(-\delta_{op} + 2(4H - y_3)\delta_{p3}\, \mathrm{M}_{ov}\tilde{\partial}_v + (4H - y_3)^2\, \mathrm{M}_{op}\tilde{\nabla}^2)\mathcal{J}_{ip}(\boldsymbol{x}, \boldsymbol{y}^{(2)})$
$\vdots$	$\vdots$

expression may be verified by adding (B.6) to (B.11) and ascertain that the no-slip condition holds on $x_3 = H$ for all i, j.

Similarly, the higher-order image tensors are found by recursively applying the reflection operations,

$$\mathcal{G}_{ij}(\boldsymbol{x}, \boldsymbol{Y}^{(m)}) = \mathrm{B}\ \mathcal{G}_{ij}(\boldsymbol{x}, \boldsymbol{y}^{(-m)}), \tag{B.12}$$

$$\mathcal{G}_{ij}(\boldsymbol{x}, \boldsymbol{Y}^{(-m)}) = \mathrm{T}\ \mathcal{G}_{ij}(\boldsymbol{x}, \boldsymbol{y}^{(m-1)}), \tag{B.13}$$

$$\mathcal{G}_{ij}(\boldsymbol{x}, \boldsymbol{y}^{(-m)}) = \mathrm{T}\ \mathcal{G}_{ij}(\boldsymbol{x}, \boldsymbol{Y}^{(m-1)}), \tag{B.14}$$

$$\mathcal{G}_{ij}(\boldsymbol{x}, \boldsymbol{y}^{(m)}) = \mathrm{B}\ \mathcal{G}_{ij}(\boldsymbol{x}, \boldsymbol{Y}^{(-m)}), \tag{B.15}$$

where $m \geqslant 1$. These replacement rules are written out for the first few images in tables B1 and B2 that give the resulting expressions of the image tensors explicitly.

Finally, adding all images together we obtain the Green's function for a Stokeslet between two parallel no-slip surfaces,

$$v_i(\boldsymbol{x}, \boldsymbol{y}, \boldsymbol{f}) = \mathcal{F}_{ij} f_j, \tag{B.16}$$

$$\mathcal{F}_{ij}(\boldsymbol{x}, \boldsymbol{y}) = \sum_{m=-\infty}^{\infty} \left[\mathcal{G}_{ij}(\boldsymbol{x}, \boldsymbol{y}^{(m)}) + \mathcal{G}_{ij}(\boldsymbol{x}, \boldsymbol{Y}^{(m)})\right]. \tag{B.17}$$

Note that the no-slip condition can be satisfied exactly on the bottom surface by adding up the reflections to $n = 1, 5, 9, 13, \ldots$ from table B2, and satisfied exactly on the top surface by adding up the reflections to $n = 3, 7, 11, 15, \ldots$. However, if symmetric flow fields are required about the channel centerline, an even number of images $n = 2, 4, 6, 8, \ldots$ must be employed.

Appendix C. Flow far-field of a three-sphere swimmer in bulk

In this appendix, we show how the flow far-field of a three-sphere swimmer can well be described by a combination of dipolar and quadrupolar flows. In the particular situation of the internal forces symmetrically distributed along the swimming axis, the dipolar contribution vanishes since the swimmer becomes invariant under time-reversal and parity transformation [154]. This type of swimmer is referred to as a self-T-dual swimmer whose leading term in the flow-far field is a quadrupole.

Firstly, we assume that the spheres have the same radius a but different oscillation amplitudes. The flow-far field is given by [17]

$$\begin{aligned} \boldsymbol{v} =& \alpha V \left(\frac{a}{s}\right)^2 \left(3\left(\hat{\boldsymbol{t}}\cdot\hat{\boldsymbol{s}}\right)^2 - 1\right)\hat{\boldsymbol{s}} \\ &+ \sigma V \left(\frac{a}{s}\right)^3 \left[3\left(5\left(\hat{\boldsymbol{t}}\cdot\hat{\boldsymbol{s}}\right)^3 - 3\left(\hat{\boldsymbol{t}}\cdot\hat{\boldsymbol{s}}\right)\right)\hat{\boldsymbol{s}}\right. \\ &\left. - \left(3\left(\hat{\boldsymbol{t}}\cdot\hat{\boldsymbol{s}}\right)^2 - 1\right)\hat{\boldsymbol{t}}\right] + \mathcal{O}\left(\frac{1}{s^4}\right), \end{aligned} \tag{C.1}$$

where the unit vector $\hat{\boldsymbol{s}} := \boldsymbol{s}/s$ and the leading order swimming velocity averaged over one period is $V = -\frac{7}{24}aK$. In addition, the dipolar and quadrupolar coefficients are given by

$$\alpha = \frac{27}{56}\frac{u_{20}^2 - u_{10}^2}{a}, \qquad \sigma = \frac{15}{56}\frac{1}{a^2}. \tag{C.2}$$

While the quadrupolar coefficient takes only positive values, the dipolar coefficient can be of different signs depending on the difference in the amplitude of the oscillations. If $|u_{20}| > |u_{10}|$, then the dipole coefficient is positive, $\alpha > 0$, and thus the swimmer is a pusher that pushes out the fluid along its swimming axis. In contrast to that, if $|u_{20}| < |u_{10}|$, the swimmer is a puller as it pulls the fluid inward along its swimming path.

It is worth noting that the aforementioned assumption $2a + |u_{10}| + |u_{20}| \ll L$ yields that α is necessarily much smaller than σ. Accordingly, the ratio between the

Table D1. The coefficients A_n, B_n and C_n of the series functions defined in equations (D.1). Here $w_1 := \sqrt{1+z^2}$ and $w_2 := \sqrt{1+4z^4}$.

A_0	$\frac{7}{24} - \frac{7}{24} w_2 w_1 - \frac{w_2}{24} + \frac{w_1}{3}$
A_2	$-\frac{35}{4} w_2 w_1 - \frac{13}{12} w_2 + \frac{14}{3} w_1$
A_4	$-\frac{931}{8} w_2 w_1 - \frac{1159}{96} w_2 + \frac{91}{3} w_1$
A_6	$-\frac{5425}{6} w_2 w_1 - \frac{2407}{32} w_2 + 172\, w_1$
A_8	$-\frac{364\,35}{8} w_2 w_1 - \frac{9203}{32} w_2 + 977\, w_1$
A_{10}	$-\frac{624\,75}{4} w_2 w_1 - \frac{225\,97}{32} w_2 + 4042\, w_1$
A_{12}	$-\frac{298\,445}{8} w_2 w_1 - \frac{4721}{4} w_2 + 105\,67\, w_1$
A_{14}	$-624\,75\, w_2 w_1 - \frac{3107}{2} w_2 + 173\,12\, w_1$
A_{16}	$-728\,70\, w_2 w_1 - 1904\, w_2 + 178\,12\, w_1$
A_{18}	$-\frac{173\,600}{3} w_2 w_1 - \frac{5768}{3} w_2 + \frac{336\,16}{3} w_1$
A_{20}	$-297\,92\, w_2 w_1 - \frac{3520}{3} w_2 + \frac{118\,40}{3} w_1$
A_{22}	$-8960\, w_2 w_1 - \frac{896}{3} w_2 + \frac{1792}{3} w_1$
A_{24}	$-\frac{3584}{3} w_2 w_1$
B_{-1}	$\frac{3}{32} w_2 w_1$
B_0	$\frac{7}{24} - \frac{7}{24} w_2 w_1 - \frac{w_2}{24} + \frac{w_1}{3}$
B_1	$\frac{45}{32} w_2 w_1$
B_2	$-\frac{35}{8} w_2 w_1 - \frac{89}{96} w_2 + \frac{8}{3} w_1$
B_3	$\frac{261}{32} w_2 w_1$
B_4	$-\frac{203}{8} w_2 w_1 - \frac{175}{24} w_2 + \frac{82}{3} w_1$
B_5	$\frac{735}{32} w_2 w_1$
B_6	$-\frac{1715}{24} w_2 w_1 - \frac{2425}{96} w_2 + \frac{208}{3} w_1$
B_7	$\frac{261}{8} w_2 w_1$
B_8	$-\frac{203}{2} w_2 w_1 - \frac{875}{24} w_2 + \frac{197}{3} w_1$
B_9	$\frac{45}{2} w_2 w_1$
B_{10}	$-70\, w_2 w_1 - \frac{91}{6} w_2 + \frac{64}{3} w_1$
B_{11}	$6\, w_2 w_1$
B_{12}	$-\frac{56}{3} w_2 w_1 - 6 w_2$
C_3	$\frac{3}{16} w_2 - 6\, w_1$
C_5	$\frac{321}{64} w_2 - 102\, w_1$
C_7	$\frac{3699}{64} w_2 - 702\, w_1$
C_9	$\frac{239\,31}{64} w_2 - 2502\, w_1$
C_{11}	$\frac{948\,69}{64} w_2 - 4842\, w_1$
C_{13}	$\frac{294\,57}{8} w_2 - 4482\, w_1$
C_{15}	$\frac{224\,19}{4} w_2 + 198\, w_1$
C_{17}	$4824\, w_2 + 4878\, w_1$
C_{19}	$1836\, w_2 + 4968\, w_1$
C_{21}	$-96\, w_2 + 2208\, w_1$
C_{23}	$-192\, w_2 + 384\, w_1$

dipolar and quadrupolar coefficients in absolute value $|\alpha/\sigma| = \frac{9}{5} a |u_{20}^2 - u_{10}^2|$ can be even three orders of magnitude smaller than 1. For instance, by taking $u_{10} = a = 0.1$ and $u_{20} = 2u_{10}$, the ratio $|\alpha/\sigma| = 5.4 \times 10^{-3}$. Even though the dipolar term persists for $u_{10} \neq u_{20}$, the flow field is primly dominated by the quadrupolar contribution, at intermediate distances from the swimmer.

We next assume that $u_{10} = u_{20}$ and consider the case in which the spheres have different sizes, as is considered in the present work. The swimming velocity averaged over one full cycle reads [14]

$$V = -\frac{21K}{8} \frac{a_1 a_2 a_3}{(a_1 + a_2 + a_3)^2} \, . \tag{C.3}$$

In addition, the dipolar and quadrupolar coefficients of the corresponding flow field are given by

$$\alpha = \frac{3}{4} \frac{a_2 - a_3}{a^2} \, , \qquad \sigma = \frac{3}{56} \frac{4\,(a_2 + a_3) - 3a}{a^3} \, , \tag{C.4}$$

where a is taken as the radius of the central sphere a_1. Remarkably, the swimmer is a pusher (puller) if $a_2 > a_3$ ($a_2 < a_3$), independently of the central sphere a. In addition, if $a < \frac{4}{3}(a_2 + a_3)$, then the quadrupolar coefficient is positive, $\sigma > 0$, a situation which characterizes swimmers with small bodies and elongated flagella. The flow far-field of the swimmer can be dipolar- or quadrupolar-dominated at intermediate distances from the swimmer, depending on the sizes of the spheres.

We finally assess the effect of the mean arm lengths on the far-field hydrodynamics. By posing $L_2 = \beta L_1 = L$ and scaling the lengths by L, the averaged swimming velocity is given by [14]

$$V = -\frac{aK}{6} \left(1 + \frac{1}{\beta^2} - \frac{1}{(1+\beta)^2} \right) \, , \tag{C.5}$$

and the dipolar and quadrupolar moments follow as

$$\alpha = \frac{3}{8a} \frac{N_\alpha}{D} (1 - \beta) \, , \qquad \sigma = \frac{3}{16a^2} \frac{N_\sigma}{D} \, , \tag{C.6}$$

where we have defined for convenience the quantities

$$N_\alpha = \beta \left(2 + 7\beta + 11\beta^2 + 7\beta^3 + 2\beta^4 \right) \, ,$$
$$N_\sigma = \beta \left(2 + 4\beta + \beta^2 - 4\beta^3 + \beta^4 + 4\beta^5 + 2\beta^6 \right) \, ,$$
$$D = 1 + 2\beta + \beta^2 + 2\beta^3 + \beta^4 \, .$$

The swimmer is a pusher (puller) if $\beta < 1$ ($\beta > 1$). Moreover, $\sigma > 0$ for all positive values of the parameter β.

Appendix D. Mathematical formulas

In this appendix, we provide explicit analytical expressions of the functions and coefficients stated in the main text.

D.1. Expressions of $A(z)$, $B(z)$ and $C(z)$ for a neutral swimmer (equal sphere radii)

Here we provide explicit analytical expressions of the functions $A(z)$, $B(z)$, and $C(z)$ defined in equation (10) of the main text, to leading order in a and as a power series in z. Defining $w_1 := \sqrt{1+z^2}$ and $w_2 := \sqrt{1+4z^4}$, we have

$$A(z) = \frac{a}{(w_1 w_2)^{13}} \sum_{n=0}^{12} A_{2n} z^{2n} \, , \tag{D.1a}$$

$$B(z) = \frac{a}{(w_1 w_2)^7} \sum_{n=-1}^{12} B_n z^n \, , \tag{D.1b}$$

$$C(z) = \frac{a}{(w_1 w_2)^{13}} \sum_{n=1}^{11} C_{2n+1} z^{2n+1} . \qquad \text{(D.1}c\text{)}$$

The series coefficients A_n, B_n, and C_n are given in table D1.

D.2. Analytical expressions for a general three-sphere swimmer in the far-field limit

The explicit analytical expression of the coefficients V_{10} and V_{20} defined in equation (18) are

$$V_{10} = -\frac{21PK}{8M^2} , \quad V_{20} = \frac{9PK\,(18 - 27S - 6P + 11Q)}{32M^3} .$$

The coefficients A_{ij}, B_{ij}, C_{ij}, and D_{ij} defined in equations (19) and (20) are given by

$$A_{23} = -\frac{63P\,(9 + 25S + 88P - 12Q)}{1024M^3} ,$$

$$D_{14} = \frac{135P}{64MN} ,$$

$$D_{22} = -\frac{189P}{256M^2} ,$$

$$D_{24} = \frac{135P\,(85Q - 18S + 542PS + 140P + 640P^2)}{2048M^2N^2} ,$$

$$B_{13} = \frac{63P}{64M} ,$$

$$B_{23} = -\frac{63P\,(9 - 6PS - 3Q + 13S + 16P)}{256M^3} ,$$

$$C_{14} = \frac{405P}{256N} ,$$

$$C_{24} = \frac{405P\,(10P + 13S)}{2048MN} ,$$

where $S = r_3 + r_2$, $P = r_3 r_2$, $Q = r_3^2 + r_2^2$, $M = 1 + S$ and $N = S + 4P$. We recall that $r_2 = a_2/a_1$ and $r_3 = a_3/a_1$.

ORCID iDs

Abdallah Daddi-Moussa-Ider https://orcid.org/0000-0002-1281-9836
Maciej Lisicki https://orcid.org/0000-0002-6976-0281
Arnold J T M Mathijssen https://orcid.org/0000-0002-9577-8928
Andreas M Menzel https://orcid.org/0000-0003-0713-4979
Hartmut Löwen https://orcid.org/0000-0001-5376-8062

References

[1] Purcell E M 1977 Life at low Reynolds number *Am. J. Phys.* **45** 3–11
[2] Lauga E and Powers T R 2009 The hydrodynamics of swimming microorganisms *Rep. Prog. Phys.* **72** 096601
[3] Elgeti J, Winkler R G and Gompper G 2015 Physics of microswimmers single particle motion and collective behavior: a review *Rep. Prog. Phys.* **78** 056601
[4] Marchetti M C, Joanny J F, Ramaswamy S, Liverpool T B, Prost J, Rao M and Simha R A 2013 Hydrodynamics of soft active matter *Rev. Mod. Phys.* **85** 1143
[5] Lauga E 2016 Bacterial hydrodynamics *Ann. Rev. Fluid Mech.* **48** 105–30
[6] Zöttl A and Stark H 2016 Emergent behavior in active colloids *J. Phys.: Condens. Matter* **28** 253001
[7] Bechinger C, Di Leonardo R, Löwen H, Reichhardt C, Volpe G and Volpe G 2016 Active particles in complex and crowded environments *Rev. Mod. Phys.* **88** 045006
[8] Happel J and Brenner H 2012 *Low Reynolds Number Hydrodynamics: with Special Applications to Particulate Media* (Berlin: Springer)
[9] Kim S and Karrila S J 2013 *Microhydrodynamics: Principles and Selected Applications* (Mineola, NY: Courier Corporation)
[10] Brennen C and Winet H 1977 Fluid mechanics of propulsion by cilia and flagella *Ann. Rev. Fluid Mech.* **9** 339–98
[11] Lauga E and Michelin S 2016 Stresslets induced by active swimmers *Phys. Rev. Lett.* **117** 148001
[12] Najafi A and Golestanian R 2004 Simple swimmer at low Reynolds number: three linked spheres *Phys. Rev.* E **69** 062901
[13] Najafi A and Golestanian R 2005 Propulsion at low Reynolds number *J. Phys.: Condens. Matter* **17** S1203
[14] Golestanian R and Ajdari A 2008 Analytic results for the three-sphere swimmer at low Reynolds number *Phys. Rev.* E **77** 036308
[15] Golestanian R and Ajdari A 2008 Mechanical response of a small swimmer driven by conformational transitions *Phys. Rev. Lett.* **100** 038101
[16] Golestanian R 2008 Three-sphere low-Reynolds-number swimmer with a cargo container *Eur. Phys. J.* E **25** 1–4
[17] Alexander G P, Pooley C M and Yeomans J M 2009 Hydrodynamics of linked sphere model swimmers *J. Phys.: Condens. Matter* **21** 204108
[18] Leoni M, Kotar J, Bassetti B, Cicuta P and Lagomarsino M C 2009 A basic swimmer at low Reynolds number *Soft Matter* **5** 472–6
[19] Grosjean G, Hubert M, Lagubeau G and Vandewalle N 2016 Realization of the Najafi–Golestanian microswimmer *Phys. Rev.* E **94** 021101
[20] Felderhof B U 2006 The swimming of animalcules *Phys. Fluids* **18** 063101
[21] Montino A and DeSimone A 2015 Three-sphere low-Reynolds-number swimmer with a passive elastic arm *Eur. Phys. J.* E **38** 42
[22] Montino A and DeSimone A 2017 Dynamics and optimal actuation of a three-sphere low-Reynolds-number swimmer with muscle-like arms *Acta Appl. Math.* **149** 53–86
[23] Pande J and Smith A-S 2015 Forces and shapes as determinants of micro-swimming: effect on synchronisation and the utilisation of drag *Soft Matter* **11** 2364–71
[24] Babel S, Löwen H and Menzel A M 2016 Dynamics of a linear magnetic microswimmer molecule *Europhys. Lett.* **113** 58003
[25] Pande J, Merchant L, Krüger T, Harting J and Smith A-S 2017 Effect of body deformability on microswimming *Soft Matter* **13** 3984–93
[26] Hosaka Y, Yasuda K, Sou I, Okamoto R and Komura S 2017 Thermally driven elastic micromachines *J. Phys. Soc. Japan* **86** 113801
[27] Pande J, Merchant L, Krüger T, Harting J and Smith A-S 2017 Setting the pace of microswimmers: when increasing viscosity speeds up self-propulsion *New J. Phys.* **19** 053024
[28] Ledesma-Aguilar R, Löwen H and Yeomans J M 2012 A circle swimmer at low Reynolds number *Eur. Phys. J.* E **35** 70
[29] Dreyfus R, Baudry J and Stone A H 2005 Purcell's rotator: mechanical rotation at low Reynolds number *Eur. Phys. J.* B **47** 161–4
[30] Ten Hagen B, Wittkowski R, Takagi D, Kümmel F, Bechinger C and Löwen H 2015 Can the self-propulsion of

anisotropic microswimmers be described by using forces and torques? *J. Phys.: Condens. Matter* **27** 194110
[31] Küchler N, Löwen H and Menzel A M 2016 Getting drowned in a swirl: deformable bead-spring model microswimmers in external flow fields *Phys. Rev.* E **93** 022610
[32] Rizvi M S, Farutin A and Misbah C 2018 Three-bead steering microswimmers *Phys. Rev.* E **97** 023102
[33] de Graaf J, Menke H, Mathijssen A J T M, Fabritius M, Holm C and Shendruk T 2016 Lattice-Boltzmann hydrodynamics of anisotropic active matter *J. Chem. Phys.* **144** 134106
[34] Mathijssen A J T M, Jeanneret R and Polin M 2018 Universal entrainment mechanism controls contact times with motile cells *Phys. Rev. Fluids* **3** 033103
[35] Vladimirov V A 2013 On the self-propulsion of an *n*-sphere micro-robot *J. Fluid Mech.* **716** R1
[36] Grégoire G and Chaté H 2004 Onset of collective and cohesive motion *Phys. Rev. Lett.* **92** 025702
[37] Mishra S, Baskaran A and Marchetti M C 2010 Fluctuations and pattern formation in self-propelled particles *Phys. Rev.* E **81** 061916
[38] Menzel A M 2012 Collective motion of binary self-propelled particle mixtures *Phys. Rev.* E **85** 021912
[39] Heidenreich S, Hess S and Klapp S H L 2011 Nonlinear rheology of active particle suspensions: insights from an analytical approach *Phys. Rev.* E **83** 011907
[40] Saintillan D 2018 Rheology of active fluids *Ann. Rev. Fluid Mech.* **50** 563–92
[41] Le Goff T, Liebchen B and Marenduzzo D 2016 Pattern formation in polymerizing actin flocks: spirals, spots, and waves without nonlinear chemistry *Phys. Rev. Lett.* **117** 238002
[42] Scholz C, Engel M and Pöschel T 2018 Rotating robots move collectively and self-organize *Nat. Commun.* **9** 931
[43] Menzel A M 2013 Unidirectional laning and migrating cluster crystals in confined self-propelled particle systems *J. Phys.: Condens. Matter* **25** 505103
[44] Kogler F and Klapp S H L 2015 Lane formation in a system of dipolar microswimmers *Europhys. Lett.* **110** 10004
[45] Romanczuk P, Chaté H, Chen L, Ngo S and Toner J 2016 Emergent smectic order in simple active particle models *New J. Phys.* **18** 063015
[46] Menzel A M 2016 On the way of classifying new states of active matter *New J. Phys.* **18** 071001
[47] Liebchen B, Cates M E and Marenduzzo D 2016 Pattern formation in chemically interacting active rotors with self-propulsion *Soft Matter* **12** 7259–64
[48] Liebchen B and Levis D 2017 Collective behavior of chiral active matter: pattern formation and enhanced flocking *Phys. Rev. Lett.* **119** 058002
[49] Hoell C, Löwen H and Menzel A M 2017 Dynamical density functional theory for circle swimmers *New J. Phys.* **19** 125004
[50] Liebchen B, Marenduzzo D and Cates M E 2017 Phoretic interactions generically induce dynamic clusters and wave patterns in active colloids *Phys. Rev. Lett.* **118** 268001
[51] Tailleur J and Cates M E 2008 Statistical mechanics of interacting run-and-tumble bacteria *Phys. Rev. Lett.* **100** 218103
[52] Buttinoni I, Bialké J, Kümmel F, Löwen H, Bechinger C and Speck T 2013 Dynamical clustering and phase separation in suspensions of self-propelled colloidal particles *Phys. Rev. Lett.* **110** 238301
[53] Palacci J, Sacanna S, Steinberg A P, Pine D J and Chaikin P M 2013 Living crystals of light-activated colloidal surfers *Science* **339** 936–40
[54] Speck T, Bialké J, Menzel A M and Löwen H 2014 Effective Cahn–Hilliard equation for the phase separation of active Brownian particles *Phys. Rev. Lett.* **112** 218304
[55] Speck T, Menzel A M, Bialké J and Löwen H 2015 Dynamical mean-field theory and weakly non-linear analysis for the phase separation of active Brownian particles *J. Chem. Phys.* **142** 224109
[56] Wensink H H, Dunkel J, Heidenreich S, Drescher K, Goldstein R E, Löwen H and Yeomans J M 2012 Meso-scale turbulence in living fluids *Proc. Natl Acad. Sci.* **109** 14308–13
[57] Wensink H H and Löwen H 2012 Emergent states in dense systems of active rods: from swarming to turbulence *J. Phys.: Condens. Matter* **24** 464130
[58] Dunkel J, Heidenreich S, Drescher K, Wensink H H, Bär M and Goldstein R E 2013 Fluid dynamics of bacterial turbulence *Phys. Rev. Lett.* **110** 228102
[59] Heidenreich S, Klapp S H L and Bär M 2014 Numerical simulations of a minimal model for the fluid dynamics of dense bacterial suspensions *J. Phys.: Conf. Ser.* **490** 012126
[60] Kaiser A, Peshkov A, Sokolov A, ten Hagen B, Löwen H and Aranson I S 2014 Transport powered by bacterial turbulence *Phys. Rev. Lett.* **112** 158101
[61] Heidenreich S, Dunkel J, Klapp S H L and Bär M 2016 Hydrodynamic length-scale selection in microswimmer suspensions *Phys. Rev.* E **94** 020601
[62] Löwen H 2016 Chirality in microswimmer motion: from circle swimmers to active turbulence *Eur. Phys. J. Spec. Top.* **225** 2319–31
[63] Squires T and Quake S 2005 Microfluidics: fluid physics at the nanoliter scale *Rev. Mod. Phys.* **77** 977
[64] Whitesides G M 2006 The origins and the future of microfluidics *Nature* **442** 368
[65] Happel J and Bryne B J 1954 Viscous flow in multiparticle systems. Motion of a sphere in a cylindrical tube *Ind. Eng. Chem.* **46** 1181–6
[66] Cui B, Diamant H and Lin B 2002 Screened hydrodynamic interaction in a narrow channel *Phys. Rev. Lett.* **89** 188302
[67] Misiunas K, Pagliara S, Lauga E, Lister J R and Keyser U F 2015 Nondecaying hydrodynamic interactions along narrow channels *Phys. Rev. Lett.* **115** 038301
[68] Stone H A, Stroock A D and Ajdari A 2004 Engineering flows in small devices: microfluidics toward a lab-on-a-chip *Annu. Rev. Fluid Mech.* **36** 381–411
[69] Lauga E, Brenner M and Stone H 2007 Microfluidics: the no-slip boundary condition *Springer Handbook of Experimental Fluid Mechanics* (Berlin: Springer) pp 1219–40
[70] Lisicki M, Cichocki B, Rogers S A, Dhont J K G and Lang P R 2014 Translational and rotational near-wall diffusion of spherical colloids studied by evanescent wave scattering *Soft Matter* **10** 4312–23
[71] Lisicki M, Cichocki B and Wajnryb E 2016 Near-wall diffusion tensor of an axisymmetric colloidal particle *J. Chem. Phys.* **145** 034904
[72] Rallabandi B, Hilgenfeldt S and Stone H A 2017 Hydrodynamic force on a sphere normal to an obstacle due to a non-uniform flow *J. Fluid Mech.* **818** 407–34
[73] Daddi-Moussa-Ider A, Lisicki M and Gekle S 2017 Mobility of an axisymmetric particle near an elastic interface *J. Fluid Mech.* **811** 210–33
[74] Daddi-Moussa-Ider A and Gekle S 2017 Hydrodynamic mobility of a solid particle near a spherical elastic membrane: axisymmetric motion *Phys. Rev.* E **95** 013108
[75] Daddi-Moussa-Ider A, Lisicki M and Gekle S 2017 Hydrodynamic mobility of a solid particle near a spherical elastic membrane. II. Asymmetric motion *Phys. Rev.* E **95** 053117

[76] Rallabandi B, Saintyves B, Jules T, Salez T, Schönecker C, Mahadevan L and Stone H A 2017 Rotation of an immersed cylinder sliding near a thin elastic coating *Phys. Rev. Fluids* **2** 074102

[77] Daddi-Moussa-Ider A, Lisicki M and Gekle S 2017 Hydrodynamic mobility of a sphere moving on the centerline of an elastic tube *Phys. Fluids* **29** 111901

[78] Frymier P D, Ford R M, Berg H C and Cummings P T 1995 Three-dimensional tracking of motile bacteria near a solid planar surface *Proc. Natl Acad. Sci.* **92** 6195–9

[79] DiLuzio W R, Turner L, Mayer M, Garstecki P, Weibel D B, Berg H C and Whitesides G M 2005 Escherichia coli swim on the right-hand side *Nature* **435** 1271–4

[80] Lauga E, DiLuzio W R, Whitesides G M and Stone H A 2006 Swimming in circles: motion of bacteria near solid boundaries *Biophys. J.* **90** 400–12

[81] Berke A P, Turner L, Berg H C and Lauga E 2008 Hydrodynamic attraction of swimming microorganisms by surfaces *Phys. Rev. Lett.* **101** 038102

[82] Drescher K, Dunkel J, Cisneros L H, Ganguly S and Goldstein R E 2011 Fluid dynamics and noise in bacterial cell–cell and cell–surface scattering *Proc. Natl Acad. Sci.* **108** 10940–5

[83] Mino G, Mallouk T E, Darnige T, Hoyos M, Dauchet J, Dunstan J, Soto R, Wang Y, Rousselet A and Clement E 2011 Enhanced diffusion due to active swimmers at a solid surface *Phys. Rev. Lett.* **106** 048102

[84] Ishimoto K and Gaffney E A 2014 A study of spermatozoan swimming stability near a surface *J. Theor. Biol.* **360** 187–99

[85] Mathijssen A J T M, Shendruk T N, Yeomans J M and Doostmohammadi A 2016 Upstream swimming in microbiological flows *Phys. Rev. Lett.* **116** 028104

[86] Lushi E, Kantsler V and Goldstein R E 2017 Scattering of biflagellate microswimmers from surfaces *Phys. Rev.* E **96** 023102

[87] Dauparas J, Das D and Lauga E 2018 Helical micropumps near surfaces *Biomicrofluidics* **12** 014108

[88] Ishimoto K and Gaffney E A 2013 Squirmer dynamics near a boundary *Phys. Rev.* E **88** 062702

[89] Contino M, Lushi E, Tuval I, Kantsler V and Polin M 2015 Microalgae scatter off solid surfaces by hydrodynamic and contact forces *Phys. Rev. Lett.* **115** 258102

[90] Dunstan J, Miño G, Clement E and Soto R 2012 A two-sphere model for bacteria swimming near solid surfaces *Phys. Fluids* **24** 011901

[91] Spagnolie S E and Lauga E 2012 Hydrodynamics of self-propulsion near a boundary: predictions and accuracy of far-field approximations *J. Fluid Mech.* **700** 105–47

[92] Uspal W E, Popescu M N, Dietrich S and Tasinkevych M 2015 Rheotaxis of spherical active particles near a planar wall *Soft Matter* **11** 6613–32

[93] Uspal W E, Popescu M N, Dietrich S and Tasinkevych M 2015 Self-propulsion of a catalytically active particle near a planar wall: from reflection to sliding and hovering *Soft Matter* **11** 434–8

[94] Simmchen J, Katuri J, Uspal W E, Popescu M N, Tasinkevych M and Sánchez S 2016 Topographical pathways guide chemical microswimmers *Nat. Commun.* **7** 10598

[95] Ibrahim Y and Liverpool T B 2015 The dynamics of a self-phoretic Janus swimmer near a wall *Europhys. Lett.* **111** 48008

[96] Mozaffari A, Sharifi-Mood N, Koplik J and Maldarelli C 2016 Self-diffusiophoretic colloidal propulsion near a solid boundary *Phys. Fluids* **28** 053107

[97] Popescu M N, Uspal W E and Dietrich S 2016 Self-diffusiophoresis of chemically active colloids *Eur. Phys. J. Spec. Top.* **225** 2189–206

[98] Rühle F, Blaschke J, Kuhr J-T and Stark H 2018 Gravity-induced dynamics of a squirmer microswimmer in wall proximity *New J. Phys.* **20** 025003

[99] Mozaffari A, Sharifi-Mood N, Koplik J and Maldarelli C 2018 Self-propelled colloidal particle near a planar wall: a Brownian dynamics study *Phys. Rev. Fluids* **3** 014104

[100] Li G-J and Ardekani A M 2014 Hydrodynamic interaction of microswimmers near a wall *Phys. Rev.* E **90** 013010

[101] Pimponi D, Chinappi M, Gualtieri P and Casciola C M 2016 Hydrodynamics of flagellated microswimmers near free-slip interfaces *J. Fluid Mech.* **789** 514–33

[102] Domínguez A, Malgaretti P, Popescu M N and Dietrich S 2016 Effective interaction between active colloids and fluid interfaces induced by Marangoni flows *Phys. Rev. Lett.* **116** 078301

[103] Dietrich K, Renggli D, Zanini M, Volpe G, Buttinoni I and Isa L 2017 Two-dimensional nature of the active Brownian motion of catalytic microswimmers at solid and liquid interfaces *New J. Phys.* **19** 065008

[104] Elgeti J and Gompper G 2009 Self-propelled rods near surfaces *Europhys. Lett.* **85** 38002

[105] Zhu L, Lauga E and Brandt L 2013 Low-Reynolds-number swimming in a capillary tube *J. Fluid Mech.* **726** 285–311

[106] Zöttl A and Stark H 2012 Nonlinear dynamics of a microswimmer in Poiseuille flow *Phys. Rev. Lett.* **108** 218104

[107] Zöttl A and Stark H 2013 Periodic and quasiperiodic motion of an elongated microswimmer in Poiseuille flow *Eur. Phys. J.* E **36** 4

[108] Najafi A, Raad S S H and Yousefi R 2013 Self-propulsion in a low-Reynolds-number fluid confined by two walls of a microchannel *Phys. Rev.* E **88** 045001

[109] Bilbao A, Wajnryb E, Vanapalli S A and Blawzdziewicz J 2013 Nematode locomotion in unconfined and confined fluids *Phys. Fluids* **25** 081902

[110] Yang F, Qian S, Zhao Y and Qiao R 2016 Self-diffusiophoresis of Janus catalytic micromotors in confined geometries *Langmuir* **32** 5580–92

[111] Elgeti J and Gompper G 2016 Microswimmers near surfaces *Eur. Phys. J. Spec. Top.* **225** 2333–52

[112] Liu C, Zhou C, Wang W and Zhang H P 2016 Bimetallic microswimmers speed up in confining channels *Phys. Rev. Lett.* **117** 198001

[113] Wioland H, Lushi E and Goldstein R E 2016 Directed collective motion of bacteria under channel confinement *New J. Phys.* **18** 075002

[114] de Graaf J, Mathijssen A J T M, Fabritius M, Menke H, Holm C and Shendruk T N 2016 Understanding the onset of oscillatory swimming in microchannels *Soft Matter* **12** 4704–8

[115] Wu H, Farutin A, Hu W-F, Thiébaud M, Rafa S, Peyla P, Lai M-C and Misbah C 2016 Amoeboid swimming in a channel *Soft Matter* **12** 7470–84

[116] de Graaf J and Stenhammar J 2017 Lattice–Boltzmann simulations of microswimmer-tracer interactions *Phys. Rev.* E **95** 023302

[117] Reigh S Y, Zhu L, Gallaire F and Lauga E 2017 Swimming with a cage: low-Reynolds-number locomotion inside a droplet *Soft Matter* **13** 3161–73

[118] Reigh S Y and Lauga E 2017 Two-fluid model for locomotion under self-confinement *Phys. Rev. Fluids* **2** 093101

[119] Spagnolie S E, Moreno-Flores G R, Bartolo D and Lauga E 2015 Geometric capture and escape of a microswimmer colliding with an obstacle *Soft Matter* **11** 3396–411

[120] Desai N, Shaik V A and Ardekani A M 2018 Hydrodynamics-mediated trapping of micro-swimmers near drops *Soft Matter* **14** 264–78

[121] Mathijssen A J T M, Doostmohammadi A, Yeomans J M and Shendruk T N 2016 Hydrodynamics of micro-swimmers in films *J. Fluid Mech.* **806** 35–70

[122] Dauparas J and Lauga E 2016 Flagellar flows around bacterial swarms *Phys. Rev. Fluids* **1** 043202

[123] Mathijssen A J T M, Figueroa-Morales N, Junot G, Clement E, Lindner A and Zöttl A 2018 Oscillatory surface rheotaxis of swimming *E. coli* bacteria (arXiv:1803.01743)

[124] Lauga E 2007 Propulsion in a viscoelastic fluid *Phys. Fluids* **19** 083104

[125] Pak O S, Zhu L, Brandt L and Lauga E 2012 Micropropulsion and microrheology in complex fluids via symmetry breaking *Phys. Fluids* **24** 103102

[126] Zhu L, Lauga E and Brandt L 2012 Self-propulsion in viscoelastic fluids: pushers versus pullers *Phys. Fluids* **24** 051902

[127] Curtis M P and Gaffney E A 2013 Three-sphere swimmer in a nonlinear viscoelastic medium *Phys. Rev.* E **87** 043006

[128] Riley E E and Lauga E 2014 Enhanced active swimming in viscoelastic fluids *Europhys. Lett.* **108** 34003

[129] Datt C, Zhu L, Elfring G J and Pak O S 2015 Squirming through shear-thinning fluids *J. Fluid Mech.* **784**

[130] Mathijssen A J T M, Doostmohammadi A, Yeomans J M and Shendruk T N 2016 Hotspots of boundary accumulation: dynamics and statistics of micro-swimmers in flowing films *J. R. Soc. Interface* **13** 20150936

[131] Gomez-Solano J R, Blokhuis A and Bechinger C 2016 Dynamics of self-propelled Janus particles in viscoelastic fluids *Phys. Rev. Lett.* **116** 138301

[132] Natale G, Datt C, Hatzikiriakos S G and Elfring G J 2017 Autophoretic locomotion in weakly viscoelastic fluids at finite Péclet number *Phys. Fluids* **29** 123102

[133] Yazdi S, Ardekani A M and Borhan A 2014 Locomotion of microorganisms near a no-slip boundary in a viscoelastic fluid *Phys. Rev.* E **90** 043002

[134] Yazdi S, Ardekani A M and Borhan A 2015 Swimming dynamics near a wall in a weakly elastic fluid *J. Nonlinear Sci.* **25** 1153–67

[135] Yazdi S and Borhan A 2017 Effect of a planar interface on time-averaged locomotion of a spherical squirmer in a viscoelastic fluid *Phys. Fluids* **29** 093104

[136] Liron N and Mochon S 1976 Stokes flow for a Stokeslet between two parallel flat plates *J. Eng. Math.* **10** 287–303

[137] Di Leonardo R, DellArciprete D, Angelani L and Iebba V 2011 Swimming with an image *Phys. Rev. Lett.* **106** 038101

[138] Swan J W and Brady J F 2007 Simulation of hydrodynamically interacting particles near a no-slip boundary *Phys. Fluids* **19** 113306

[139] Bhattacharya S and Bławzdziewicz J 2002 Image system for Stokes-flow singularity between two parallel planar walls *J. Math. Phys.* **43** 5720–31

[140] Bhattacharya S, Bławzdziewicz J and Wajnryb E 2005 Hydrodynamic interactions of spherical particles in suspensions confined between two planar walls *J. Fluid Mech.* **541** 263–92

[141] Bhattacharya S, Bławzdziewicz J and Wajnryb E 2005 Many-particle hydrodynamic interactions in parallel-wall geometry: Cartesian-representation method *Physica* A **356** 294–340

[142] Blake J R 1971 A note on the image system for a Stokeslet in a no-slip boundary *Math. Proc. Camb. Phil. Soc.* **70** 303–10

[143] Oseen C W 1927 *Neuere Methoden und Ergebnisse in der Hydrodynamik* (Leipzig: Akademische Verlagsgesellschaft m. b. H.)

[144] Press W H 1992 *The Art of Scientific Computing* (Cambridge: Cambridge University Press)

[145] Daddi-Moussa-Ider A, Lisicki M, Hoell C and Löwen H 2018 Swimming trajectories of a three-sphere microswimmer near a wall *J. Chem. Phys.* **148** 134904

[146] Lopez D and Lauga E 2014 Dynamics of swimming bacteria at complex interfaces *Phys. Fluids* **26** 400–12

[147] Schaar K, Zöttl A and Stark H 2015 Detention times of microswimmers close to surfaces: influence of hydrodynamic interactions and noise *Phys. Rev. Lett.* **115** 038101

[148] Bickel T 2007 Hindered mobility of a particle near a soft interface *Phys. Rev.* E **75** 041403

[149] Bickel T 2006 Brownian motion near a liquid-like membrane *Eur. Phys. J.* E **20** 379–85

[150] Daddi-Moussa-Ider A and Gekle S 2018 Brownian motion near an elastic cell membrane: a theoretical study *Eur. Phys. J.* E **41** 19

[151] Daddi-Moussa-Ider A, Guckenberger A and Gekle S 2016 Long-lived anomalous thermal diffusion induced by elastic cell membranes on nearby particles *Phys. Rev.* E **93** 012612

[152] Abramowitz M and Stegun I A 1972 *Handbook of Mathematical Functions* vol 1 (New York: Dover)

[153] Ozarkar S S and Sangani A S 2008 A method for determining Stokes flow around particles near a wall or in a thin film bounded by a wall and a gas-liquid interface *Phys. Fluids* **20** 063301

[154] Pooley C M, Alexander G P and Yeomans J M 2007 Hydrodynamic interaction between two swimmers at low Reynolds number *Phys. Rev. Lett.* **99** 228103

P7 Membrane penetration and trapping of an active particle

Reproduced from

A. Daddi-Moussa-Ider, S. Goh, B. Liebchen, C. Hoell, A. J. T. M. Mathijssen,
F. Guzmán-Lastra, C. Scholz, A. M. Menzel, and H. Löwen,
Membrane penetration and trapping of an active particle,
J. Chem. Phys. **150**, 064906 (2019),
with the permission of *AIP Publishing.*

Digital Object Identifier (DOI): `https://doi.org/10.1063/1.5080807`

Statement of contribution

I contributed to the theoretical description of the one-dimensional model membrane and performed the analytical calculation for the case of fast orientational relaxation. I participated in the discussion and interpretation of the results, including the steady-state solution of the membrane displacement, when the approaching active particle is being trapped, and the corresponding dynamical solution. Subsequently, I contributed to drafting the parts of the manuscript concerning these solutions and the case of fast orientational relaxation. Moreover, I participated in editing the text and finalizing the manuscript. My work concerning this paper was supervised by ADMI, AMM, and HL.

Copyright and license notice

The Journal of Chemical Physics ARTICLE scitation.org/journal/jcp

Membrane penetration and trapping of an active particle

Cite as: J. Chem. Phys. 150, 064906 (2019); doi: 10.1063/1.5080807
Submitted: 12 November 2018 • Accepted: 23 January 2019 •
Published Online: 12 February 2019

View Online Export Citation CrossMark

Abdallah Daddi-Moussa-Ider,[1,a)] Segun Goh,[1] Benno Liebchen,[1] Christian Hoell,[1] Arnold J. T. M. Mathijssen,[2] Francisca Guzmán-Lastra,[1,3] Christian Scholz,[1] Andreas M. Menzel,[1] and Hartmut Löwen[1,b)]

AFFILIATIONS

[1] Institut für Theoretische Physik II: Weiche Materie, Heinrich-Heine-Universität Düsseldorf, Universitätsstraße 1, 40225 Düsseldorf, Germany
[2] Department of Bioengineering, Stanford University, 443 Via Ortega, Stanford, California 94305, USA
[3] Facultad de Ciencias, Universidad Mayor, Ave. Manuel Montt 367, Providencia, Santiago de Chile, Chile

Note: This article is part of the Special Topic "Chemical Physics of Active Matter" in J. Chem. Phys.
[a)] **Electronic mail:** abdallah.daddi.moussa.ider@uni-duesseldorf.de
[b)] **Electronic mail:** hartmut.loewen@uni-duesseldorf.de

ABSTRACT

The interaction between nano- or micro-sized particles and cell membranes is of crucial importance in many biological and biomedical applications such as drug and gene delivery to cells and tissues. During their cellular uptake, the particles can pass through cell membranes via passive endocytosis or by active penetration to reach a target cellular compartment or organelle. In this manuscript, we develop a simple model to describe the interaction of a self-driven spherical particle (moving through an effective constant active force) with a minimal membrane system, allowing for both penetration and trapping. We numerically calculate the state diagram of this system, the membrane shape, and its dynamics. In this context, we show that the active particle may either get trapped near the membrane or penetrate through it, where the membrane can either be permanently destroyed or recover its initial shape by self-healing. Additionally, we systematically derive a continuum description allowing us to accurately predict most of our results analytically. This analytical theory helps in identifying the generic aspects of our model, suggesting that most of its ingredients should apply to a broad range of membranes, from simple model systems composed of magnetic microparticles to lipid bilayers. Our results might be useful to predict the mechanical properties of synthetic minimal membranes.

I. INTRODUCTION

Biological membranes play a crucial role in a large variety of cellular processes and serve as a barrier to protect the interior of living cells from unwanted agents and harmful external influences.[1–7] The interaction between particles and cell membranes is of crucial importance in a variety of biomedical applications, including targeted phototherapy, intracellular imaging, and diagnostic assays.[8–10] Once injected into a living organism, particle uptake can be achieved via passive mechanisms[11–15] or can be mediated by active processes involving cellular energy input.[16–19] Considerable research advances have been made over the last few years in understanding the penetration of particles into cell membranes. Previous studies have shown that the particle uptake by living cells is strongly affected by the particle properties[20–24] and the physicochemical and functional properties of the membrane.[25–30]

As a simple framework for studying basic mechanisms of cell penetration, artificial model membranes provide a basis for understanding the complex interactions within living cells. For example, the formation of a desired target membrane

The Journal of Chemical Physics ARTICLE scitation.org/journal/jcp

structure can be driven by an entropic mechanism[31] or can be achieved using controlled external fields.[32–37] In particular, self-assembled colloidal membranes have offered a novel framework for studying fundamental physical problems, such as geometric frustration in artificial spin-ice systems,[38–40] and can conveniently be built from isolated microparticles with adjustable interactions.[41–49] For this purpose, various types of interparticle interactions could be exploited, among which magnetic attraction stands out.

One possibility is to construct membranes from colloidal magnetic particles that, in other situations, serve as building blocks of magnetically self-assembled chains and sheets. Magnetic nanoparticles (MNPs)[50,51] are well-established nanocomponents, owing to their diverse promising technological and biomedical applications. Notable examples include their potential use as drug delivery agents[52–54] or as mediators to convert electromagnetic energy into heat (hyperthermia).[55] By binding MNPs to the surface of living cells, the membrane mechanical properties can conveniently be tuned by an external magnetic field.[56–58] Furthermore, magnetic colloidal and nanoparticles have proved to be useful in the design of optical stimuli-responsive materials[59–62] and in the development of artificial self-propelling active microswimmers.[63–77] Meanwhile, the dynamical properties of self-propelled active polymers and filaments have been investigated.[78–81] Additional studies include the dynamics of semi-flexible polymer chains in the presence of nanoparticles[82] and the behavior of polymers in a crowded solution of active particles.[83]

Here, we develop a minimal model for a (non-fluctuating) membrane made of dipolar (e.g., electric or magnetic) particles sterically interacting with a constantly driven "active" particle.[84–92] This particle may represent, e.g., a swimming microorganism[68,69] or a synthetic micro- or nanomachine that can be manipulated under the action of controlled external fields.[93–96] Here, we focus on the case in which the persistence length of the trajectory of the active particle is large compared to its initial distance from the membrane, i.e., the particle essentially moves along a straight line towards the membrane.

In general, active particles can reach normally inaccessible areas inside living organisms and can perform delicate and precise tasks, holding great promise for prospective biomedical applications such as precision nanosurgery[97–99] or transport of therapeutic substances to tumor and inflammation sites.[100–102] Direct experimental observations have recently demonstrated the self-driven motion of acoustically powered active nanorods inside living HeLa cells.[103] These nanomotors have been shown to bump into cell organelles and exhibit directional motion and spinning inside the cells. A detailed modeling of the interactions of active particles and (cell) membranes may help to shed light on our understanding of the processes driving particle motion in living and synthetic cell components. Additionally, a fundamental understanding of these processes helps to improve the controllability of micro- and nanoparticle-based agents in complex environments. Potentially, this might be relevant for novel therapeutic drug targets for health therapy. One step in this direction has been taken recently specifically for self-propelled particles interacting with a moving potential interpreted as a semipermeable membrane,[104] identifying an enhanced particle accumulation in front of the membrane accompanied with an increased drag force. Experimentally, the mechanical pressure exerted by a set of both passive isotropic and self-propelled polar disks onto flexible unidimensional model membranes has been studied.[105]

In the present work, we investigate a membrane model self-assembled from dipolar spheres arranged along a chain in the two-dimensional space. Their dipole moment can arise either from an unscreened magnetic or electric moment or from screened short-ranged electric interactions, also arising from polar colloidal clusters.[106] It has previously been shown that a chain of magnetic particles can exhibit intrinsic mechanical properties reminiscent of elastic strings or rods[107–112] depending on the additional particle interactions. In colloidal suspensions, magnetic interactions often cause flocculation due to the strong attraction at short distances.[113] Such effects are usually counterbalanced by repulsive steric interactions that prevent overlapping particle volumes at finite concentrations.[114–116] Additional elastic interactions may be considered in the form of harmonic springs. Particle systems subject to combinations of magnetic, steric, and elastic interactions have widely been utilized as a model system for ferrofluids and ferrogels.[117–126]

Using our simple model membrane as a basis to study the penetration process by a self-driven particle (moving under the action of a constant driving force), we obtain dynamical state diagrams indicating trapping and penetration states. We further observe penetration events with or without subsequent healing of the membrane depending on the range of the interactions between the membrane particles. Considering a chain of dipolar spheres, we derive a continuum theory[125,127] and we probe the particle displacement and dipole reorientation caused by the self-driven particle in the small-deformation regime. Good quantitative agreement is found between the theoretical results and numerical simulations.

The remaining part of the paper is organized as follows: in Sec. II, we present the system setup and derive from the potential energy the governing equations for the displacement and orientation fields of the dipolar spheres. We then present in Sec. III state diagrams indicating the possible steady configurations of the system. Moreover, we probe the transition between the dynamical states. In Sec. IV, we devise a linearized analytical theory that describes the temporal evolution of the membrane and we provide solutions for the trapping state in Sec. V. Concluding remarks are contained in Sec. VI.

II. SYSTEM SETUP

We consider in two spatial dimensions a simple model membrane composed of a chain of N identical dipolar particles of radius a and dipole moment $\boldsymbol{m}$. Here, we assume that the dipole moments rotate rigidly with the particles. The

The Journal of Chemical Physics ARTICLE scitation.org/journal/jcp

membrane is fully immersed in a Newtonian viscous fluid of constant dynamic viscosity η. We support the chain at its extremities such that the particles on both ends are fixed in space. Moreover, we neglect Brownian noise, which should play only a minor role when considering a large membrane and large self-driven particles or systems at low temperatures. In the resulting equilibrium configuration, the dipolar particles are uniformly distributed along the chain and aligned along the x direction (Fig. 1). We denote by h the interparticle distance, initially set identical for all particles, and by $L = hN$ the total length of the chain.

A. Potential energy of the membrane

Next, we assume that the membrane particles are subject to three types of mutual interactions, namely, dipolar, steric, and elastic interactions. Accordingly, the system potential energy governing the time evolution of the membrane can be written as

$$\mathcal{U} = \mathcal{U}_M + \mathcal{U}_S + \mathcal{U}_E, \tag{1}$$

where $\mathcal{U}_M$, $\mathcal{U}_S$, and $\mathcal{U}_E$ are contributions stemming from the dipolar, steric, and elastic interactions, respectively. In this study, we neglect for simplicity the fluid-mediated hydrodynamic interactions between the particles.

In the following, $\boldsymbol{m}_i$ denotes the dipole moment of the ith membrane particle, $i = 1, \ldots, N$. It is assumed that the magnitudes of the dipole moments are equal and constant for all the membrane particles, $m = |\boldsymbol{m}_i|$. Then, the dipolar part of the potential energy may be expressed as[128]

$$\mathcal{U}_M = \frac{\mu_0 m^2}{4\pi} \sum_{\substack{i,j=1 \\ j<i}}^{N} \frac{1}{r_{ij}^3} \left(\hat{\boldsymbol{m}}_i \cdot \hat{\boldsymbol{m}}_j - 3\left(\hat{\boldsymbol{m}}_i \cdot \hat{\boldsymbol{r}}_{ij}\right)\left(\hat{\boldsymbol{m}}_j \cdot \hat{\boldsymbol{r}}_{ij}\right)\right), \tag{2}$$

where μ_0 is the magnetic vacuum permeability, $\hat{\boldsymbol{m}}_i = \boldsymbol{m}_i/m$ gives the orientation of the ith dipole moment, $\boldsymbol{r}_{ij} = \boldsymbol{r}_i - \boldsymbol{r}_j$ denotes the distance vector from particle j to particle i, $r_{ij} = |\boldsymbol{r}_{ij}|$ is its magnitude, and $\hat{\boldsymbol{r}}_{ij} = \boldsymbol{r}_{ij}/r_{ij}$ stands for the corresponding unit vector.

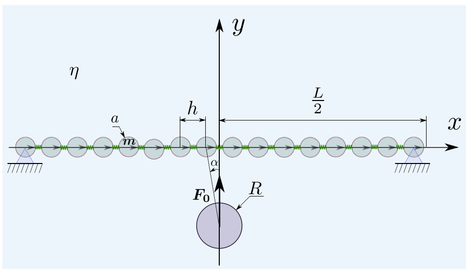

FIG. 1. Illustration of the system setup. Under the action of an effective propulsion force $\boldsymbol{F}_0$, a solid spherical particle of radius R approaches a membrane composed of N identical magnetic spheres of radius a and dipole moment $\boldsymbol{m}$. The membrane particles are initially equidistant with distance h from one another. We denote by L the total length of the membrane. The particles composing the membrane are subject to dipolar, steric, and elastic interactions. The system is immersed in a bulk liquid of constant dynamic viscosity η.

In order to avoid aggregation of the dipolar particles, we consider a repulsive Weeks–Chandler–Andersen (WCA) pair potential. The corresponding potential energy reads[129]

$$\mathcal{U}_S = 4\epsilon \sum_{\substack{i,j=1 \\ j<i}}^{N} N_{ij} \left(\frac{\sigma}{r_{ij}}\right)^6 \left(\left(\frac{\sigma}{r_{ij}}\right)^6 - 1\right) + \epsilon, \tag{3}$$

where we have defined the shorthand notation $N_{ij} = H\left(r_C - r_{ij}\right)$, with $H(\cdot)$ being the Heaviside step function and $r_C = 2^{1/6}\sigma$ denoting a cutoff radius beyond which the potential energy is set to zero. Here, $\sigma = 2a$ is the particle diameter and ϵ is an energy scale associated with the hardness of the potential.

In addition, we allow for harmonic elastic-like interactions among adjacent particles. These interactions are included such as springs of constant stiffness k and rest length r_0. The corresponding potential energy is given by

$$\mathcal{U}_E = \frac{k}{2} \sum_{i=1}^{N-1} (r_{i,i+1} - r_0)^2. \tag{4}$$

Consequently, the resulting force and torque acting on the ith sphere are calculated from the system potential energy as[66] $\mathbf{F}_i = -\partial\mathcal{U}/\partial\boldsymbol{r}_i$ and $\mathbf{T}_i = -\hat{\boldsymbol{m}}_i \times (\partial\mathcal{U}/\partial\hat{\boldsymbol{m}}_i)$. We obtain

$$\begin{aligned}\mathbf{F}_i = {}& \frac{3\mu_0 m^2}{4\pi} \sum_{\substack{j=1 \\ j\neq i}}^{N} \frac{1}{r_{ij}^4} \Big(\left(\hat{\boldsymbol{m}}_j \cdot \hat{\boldsymbol{r}}_{ij}\right)\hat{\boldsymbol{m}}_i + \left(\hat{\boldsymbol{m}}_i \cdot \hat{\boldsymbol{r}}_{ij}\right)\hat{\boldsymbol{m}}_j \\ & + \left(\hat{\boldsymbol{m}}_i \cdot \hat{\boldsymbol{m}}_j\right)\hat{\boldsymbol{r}}_{ij} - 5\left(\hat{\boldsymbol{m}}_i \cdot \hat{\boldsymbol{r}}_{ij}\right)\left(\hat{\boldsymbol{m}}_j \cdot \hat{\boldsymbol{r}}_{ij}\right)\hat{\boldsymbol{r}}_{ij}\Big) \\ & + 48\epsilon \sum_{\substack{j=1 \\ j\neq i}}^{N} N_{ij} \left(\frac{\sigma}{r_{ij}}\right)^6 \left(\left(\frac{\sigma}{r_{ij}}\right)^6 - \frac{1}{2}\right)\frac{\hat{\boldsymbol{r}}_{ij}}{r_{ij}} + k \sum_{\substack{j=i-1 \\ j\neq i}}^{i+1} \left(\frac{r_0}{r_{ij}} - 1\right)\boldsymbol{r}_{ij}\end{aligned} \tag{5}$$

and

$$\mathbf{T}_i = -\frac{\mu_0 m^2}{4\pi} \sum_{\substack{j=1 \\ j\neq i}}^{N} \frac{\hat{\boldsymbol{m}}_i \times \mathbf{c}_{ij}}{r_{ij}^3}, \tag{6}$$

where we have defined, for convenience, the dimensionless vector $\mathbf{c}_{ij} = \hat{\boldsymbol{m}}_j - 3\left(\hat{\boldsymbol{m}}_j \cdot \hat{\boldsymbol{r}}_{ij}\right)\hat{\boldsymbol{r}}_{ij}$.

B. Dynamical equations

Assuming low-Reynolds-number hydrodynamics,[130] the moments of the particle velocities are related to the moments of the hydrodynamic forces acting on them via the mobility functions.[131,132] Neglecting mutual hydrodynamic interactions between the particles yields

$$\mathbf{V}_i = \mu\left(\mathbf{F}_i + \mathbf{F}_i^{\text{ext}}\right), \qquad \boldsymbol{\Omega}_i = \gamma\,\mathbf{T}_i, \tag{7}$$

where $\mathbf{V}_i$ and $\boldsymbol{\Omega}_i$ denote the linear and angular velocities of the ith membrane particle, respectively. Here, $\mu =$

The Journal of Chemical Physics ARTICLE scitation.org/journal/jcp

$1/(6\pi\eta a)$ and $\gamma = 1/(8\pi\eta a^3)$ are the translational and rotational mobilities for a sphere as given by the Stokes formulas, respectively. Moreover, $\mathbf{F}_i^{ext}$ is the external force resulting from the steric interaction with the self-driven particle that is moving under the action of a constant driving force $\mathbf{F}_0 = F_0\,\hat{\mathbf{e}}_y$. Here, we assume that the self-driven spherical particle of radius R interacts with membrane particles via the same soft repulsive WCA pair potential stated by Eq. (3) for $\sigma = a + R$.

Then, the equation of motion for the translational degrees of freedom reads

$$\frac{d\mathbf{r}_i}{dt} = \mathbf{V}_i. \tag{8}$$

Similarly, the equation governing the temporal evolution of the orientation of the ith particle is given by

$$\frac{d\hat{\mathbf{m}}_i}{dt} = \mathbf{\Omega}_i \times \hat{\mathbf{m}}_i, \tag{9}$$

which can be rewritten as

$$\frac{d\hat{\mathbf{m}}_i}{dt} = \frac{\gamma\mu_0 m^2}{4\pi}\sum_{\substack{j=1\\ j\neq i}}^{N}\frac{1}{r_{ij}^3}\Big(\big(\hat{\mathbf{m}}_i\cdot\mathbf{c}_{ij}\big)\hat{\mathbf{m}}_i - \mathbf{c}_{ij}\Big), \tag{10}$$

by making use of Eqs. (6) and (7).

Considering now two-dimensional orientation vectors in the (xy) plane, the particle orientations are represented in the Cartesian basis system as $\hat{\mathbf{m}}_i = (\cos\phi_i, \sin\phi_i)$ with the angle ϕ_i measured relatively to the x direction. Furthermore, the angular velocity vector then possesses only one single component (along the z direction). Hence, the temporal evolution of the orientation angle of the ith particle is calculated as

$$\frac{d\phi_i}{dt} = \mathbf{\Omega}_i\cdot\hat{\mathbf{e}}_z = \gamma(\mathbf{T}_i\cdot\hat{\mathbf{e}}_z). \tag{11}$$

We now introduce an additional cutoff length $\ell = 3h/2$ for the dipolar and elastic interactions. That is, we multiply a Heaviside function of the form $H(\ell - r_{ij})$ to Eqs. (5) and (6). Accordingly, these interactions are now truncated beyond next-nearest neighbors. Such a cutoff can be reasonable for screened electric dipolar interactions. This assumption does not significantly change our results except for the membrane destruction state of absent-healing (see below), the occurrence of which hinges on the cutoff.

III. STATE DIAGRAM

As an initial configuration of the membrane, the interparticle distance h is taken equal to the cutoff radius r_C beyond which the steric forces vanish. Moreover, we assume that the rest length of the springs is equal to this initial interparticle equilibrium distance, i.e., $r_0 = 2^{1/6}a$.

Our parameter space has four essential dimensions. The two dimensionless numbers

$$E_1 = \frac{\mu_0 m^2}{4\pi a^3\epsilon}, \qquad E_2 = \frac{aF_0}{\epsilon} \tag{12}$$

quantify the importance of the attractive dipolar force ($\sim\mu_0 m^2/a^4$) and of the active force F_0 relative to the repulsive steric force ($\sim\epsilon/a$) at particle contact, respectively. These two parameters will be denominated as reduced dipole strength and reduced activity, respectively. One additional dimensionless number

$$\kappa = \frac{\pi}{6}\frac{kh^5}{\mu_0 m^2} \tag{13}$$

corresponds to the ratio of the elastic to the dipolar interactions. Moreover, we define the dimensionless number

$$\delta = \frac{R}{a} \tag{14}$$

as the ratio of the radius of the active particle relative to that of the membrane particle. The parameters κ and δ will be denominated as reduced stiffness and size ratio, respectively. For future reference, we also introduce a dimensionless number quantifying the ratio of the driving and dipolar forces in the form

$$P_0 = \frac{1}{12}\left(\frac{h}{a}\right)^4\frac{E_2}{E_1}. \tag{15}$$

The latter will serve as our key control parameter discriminating trapped from penetrating states as detailed below. We note that $h/a = 2^{7/6}$ is kept constant such that P_0 is fully determined from the ratio E_2/E_1.

In Fig. 2, we present state diagrams identifying the possible dynamical states of the system in the plane of the two control parameters E_1 and E_2. The diagrams are constructed by numerical integration of the dynamical equations of motion using the 4th-order Runge-Kutta scheme with adaptive time step.[133] Results are shown for three values of the reduced stiffness κ which span a wide range of values to be expected in various situations. Here, we set $N = 20$ and $\delta = 1$. We have tested the robustness of the state diagrams by varying the number of membrane particles and have found no qualitative difference. Depending on the combination of the relevant control parameters, the self-driven particle either penetrates or remains in direct contact with the membrane (trapping state). In the latter case, the particle is essentially held back due to the steric interactions with the membrane particles. Furthermore, two penetration regimes are identified depending on whether the membrane self-heals and recovers its initial undeformed shape (red triangles) or remains damaged after the particle reaches the other side [green disks in (c)]. Qualitatively, penetration scenarios are observed for higher values of P_0 that indicate larger driving forces or smaller restoring dipolar forces than those in the trapped state. For $\kappa \gg 1$, penetration happens when

$$\frac{P_0}{\kappa} = \frac{2F_0}{kh} \gtrsim 1, \tag{16}$$

i.e., when the active force is larger than the overall elastic and dipolar restoring forces of a membrane particle with its two neighbors. After membrane penetration, self-healing always occurs for non- or weakly elastic membranes, for the

The Journal of Chemical Physics ARTICLE scitation.org/journal/jcp

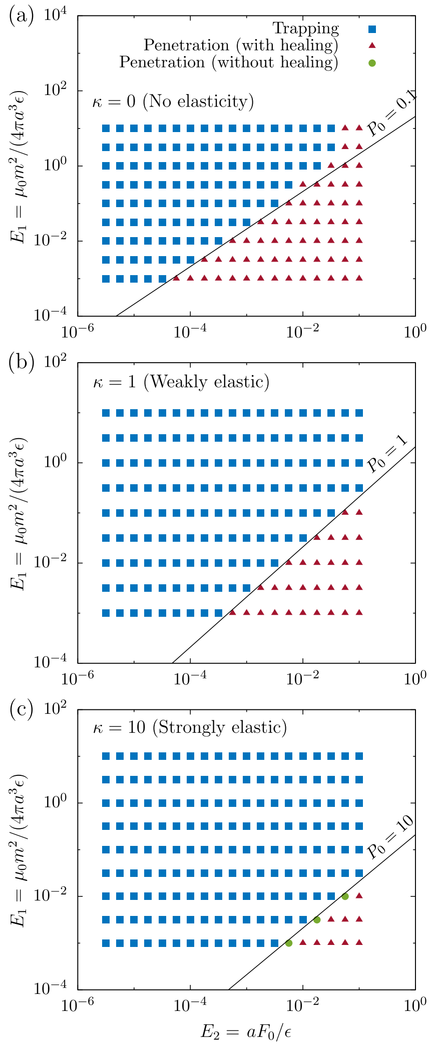

FIG. 2. Ability of penetration or trapping as a function of elasticity. Shown are state diagrams for (a) κ = 0, (b) κ = 1, and (c) κ = 10. Symbols represent the final states obtained from numerical integration of the dynamical equations, given by Eqs. (5)–(11). Here, membranes consisting of N = 20 dipolar particles have been examined and we set the size ratio δ = 1. Depending on the values of the dimensionless numbers E_1 and E_2, the active particle is either trapped (blue squares) or passes through the membrane to reach the other side. After full penetrations, the membrane either shows a self-healing ability (red triangles) or remains permanently damaged (green disks). The latter behavior is only observed in the case of strongly elastic membranes shown in (c) for the present set of parameters. The solid lines display the estimates of the transition line between the states.

present set of parameters. In contrast to this, the membrane may remain permanently damaged for strongly elastic membranes, see Fig. 2(c). Besides, the elastic interactions cause a noticeable "shifting" of the transition line between the penetration and trapping states. Apart from this, they do not qualitatively alter our results and will therefore be omitted in most of our later calculations. It is worth noting that the detailed form of the steric repulsion may not be important as long as the reduced dipole strength $E_1 \ll 1$. An alternative could be the use of hard-core interactions. However, a softer potential is adopted here for numerical convenience to prevent the interparticle forces from diverging during the evolution dynamics.

We now describe the dynamical scenarios of the trapped and penetrating states depicted in Fig. 3. First, we examine the time evolution of membrane configurations. At the initial stage of the dynamics, the active particle pushes the membrane and subsequently bends the membrane, as shown in Figs. 3(a), 3(c), and 3(e). If the active force is strong enough ($P_0 \gg 1$), such deformation persistently increases and induces a growing distance between the two center particles of the chain, giving rise to a weakening of their mutual dipolar attraction. Consequently, the active particle penetrates through the membrane, see Figs. 3(c) and 3(e). Depending on the size of the active particle relative to that of the membrane particles, the membrane either closes again to recover its initial aligned configuration [self-healing behavior shown in (c) for δ = 1] or remains permanently deformed [as shown for δ = 5 in (e)]. In addition, we observe that the penetration event is also accompanied by a slight abrupt increase in the particle speed [small cusp occurring in (d) at $t/t_S \simeq 0.6$ and in (f) at $t/t_S \simeq 1.6$]. This small augmentation of speed is due to the steric interactions which support the particle motion at this final stage when the penetrated particle is sterically repelled by the nearby membrane particles. In sharp contrast, when $P_0 \ll 1$, the membrane develops a triangular profile, reaching a steady state without allowing the self-driven particle to pass, see Fig. 3(e). This trapping behavior is investigated in more detail in Secs. IV and V. Meanwhile, both scenarios can also be understood in terms of the velocity profiles of the self-driven particle presented in Figs. 3(b), 3(d), and 3(f). Since the dynamics are overdamped, the velocity can be interpreted as the total net force exerted on the particle. Accordingly, membrane penetration occurs when the external driving force remains larger than the membrane restoring forces.

In order to explore the membrane behavior in the penetration state in more detail, we present in Fig. 4 a state diagram in the parameter space (δ, E_2). Here, we keep the other parameters fixed at κ = 0, $E_1 = 10^{-2}$, and N = 20. We observe that the transition between the trapping and penetration states can only be enabled by increasing the reduced activity E_2, regardless of the size ratio δ. However, the latter strongly affects the membrane behavior in the penetration scenario. In the considered range of parameters, lower values of δ lead to self-healing, while larger values imply permanent damage of the membrane. The observed suppression of the healing behavior for large enough penetrating particles can be

The Journal of Chemical Physics ARTICLE scitation.org/journal/jcp

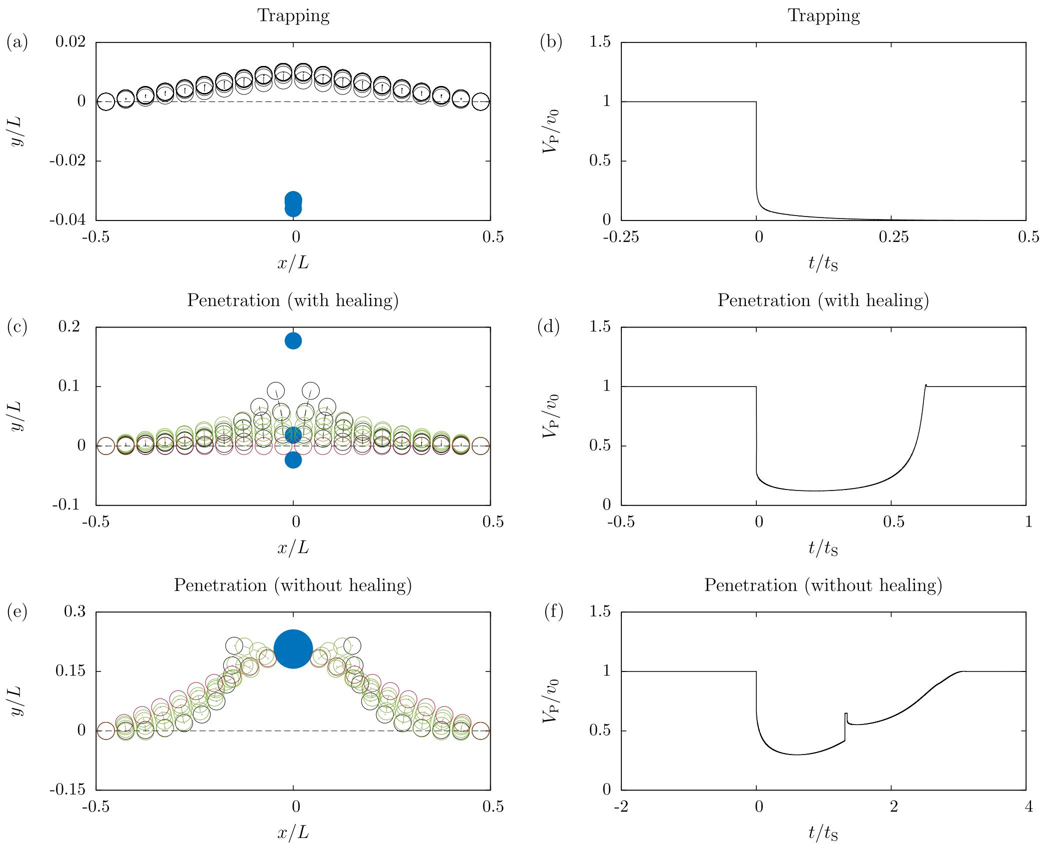

FIG. 3. Membrane dynamics of trapping and penetration states. (a) Frame series in the trapping state for $N = 20$, $\kappa = 0$, $\delta = 1$, $E_1 = 1$, and $E_2 = 10^{-2}$. Here, the frames are displayed every $0.2t_S$, where $t_S = \eta L^3/\epsilon$ is the simulation time unit. (b) Time evolution of the translational velocity of the active particle in the trapping state. (c) Frame series of the membrane conformation during the penetration state with healing, using the same set of parameters as in (a), except for $E_1 = 0.1$. The frames are displayed in time every $0.6t_S$. The black and green circles represent the positions of the membrane particles before and after the active particle (blue disk) reaches the upper side, respectively. As shown, the membrane recovers its original conformation after the active particle has passed (red circles). Panel (d) shows the corresponding translational velocity of the active particle versus time. (e) Frame series of the membrane shape during the penetration state without healing, using the same parameters as in (c), except for $R = 5a$. The frames are displayed every $6t_S$ in time with the same color as in (c). Circles shown in red represent the steady positions of the membrane particles. Panel (f) displays the corresponding time evolution of the active particle. We note that the particles in (a), (c), and (e) are not plotted to scale. Accordingly, the shown circles and disks only correspond to the positions of the centers of the particles. [The membrane particles and the driven particle in (a) are actually in contact, but the scales on the ordinate and abscissa are pronouncedly different.] Time $t = 0$ in (b), (d), and (f) corresponds to the moment when the active particle and the membrane begin to mutually interact.

understood by the fact that the mutual distance between the two central beads becomes larger than the cutoff distance ℓ, which could represent the average distance between cytoskeletal cross-linkers for biological membranes. If these links are broken by large active particles, the attractive interactions between the membrane particles vanish. Consequently, the membrane is split up and remains permanently destroyed, or at least until other mechanisms help the membrane to regenerate. Without the cutoff, the membrane because of the long-ranged forces always heals after a penetration event.

IV. ANALYTICAL THEORY

To proceed analytically, we restrict ourselves to the small-deformation regime. Then, we linearize the dynamical equations and solve for the membrane displacement and dipole orientation fields.

The Journal of Chemical Physics ARTICLE scitation.org/journal/jcp

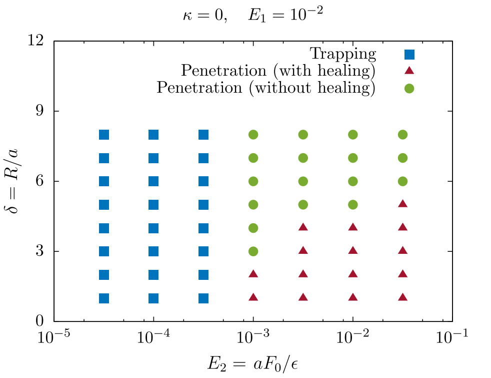

FIG. 4. State diagram of trapping and penetration in the parameter space of size ratio δ and reduced activity E_2, while keeping the reduced stiffness $\kappa = 0$ and the reduced dipole strength $E_1 = 10^{-2}$. Here, we have examined membranes consisting of $N = 20$ dipolar particles. Symbols represent the final dynamical state obtained from numerical integration of Eqs. (5)–(11).

A. Evolution of the membrane particles

In the deformed configuration, the position vector of each dipolar particle in the laboratory frame of reference can be written as $\boldsymbol{r}_i = (d_i + u_i)\hat{\boldsymbol{e}}_x + \rho_i\hat{\boldsymbol{e}}_y$, wherein $d_i = h(i - N/2)$, $i = 1, \ldots, N$, represents the equilibrium x positions of the particles in the initial configuration. Without loss of generality, we consider here only even numbers of N. In addition, u_i and ρ_i denote the membrane displacements along the x and y directions, respectively.

We assume that the active particle has a radius comparable to that of the membrane particles. For the dipolar particles that are not at the chain ends, i.e., for $i = 2, \ldots, N - 1$, the projection of the dynamic equations governing the translational motion of the ith sphere, given by Eq. (8), can be presented in a linearized form as

$$\frac{1}{A}\frac{du_i}{dt} = \frac{72\epsilon\mu}{Ah^2}\left((u_{i+1} - u_i)N_{i,i+1} - (u_i - u_{i-1})N_{i,i-1}\right) + 2(\kappa - 1)\frac{u_{i+1} - 2u_i + u_{i-1}}{h^2} - \frac{\mu F_{\parallel i}}{A}, \tag{17a}$$

$$\frac{1}{A}\frac{d\rho_i}{dt} = \frac{\rho_{i+1} - 2\rho_i + \rho_{i-1}}{h^2} - \frac{\phi_{i+1} - \phi_{i-1}}{4h} + \frac{\mu F_{\perp i}}{A}, \tag{17b}$$

where we have defined $A := 3\mu_0 m^2\mu/(\pi h^3)$, a parameter that has the dimension of a diffusion coefficient. We assume that $r_{i,i\pm1} < \ell$ always holds in the small-deformation regime considered here. Moreover, $F_{\parallel i} = F_i \sin\alpha$ and $F_{\perp i} = F_i\cos\alpha$, where $F_i = F(\delta_{i,N/2} + \delta_{i,N/2+1})$ is the magnitude of the force acting on the two central particles due to the steric interactions with the active particle. Thus, $F_i = F$ if $i \in \{N/2, N/2 + 1\}$ and $F_i = 0$ otherwise. This implies that the active particle is exactly positioned between the central two beads of the membrane. We have also explored the situation, where N is an odd number, in which the external force is only exerted to the center particle and have found quantitatively similar results. Continuing, α is the angle formed by the y axis and the line connecting the center of the self-driven particle to that of the closest membrane particle (see Fig. 1). This angle is defined as negative for clockwise rotation from the y axis. Notably, the dipolar interactions manifest themselves in both the longitudinal and transverse force balance equations, whereas the steric and elastic interactions are (at linear order) only involved in the longitudinal force balance equation. This behavior resembles that of elastic membranes, where stretching and bending effects are predominately pronounced along the tangential and normal traction jumps, respectively.[134–138] Therefore, our self-assembled chains can be used as a minimal model membrane with effective stretching and bending moduli, in analogy to purely elastic membranes with stretching and bending deformation modes.

Similarly, we proceed with the torque balance given by Eq. (11), and derive an approximate equation for the rotational motion of the membrane particles. Upon linearization, we obtain

$$\frac{d\phi_i}{dt} = \frac{B}{2}\left(\frac{\rho_{i+1} - \rho_{i-1}}{h} - \frac{\phi_{i+1} + \phi_{i-1} + 4\phi_i}{3}\right), \tag{18}$$

where we have defined a parameter $B := 3A/(8a^2)$ with the dimension of inverse time. We also used the fact that the translational and rotational mobilities of a sphere are related via $\gamma/\mu = 3/(4a^2)$.

The two particles located at the membrane extremities remain fixed in space (zero displacement) and are not subject to any dipolar torques. The latter could be achieved, for instance, if for the two particles at the ends of the membrane the dipole moment can freely rotate inside the particle, relatively to the particle frame. Therefore, Eqs. (17) and (18) are subject to the boundary conditions

$$u_i = \rho_i = 0 \ \text{ for } \ i \in \{1, N\}, \tag{19a}$$

$$\phi_2 + 2\phi_1 - 3\frac{\rho_2}{h} = 0, \tag{19b}$$

$$\phi_{N-1} + 2\phi_N + 3\frac{\rho_{N-1}}{h} = 0. \tag{19c}$$

B. Evolution of the active particle

The active particle is subject to the constant force $\mathbf{F}_0$ acting along the y direction in addition to the resistive forces due to the steric interactions with the two central particles. Denoting by $\mu_P = 1/(6\pi\eta R)$ the translational mobility function of the self-driven particle, the governing equation for the translational motion along the y direction reads

$$\frac{1}{\mu_P}\frac{dy_P}{dt} = F_0 - 2F\cos\alpha. \tag{20}$$

For future reference, we define r as the steady center-to-center distance separating the self-driven particle from the central particles in the trapping state. For an interparticle distance $r \lesssim r_C$, the magnitude of the WCA force acting on a

The Journal of Chemical Physics ARTICLE scitation.org/journal/jcp

central particle can, to leading order, be approximated by

$$F = \frac{36 \cdot 2^{2/3}\epsilon}{\sigma}\left(2^{1/6} - \frac{r}{\sigma}\right), \tag{21}$$

where $\sigma = a + R$.

Inserting the latter equation into Eq. (20) and setting the left-hand side to zero, the steady-state distance separating the self-driven particle from the central particles is given by

$$r = \frac{h}{2}\left(1 + \frac{R}{a}\right)\left(1 - \frac{E_2}{288}\left(1 + \frac{R}{a}\right)\frac{h}{a\cos\alpha}\right), \tag{22}$$

where we have used the constraint that $h/a = 2^{7/6}$.

Equations (17) and (18) form $3(N-2)$ ordinary differential equations in time for the unknown displacement and orientation fields. These equations are subject to the six boundary conditions given by Eqs. (19) in addition to the initial conditions of vanishing displacement and orientation fields. In the steady state, the problem reduces to finding the solution of a set of recurrence equations relating the positions and orientations of adjacent spheres. In Sec. V, we present an analytical solution of the resulting recurrence problem. In addition, we show that the underlying equations for the motion of the membrane particles can conveniently be presented in the continuous limit using partial differential equations that describe the temporal and spatial evolution of the membrane displacement and dipole orientation.

V. SOLUTION FOR THE TRAPPING STATE

A. Steady solution of the recurrence problem

For $E_2 \ll 1$, it follows from Eq. (22) that $r \sim h(1+\delta)/2$, where again $\delta = R/a$. Assuming that $|u_i| \ll h$, for $i = 1, \ldots, N$, yields $\sin\alpha \simeq h/(2r)$. As a result, $\alpha \simeq \arcsin(1/(1+\delta))$.

Due to the symmetry of the problem with respect to the membrane center, it is sufficient to solve the recurrence problem for $i \in \{1, \ldots, M\}$, where $M := N/2$. In the steady state, it follows readily from the force balance Eq. (20) that $F = F_0/(2\cos\alpha)$, where $\cos\alpha \simeq \left(1 - 1/(1+\delta)^2\right)^{1/2}$.

1. Longitudinal displacement

The mutual distance between adjacent particles in the trapping state is significantly larger than the cutoff distance. Therefore, the steric interactions between membrane particles vanish, and only the elastic and dipolar interactions are relevant.

Assuming that $\kappa \neq 1$, Eq. (17a) that governs the final steady-state membrane displacement along the x direction, for $1 < i < M$, can be written as

$$u_{i+1} - 2u_i + u_{i-1} = 0. \tag{23}$$

The latter expression is subject to the boundary condition $u_{M-1} - 3u_M = Kh$, which follows from setting $i = M$ in Eq. (17a) and using the fact that $u_{M+1} = -u_M$ as required by symmetry considerations. Here, we have defined for convenience the dimensionless number

$$K = \frac{P_0}{4(\kappa - 1)(1+\delta)}, \tag{24}$$

where we have used the approximation $\sin\alpha \simeq 1/(1+\delta)$. The solution of the resulting linear homogeneous second-order recurrence problem satisfying the zero-displacement boundary condition $u_1 = 0$ is given by

$$\frac{u_i}{h} = -\frac{i-1}{N-1}K. \tag{25}$$

The maximum displacement occurs for $i = M$ and amounts to $u_M = -(M-1)Kh/(2M-1)$.

For $\kappa = 1$, the dipolar forces are balanced by the elastic forces. Consequently, the membrane to linear order primarily undergoes motion along the transverse direction.

We further note that for $\kappa \leq 1$ the elastic forces cannot stabilize the system as the dipolar attraction overwhelms the elastic repulsion. Since its ends are fixed, the membrane would tear itself apart. The steric repulsions in this situation prevent the collapse of the system.

2. Transverse displacement and dipole orientation

We next consider the displacement field induced along the transverse direction and examine the rotation of the dipoles. For $1 < i < M$, Eqs. (17b) and (18) are written in the steady trapping state as

$$\frac{1}{h}(\rho_{i+1} - 2\rho_i + \rho_{i-1}) - \frac{1}{4}(\phi_{i+1} - \phi_{i-1}) = 0, \tag{26a}$$

$$\frac{1}{h}(\rho_{i+1} - \rho_{i-1}) - \frac{1}{3}(\phi_{i+1} + 4\phi_i + \phi_{i-1}) = 0. \tag{26b}$$

For the solution of the coupled recurrence relations at hand, it is convenient to rearrange the equations in such a way as to decouple the transverse displacement from the dipole orientation. To this end, we define the displacement gradient as $D_i = (\rho_i - \rho_{i-1})/h$. Accordingly, Eqs. (26) can be rewritten as

$$D_{i+1} - D_i = \frac{1}{4}(\phi_{i+1} - \phi_{i-1}), \tag{27a}$$

$$D_{i+1} + D_i = \frac{1}{3}(\phi_{i+1} + 4\phi_i + \phi_{i-1}). \tag{27b}$$

Then, Eqs. (27) can be rearranged to obtain

$$D_i = \frac{2}{3}\phi_{i-1} + \frac{7\phi_i + \phi_{i-2}}{24} = \frac{2}{3}\phi_i + \frac{7\phi_{i-1} + \phi_{i+1}}{24}. \tag{28}$$

The latter equation can further be rearranged to obtain the following recurrence relation for the orientation field:

$$\phi_{i+1} - \phi_{i-2} + 9(\phi_i - \phi_{i-1}) = 0. \tag{29}$$

In order to solve the resulting linear homogeneous third-order recurrence problem and find the general term of ϕ_i, we use the classical approach based on the *distinct roots theorem*.[139] Correspondingly, we search for solutions of the recurrence relation in the form of $\phi_i = c/p^i$. Substituting into

The Journal of Chemical Physics ARTICLE scitation.org/journal/jcp

Eq. (29) yields the characteristic equation of the recurrence problem,

$$p^3 + 9p^2 - 9p - 1 = 0, \tag{30}$$

the solutions of which, often called the characteristic roots of the recurrence relation, are $p = 1$ and $p_\pm := -5 \pm 2\sqrt{6}$. Then, the general solution for the orientation field is given by

$$\phi_i = C + C_- p_-^i + C_+ p_+^i, \tag{31}$$

where the constants $C_\pm$ and C are to be determined from the boundary conditions. We note that p_+ and p_- are the multiplicative inverse of each other, i.e., $p_+ p_- = 1$.

Upon substitution of the expression of the orientation field given by Eq. (31) into Eq. (28), the general solution for the displacement gradient is obtained as

$$D_i = C + C_-\left(-1 + \tfrac{\sqrt{6}}{2}\right)p_-^i + C_+\left(-1 - \tfrac{\sqrt{6}}{2}\right)p_+^i. \tag{32}$$

For the determination of the three unknown coefficients C and $C_\pm$, we make use of the boundary conditions,

$$3D_2 - (\phi_2 + 2\phi_1) = 0, \tag{33a}$$

$$D_M - \frac{1}{4}(\phi_M + \phi_{M-1}) = \frac{P_0}{2}, \tag{33b}$$

$$D_M - \phi_M - \frac{\phi_{M-1}}{3} = 0, \tag{33c}$$

after noting that $\rho_{M+1} = \rho_M$ and $\phi_{M+1} = -\phi_M$. Here, $P_0 = \mu F_0 h/A$ is the dimensionless parameter defined earlier in Eq. (15).

Next, from Eqs. (31) to (33), the unknown coefficients are determined as

$$C = -W\left(12Q_{M-1} + 117Q_M + \sqrt{6}(5S_{M-1} + 48S_M)\right),$$
$$C_\pm = W\left(\pm 12 + 5\sqrt{6}\right),$$

where we have defined

$$S_i = p_+^i + p_-^i, \qquad Q_i = p_+^i - p_-^i. \tag{34}$$

Moreover, $W = P_0/\left(3Q_M + \sqrt{6}S_M\right)$.

The transverse displacement field of the ith membrane particle can then be calculated from the displacement gradient as

$$\rho_i = h\sum_{j=2}^{i} D_j, \tag{35}$$

which, using $\rho_1 = 0$, reads

$$\frac{\rho_i}{h} = (i-1)C + C_-\left(-1 + \tfrac{5\sqrt{6}}{12}\right)\left(49 + 20\sqrt{6} - p_-^{i+1}\right)$$
$$+ C_+\left(1 + \tfrac{5\sqrt{6}}{12}\right)\left(-49 + 20\sqrt{6} + p_+^{i+1}\right). \tag{36}$$

In the limit of $M \to \infty$ (and thus $h \to 0$ for fixed L), we get $C = P_0$ and $C_- = C_+ = 0$. Defining a continuum variable as $x/L = ((i-1)/(M-1) - 1)/2$ for $1 \le i \le M$ such that $x/L \in [-1/2, 0)$, Eq. (36) can be written in the continuum limit, for x notably smaller than zero, as

$$\lim_{M\to\infty} \phi(x) = P_0, \tag{37a}$$

$$\lim_{M\to\infty} \rho(x) = P_0\left(\frac{L}{2} + x\right). \tag{37b}$$

It is worth mentioning that our approximation is valid in the small deformation regime for which $P_0 \ll 1$. From parity considerations, consequently $\phi(-x) = -\phi(x)$ and $\rho(-x) = \rho(x)$. Thus, the transverse displacement reaches its maximum value at the membrane center, for $x = 0$.

In the following, we will approach the problem differently by utilizing a continuum description of the governing equations to yield analytical expressions for the membrane deformation not only in the steady state but also in the transient state.

B. Continuum description

In order to obtain a continuum description of the membrane deformation and dipole orientations, we present the transverse displacement field in the form $\rho_{i+s} = \exp(shD)\rho(x)$, and analogously for u_{i+s} and ϕ_{i+s}, wherein s is a relative integer and $D := \partial/\partial x$ denotes the differential operator with respect to the spatial coordinate. Expanding the exponential argument in powers of shD, we obtain for ρ_{i+s} up to second order[140]

$$\rho_{i+s} = \left(1 + sh\frac{\partial}{\partial x} + \frac{(sh)^2}{2}\frac{\partial^2}{\partial x^2} + \cdots\right)\rho(x), \tag{38}$$

and analogously expressions for u_{i+s} and ϕ_{i+s}.

Using this representation, Eqs. (17) can be written in the continuum limit as

$$u_{,t} = 2A(\kappa - 1)u_{,xx}, \tag{39a}$$

$$\rho_{,t} = A\left(\rho_{,xx} - \frac{\phi_{,x}}{2}\right) + \mu\left(F_0 - \frac{y_{P,t}}{\mu_P}\right)h\,\delta(x), \tag{39b}$$

for $-L/2 \le x \le L/2$. Here, commas in the subscripts denote partial derivative with respect to the arguments listed in the subscripts. We have neglected the steric interactions along the longitudinal direction as they usually have a vanishing contribution to the force balance in the trapping state, during which the membrane is stretched. In addition, the discrete force $F_i = F(\delta_{i,M} + \delta_{i,M+1})$ has now been transformed into a point force $2Fh\,\delta(x)$ oriented along the y direction, where the prefactor h has been introduced so as to ensure the right physical dimension. Accordingly, $\alpha \to 0$ holds in the continuum limit since $a \to 0$ leads to $\delta \to \infty$ for R remaining finite. Thus the longitudinal component of the force $F_\parallel$ vanishes.

Similarly, the continuum version of the equation governing the orientation dynamics of the dipoles, given in a discrete form by Eq. (18), reads

$$\phi_{,t} = B(\rho_{,x} - \phi). \tag{40}$$

Equations (39) and (40) are subject to the initial conditions at $t = 0$ of vanishing displacement and orientation, in addition to the boundary conditions of zero displacement and torque at $x = \pm L/2$. It is worth mentioning that A and B are considered

The Journal of Chemical Physics ARTICLE scitation.org/journal/jcp

here as constant membrane properties and are therefore not affected by the limit $h \to 0$.

1. Steady state

We first look for analytical solutions of the continuum model equations in the steady state of motion. It follows from Eq. (39a) that the steady longitudinal displacement in the trapping state satisfies $u_{,xx} = 0$. Since $u(x = 0) = 0$, as required by symmetry considerations, the longitudinal displacement necessarily vanishes upon application of the boundary conditions. Therefore, the membrane particles only displace along the y direction in the considered continuum limit.

As for the transverse displacement, Eq. (39b) simplifies in the steady state to

$$\rho_{,xx} - \frac{\phi_{,x}}{2} + P_0\,\delta(x) = 0, \tag{41}$$

while Eq. (40) leads to $\phi = \rho_{,x}$. As a result, the steady orientation of the dipoles is solely given by the displacement gradient. The present situation is analogous to that known in the context of Kirchhoff–Love theory of elastic beams or plates.[141] Thus, the transverse displacement of the continuous membrane is governed by the following second-order differential equation:

$$\rho_{,xx} + 2P_0\,\delta(x) = 0, \tag{42}$$

the solution of which (that satisfies the boundary conditions) is given by

$$\rho(x) = P_0\left(\frac{L}{2} - |x|\right), \tag{43a}$$

$$\phi(x) = -P_0\,\mathrm{sgn}(x), \tag{43b}$$

where $\mathrm{sgn}(x) := x/|x|$ denotes the sign function. These results are in full agreement with Eqs. (37) that have been obtained for $x < 0$ by taking the corresponding continuum limit in the discrete description.

The membrane undergoes a maximum deformation at its center, which, for $h = L/N$ and $h/a = 2^{7/6}$, is given by

$$\frac{\rho_{\mathrm{Max}}}{L} = \frac{P_0}{2} = 4\pi c\,\frac{a^4 F_0}{\mu_0 m^2}, \tag{44}$$

where $c = 2^{5/3}/3 \approx 1.06$ is a numerical prefactor. The latter result indicates that the maximum deflection of the membrane scales linearly with the magnitude of the active force but does not depend on the nature of the steric interactions causing the membrane to deform.

In Fig. 5, we present the steady-state profiles of (a) the transverse displacement $\rho(x)$ and (b) the orientation $\phi(x)$ for various values of E_2, while keeping the other parameters constant at $E_1 = 1$ and $N = 20$. Here, the numerical solutions of the nonlinear equations are indicated by circles, and the results of the corresponding recurrence solution of the linear discrete problem—closely matching the numerical solution—are denoted by squares. Solid lines present the continuum solutions for the same set of parameters.

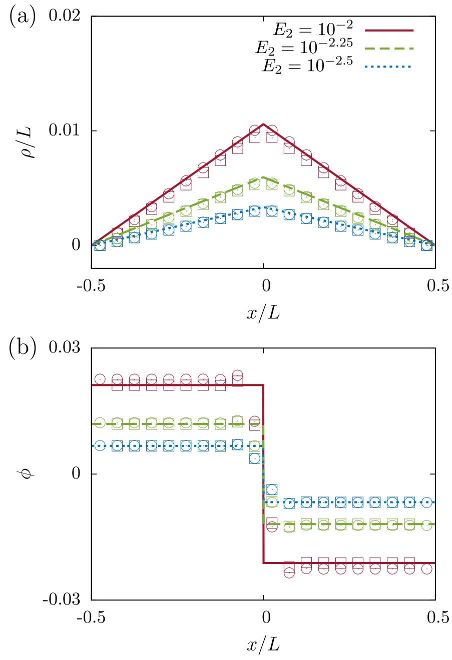

FIG. 5. Steady-state solutions in the trapping state. (a) Scaled membrane deformation ρ/L and (b) local membrane orientation ϕ as functions of x (the self-driven particle is located at $x = 0$), both for systems with $E_1 = 1$, $N = 20$, and varying values of E_2. Circles indicate the results of numerical simulations obtained by solving the nonlinear dynamical equations, squares denote the solutions of the recurrence problem given by Eqs. (31) and (36), and solid lines are the analytical predictions described by Eqs. (43) obtained from a continuum formulation. All these approaches lead to triangular profiles for $\rho(x)$ and square-like ones for $\phi(x)$, showing strong quantitative agreement without the introduction of any fitting parameters.

While the continuum description always leads to ideal triangular and square profiles for $\rho(x)$ and $\phi(x)$, respectively, the numerical solution of the nonlinear problem shows deviations from these shapes. The differences are most probably due to the finite size of the active particle which has not been taken into account in the present continuum description. Finally, we remark that even though no fitting parameters have been introduced, the results still closely match each other, reinforcing the applicability of our approximate analytical approach to predict the shape of our minimal membrane model under the influence of a localized destroying force.

2. Transient behavior

Having presented analytical solutions of the continuum equations of motion in the steady state, assessed the appropriateness and judged the accuracy of our linearized

The Journal of Chemical Physics ARTICLE scitation.org/journal/jcp

analytical theory, we next address the membrane deformation and dipole orientation in the transient regime. The solution to this mathematical problem can be obtained by *finite* Fourier transforms in space of the governing equations and solving the resulting ordinary differential equations in time.

For this purpose, we define the basis functions

$$c_q(x) = \cos\left(H_q x\right), \qquad s_q(x) = \sin\left(H_q x\right), \tag{45}$$

where $H_q = (2q - 1)\pi/L$ with $q = 1, 2, \ldots$ denoting the variable that sets the coordinates in Fourier space. Then the displacement and orientation fields can be expressed in terms of Fourier series in space as[142]

$$\rho(x,t) = \frac{2}{L}\sum_{q\geq 1}\hat{\rho}(q,t)\, c_q(x), \tag{46a}$$

$$\phi(x,t) = \frac{2}{L}\sum_{q\geq 1}\hat{\phi}(q,t)\, s_q(x), \tag{46b}$$

where $\hat{\rho}$ and $\hat{\phi}$ are the Fourier coefficients, defined as

$$\hat{\rho}(q,t) = \int_{-\frac{L}{2}}^{\frac{L}{2}} \rho(x,t)\, c_q(x)\, dx, \tag{47a}$$

$$\hat{\phi}(q,t) = \int_{-\frac{L}{2}}^{\frac{L}{2}} \phi(x,t)\, s_q(x)\, dx. \tag{47b}$$

The form of the Fourier representation given by Eqs. (46) follows from the boundary conditions to ensure at any time that $\rho(\pm L/2,\, t) = 0$ and $\phi_{,x}(\pm L/2,\, t) = 0$. We note that the basis functions $c_q(x)$ and $s_q(x)$ satisfy the orthogonality relations

$$\int_{-\frac{L}{2}}^{\frac{L}{2}} c_p(x)c_q(x)\, dx = \int_{-\frac{L}{2}}^{\frac{L}{2}} s_p(x)s_q(x)\, dx = \frac{L}{2}\,\delta_{pq}. \tag{48}$$

Transforming Eqs. (39b) and (40) into spatial Fourier space yields

$$\frac{\hat{\rho}_{,t}}{A} = -H_q\left(H_q\hat{\rho} + \frac{\hat{\phi}}{2}\right) + P_0\left(1 - \frac{y_{P,t}}{v_0}\right), \tag{49a}$$

$$\frac{\hat{\phi}_{,t}}{B} = -H_q\hat{\rho} - \hat{\phi}, \tag{49b}$$

where $v_0 = \mu_P F_0$ is the bulk velocity of the active particle.

For a closure of the above set of equations, we require that the instantaneous distance between the self-driven particle and the membrane center remains constant during the system evolution such that $y_{P,t} = \rho_{,t}(x = 0, t)$. However, in order to be able to make analytical progress, we further assume that after a brief transient evolution, $|y_{P,t}| \ll v_0$ holds, and thus the term involving $y_{P,t}$ can be neglected. This is equivalent to assuming that the active particle instantaneously attains its terminal velocity when the interaction with the membrane takes place.

The solution of the system of differential equations given by Eqs. (49) can more easily be obtained using the Laplace transform technique.[143] In the following, the Laplace-transformed function pairs are distinguished only by their argument while the hat is reserved to denote the spatial Fourier transforms. By employing the initial conditions $\hat{\rho}(q, t = 0) = \hat{\phi}(q, t = 0) = 0$, we obtain

$$\frac{s}{A}\,\hat{\rho}(q,s) = -H_q\left(H_q\hat{\rho}(q,s) + \frac{\hat{\phi}(q,s)}{2}\right) + \frac{P_0}{s}, \tag{50a}$$

$$\frac{s}{B}\,\hat{\phi}(q,s) = -H_q\hat{\rho}(q,s) - \hat{\phi}(q,s). \tag{50b}$$

Solving these equations for $\hat{\rho}(q,s)$ and $\hat{\phi}(q,s)$ yields

$$\hat{\rho}(q,s) = \frac{2A(B+s)P_0}{Q}, \tag{51a}$$

$$\hat{\phi}(q,s) = -\frac{2H_q ABP_0}{Q}, \tag{51b}$$

where the denominator is given by

$$Q = s\left(2s^2 + 2(B + AH_q^2)s + ABH_q^2\right).$$

The inverse Laplace transform can readily be obtained from the standard approach of partial fraction decomposition and using tables of Laplace transforms, which yields

$$\hat{\rho}(q,t) = \frac{2P_0}{H_q^2}\left(1 - e^{-\beta t}\left(\cosh(\tau t) + \frac{B}{2\tau}\,\sinh(\tau t)\right)\right),$$

$$\hat{\phi}(q,t) = -\frac{2P_0}{H_q}\left(1 - e^{-\beta t}\left(\cosh(\tau t) + \frac{\beta}{\tau}\,\sinh(\tau t)\right)\right),$$

where we have defined the parameters τ and β, with inverse time dimension, as

$$\tau = \frac{1}{2}\sqrt{B^2 + A^2H_q^4}, \qquad \beta = \frac{1}{2}\left(B + AH_q^2\right). \tag{52}$$

A typical transient behavior is shown in Fig. 6 presenting (a) the membrane transverse displacement $\rho(x, t)$ and (b) the dipole orientation $\phi(x, t)$ at various times t using the parameters $E_1 = 1$, $E_2 = 10^{-2}$, and $N = 20$. Here, symbols indicate the numerical solutions for a discrete membrane and solid lines represent the analytical solutions of the continuum theory outlined above. Again, without fitting parameters, there is strong qualitative and quantitative agreement between both approaches.

The transverse displacement profile features at early times a small central dent, which then more and more expands as time evolves. This leads to a significant kink at the center and, finally, to the triangular shape in the steady state. At all times, the symmetry $\rho(-x, t) = \rho(x, t)$ is fulfilled. Similarly, for the dipole orientation, smooth transitions take place from a small "orientation jump" in the center and vanishing initial orientations elsewhere to a full-chain square-like profile in the steady state. The discrete case features a significantly less pronounced change in orientation for the two central spheres at all times.

Finally, we address the transient behavior in the particular situation of fast orientational relaxation, for which $B \gg Aq^2$. Setting $\phi_{,t} = 0$ in Eq. (40) yields

The Journal of Chemical Physics ARTICLE scitation.org/journal/jcp

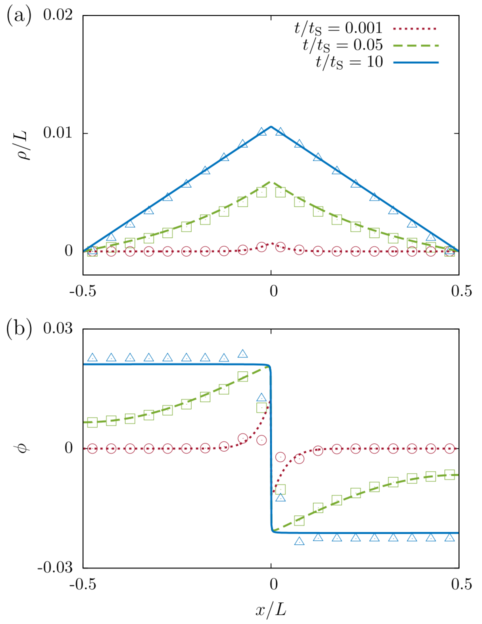

FIG. 6. Dynamic solutions for the trapping scenario. (a) Scaled transient membrane deformation profile $\rho(x, t)/L$ and (b) membrane orientation profile $\phi(x, t)$ calculated at times t/t_S = 0.001, 0.05, 10, where $t_S = \eta L^3/\epsilon$ for N = 20, E_1 = 1, and $E_2 = 10^{-2}$. Here, symbols are numerical simulation results and solid lines give the corresponding analytical results according to Eqs. (46). Both approaches show qualitative and quantitative agreement in their description of the transition from the small central perturbations at early times to the steady state for $t \to \infty$ (see also Fig. 5 for a detailed display of the latter).

$$\phi = \rho_{,x}. \tag{53}$$

Accordingly, the dipole orientation follows instantaneously the slope of the membrane. Inserting Eq. (53) into Eq. (39b) yields

$$\rho_{,t} = \frac{A}{2}\rho_{,xx} + \mu h F_0\,\delta(x), \tag{54}$$

where $y_{P,t}$ has been neglected along the same lines as discussed above.

Equation (54) has the form of a diffusion equation with a point source localized in space, subject to the initial condition $\rho(x, t = 0) = 0$, in addition to the Dirichlet-type boundary conditions $\rho(x = \pm L/2, t) = 0$. The solution of this equation has been obtained by Sommerfeld[144] and is expressed as

$$\rho(x,t) = \frac{AP_0}{2L}\int_0^t \left(\vartheta\left(\frac{x}{2L},t'\right) - \vartheta\left(\frac{x+L}{2L},t'\right)\right)dt', \tag{55}$$

with Jacobi theta functions[145]

$$\vartheta(\xi,t) = 1 + 2\sum_{n=1}^{\infty} e^{-\delta_n t}\cos(2n\pi\xi), \tag{56}$$

where we have defined

$$\delta_n = \frac{n^2\pi^2 A}{2L^2}. \tag{57}$$

This leads to the scaled displacement

$$\frac{\rho(x,t)}{L} = \frac{4P_0}{\pi^2}\sum_{n=1}^{\infty}\frac{1-e^{-\delta_{2n-1}t}}{(2n-1)^2}\cos\left((2n-1)\frac{\pi x}{L}\right), \tag{58}$$

which reproduces the steady-state solution given by Eq. (36) as shown below. In particular, the long-time behavior is dominated by the first term (n = 1), which approaches the limit exponentially with a characteristic decay time $2L^2/(\pi^2 A)$. Additionally, the orientation follows forthwith from Eq. (53) as

$$\phi(x,t) = -\frac{4P_0}{\pi}\sum_{n=1}^{\infty}\frac{1-e^{-\delta_{2n-1}t}}{2n-1}\sin\left((2n-1)\frac{\pi x}{L}\right). \tag{59}$$

In the limit $t \to \infty$, we obtain

$$\lim_{t\to\infty}\frac{\rho(x,t)}{L} = \frac{4P_0}{\pi^2}\sum_{n=1}^{\infty}\frac{\cos\left((2n-1)\frac{\pi x}{L}\right)}{(2n-1)^2}, \tag{60a}$$

$$\lim_{t\to\infty}\phi(x,t) = -\frac{4P_0}{\pi}\sum_{n=1}^{\infty}\frac{\sin\left((2n-1)\frac{\pi x}{L}\right)}{2n-1}, \tag{60b}$$

which correspond, respectively, to the Fourier series representation of the triangle and square wave functions of frequency $2\pi/L$. The maximum membrane displacement is calculated as

$$\lim_{t\to\infty}\frac{\rho(0,t)}{L} = \frac{4P_0}{\pi^2}\sum_{n=1}^{\infty}\frac{1}{(2n-1)^2} = \frac{P_0}{2}, \tag{61}$$

in agreement with the result obtained earlier from the steady differential equations, as given by Eq. (44).

VI. CONCLUSIONS

In this article, we explored the interactions between an active particle and a minimal model membrane. Since we concentrate on a two-dimensional setup, our results could, for instance, in experiments be readily compared with the behavior of a self-driven particle on a substrate, colliding with a straightened chain of mutually attractive dipolar spheres. We demonstrated that the particle may either get trapped by the membrane or penetrate through it, where the membrane can either be permanently damaged or recover by self-healing. State diagrams are presented that carefully map out which state occurs as a function of only a few generic parameters: membrane elasticity, bending stiffness, strength and size of the active particle. Our analytical theory further predicts the shape and the dynamics of the membrane, in close quantitative agreement with our numerical simulations. Our results suggest that the microscopic details of the interactions among membrane components (particles) are largely insignificant to the overall behavior of the membrane. Thus, our results might be broadly applicable to describe the experiments of micro-swimmers interacting with membranes, such as synthetic microbots colliding with a lipid bilayer or microbes with a membrane synthesized from dipolar microparticles. In this context, it would be interesting to extend our model to account for Brownian noise acting on the membrane and the self-driven particle as well. This might, for instance, support the membrane in healing after being destroyed by the penetrating active particle.

ACKNOWLEDGMENTS

A.D.M.I., A.M.M., and H.L. thank Joachim Clement for a stimulating discussion. The authors are indebted to Maciej Lisicki and Shang Yik Reigh for helpful comments and suggestions, and gratefully acknowledge support from the DFG (Deutsche Forschungsgemeinschaft) through the Project Nos. DA 2107/1-1, SCHO 1700/1-1, ME 3571/2-2, and LO 418/16-3. S.G. gratefully acknowledges funding from the Alexander von Humboldt Foundation. The work of A.J.T.M.M. was supported by a cross-disciplinary fellowship from the Human Frontier Science Program Organization (No. HFSPO–LT001670/2017). F.G.-L. acknowledges support from the Millennium Nucleus "Physics of Active Matter" of the Millennium Scientific Initiative of the Ministry of Economy, Development and Tourism, Chile.

REFERENCES

[1] K. T. Kaljot, R. D. Shaw, D. H. Rubin, and H. B. Greenberg, "Infectious rotavirus enters cells by direct cell membrane penetration, not by endocytosis," J. Virol. **62**, 1136–1144 (1988), available at https://jvi.asm.org/content/62/4/1136.

[2] H. Lodish, A. Berk, S. L. Zipursky, P. Matsudaira, D. Baltimore, J. Darnell *et al.*, *Molecular Cell Biology* (W. H. Freeman, New York, 1995), Vol. 3.

[3] G. Seisenberger, M. U. Ried, T. Endreß, H. Büning, M. Hallek, and C. Bräuchle, "Real-time single-molecule imaging of the infection pathway of an adeno-associated virus," Science **294**, 1929–1932 (2001).

[4] K. Saar, M. Lindgren, M. Hansen, E. Eiríksdóttir, Y. Jiang, K. Rosenthal-Aizman, M. Sassian, and Ü. Langel, "Cell-penetrating peptides: A comparative membrane toxicity study," Anal. Biochem. **345**, 55–65 (2005).

[5] G. Karp, *Cell and Molecular Biology: Concepts and Experiments* (Wiley, Hoboken, NJ, 2008).

[6] Y. Li, H. Yuan, A. von dem Bussche, M. Creighton, R. H. Hurt, A. B. Kane, and H. Gao, "Graphene microsheets enter cells through spontaneous membrane penetration at edge asperities and corner sites," Proc. Natl. Acad. Sci. U. S. A. **110**, 12295–12300 (2013).

[7] A. R. Liboff, "Magnetic correlates in electromagnetic consciousness," Electromagn. Biol. Med. **35**, 228–236 (2016).

[8] Y. Xia, "Nanomaterials at work in biomedical research," Nat. Mater. **7**, 758 (2008).

[9] D. K. Kirui, D. A. Rey, and C. A. Batt, "Gold hybrid nanoparticles for targeted phototherapy and cancer imaging," Nanotechnology **21**, 105105 (2010).

[10] J. S. Suk, Q. Xu, N. Kim, J. Hanes, and L. M. Ensign, "PEGylation as a strategy for improving nanoparticle-based drug and gene delivery," Adv. Drug Delivery Rev. **99**, 28–51 (2016).

[11] C. Lanvers-Kaminsky, A. am Zehnhoff-Dinnesen, R. Parfitt, and G. Ciarimboli, "Drug-induced ototoxicity: Mechanisms, pharmacogenetics, and protective strategies," Clin. Pharmacol. Ther. **101**, 491–500 (2017).

[12] K. B. Jirage, J. C. Hulteen, and C. R. Martin, "Nanotubule-based molecular-filtration membranes," Science **278**, 655–658 (1997).

[13] S. Y. Yang, I. Ryu, H. Y. Kim, J. K. Kim, S. K. Jang, and T. P. Russell, "Nanoporous membranes with ultrahigh selectivity and flux for the filtration of viruses," Adv. Mater. **18**, 709–712 (2006).

[14] A. Kalra, S. Garde, and G. Hummer, "Osmotic water transport through carbon nanotube membranes," Proc. Natl. Acad. Sci. U. S. A. **100**, 10175–10180 (2003).

[15] P. Nelson, *Biological Physics* (W. H. Freeman, New York, 2004).

[16] H. Nikaido and M. H. Saier, "Transport proteins in bacteria: Common themes in their design," Science **258**, 936–942 (1992).

[17] M. Palacín, R. Estévez, J. Bertran, and A. Zorzano, "Molecular biology of mammalian plasma membrane amino acid transporters," Physiol. Rev. **78**, 969–1054 (1998).

[18] E. R. Kandel, J. H. Schwartz, T. M. Jessell, D. of Biochemistry, M. B. T. Jessell, S. Siegelbaum, and A. Hudspeth, *Principles of Neural Science* (McGraw-Hill, New York, 2000), Vol. 4.

[19] I. A. Simpson, A. Carruthers, and S. J. Vannucci, "Supply and demand in cerebral energy metabolism: The role of nutrient transporters," J. Cereb. Blood Flow Metab. **27**, 1766–1791 (2007).

[20] M. Yu, L. Xu, F. Tian, Q. Su, N. Zheng, Y. Yang, J. Wang, A. Wang, C. Zhu, S. Guo *et al.*, "Rapid transport of deformation-tuned nanoparticles across biological hydrogels and cellular barriers," Nat. Commun. **9**, 2607 (2018).

[21] A. J. T. M. Mathijssen, R. Jeanneret, and M. Polin, "Universal entrainment mechanism controls contact times with motile cells," Phys. Rev. Fluids **3**, 033103 (2018).

[22] C. Gräfe, I. Slabu, F. Wiekhorst, C. Bergemann, F. von Eggeling, A. Hochhaus, L. Trahms, and J. Clement, "Magnetic particle spectroscopy allows precise quantification of nanoparticles after passage through human brain microvascular endothelial cells," Phys. Med. Biol. **61**, 3986 (2016).

[23] F. Schlenk, S. Werner, M. Rabel, F. Jacobs, C. Bergemann, J. H. Clement, and D. Fischer, "Comprehensive analysis of the *in vitro* and ex ovo hemocompatibility of surface engineered iron oxide nanoparticles for biomedical applications," Arch. Toxicol. **91**, 3271–3286 (2017).

[24] E. K. Müller, C. Gräfe, F. Wiekhorst, C. Bergemann, A. Weidner, S. Dutz, and J. H. Clement, "Magnetic nanoparticles interact and pass an *in vitro* co-culture blood-placenta barrier model," Nanomaterials **8**, 108 (2018).

[25] B. D. Chithrani, A. A. Ghazani, and W. C. W. Chan, "Determining the size and shape dependence of gold nanoparticle uptake into mammalian cells," Nano Lett. **6**, 662–668 (2006).

[26] J. Lin, H. Zhang, Z. Chen, and Y. Zheng, "Penetration of lipid membranes by gold nanoparticles: Insights into cellular uptake, cytotoxicity, and their relationship," ACS Nano **4**, 5421–5429 (2010).

[27] K. Yang and Y. Q. Ma, "Computer simulation of the translocation of nanoparticles with different shapes across a lipid bilayer," Nat. Nanotechnol. **5**, 579–583 (2010).

[28] T. Dos Santos, J. Varela, I. Lynch, A. Salvati, and K. A. Dawson, "Quantitative assessment of the comparative nanoparticle-uptake efficiency of a range of cell lines," Small **7**, 3341–3349 (2011).

[29] S. Dasgupta, T. Auth, and G. Gompper, "Shape and orientation matter for the cellular uptake of nonspherical particles," Nano Lett. **14**, 687–693 (2014).

[30] S. Dasgupta, T. Auth, and G. Gompper, "Nano- and microparticles at fluid and biological interfaces," J. Phys.: Condens. Matter **29**, 373003 (2017).

[31] E. Barry and Z. Dogic, "Entropy driven self-assembly of nonamphiphilic colloidal membranes," Proc. Natl. Acad. Sci. U. S. A. **107**, 10348–10353 (2010).

[32] K. Zahn and G. Maret, "Two-dimensional colloidal structures responsive to external fields," Curr. Opin. Colloid Interface Sci. **4**, 60–65 (1999).

[33] M. Mittal and E. M. Furst, "Electric field-directed convective assembly of ellipsoidal colloidal particles to create optically and mechanically anisotropic thin films," Adv. Funct. Mater. **19**, 3271–3278 (2009).

[34] N. Osterman, I. Poberaj, J. Dobnikar, D. Frenkel, P. Ziherl, and D. Babić, "Field-induced self-assembly of suspended colloidal membranes," Phys. Rev. Lett. **103**, 228301 (2009).

[35] E. C. Oğuz, M. Marechal, F. Ramiro-Manzano, I. Rodriguez, R. Messina, F. J. Meseguer, and H. Löwen, "Packing confined hard spheres denser with adaptive prism phases," Phys. Rev. Lett. **109**, 218301 (2012).

The Journal of Chemical Physics ARTICLE scitation.org/journal/jcp

[36] J. Dobnikar, A. Snezhko, and A. Yethiraj, "Emergent colloidal dynamics in electromagnetic fields," Soft Matter **9**, 3693–3704 (2013).
[37] I. Williams, E. C. Oğuz, T. Speck, P. Bartlett, H. Löwen, and C. P. Royall, "Transmission of torque at the nanoscale," Nat. Phys. **12**, 98 (2016).
[38] A. Ortiz-Ambriz and P. Tierno, "Engineering of frustration in colloidal artificial ices realized on microfeatured grooved lattices," Nat. Commun. **7**, 10575 (2016).
[39] J. Loehr, A. Ortiz-Ambriz, and P. Tierno, "Defect dynamics in artificial colloidal ice: Real-time observation, manipulation, and logic gate," Phys. Rev. Lett. **117**, 168001 (2016).
[40] P. Tierno, "Geometric frustration of colloidal dimers on a honeycomb magnetic lattice," Phys. Rev. Lett. **116**, 038303 (2016).
[41] W. Shenton, S. A. Davis, and S. Mann, "Directed self-assembly of nanoparticles into macroscopic materials using antibody–antigen recognition," Adv. Mater. **11**, 449–452 (1999).
[42] M. Grzelczak, J. Vermant, E. M. Furst, and L. M. Liz-Marzán, "Directed self-assembly of nanoparticles," ACS Nano **4**, 3591–3605 (2010).
[43] V. Froltsov, R. Blaak, C. Likos, and H. Löwen, "Crystal structures of two-dimensional magnetic colloids in tilted external magnetic fields," Phys. Rev. E **68**, 061406 (2003).
[44] V. Froltsov, C. N. Likos, H. Löwen, C. Eisenmann, U. Gasser, P. Keim, and G. Maret, "Anisotropic mean-square displacements in two-dimensional colloidal crystals of tilted dipoles," Phys. Rev. E **71**, 031404 (2005).
[45] Y. Lin, A. Böker, J. He, K. Sill, H. Xiang, C. Abetz, X. Li, J. Wang, T. Emrick, S. Long *et al.*, "Self-directed self-assembly of nanoparticle/copolymer mixtures," Nature **434**, 55 (2005).
[46] D. Heinrich, A. R. Goñi, T. Osan, L. Cerioni, A. Smessaert, S. H. Klapp, J. Faraudo, D. J. Pusiol, and C. Thomsen, "Effects of magnetic field gradients on the aggregation dynamics of colloidal magnetic nanoparticles," Soft Matter **11**, 7606–7616 (2015).
[47] A. B. Yener and S. H. Klapp, "Self-assembly of three-dimensional ensembles of magnetic particles with laterally shifted dipoles," Soft Matter **12**, 2066–2075 (2016).
[48] S. D. Peroukidis and S. H. L. Klapp, "Orientational order and translational dynamics of magnetic particle assemblies in liquid crystals," Soft Matter **12**, 6841–6850 (2016).
[49] B. Bharti, F. Kogler, C. K. Hall, S. H. Klapp, and O. D. Velev, "Multidirectional colloidal assembly in concurrent electric and magnetic fields," Soft Matter **12**, 7747–7758 (2016).
[50] Q. A. Pankhurst, J. Connolly, S. Jones, and J. Dobson, "Applications of magnetic nanoparticles in biomedicine," J. Phys. D: Appl. Phys. **36**, R167 (2003).
[51] A.-H. Lu, E. L. Salabas, and F. Schüth, "Magnetic nanoparticles: Synthesis, protection, functionalization, and application," Angew. Chem., Int. Ed. **46**, 1222–1244 (2007).
[52] S. Naahidi, M. Jafari, F. Edalat, K. Raymond, A. Khademhosseini, and P. Chen, "Biocompatibility of engineered nanoparticles for drug delivery," J. Controlled Release **166**, 182–194 (2013).
[53] H. Al-Obaidi and A. T. Florence, "Nanoparticle delivery and particle diffusion in confined and complex environments," J. Drug Delivery Sci. Technol. **30**, 266–277 (2015).
[54] J. Liu, T. Wei, J. Zhao, Y. Huang, H. Deng, A. Kumar, C. Wang, Z. Liang, X. Ma, and X.-J. Liang, "Multifunctional aptamer-based nanoparticles for targeted drug delivery to circumvent cancer resistance," Biomaterials **91**, 44–56 (2016).
[55] J. Gao, H. Gu, and B. Xu, "Multifunctional magnetic nanoparticles: Design, synthesis, and biomedical applications," Acc. Chem. Res. **42**, 1097–1107 (2009).
[56] N. Wang, J. Butler, and D. Ingber, "Mechanotransduction across the cell surface and through the cytoskeleton," Science **260**, 1124–1127 (1993).
[57] J. Dobson, "Remote control of cellular behaviour with magnetic nanoparticles," Nat. Nanotechnol. **3**, 139 (2008).
[58] Q. A. Pankhurst, N. T. K. Thanh, S. K. Jones, and J. Dobson, "Progress in applications of magnetic nanoparticles in biomedicine," J. Phys. D: Appl. Phys. **42**, 224001 (2009).
[59] M. Ewerlin, D. Demirbas, F. Brüssing, O. Petracic, A. A. Ünal, S. Valencia, F. Kronast, and H. Zabel, "Magnetic dipole and higher pole interaction on a square lattice," Phys. Rev. Lett. **110**, 177209 (2013).
[60] L. Spiteri and R. Messina, "Columnar aggregation of dipolar chains," Europhys. Lett. **120**, 36001 (2017).
[61] R. Messina, L. A. Khalil, and I. Stanković, "Self-assembly of magnetic balls: From chains to tubes," Phys. Rev. E **89**, 011202 (2014).
[62] R. Messina and I. Stanković, "Assembly of magnetic spheres in strong homogeneous magnetic field," Physica A **466**, 10–20 (2017).
[63] F. Guzmán-Lastra, A. Kaiser, and H. Löwen, "Fission and fusion scenarios for magnetic microswimmer clusters," Nat. Commun. **7**, 13519 (2016).
[64] F. Martinez-Pedrero, A. Ortiz-Ambriz, I. Pagonabarraga, and P. Tierno, "Colloidal microworms propelling via a cooperative hydrodynamic conveyor belt," Phys. Rev. Lett. **115**, 138301 (2015).
[65] A. Kaiser, K. Popowa, and H. Löwen, "Active dipole clusters: From helical motion to fission," Phys. Rev. E **92**, 012301 (2015).
[66] S. Babel, H. Löwen, and A. M. Menzel, "Dynamics of a linear magnetic 'microswimmer molecule'," Europhys. Lett. **113**, 58003 (2016).
[67] A. J. T. M. Mathijssen, A. Doostmohammadi, J. M. Yeomans, and T. N. Shendruk, "Hydrodynamics of microswimmers in films," J. Fluid Mech. **806**, 35–70 (2016).
[68] J. Elgeti, R. G. Winkler, and G. Gompper, "Physics of microswimmers–Single particle motion and collective behavior: A review," Rep. Prog. Phys. **78**, 056601 (2015).
[69] C. Bechinger, R. Di Leonardo, H. Löwen, C. Reichhardt, G. Volpe, and G. Volpe, "Active particles in complex and crowded environments," Rev. Mod. Phys. **88**, 045006 (2016).
[70] J. de Graaf, H. Menke, A. J. T. M. Mathijssen, M. Fabritius, C. Holm, and T. Shendruk, "Lattice-Boltzmann hydrodynamics of anisotropic active matter," J. Chem. Phys. **144**, 134106 (2016).
[71] F. Martinez-Pedrero, E. Navarro-Argemí, A. Ortiz-Ambriz, I. Pagonabarraga, and P. Tierno, "Emergent hydrodynamic bound states between magnetically powered micropropellers," Sci. Adv. **4**, eaap9379 (2018).
[72] A. Daddi-Moussa-Ider, M. Lisicki, C. Hoell, and H. Löwen, "Swimming trajectories of a three-sphere microswimmer near a wall," J. Chem. Phys. **148**, 134904 (2018).
[73] A. Daddi-Moussa-Ider, M. Lisicki, A. J. T. M. Mathijssen, C. Hoell, S. Goh, J. Bławzdziewicz, A. M. Menzel, and H. Löwen, "State diagram of a three-sphere microswimmer in a channel," J. Phys.: Condens. Matter **30**, 254004 (2018).
[74] J. García-Torres, C. Calero, F. Sagués, I. Pagonabarraga, and P. Tierno, "Magnetically tunable bidirectional locomotion of a self-assembled nanorod-sphere propeller," Nat. Commun. **9**, 1663 (2018).
[75] T. Yu, P. Chuphal, S. Thakur, S.-Y. Reigh, D. P. Singh, and P. Fischer, "Chemical micromotors self-assemble and self-propel by spontaneous symmetry breaking," Chem. Commun. **54**, 11933 (2018).
[76] A. J. Mathijssen, F. Guzmán-Lastra, A. Kaiser, and H. Löwen, "Nutrient transport driven by microbial active carpets," Phys. Rev. Lett. **121**, 248101 (2018).
[77] A. Daddi-Moussa-Ider and A. M. Menzel, "Dynamics of a simple model microswimmer in an anisotropic fluid: Implications for alignment behavior and active transport in a nematic liquid crystal," Phys. Rev. Fluids **3**, 094102 (2018).
[78] A. Kaiser, S. Babel, B. ten Hagen, C. von Ferber, and H. Löwen, "How does a flexible chain of active particles swell?," J. Chem. Phys. **142**, 124905 (2015).
[79] R. G. Winkler, J. Elgeti, and G. Gompper, "Active polymers–emergent conformational and dynamical properties: A brief review," J. Phys. Soc. Jpn. **86**, 101014 (2017).
[80] A. Martín-Gómez, G. Gompper, and R. Winkler, "Active brownian filamentous polymers under shear flow," Polymers **10**, 837 (2018).
[81] Ö. Duman, R. E. Isele-Holder, J. Elgeti, and G. Gompper, "Collective dynamics of self-propelled semiflexible filaments," Soft Matter **14**, 4483–4494 (2018).

The Journal of Chemical Physics ARTICLE scitation.org/journal/jcp

[82]Y. Peng, H. Zhang, X.-W. Huang, J.-H. Huang, and M.-B. Luo, "Monte Carlo simulation on the dynamics of a semi-flexible polymer in the presence of nanoparticles," Phys. Chem. Chem. Phys. **20**, 26333–26343 (2018).
[83]J. Shin, A. G. Cherstvy, W. K. Kim, and R. Metzler, "Facilitation of polymer looping and giant polymer diffusivity in crowded solutions of active particles," New J. Phys. **17**, 113008 (2015).
[84]B. ten Hagen, S. van Teeffelen, and H. Löwen, "Brownian motion of a self-propelled particle," J. Phys.: Condens. Matter **23**, 194119 (2011).
[85]R. Wittkowski and H. Löwen, "Self-propelled brownian spinning top: Dynamics of a biaxial swimmer at low Reynolds numbers," Phys. Rev. E **85**, 021406 (2012).
[86]A. Kaiser, H. Wensink, and H. Löwen, "How to capture active particles," Phys. Rev. Lett. **108**, 268307 (2012).
[87]H. H. Wensink and H. Löwen, "Emergent states in dense systems of active rods: From swarming to turbulence," J. Phys.: Condens. Matter **24**, 464130 (2012).
[88]F. Kümmel, B. ten Hagen, R. Wittkowski, I. Buttinoni, R. Eichhorn, G. Volpe, H. Löwen, and C. Bechinger, "Circular motion of asymmetric self-propelling particles," Phys. Rev. Lett. **110**, 198302 (2013).
[89]B. ten Hagen, F. Kümmel, R. Wittkowski, D. Takagi, H. Löwen, and C. Bechinger, "Gravitaxis of asymmetric self-propelled colloidal particles," Nat. Commun. **5**, 4829 (2014).
[90]B. ten Hagen, R. Wittkowski, D. Takagi, F. Kümmel, C. Bechinger, and H. Löwen, "Can the self-propulsion of anisotropic microswimmers be described by using forces and torques?," J. Phys.: Condens. Matter **27**, 194110 (2015).
[91]T. Speck and R. L. Jack, "Ideal bulk pressure of active brownian particles," Phys. Rev. E **93**, 062605 (2016).
[92]M. Driscoll and B. Delmotte, "Leveraging collective effects in externally driven colloidal suspensions: Experiments and simulations," Curr. Opin. Colloid Interface Sci. **40**, 42 (2018).
[93]W. Gao, X. Feng, A. Pei, C. R. Kane, R. Tam, C. Hennessy, and J. Wang, "Bioinspired helical microswimmers based on vascular plants," Nano Lett. **14**, 305–310 (2013).
[94]W. Gao and J. Wang, "Synthetic micro/nanomotors in drug delivery," Nanoscale **6**, 10486–10494 (2014).
[95]C. Scholz, M. Engel, and T. Pöschel, "Rotating robots move collectively and self-organize," Nat. Commun. **9**, 931 (2018).
[96]C. Scholz, S. Jahanshahi, A. Ldov, and H. Löwen, "Inertial delay of self-propelled particles," Nat. Commun. **9**, 5156 (2018).
[97]B. J. Nelson, I. K. Kaliakatsos, and J. J. Abbott, "Microrobots for minimally invasive medicine," Annu. Rev. Biomed. Eng. **12**, 55–85 (2010).
[98]W. Xi, A. A. Solovev, A. N. Ananth, D. H. Gracias, S. Sanchez, and O. G. Schmidt, "Rolled-up magnetic microdrillers: Towards remotely controlled minimally invasive surgery," Nanoscale **5**, 1294–1297 (2013).
[99]L. K. Abdelmohsen, F. Peng, Y. Tu, and D. A. Wilson, "Micro-and nanomotors for biomedical applications," J. Mater. Chem. B **2**, 2395–2408 (2014).
[100]J. Wang and W. Gao, "Nano/microscale motors: Biomedical opportunities and challenges," ACS Nano **6**, 5745–5751 (2012).
[101]W. Wang, W. Duan, S. Ahmed, T. E. Mallouk, and A. Sen, "Small power: Autonomous nano-and micromotors propelled by self-generated gradients," Nano Today **8**, 531–554 (2013).
[102]W. F. Paxton, K. C. Kistler, C. C. Olmeda, A. Sen, S. K. St. Angelo, Y. Cao, T. E. Mallouk, P. E. Lammert, and V. H. Crespi, "Catalytic nanomotors: Autonomous movement of striped nanorods," J. Am. Chem. Soc. **126**, 13424–13431 (2004).
[103]W. Wang, S. Li, L. Mair, S. Ahmed, T. J. Huang, and T. E. Mallouk, "Acoustic propulsion of nanorod motors inside living cells," Angew. Chem., Int. Ed. **53**, 3201–3204 (2014).
[104]U. Marini Bettolo Marconi, A. Sarracino, C. Maggi, and A. Puglisi, "Self-propulsion against a moving membrane: Enhanced accumulation and drag force," Phys. Rev. E **96**, 032601 (2017).
[105]G. Junot, G. Briand, R. Ledesma-Alonso, and O. Dauchot, "Active versus passive hard disks against a membrane: Mechanical pressure and instability," Phys. Rev. Lett. **119**, 028002 (2017).
[106]A. F. Demirörs, J. C. Stiefelhagen, T. Vissers, F. Smallenburg, M. Dijkstra, A. Imhof, and A. van Blaaderen, "Long-ranged oppositely charged interactions for designing new types of colloidal clusters," Phys. Rev. X **5**, 021012 (2015).
[107]D. Vella, E. du Pontavice, C. L. Hall, and A. Goriely, "The magneto-elastica: From self-buckling to self-assembly," Proc. R. Soc. A **470**, 20130609 (2014).
[108]C. Hall, D. Vella, and A. Goriely, "The mechanics of a chain or ring of spherical magnets," SIAM J. Appl. Math. **73**, 2029–2054 (2013).
[109]B. Kiani, D. Faivre, and S. Klumpp, "Elastic properties of magnetosome chains," New J. Phys. **17**, 043007 (2015).
[110]S. Klumpp, C. T. Lefèvre, M. Bennet, and D. Faivre, "Swimming with magnets: From biological organisms to synthetic devices," Phys. Rep. **789**, 1–54 (2019).
[111]H.-H. Boltz and S. Klumpp, "Buckling of elastic filaments by discrete magnetic moments," Eur. Phys. J. E **40**, 86 (2017).
[112]F. Deißenbeck, H. Löwen, and E. C. Oğuz, "Ground state of dipolar hard spheres confined in channels," Phys. Rev. E **97**, 052608 (2018).
[113]A. P. Philipse, M. P. B. van Bruggen, and C. Pathmamanoharan, "Magnetic silica dispersions: Preparation and stability of surface-modified silica particles with a magnetic core," Langmuir **10**, 92–99 (1994).
[114]A. P. Gast and L. Leibler, "Interactions of sterically stabilized particles suspended in a polymer solution," Macromolecules **19**, 686–691 (1986).
[115]G. Nägele, "On the dynamics and structure of charge-stabilized suspensions," Phys. Rep. **272**, 215–372 (1996).
[116]M. Eshraghi and J. Horbach, "Molecular dynamics simulation of charged colloids confined between hard walls: Pre-melting and pre-freezing across the BCC–fluid coexistence," Soft Matter **14**, 4141–4149 (2018).
[117]G. Filipcsei, I. Csetneki, A. Szilágyi, and M. Zrínyi, "Magnetic field-responsive smart polymer composites," Adv. Polym. Sci. **206**, 137–189 (2007).
[118]N. Frickel, R. Messing, and A. M. Schmidt, "Magneto-mechanical coupling in $CoFe_2O_4$-linked PAAm ferrohydrogels," J. Mater. Chem. **21**, 8466–8474 (2011).
[119]P. Ilg, "Stimuli-responsive hydrogels cross-linked by magnetic nanoparticles," Soft Matter **9**, 3465–3468 (2013).
[120]P. Cremer, H. Löwen, and A. M. Menzel, "Tailoring superelasticity of soft magnetic materials," Appl. Phys. Lett. **107**, 171903 (2015).
[121]P. Cremer, H. Löwen, and A. M. Menzel, "Superelastic stress–strain behavior in ferrogels with different types of magneto-elastic coupling," Phys. Chem. Chem. Phys. **18**, 26670–26690 (2016).
[122]G. Pessot, H. Löwen, and A. M. Menzel, "Dynamic elastic moduli in magnetic gels: Normal modes and linear response," J. Chem. Phys. **145**, 104904 (2016).
[123]V. Yannopapas, S. H. Klapp, and S. D. Peroukidis, "Magneto-optical properties of liquid-crystalline ferrofluids," Opt. Mater. Express **6**, 2681–2688 (2016).
[124]P. Cremer, M. Heinen, A. M. Menzel, and H. Löwen, "A density functional approach to ferrogels," J. Phys.: Condens. Matter **29**, 275102 (2017).
[125]S. Goh, A. M. Menzel, and H. Löwen, "Dynamics in a one-dimensional ferrogel model: Relaxation, pairing, shock-wave propagation," Phys. Chem. Chem. Phys. **20**, 15037–15051 (2018).
[126]A. M. Menzel, "Mesoscopic characterization of magnetoelastic hybrid materials: Magnetic gels and elastomers, their particle-scale description, and scale-bridging links," Arch. Appl. Mech. **89**, 17–45 (2019).
[127]M. Doi and S. F. Edwards, *The Theory of Polymer Dynamics* (Clarendon Press, Oxford, 1986).
[128]J. D. Jackson, *Classical Electrodynamics* (John Wiley & Sons, New Jersey, 2012).
[129]J. D. Weeks, D. Chandler, and H. C. Andersen, "Role of repulsive forces in determining the equilibrium structure of simple liquids," J. Chem. Phys. **54**, 5237–5247 (1971).
[130]J. Happel and H. Brenner, *Low Reynolds Number Hydrodynamics: With Special Applications to Particulate Media* (Springer Science & Business Media, The Netherlands, 2012).

[131] S. Kim and S. J. Karrila, *Microhydrodynamics: Principles and Selected Applications* (Courier Corporation, 2013).

[132] F. Balboa-Usabiaga, B. Kallemov, B. Delmotte, A. Bhalla, B. Griffith, and A. Donev, "Hydrodynamics of suspensions of passive and active rigid particles: A rigid multiblob approach," Commun. Appl. Math. Comput. Sci. **11**, 217–296 (2017).

[133] W. H. Press, B. P. Flannery, S. A. Teukolsky, and W. T. Vetterling, *Numerical Recipes* (Cambridge University Press Cambridge, 1989), Vol. 2.

[134] A. Daddi-Moussa-Ider, A. Guckenberger, and S. Gekle, "Long-lived anomalous thermal diffusion induced by elastic cell membranes on nearby particles," Phys. Rev. E **93**, 012612 (2016).

[135] A. Daddi-Moussa-Ider, M. Lisicki, and S. Gekle, "Mobility of an axisymmetric particle near an elastic interface," J. Fluid Mech. **811**, 210–233 (2017).

[136] A. Daddi-Moussa-Ider, "Diffusion of nanoparticles nearby elastic cell membranes: A theoretical study," Ph.D. thesis, University of Bayreuth, 2017.

[137] A. Daddi-Moussa-Ider and S. Gekle, "Brownian motion near an elastic cell membrane: A theoretical study," Eur. Phys. J. E **41**, 19 (2018).

[138] A. Daddi-Moussa-Ider, B. Rallabandi, S. Gekle, and H. A. Stone, "A reciprocal theorem for the prediction of the normal force induced on a particle translating parallel to an elastic membrane," Phys. Rev. Fluids **3**, 084101 (2018).

[139] W. Rudin, *Principles of Mathematical Analysis* (McGraw-Hill, New York, 1976), Vol. 3.

[140] K. Kumar, "On expanding the exponential," J. Math. Phys. **6**, 1928–1934 (1965).

[141] S. Timoshenko and Woinowsky-Krieger, *Theory of Plates and Shells* (McGraw-Hill, New York, 1959), Vol. 2.

[142] R. Bracewell, *The Fourier Transform and its Applications* (McGraw-Hill, Pennsylvania, 1999).

[143] D. V. Widder, *Laplace Transform (PMS-6)* (Princeton University Press, New Jersey, 2015).

[144] A. Sommerfeld, *Partial Differential Equations in Physics* (Academic Press, 1949), Vol. 1.

[145] M. Abramowitz and I. A. Stegun, *Handbook of Mathematical Functions* (Dover, New York, 1972), Vol. 5.

P8 Creeping motion of a solid particle inside a spherical elastic cavity: II. Asymmetric motion

Reproduced from

C. Hoell, H. Löwen, A. M. Menzel, and A. Daddi-Moussa-Ider,
Creeping motion of a solid particle inside a spherical elastic cavity: II. Asymmetric motion,
Eur. Phys. J. E **42**, 89 (2019),
EDP Sciences/Società Italiana di Fisica/Springer-Verlag GmbH Germany, part of Springer Nature.

Digital Object Identifier (DOI): `https://doi.org/10.1140/epje/i2019-11853-4`

Statement of contribution

ADMI conceived the study and performed the numerical simulations. ADMI and I carried out the analytical calculations, involving a decomposition of the fluid flow using spherical harmonics and deriving the solutions in this framework. ADMI and I drafted the manuscript. All authors discussed and interpreted the results, edited the text, and finalized the manuscript. My work concerning this paper was supervised by ADMI, AMM, and HL.

Copyright and license notice

Eur. Phys. J. E (2019) **42**: 89
DOI 10.1140/epje/i2019-11853-4

THE EUROPEAN PHYSICAL JOURNAL E

Regular Article

Creeping motion of a solid particle inside a spherical elastic cavity: II. Asymmetric motion

Christian Hoell[a], Hartmut Löwen, Andreas M. Menzel, and Abdallah Daddi-Moussa-Ider[b]

Institut für Theoretische Physik II: Weiche Materie, Heinrich-Heine-Universität Düsseldorf, Universitätsstraße 1, 40225 Düsseldorf, Germany

Received 1 March 2019 and Received in final form 10 May 2019
Published online: 16 July 2019

Abstract. An analytical method is proposed for computing the low-Reynolds-number hydrodynamic mobility function of a small colloidal particle asymmetrically moving inside a large spherical elastic cavity, the membrane of which is endowed with resistance toward shear and bending. In conjunction with the results obtained in the first part (A. Daddi-Moussa-Ider, H. Löwen, S. Gekle, Eur. Phys. J. E **41**, 104 (2018)), in which the axisymmetric motion normal to the surface of an elastic cavity is investigated, the general motion for an arbitrary force direction can now be addressed. The elastohydrodynamic problem is formulated and solved using the classic method of images through expressing the hydrodynamic flow fields as a multipole expansion involving higher-order derivatives of the free-space Green's function. In the quasi-steady limit, we demonstrate that the particle self-mobility function of a particle moving tangent to the surface of the cavity is larger than that predicted inside a rigid stationary cavity of equal size. This difference is justified by the fact that a stationary rigid cavity introduces additional hindrance to the translational motion of the encapsulated particle, resulting in a reduction of its hydrodynamic mobility. Furthermore, the motion of the cavity is investigated, revealing that the translational pair (composite) mobility, which linearly couples the velocity of the elastic cavity to the force exerted on the solid particle, is solely determined by membrane shear properties. Our analytical predictions are favorably compared with fully-resolved computer simulations based on a completed-double-layer boundary integral method.

1 Introduction

Many industrial and biological transport processes on the microscale predominantly occur under confinement, where hydrodynamic interactions with boundaries drastically alter the diffusive behavior of microparticles in viscous media. Prime examples include particle sorting in microfabricated fluidic devices [1–5], membrane separation and purification in pharmaceutical industry [6–8], as well as intracellular drug delivery and targeting via multifunctional nanocarriers, which release therapeutic agents in disease regions such as tumor or inflammation sites [9–16]. The uptake by cell membranes occurs via endocytosis or by direct penetration to reach target cellular compartments.

At small length scales, fluid flows are characterized by small Reynolds numbers, implying that viscous forces dominate inertial forces. In these situations, the fluid-mediated hydrodynamic interactions are fully encoded in the mobility tensor, which linearly couples the velocities of microparticles to the forces and torques exerted on them [17–19]. Even for simple geometric confinements, finding closed analytical solutions of diverse flow problems can be challenging. Most theoretical approaches are based on the method of images, consisting of a set of (typically higher-order) singularities that are required to satisfy the prescribed boundary conditions at the confining boundaries [20]. Using this approach, the solution of the Stokes equations in the presence of a point force singularity acting in a fluid domain bounded by a rigid spherical cavity has been obtained by Oseen [21]. Extensions of Oseen's solution have further been proposed [22–29]. A particularly more compliant solution that separately considers both axisymmetric and asymmetric Stokeslets has later been presented by Maul and Kim [30, 31]. Meanwhile, the hydrodynamic coupling and rotational mobilities have been calculated for point-like particles [32]. In this context, the low-Reynolds-number swimming inside spherical containers has also attracted some attention [33–38].

In this manuscript, we examine the slow translational motion of a small colloidal particle moving inside

[a] e-mail: `christian.hoell@uni-duesseldorf.de`
[b] e-mail: `abdallah.daddi.moussa.ider@uni-duesseldorf.de`

a large spherical elastic cavity (that itself is floating in an infinitely-extended viscous fluid). This setup may be viewed as a relevant model system for transport processes within biological media, such as elastic cell membranes. The cavity membrane is modeled as a two-dimensional hyperelastic sheet, endowed with resistance toward shear elasticity and bending rigidity. This model has previously been employed to address the effect of elastic confinements on the diffusive behavior of colloidal particles moving close to planar [39,40] or curved elastic membranes [41–44].

The present article is a natural extension of a preceding paper [45] (hereinafter referred to as part I), where the axisymmetric motion was examined. The goal of the current study is to supplement and complement our previous results by quantifying the effect of the confining elastic cavity on the asymmetric motion of an encapsulated particle located at arbitrary position within the cavity. Our approach is based on the method of images employed by Fuentes and collaborators [46,47], who examined theoretically the hydrodynamic interactions between two unequally-sized spherical viscous drops at moderately small separations. Our analytical investigations proceed through the calculation of Green's functions associated with a point force acting inside a spherical elastic cavity. The problem treated here does not possess the symmetry properties of the simpler axisymmetric case considered in part I. This makes it necessary to employ an alternative mathematical framework to obtain the solution of the flow problem for the asymmetric case. The calculated hydrodynamic flow field is used to determine the frequency-dependent mobility functions for an enclosed point particle. This approximation is reasonable if the separation distance between the particle and the cavity surface is large compared to the particle size. Particularly, inside our deformable cavity, the mobility in the quasi-steady limit of vanishing frequency is shown to be always larger than the one predicted inside a rigid cavity with no-slip boundary condition. Our theoretical results favorably compare to numerical simulations.

The remainder of the paper is organized as follows. In sect. 2, we use the multipole expansion method to find solutions of the elastohydrodynamic problem for the fluid inside and outside the cavity. We then provide in sect. 3 analytical expressions of the hydrodynamic self-mobility function for a particle moving tangent to the surface of the cavity. In sect. 4, we assess the motion of the large cavity and determine the deformation field induced by the motion of the particle. We provide in sect. 5 concluding remarks summarizing our findings. The appendix contains explicit expressions for the series coefficients arising from the multipole expansion.

2 Singularity solution

We examine the low-Reynolds-number motion of a small sphere of radius b situated inside a large spherical elastic cavity of radius a. The fluid inside and outside the cavity is characterized by a constant dynamic viscosity η, and the flow is assumed to be incompressible. The center of

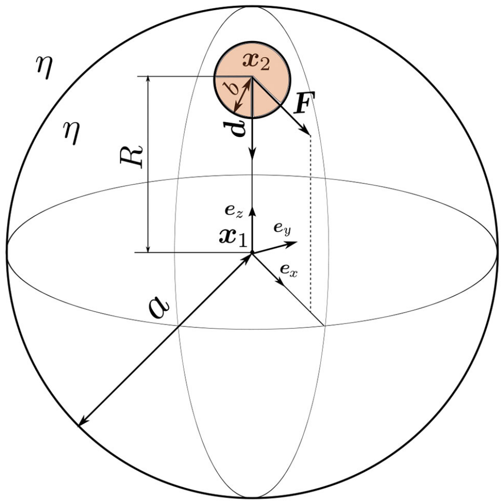

Fig. 1. Graphical illustration of the system setup. A small spherical particle of radius b is located at $\boldsymbol{x}_2 = R\boldsymbol{e}_z$ inside an elastic spherical cavity of radius a positioned at $\boldsymbol{x}_1$. The fluid on both sides of the cavity is characterized by a constant dynamic viscosity η. In an asymmetric configuration, the force is directed perpendicular to the unit vector $\boldsymbol{d} = (\boldsymbol{x}_1 - \boldsymbol{x}_2)/R$.

the cavity at $\boldsymbol{x}_1$ coincides with the origin of the spherical coordinate system. The solid particle located at position $\boldsymbol{x}_2 = R\boldsymbol{e}_z$ is moving under the action of an asymmetric external force $\boldsymbol{F} \perp \boldsymbol{e}_z$. An illustration of the system under consideration is shown in fig. 1.

The physical problem is thus equivalent to solving the forced Stokes equations inside the cavity [17,18],

$$\eta \boldsymbol{\nabla}^2 \boldsymbol{v}^{(i)} - \boldsymbol{\nabla} p^{(i)} + \boldsymbol{F}\delta\left(\boldsymbol{x} - \boldsymbol{x}_2\right) = 0, \tag{1a}$$

$$\boldsymbol{\nabla} \cdot \boldsymbol{v}^{(i)} = 0, \tag{1b}$$

and homogeneous (force-free) equations for the outer fluid,

$$\eta \boldsymbol{\nabla}^2 \boldsymbol{v}^{(o)} - \boldsymbol{\nabla} p^{(o)} = 0, \tag{2a}$$

$$\boldsymbol{\nabla} \cdot \boldsymbol{v}^{(o)} = 0, \tag{2b}$$

wherein $\boldsymbol{v}^{(i)}$ and $\boldsymbol{v}^{(o)}$ denote the flow velocity fields for the inner and outer fluids, respectively, and $p^{(i)}$ and $p^{(o)}$ are the corresponding pressure fields. Equations (1) and (2) are subject to the regularity conditions

$$\left|\boldsymbol{v}^{(i)}\right| < \infty \quad \text{as } r \to 0, \tag{3a}$$

$$\boldsymbol{v}^{(o)} \to \boldsymbol{0} \quad \text{as } r \to \infty, \tag{3b}$$

in addition to the standard boundary conditions of continuity of the velocity field and discontinuity of the hydrodynamic stresses at the cavity surface. In the present work, we assume that the cavity undergoes a small deformation only, so that the boundary conditions are evaluated at the undeformed surface of reference at $r = a$. Specifically,

$$\boldsymbol{v}^{(o)} - \boldsymbol{v}^{(i)}\Big|_{r=a} = \boldsymbol{0}, \tag{4a}$$

$$\left(\boldsymbol{\sigma}^{(o)} - \boldsymbol{\sigma}^{(i)}\right) \cdot \boldsymbol{e}_r\Big|_{r=a} = \Delta\boldsymbol{f}^{\mathrm{S}} + \Delta\boldsymbol{f}^{\mathrm{B}}, \tag{4b}$$

where $\boldsymbol{\sigma} = -p\boldsymbol{I} + 2\eta\boldsymbol{E}$ is the viscous stress tensor. Here, $\boldsymbol{E} = (\boldsymbol{\nabla v} + \boldsymbol{\nabla v}^{\mathrm{T}})/2$ denotes the rate-of-strain tensor, the components of which are given in spherical coordinates by

$$\sigma_{\theta r} = \eta\left(v_{\theta,r} - \frac{v_\theta + v_{r,\theta}}{r}\right), \tag{5a}$$

$$\sigma_{\phi r} = \eta\left(v_{\phi,r} + \frac{v_{r,\phi} - v_\phi}{r\sin\theta}\right), \tag{5b}$$

$$\sigma_{rr} = -p + 2\eta v_{r,r}, \tag{5c}$$

where ϕ and θ, respectively, denote the azimuthal and polar angles, such that $(\phi,\theta) \in [0, 2\pi) \times [0, \pi]$ describes a point on the surface of the unit sphere. Furthermore, by convention, indices after a comma stand for the corresponding partial derivatives, *e.g.*, $v_{r,r} = \partial v_r/\partial r$. Additionally, $\Delta\boldsymbol{f}^{\mathrm{S}}$ and $\Delta\boldsymbol{f}^{\mathrm{B}}$ denote the traction jumps stemming from shear and bending deformation modes, respectively. We further remark that, if the membrane cavity undergoes a large deformation, the boundary conditions should rather be evaluated at the displaced membrane positions, see, *e.g.*, refs. [48–54].

In this work, we model the elastic cavity as a spherical hyperelastic shell of vanishing thickness, the deformation of which is governed by the shear elasticity model proposed by Skalak [55] that is commonly employed when modeling, *e.g.*, the membranes of red blood cells [56, 57]. Specifically, the areal strain energy density of the Skalak model is given by [58]

$$E = \frac{\kappa_{\mathrm{S}}}{12}\left(\left(I_1^2 + 2I_1 - 2I_2\right) + CI_2^2\right), \tag{6}$$

where I_1 and I_2 stand for the invariants of the right Cauchy-Green deformation tensor [59,60], and $C = \kappa_{\mathrm{A}}/\kappa_{\mathrm{S}}$ is the Skalak coefficient representing the ratio between the area dilatation modulus κ_{A} and shear modulus κ_{S} [55]. For $C = 1$, the Skalak model is equivalent to the classical Neo-Hookean model for small membrane deformations [61].

Accordingly, the linearized traction jump due to shear is expressed in terms of the deformation field $\boldsymbol{u}$, and can be split into an axisymmetric and an asymmetric part as

$$\Delta\boldsymbol{f}^{\mathrm{S}} = \Delta\boldsymbol{f}^{\mathrm{S}}\big|_{\mathrm{Axi}} + \Delta\boldsymbol{f}^{\mathrm{S}}\big|_{\mathrm{Asy}}, \tag{7}$$

where

$$\begin{aligned}
\Delta f_\theta^{\mathrm{S}}\big|_{\mathrm{Axi}} &= -\frac{2\kappa_{\mathrm{S}}}{3}\big(2\xi_- u_{r,\theta} + \lambda\left(u_{\theta,\theta\theta} + u_{\theta,\theta}\cot\theta\right) \\
&\quad - u_\theta\left(\lambda\cot^2\theta + \lambda - 1\right)\big), \\
\Delta f_\phi^{\mathrm{S}}\big|_{\mathrm{Axi}} &= 0, \\
\Delta f_r^{\mathrm{S}}\big|_{\mathrm{Axi}} &= \frac{4\kappa_{\mathrm{S}}}{3}\,\xi_-\left(2u_r + u_{\theta,\theta} + u_\theta\cot\theta\right),
\end{aligned}$$

and

$$\begin{aligned}
\Delta f_\theta^{\mathrm{S}}\big|_{\mathrm{Asy}} &= -\frac{2\kappa_{\mathrm{S}}}{3}\left(\xi_-\frac{u_{\phi,\phi\theta}}{\sin\theta} + \frac{u_{\theta,\phi\phi}}{2\sin^2\theta} - \xi_+\frac{\cot\theta}{\sin\theta}\,u_{\phi,\phi}\right), \\
\Delta f_\phi^{\mathrm{S}}\big|_{\mathrm{Asy}} &= -\frac{2\kappa_{\mathrm{S}}}{3}\left(\lambda\frac{u_{\phi,\phi\phi}}{\sin^2\theta} + \frac{u_{\phi,\theta\theta}}{2} + \frac{\xi_-}{\sin\theta}\left(2u_{r,\phi} + u_{\theta,\phi\theta}\right)\right. \\
&\quad \left. + \left(1 - \cot^2\theta\right)\frac{u_\phi}{2} + \frac{u_{\phi,\theta}}{2}\cot\theta + \xi_+\frac{\cot\theta}{\sin\theta}u_{\theta,\phi}\right), \\
\Delta f_r^{\mathrm{S}}\big|_{\mathrm{Asy}} &= \frac{4\kappa_{\mathrm{S}}}{3}\,\frac{\xi_-}{\sin\theta}\,u_{\phi,\phi},
\end{aligned}$$

for the axisymmetric and asymmetric parts, respectively. Here, the asymmetric part includes all terms that depend on u_ϕ or involve derivatives with respect to ϕ. Moreover, we have defined

$$\lambda := 1 + C = 1 + \frac{\kappa_{\mathrm{A}}}{\kappa_{\mathrm{S}}}, \tag{8a}$$

$$\xi_\pm = \lambda \pm \frac{1}{2}. \tag{8b}$$

In addition, we introduce a resistance toward bending following the Helfrich model [62–64]. The areal bending energy density thus is described by a curvature-elastic continuum model of a quadratic form given by [65]

$$E_{\mathrm{B}} = 2\kappa_{\mathrm{B}}\left(H - H_0\right)^2, \tag{9}$$

wherein κ_{B} denotes the bending modulus, H_0 stands for the spontaneous curvature (here taken as the corresponding value for the initial undeformed sphere), and $H := b_\alpha^\alpha/2$ (summing over repeated indices) is the mean curvature, with b_α^β being the corresponding component of the curvature tensor [66].

The traction jump equation across the membrane as derived from this model reads [65]

$$\Delta\boldsymbol{f} = -2\kappa_{\mathrm{B}}\left(2(H^2 - K + H_0H) + \Delta_\|\right)(H - H_0)\,\boldsymbol{n}, \tag{10}$$

where $\boldsymbol{n}$ is the outward-pointing unit normal vector to the spherical cavity, $K := \det b_\alpha^\beta$ stands for the Gaussian curvature, and $\Delta_\|$ denotes the Laplace-Beltrami operator [67]. Accordingly, bending introduces a traction jump along the normal direction which can be split into an axisymmetric and an asymmetric part as

$$\Delta f_r^{\mathrm{B}} = \Delta f_r^{\mathrm{B}}\big|_{\mathrm{Axi}} + \Delta f_r^{\mathrm{B}}\big|_{\mathrm{Asy}}, \tag{11}$$

where

$$\begin{aligned}
\Delta f_r^{\mathrm{B}}\big|_{\mathrm{Axi}} &= \kappa_{\mathrm{B}}\big(4u_r + T\left(5 + T^2\right)u_{r,\theta} \\
&\quad + \left(2 - T^2\right)u_{r,\theta\theta} + 2Tu_{r,\theta\theta\theta} + u_{r,\theta\theta\theta\theta}\big), \\
\Delta f_r^{\mathrm{B}}\big|_{\mathrm{Asy}} &= \kappa_{\mathrm{B}}\left(1 + T^2\right)\big(2u_{r,\phi\phi\theta\theta} + 2\left(3 + 2T^2\right)u_{r,\phi\phi} \\
&\quad - 2Tu_{r,\phi\phi\theta} + \left(1 + T^2\right)u_{r,\phi\phi\phi\phi}\big),
\end{aligned}$$

and where we have used the shorthand notation $T := \cot\theta$. We note that bending as derived from Helfrich's model does not introduce discontinuities along the tangential directions. Accordingly, $\Delta f_\theta^{\mathrm{B}} = \Delta f_\phi^{\mathrm{B}} = \boldsymbol{0}$. These traction jumps reduce to the axisymmetric case considered in part I [45] for which $\Delta \boldsymbol{f}^{\mathrm{S}}|_{\mathrm{Asy}} = \Delta \boldsymbol{f}^{\mathrm{B}}|_{\mathrm{Asy}} = \mathbf{0}$. In this situation, $u_\phi = 0$ and all derivatives with respect to ϕ drop out.

A closure of the problem is achieved by requiring a no-slip boundary condition at the undisplaced membrane. Accordingly, the velocity field at $r = a$ is assumed to be equal to that of the displaced material points of the elastic cavity, *i.e.*,

$$\boldsymbol{v}|_{r=a} = \frac{\mathrm{d}\boldsymbol{u}}{\mathrm{d}t}\,, \tag{12}$$

which can be written in Fourier space as

$$\boldsymbol{v}|_{r=a} = i\omega\, \boldsymbol{u}. \tag{13}$$

Our resolution methodology proceeds through writing the solution of the elastohydrodynamic problem inside the cavity as

$$\boldsymbol{v}^{(i)} = \boldsymbol{v}^{\mathrm{S}} + \boldsymbol{v}^{*}, \tag{14}$$

where $\boldsymbol{v}^{\mathrm{S}} = \boldsymbol{\mathcal{G}}(\boldsymbol{x} - \boldsymbol{x}_2) \cdot \boldsymbol{F}$ represents the velocity field induced by a point-force singularity acting at position $\boldsymbol{x}_2$ in an unbounded fluid – *i.e.*, in the absence of the cavity – and $\boldsymbol{v}^*$ is the complementary term that is required to satisfy the imposed boundary conditions at the cavity. This type of complementary solution is often termed as the image system solution or sometimes known under the name of reflected flow field [20, 68].

We now briefly outline the main steps in our resolution approach. First, we express the Stokeslet solution in terms of harmonics, which are then rewritten in terms of harmonics relative to the origin via the Legendre expansion [69]. Second, the reflected flow field and the solution outside the cavity are expressed using Lamb's general solution [70] with interior and exterior harmonics, respectively. This gives us a complete solution form involving a set of unknown series coefficients. These coefficients are determined from the underlying boundary conditions imposed at the cavity surface. Finally, the solution of the flow problem can then be employed to assess the effect of the confining cavity on the motion of the encapsulated spherical particle.

2.1 Stokeslet representation

For the remainder of this paper, we will scale all the lengths by the cavity radius a. In analogy with part I, we begin by writing the Stokeslet singularity located at position $\boldsymbol{x}_2$ as

$$\boldsymbol{v}^{\mathrm{S}} = \boldsymbol{\mathcal{G}}\left(\boldsymbol{x} - \boldsymbol{x}_2\right) \cdot \boldsymbol{F} = \frac{1}{8\pi\eta}\left(\frac{\mathbf{1}}{s} + \frac{\boldsymbol{s}\boldsymbol{s}}{s^3}\right) \cdot \boldsymbol{F}, \tag{15}$$

where we have defined $\boldsymbol{s} := \boldsymbol{x} - \boldsymbol{x}_2$ and $s := |\boldsymbol{s}|$. Here, $\mathbf{1}$ is the unit tensor. Using Legendre expansion, the harmonics located at $\boldsymbol{x}_2$ can conveniently be expressed in terms of harmonics centered at $\boldsymbol{x}_1$ as

$$\frac{1}{s} = \sum_{n=0}^{\infty} R^n \varphi_n(r, \theta). \tag{16}$$

Here, φ_n are harmonics of degree n, which are related to Legendre polynomials by [71]

$$\varphi_n(r, \theta) := \frac{(\boldsymbol{d} \cdot \boldsymbol{\nabla})^n}{n!} \frac{1}{r} = \frac{1}{r^{n+1}} P_n(\cos\theta),$$

where $\boldsymbol{d} := (\boldsymbol{x}_1 - \boldsymbol{x}_2)/R$ is a unit vector, $\boldsymbol{r} = \boldsymbol{x} - \boldsymbol{x}_1$ is the position vector in the spherical coordinate system centered at the cavity center, and $r := |\boldsymbol{r}|$. The dyadic product in eq. (15) can be written as

$$\frac{\boldsymbol{s}\boldsymbol{s}}{s^3} = \boldsymbol{s}\, \boldsymbol{\nabla}_2 \left(\frac{1}{s}\right), \tag{17}$$

with $\boldsymbol{\nabla}_2 := \partial/\partial \boldsymbol{x}_2$. By making use of eq. (16), the derivatives with respect to $\boldsymbol{x}_2$ can readily be taken care of by noting that

$$\boldsymbol{\nabla}_2 R^n = -nR^{n-1}\boldsymbol{d}, \qquad (\boldsymbol{d} \cdot \boldsymbol{\nabla}_2)\, \boldsymbol{d} = \mathbf{0}. \tag{18}$$

In the present work, we focus our attention on the asymmetric situation in which the force is purely tangent to the membrane surface and thus $\boldsymbol{F} \cdot \boldsymbol{d} = 0$. By taking this into consideration, the Stokeslet stated in eq. (15) can therefore be expressed as

$$\begin{aligned} 8\pi\eta \boldsymbol{v}^{\mathrm{S}} = {} & \boldsymbol{F} \sum_{n=0}^{\infty} R^n\, \varphi_n - \boldsymbol{r} \sum_{n=1}^{\infty} R^{n-1} \left(\boldsymbol{F} \cdot \boldsymbol{\nabla}\right) \varphi_{n-1} \\ & - \boldsymbol{d} \sum_{n=1}^{\infty} R^n \left(\boldsymbol{F} \cdot \boldsymbol{\nabla}\right) \varphi_{n-1}. \end{aligned}$$

Accordingly, the Stokeslet solution has now been expressed in terms of spherical harmonics positioned at the origin. By defining $\boldsymbol{t} = \boldsymbol{F} \times \boldsymbol{d}$, we have the recurrence relation

$$\boldsymbol{d}(\boldsymbol{F} \cdot \boldsymbol{\nabla})\varphi_n = (\boldsymbol{t} \times \boldsymbol{\nabla})\varphi_n + (n+1)\boldsymbol{F}\varphi_{n+1}. \tag{19}$$

In addition, imposing $\boldsymbol{F} \cdot \boldsymbol{d} = 0$ yields

$$\begin{aligned} (2n+1)(n+1)\boldsymbol{F}\varphi_n = {} & -(2n+3)\boldsymbol{r}\psi_n - r^2 \boldsymbol{\nabla}\psi_n \\ & + \boldsymbol{\nabla}\psi_{n-2} - (2n+1)\boldsymbol{\gamma}_{n-1}, \end{aligned} \tag{20}$$

where the harmonics ψ_n and $\boldsymbol{\gamma}_n$ are, respectively, defined as

$$\psi_n = (\boldsymbol{F} \cdot \boldsymbol{\nabla})\varphi_n, \qquad \boldsymbol{\gamma}_n = (\boldsymbol{t} \times \boldsymbol{\nabla})\varphi_n. \tag{21}$$

These are related to each other via $\psi_n = \boldsymbol{\gamma}_n \cdot \boldsymbol{d}$.

In the following, the functions $\boldsymbol{\nabla}\psi_n$, $\boldsymbol{r}\psi_n$, and $\boldsymbol{\gamma}_n$ are chosen as vector basis functions to be used for expanding the velocity and pressure fields. Accordingly, the Stokeslet solution can be written in a final form as

$$\begin{aligned} 8\pi\eta \boldsymbol{v}^{\mathrm{S}} = {} & \sum_{n=1}^{\infty} \left(\frac{(n-2)R^{n-1}}{(2n-1)n} r^2 - \frac{nR^{n+1}}{(n+2)(2n+3)} \right) \boldsymbol{\nabla}\psi_{n-1} \\ & - \frac{2R^n}{n+1}\, \boldsymbol{\gamma}_{n-1} - \frac{2(n+1)R^{n-1}}{n(2n-1)}\, \boldsymbol{r}\psi_{n-1}. \end{aligned} \tag{22}$$

We next proceed to deriving analogous expansions for the flow fields inside and outside the spherical cavity.

2.2 The image system solution

The solution for the flow field in a spherical domain possesses a generic form known as Lamb's general solution [18, 70]. It involves three sets of unknown coefficients to be determined from the underlying boundary conditions, and can be written for an asymmetric situation as

$$8\pi\eta \boldsymbol{v}^* = \sum_{n=1}^{\infty} \left(a_n \boldsymbol{\sigma}_{n1} + b_n \boldsymbol{\sigma}_{n2} + c_n \boldsymbol{\sigma}_{n3} \right), \tag{23}$$

where we have defined

$$\boldsymbol{\sigma}_{n1} = \frac{n+3}{2n} r^{2n+3} \boldsymbol{\nabla}\psi_{n-1} + \frac{(n+1)(2n+3)}{2n} r^{2n+1} \boldsymbol{r}\psi_{n-1},$$
$$\boldsymbol{\sigma}_{n2} = \frac{r^{2n+1}}{n} \boldsymbol{\nabla}\psi_{n-1} + \frac{2n+1}{n} r^{2n-1} \boldsymbol{r}\psi_{n-1},$$
$$\boldsymbol{\sigma}_{n3} = r^{2n-1} \boldsymbol{\gamma}_{n-1} + (2n-1) r^{2n-3} (\boldsymbol{t} \times \boldsymbol{r}) \varphi_{n-1}.$$

Here, a_n, b_n, and c_n are free parameters that will be determined from the boundary conditions. It is worth noting that the present solution involves three unknown coefficients for each n, while the simpler axisymmetric motion considered in part I only involves two sets of coefficients. Unfortunately, this also means that we are not able to proceed as for the axisymmetric case, but have to derive the solutions using a notably different framework.

2.3 The exterior solution

The solution on the outside of the spherical cavity can be expressed in terms of exterior harmonics using Lamb's general solution as

$$8\pi\eta \boldsymbol{v}^{(o)} = \sum_{n=1}^{\infty} \Bigg(A_n \left(\frac{n-2}{2(n+1)} r^2 \boldsymbol{\nabla}\psi_{n-1} - \boldsymbol{r}\psi_{n-1} \right) - \frac{B_n}{n+1} \boldsymbol{\nabla}\psi_{n-1} + C_n \boldsymbol{\gamma}_{n-1} \Bigg). \tag{24}$$

The latter expression can be deduced from the solution for the inner fluid given by eq. (23) by making use of the substitution $n \leftarrow -(n+1)$.

The six unknown coefficients (a_n, b_n, and c_n for the image system solution, and A_n, B_n, and C_n for the exterior flow) can now be determined from the underlying boundary conditions of continuity of the flow velocity field and discontinuity of the hydrodynamic stress tensor across the membrane.

2.4 Velocity projections

Before proceeding with the determination of the unknown series coefficients, it is convenient to state explicitly the projected expressions of the velocity field along the radial and tangential directions.

2.4.1 Radial velocities

The radial projection of the three vector basis functions are given by

$$\boldsymbol{e}_r \cdot \boldsymbol{\nabla}\psi_{n-1} = -\frac{n+1}{r} \psi_{n-1}, \tag{25a}$$
$$\boldsymbol{e}_r \cdot \boldsymbol{r}\psi_{n-1} = r\psi_{n-1}, \tag{25b}$$
$$\boldsymbol{e}_r \cdot \boldsymbol{\gamma}_{n-1} = -\frac{1}{r} \psi_{n-2}. \tag{25c}$$

In addition to that, since $\boldsymbol{e}_r$ and $\boldsymbol{r}$ are collinear, the scalar triple product $\boldsymbol{e}_r \cdot (\boldsymbol{t} \times \boldsymbol{r}) \varphi_{n-1}$ vanishes. Moreover, the projection of eq. (20) onto the radial direction yields

$$\boldsymbol{e}_r \cdot \boldsymbol{F}\varphi_n = \frac{1}{2n+1} \left(\frac{\psi_{n-2}}{r} - r\psi_n \right). \tag{26}$$

By making use of eqs. (25) and (26) in the radial projection of eqs. (22), (24), and (23), the components of the fluid velocity fields along the radial direction can thus be expressed in terms of the harmonics ψ_n as

$$8\pi\eta v_r^{\mathrm{S}} = \sum_{n=1}^{\infty} \left(\frac{n+3}{2n+3} \frac{R^2}{r^2} - \frac{n+1}{2n-1} \right) R^{n-1} r\psi_{n-1}, \tag{27a}$$
$$8\pi\eta v_r^* = \sum_{n=1}^{\infty} \left(\frac{n+1}{2} a_n r^2 + b_n - c_{n+1} \right) r^{2n} \psi_{n-1}, \tag{27b}$$
$$8\pi\eta v_r^{(o)} = \sum_{n=1}^{\infty} \left(-\frac{nr}{2} A_n + \frac{B_n}{r} - \frac{C_{n+1}}{r} \right) \psi_{n-1}. \tag{27c}$$

2.4.2 Tangential velocities

As for the tangential direction, we define the projection operator $\boldsymbol{\Pi} := \boldsymbol{1} - \boldsymbol{e}_r\boldsymbol{e}_r$, which projects vectors on a plane tangent to the surface of the spherical cavity. By applying the projection operator to eq. (20), we readily obtain

$$(\boldsymbol{\Pi}\boldsymbol{F})\varphi_n = \frac{1}{n+1} \left(\frac{1}{2n+1} \left(\boldsymbol{\Psi}_{n-2} - r^2 \boldsymbol{\Psi}_n \right) - \boldsymbol{\Gamma}_{n-1} \right), \tag{28}$$

where we have defined the vector harmonics

$$\boldsymbol{\Gamma}_n := \boldsymbol{\Pi}\boldsymbol{\gamma}_n, \qquad \boldsymbol{\Psi}_n := \boldsymbol{\Pi}\boldsymbol{\nabla}\psi_n.$$

Additionally, the tangential projection of $(\boldsymbol{t} \times \boldsymbol{r})\varphi_n$ can be taken care of by noting that

$$\boldsymbol{\Pi}(\boldsymbol{t} \times \boldsymbol{r})\varphi_{n-1} = \frac{1}{2n-1} \Bigg(\frac{1}{n-1} \left(\boldsymbol{\Psi}_{n-4} - r^2 \boldsymbol{\Psi}_{n-2} \right) - \frac{n-2}{n-1} \boldsymbol{\Gamma}_{n-3} - r^2 \boldsymbol{\Gamma}_{n-1} \Bigg). \tag{29}$$

Applying the projection relations stated by eqs. (28) and (29) to eqs. (22), (24), and (23), we finally obtain

see eqs. (30) *on the next page*

$$8\pi\eta\,\boldsymbol{\Pi}\boldsymbol{v}^{\mathrm{S}} = \sum_{n=1}^{\infty}\left(\frac{(n-2)\,R^{n-1}}{(2n-1)n}\,r^2 - \frac{nR^{n+1}}{(n+2)(2n+3)}\right)\boldsymbol{\Psi}_{n-1} + \sum_{n=0}^{\infty} -\frac{2R^{n+1}}{n+2}\,\boldsymbol{\Gamma}_n, \tag{30a}$$

$$8\pi\eta\,\boldsymbol{\Pi}\boldsymbol{v}^{*} = \sum_{n=1}^{\infty}\left(\frac{r^{2n+3}}{n+2}\,c_{n+3} - \frac{r^{2n+1}}{n}\,c_{n+1} + \frac{r^{2n+1}}{n}\,b_n + \frac{n+3}{2n}\,r^{2n+3}a_n\right)\boldsymbol{\Psi}_{n-1} + \sum_{n=0}^{\infty} -\frac{n+1}{n+2}\,r^{2n+3}c_{n+3}\,\boldsymbol{\Gamma}_n, \tag{30b}$$

$$8\pi\eta\,\boldsymbol{\Pi}\boldsymbol{v}^{(o)} = \sum_{n=1}^{\infty}\frac{1}{n+1}\left(\frac{n-2}{2}\,r^2 A_n - B_n\right)\boldsymbol{\Psi}_{n-1} + \sum_{n=0}^{\infty} C_{n+1}\boldsymbol{\Gamma}_n. \tag{30c}$$

2.5 Determination of the series coefficients

To determine the unknown coefficients, we have to make recourse to the orthogonality properties of spherical harmonics [72]. For this purpose, we introduce the following notation to describe the average of a given quantity $Q(\phi,\theta)$ over the surface of a sphere. Specifically, this means

$$\langle Q\rangle := \frac{1}{2\pi}\int_0^{2\pi}\int_0^{\pi} Q(\phi,\theta)\sin\theta\,\mathrm{d}\theta\,\mathrm{d}\phi. \tag{31}$$

At the surface of the cavity, *i.e.*, for $r=1$, the harmonics φ_n and ψ_n satisfy the orthogonality relations

$$\langle\varphi_{m-1}\varphi_{n-1}\rangle|_{r=1} = \frac{2}{2n+1}\,\delta_{mn}, \tag{32a}$$

$$\langle\psi_{m-1}\psi_{n-1}\rangle|_{r=1} = \frac{n(n+1)}{2n+1}\,\delta_{mn}, \tag{32b}$$

where δ_{mn} denotes the Kronecker symbol, *i.e.*, the above terms vanish for $m\neq n$. Moreover, the vector harmonics $\boldsymbol{\Psi}_{n-1}$ and $\boldsymbol{\Gamma}_n$ satisfy at $r=1$ the orthogonality properties

$$\langle\boldsymbol{\Psi}_{m-1}\cdot\boldsymbol{\Psi}_{n-1}\rangle|_{r=1} = \frac{n^2(n+1)^2}{2n+1}\,\delta_{mn}, \tag{33a}$$

$$\langle\boldsymbol{\Gamma}_{m}\cdot\boldsymbol{\Gamma}_{n}\rangle|_{r=1} = \frac{4(n+1)^3}{(2n+1)(2n+3)}\,\delta_{mn}, \tag{33b}$$

$$\langle\boldsymbol{\Psi}_{m-1}\cdot\boldsymbol{\Gamma}_{n}\rangle|_{r=1} = \frac{n^2(n+1)}{2n+1}\,\delta_{mn}. \tag{33c}$$

We further note that their derivatives with respect to r (needed in the calculation of the stress jumps) satisfy the recurrence relations

$$\left(\boldsymbol{\Psi}_{n-1,r} + (n+2)\boldsymbol{\Psi}_{n-1}\right)|_{r=1} = 0, \tag{34a}$$

$$\left(\boldsymbol{\Gamma}_{n,r} + (n+2)\boldsymbol{\Gamma}_{n}\right)|_{r=1} = 0. \tag{34b}$$

2.5.1 Pressure field

Knowing the velocity fields on both sides of the elastic cavity, the inner and outer pressure fields can readily be calculated from the fluid motion equations. The solution inside the spherical cavity, which comprises both contributions from the Stokeslet and the image system solution, can be expressed in terms of a multipole expansion as

$$8\pi p^{(i)} = \sum_{n=1}^{\infty}\left(-2R^{n-1} + \frac{(n+1)(2n+3)}{n}\,r^{2n+1}a_n\right)\psi_{n-1}.$$

Outside the cavity, only the exterior harmonics that decay at larger distances should be accounted for, thus excluding contributions of the form $r^{2n+1}\psi_{n-1}$. After some algebra, we obtain

$$8\pi p^{(o)} = \sum_{n=1}^{\infty} -\frac{n(2n-1)}{n+1}\,A_n\psi_{n-1}.$$

2.5.2 Continuity of velocity

The projections of the fluid velocity field along the radial and tangential directions can be presented in a generic form as

$$v_r^{(q)} = \sum_{n=1}^{\infty}\rho_n^{(q)}\psi_{n-1}, \tag{35a}$$

$$\boldsymbol{\Pi}\boldsymbol{v}^{(q)} = \sum_{n=1}^{\infty}\alpha_n^{(q)}\boldsymbol{\Psi}_{n-1} + \sum_{n=0}^{\infty}\beta_n^{(q)}\boldsymbol{\Gamma}_n, \tag{35b}$$

wherein $q=i$ holds for the fluid on the inside, and $q=o$ for the fluid on the outside. Moreover, $\rho_n^{(q)}$, $\alpha_n^{(q)}$, and $\beta_n^{(q)}$, for $q\in\{i,o\}$, are radially symmetric series functions that can readily be obtained by identification with eqs. (27) and (30) giving the radial and tangential velocities, respectively.

The unknown coefficients inside the cavity can conveniently be expressed in terms of those outside thanks to the natural continuity of the velocity field across the membrane. By making use of the orthogonality properties of the basis functions, we obtain

$$a_n = \frac{n(2n-1)}{2(n+1)}\,A_n - \frac{2n+1}{n+1}\,B_n + \frac{2n+1}{n+1}\,C_{n+1} + R^{n-1}\left(\frac{(n+3)(2n+1)}{(n+1)(2n+3)}\,R^2 - 1\right), \tag{36a}$$

$$b_n = -\frac{n(2n+1)}{4}\,A_n + \frac{2n+3}{2}\,B_n - \frac{2n+3}{2}\,C_{n+1} - \frac{n\,C_{n-1}}{n-1} + R^{n-1}\left(\frac{2n^3+n^2-10n+3}{2(2n-1)(n-1)} - \frac{n+3}{2}R^2\right), \tag{36b}$$

$$c_n = -\frac{(n-1)C_{n-2} + 2R^{n-2}}{n-2}. \tag{36c}$$

$$\tilde{\alpha}_n + \frac{\tilde{\beta}_n}{n+1}\bigg|_{r=1} = \alpha\left(\left(\alpha_n^{(o)} + \frac{\beta_n^{(o)}}{n+1}\right)\big(n(n+1)\lambda - 1\big) - (2\lambda-1)\rho_n^{(o)}\right)\bigg|_{r=1}, \tag{39a}$$

$$\tilde{\alpha}_n + \frac{4(n+1)^2}{(2n+3)n^2}\,\tilde{\beta}_n\bigg|_{r=1} = \alpha\left(\big(n(n+1)\lambda-1\big)\alpha_n^{(o)} - (2\lambda-1)\rho_n^{(o)} + \left(\frac{12+22n+13n^2+2n^3}{2n(2n+3)} + \lambda n\right)\beta_n^{(o)}\right)\bigg|_{r=1}. \tag{39b}$$

2.5.3 Discontinuity of stress tensor

Expressions for the unknown coefficients A_n, B_n, and C_n associated with the outer fluid can be obtained from the traction jump equations across the membrane. For the sake of clarity, and to make the calculations traceable, we will consider in the following the effects of shear and bending deformation modes separately.

a) Pure shear. The tangential traction jump equations due to shear can conveniently be cast in the form

$$\sum_{n=1}^{\infty}\tilde{\alpha}_n\boldsymbol{\Psi}_{n-1} + \sum_{n=0}^{\infty}\tilde{\beta}_n\boldsymbol{\Gamma}_n\bigg|_{r=1} = \sum_{n=1}^{\infty}\alpha_n^{(o)}\boldsymbol{F}_n + \sum_{n=0}^{\infty}\beta_n^{(o)}\boldsymbol{G}_n + \sum_{n=1}^{\infty}\rho_n^{(o)}\boldsymbol{f}_n\bigg|_{r=1}, \tag{37}$$

where we have defined

$$\tilde{\alpha}_n = \alpha_{n,r}^{(o)} - \alpha_{n,r}^{(i)} - (n+2)\left(\alpha_n^{(o)} - \alpha_n^{(i)}\right),$$
$$\tilde{\beta}_n = \beta_{n,r}^{(o)} - \beta_{n,r}^{(i)} - (n+2)\left(\beta_n^{(o)} - \beta_n^{(i)}\right).$$

Here, $\boldsymbol{F}_n$, $\boldsymbol{G}_n$, and $\boldsymbol{f}_n$ are known series vectors, the expressions of which can be obtained by identification with eq. (4b) upon substitution of the tangential velocity field from eq. (30). They satisfy the orthogonality relations

$$\langle \boldsymbol{F}_n\cdot\boldsymbol{\Psi}_{m-1}\rangle|_{r=1} = n(n+1)\big(n(n+1)\lambda-1\big)S_n\delta_{mn},$$
$$\langle \boldsymbol{G}_n\cdot\boldsymbol{\Psi}_{m-1}\rangle|_{r=1} = n\big(n(n+1)\lambda-1\big)S_n\delta_{mn},$$
$$\langle \boldsymbol{f}_n\cdot\boldsymbol{\Psi}_{m-1}\rangle|_{r=1} = -n(n+1)\,(2\lambda-1)\,S_n\delta_{mn},$$

with the basis vector harmonics $\boldsymbol{\Psi}_{m-1}$, and

$$\langle \boldsymbol{F}_n\cdot\boldsymbol{\Gamma}_m\rangle|_{r=1} = n\big(n(n+1)\lambda-1\big)S_n\delta_{mn},$$
$$\langle \boldsymbol{G}_n\cdot\boldsymbol{\Gamma}_m\rangle|_{r=1} = \frac{S_nW_n}{2n+3}\,\delta_{mn},$$
$$\langle \boldsymbol{f}_n\cdot\boldsymbol{\Gamma}_m\rangle|_{r=1} = -n\,(2\lambda-1)\,S_n\delta_{mn},$$

with $\boldsymbol{\Gamma}_n$, where we have defined

$$S_n = \frac{\alpha n(n+1)}{2n+1},$$
$$W_n = 6 + 11n + \frac{13}{2}\,n^2 + n^3 + n^2(2n+3)\lambda,$$

with

$$\alpha = \frac{2\kappa_S}{3\eta i\omega} \tag{38}$$

being the shear number. Combining these equations with the orthogonality relations given by eqs. (33) yields

see eqs. (39) *above*

Using our representation, the normal traction jump due to shear reads

$$\sum_{n=1}^{\infty}\left(p_n^{(o)} - p_n^{(i)}\right)\psi_{n-1}\bigg|_{r=1} = \alpha(2\lambda-1)\sum_{n=1}^{\infty}\left(\rho_{n,r}^{(o)} - (n+1)\rho_n^{(o)}\right)\psi_{n-1}\bigg|_{r=1}, \tag{40}$$

which, upon using the orthogonality property of ψ_{n-1}, yields

$$p_n^{(o)} - p_n^{(i)}\Big|_{r=1} = \alpha(2\lambda-1)\left(\rho_{n,r}^{(o)} - (n+1)\rho_n^{(o)}\right)\Big|_{r=1}. \tag{41}$$

By combining eqs. (36), (39), and (41), the unknown series coefficients for the outer fluid can be obtained and cast in the form

$$A_n = -\frac{(n+1)(2n+1)}{K_3}\left(K_1\,R^{n+1} + K_2\,R^{n-1}\right), \tag{42a}$$

$$B_n = \frac{K_4}{K_5}\,A_n + \frac{1}{K_7}\left(K_6\,R^{n+1} + K_8\,R^{n-1}\right), \tag{42b}$$

$$C_n = -\frac{2n+1}{K_9}\,R^n, \tag{42c}$$

where $K_1,\dots,K_9$ are rather complex functions of α,λ and n, the expressions of which are explicitly provided in the appendix. In the limit $i\alpha\to\infty$, which physically corresponds to a cavity membrane with an infinite shear elasticity modulus (or equivalently to a vanishing actuation frequency), the expressions of the series coefficients inside the cavity reduce to

$$\lim_{\alpha\to\infty} a_n = \frac{(n+3)(2n+1)}{(n+1)(2n+3)}\,R^{n+1} - R^{n-1}, \tag{43a}$$

$$\lim_{\alpha\to\infty} b_n = \frac{2n^3+n^2-10n+3}{2(n-1)(2n-1)}\,R^{n-1} - \frac{n+3}{2}\,R^{n+1}, \tag{43b}$$

$$\lim_{\alpha\to\infty} c_n = -\frac{2}{n-2}\,R^{n-2}. \tag{43c}$$

In this limit, A_n, B_n, and C_n vanish except for $n=1$, where $(A_1,B_1,C_1) = (4, 2/3, -R)$. It is worthwhile to note that the coefficients given by eqs. (43) correspond to the solution for an asymmetric point force acting inside a rigid cavity with no-slip boundary conditions.

b) Pure bending. We now use a similar resolution procedure to determine the unknown series coefficients for a cavity membrane with pure bending resistance, such as that of a fluid vesicle or a liposome used as a vehicle for pharmaceutical drugs [73–75]. Since the tangential components of the traction are continuous, we obtain

$$\sum_{n=1}^{\infty} \tilde{\alpha}_n \boldsymbol{\Psi}_{n-1} + \sum_{n=0}^{\infty} \tilde{\beta}_n \boldsymbol{\Gamma}_n \bigg|_{r=1} = \boldsymbol{0}, \tag{44}$$

which, after applying the orthogonality properties given by eqs. (33), leads to

$$\tilde{\alpha}_n|_{r=1} = \tilde{\beta}_n|_{r=1} = 0. \tag{45}$$

The normal traction jump due to bending as derived from the Helfrich model reads

$$\sum_{n=1}^{\infty} \left(p_n^{(o)} - p_n^{(i)}\right)\psi_{n-1}\bigg|_{r=1} = \sum_{n=1}^{\infty} -\rho_n^{(o)} H_n \bigg|_{r=1}, \tag{46}$$

which, upon using the orthogonality relation

$$\langle H_n \psi_{m-1}\rangle|_{r=1} = \alpha_{\mathrm{B}} \frac{n(n+1)(n-1)^2(n+2)^2}{2n+1}\, \delta_{mn}, \tag{47}$$

leads to

$$p_n^{(o)} - p_n^{(i)}\Big|_{r=1} = -\alpha_{\mathrm{B}}(n-1)^2(n+2)^2 \rho_n^{(o)}\Big|_{r=1}, \tag{48}$$

wherein

$$\alpha_{\mathrm{B}} = \frac{\kappa_{\mathrm{B}}}{\eta i \omega} \tag{49}$$

denotes the bending number.

By combining eqs. (45) and (48) with eqs. (36), the unknown series coefficients for the fluid on the outside can be cast in the form

$$A_n = \frac{n+1}{Q_3}\left(Q_1 R^{n+1} + Q_2 R^{n-1}\right), \tag{50a}$$

$$B_n = \frac{1}{Q_7}\left(Q_4 A_n + Q_5 R^{n+1} + Q_6 R^{n-1}\right), \tag{50b}$$

$$C_n = -\frac{2}{n+1} R^n, \tag{50c}$$

where $Q_1, \ldots, Q_7$ are complicated functions of α_{B}, λ, and n which are given in the Appendix. In the limit $i\alpha_{\mathrm{B}} \to \infty$, corresponding to an infinite membrane bending modulus, or to a vanishing forcing frequency, the series coefficients are given by

$$\lim_{\alpha_{\mathrm{B}}\to\infty} a_n = \frac{(n+3)(2n-1)}{2(n+1)(2n+3)} R^{n+1} - \frac{R^{n-1}}{2}, \tag{51a}$$

$$\lim_{\alpha_{\mathrm{B}}\to\infty} b_n = -\frac{n+3}{4} R^{n+1} + \frac{(n+1)(2n+3)}{4(2n-1)} R^{n-1}, \tag{51b}$$

$$\lim_{\alpha_{\mathrm{B}}\to\infty} c_n = 0 \tag{51c}$$

for the inner fluid, and

$$\lim_{\alpha_{\mathrm{B}}\to\infty} A_n = \frac{1}{2n}\left((n+3)R^{n+1} - (n+1)R^{n-1}\right), \tag{52a}$$

$$\lim_{\alpha_{\mathrm{B}}\to\infty} B_n = -\frac{n+1}{4} R^{n-1} + \frac{n^2+5n-2}{4(n+2)} R^{n+1}, \tag{52b}$$

$$\lim_{\alpha_{\mathrm{B}}\to\infty} C_n = -\frac{2}{n+1} R^n \tag{52c}$$

for the outer fluid when $n \geq 2$. In addition, $(A_1, B_1, C_1) = (4, 2R^2/15, -R)$.

c) Combined shear and bending. An analogous resolution strategy can be adopted for the determination of the sum coefficients when the membrane is simultaneously endowed with both a resistance toward shear and bending. Analytical expressions of the coefficients can readily be obtained using computer algebra systems but these are not provided here due to their complexity and lengthiness. It is noteworthy that, in contrast to planar elastic membranes, a coupling between shear and bending deformation modes has been observed for curved membranes.

3 Hydrodynamic mobility

The calculation of the flow field presented in the previous section can be utilized to assess the effect of the confining cavity on the motion of the encapsulated particle. This effect is quantified by the hydrodynamic self-mobility function μ, which relates the translational velocity of a colloidal particle to the force exerted on its surface.

We now assume an arbitrary time-dependent external force $\boldsymbol{F}_2$ to be acting on the spherical particle positioned at $\boldsymbol{x}_2$. The zeroth-order solution for the translational velocity of the solid particle can readily be obtained from the Stokeslet solution as $\boldsymbol{V}_2^{(0)} = \mu_0 \boldsymbol{F}_2$, where $\mu_0 = 1/(6\pi\eta b)$ is the usual Stokes mobility for a sphere moving in an unconfined viscous fluid. The leading-order correction to the hydrodynamic self-mobility can be calculated from the reflected flow field as

$$\boldsymbol{v}^*|_{\boldsymbol{x}=\boldsymbol{x}_2} = \Delta\mu \boldsymbol{F}_2. \tag{53}$$

The latter result is often denominated as the mobility correction in the point-particle approximation [76, 77]. Higher-order correction terms can be obtained by employing a combination of the multipole expansion and the Faxén theorem [78, 79]. However, we will show in the sequel that this approximation, despite its simplicity, can surprisingly lead to a good prediction of the mobility correction when comparing with fully-resolved computer simulations.

By making use of the relations

$$\boldsymbol{\nabla}\psi_{n-1}|_{\boldsymbol{r}=\boldsymbol{x}_2} = -\frac{n(n+1)}{2R^{n+2}} \boldsymbol{F}_2, \tag{54a}$$

$$\boldsymbol{\gamma}_{n-1}|_{\boldsymbol{r}=\boldsymbol{x}_2} = -\frac{n}{R^{n+1}} \boldsymbol{F}_2, \tag{54b}$$

$$(\boldsymbol{t}\times\boldsymbol{r})\,\varphi_{n-1}|_{\boldsymbol{r}=\boldsymbol{x}_2} = \frac{\boldsymbol{F}_2}{R^{n-1}}, \tag{54c}$$

$$\boldsymbol{r}\psi_{n-1}|_{\boldsymbol{r}=\boldsymbol{x}_2} = \boldsymbol{0}, \tag{54d}$$

in addition to inserting eq. (23) into eq. (53), we write the scaled mobility correction as

$$\frac{\Delta\mu}{\mu_0} = \frac{3b}{4} \sum_{n=1}^{\infty} \Bigg(- \frac{(n+1)(n+3)}{4}\, R^3 a_n - \frac{n+1}{2}\, R b_n + (n-1) c_n \Bigg) R^{n-2}, \tag{55}$$

where we have used the relation $P_n'(1) = n(n+1)/2$ for the derivative at the end point. We further remark that $R \in [0,1)$ because all distances have been scaled by the cavity radius a. The general term in the latter series, which we denote by $f_n(\alpha, R)$, has an asymptotic behavior at infinity that does not depend on the shear and bending properties of the membrane. Specifically, we obtain as $n \to \infty$

$$f_n(\alpha, R) = \frac{3b}{16}\, n^2 \left(1-R^2\right)^2 R^{2n-2} + \mathcal{O}\left(nR^{2n}\right). \tag{56}$$

In particular, for $R = 0$, the mobility correction simplifies to

$$\left.\frac{\Delta\mu}{\mu_0}\right|_{R=0} = -\frac{3b}{4}\,(b_1 - c_2) = -\frac{5b}{4}\,\frac{\alpha(2\lambda-1)}{5+\alpha(2\lambda-1)}\,, \tag{57}$$

in full agreement with the result obtained in part I for a particle concentric with the elastic cavity. We recall that the shear number α has previously been defined by eq. (38), and the dimensionless parameter λ associated with the Skalak ratio has been defined by eq. (8a).

In the quasi-steady limit of vanishing frequency, the scaled correction to the mobility reads

$$\lim_{\alpha\to\infty} \frac{\Delta\mu}{\mu_0} = \frac{\Delta\mu_{\mathrm{R}}}{\mu_0} + b\left(1 + \frac{3R^2}{4}\right), \tag{58}$$

wherein $\Delta\mu^{\mathrm{R}}/\mu_0$ is the scaled correction to the particle mobility associated with asymmetric motion inside a rigid spherical cavity. This correction can readily be obtained by substituting the series coefficients given by eq. (43) into eq. (55) to obtain

$$\frac{\Delta\mu_{\mathrm{R}}}{\mu_0} = \sum_{n=1}^{\infty} \lim_{\alpha\to\infty} \frac{\Delta\mu}{\mu_0} = -\frac{9b}{16}\,\frac{4-3R^2+R^4}{1-R^2}\,, \tag{59}$$

in agreement with the results by Aponte-Rivera and Zia [80–82], who provided the elements of the grand mobility tensor for general motion inside a rigid cavity. Interestingly, the particle mobility in the limit of infinite stiffness is found to be always larger than that inside a rigid cavity with no-slip velocity boundary condition on its interior surface. Mathematically, this behavior can be justified by the fact that the limit and sum operators cannot generally be swapped in every situation. In fact, using Fatou's Lemma [83], it can be shown that

$$\lim_{\alpha\to\infty} \sum_{n=1}^{\infty} |f_n(\alpha,R)| \ge \sum_{n=1}^{\infty} \lim_{\alpha\to\infty} |f_n(\alpha,R)|\,. \tag{60}$$

That is, evaluating the sum over n before taking the limit $\alpha \to \infty$ (as for an elastic cavity) could lead, under some circumstances, to a larger value in magnitude compared to the case in which the sum is taken after taking the limit (as it is the case for a rigid cavity). This is explained by the fact that the dominated convergence theorem does not apply for the series function at hand [84].

We further mention that the same limit given by eq. (58) is obtained when the cavity membrane only possesses resistance toward shear. In the limit of infinite cavity radius, the classic result for motion parallel to a planar hard wall is recovered. Specifically,

$$\lim_{a\to\infty} \frac{\Delta\mu_{\mathrm{R}}}{\mu_0} = -\frac{9}{16}\,\frac{b}{h}\,, \tag{61}$$

wherein $h = 1-R$ denotes the distance between the center of the particle and the closest point of the cavity membrane.

Next, we consider an idealized cavity membrane with pure bending resistance and calculate the correction to the self-mobility function in the limit of $\alpha_{\mathrm{B}} \to \infty$, corresponding to an infinite bending modulus or to particle motion in the quasi-steady limit of vanishing frequency. After some algebra, we obtain

$$\lim_{\alpha_{\mathrm{B}}\to\infty} \frac{\Delta\mu}{\mu_0} = \frac{\Delta\mu_{\mathrm{D}}}{\mu_0} + \frac{3b}{40}\left(5-2R^2\right)^2, \tag{62}$$

wherein $\Delta\mu_{\mathrm{D}}/\mu_0$ is the scaled correction to the particle mobility for motion inside a spherical drop of infinite surface tension (with vanishing normal velocity on its surface), given by

$$\frac{\Delta\mu_{\mathrm{D}}}{\mu_0} = \sum_{n=1}^{\infty} \lim_{\alpha_{\mathrm{B}}\to\infty} \frac{\Delta\mu}{\mu_0} = -\frac{3b}{32}\,\frac{20-15R^2-3R^4}{1-R^2}\,. \tag{63}$$

Again, the particle mobility in the vanishing-frequency limit for a membrane with pure bending is found to be always larger than that inside a spherical drop. Notably, the mobility correction vanishes in the concentric configuration corresponding to $R = 0$ where the system behavior is solely determined by membrane shear properties. This is in agreement with the results of part I obtained by exactly solving the fluid motion equations for an extended particle of finite size concentric with an elastic cavity.

In the limit of infinite cavity radius, we recover the mobility correction near a planar fluid-fluid interface,

$$\lim_{a\to\infty} \frac{\Delta\mu_{\mathrm{D}}}{\mu_0} = -\frac{3}{32}\,\frac{b}{h}\,, \tag{64}$$

in agreement with the result by Lee and Leal [85].

In the following, we assess the appropriateness and validity of our analytical calculations by direct comparison with computer simulations based on a completed-double-layer boundary integral method [86]. The method is perfectly suited for solving numerically diverse flow problems in the Stokes regime involving both rigid and elastic boundaries. For technical details regarding the computational method and its numerical implementation, we refer the reader to refs. [87] and [88].

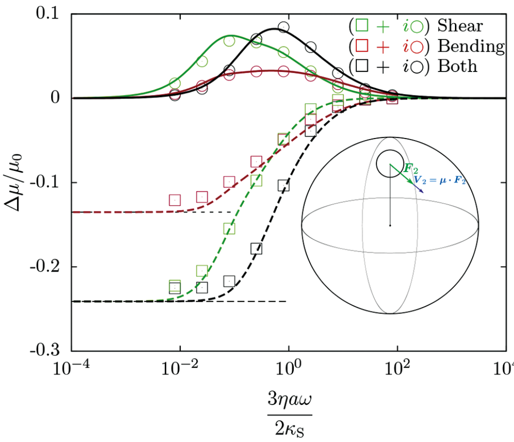

Fig. 2. Variation of the correction to the self-mobility function inside a spherical elastic cavity (scaled by the bulk mobility) *versus* the scaled frequency. The physical setup is sketched in the inset. Squares (□) and circles (○) indicate the real and, respectively, imaginary parts of the mobility correction as obtained from the full boundary integral simulations performed for a cavity membrane endowed with pure shear (green), pure bending (red), or coupled shear and bending (black). Solid and dashed lines give the corresponding analytical predictions (as described in the main text), which closely follow the numerical results. Thin black horizontal dashed lines represent the vanishing-frequency limits. Here, $b = 1/10$, $R = 4/5$, and $\kappa_B/(\kappa_S a^2) = 2/75$.

To probe the effect of the confining elastic cavity on the motion of an encapsulated particle, we present in fig. 2 the variations of the scaled correction to the self-mobility as a function of the forcing frequency, for a cavity membrane possessing only shear (green), only bending (red), or both shear and bending deformation modes (black). Here, the particle of radius $b = 1/10$ is positioned at $R = 4/5$ from the cavity center. We observe that the real (reactive) part of the mobility correction (shown as dashed lines) is a monotonically increasing function with frequency and approaches zero for larger forcing frequencies. In contrast to that, the imaginary (dissipative) part (shown as solid lines) exhibits the typical bell-shaped profile which peaks at around $\omega \sim \kappa_S/(\eta a)$. In the low-frequency regime, the mobility correction approaches the plateau values predicted by eqs. (58) and (62) for a cavity membrane with only shear elasticity or pure bending, respectively. Overall, there is strong quantitative agreement between the full numerical solutions (symbols) and the theoretical predictions. The small observed discrepancy notably for the real part in the low-frequency regime is most probably due to the finite size effect, because the analytical predictions are based on the point-particle approximation, whereas the numerical simulations necessarily account for the finite radius of the solid particle.

4 Cavity motion and membrane deformation

4.1 Pair (composite) mobility

The hydrodynamic self-mobility discussed in sect. 3 represents the particle response function to an external force. In this regard, one can also define an analogous response function for the whole elastic cavity and its interior, that relates the translational velocity $\boldsymbol{V}_1$ of the cavity centroid to the force $\boldsymbol{F}_2$ exerted on the encapsulated particle via $\boldsymbol{V}_1 = \boldsymbol{\mu}^{\mathrm{P}} \cdot \boldsymbol{F}_2$. In accordance to part I, we call the tensor $\boldsymbol{\mu}^{\mathrm{P}}$ the pair (composite) mobility. By symmetry, $\boldsymbol{V}_1 \| \boldsymbol{F}_2$ holds, so that the components of $\boldsymbol{\mu}^{\mathrm{P}}$ reduce to a single entry μ^{P} connecting the corresponding magnitudes via $V_1 = \mu^{\mathrm{P}} F_2$.

Without loss of generality, we assume in the following that $\boldsymbol{F}_2$ is exerted along the x-direction. Accordingly, the translational velocity of the elastic cavity can be calculated by integration over the fluid domain inside the cavity as [89]

$$V_1(\omega) = \frac{1}{\Omega} \int_0^1 \mathrm{d}r \int_0^{2\pi} \mathrm{d}\phi \int_0^{\pi} \mathrm{d}\theta \, v_x^{(i)}(r,\phi,\theta,\omega) \, r^2 \sin\theta, \tag{65}$$

where $\Omega = 4\pi/3$ is the scaled volume of the undeformed cavity, and

$$v_x^{(i)} = \left(v_r^{(i)} \sin\theta + v_\theta^{(i)} \cos\theta \right) \cos\phi - v_\phi^{(i)} \sin\phi. \tag{66}$$

The resulting frequency-dependent pair mobility function is obtained as

$$\mu^{\mathrm{P}} = -\frac{1}{8\pi\eta} \left(\frac{4R^2}{5} - 2 + a_1 + b_1 - c_2 \right), \tag{67}$$

so that only the term corresponding to $n = 1$ remains after volume integration. Upon simplification and rearrangement, the result can be presented in a scaled form as

$$6\pi\eta\mu^{\mathrm{P}} = \frac{3}{2} - \frac{3}{5} R^2 - \frac{5 - 6R^2}{10} \frac{\alpha(2\lambda - 1)}{5 + \alpha(2\lambda - 1)}, \tag{68}$$

where the parameters α and λ are defined by eq. (38) and eq. (8a), respectively.

Consequently, μ^{P} depends only on the membrane shear properties and can be described by a simple Debye model with a single relaxation time $\tau/\tau_S = 15/(2(2\lambda-1))$, where $\tau_S = a\eta/\kappa_S$ is a characteristic time scale for shear. Remarkably, the pair mobility can also become independent of frequency for $R = \sqrt{30}/6 \approx 9/10$, a value for which $6\pi\eta\mu^{\mathrm{P}} = 1$. Nevertheless, as $R \sim 1$, it becomes essential to ensure that the inequality $R + b \ll 1$ remains satisfied, for the point-particle approximation employed here to be applicable.

In fig. 3, we show the variations of the pair mobility (scaled by $6\pi\eta$) as a function of the scaled frequency. Results are shown for a cavity membrane with pure shear (green), pure bending (red), and both shear and bending (black). The pair mobility for a bending-only membrane remains unchanged upon varying the frequency and

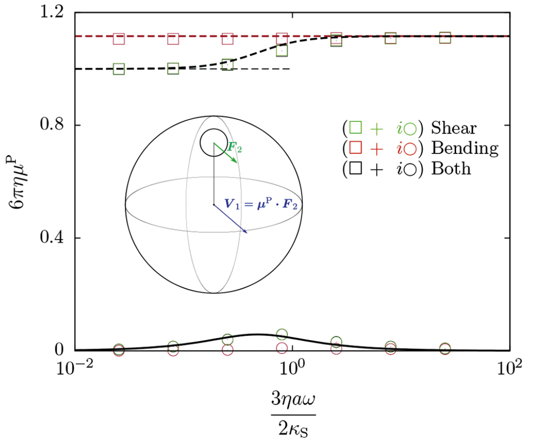

Fig. 3. Variation of the scaled pair mobility function (bridging between the translational velocity of the cavity and the external force exerted on the solid particle, as sketched in the inlet) as a function of the scaled frequency. The theoretical predictions are shown as dashed and solid lines, for the reactive and dissipative parts, respectively. Symbols (same as fig. 2) represent the boundary integral simulations results. The other system parameters are the same as in fig. 2. In this plot, the pure-shear data points (green) mostly overlap with those for coupled shear and bending (black).

amounts to $3/2 - 3R^2/5$. In contrast to that, the reactive part for a membrane possessing a shear resistance shows a logistic sigmoid curve varying between 1 (when $\alpha \to \infty$) and $3/2 - 3R^2/5$ (when $\alpha = 0$), whereas the dissipative part exhibits a Gaussian-like – or – bell-shaped profile. In all cases, there is strong agreement between the series-expansion theory (solid lines) and the full numerical solutions (symbols), confirming our theoretical predictions that the pair mobility is solely dependent on membrane shear properties (and independent of bending properties).

In analogy to the above discussion of the translational motion of the cavity in the presence of a force acting on the enclosed particle, one can also consider the corresponding rotational response. The angular velocity $\boldsymbol{\Omega}$ of the cavity is (due to symmetry) of the form $\boldsymbol{\Omega} = \Omega \boldsymbol{e}_y$ and has to fulfill $\boldsymbol{v}^{(q)}(\boldsymbol{r}) = \boldsymbol{\Omega} \times \boldsymbol{r}$ at the surface of the cavity ($r = 1$), with $q \in \{i, o\}$. After some algebra, one obtains

$$\Omega = \frac{3}{4} \left\langle \boldsymbol{e}_y \cdot \left(\boldsymbol{r} \times \boldsymbol{v}^{(q)} \right) \Big|_{r=1} \right\rangle = \frac{FR}{8\pi\eta} \qquad (69)$$

upon inserting our solution for the flow field, with angular brackets again denoting the surface average defined in eq. (31). Here, we find the same value of Ω for the different series coefficients obtained for pure shear, pure bending, as well as combined shear and bending. Additionally, we note that only the term $\propto \boldsymbol{\Gamma}_0$ in eqs. (35) contributes to the rotation of the cavity, while all other terms lead to vanishing contributions. Accordingly, the angular velocity effectively stems only from the Stokeslet solution and does not depend on membrane shear and bending properties.

4.2 Membrane deformation

The elastic deformation of the membrane can be assessed by calculating the displacement field $\boldsymbol{u}(\theta, \phi, \omega)$ resulting from the external force acting on the particle. This field quantifies the motion of the material points of the cavity membrane relative to their initial positions in the undeformed state. In the small deformation regime, the displacement field can readily be obtained from the no-slip boundary condition given by eq. (13), to obtain

$$8\pi\eta i\omega\, u_r = \sum_{n=1}^{\infty} \left(-\frac{n}{2} A_n + B_n - C_{n+1} \right) \psi_{n-1},$$

$$8\pi\eta i\omega\, \boldsymbol{\Pi u} = \sum_{n=1}^{\infty} \left(\frac{n-2}{2} A_n - B_n \right) \frac{\boldsymbol{\Psi}_{n-1}}{n+1} + \sum_{n=0}^{\infty} C_{n+1} \boldsymbol{\Gamma}_n.$$

We now define the reaction tensor $\boldsymbol{R}$, a frequency-dependent tensorial quantity relating the membrane displacement field of the cavity to the asymmetric point force as [77]

$$\boldsymbol{u}(\phi, \theta, \omega) = \boldsymbol{R}(\phi, \theta, \omega) \cdot \boldsymbol{F}(\omega). \qquad (70)$$

By considering a harmonic oscillation of the form $\boldsymbol{F} = \boldsymbol{K} e^{i\omega_0 t}$, of amplitude $\boldsymbol{K}$ and frequency ω_0, the membrane displacement in real space can readily be obtained from inverse Fourier transform as [90]

$$\boldsymbol{u}(\phi, \theta, t) = \boldsymbol{R}(\phi, \theta, \omega_0) \cdot \boldsymbol{K} e^{i\omega_0 t}. \qquad (71)$$

An exemplary displacement field is displayed in fig. 4 as a function of the polar angle for three different forcing frequencies. The azimuthal angle ϕ is chosen to represent the planes of maximum deformation for the respective components, as described in the figure caption. Here, the cavity membrane is endowed with both shear and bending rigidities. We observe that the radial component u_r vanishes at the upper pole and shows a peak around $\theta/\pi \approx 1/8$, before decaying quasi-linearly to zero upon increasing θ. The in-plane displacements u_θ and u_ϕ display a maximum value at the upper pole, and monotonically decay as θ increases. Our analytical predictions are in good agreement with numerical simulations. Notably, we observe a small deviation in the plot for u_r shown in panel (a) which is most probably due to a finite-sized effect. In contrast to the axisymmetric case discussed in part I, the deformation here is (in general) largest in the tangential direction.

In typical biological situations, the forces that could be exerted by optical tweezers on particles are of the order of 1 pN [91]. The spherical cavity may have a radius of 10^{-6} m and a shear modulus of $\kappa_{\mathrm{S}} = 5 \times 10^{-6}$ N/m [56]. For a scaled frequency $(3\eta a\omega)/(2\kappa_{\mathrm{S}}) = 4$, the membrane cavity is expected to undergo a maximal deformation of only about 1% of its initial undeformed radius. Consequently, cavity deformations and deviations from the spherical shape are notably small.

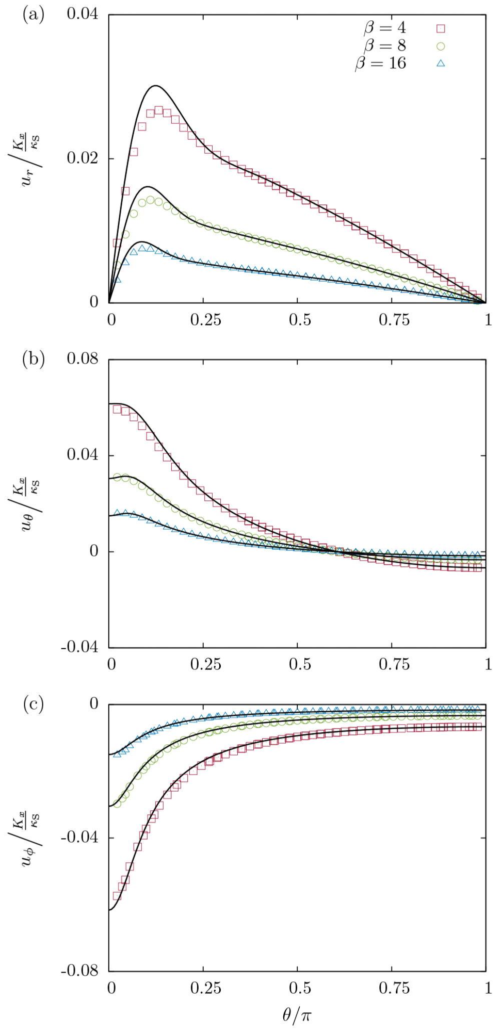

Fig. 4. Scaled membrane displacement field. (a) Radial, (b) circumferential, and (c) azimuthal components of the displacement field as a function of the polar angle θ for three scaled forcing frequencies (with $\beta = (3\eta a\omega)/(2\kappa_S)$), evaluated at quarter oscillation period for $t\omega_0 = \pi/2$. The components of the local displacement fields are shown for their respective planes of maximum deformation ($\phi = 0$ for u_r and u_θ and $\phi = \pi/2$ for u_ϕ). Numerical results obtained for coupled shear and bending are shown as symbols (as indicated in the legend), while the solid lines represent the corresponding, closely matching theoretical predictions.

5 Conclusions

In summary, we have presented an analytical theory to describe the low-Reynolds-number motion of a spherical particle moving inside a spherical membrane cavity endowed with both shear elasticity and bending rigidity. Here, we have focused on the situation in which the force exerted on the particle is directed tangent to the surface of the cavity. Together with the axisymmetric results obtained in an earlier paper [45], the solution of the elastohydrodynamic problem for a point force acting inside a spherical elastic cavity is thus obtained.

We have expressed the solution of the flow problem using the method of images. For this purpose, the hydrodynamic flow field is represented by a multipole expansion, summing over modes in terms of spherical harmonics, in analogy with familiar methods in electrostatics. The unknown series coefficients associated with each mode have been determined analytically from the prescribed boundary conditions of continuity of the fluid velocity field at the membrane cavity and discontinuity of hydrodynamic stresses as derived from Skalak and Helfrich elasticity models, associated with shear and bending deformation modes, respectively.

We have then explored the role of confinement on the motion of the encapsulated particle by calculating the frequency-dependent mobility functions. The latter linearly couple the translational velocity of the particle to the external force exerted on it. In the quasi-steady limit of vanishing actuation frequency, we have demonstrated that the hydrodynamic mobility inside a spherical elastic cavity is always larger than that predicted inside a rigid cavity of equal size with no-slip surface conditions. In addition, we have quantified the translational and rotational motion of the confining cavity, finding that the translational pair (composite) mobility is uniquely determined by membrane shear elasticity and that bending does not play a role in the dynamics of the cavity. We have further assessed the membrane deformation caused by the motion of the particle, showing that the cavity membrane primarily experiences deformation along the tangential direction.

Finally, we have assessed the appropriateness and applicability of our theoretical approach by supplementing our analytical calculations with fully-resolved computer simulations of truly-extended particles using the boundary integral method. Good agreement is obtained between theoretical predictions and numerical simulations over the full range of applied forcing frequencies. The developed method may find applications in the simulation of hydrodynamically interacting microparticles confined by a spherical elastic cavity, or medical capsules that are directed to a requested site by magnetic forces acting on incorporated magnetic particles.

We would like to thank Stephan Gekle and the Biofluid Simulation and Modeling group at the University of Bayreuth, where the boundary integral code used in this work has been developed. The authors gratefully acknowledge support from the DFG (Deutsche Forschungsgemeinschaft) through the projects LO 418/17-2 (HL), ME 3571/2-2 (AMM), and DA 2107/1-1 (ADMI).

Author contribution statement

ADMI conceived the study and performed the numerical simulations. CH and ADMI carried out the analytical calculations and drafted the manuscript. CH, HL, AMM, and ADMI discussed and interpreted the results, edited the text, and finalized the manuscript.

Publisher's Note The EPJ Publishers remain neutral with regard to jurisdictional claims in published maps and institutional affiliations.

Appendix A. Expression of the coefficients

In this appendix, we provide explicit expressions for the coefficients stated in eqs. (42) and (50) of the main body of the paper. For an idealized membrane with pure shear, the coefficients are given by

$$K_1 = \alpha\lambda\, n\,(n-1)\,(n+3)\,(n+2),$$

$$K_2 = (n+1)(2n+1)\big(\alpha n^4\lambda + 4\alpha n^3\lambda + (8-2\alpha+5\alpha\lambda)n^2 + (16-4\alpha+2\alpha\lambda)\,n+6\big),$$

$$K_3 = n\,\big(4\,\alpha\lambda n^5 + (-\alpha^2+10\alpha\lambda+16+2\,\alpha^2\lambda)\,n^4 + (32+6\alpha\lambda+4\alpha^2\lambda-2\alpha^2)\,n^3 + (\alpha^2-2\alpha^2\lambda+8-\alpha\lambda)\,n^2 - (4\alpha^2\lambda+\alpha\lambda-2\alpha^2+8+6\alpha)\,n-3-3\alpha\big),$$

$$K_4 = n\,\left(\alpha n^3\lambda + (\alpha\lambda+4-\alpha)\,n^2 - 2\alpha n + 2\alpha - 1\right),$$

$$K_5 = 2\left(\alpha\lambda n^3 + (3\alpha\lambda+4-\alpha)n^2 + (2\alpha\lambda-2\alpha+8)n+3\right),$$

$$K_6 = -(n+1)\,n\,\big(-2\alpha n^3 + (-8-15\alpha+8\alpha\lambda)\,n^2 + (-43\alpha+28\alpha\lambda-16)\,n - 42\alpha + 24\alpha\lambda - 6\big),$$

$$K_7 = (n+2)\,(\alpha n^2 + (3\alpha+4)\,n+6)\,K_5,$$

$$K_8 = -(n+1)\,(n+2)\,(2n+1)\,(\alpha n^2 + (3\alpha+4)\,n+6),$$

$$K_9 = \frac{1}{4}\left(\alpha n^3 + (2\alpha+4)\,n^2 + (6-\alpha)\,n - 2\alpha + 2\right),$$

where we recall that $\alpha = 2\kappa_S/(3\eta i\omega)$ is the shear number, and $\lambda = C+1$ is the dimensionless parameter associated with the Skalak ratio. For an idealized membrane with pure bending resistance, the corresponding coefficients read

$$Q_1 = \alpha_B\, n\,(n+3)\,(n+2)^2\,(n-1)^2,$$

$$Q_2 = -\alpha_B\, n^6 - 3\alpha_B\, n^5 + \alpha_B\, n^4 + 7\alpha_B\, n^3 + 8\,n^2 + (16-4\alpha_B)\;n+6,$$

$$Q_3 = n\,\big(2\alpha_B\, n^6 + 6\alpha_B\, n^5 - 2\alpha_B\, n^4 + (8-14\alpha_B)\,n^3 + 12\,n^2 + (-2+8\alpha_B)\,n-3\big),$$

$$Q_4 = n\,\big(\alpha_B\, n^7 + 10\alpha_B\, n^6 + 17\alpha_B\, n^5 + (4-20\alpha_B)\,n^4 + (40-40\alpha_B)\,n^3 + (16\alpha_B+47)\,n^2 + (-10+16\alpha_B)\,n-12\big),$$

$$Q_5 = -2\,n\,(n+1)\,(n+2)\,\big(\alpha_B\, n^4 + 4\alpha_B\, n^3 - 3\alpha_B\, n^2 - (2+10\alpha_B)\,n - 1 + 8\alpha_B\big),$$

$$Q_6 = 2\,(n+1)\,\big(\alpha_B\, n^6 + 2\alpha_B\, n^5 - 3\alpha_B\, n^4 - (4\alpha_B+2)\,n^3 + (-21+4\alpha_B)\,n^2 - 34\,n - 12\big),$$

$$Q_7 = 2\,(n+2)^2\,\big(\alpha_B\, n^5 + 2\alpha_B\, n^4 - 3\alpha_B\, n^3 + 4\,n^2 - 4\alpha_B\, n^2 + (4\alpha_B+8)\,n+3\big),$$

wherein $\alpha_B = \kappa_B/(\eta i\omega)$ denotes the bending number.

References

1. H.A. Stone, A.D. Stroock, A. Ajdari, Annu. Rev. Fluid Mech. **36**, 381 (2004).
2. A.Y. Fu, C. Spence, A. Scherer, F.H. Arnold, S.R. Quake, Nat. Biotechnol. **17**, 1109 (1999).
3. H. Lu, S. Gaudet, M.A. Schmidt, K.F. Jensen, Anal. Chem. **76**, 5705 (2004).
4. D. Huh, W. Gu, Y. Kamotani, J.B. Grotberg, S. Takayama, Physiol. Meas. **26**, R73 (2005).
5. L. Schmid, D.A. Weitz, T. Franke, Lab Chip **14**, 3710 (2014).
6. S. Darvishmanesh, L. Firoozpour, J. Vanneste, P. Luis, J. Degrève, B. Van der Bruggen, Green Chem. **13**, 3476 (2011).
7. A. Adamo, P.L. Heider, N. Weeranoppanant, K.F. Jensen, Ind. Eng. Chem. Res. **52**, 10802 (2013).
8. B. Gutmann, D. Cantillo, C.O. Kappe, Angew. Chem. Int. Ed. **54**, 6688 (2015).
9. Y.L. Colson, M.W. Grinstaff, Adv. Mater. **24**, 3878 (2012).
10. H. Hillaireau, P. Couvreur, Cell. Mol. Life Sci. **66**, 2873 (2009).
11. J. Liu, T. Wei, J. Zhao, Y. Huang, H. Deng, A. Kumar, C. Wang, Z. Liang, X. Ma, X.J. Liang, Biomaterials **91**, 44 (2016).
12. H. Maeda, H. Nakamura, J. Fang, Adv. Drug Deliv. Rev. **65**, 71 (2013).
13. S. Naahidi, M. Jafari, F. Edalat, K. Raymond, A. Khademhosseini, P. Chen, J. Control. Release **166**, 182 (2013).
14. J.M. Rosenholm, C. Sahlgren, M. Linden, Nanoscale **2**, 1870 (2010).
15. R. Singh, J.W. Lillard, Exp. Mol. Pathol. **86**, 215 (2009).
16. L.M. Bareford, P.W. Swaan, Adv. Drug Deliv. Rev. **59**, 748 (2007).
17. J. Happel, H. Brenner, *Low Reynolds Number Hydrodynamics: With Special Applications to Particulate Media*, Vol. **1** (Springer Netherlands, Dordrecht, Netherlands, 2012).
18. S. Kim, S.J. Karrila, *Microhydrodynamics: Principles and Selected Applications* (Dover Publications, Mineola, New York, 2013).
19. L.G. Leal, Annu. Rev. Fluid Mech. **12**, 435 (1980).
20. J.R. Blake, Math. Proc. Camb. Philos. Soc. **70**, 303 (1971).
21. C.W. Oseen, *Neuere Methoden und Ergebnisse in der Hydrodynamik* (Akademische Verlagsgesellschaft, Leipzig, Germany, 1928).
22. S.F.J. Butler, Math. Proc. Cambridge Philos. Soc. **49**, 169 (1953).
23. W.D. Collins, Mathematika **1**, 125 (1954).
24. H. Hasimoto, J. Phys. Soc. Jpn. **11**, 793 (1956).
25. H. Hasimoto, J. Phys. Soc. Jpn. **61**, 3027 (1992).
26. H. Hasimoto, Phys. Fluids **9**, 1838 (1997).
27. R. Shail, Quart. J. Mech. Appl. Math. **40**, 223 (1987).
28. R. Shail, S.H. Onslow, Mathematika **35**, 233 (1988).

29. A. Sellier, Comput. Model. Eng. Sci. **25**, 165 (2008).
30. C. Maul, S. Kim, Phys. Fluids **6**, 2221 (1994).
31. C. Maul, S. Kim, in *The Centenary of a Paper on Slow Viscous Flow by the Physicist H.A. Lorentz* (Springer Netherlands, Dordrecht, Netherlands, 1996) pp. 119–130.
32. B.U. Felderhof, A. Sellier, J. Chem. Phys. **136**, 054703 (2012).
33. D. Tsemakh, O.M. Lavrenteva, A. Nir, Int. J. Multiph. Flow **30**, 1337 (2004).
34. O.M. Lavrenteva, D. Tsemakh, A. Nir, Fluid Dyn. Mater. Process. **1**, 131 (2005).
35. S.Y. Reigh, L. Zhu, F. Gallaire, E. Lauga, Soft Matter **13**, 3161 (2017).
36. L. Zhu, F. Gallaire, Phys. Rev. Lett. **119**, 064502 (2017).
37. S.Y. Reigh, E. Lauga, Phys. Rev. Fluids **2**, 093101 (2017).
38. V.A. Shaik, V. Vasani, A.M. Ardekani, J. Fluid Mech. **851**, 187 (2018).
39. A. Daddi-Moussa-Ider, A. Guckenberger, S. Gekle, Phys. Rev. E **93**, 012612 (2016).
40. A. Daddi-Moussa-Ider, S. Gekle, Eur. Phys. J. E **41**, 19 (2018).
41. A. Daddi-Moussa-Ider, S. Gekle, Phys. Rev. E **95**, 013108 (2017).
42. A. Daddi-Moussa-Ider, M. Lisicki, S. Gekle, Phys. Rev. E **95**, 053117 (2017).
43. A. Daddi-Moussa-Ider, M. Lisicki, S. Gekle, Phys. Fluids **29**, 111901 (2017).
44. A. Daddi-Moussa-Ider, M. Lisicki, S. Gekle, Acta Mech. **229**, 149 (2018).
45. A. Daddi-Moussa-Ider, H. Löwen, S. Gekle, Eur. Phys. J. E **41**, 104 (2018).
46. Y.O. Fuentes, S. Kim, D.J. Jeffrey, Phys. Fluids **31**, 2445 (1988).
47. Y.O. Fuentes, S. Kim, D.J. Jeffrey, Phys. Fluids **1**, 61 (1989).
48. K. Sekimoto, L. Leibler, Europhys. Lett. **23**, 113 (1993).
49. S.J. Weekley, S.L. Waters, O.E. Jensen, Q. J. Mech. Appl. Math. **59**, 277 (2006).
50. T. Salez, L. Mahadevan, J. Fluid Mech. **779**, 181 (2015).
51. B. Saintyves, T. Jules, T. Salez, L. Mahadevan, Proc. Natl. Acad. Sci. U.S.A. **113**, 5847 (2016).
52. B. Rallabandi, B. Saintyves, T. Jules, T. Salez, C. Schönecker, L. Mahadevan, H.A. Stone, Phys. Rev. Fluids **2**, 074102 (2017).
53. A. Daddi-Moussa-Ider, B. Rallabandi, S. Gekle, H.A. Stone, Phys. Rev. Fluids **3**, 084101 (2018).
54. B. Rallabandi, N. Oppenheimer, M.Y.B. Zion, H.A. Stone, Nat. Phys. **14**, 1211 (2018).
55. R. Skalak, A. Tozeren, R.P. Zarda, S. Chien, Biophys. J. **13**, 245 (1973).
56. J.B. Freund, Annu. Rev. Fluid Mech. **46**, 67 (2014).
57. T. Krüger, *Computer Simulation Study of Collective Phenomena in Dense Suspensions of Red Blood Cells under Shear* (Vieweg+Teubner Verlag, Wiesbaden, Germany, 2012).
58. T. Krüger, F. Varnik, D. Raabe, Comput. Math. Appl. **61**, 3485 (2011).
59. A.E. Green, J.C. Adkins, *Large Elastic Deformations and Non-linear Continuum Mechanics* (Oxford University Press, Oxford, UK, 1960).
60. L. Zhu, PhD Thesis (2014).
61. E. Lac, D. Barthès-Biesel, N.A. Pelekasis, J. Tsamopoulos, J. Fluid Mech. **516**, 303 (2004).
62. W. Helfrich, Z. Naturforsch. C **28**, 693 (1973).
63. K. Berndl, J. Käs, R. Lipowsky, E. Sackmann, U. Seifert, Europhys. Lett. **13**, 659 (1990).
64. U. Seifert, Adv. Phys. **46**, 13 (1997).
65. A. Guckenberger, S. Gekle, J. Phys.: Condens. Matter **29**, 203001 (2017).
66. S. Kobayashi, K. Nomizu, *Foundations of Differential Geometry*, Vol. **1** (Interscience Publishers, New York, 1963).
67. M. Deserno, Chem. Phys. Lipids **185**, 11 (2015).
68. J.R. Blake, A.T. Chwang, J. Eng. Math. **8**, 23 (1974).
69. D. Zill, W.S. Wright, M.R. Cullen, *Advanced Engineering Mathematics* (Jones & Bartlett Learning, Burlington, Massachusetts, 2011).
70. H. Lamb, *Hydrodynamics* (Cambridge University Press, Cambridge, UK, 1932).
71. M. Abramowitz, I.A. Stegun, *Handbook of Mathematical Functions*, Vol. **1** (Dover Publications, Mineola, New York, 1972).
72. A.R. Edmonds, *Angular Momentum in Quantum Mechanics*, Vol. **4** (Princeton University Press, Princeton, New Jersey, 1996).
73. Y. Rui, S. Wang, P.S. Low, D.H. Thompson, J. Am. Chem. Soc. **120**, 11213 (1998).
74. V.P. Torchilin, Nat. Rev. Drug Discov. **4**, 145 (2005).
75. C. Zylberberg, S. Matosevic, Drug Deliv. **23**, 3319 (2016).
76. T. Bickel, Eur. Phys. J. E **20**, 379 (2006).
77. T. Bickel, Phys. Rev. E **75**, 041403 (2007).
78. J.W. Swan, J.F. Brady, Phys. Fluids **19**, 113306 (2007).
79. J.W. Swan, J.F. Brady, Phys. Fluids **22**, 103301 (2010).
80. C. Aponte-Rivera, R.N. Zia, Phys. Rev. Fluids **1**, 023301 (2016).
81. C. Aponte-Rivera, Y. Su, R.N. Zia, J. Fluid Mech. **836**, 413 (2018).
82. C. Aponte-Rivera, PhD Thesis, Cornell University, USA (2017).
83. N.L. Carothers, *Real Analysis* (Cambridge University Press, Cambridge, UK, 2000).
84. P. Billingsley, *Convergence of Probability Measures* (John Wiley & Sons, Hoboken, New Jersey, 2013).
85. S.H. Lee, R.S. Chadwick, L.G. Leal, J. Fluid Mech. **93**, 705 (1979).
86. C. Pozrikidis, J. Comput. Phys. **169**, 250 (2001).
87. A. Daddi-Moussa-Ider, A. Guckenberger, S. Gekle, Phys. Fluids **28**, 071903 (2016).
88. A. Guckenberger, M.P. Schraml, P.G. Chen, M. Leonetti, S. Gekle, Comput. Phys. Commun. **207**, 1 (2016).
89. B.U. Felderhof, Phys. Rev. E **89**, 033001 (2014).
90. R. Bracewell, *The Fourier Transform and Its Applications* (McGraw-Hill, New York, 1999).
91. G. Cipparrone, I. Ricardez-Vargas, P. Pagliusi, C. Provenzano, Opt. Express **18**, 6008 (2010).

P9 Frequency-dependent higher-order Stokes singularities near a planar elastic boundary: implications for the hydrodynamics of an active microswimmer near an elastic interface

Reproduced from

A. Daddi-Moussa-Ider, C. Kurzthaler, C. Hoell, A. Zöttl, M. Mirzakhanloo, M.-R. Alam, A. M. Menzel, H. Löwen, and S. Gekle,
Frequency-dependent higher-order Stokes singularities near a planar elastic boundary: implications for the hydrodynamics of an active microswimmer near an elastic interface,
Phys. Rev. E **100**, 032610 (2019),
published by the *American Physical Society.*

Digital Object Identifier (DOI):
`https://doi.org/10.1103/PhysRevE.100.032610`

Statement of contribution

I contributed to the theoretical description, concerning the elastic response of the interface and the resulting hydrodynamic interactions, as well as to the discussion and interpretation of the results, in particular with respect to the effects of a force dipole and of a rotlet dipole. Subsequently, I contributed to drafting the corresponding parts of the manuscript. Moreover, I participated in editing the text and finalizing the manuscript. My work here was supervised by ADMI, AMM, and HL.

Copyright and license notice

PHYSICAL REVIEW E **100**, 032610 (2019)

Frequency-dependent higher-order Stokes singularities near a planar elastic boundary: Implications for the hydrodynamics of an active microswimmer near an elastic interface

Abdallah Daddi-Moussa-Ider,[1,*] Christina Kurzthaler,[2] Christian Hoell,[1] Andreas Zöttl,[3] Mehdi Mirzakhanloo,[4] Mohammad-Reza Alam,[4] Andreas M. Menzel,[1] Hartmut Löwen,[1] and Stephan Gekle[5]

[1] *Institut für Theoretische Physik II: Weiche Materie, Heinrich-Heine-Universität Düsseldorf, Universitätsstraße 1, 40225 Düsseldorf, Germany*

[2] *Department of Mechanical and Aerospace Engineering, Princeton University, Princeton, New Jersey 08544, USA*

[3] *Institute for Theoretical Physics, Technische Universität Wien, Wiedner Hauptstraße 8-10, 1040 Wien, Austria*

[4] *Department of Mechanical Engineering, University of California, Berkeley, California 94720, USA*

[5] *Biofluid Simulation and Modeling, Theoretische Physik VI, Universität Bayreuth, Universitätsstraße 30, 95440 Bayreuth, Germany*

(Received 16 July 2019; published 30 September 2019)

The emerging field of self-driven active particles in fluid environments has recently created significant interest in the biophysics and bioengineering communities owing to their promising future for biomedical and technological applications. These microswimmers move autonomously through aqueous media, where under realistic situations they encounter a plethora of external stimuli and confining surfaces with peculiar elastic properties. Based on a far-field hydrodynamic model, we present an analytical theory to describe the physical interaction and hydrodynamic couplings between a self-propelled active microswimmer and an elastic interface that features resistance toward shear and bending. We model the active agent as a superposition of higher-order Stokes singularities and elucidate the associated translational and rotational velocities induced by the nearby elastic boundary. Our results show that the velocities can be decomposed in shear and bending related contributions which approach the velocities of active agents close to a no-slip rigid wall in the steady limit. The transient dynamics predict that contributions to the velocities of the microswimmer due to bending resistance are generally more pronounced than those due to shear resistance. Bending can enhance (suppress) the velocities resulting from higher-order singularities whereas the shear related contribution decreases (increases) the velocities. Most prominently, we find that near an elastic interface of only energetic resistance toward shear deformation, such as that of an elastic capsule designed for drug delivery, a swimming bacterium undergoes rotation of the same sense as observed near a no-slip wall. In contrast to that, near an interface of only energetic resistance toward bending, such as that of a fluid vesicle or liposome, we find a reversed sense of rotation. Our results provide insight into the control and guidance of artificial and synthetic self-propelling active microswimmers near elastic confinements.

DOI: 10.1103/PhysRevE.100.032610

I. INTRODUCTION

Artificial nano- and microscale machines hold great potential for future biomedical applications such as precision nanosurgery, biopsy, or transport of radioactive substances to tumor sites [1–3]. These active particles have the ability to move autonomously in biofluids and could reach inaccessible areas of the body to perform delicate and precise tasks. Recent advances in the field have provided a fundamental understanding of various physical phenomena arising in active matter systems [4–12], which exhibit strikingly different behavior than their passive counterparts. Suspensions of active agents display fascinating collective behavior and unusual spatiotemporal patterns, including propagating density waves [13–15], motility-induced phase separation [16–20], and the emergence of active turbulence [21–26].

While passive particles can be set into motion under the action of an external field, active particles self-propel by converting energy from their environment into mechanical work. At low Reynolds numbers, microswimmers have to employ effective self-propulsion mechanisms that break the time-reversal symmetry of the Stokes flow [4], a property commonly referred to as Purcell's scallop theorem [27–30]. For instance, many biological microswimmers perform a nonreciprocal deformation cycle of their body via, e.g., rotating flagella or beating cilia [31–34], whereas synthetic microswimmers move via phoretic effects caused by their asymmetric surface properties [35–43], or by nonreciprocal deformation of their shape [44–55].

In many biologically relevant situations, motion occurs in the presence of surfaces that significantly modify the hydrodynamic flows and thereby strongly affect the transport properties, function, and survival of suspended particles and microorganisms. Confining boundaries play an important role in many engineering and biological processes ranging from the rheology of colloidal suspensions [56–58] to the transport of nanoparticles and various molecules through micro- and nanochannels [59,60]. Moreover, microswimmers encounter in their natural habitats a plethora of different types of

[*] abdallah.daddi.moussa.ider@uni-duesseldorf.de

surfaces with various geometric and elastic properties. Examples include sperm cells in the female reproductive tract [61], bacterial pathogens in microvasculature channels [62], or bacteria in biofilms [63]. Thus, surface related effects on their motility may entail important consequences for a large number of biological systems, including biofilm formation, bacterial adhesion, and microbial activity [64,65].

Transport properties of active agents near a no-slip rigid planar wall reveal various interesting features [66–83], including their escape from the wall, a stationary hovering state, or gliding along the boundary maintaining a constant orientation during their navigation. Interestingly, flagellated bacteria display circular swimming trajectories close to surfaces as a consequence of hydrodynamic couplings [84]. Their swimming direction can be qualitatively influenced by the nature of the boundary conditions at the interface such that, e.g., the circular motion is reversed at a free air-liquid interface when compared to a no-slip wall [85]. Bacterial swimming in the close vicinity of a boundary has been addressed theoretically using a two-dimensional singularity model combined with a complex variable approach [86], a resistive force theory [87], or a multipole expansion technique [85]. Further, it has been shown that the presence of a nearby wall can lead to a change in the waveform assumed by actuated flagella causing a strong alteration of the resulting propulsive force [88]. Under applied shear flow, swimming bacteria [89–95] and sperm cells [96–98] near surfaces may inhibit their circular motion and exhibit rheotaxis leading to motion against imposed shear flow. Likewise, the rheotactic behavior of a self-diffusiophoretic particle has been investigated numerically by means of boundary integral simulations [99]. Direct measurements of the flow field generated by individual swimming *E. coli* both far from and near a solid surface have revealed the relative importance of fluid dynamics and rotational diffusion in bacterial locomotion [100]. More recently, it has been shown that *E. coli* bacteria use transient adhesion to nearby surfaces as a generic mechanism to regulate their motility and transport properties in confinements [101]. Remarkably, a nearby wall alone can enable self-phoresis of homogeneous and isotropic active particles [102]. The behavior of self-propelled nano- and micro-rods in a channel has further been investigated theoretically and numerically [103–109].

Unlike fluid-fluid or fluid-solid interfaces, elastic boundaries generically stand apart because they endow the system with memory. Such an effect results in a long-lasting anomalous subdiffusive behavior on nearby particles [110–113]. The emerging subdiffusion can significantly enhance residence time and binding rates and thus may increase the probability to trigger the uptake of particles by living cell membranes via endocytosis [114,115]. Moreover, theoretical investigations of model microswimmers immersed in an elastic channel have predicted an enhancement in swimming speed as the swimmers deform the flexible boundaries via hydrodynamic flows [116]. In addition, it has been demonstrated that reciprocal motion close to a deformable interface can circumvent the scallop theorem and result in a net propulsion of microswimmers at low Reynolds numbers [117]. Theoretically, the motion of a passive particle near a fluid membrane possessing surface tension [118,119], bending resistance [120], or surface elasticity [121,122] has thoroughly been studied. The corresponding diffusion coefficient in the steady limit is found to be universal and identical to that predicted near a hard wall with no-slip boundary conditions [121].

Here, we investigate the influence of nearby elastic boundaries possessing resistance toward shear and bending on the dynamics of microswimmers at low Reynolds number. Our analytical approach is based on the far-field hydrodynamic multipole representation of active microswimmers and valid in the small-deformation regime. We find that the shear- and bending related contributions to the overall induced translational and rotational velocities resulting from the hydrodynamic interactions with an elastic interface may have promotive or suppressive effects. In the steady limit, the swimming velocities are found to be independent of the membrane elastic properties and to approach the corresponding values near a no-slip wall.

The remainder of the paper is organized as follows. In Sec. II, we present the governing equations of low-Reynolds-number fluid motion and introduce, in the small deformation regime, a relevant model for an elastic interface featuring resistance toward both shear and bending. In addition, we describe in terms of the multipole expansion of the Stokes equations the self-generated flow field induced by an active microswimmer near an elastic interface. We then evaluate in Sec. III the induced swimming velocities due to hydrodynamic interactions with the interface and discuss the interplay between shear and bending deformation modes, as well as their corresponding roles in the overall dynamics. Concluding remarks are contained in Sec. IV. Some mathematical details, which are not essential for the understanding of the key messages of our analytical approach, are relegated to the Appendices.

II. THEORETICAL DESCRIPTION

We consider the behavior of an axisymmetric microswimmer near a planar elastic interface of infinite extent in the xy plane, i.e., the z direction is directed normal to that plane. The swimmer is modeled as a prolate spheroid of short semiaxis a and long semiaxis c, trapped above the elastic interface at position $z = h$. Here, we adopt a local coordinate system attached to the swimmer such that $\theta \in [-\pi/2, \pi/2]$ is the pitch angle and $\varphi \in [0, 2\pi)$ is the azimuthal orientation in the xy plane (see Fig. 1 for a graphical illustration of the system setup).

We model the swimming behavior in the far-field limit (i.e., $c \ll h$) by using a combination of fundamental solutions to the Stokes equations in the vicinity of an elastic interface [123,124]. Further details on the swimmer model are provided after stating the exact Green's functions for a point-force singularity near a planar elastic boundary and derivation of the corresponding higher-order singularities that are obtained via a multipole expansion (see Sec. III).

A. Low-Reynolds-number hydrodynamics: Stokes equations

For a viscous, incompressible Newtonian fluid, the Navier-Stokes equations in the overdamped, low-Reynolds-number

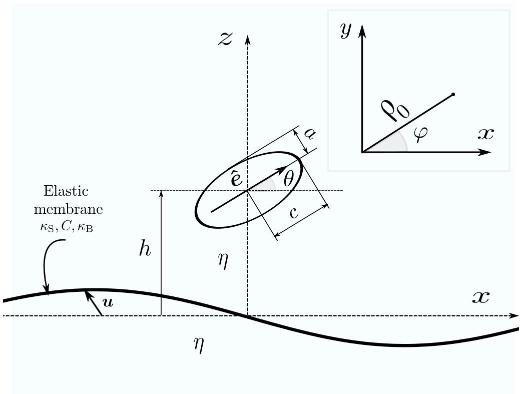

FIG. 1. Illustration of the system setup. An axisymmetric active microswimmer modeled as a prolate spheroid is trapped at $z = h$ above an elastic interface infinitely extended in the xy plane. The lengths of the short and long semiaxes are denoted by a and c, respectively. Setting the orientation of the swimmer, the unit vector $\hat{\boldsymbol{e}}$ points along the symmetry axis of the swimmer. The pitch angle of the swimmer relative to the horizontal plane is denoted by $\theta \in [-\pi/2, \pi/2]$ (the complement of the polar angle in spherical coordinates). On both sides of the elastic interface, the surrounding fluid is Newtonian and characterized by the same dynamic viscosity η. The figure shown in the inset is a top view of the local reference frame associated with the microswimmer, where ρ_0 is the radial distance and $\varphi \in [0, 2\pi)$ is the azimuthal orientation.

limit simplify to the time-independent Stokes equations [6,27]

$$\eta\nabla^2 \boldsymbol{v}(\boldsymbol{r}) - \nabla p(\boldsymbol{r}) + \boldsymbol{f}_B(\boldsymbol{r}) = 0, \tag{1a}$$

$$\nabla \cdot \boldsymbol{v}(\boldsymbol{r}) = 0, \tag{1b}$$

where $\boldsymbol{r}$ denotes the spatial coordinate, η is the shear viscosity, $\boldsymbol{v}$ denotes the fluid velocity, p is the pressure field, and $\boldsymbol{f}_B$ here represents the body force density acting on the fluid domain by the immersed objects.

The fundamental solution of the Stokes equations for a point-force singularity $\boldsymbol{f}_B = \boldsymbol{f}\delta(\boldsymbol{r} - \boldsymbol{r}_0)$ (Stokeslet) placed at position $\boldsymbol{r}_0$ in an otherwise quiescent unbounded (infinite) fluid domain is expressed in terms of the free-space Green's function given by the Oseen tensor [125,126]. Assuming that the point force is directed along the unit vector $\hat{\boldsymbol{e}}$ such that $\boldsymbol{f} = f\hat{\boldsymbol{e}}$, the induced flow and pressure fields read

$$\boldsymbol{v}_S^\infty(\boldsymbol{r}) = \frac{f}{8\pi\eta}\boldsymbol{G}^\infty(\boldsymbol{r}, \boldsymbol{r}_0; \hat{\boldsymbol{e}}), \quad p_S^\infty(\boldsymbol{r}) = \frac{f}{4\pi}P^\infty(\boldsymbol{r}, \boldsymbol{r}_0; \hat{\boldsymbol{e}}), \tag{2}$$

where the Stokeslet solution is given by $\boldsymbol{G}^\infty(\boldsymbol{r}, \boldsymbol{r}_0; \hat{\boldsymbol{e}}) = (\hat{\boldsymbol{e}} + (\hat{\boldsymbol{e}} \cdot \hat{\boldsymbol{s}})\hat{\boldsymbol{s}})/s$, with $\boldsymbol{s} = \boldsymbol{r} - \boldsymbol{r}_0$, $s = |\boldsymbol{s}|$ denoting the distance from the singularity position, and $\hat{\boldsymbol{s}} = \boldsymbol{s}/s$. Likewise, the corresponding solution for the pressure field is $P^\infty(\boldsymbol{r}, \boldsymbol{r}_0; \hat{\boldsymbol{e}}) = \hat{\boldsymbol{e}} \cdot \hat{\boldsymbol{s}}/s^2$.

B. Model for the elastic interface

The interface is modeled as a two-dimensional elastic sheet made of a hyperelastic material featuring resistance toward both shear and bending. Shear elasticity of the interface is described by the well-established Skalak model [127], which is commonly utilized as a practical model for the description of red blood cell membranes [128–131]. The interface resistance toward bending is described by the Helfrich model [132–135].

For an elastic interface infinitely extended in the xy plane, the linearized tangential and normal traction jumps across the interface due to shear and bending deformation modes are expressed in terms of the displacement field $\boldsymbol{u}$ of the interface relative to the initial planar configuration via [110]

$$[\sigma_{zj}] = -\frac{\kappa_S}{3}[\Delta_\parallel u_j + (1 + 2C)\partial_j\epsilon], \quad j \in \{x, y\}, \tag{3a}$$

$$[\sigma_{zz}] = \kappa_B\Delta_\parallel^2 u_z, \tag{3b}$$

where κ_S is the shear modulus, $C = \kappa_A/\kappa_S$ denotes the Skalak parameter (with the area expansion modulus κ_A), and κ_B is the bending modulus. Here we use the notation $[\sigma_{ij}] = \sigma_{ij}(z = 0^+) - \sigma_{ij}(z = 0^-)$ to denote the jump in the viscous stress tensor across the elastic interface. In addition, $\epsilon = \partial_x u_x + \partial_y u_y$ denotes the dilatation function, and $\Delta_\parallel = \partial_x^2 + \partial_y^2$ stands for the Laplace-Beltrami operator [136]. The normal components of the hydrodynamic stress tensor are expressed in the Cartesian coordinate system in the usual way as $\sigma_{zj} = -p\delta_{zj} + \eta(\partial_j v_z + \partial_z v_j)$.

To relate the displacement of the elastic interface to the fluid velocity field, we impose a hydrodynamic no-slip boundary condition. The latter, in Fourier space, takes a particularly simple form in the small-deformation regime. Specifically [118],

$$\boldsymbol{v}|_{z=0} = i\omega\boldsymbol{u}, \tag{4}$$

with ω being the frequency in the Fourier domain. Accordingly, the components of the fluid velocity field evaluated at the surface of reference $z = 0$ are assumed to coincide with those of the material points composing the deformable interface. The particular case of zero frequency corresponds to the "stick" boundary condition which applies for an infinitely-extended rigid wall [121]. It is worth mentioning that, if the elastic interface undergoes a larger deformation, the no-slip condition stated by Eq. (4) takes a nonlinear form because the condition has to be applied at the deformed interface. This situation has been considered, for instance, in Refs. [137–144]. Since our attention here is restricted to the system behavior in the small-deformation regime, for which $|\boldsymbol{u}| \ll h$, applying the no-slip boundary condition at the position of the undisplaced interface is appropriate for our theoretical analysis.

As described in detail in Refs. [110,112], the behavior of a particle close to an elastic interface can conveniently be characterized in terms of the two dimensionless parameters

$$\beta = \frac{6Bh\eta\omega}{\kappa_S}, \quad \beta_B = 2h\left(\frac{4\eta\omega}{\kappa_B}\right)^{1/3}, \tag{5}$$

where $B = 2/(1 + C)$. Note that both β and $\beta_B^3 \propto \omega$, and can thus be viewed as dimensionless frequencies associated with shear and bending deformation modes, respectively.

The exact Green's functions for a point-force singularity acting close to an elastic interface possessing shear and bending rigidities have recently been calculated by some of us (see, e.g., Refs. [110,113] for details of the derivation). The $\hat{\boldsymbol{e}}$-directed Stokeslet near the elastic interface can be obtained from the tensorial description of the Green's function via

$$\boldsymbol{G}(\boldsymbol{r}, \boldsymbol{r}_0; \hat{\boldsymbol{e}}) = 8\pi\eta\, \boldsymbol{\mathcal{G}}(\boldsymbol{r}, \boldsymbol{r}_0) \cdot \hat{\boldsymbol{e}}. \tag{6}$$

The *frequency-dependent* Green's functions $\boldsymbol{\mathcal{G}}$ associated with a point force exerted at position $\boldsymbol{r}_0$ above an elastic interface can be derived using a standard two-dimensional Fourier-transform technique [118,120] and applying the underlying boundary conditions at the planar surface of reference. Accordingly, the Green's functions can be expressed in terms of convergent infinite integrals over the wave number. Explicit analytical expressions of the components of the Green's functions due to a Stokeslet near an elastic interface are listed for convenience in Appendix A.

C. Multipole expansion

The flow field generated by a microswimmer can be decomposed into a multipole expansion of the solution of the Stokes equations [Eq. (1)] near an elastic interface. Then, the linearity of the Stokes equations permits the description of the far-field flow induced by a microswimmer in terms of a superposition of different singularity solutions [124]. While the leading-order flow field of a driven particle is a force monopole (Stokeslet) field which decays as s^{-1}, force- and torque-free microswimmers typically create a force dipole field in leading order [4,6] which decays as s^{-2}. The next-higher-order singularities are the force quadrupole, source dipole, and rotlet dipole, which all decay as s^{-3}. The Green's functions for higher-order singularities can be obtained as derivatives of the Stokeslet solution [123]. For example, for a force dipole (D),

$$\boldsymbol{G}_{\mathrm{D}}(\boldsymbol{r}, \boldsymbol{r}_0; \hat{\boldsymbol{e}}, \boldsymbol{a}) = (\boldsymbol{a} \cdot \boldsymbol{\nabla}_0)\boldsymbol{G}(\boldsymbol{r}, \boldsymbol{r}_0; \hat{\boldsymbol{e}}), \tag{7}$$

wherein $\boldsymbol{\nabla}_0$ denotes the nabla (gradient) operator taken with respect to the singularity position $\boldsymbol{r}_0$. The force quadrupole (Q) can then be determined from the force dipole as

$$\boldsymbol{G}_{\mathrm{Q}}(\boldsymbol{r}, \boldsymbol{r}_0; \hat{\boldsymbol{e}}, \boldsymbol{a}, \boldsymbol{b}) = (\boldsymbol{b} \cdot \boldsymbol{\nabla}_0)\boldsymbol{G}_{\mathrm{D}}(\boldsymbol{r}, \boldsymbol{r}_0; \hat{\boldsymbol{e}}, \boldsymbol{a}). \tag{8}$$

In addition, we define the source dipole (SD) singularity which can be derived from a singular potential solution satisfying the Laplace equation [124]. It can be expressed in terms of the Stokeslet solution via

$$\boldsymbol{G}_{\mathrm{SD}}(\boldsymbol{r}, \boldsymbol{r}_0; \hat{\boldsymbol{e}}) = -\tfrac{1}{2}\, \boldsymbol{\nabla}_0^2 \boldsymbol{G}(\boldsymbol{r}, \boldsymbol{r}_0; \hat{\boldsymbol{e}}). \tag{9}$$

Further, we define the rotlet dipole (RD) singularity as

$$\boldsymbol{G}_{\mathrm{RD}}(\boldsymbol{r}, \boldsymbol{r}_0; \hat{\boldsymbol{e}}, \boldsymbol{c}) = \boldsymbol{c} \cdot \boldsymbol{\nabla}_0 \boldsymbol{G}_{\mathrm{R}}(\boldsymbol{r}, \boldsymbol{r}_0; \hat{\boldsymbol{e}}), \tag{10}$$

where the Green's function for the rotlet (R) is obtained as

$$\boldsymbol{G}_{\mathrm{R}}(\boldsymbol{r}, \boldsymbol{r}_0; \hat{\boldsymbol{e}}) = \tfrac{1}{2}[\boldsymbol{G}_{\mathrm{D}}(\boldsymbol{r}, \boldsymbol{r}_0; \boldsymbol{b}, \boldsymbol{a}) - \boldsymbol{G}_{\mathrm{D}}(\boldsymbol{r}, \boldsymbol{r}_0; \boldsymbol{a}, \boldsymbol{b})], \tag{11}$$

where $\boldsymbol{a}$ and $\boldsymbol{b}$ are unit vectors with $\boldsymbol{a} \times \boldsymbol{b} = \hat{\boldsymbol{e}}$ ($\times$ denotes the cross product). Note that the rotlet is the leading-order flow field of a force-free particle but where an external torque is applied. The flow field due to a rotlet dipole can further be expanded as a combination of two force quadrupoles as

$$\boldsymbol{G}_{\mathrm{RD}}(\boldsymbol{r}, \boldsymbol{r}_0; \hat{\boldsymbol{e}}, \boldsymbol{c}) = \tfrac{1}{2}[\boldsymbol{G}_{\mathrm{Q}}(\boldsymbol{r}, \boldsymbol{r}_0; \boldsymbol{b}, \boldsymbol{a}, \boldsymbol{c}) - \boldsymbol{G}_{\mathrm{Q}}(\boldsymbol{r}, \boldsymbol{r}_0; \boldsymbol{a}, \boldsymbol{b}, \boldsymbol{c})].$$

Expressions of the higher-order Stokes singularities in an unbounded (infinite) fluid are provided in Appendix B.

In the presence of external forces and torques acting on the microswimmer, the Stokeslet, $\boldsymbol{G}(\boldsymbol{r}, \boldsymbol{r}_0; \hat{\boldsymbol{e}})$, and rotlet $\boldsymbol{G}_{\mathrm{R}}(\boldsymbol{r}, \boldsymbol{r}_0; \hat{\boldsymbol{e}})$, solutions have to be added to our description. Collecting results, the self-generated flow field induced by an axially symmetric microswimmer initially located at position $\boldsymbol{r}_0$ and oriented along the direction of the unit vector $\hat{\boldsymbol{e}}$ can be written up to third order in inverse distance from the swimmer location as

$$\boldsymbol{v}(\boldsymbol{r}) = \boldsymbol{v}_{\mathrm{S}}(\boldsymbol{r}) + \boldsymbol{v}_{\mathrm{R}}(\boldsymbol{r}) + \boldsymbol{v}_{\mathrm{D}}(\boldsymbol{r}) + \boldsymbol{v}_{\mathrm{SD}}(\boldsymbol{r}) + \boldsymbol{v}_{\mathrm{Q}}(\boldsymbol{r}) + \boldsymbol{v}_{\mathrm{RD}}(\boldsymbol{r}), \tag{12}$$

where we have defined the velocities

$$\begin{aligned} \boldsymbol{v}_{\mathrm{S}}(\boldsymbol{r}) &= \alpha_{\mathrm{S}}\, \boldsymbol{G}(\hat{\boldsymbol{e}}), & \boldsymbol{v}_{\mathrm{R}}(\boldsymbol{r}) &= \alpha_{\mathrm{R}}\, \boldsymbol{G}_{\mathrm{R}}(\hat{\boldsymbol{e}}), \\ \boldsymbol{v}_{\mathrm{D}}(\boldsymbol{r}) &= \alpha_{\mathrm{D}}\, \boldsymbol{G}_{\mathrm{D}}(\hat{\boldsymbol{e}}, \hat{\boldsymbol{e}}), & \boldsymbol{v}_{\mathrm{SD}}(\boldsymbol{r}) &= \alpha_{\mathrm{SD}}\, \boldsymbol{G}_{\mathrm{SD}}(\hat{\boldsymbol{e}}), \\ \boldsymbol{v}_{\mathrm{Q}}(\boldsymbol{r}) &= \alpha_{\mathrm{Q}}\, \boldsymbol{G}_{\mathrm{Q}}(\hat{\boldsymbol{e}}, \hat{\boldsymbol{e}}, \hat{\boldsymbol{e}}), & \boldsymbol{v}_{\mathrm{RD}}(\boldsymbol{r}) &= \alpha_{\mathrm{RD}}\, \boldsymbol{G}_{\mathrm{RD}}(\hat{\boldsymbol{e}}, \hat{\boldsymbol{e}}), \end{aligned}$$

not writing the dependence of the flow singularities on $\boldsymbol{r}$ and $\boldsymbol{r}_0$ explicitly any longer.

The Stokeslet coefficient α_{S} has dimension of $(\text{length})^2(\text{time})^{-1}$, the rotlet coefficient α_{R} and dipolar coefficient α_{D} have dimension of $(\text{length})^3(\text{time})^{-1}$, whereas the remaining higher-order multipole coefficients α_{SD}, α_{Q}, and α_{RD} have dimensions of $(\text{length})^4(\text{time})^{-1}$. The magnitude and sign of these coefficients depend on the propulsion mechanism as well as on the swimmer shape. For a valuable discussion on the physical meaning and interpretation of these singularities, we refer the reader to recent works by Spagnolie and Lauga [124] and Mathijssen *et al.* [145].

III. SWIMMING NEAR AN ELASTIC INTERFACE

In the presence of confining boundaries, the swimming direction $\hat{\boldsymbol{e}}$ of the microswimmer and its distance h from the boundary dictate the hydrodynamic flows, as sketched in Fig. 1. The orientation $\hat{\boldsymbol{e}}$ is described by the unit vector

$$\hat{\boldsymbol{e}} = (\cos\theta\cos\varphi, \cos\theta\sin\varphi, \sin\theta), \tag{13}$$

where, again, θ denotes the pitch angle (such that $\theta = 0$ corresponds to a swimmer that is aligned parallel to the interface), and φ is the azimuthal orientation that we, without loss of generality, set initially to zero.

The total self-generated flow field of the swimmer expressed by Eq. (12) can be decomposed into terms of the bulk contribution $\boldsymbol{v}^\infty$ and a correction $\boldsymbol{v}^*$ that is required to satisfy the boundary conditions at the elastic interface:

$$\boldsymbol{v} = \boldsymbol{v}^\infty + \boldsymbol{v}^*. \tag{14}$$

The latter encompasses the Stokeslet contribution to the flow field that we have determined in previous works [110,146] in addition to the higher-order singularity solutions that we calculate here. It is worth emphasizing that $\boldsymbol{v}_\infty$ is the sum of the bulk flow fields of the different multipoles such that

$$\boldsymbol{v}^\infty = \lim_{\beta, \beta_{\mathrm{B}} \to \infty} \boldsymbol{v}. \tag{15}$$

The induced translational and rotational velocities due to the fluid-mediated hydrodynamic interactions between the elastic interface and a microswimmer of prolate ellipsoidal shape located at position $\boldsymbol{r}_0$ are provided by Faxén's laws [126] as

$$\boldsymbol{v}^{\mathrm{HI}} = \boldsymbol{v}^*(\boldsymbol{r})|_{\boldsymbol{r}=\boldsymbol{r}_0}, \tag{16a}$$

$$\boldsymbol{\Omega}^{\mathrm{HI}} = \tfrac{1}{2}\nabla \times \boldsymbol{v}^*(\boldsymbol{r}) + \Gamma\hat{\boldsymbol{e}} \times (\boldsymbol{E}^*(\boldsymbol{r}) \cdot \hat{\boldsymbol{e}})|_{\boldsymbol{r}=\boldsymbol{r}_0}. \tag{16b}$$

These expressions have been restricted to leading order in swimmer length c. Here, $\boldsymbol{E}^* = [\nabla \boldsymbol{v}^* + (\nabla \boldsymbol{v}^*)^{\mathrm{T}}]/2$ is the rate-of-strain tensor associated with the reflected flow, with T denoting the transpose. Further, $\Gamma = (\gamma^2 - 1)/(\gamma^2 + 1) \in [0, 1)$ is a shape factor (also known as the Bretherton constant [147,148]) that depends on the aspect ratio γ of the prolate spheroidal microswimmer, defined as the ratio of major to minor semiaxes, i.e., $\gamma = c/a \geqslant 1$. It vanishes for a sphere and approaches 1 for needlelike particles of large aspect ratio. Higher-order correction terms in Γ to the induced hydrodynamic fields can be obtained using the multipole method (see, e.g., Ref. [146]).

Due to the linearity of the Stokes equations [Eqs. (1)] we can consider the effect of each higher-order singularity on the swimming behavior independently. Thus, in the following we provide solutions for the translational and rotational velocities, $\boldsymbol{v}^{\mathrm{HI}}$ and $\boldsymbol{\Omega}^{\mathrm{HI}}$, induced by fluid-mediated hydrodynamic couplings of the individual contributions with the nearby elastic boundary.

Remarkably, the total velocities due to hydrodynamic interactions with an elastic interface endowed simultaneously with both shear and bending resistances can be written as a superposition of the velocities induced by hydrodynamic interactions with an interface of pure shear ($\beta_{\mathrm{B}} \to \infty$) and pure bending ($\beta \to \infty$) resistances. Accordingly, the total wall-induced linear and angular velocities can be obtained by evaluating both contributions independently:

$$\boldsymbol{v}^{\mathrm{HI}} = \boldsymbol{v}^{\mathrm{HI}}|_{\mathrm{S}} + \boldsymbol{v}^{\mathrm{HI}}|_{\mathrm{B}}, \tag{17a}$$

$$\boldsymbol{\Omega}^{\mathrm{HI}} = \boldsymbol{\Omega}^{\mathrm{HI}}|_{\mathrm{S}} + \boldsymbol{\Omega}^{\mathrm{HI}}|_{\mathrm{B}}, \tag{17b}$$

where the subscripts S and B stand for shear and bending, respectively. However, it is worth mentioning that this is only true for a planar elastic interface. For curved interfaces, a coupling between shear and bending deformation modes exists [149–153].

Near a no-slip wall, the induced hydrodynamic interactions of the multipole flow fields created by a microswimmer located at a given position and orientation are independent of time [124] (assuming that the strengths of the singularities are constant). This is in contrast to an elastic interface where memory effects can lead to time-dependent contributions $\boldsymbol{v}^{\mathrm{HI}}(t)$ and $\boldsymbol{\Omega}^{\mathrm{HI}}(t)$. One way to realize such a time dependence is to assume that the microswimmer is initially at rest with a given orientation (θ, φ) at a distance h from the interface and suddenly starts to swim and sets the surrounding fluid into motion at time $t = 0$. However, we do not allow the microswimmer to actually *move* towards the interface but its position and orientation are kept fixed by applying just the right external forces $\boldsymbol{F}^{\mathrm{ext}}$ and torques $\boldsymbol{T}^{\mathrm{ext}}$, e.g., via optical traps, aligning magnetic fields, or other micromanipulation techniques. Denoting by v_0 the bulk swimming speed, i.e., in the absence of the confining interface, the swimming velocities and rotation rates are related to the external forces and torques required to trap the swimmer near the interface via

$$\begin{pmatrix} v_0\hat{\boldsymbol{e}} + \boldsymbol{v}^{\mathrm{HI}}(t) \\ \boldsymbol{\Omega}^{\mathrm{HI}}(t) \end{pmatrix} + \boldsymbol{\mu} \cdot \begin{pmatrix} \boldsymbol{F}^{\mathrm{ext}}(t) \\ \boldsymbol{T}^{\mathrm{ext}}(t) \end{pmatrix} = \boldsymbol{0}. \tag{18}$$

Note, the forces and torques are zero for $t < 0$, but finite and time dependent for $t \geqslant 0$, when the flow fields created by the microswimmers interact with the elastic interface. Here $\boldsymbol{\mu}$ is the position- and orientation-dependent hydrodynamic grand mobility tensor of a spheroid near an elastic interface [146]. We have neglected thermal fluctuations and all possible steric interactions with the interface. We were able to calculate $\boldsymbol{v}^{\mathrm{HI}}(t)$ and $\boldsymbol{\Omega}^{\mathrm{HI}}(t)$ for all considered multipole flows. The solutions for $\boldsymbol{v}^{\mathrm{HI}}(t)$ are shown in Tables VI and VII. Similar expressions exist for $\boldsymbol{\Omega}^{\mathrm{HI}}(t)$ but they are not shown here because of their complexity and lengthiness.

In the following we discuss the different contributions stemming from the different multipoles. Before doing so, we present typical numbers which we used to produce the results shown below. The shear and bending properties of the elastic surface entail a characteristic time scale of shear as $T_{\mathrm{S}} = 6\eta h/(B\kappa_{\mathrm{S}})$, in addition to a characteristic time scale of bending as $T_{\mathrm{B}} = 8\eta h^3/\kappa_{\mathrm{B}}$ [110]. Thus, we define the scaled times $\tau_{\mathrm{S}} = t/T_{\mathrm{S}}$ and $\tau_{\mathrm{B}} = t/T_{\mathrm{B}}$ associated with shear and bending deformation modes, respectively. Note that, for $h = [3\kappa_{\mathrm{B}}/(4B\kappa_{\mathrm{S}})]^{1/2}$, it follows that $T_{\mathrm{S}} = T_{\mathrm{B}}$. This corresponds to the situation in which both shear and bending equally manifest themselves in the system at intermediate time scales [111]. In typical situations [128], elastic red blood cells have a shear modulus $\kappa_{\mathrm{S}} = 5 \times 10^{-6}$ N/m, a Skalak ratio $C = 100$, and a bending modulus $\kappa_{\mathrm{B}} = 2 \times 10^{-19}$ N m. By considering a dynamic viscosity of the surrounding Newtonian viscous fluid $\eta = 1.2 \times 10^{-3}$ Pa s, as well as a micron-sized swimmer of size $a = 10^{-6}$ m located above the interface at $h = 5a$, it follows that $T_{\mathrm{S}} \simeq 0.36$ s and $T_{\mathrm{B}} = 6$ s. Therefore, at later times, bending effects are expected to manifest themselves in a more pronounced way than shear. For the results presented below, we use $\tau := \tau_{\mathrm{S}} = 16\tau_{\mathrm{B}}$ as the scaled time of the system.

We distinguish contributions relevant for force- and torque-free swimming and contributions stemming from external forcing, where particular focus lies on a trapped microswimmer in the vicinity of an elastic interface.

A. Force- and torque-free contribution

Here we discuss the swimming behavior of an active agent near an elastic boundary by following the theoretical framework discussed in Sec. II. We consider different higher-order singularities that describe features of the swimming motion of a variety of active agents. In addition to the leading-order far field of a microswimmer in terms of a force dipole ($1/s^2$), we consider further details of the propulsion mechanisms that contribute to the flow field with the order of $1/s^3$. These include, for example, contributions of the finite size cell body, the anisotropy in the swimming mechanism, and the rotation or counter-rotation of body parts during swimming. Yet, the importance of the contribution of each of these singularities depends strongly on the geometry of the active agent, its swimming mechanism, and its distance from the elastic interface.

1. Force dipole

The flow field induced by a force dipole, $\boldsymbol{v}_\mathrm{D}(\boldsymbol{r}) = \alpha_\mathrm{D}\, \boldsymbol{G}_\mathrm{D}(\hat{\boldsymbol{e}}, \hat{\boldsymbol{e}})$, is the leading contribution to describe the hydrodynamics of many microswimmers, which are net force free by definition [27]. The sign of the dipolar coefficient α_D distinguishes between *pusher* ($\alpha_\mathrm{D} > 0$) and *puller* ($\alpha_\mathrm{D} < 0$) microswimmers. Some bacterial microorganisms, such as *E. coli*, exploit (bundles of) helical filaments called flagella for their propulsion, the rotation of which causes the entire bacterium to move forward in a corkscrewlike motion [154–156]. Here, the translation-rotation coupling of the hydrodynamic friction of the flagellum yields a net propulsion of the swimmer. Since these swimmers push out the fluid along their swimming axis, they are referred to as pushers. Another broad class of microswimmers, including, for example, the algae *Chlamydomonas reinhardtii* [157], pull in (averaged over one whole swimming stroke) the fluid along the axis parallel to their swimming direction, and are thus classified as pullers.

Both pushers and pullers may conveniently be modeled, e.g., via minimal models based on the insertion of force centers that co-move with the body of the swimmer [158–162], or as squirmers [163–165]. The latter are driven by prescribed tangential velocities at their (spherical or ellipsoidal) surfaces and were introduced to model microorganisms that self-propel by the beating of cilia covering their bodies [31–33,166]. The squirmer model has been previously used to address, e.g., the hydrodynamic interaction between two swimmers [167,168], the influence of an imposed external flow field on the swimming behavior [169,170], or low-Reynolds-number locomotion in complex fluids [171–174].

We now return to the mathematical problem and remark that a tilted force dipole (that is directed along $\hat{\boldsymbol{e}}$) can be expressed in terms of force dipoles aligned parallel and perpendicular to the elastic interface as [85]

$$\boldsymbol{G}_\mathrm{D}(\hat{\boldsymbol{e}}, \hat{\boldsymbol{e}}) = \boldsymbol{G}_\mathrm{D}(\hat{\boldsymbol{e}}_x, \hat{\boldsymbol{e}}_x)\cos^2\theta + \boldsymbol{G}_\mathrm{D}(\hat{\boldsymbol{e}}_z, \hat{\boldsymbol{e}}_z)\sin^2\theta + \boldsymbol{G}_\mathrm{SS}(\hat{\boldsymbol{e}}_x, \hat{\boldsymbol{e}}_z)\sin(2\theta), \tag{19}$$

where $\boldsymbol{G}_\mathrm{SS}$ is the symmetric part of the force dipole, commonly referred to as stresslet, $\boldsymbol{G}_\mathrm{SS}(\boldsymbol{a}, \boldsymbol{b}) = [\boldsymbol{G}_\mathrm{D}(\boldsymbol{b}, \boldsymbol{a}) + \boldsymbol{G}_\mathrm{D}(\boldsymbol{a}, \boldsymbol{b})]/2$. By inserting the Stokeslet solution (see Appendix A) into Eq. (7), the self-generated dipolar flow field $\boldsymbol{v}_\mathrm{D}(\boldsymbol{r})$ can be evaluated and expressed in terms of infinite integrals over the wave number. The frequency-dependent components of the induced translational, $\boldsymbol{v}^\mathrm{HI}$, and rotational, $\boldsymbol{\Omega}^\mathrm{HI}$, velocities, of the microswimmer resulting from dipolar interactions with the elastic interface, as given by Eq. (16), are listed in integral form in Table IV of Appendix C. The velocities in Fourier space depend on the dipolar coefficient α_D, the distance h from the elastic interface, the orientation θ of the swimmer with respect to the interface, as well as the dimensionless frequencies β and β_B, reflecting shear and bending contributions, respectively.

In Figs. 2(a)–2(c), we present the time evolution of the induced swimming velocities and rotation rates due to dipolar hydrodynamic interactions with a planar elastic interface. The latter has only energetic resistance toward shear (green), only energetic resistance toward bending (red), or simultaneously possesses both shear and bending resistances (black). Here, we consider a spheroidal swimmer with an aspect ratio $\gamma = 4$ (corresponding to a shape factor $\Gamma = 15/17$), as measured experimentally for the bacterium *Bacillus subtilis* [175]. The swimmer is inclined by a pitch angle $\theta = \pi/6$ with respect to the horizontal direction. Results are rendered dimensionless by scaling with the corresponding hard wall limits listed in Table I. As already mentioned, the total swimming velocity near a planar interface with both shear and bending resistance is obtained by linearly superimposing the individual contributions stemming from each deformation mode.

The translational and rotational velocities of the microswimmer induced by the presence of the elastic interface amount to small values at short times ($\tau \ll 1$), because the interface is still relatively undeformed and therefore hardly imposes any elastic resistance toward the flow field induced by the microswimmer. Consequently, the system exhibits initially a "bulklike" behavior. For increasing times, such that $\tau \simeq 1$, the presence of the elastic interface becomes more noticeable. The induced swimming velocities monotonically increase in magnitude before reaching at long times ($\tau \gg 1$) the steady limits. These correspond to the velocities induced near a no-slip wall and are independent of the membrane shear and bending properties. Therefore, the elasticity of the boundary only contributes at intermediate time scales to the temporal changes of the swimming behavior, whereas, in the steady state, the swimmer essentially experiences the response of the fully deformed interface that does not change its overall shape of deformation any longer. It is worth emphasizing that the hard wall limits are reached (if and) only if the interface is simultaneously endowed with resistance toward shear and bending. Interestingly, at intermediate time scales, the shear related contribution to the rotational velocity [Fig. 2(c)] exceeds to a certain extent its steady value.

In the steady limit, the sign and magnitude of the swimming velocities are strongly dependent on the dipolar coefficient α_D as well as on the pitch angle θ. In this situation, because $v_{z\mathrm{D}}^\mathrm{HI} \propto -\alpha_\mathrm{D}(3\cos^2\theta - 2)$ for all interface types (see Table I), it follows that, for a small pitch angle, such that $|\theta| < \arccos(\sqrt{6}/3)$, a pusher-type microswimmer ($\alpha_\mathrm{D} > 0$) tends to be attracted toward the interface, while a puller ($\alpha_\mathrm{D} < 0$) tends to be repelled away from it. This behavior is purely hydrodynamic in origin as has been discussed earlier by Lauga and collaborators for the case of a hard wall [124,176]. In particular, the hard wall limits are predominately determined by the bending related contribution. This implies that, for the dipolar hydrodynamic interactions, the effect due to the bending rigidity is more pronounced than that due to shear. In addition, since $\Omega_{y\mathrm{D}}^\mathrm{HI} \propto \alpha_\mathrm{D}\sin(2\theta)$, a pusher-type swimmer tends to be oriented along the parallel direction ($\theta = 0$ is a stable fixed point), while the interface tends to align a puller in the direction normal to the interface ($\theta = \pm\pi/2$). Hence, in the absence of external trapping, a puller will tend to swim either toward or away from the interface, depending on whether it is initially pitched toward ($\theta < 0$) or away from the interface ($\theta > 0$). Particularly, the extensional flow and the shear related contribution to the rotation rate vanish for a sphere ($\Gamma = 0$). In such a case, the reorientation

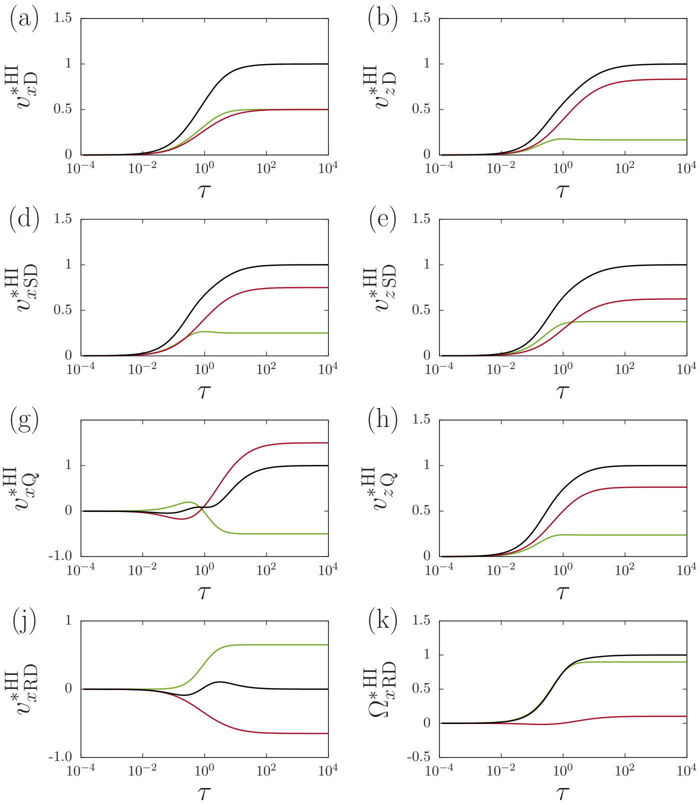

FIG. 2. Evolution of the scaled induced translational and rotational swimming velocities associated with a force dipole (a–c), source dipole (d–f), force quadrupole (g–i), and rotlet dipole (j–l), resulting from hydrodynamic interactions with a planar elastic interface of pure shear (green), pure bending (red), or both shear and bending (black) resistances. The swimmer has an aspect ratio $\gamma = 4$ and is oriented by a pitch angle $\theta = \pi/6$ relative to the horizontal direction. Here, the velocities are scaled by the corresponding hard wall limits listed in Table I, except that the x component of the rotlet dipolar contribution shown in panel (j) is scaled by $\alpha_{\mathrm{RD}}/(8h^4)$ (because this component vanishes in the steady limit). The scaled time is $\tau := \tau_{\mathrm{S}} = 16\tau_{\mathrm{B}}$.

of the swimmer is solely dictated by the interface bending properties.

In addition to the leading-order contribution of a force dipole, next-higher-order singularity solutions are useful to describe details of the propulsion mechanism of an active agent. The time-dependent translational and rotational velocities induced by higher-order singularities close to the elastic surface for the start-up motion from static condition are presented in Table VI of Appendix C, and the steady limits are shown in Table I.

2. *Source dipole*

The far-field hydrodynamic flows induced by the finite size of a swimming object can be described by a *source dipole*, $\boldsymbol{v}_{\mathrm{SD}}(\boldsymbol{r}) = \alpha_{\mathrm{SD}}\boldsymbol{G}_{\mathrm{SD}}(\hat{\boldsymbol{e}})$. For the type of microswimmers that propel themselves by means of activity on their surfaces, as it is the case for many active colloidal particles [37,38,177] or ciliated microorganisms [28,34], a source dipolar coefficient $\alpha_{\mathrm{SD}} > 0$ is expected. In contrast to that, it is expected that $\alpha_{\mathrm{SD}} < 0$ for nonciliated but flagellated microswimmers [145].

We now consider the scenario of a microswimmer initially at rest before starting to pump the fluid, in a way analogous to what we have introduced in the previous discussion regarding the force dipole contribution. The respective scaled induced translational and rotational velocities resulting from source dipolar hydrodynamic interactions exhibit a similar logistic sigmoid curve varying between 0 and 1 [see Figs. 2(d)–2(f)]. Similar as for the force dipole contribution, at long times the corresponding values of a no-slip wall are approached. The bending related contribution to the swimming velocities is found to be once again more pronounced than that due to shear resistance.

For all types of interface, the induced normal swimming velocity in the steady limit can be cast into the form $v_{z\mathrm{SD}}^{\mathrm{HI}} \propto -\alpha_{\mathrm{SD}} \sin\theta$. Therefore, the swimmer tends to be attracted to the interface for $\alpha_{\mathrm{SD}} > 0$ when it is oriented toward it ($\theta < 0$) and tends to be repelled from the interface otherwise.

TABLE I. Expressions of the induced translational and rotational swimming velocities resulting from force dipolar, source dipolar, force quadrupolar, and rotlet dipolar hydrodynamic interactions with a planar elastic interface in the steady limit. Here, $n = 2$ for the force dipole and $n = 3$ for the source dipole and force quadrupole. The swimming velocities near a no-slip hard wall are obtained by linear superposition of the shear- and bending related contributions.

Interface type	$h^n v_x^{\mathrm{HI}}$	$h^n v_z^{\mathrm{HI}}$	$h^{n+1} \Omega_y^{\mathrm{HI}}$
		Force dipole	
Shear	$\frac{3\alpha_\mathrm{D}}{16} \sin(2\theta)$	$-\frac{\alpha_\mathrm{D}}{16}(3\cos^2\theta - 2)$	$\frac{3\alpha_\mathrm{D}}{64}\, \Gamma \sin(2\theta)\cos^2\theta$
Bending	$\frac{3\alpha_\mathrm{D}}{16} \sin(2\theta)$	$-\frac{5\alpha_\mathrm{D}}{16}(3\cos^2\theta - 2)$	$\frac{3\alpha_\mathrm{D}}{64} \sin(2\theta)[4 + \Gamma(4 - 3\cos^2\theta)]$
Hard wall	$\frac{3\alpha_\mathrm{D}}{8} \sin(2\theta)$	$-\frac{3\alpha_\mathrm{D}}{8}(3\cos^2\theta - 2)$	$\frac{3\alpha_\mathrm{D}}{32} \sin(2\theta)[2 + \Gamma(2 - \cos^2\theta)]$
		Source dipole	
Shear	$-\frac{\alpha_\mathrm{SD}}{16} \cos\theta$	$-\frac{3\alpha_\mathrm{SD}}{8} \sin\theta$	$-\frac{3\alpha_\mathrm{SD}}{16} \cos\theta[1 + \Gamma(2 - \cos^2\theta)]$
Bending	$-\frac{3\alpha_\mathrm{SD}}{16} \cos\theta$	$-\frac{5\alpha_\mathrm{SD}}{8} \sin\theta$	$-\frac{3\alpha_\mathrm{SD}}{16} \cos\theta[1 + 2\Gamma(2 - \cos^2\theta)]$
Hard wall	$-\frac{\alpha_\mathrm{SD}}{4} \cos\theta$	$-\alpha_\mathrm{SD} \sin\theta$	$-\frac{3\alpha_\mathrm{SD}}{16} \cos\theta[2 + 3\Gamma(2 - \cos^2\theta)]$
		Force quadrupole	
Shear	$\frac{\alpha_\mathrm{Q}}{32} \cos\theta(21\cos^2\theta - 16)$	$\frac{3\alpha_\mathrm{Q}}{8} \sin\theta\cos^2\theta$	$\frac{3\alpha_\mathrm{Q}}{64} \cos\theta[3\Gamma\cos^4\theta + 2(1 - 2\Gamma)\cos^2\theta + 8\Gamma]$
Bending	$\frac{3\alpha_\mathrm{Q}}{32} \cos\theta(11\cos^2\theta - 8)$	$\frac{\alpha_\mathrm{Q}}{8} \sin\theta(15\cos^2\theta - 4)$	$\frac{3\alpha_\mathrm{Q}}{64} \cos\theta[-9\Gamma\cos^4\theta + 2(11 + 8\Gamma)\cos^2\theta + 8(\Gamma - 2)]$
Hard wall	$\frac{\alpha_\mathrm{Q}}{16} \cos\theta(27\cos^2\theta - 20)$	$\frac{\alpha_\mathrm{Q}}{4} \sin\theta(9\cos^2\theta - 2)$	$\frac{3\alpha_\mathrm{Q}}{32} \cos\theta[-3\Gamma\cos^4\theta + 6(\Gamma + 2)\cos^2\theta + 8(\Gamma - 1)]$
Interface type	$h^3 v_x^{\mathrm{HI}}$	$h^4 \Omega_x^{\mathrm{HI}}$	$h^4 \Omega_z^{\mathrm{HI}}$
		Rotlet dipole	
Shear	$\frac{3\alpha_\mathrm{RD}}{32} \sin(2\theta)$	$\frac{3\alpha_\mathrm{RD}}{16} \sin(2\theta)$	$-\frac{3\alpha_\mathrm{RD}}{32}(3\cos^2\theta - 2)$
Bending	$-\frac{3\alpha_\mathrm{RD}}{32} \sin(2\theta)$	$\frac{3\alpha_\mathrm{RD}}{64} \sin(2\theta)[2 + \Gamma(3\cos^2\theta - 4)]$	$\frac{3\alpha_\mathrm{RD}}{32}\, \Gamma\cos^2\theta(4 - 3\cos^2\theta)$
Hard wall	0	$\frac{3\alpha_\mathrm{RD}}{64} \sin(2\theta)[6 + \Gamma(3\cos^2\theta - 4)]$	$-\frac{3\alpha_\mathrm{RD}}{32}[3\Gamma\cos^4\theta + (3 - 4\Gamma)\cos^2\theta - 2]$

Moreover, since $\Omega_{y\mathrm{SD}}^{\mathrm{HI}} \propto -\alpha_\mathrm{SD}\cos\theta$ it follows that $\theta = \pi/2$ is a stable fixed point for $\alpha_\mathrm{SD} > 0$, thus favoring the escape of the swimmer from the interface in the absence of external trapping. In contrast to that, $\theta = -\pi/2$ is a stable fixed point for $\alpha_\mathrm{SD} < 0$, leading to hydrodynamic trapping of the swimmer near the interface.

3. Force quadrupole

The flow fields generated by a fore-aft asymmetry of the propulsion mechanism can be captured in terms of a *force quadrupole* $\boldsymbol{v}_\mathrm{Q}(\boldsymbol{r}) = \alpha_\mathrm{Q}\boldsymbol{G}_\mathrm{Q}(\hat{\boldsymbol{e}}, \hat{\boldsymbol{e}}, \hat{\boldsymbol{e}})$. Such contributions play a pivotal role for flagellated microorganisms, such as bacteria [178] and sperms [179], where an asymmetry between the length of the forward-pushing cell and the flagella impacts the propulsive force distribution along the agent and thereby the hydrodynamic flows. Resulting effects have been found to induce correlated motion between adjacently swimming bacteria [178]. It is expected that $\alpha_\mathrm{Q} > 0$ for microswimmers with large cell bodies and short flagella, while $\alpha_\mathrm{Q} < 0$ holds for long-flagellated microorganisms with small cell bodies [124,145].

Interestingly, the translational velocity $v_{x\mathrm{Q}}^{\mathrm{HI}}$ induced by a force quadrupole parallel to an elastic surface displays at intermediate time scales a weakly nonmonotonic behavior before reaching the steady state [see Fig. 2(g)]. In particular, the velocity induced by a surface with pure shear resistance displays the opposite effect to the one induced by a surface with bending resistance at long times considering the present set of parameters. This implies that, e.g., if bending resistance increases the swimming velocity tangent to the interface, then shear resistance decreases it and vice versa. The induced translational velocity perpendicular to the elastic boundary and the rotational velocity quasimonotonically increase in magnitude over time as resulting from adding both shear and bending contributions [see Figs. 2(h) and 2(i)]. Notably, the bending effect is once again more pronounced than the one associated with shear. In the steady state, the translational and rotational velocities approach those induced by a rigid wall, as has been observed for the other higher-order singularity solutions presented above.

Depending on the types of interface, the force quadrupole coefficient, and the pitch angle, quadrupolar hydrodynamic interactions in the steady limit may lead to attraction or repulsion of swimming microorganisms in a complex way. Considering an interface with only energetic resistance toward shear, we find that $v_{z\mathrm{Q}}^{\mathrm{HI}} \propto \alpha_\mathrm{Q}\sin\theta$. Thus, the swimmer tends to be repelled from the interface when α_Q and θ have both the same sign, and tends to be attracted toward the interface otherwise. An analogous discussion holds as well for an interface with only energetic resistance toward bending, or for an interface with both shear and bending deformation modes, provided that $|\theta| < \arccos(2\sqrt{15}/15)$ in the former and $|\theta| < \arccos(\sqrt{2}/3)$ in the latter case.

Next, considering an interface with energetic resistance only toward shear, the rotation rate in the steady state $\Omega_{y\mathrm{Q}}^{\mathrm{HI}} \propto \alpha_\mathrm{Q}\cos\theta$. Thus, the swimmer in the absence of external trapping tends to rotate toward the interface when $\alpha_\mathrm{Q} > 0$, and away from the interface when $\alpha_Q < 0$. For an elastic interface possessing pure bending resistance, the swimmer may also assume in the steady state an oblique alignment along a pitch angle $\theta = \pm\theta_\Gamma$, where

$$\theta_\Gamma = \arccos\left(\frac{1}{3}\sqrt{8 + \frac{11}{\Gamma} - \sqrt{136 + \frac{32}{\Gamma} + \frac{121}{\Gamma^2}}}\right).$$

Consequently, for $\alpha_Q > 0$, force quadrupolar hydrodynamic interactions tend to orient the swimmer along $\theta = -\theta_\Gamma$ when $\theta < \theta_\Gamma$, and along $\theta = \pi/2$ otherwise. In contrast to that, for $\alpha_Q < 0$, the swimmer tends to be reoriented toward $\theta = \theta_\Gamma$ when $\theta > -\theta_\Gamma$, and along $\theta = -\pi/2$ otherwise. An analogous discussion holds when the interface is endowed with both shear and bending resistances in the steady limit (hard wall), where the oblique alignment in this situation is found to be along

$$\theta_\Gamma = \arccos\left(\sqrt{1 + \frac{2}{\Gamma} - \sqrt{\frac{11}{3} + \frac{4}{3\Gamma} + \frac{4}{\Gamma^2}}}\right).$$

4. Rotlet dipole

In addition, the flow field produced by flagellated microorganisms can be altered by rotation of their body parts, such as the rotation of their flagella bundle and the counter-rotation of the cell body in *E. coli* bacteria [84]. The induced flow far field can be included at lowest order in terms of a *rotlet dipole*, $\boldsymbol{v}_{\mathrm{RD}}(\boldsymbol{r}) = \alpha_{\mathrm{RD}}\, \boldsymbol{G}_{\mathrm{RD}}(\hat{\boldsymbol{e}}, \hat{\boldsymbol{e}})$. A tilted rotlet dipole can conveniently be expanded as a combination of rotlet dipoles orientated parallel and perpendicular to the interface as

$$\begin{aligned}\boldsymbol{G}_{\mathrm{RD}}(\hat{\boldsymbol{e}}, \hat{\boldsymbol{e}}) &= \boldsymbol{G}_{\mathrm{RD}}(\hat{\boldsymbol{e}}_x, \hat{\boldsymbol{e}}_x)\cos^2\theta + \boldsymbol{G}_{\mathrm{RD}}(\hat{\boldsymbol{e}}_z, \hat{\boldsymbol{e}}_z)\sin^2\theta \\ &\quad + \boldsymbol{G}_{\mathrm{RR}}(\hat{\boldsymbol{e}}_x, \hat{\boldsymbol{e}}_z)\sin(2\theta),\end{aligned} \tag{20}$$

where $\boldsymbol{G}_{\mathrm{RR}}(\boldsymbol{a}, \boldsymbol{b}) = [\boldsymbol{G}_{\mathrm{RD}}(\boldsymbol{a}, \boldsymbol{b}) + \boldsymbol{G}_{\mathrm{RD}}(\boldsymbol{b}, \boldsymbol{a})]/2$ denotes the symmetric part of the rotlet dipole. Similar to the force quadrupole contribution, the induced swimming velocity parallel to the elastic surface displays a nonmonotonic behavior before approaching zero at long times [see Fig. 2(j)]. In addition, the shear- and bending related parts may have opposite contributions to the overall translational velocity tangent to the interface. At long times, again the velocities of a microswimmer induced by a rigid, no-slip wall are recovered.

Interestingly, the rotation rate around the swimmer body is found to be shear dominated where bending does not play a significant role [Fig. 2(k)]. Moreover, the rotlet-dipolar hydrodynamic interactions induce a nonvanishing rotation rate about an axis perpendicular to the interface [see Fig. 2(l)]. This naturally leads in the absence of external trapping to an overall "swimming in circles," as has been previously reported for *E. coli* near walls [84,180] and explained via corresponding theoretical studies that include phenomenological representations of the rotating flagella [81,181]. As this component vanishes for the other singularities discussed above, we thus expect the introduction of a rotlet dipole to be the simplest possible hydrodynamic modeling of this circling behavior near surfaces. Remarkably, this rotation rate is independent of the shape factor Γ in the shear related part but vanishes for a sphere ($\Gamma = 0$) in the bending related part. Considering a swimmer that is aligned parallel to the interface ($\theta = 0$) in the steady limit, we obtain

$$\Omega_{z\mathrm{RD}}^{\mathrm{HI}}\big|_{\mathrm{S}} = -\frac{3\alpha_{\mathrm{RD}}}{32h^4}, \tag{21a}$$

$$\Omega_{z\mathrm{RD}}^{\mathrm{HI}}\big|_{\mathrm{B}} = \frac{3\alpha_{\mathrm{RD}}}{32h^4}\,\Gamma, \tag{21b}$$

$$\Omega_{z\mathrm{RD}}^{\mathrm{HI}}\big|_{\mathrm{S+B}} = -\frac{3\alpha_{\mathrm{RD}}}{32h^4}(1 - \Gamma). \tag{21c}$$

Therefore, assuming that $\alpha_{\mathrm{RD}} > 0$, circular motion is expected to be clockwise (when viewed from top) near an interface with pure shear or with both shear and bending rigidities [Eqs. (21a) and (21c)], and counterclockwise near an interface with pure bending [Eq. (21b)]. This is in agreement with the behavior observed for a torque-free doublet of counter-rotating spheres around its center near an elastic interface [182]. It is worth mentioning that, in the steady limit, the system behavior near an interface with pure bending resistance is analogous to that near a flat fluid-fluid interface separating two immiscible fluids with the same viscosity contrast.

B. Contributions due to external forces and torques

Nature offers a plethora of external stimuli and forces that impact the swimming motion of active agents. Examples include gravitational fields [183–186]. The far-field hydrodynamics of externally trapped self-propelled particles near elastic boundaries can readily be captured in terms of a Stokeslet and rotlet solution to the Stokes equation. The corresponding translational and rotational velocities as functions of time as well as the steady limits are presented in Tables II and VI.

1. Stokeslet

In the presence of an external force, the *Stokeslet* singularity can be used to capture the associated hydrodynamic flow [157] and calculate the induced velocity of the microswimmer as $\boldsymbol{v}_{\mathrm{S}}(\boldsymbol{r}) = \alpha_{\mathrm{S}}\, \boldsymbol{G}(\hat{\boldsymbol{e}})$. Similar as before, a tilted Stokeslet can be decomposed into a superposition of Stokeslets directed parallel and perpendicular to the interface as $\boldsymbol{G}(\hat{\boldsymbol{e}}) = \boldsymbol{G}(\hat{\boldsymbol{e}}_x)\cos\theta + \boldsymbol{G}(\hat{\boldsymbol{e}}_y)\sin\theta$. In contrast to the higher-order singularities used to model force-free swimming, the Stokeslet introduces a far field of the fluid flow that decays as $1/h$ and thus represents the leading-order contribution.

In Figs. 3(a)–3(c), we present the variations of the induced swimming velocities due to a Stokeslet singularity acting near a planar elastic interface with pure shear (green), pure bending (red), or both shear and bending deformation modes (black), using the same parameters as in Fig. 2. While resistance toward shear manifests itself in a more pronounced way for the translational motion parallel to the interface, the effect of bending is dominant for the translational motion normal to the interface and for the rotation rate.

In the remainder of our discussion, we assume that the Stokeslet coefficient $\alpha_{\mathrm{S}} > 0$. Correspondingly, the swimmer in the steady state tends to be attracted to the interface when $\theta > 0$, and repelled from it when $\theta < 0$. Near an interface with resistance only to shear such that $\Gamma \leqslant 2/3$ (or $\gamma \leqslant \sqrt{5}$), it follows that $\Omega_{y\mathrm{S}}^{\mathrm{HI}} \propto \cos\theta$. Therefore, the swimmer tends to be reoriented toward the interface ($\theta = -\pi/2$). In contrast

TABLE II. Expressions of the induced translational and rotational swimming velocities resulting from Stokeslet and rotlet near an elastic interface in the quasisteady limit of vanishing frequency, or equivalently for $t \to \infty$. The swimming velocities near a no-slip hard wall are obtained by linear superposition of the shear- and bending related contributions in the vanishing-frequency limit.

Interface type	hv_x^{HI}	hv_z^{HI}	$h^2\Omega_y^{\mathrm{HI}}$
		Stokeslet	
Shear	$-\frac{5\alpha_S}{8}\cos\theta$	$-\frac{\alpha_S}{4}\sin\theta$	$\frac{\alpha_S}{16}\cos\theta(2-3\Gamma\cos^2\theta)$
Bending	$-\frac{\alpha_S}{8}\cos\theta$	$-\frac{5\alpha_S}{4}\sin\theta$	$-\frac{\alpha_S}{16}\cos\theta[2+3\Gamma(4-3\cos^2\theta)]$
Hard wall	$-\frac{3\alpha_S}{4}\cos\theta$	$-\frac{3\alpha_S}{2}\sin\theta$	$-\frac{3\alpha_S}{8}\Gamma\cos\theta(1+\sin^2\theta)$
Interface type	$h^2v_y^{\mathrm{HI}}$	$h^3\Omega_x^{\mathrm{HI}}$	$h^3\Omega_z^{\mathrm{HI}}$
		Rotlet	
Shear	$-\frac{\alpha_R}{8}\cos\theta$	$-\frac{3\alpha_R}{16}\cos\theta$	$-\frac{\alpha_R}{8}\sin\theta$
Bending	$\frac{\alpha_R}{8}\cos\theta$	$-\frac{\alpha_R}{16}\cos\theta(2-3\Gamma\sin^2\theta)$	$-\frac{3\alpha_R}{16}\Gamma\sin\theta\cos^2\theta$
Hard wall	0	$-\frac{\alpha_R}{16}\cos\theta(5-3\Gamma\sin^2\theta)$	$-\frac{\alpha_R}{16}\sin\theta(2+3\Gamma\cos^2\theta)$

to that, for $\Gamma > 2/3$, the swimmer tends to align along the oblique direction given by $\theta_\Gamma = \arccos[\sqrt{6\Gamma}/(3\Gamma)]$ when $\theta > -\theta_\Gamma$, and along $\theta = -\pi/2$ otherwise. Near an interface of either pure bending resistance or both shear and bending resistance, $\Omega_{y\mathrm{S}}^{\mathrm{HI}} \propto -\cos\theta$, leading to swimmer reorientation away from the interface ($\theta = \pi/2$). Notably, $\Omega_{y\mathrm{S}}^{\mathrm{HI}}$ vanishes in the hard wall limit for a spherical microswimmer ($\Gamma = 0$).

2. Rotlet

The far field of an external torque applied to the microswimmer can be described in terms of a *rotlet singularity*. The rotlet related contribution to the induced translational velocity resulting from hydrodynamic interactions with the elastic interface has a single nonvanishing component along the y direction, for which both shear and bending have equal but opposite contributions to the overall dynamics [see Fig. 3(d)]. For the induced rotation rates [Figs. 3(e) and 3(f)], the relative importance of shear and bending elasticity depends strongly on the swimmer geometry and orientation. Analogously to a rotlet dipole, the induced rotational velocity normal to the interface is independent of the shape factor Γ near an interface of only shear resistance, and vanishes for a spherical microswimmer ($\Gamma = 0$) near an interface of resistance only to bending.

C. Long-time decay of swimming velocities

Finally, we briefly comment on the leading-order behavior of the hydrodynamically induced swimming velocities at long times in approaching the steady limits. Results are summarized in Table III for various singularity and interface types.

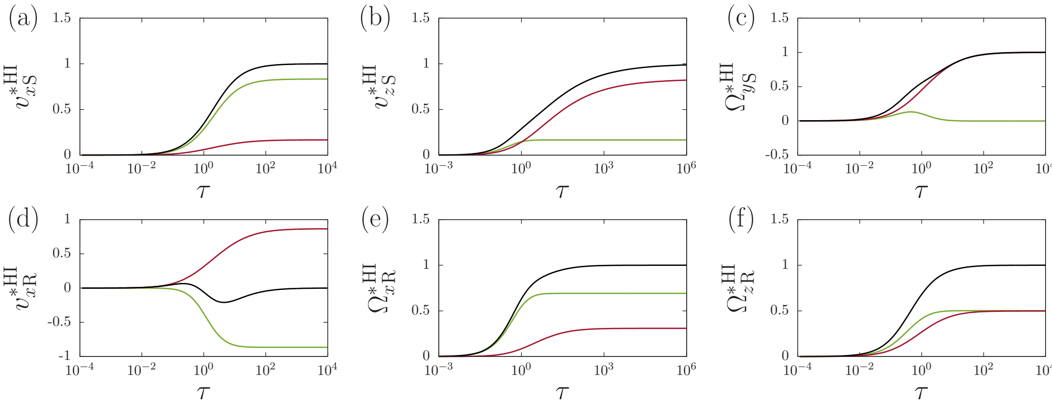

FIG. 3. Evolution of the scaled swimming velocities associated with a Stokeslet (a–c) and rotlet (d–f) due to hydrodynamic interactions with an elastic interface showing pure shear (green), pure bending (red), or both shear and bending rigidities (black). Here, the swimmer has an aspect ratio $\gamma = 4$ and an orientation $\theta = \pi/6$ with respect to the horizontal direction. The velocities are scaled by the corresponding hard wall values except that the x component of the rotlet contribution is scaled by $\alpha_R/(8h^4)$. We set $\tau := \tau_S = 16\tau_B$.

TABLE III. Expressions of the long-time decay of the swimming velocities due to dipolar, source dipolar, quadrupolar, and rotlet dipolar hydrodynamic interactions with an elastic interface. Here, $\tau_S = t/T_S$ and $\tau_B = t/T_B$ with $T_S = 6\eta h/(B\kappa_S)$ and $T_B = 8\eta h^3/\kappa_B$ are characteristic time scales associated with shear and bending deformation modes, respectively.

Interface type	v_x^{HI}	v_z^{HI}	Ω_y^{HI}
		Force dipole	
Shear	τ_S^{-2}	τ_S^{-3}	τ_S^{-3}
Bending	$\tau_B^{-4/3}$	τ_B^{-1}	$\tau_B^{-4/3}$
		Source dipole/Force quadrupole	
Shear	τ_S^{-3}	τ_S^{-4}	τ_S^{-4}
Bending	$\tau_B^{-4/3}$	τ_B^{-1}	$\tau_B^{-4/3}$
		Stokeslet	
Shear	τ_S^{-1}	τ_S^{-3}	τ_S^{-2}
Bending	τ_B^{-1}	$\tau_B^{-1/3}$	τ_B^{-1}
Interface type	v_y^{HI}	Ω_x^{HI}	Ω_z^{HI}
		Rotlet dipole	
Shear	τ_S^{-3}	τ_S^{-4}	τ_S^{-4}
Bending	$\tau_B^{-4/3}$	$\tau_B^{-4/3}$	$\tau_B^{-5/3}$
		Rotlet	
Shear	τ_S^{-2}	τ_S^{-3}	τ_S^{-3}
Bending	τ_B^{-1}	τ_B^{-1}	$\tau_B^{-4/3}$

For higher-order singularities, the rotation rates are found to decay similarly or much faster than the translational swimming velocities. Most importantly, the shear related contributions to the swimming velocities experience a faster decay in time compared to those related to bending. Therefore, the system behavior is shear dominated at early times, while bending is expected to play the more dominant role at later times.

IV. CONCLUSION

We have derived exact solutions for the translational and angular velocities of a trapped microswimmer in the vicinity of a deformable surface that features resistance towards bending and shear. Based on far-field calculations we show that the velocities can be decomposed into bending and shear related contributions, which can display opposed behavior; i.e., while one of them enhances the velocities, the other decreases them and vice versa. In particular, the elastic properties of the interface introduce history to the hydrodynamic couplings, which manifests itself in time-dependent translational and rotational velocities of the approaching microswimmer. These velocities strongly depend on the swimming direction, the distance from the interface, the body shape, and details of the swimming mechanism encoded in the singularity coefficients. By accounting for both bending and shear resistances, the steady-state velocities agree with those of an active agent close to a planar, rigid wall.

Our results provide a detailed analysis of far-field hydrodynamic interactions of trapped, self-propelled particles with a deformable surface and are expected to contribute to our understanding of microswimmer motion in their natural surroundings. Based on the proposed theoretical framework, future investigations could elucidate the spatiotemporal behavior of freely moving microswimmers near an elastic interface and analyze more closely the potential accumulation of microswimmers at the deformable surface in comparison to a rigid wall [176]. Moreover, an additional, intrinsic curvature of the surface can be included in our model [150,187], which could provide a fundamental ingredient for our understanding of microswimmer entrapment and accumulation in realistic biological setups.

ACKNOWLEDGMENTS

We thank Arnold J. T. M. Mathijssen and Maciej Lisicki for invaluable discussions. A.D.-M.I., A.M.M., and H.L. gratefully acknowledge support from the Deutsche Forschungsgemeinschaft (DFG) through Projects No. DA 2107/1-1, No. ME 3571/2-2, and No. LO 418/16-3. C.K. gratefully acknowledges support from the Austrian Science Fund (FWF) via the Erwin Schrödinger Fellowship (Grant No. J 4321-N27). A.Z. acknowledges support from the FWF through a Lise Meitner Fellowship (Grant No. M 2458-N36). M.M. and M.-R.A. acknowledge the support of the National Science Foundation via Grant No. CMMI-1562871. S.G. thanks the Volkswagen Foundation and the DFG (Grant No. SFB-TRR 225, Subproject No. B07, 326998133) for financial support."

APPENDIX A: GREEN'S FUNCTIONS FOR A STOKESLET NEAR AN ELASTIC INTERFACE

The components of the Green's functions can be expressed in terms of convergent improper (infinite) integrals over the wave number and assume the following form:

$$\mathcal{G}_{xx} = \frac{1}{4\pi}\int_0^\infty dq\, q\, [\tilde{\mathcal{G}}_+ J_0(q\rho_0) + \tilde{\mathcal{G}}_- J_2(q\rho_0)\cos(2\varphi)],$$

$$\mathcal{G}_{yy} = \frac{1}{4\pi}\int_0^\infty dq\, q\, [\tilde{\mathcal{G}}_+ J_0(q\rho_0) - \tilde{\mathcal{G}}_- J_2(q\rho_0)\cos(2\varphi)],$$

$$\mathcal{G}_{zz} = \frac{1}{2\pi}\int_0^\infty dq\, q\, \tilde{\mathcal{G}}_{zz} J_0(q\rho_0),$$

$$\mathcal{G}_{xy} = \frac{1}{4\pi}\int_0^\infty dq\, q\, \tilde{\mathcal{G}}_- J_2(q\rho_0)\sin(2\varphi),$$

$$\mathcal{G}_{rz} = \frac{i}{2\pi}\int_0^\infty dq\, q\, \tilde{\mathcal{G}}_{lz} J_1(q\rho_0),$$

$$\mathcal{G}_{zr} = \frac{i}{2\pi}\int_0^\infty dq\, q\, \tilde{\mathcal{G}}_{zl} J_1(q\rho_0),$$

wherein $\rho_0 = \sqrt{(x-x_0)^2 + (y-y_0)^2}$ denotes the radial distance and $\varphi := \arctan[(y-y_0)/(x-x_0)]$ is the azimuthal angle (see inset of Fig. 1). Here $J_n(\cdot)$ represents the nth-order Bessel function of the first kind [188] and we introduce

$$\tilde{\mathcal{G}}_\pm(q, z, \omega) := \tilde{\mathcal{G}}_{tt}(q, z, \omega) \pm \tilde{\mathcal{G}}_{ll}(q, z, \omega),$$

TABLE IV. Expressions of the frequency-dependent evolutions of the induced-swimming velocities resulting from hydrodynamic interactions with the elastic interface. Here, we have used the abbreviation $S = 2Bu^2 + (B+2)i\beta u - \beta^2$.

Velocity component	Expression
	Force dipole
$v_{x\mathrm{D}}^{\mathrm{HI}}$	$\frac{\alpha_\mathrm{D}\sin(2\theta)}{2h^2}\int_0^\infty du\left(\frac{N_\mathrm{D}^\mathrm{S}}{S} + \frac{8u^6}{8u^3+i\beta_\mathrm{B}^3}\right)e^{-2u}$
$v_{z\mathrm{D}}^{\mathrm{HI}}$	$\frac{\alpha_\mathrm{D}(2-3\cos^2\theta)}{h^2}\int_0^\infty du\left(\frac{u^3(u-1)}{2u+i\beta} + \frac{4u^5(u+1)}{8u^3+i\beta_\mathrm{B}^3}\right)e^{-2u}$
$\Omega_{y\mathrm{D}}^{\mathrm{HI}}$	$\frac{\sin(2\theta)}{24h^3}\int_0^\infty du\left(\frac{u^3}{S}\left(H_\mathrm{D}^\mathrm{S} + A_\mathrm{D}^\mathrm{S}\cos^2\theta\right) + \frac{12u^6}{8u^3+i\beta_\mathrm{B}^3}[8 + \Gamma u(4-3\cos^2\theta)]\right)e^{-2u}$
	Source dipole
$v_{x\mathrm{SD}}^{\mathrm{HI}}$	$-\frac{\alpha_\mathrm{SD}\cos\theta}{h^3}\int_0^\infty du\left(\frac{N_\mathrm{SD}^\mathrm{S}}{S} + \frac{4u^6}{8u^3+i\beta_\mathrm{B}^3}\right)e^{-2u}$
$v_{z\mathrm{SD}}^{\mathrm{HI}}$	$-\frac{\alpha_\mathrm{SD}\sin\theta}{h^3}\int_0^\infty du\left(\frac{2u^4}{2u+i\beta} + \frac{8u^5(1+u)}{8u^3+i\beta_\mathrm{B}^3}\right)e^{-2u}$
$\Omega_{y\mathrm{SD}}^{\mathrm{HI}}$	$-\frac{\alpha_\mathrm{SD}\cos\theta}{h^4}\int_0^\infty du\left(\frac{u^4}{S}\left(H_\mathrm{SD}^\mathrm{S} + A_\mathrm{SD}^\mathrm{S}\cos^2\theta\right) + \frac{4u^6}{8u^3+i\beta_\mathrm{B}^3}[1 + \Gamma u(2-\cos^2\theta)]\right)e^{-2u}$
	Force quadrupole
$v_{x\mathrm{Q}}^{\mathrm{HI}}$	$\frac{\alpha_\mathrm{Q}\cos\theta}{4h^3}\int_0^\infty du\left(\frac{u^3}{S}\left(N_\mathrm{Q}^\mathrm{S} + M_\mathrm{Q}^\mathrm{S}\cos^2\theta\right) + \frac{4u^6}{8u^3+i\beta_\mathrm{B}^3}[4u(2-3u) + (15u-8)\cos^2\theta]\right)e^{-2u}$
$v_{z\mathrm{Q}}^{\mathrm{HI}}$	$\frac{\alpha_\mathrm{Q}\sin\theta}{h^3}\int_0^\infty du\left(\frac{u^4}{2u+i\beta}[2(2-u) + (5u-8)\cos^2\theta] + \frac{4u^5(1+u)}{8u^3+i\beta_\mathrm{B}^3}[2(1-u) + (5u-3)\cos^2\theta]\right)e^{-2u}$
$\Omega_{y\mathrm{Q}}^{\mathrm{HI}}$	$\frac{\alpha_\mathrm{Q}\cos\theta}{8h^4}\int_0^\infty du\left(\frac{u^4}{S}\left(W_\mathrm{Q}^\mathrm{S}\cos^4\theta + A_\mathrm{Q}^\mathrm{S}\cos^2\theta + H_\mathrm{Q}^\mathrm{S}\right) + \frac{u^6}{8u^3+i\beta_\mathrm{B}^3}\left(W_\mathrm{Q}^\mathrm{B}\cos^4\theta + A_\mathrm{Q}^\mathrm{B}\cos^2\theta + H_\mathrm{Q}^\mathrm{B}\right)\right)e^{-2u}$
	Rotlet dipole
$v_{y\mathrm{RD}}^{\mathrm{HI}}$	$\frac{\alpha_\mathrm{RD}\sin(2\theta)}{h^3}\int_0^\infty du\left(\frac{N_\mathrm{RD}^\mathrm{S}}{4S} - \frac{2u^6}{8u^3+i\beta_\mathrm{B}^3}\right)e^{-2u}$
$\Omega_{x\mathrm{RD}}^{\mathrm{HI}}$	$\frac{\alpha_\mathrm{RD}\sin(2\theta)}{16h^4}\int_0^\infty du\left(\frac{u^4}{S}\left(G_\mathrm{RD}^\mathrm{S} + K_\mathrm{RD}^\mathrm{S}\cos^2\theta\right) + \frac{8u^6}{8u^3+i\beta_\mathrm{B}^3}[4(1-\Gamma u) + 3\Gamma u\cos^2\theta]\right)e^{-2u}$
$\Omega_{z\mathrm{RD}}^{\mathrm{HI}}$	$\frac{\alpha_\mathrm{RD}}{8h^4}\int_0^\infty du\left(\frac{u^4}{S}\left(W_\mathrm{RD}^\mathrm{S}\cos^4\theta + A_\mathrm{RD}^\mathrm{S}\cos^2\theta + H_\mathrm{RD}^\mathrm{S}\right) + \frac{8\Gamma u^7}{8u^3+i\beta_\mathrm{B}^3}[(4-3\cos^2\theta)\cos^2\theta]\right)e^{-2u}$
	Stokeslet
$v_{x\mathrm{S}}^{\mathrm{HI}}$	$-\frac{\alpha_\mathrm{S}\cos\theta}{h}\int_0^\infty du\left(\frac{N_\mathrm{S}^\mathrm{S}}{S} + \frac{4u^5}{8u^3+i\beta_\mathrm{B}^3}\right)e^{-2u}$
$v_{z\mathrm{S}}^{\mathrm{HI}}$	$-\frac{\alpha_\mathrm{S}\sin\theta}{h}\int_0^\infty du\left(\frac{2u^3}{2u+i\beta} + \frac{8u^3(u+1)^2}{8u^3+i\beta_\mathrm{B}^3}\right)e^{-2u}$
$\Omega_{y\mathrm{S}}^{\mathrm{HI}}$	$-\frac{\alpha_\mathrm{S}\cos\theta}{h^2}\int_0^\infty du\left(\frac{u^2}{2S}\left(H_\mathrm{S}^\mathrm{S} + A_\mathrm{S}^\mathrm{S}\cos^2\theta\right) + \frac{4u^5}{8u^3+i\beta_\mathrm{B}^3}[1 + 2\Gamma u + 3\Gamma - \Gamma(u+3)\cos^2\theta]\right)e^{-2u}$
	Rotlet
$v_{y\mathrm{R}}^{\mathrm{HI}}$	$\frac{\alpha_\mathrm{R}\cos\theta}{2h^2}\int_0^\infty du\left(\frac{H_\mathrm{R}^\mathrm{S}}{S} + \frac{8u^5}{8u^3+i\beta_\mathrm{B}^3}\right)e^{-2u}$
$\Omega_{x\mathrm{R}}^{\mathrm{HI}}$	$\frac{\alpha_\mathrm{R}\cos\theta}{h^3}\int_0^\infty du\left(\frac{u^3}{4S}\left(G_\mathrm{R}^\mathrm{S} + K_\mathrm{R}^\mathrm{S}\cos^2\theta\right) - \frac{4u^5}{8u^3+i\beta_\mathrm{B}^3}(1 - \Gamma u + \Gamma u\cos^2\theta)\right)e^{-2u}$
$\Omega_{z\mathrm{R}}^{\mathrm{HI}}$	$\frac{\alpha_\mathrm{R}\sin\theta}{h^3}\int_0^\infty du\left(\frac{u^3}{4S}\left(H_\mathrm{R}^\mathrm{S} + K_\mathrm{R}^\mathrm{S}\cos^2\theta\right) - \frac{4u^6}{8u^3+i\beta_\mathrm{B}^3}\,\Gamma\cos^2\theta\right)e^{-2u}$

with

$$\tilde{\mathcal{G}}_{ll} = \frac{1}{4\eta q}\left[(1-q|z-h|)e^{-q|z-h|} + \left(\frac{2iqh(1-qh)(1-qz)}{\beta - 2iqh} + \frac{8iq^5zh^4}{\beta_\mathrm{B}^3 - 8i(qh)^3}\right)e^{-q(z+h)}\right],$$

$$\tilde{\mathcal{G}}_{tt} = \frac{1}{2\eta q}\left(e^{-q|z-h|} + \frac{iBqh}{\beta - iBqh}e^{-q(z+h)}\right).$$

TABLE V. Expressions of the frequency-dependent coefficients appearing in Table IV.

Coefficient	Expression
$N_{\mathrm{D}}^{\mathrm{S}}$	$u^2[(2u^2-4u+B+2)i\beta+2Bu(u^2-2u+2)]$
$H_{\mathrm{D}}^{\mathrm{S}}$	$3\Gamma[2(2u^2-4u+2-B)i\beta+4Bu^2(u-2)]+6[(4u-B-4)i\beta+2Bu(2u-3)]$
$A_{\mathrm{D}}^{\mathrm{S}}$	$3\Gamma[3(-u^2+2u+B-1)i\beta+3Bu(-u^2+2u+1)]$
$N_{\mathrm{SD}}^{\mathrm{S}}$	$u^3(Bu+i\beta)(u-1)$
$H_{\mathrm{SD}}^{\mathrm{S}}$	$2(Bu+i\beta)[1+2\Gamma(u-1)]$
$A_{\mathrm{SD}}^{\mathrm{S}}$	$-(Bu+i\beta)\Gamma(u-1)$
$N_{\mathrm{Q}}^{\mathrm{S}}$	$-[4i\beta(3u^2-8u+5+B)+4Bu(3u^2-8u+7)]$
$M_{\mathrm{Q}}^{\mathrm{S}}$	$(15u^2-38u+5B+23)i\beta+Bu(15u^2-38u+33)$
$W_{\mathrm{Q}}^{\mathrm{S}}$	$\Gamma[6i\beta(B-2-u^2+3u)-6Bu^2(u-3)]$
$A_{\mathrm{Q}}^{\mathrm{S}}$	$2Bu(15u-28)+\Gamma(i\beta(26-9B+12u^2-38u)+2Bu(6u^2-19u+4))+i\beta(30u-5B-46)$
$H_{\mathrm{Q}}^{\mathrm{S}}$	$\Gamma[4i\beta(2u+B-2)+8Bu^2]-24Bu(u-2)+4i\beta(10+B-6u)$
$W_{\mathrm{Q}}^{\mathrm{B}}$	$24\Gamma u(1-u)$
$A_{\mathrm{Q}}^{\mathrm{B}}$	$8[15u-8+\Gamma u(6u-7)]$
$H_{\mathrm{Q}}^{\mathrm{B}}$	$32(2-3u+\Gamma u)$
$N_{\mathrm{RD}}^{\mathrm{S}}$	$2u^3[(1+B-u)i\beta+Bu(3-u)]$
$K_{\mathrm{RD}}^{\mathrm{S}}$	$\Gamma[6Bu(u-2)-3i\beta(2+B-2u)]$
$G_{\mathrm{RD}}^{\mathrm{S}}$	$\Gamma[4i\beta(2+B-2u)-8Bu(u-2)]+16Bu+4i\beta(2+B)$
$W_{\mathrm{RD}}^{\mathrm{S}}$	$\Gamma[3i\beta(2+B-2u)+6Bu(2-u)]$
$A_{\mathrm{RD}}^{\mathrm{S}}$	$\Gamma[4i\beta(2u-2-B)+8Bu(u-2)]-6B(2u+i\beta)$
$H_{\mathrm{RD}}^{\mathrm{S}}$	$4B(2u+i\beta)$
$N_{\mathrm{S}}^{\mathrm{S}}$	$u[(u^2-2u+B+1)i\beta+Bu(u^2-2u+3)]$
$H_{\mathrm{S}}^{\mathrm{S}}$	$\Gamma[(4u^2-2u-B-2)i\beta+2Bu(2u^2-u-2)]+(2u-2-B)i\beta+2Bu(u-2)$
$A_{\mathrm{S}}^{\mathrm{S}}$	$-\Gamma[2(u^2+u-2-B)i\beta+2Bu(u^2+u-4)]$
$H_{\mathrm{R}}^{\mathrm{S}}$	$u^2[(2u-2-B)i\beta+2Bu(u-2)]$
$K_{\mathrm{R}}^{\mathrm{S}}$	$\Gamma[(-4u+B+4)i\beta-2Bu(2u-3)]$
$G_{\mathrm{R}}^{\mathrm{S}}$	$-K_{\mathrm{R}}^{\mathrm{S}}-6Bu-(B+4)i\beta$
$H_{\mathrm{R}}^{\mathrm{S}}$	$-2B(2u+i\beta)$

The remaining Green's functions in Fourier space read

$$\tilde{\mathcal{G}}_{zz}=\frac{1}{4\eta q}\left[(1+q|z-h|)e^{-q|z-h|}+\left(\frac{2iq^3zh^2}{\beta-2iqh}+\frac{8i(qh)^3(1+qz)(1+qh)}{\beta_{\mathrm{B}}^3-8i(qh)^3}\right)e^{-q(z+h)}\right],$$

$$\tilde{\mathcal{G}}_{lz}=\frac{i}{4\eta q}\left[-q(z-h)e^{-q|z-h|}+\left(\frac{2i(qh)^2(1-qz)}{\beta-2iqh}-\frac{8iq^4zh^3(1+qh)}{\beta_{\mathrm{B}}^3-8i(qh)^3}\right)e^{-q(z+h)}\right],$$

$$\tilde{\mathcal{G}}_{zl}=\frac{i}{4\eta q}\left[-q(z-h)e^{-q|z-h|}+\left(-\frac{2iq^2zh(1-qh)}{\beta-2iqh}+\frac{8iq^4h^4(1+qz)}{\beta_{\mathrm{B}}^3-8i(qh)^3}\right)e^{-q(z+h)}\right].$$

The Green's functions comprise both bulk contributions and the frequency-dependent corrections due to the presence of the elastic interface. The terms involving β and β_{B} are, respectively, contributions associated with shear and bending. Moreover, the remaining components of the Green's functions can readily be obtained from the usual transformation relations. Specifically, this means $\mathcal{G}_{xz}=\mathcal{G}_{rz}\cos\varphi$, $\mathcal{G}_{yz}=\mathcal{G}_{rz}\sin\varphi$, $\mathcal{G}_{zx}=\mathcal{G}_{zr}\cos\varphi$, $\mathcal{G}_{zy}=\mathcal{G}_{zr}\sin\varphi$, and $\mathcal{G}_{yx}=\mathcal{G}_{xy}$. In the quasisteady limit of vanishing frequency ($\beta=\beta_{\mathrm{B}}=0$), the Green's functions reduce to the well-known Blake tensor near a no-slip wall [189,190]. Physically, this limit corresponds to an infinitely stiff wall, for which the displacement field at the interface identically vanishes.

TABLE VI. Expressions of the time-dependent evolutions of the induced-swimming velocities due to hydrodynamic interactions with the elastic interface. Here, $\xi(u) = e^{-2u} - e^{-2u(1+\tau_B u^2)}$ is a bending related dimensionless function.

Velocity component	Expression
	Force dipole
$v_{x\mathrm{D}}^{\mathrm{HI}}$	$\frac{\alpha_\mathrm{D}\sin(2\theta)}{2h^2}\left(\frac{\tau_\mathrm{S} J_\mathrm{D}^\mathrm{S}}{8(1+\tau_\mathrm{S})^4(2+B\tau_\mathrm{S})^2} + \int_0^\infty du\, u^3\xi(u)\right)$
$v_{z\mathrm{D}}^{\mathrm{HI}}$	$-\frac{\alpha_\mathrm{D}(2-3\cos^2\theta)}{2h^2}\left(\frac{\tau_\mathrm{S}\left(\tau_\mathrm{S}^3+4\tau_\mathrm{S}^2+6\tau_\mathrm{S}+6\right)}{8(\tau_\mathrm{S}+1)^4} + \int_0^\infty du\,(1+u)u^2\xi(u)\right)$
	Source dipole
$v_{x\mathrm{SD}}^{\mathrm{HI}}$	$-\frac{\alpha_\mathrm{SD}\cos\theta}{2h^3}\left(\frac{\tau_\mathrm{S}\left(\tau_\mathrm{S}^3+4\tau_\mathrm{S}^2+6\tau_\mathrm{S}+6\right)}{8(1+\tau_\mathrm{S})^4} + \int_0^\infty du\, u^3\xi(u)\right)$
$v_{z\mathrm{SD}}^{\mathrm{HI}}$	$-\frac{\alpha_\mathrm{SD}\sin\theta}{h^3}\left(\frac{3\tau_\mathrm{S}(2+\tau_\mathrm{S})\left(\tau_\mathrm{S}^2+2\tau_\mathrm{S}+2\right)}{8(1+\tau_\mathrm{S})^4} + \int_0^\infty du\,(1+u)u^2\xi(u)\right)$
	Force quadrupole
$v_{x\mathrm{Q}}^{\mathrm{HI}}$	$\frac{\alpha_\mathrm{Q}\cos\theta}{8h^3}\left(\frac{\tau_\mathrm{S}}{4(1+\tau_\mathrm{S})^5(2+B\tau_\mathrm{S})^3}\left(Y_\mathrm{Q}^\mathrm{S}\cos^2\theta - J_\mathrm{Q}^\mathrm{S}\right) + \int_0^\infty du\, u^3\left(2-2u+(5u-3)\cos^2\theta\right)\xi(u)\right)$
$v_{z\mathrm{Q}}^{\mathrm{HI}}$	$\frac{\alpha_\mathrm{Q}\sin\theta}{2h^3}\left(\frac{3\tau_\mathrm{S}}{4(1+\tau_\mathrm{S})^5}\left(R_\mathrm{Q}^\mathrm{S}\cos^2\theta - 2\right) + \int_0^\infty du\,(1+u)\,u^2\,(8-12u+(15u-8)\cos^2\theta)\xi(u)\right)$
	Rotlet dipole
$v_{y\mathrm{RD}}^{\mathrm{HI}}$	$\frac{\alpha_\mathrm{RD}\sin(2\theta)}{4h^3}\left(\frac{\tau_\mathrm{S} J_\mathrm{RD}^\mathrm{S}}{8(1+\tau_\mathrm{S})^4(2+B\tau_\mathrm{S})^3} - \int_0^\infty du\, u^3\xi(u)\right)$
	Stokeslet
$v_{x\mathrm{S}}^{\mathrm{HI}}$	$-\frac{\alpha_\mathrm{S}\cos\theta}{2h}\left(\frac{\tau_\mathrm{S} J_\mathrm{S}^\mathrm{S}}{4(1+\tau_\mathrm{S})^3(2+B\tau_\mathrm{S})} + \int_0^\infty du\, u^2\xi(u)\right)$
$v_{z\mathrm{S}}^{\mathrm{HI}}$	$-\frac{\alpha_\mathrm{S}\sin\theta}{h}\left(\frac{\tau_\mathrm{B}\left(\tau_\mathrm{B}^2+3\tau_\mathrm{B}+3\right)}{4(1+\tau_\mathrm{B})^3} + \int_0^\infty du\,(1+u)^2\xi(u)\right)$
	Rotlet
$v_{y\mathrm{R}}^{\mathrm{HI}}$	$\frac{\alpha_\mathrm{R}\cos\theta}{h^2}\left(-\frac{\tau_\mathrm{S} J_\mathrm{R}^\mathrm{S}}{8(1+\tau_\mathrm{S})^3(2+B\tau_\mathrm{S})^2} + \int_0^\infty du\, u^2\xi(u)\right)$

APPENDIX B: HIGHER-ORDER SINGULARITIES IN AN UNBOUNDED FLUID DOMAIN

In this Appendix, we provide for completeness analytical expressions of the higher-order Stokes singularities in an unbounded fluid domain, i.e., in the absence of the confining elastic interface. By making use of the analytical recipes introduced in Sec. II C, we readily obtain

$$\boldsymbol{G}_\mathrm{R}^\infty = \frac{1}{s^2}(\hat{\boldsymbol{e}} \times \hat{\boldsymbol{s}}),$$

$$\boldsymbol{G}_\mathrm{D}^\infty = \frac{1}{s^2}[3(\hat{\boldsymbol{e}} \cdot \hat{\boldsymbol{s}})^2 - 1]\hat{\boldsymbol{s}},$$

$$\boldsymbol{G}_\mathrm{SD}^\infty = \frac{1}{s^3}[3(\hat{\boldsymbol{e}} \cdot \hat{\boldsymbol{s}})\hat{\boldsymbol{s}} - \hat{\boldsymbol{e}}],$$

$$\boldsymbol{G}_\mathrm{Q}^\infty = \frac{1}{s^3}\{3[5(\hat{\boldsymbol{e}} \cdot \hat{\boldsymbol{s}})^3 - 3(\hat{\boldsymbol{e}} \cdot \hat{\boldsymbol{s}})]\hat{\boldsymbol{s}} - [3(\hat{\boldsymbol{e}} \cdot \hat{\boldsymbol{s}})^2 - 1]\hat{\boldsymbol{e}}\},$$

$$\boldsymbol{G}_\mathrm{RD}^\infty = \frac{3}{s^3}(\hat{\boldsymbol{e}} \cdot \hat{\boldsymbol{s}})(\hat{\boldsymbol{e}} \times \hat{\boldsymbol{s}}),$$

where, again, $\boldsymbol{s} = \boldsymbol{r} - \boldsymbol{r}_0$ denotes the position vector relative to the singularity location, $s = |\boldsymbol{s}|$, $\hat{\boldsymbol{s}} = \boldsymbol{s}/s$, and $\hat{\boldsymbol{e}}$ stands for the orientation unit vector of the swimmer as defined by Eq. (13) of the main body of the paper. Notably, the rotlet and force dipole decay in the far-field limit as $1/s^2$, whereas the source dipole, force quadrupole, and rotlet dipole undergo a faster decay as $1/s^3$.

APPENDIX C: EXPRESSION OF THE INDUCED-SWIMMING VELOCITIES IN THE FREQUENCY AND TEMPORAL DOMAINS

Here, we present the main mathematical expressions obtained in this paper in the form of tables. We provide in Tables IV and V explicit analytical expressions of the frequency-dependent translational swimming velocities and rotation rates resulting from the fluid-mediated hydrodynamic interactions with a nearby planar elastic interface. In Tables VI and VII, we list the corresponding expressions in the temporal domain for the startup motion from static conditions. As already mentioned in the main text, only the induced translational swimming velocities in the temporal domain are provided. The rotation rates have rather lengthy and complex analytical expressions and thus are not listed here.

TABLE VII. Expressions of the time-dependent coefficients appearing in Table VI.

Coefficient	Expression
$J_{\mathrm{D}}^{\mathrm{S}}$	$3B^2\tau_{\mathrm{S}}^5 + 12B(1+B)\tau_{\mathrm{S}}^4 + 4[1+4B(B+3)]\tau_{\mathrm{S}}^3 + 4[4+B(3B+16)]\tau_{\mathrm{S}}^2 + 2[8+B(B+24)]\tau_{\mathrm{S}} + 8(B+2)$
$Y_{\mathrm{Q}}^{\mathrm{S}}$	$21B^3\tau_{\mathrm{S}}^7 + 21B^2(6+5B)\tau_{\mathrm{S}}^6 + 42B[5B+6(B+3)]\tau_{\mathrm{S}}^5 + [187B^3 + 1260B(B+1) + 88]\tau_{\mathrm{S}}^4 + 2(58B^3 + 561B^2 + 1260B + 220)\tau_{\mathrm{S}}^3 + 2(5B^3 + 348B^2 + 1122B + 440)\tau_{\mathrm{S}}^2 + 12(5B^2 + 116B + 58)\tau_{\mathrm{S}} + 24(5B + 22)$
$J_{\mathrm{Q}}^{\mathrm{S}}$	$16B^3\tau_{\mathrm{S}}^7 + 16B^2(5B+6)\tau_{\mathrm{S}}^6 + 32B(5B^2 + 15B + 6)\tau_{\mathrm{S}}^5 + 4[35B^3 + 240B(B+1) + 16]\tau_{\mathrm{S}}^4 + 8(11B^3 + 105B^2 + 240B + 40)\tau_{\mathrm{S}}^3 + 8(B^3 + 66B^2 + 210B + 80)\tau_{\mathrm{S}}^2 + 48(B^2 + 22B + 10)\tau_{\mathrm{S}} + 96(B+4)$
$R_{\mathrm{Q}}^{\mathrm{S}}$	$\tau_{\mathrm{S}}^4 + 5\tau_{\mathrm{S}}^3 + 10\tau_{\mathrm{S}}^2 + 10\tau_{\mathrm{S}} + 9$
$J_{\mathrm{RD}}^{\mathrm{S}}$	$3B^3\tau_{\mathrm{S}}^6 + 6B^2(2B+3)\tau_{\mathrm{S}}^5 + 18B(B^2 + 4B + 2)\tau_{\mathrm{S}}^4 + 2(5B^3 + 54B^2 + 72B - 4)\tau_{\mathrm{S}}^3 + 4(B^3 + 15B^2 + 54B - 8)\tau_{\mathrm{S}}^2 + 24(B^2 + 5B - 2)\tau_{\mathrm{S}} + 48(B-1)$
$J_{\mathrm{S}}^{\mathrm{S}}$	$5B\tau_{\mathrm{S}}^3 + (2+13B)\tau_{\mathrm{S}}(1+\tau_{\mathrm{S}}) + 2(1+2B)$
$J_{\mathrm{R}}^{\mathrm{S}}$	$B^2\tau_{\mathrm{S}}^4 + B(4+3B)\tau_{\mathrm{S}}^3 + 2B(6+B)\tau_{\mathrm{S}}^2 + B(8+B)\tau_{\mathrm{S}} - 4(1-B)$

[1] J. Wang and W. Gao, Nano/microscale motors: Biomedical opportunities and challenges, ACS Nano **6**, 5745 (2012).
[2] W. Wang, W. Duan, S. Ahmed, T. E. Mallouk, and A. Sen, Small power: Autonomous nano-and micromotors propelled by self-generated gradients, Nano Today **8**, 531 (2013).
[3] W. F. Paxton, K. C. Kistler, C. C. Olmeda, A. Sen, S. K. St. Angelo, Y. Cao, T. E. Mallouk, P. E. Lammert, and V. H. Crespi, Catalytic nanomotors: Autonomous movement of striped nanorods, J. Am. Chem. Soc. **126**, 13424 (2004).
[4] E. Lauga and T. R. Powers, The hydrodynamics of swimming microorganisms, Rep. Prog. Phys. **72**, 096601 (2009).
[5] M. C. Marchetti, J. F. Joanny, S. Ramaswamy, T. B. Liverpool, J. Prost, M. Rao, and R. A. Simha, Hydrodynamics of soft active matter, Rev. Mod. Phys. **85**, 1143 (2013).
[6] J. Elgeti, R. G. Winkler, and G. Gompper, Physics of microswimmers—single particle motion and collective behavior: A review, Rep. Prog. Phys. **78**, 056601 (2015).
[7] A. M. Menzel, Tuned, driven, and active soft matter, Phys. Rep. **554**, 1 (2015).
[8] C. Bechinger, R. Di Leonardo, H. Löwen, C. Reichhardt, G. Volpe, and G. Volpe, Active particles in complex and crowded environments, Rev. Mod. Phys. **88**, 045006 (2016).
[9] A. Zöttl and H. Stark, Emergent behavior in active colloids, J. Phys.: Condens. Matter **28**, 253001 (2016).
[10] E. Lauga, Bacterial hydrodynamics, Ann. Rev. Fluid Mech. **48**, 105 (2016).
[11] P. Illien, R. Golestanian, and A. Sen, "Fuelled" motion: Phoretic motility and collective behaviour of active colloids, Chem. Soc. Rev. **46**, 5508 (2017).
[12] K. K. Dey, Dynamic coupling at low Reynolds number, Angew. Chem. Int. Ed. **58**, 2208 (2019).
[13] G. Grégoire and H. Chaté, Onset of Collective and Cohesive Motion, Phys. Rev. Lett. **92**, 025702 (2004).
[14] S. Mishra, A. Baskaran, and M. C. Marchetti, Fluctuations and pattern formation in self-propelled particles, Phys. Rev. E **81**, 061916 (2010).
[15] A. M. Menzel, Collective motion of binary self-propelled particle mixtures, Phys. Rev. E **85**, 021912 (2012).
[16] J. Tailleur and M. E. Cates, Statistical Mechanics of Interacting Run-and-Tumble Bacteria, Phys. Rev. Lett. **100**, 218103 (2008).
[17] J. Palacci, S. Sacanna, A. P. Steinberg, D. J. Pine, and P. M. Chaikin, Living crystals of light-activated colloidal surfers, Science **339**, 936 (2013).
[18] I. Buttinoni, J. Bialké, F. Kümmel, H. Löwen, C. Bechinger, and T. Speck, Dynamical Clustering and Phase Separation in Suspensions of Self-Propelled Colloidal Particles, Phys. Rev. Lett. **110**, 238301 (2013).
[19] T. Speck, J. Bialké, A. M. Menzel, and H. Löwen, Effective Cahn-Hilliard Equation for the Phase Separation of Active Brownian Particles, Phys. Rev. Lett. **112**, 218304 (2014).
[20] T. Speck, A. M. Menzel, J. Bialké, and H. Löwen, Dynamical mean-field theory and weakly non-linear analysis for the phase separation of active Brownian particles, J. Chem. Phys. **142**, 224109 (2015).
[21] H. H. Wensink, J. Dunkel, S. Heidenreich, K. Drescher, R. E. Goldstein, H. Löwen, and J. M. Yeomans, Meso-scale turbulence in living fluids, Proc. Natl. Acad. Sci. USA **109**, 14308 (2012).
[22] H. H. Wensink and H. Löwen, Emergent states in dense systems of active rods: From swarming to turbulence, J. Phys.: Condens. Matter **24**, 464130 (2012).
[23] J. Dunkel, S. Heidenreich, K. Drescher, H. H. Wensink, M. Bär, and R. E. Goldstein, Fluid Dynamics of Bacterial Turbulence, Phys. Rev. Lett. **110**, 228102 (2013).
[24] S. Heidenreich, S. H. L. Klapp, and M. Bär, Numerical simulations of a minimal model for the fluid dynamics of dense bacterial suspensions, J. Phys. Conf. Ser. **490**, 012126 (2014).
[25] A. Kaiser, A. Peshkov, A. Sokolov, B. ten Hagen, H. Löwen, and I. S. Aranson, Transport Powered by Bacterial Turbulence, Phys. Rev. Lett. **112**, 158101 (2014).
[26] S. Heidenreich, J. Dunkel, S. H. L. Klapp, and M. Bär, Hydrodynamic length-scale selection in microswimmer suspensions, Phys. Rev. E **94**, 020601(R) (2016).
[27] E. M. Purcell, Life at low Reynolds number, Am. J. Phys. **45**, 3 (1977).

[28] H. A. Stone and A. D. T. Samuel, Propulsion of Microorganisms by Surface Distortions, Phys. Rev. Lett. **77**, 4102 (1996).
[29] E. Lauga, Enhanced Diffusion by Reciprocal Swimming, Phys. Rev. Lett. **106**, 178101 (2011).
[30] E. Lauga, Life around the scallop theorem, Soft Matter **7**, 3060 (2011).
[31] M. J. Lighthill, On the squirming motion of nearly spherical deformable bodies through liquids at very small Reynolds numbers, Comm. Pure Appl. Math. **5**, 109 (1952).
[32] J. R. Blake, A spherical envelope approach to ciliary propulsion, J. Fluid Mech. **46**, 199 (1971).
[33] C. Brennen and H. Winet, Fluid mechanics of propulsion by cilia and flagella, Ann. Rev. Fluid Mech. **9**, 339 (1977).
[34] S. Sareh, J. Rossiter, A. Conn, K. Drescher, and R. E. Goldstein, Swimming like algae: Biomimetic soft artificial cilia, J. Royal Soc. Interface **10**, 20120666 (2013).
[35] R. Golestanian, T. B. Liverpool, and A. Ajdari, Propulsion of a Molecular Machine by Asymmetric Distribution of Reaction Products, Phys. Rev. Lett. **94**, 220801 (2005).
[36] R. Golestanian, T. B. Liverpool, and A. Ajdari, Designing phoretic micro-and nano-swimmers, New J. Phys. **9**, 126 (2007).
[37] J. R. Howse, R. A. L. Jones, A. J. Ryan, T. Gough, R. Vafabakhsh, and R. Golestanian, Self-Motile Colloidal Particles: From Directed Propulsion to Random Walk, Phys. Rev. Lett. **99**, 048102 (2007).
[38] B. Liebchen, M. E. Cates, and D. Marenduzzo, Pattern formation in chemically interacting active rotors with self-propulsion, Soft Matter **12**, 7259 (2016).
[39] N. Sharifi-Mood, J. Koplik, and C. Maldarelli, Diffusiophoretic self-propulsion of colloids driven by a surface reaction: The sub-micron particle regime for exponential and van der Waals interactions, Phys. Fluids **25**, 012001 (2013).
[40] S. Michelin and E. Lauga, Phoretic self-propulsion at finite Péclet numbers, J. Fluid Mech. **747**, 572 (2014).
[41] M. N. Popescu, W. E. Uspal, and S. Dietrich, Self-diffusiophoresis of chemically active colloids, Eur. Phys. J. Special Topics **225**, 2189 (2016).
[42] C. Kurzthaler, C. Devailly, J. Arlt, T. Franosch, W. C. K. Poon, V. A. Martinez, and A. T. Brown, Probing the Spatiotemporal Dynamics of Catalytic Janus Particles with Single-Particle Tracking and Differential Dynamic Microscopy, Phys. Rev. Lett. **121**, 078001 (2018).
[43] A. Varma, T. D. Montenegro-Johnson, and S. Michelin, Clustering-induced self-propulsion of isotropic autophoretic particles, Soft Matter **14**, 7155 (2018).
[44] A. Najafi and R. Golestanian, Simple swimmer at low Reynolds number: Three linked spheres, Phys. Rev. E **69**, 062901 (2004).
[45] A. Najafi and R. Golestanian, Propulsion at low Reynolds number, J. Phys.: Condens. Matter **17**, S1203 (2005).
[46] R. Dreyfus, J. Baudry, M. L. Roper, M. Fermigier, H. A. Stone, and J. Bibette, Microscopic artificial swimmers, Nature (London) **437**, 862 (2005).
[47] R. Golestanian and A. Ajdari, Analytic results for the three-sphere swimmer at low Reynolds number, Phys. Rev. E **77**, 036308 (2008).
[48] A. Snezhko, M. Belkin, I. S. Aranson, and W.-K. Kwok, Self-Assembled Magnetic Surface Swimmers, Phys. Rev. Lett. **102**, 118103 (2009).
[49] R. Ledesma-Aguilar, H. Löwen, and J. M. Yeomans, A circle swimmer at low Reynolds number, Eur. Phys. J. E **35**, 1 (2012).
[50] D. Klotsa, K. A. Baldwin, R. J. A. Hill, R. M. Bowley, and M. R. Swift, Propulsion of a Two-Sphere Swimmer, Phys. Rev. Lett. **115**, 248102 (2015).
[51] G. Grosjean, M. Hubert, G. Lagubeau, and N. Vandewalle, Realization of the Najafi-Golestanian microswimmer, Phys. Rev. E **94**, 021101(R) (2016).
[52] B. Nasouri, A. Khot, and G. J. Elfring, Elastic two-sphere swimmer in Stokes flow, Phys. Rev. Fluids **2**, 043101 (2017).
[53] M. Mirzakhanloo, M. A. Jalali, and M.-R. Alam, Hydrodynamic choreographies of microswimmers, Sci. Rep. **8**, 3670 (2018).
[54] B. Nasouri, A. Vilfan, and R. Golestanian, Efficiency limits of the three-sphere swimmer, Phys. Rev. Fluids **4**, 073101 (2019).
[55] A. Sukhov, S. Ziegler, Q. Xie, O. Trosman, J. Pande, G. Grosjean, M. Hubert, N. Vandewalle, A.-S. Smith, and J. Harting, Resonant motion of triangular magnetocapillary swimmers, J. Chem. Phys. (2019).
[56] H. Löwen, Melting, freezing and colloidal suspensions, Phys. Rep. **237**, 249 (1994).
[57] L. Isa, R. Besseling, A. N. Morozov, and W. C. K. Poon, Velocity Oscillations in Microfluidic Flows of Concentrated Colloidal Suspensions, Phys. Rev. Lett. **102**, 058302 (2009).
[58] S. H. L. Klapp, Y. Zeng, D. Qu, and R. von Klitzing, Surviving Structure in Colloidal Suspensions Squeezed from 3D to 2D, Phys. Rev. Lett. **100**, 118303 (2008).
[59] S. M. Stavis, J. B. Edel, K. T. Samiee, and H. G. Craighead, Single molecule studies of quantum dot conjugates in a submicrometer fluidic channel, Lab Chip **5**, 337 (2005).
[60] D. Huh, K. L. Mills, X. Zhu, M. A. Burns, M. D. Thouless, and S. Takayama, Tuneable elastomeric nanochannels for nanofluidic manipulation, Nat. Mater. **6**, 424 (2007).
[61] R. Nosrati, A. Driouchi, C. M. Yip, and D. Sinton, Two-dimensional slither swimming of sperm within a micrometre of a surface, Nat. Commun. **6**, 8703 (2015).
[62] T. J. Moriarty, M. U. Norman, P. Colarusso, T. Bankhead, P. Kubes, and G. Chaconas, Real-time high resolution 3D imaging of the lyme disease spirochete adhering to and escaping from the vasculature of a living host, PLoS Pathog. **4**, e1000090 (2008).
[63] M. G. Mazza, The physics of biofilms–an introduction, J. Phys. D **49**, 203001 (2016).
[64] M. C. van Loosdrecht, J. Lyklema, W. Norde, and A. Zehnder, Influence of interfaces on microbial activity, Microbiol. Mol. Biol. Rev. **54**, 75 (1990).
[65] G. O'Toole, H. B. Kaplan, and R. Kolter, Biofilm formation as microbial development, Ann. Rev. Microbiol. **54**, 49 (2000).
[66] R. Zargar, A. Najafi, and M. F. Miri, Three-sphere low-Reynolds-number swimmer near a wall, Phys. Rev. E **80**, 026308 (2009).
[67] K. Ishimoto and E. A. Gaffney, Squirmer dynamics near a boundary, Phys. Rev. E **88**, 062702 (2013).
[68] K. Ishimoto and E. A. Gaffney, A study of spermatozoan swimming stability near a surface, J. Theor. Biol. **360**, 187 (2014).
[69] G. J. Li and A. M. Ardekani, Hydrodynamic interaction of microswimmers near a wall, Phys. Rev. E **90**, 013010 (2014).

[70] W. E. Uspal, M. N. Popescu, S. Dietrich, and M. Tasinkevych, Self-propulsion of a catalytically active particle near a planar wall: From reflection to sliding and hovering, Soft Matter **11**, 434 (2015).
[71] Y. Ibrahim and T. B. Liverpool, The dynamics of a self-phoretic Janus swimmer near a wall, Europhys. Lett. **111**, 48008 (2015).
[72] K. Schaar, A. Zöttl, and H. Stark, Detention Times of Microswimmers Close to Surfaces: Influence of Hydrodynamic Interactions and Noise, Phys. Rev. Lett. **115**, 038101 (2015).
[73] S. Das, A. Garg, A. I. Campbell, J. Howse, A. Sen, D. Velegol, R. Golestanian, and S. J. Ebbens, Boundaries can steer active Janus spheres, Nat. Commun. **6**, 8999 (2015).
[74] A. Mozaffari, N. Sharifi-Mood, J. Koplik, and C. Maldarelli, Self-diffusiophoretic colloidal propulsion near a solid boundary, Phys. Fluids **28**, 053107 (2016).
[75] J. Simmchen, J. Katuri, W. E. Uspal, M. N. Popescu, M. Tasinkevych, and S. Sánchez, Topographical pathways guide chemical microswimmers, Nat. Commun. **7**, 10598 (2016).
[76] J. S. Lintuvuori, A. T. Brown, K. Stratford, and D. Marenduzzo, Hydrodynamic oscillations and variable swimming speed in squirmers close to repulsive walls, Soft Matter **12**, 7959 (2016).
[77] E. Lushi, V. Kantsler, and R. E. Goldstein, Scattering of biflagellate microswimmers from surfaces, Phys. Rev. E **96**, 023102 (2017).
[78] K. Ishimoto, Guidance of microswimmers by wall and flow: Thigmotaxis and rheotaxis of unsteady squirmers in two and three dimensions, Phys. Rev. E **96**, 043103 (2017).
[79] F. Rühle, J. Blaschke, J.-T. Kuhr, and H. Stark, Gravity-induced dynamics of a squirmer microswimmer in wall proximity, New J. Phys. **20**, 025003 (2018).
[80] A. Mozaffari, N. Sharifi-Mood, J. Koplik, and C. Maldarelli, Self-propelled colloidal particle near a planar wall: A Brownian dynamics study, Phys. Rev. Fluids **3**, 014104 (2018).
[81] A. Daddi-Moussa-Ider, M. Lisicki, C. Hoell, and H. Löwen, Swimming trajectories of a three-sphere microswimmer near a wall, J. Chem. Phys. **148**, 134904 (2018).
[82] Z. Shen, A. Würger, and J. S. Lintuvuori, Hydrodynamic interaction of a self-propelling particle with a wall, Eur. Phys. J. E **41**, 39 (2018).
[83] M. Mirzakhanloo and M.-R. Alam, Flow characteristics of chlamydomonas result in purely hydrodynamic scattering, Phys. Rev. E **98**, 012603 (2018).
[84] E. Lauga, W. R. DiLuzio, G. M. Whitesides, and H. A. Stone, Swimming in circles: Motion of bacteria near solid boundaries, Biophys. J. **90**, 400 (2006).
[85] D. Lopez and E. Lauga, Dynamics of swimming bacteria at complex interfaces, Phys. Fluids **26**, 071902 (2014).
[86] D. Crowdy, S. Lee, O. Samson, E. Lauga, and A. E. Hosoi, A two-dimensional model of low-Reynolds number swimming beneath a free surface, J. Fluid Mech. **681**, 24 (2011).
[87] R. Di Leonardo, D. Dell–Arciprete, L. Angelani, and V. Iebba, Swimming with an Image, Phys. Rev. Lett. **106**, 038101 (2011).
[88] A. A. Evans and E. Lauga, Propulsion by passive filaments and active flagella near boundaries, Phys. Rev. E **82**, 041915 (2010).
[89] J. Hill, O. Kalkanci, J. L. McMurry, and H. Koser, Hydrodynamic Surface Interactions Enable *Escherichia coli* to Seek Efficient Routes to Swim Upstream, Phys. Rev. Lett. **98**, 068101 (2007).
[90] T. Kaya and H. Koser, Direct upstream motility in *Escherichia coli*, Biophys. J. **102**, 1514 (2012).
[91] E. Altshuler, G. Mino, C. Pérez-Penichet, L. del Río, A. Lindner, A. Rousselet, and E. Clément, Flow-controlled densification and anomalous dispersion of *E. coli* through a constriction, Soft Matter **9**, 1864 (2013).
[92] R. Rusconi, J. S. Guasto, and R. Stocker, Bacterial transport suppressed by fluid shear, Nat. Phys. **10**, 212 (2014).
[93] N. Figueroa-Morales, G. L. Mino, A. Rivera, R. Caballero, E. Clément, E. Altshuler, and A. Lindner, Living on the edge: Transfer and traffic of *E. coli* in a confined flow, Soft Matter **11**, 6284 (2015).
[94] A. J. T. M. Mathijssen, T. N. Shendruk, J. M. Yeomans, and A. Doostmohammadi, Upstream Swimming in Microbiological Flows, Phys. Rev. Lett. **116**, 028104 (2016).
[95] A. J. T. M. Mathijssen, N. Figueroa-Morales, G. Junot, E. Clement, A. Lindner, and A. Zöttl, Oscillatory surface rheotaxis of swimming *E. coli* bacteria, Nat. Commun. **10**, 3434 (2019).
[96] F. P. Bretherton and N. M. V. Rothschild, Rheotaxis of spermatozoa, Proc. R. Soc. London **153**, 490 (1961).
[97] V. Kantsler, J. Dunkel, M. Blayney, and R. E. Goldstein, Rheotaxis facilitates upstream navigation of mammalian sperm cells, eLife **3**, e02403 (2014).
[98] C.-k. Tung, F. Ardon, A. Roy, D. L. Koch, S. S. Suarez, and M. Wu, Emergence of Upstream Swimming Via a Hydrodynamic Transition, Phys. Rev. Lett. **114**, 108102 (2015).
[99] W. E. Uspal, M. N. Popescu, S. Dietrich, and M. Tasinkevych, Rheotaxis of spherical active particles near a planar wall, Soft Matter **11**, 6613 (2015).
[100] K. Drescher, J. Dunkel, L. H. Cisneros, S. Ganguly, and R. E. Goldstein, Fluid dynamics and noise in bacterial cell–cell and cell–surface scattering, Proc. Natl. Acad. Sci. USA **108**, 10940 (2011).
[101] E. P. Ipiña, S. Otte, R. Pontier-Bres, D. Czerucka, and F. Peruani, Bacteria display optimal transport near surfaces, Nat. Phys. **15**, 610 (2019).
[102] E. Yariv, Wall-induced self-diffusiophoresis of active isotropic colloids, Phys. Rev. Fluids **1**, 032101 (2016).
[103] J. Elgeti and G. Gompper, Self-propelled rods near surfaces, Europhys. Lett. **85**, 38002 (2009).
[104] J. Elgeti and G. Gompper, Microswimmers near surfaces, Eur. Phys. J. Special Topics **225**, 2333 (2016).
[105] A. Daddi-Moussa-Ider, M. Lisicki, A. J. T. M. Mathijssen, C. Hoell, S. Goh, J. Bławzdziewicz, A. M. Menzel, and H. Löwen, State diagram of a three-sphere microswimmer in a channel, J. Phys.: Condens. Matter **30**, 254004 (2018).
[106] H. Wioland, E. Lushi, and R. E. Goldstein, Directed collective motion of bacteria under channel confinement, New J. Phys. **18**, 075002 (2016).
[107] M. Theers, E. Westphal, G. Gompper, and R. G. Winkler, Modeling a spheroidal microswimmer and cooperative swimming in a narrow slit, Soft Matter **12**, 7372 (2016).
[108] J. de Graaf, A. J. Mathijssen, M. Fabritius, H. Menke, C. Holm, and T. N. Shendruk, Understanding the onset of oscillatory swimming in microchannels, Soft Matter **12**, 4704 (2016).

[109] M. Kuron, P. Stärk, C. Burkard, J. de Graaf, and C. Holm, A lattice Boltzmann model for squirmers, J. Chem. Phys. **150**, 144110 (2019).

[110] A. Daddi-Moussa-Ider, A. Guckenberger, and S. Gekle, Long-lived anomalous thermal diffusion induced by elastic cell membranes on nearby particles, Phys. Rev. E **93**, 012612 (2016).

[111] A. Daddi-Moussa-Ider, A. Guckenberger, and S. Gekle, Particle mobility between two planar elastic membranes: Brownian motion and membrane deformation, Phys. Fluids **28**, 071903 (2016).

[112] A. Daddi-Moussa-Ider and S. Gekle, Hydrodynamic interaction between particles near elastic interfaces, J. Chem. Phys. **145**, 014905 (2016).

[113] A. Daddi-Moussa-Ider and S. Gekle, Brownian motion near an elastic cell membrane: A theoretical study, Eur. Phys. J. E **41**, 19 (2018).

[114] L. Xiao, L. Wei, C. Liu, Y. He, and E. S. Yeung, Unsynchronized translational and rotational diffusion of nanocargo on a living cell membrane, Angew. Chem. Int. Ed. **51**, 4181 (2012).

[115] F. Jünger, F. Kohler, A. Meinel, T. Meyer, R. Nitschke, B. Erhard, and A. Rohrbach, Measuring local viscosities near plasma membranes of living cells with photonic force microscopy, Biophys. J. **109**, 869 (2015).

[116] R. Ledesma-Aguilar and J. M. Yeomans, Enhanced Motility of a Microswimmer in Rigid and Elastic Confinement, Phys. Rev. Lett. **111**, 138101 (2013).

[117] R. Trouilloud, S. Y. Tony, A. E. Hosoi, and E. Lauga, Soft Swimming: Exploiting Deformable Interfaces for Low Reynolds Number Locomotion, Phys. Rev. Lett. **101**, 048102 (2008).

[118] T. Bickel, Hindered mobility of a particle near a soft interface, Phys. Rev. E **75**, 041403 (2007).

[119] T. Bickel, Probing nanoscale deformations of a fluctuating interface, Europhys. Lett. **106**, 16004 (2014).

[120] T. Bickel, Brownian motion near a liquid-like membrane, Eur. Phys. J. E **20**, 379 (2006).

[121] B. U. Felderhof, Effect of surface tension and surface elasticity of a fluid-fluid interface on the motion of a particle immersed near the interface, J. Chem. Phys. **125**, 144718 (2006).

[122] B. U. Felderhof, Effect of surface elasticity on the motion of a droplet in a viscous fluid, J. Chem. Phys. **125**, 124904 (2006).

[123] A. T. Chwang and T. Y.-T. Wu, Hydromechanics of low-Reynolds-number flow. Part 2. Singularity method for Stokes flows, J. Fluid Mech. **67**, 787 (1975).

[124] S. E. Spagnolie and E. Lauga, Hydrodynamics of self-propulsion near a boundary: Predictions and accuracy of far-field approximations, J. Fluid Mech. **700**, 105 (2012).

[125] J. Happel and H. Brenner, *Low Reynolds Number Hydrodynamics: With Special Applications to Particulate Media* (Springer, New York, 2012), Vol. 1.

[126] S. Kim and S. J. Karrila, *Microhydrodynamics: Principles and Selected Applications* (Courier, New York, 2013).

[127] R. Skalak, A. Tozeren, R. P. Zarda, and S. Chien, Strain energy function of red blood cell membranes, Biophys. J. **13**, 245 (1973).

[128] J. B. Freund, Numerical simulation of flowing blood cells, Annu. Rev. Fluid Mech. **46**, 67 (2014).

[129] T. Krüger, F. Varnik, and D. Raabe, Efficient and accurate simulations of deformable particles immersed in a fluid using a combined immersed boundary lattice Boltzmann finite element method, Comput. Math. Appl. **61**, 3485 (2011).

[130] T. Krüger, *Computer Simulation Study of Collective Phenomena in Dense Suspensions of Red Blood Cells Under Shear* (Springer, New York, 2012).

[131] D. Barthès-Biesel, Motion and deformation of elastic capsules and vesicles in flow, Ann. Rev. Fluid Mech. **48**, 25 (2016).

[132] W. Helfrich, Elastic properties of lipid bilayers - theory and possible experiments, Z. Naturf. C. **28**, 693 (1973).

[133] U. Seifert, Configurations of fluid membranes and vesicles, Adv. Phys. **46**, 13 (1997).

[134] A. Guckenberger, M. P. Schraml, P. G. Chen, M. Leonetti, and S. Gekle, On the bending algorithms for soft objects in flows, Comput. Phys. Commun. **207**, 1 (2016).

[135] A. Guckenberger and S. Gekle, Theory and algorithms to compute Helfrich bending forces: A review, J. Phys.: Condens. Matter **29**, 203001 (2017).

[136] M. Deserno, Fluid lipid membranes: From differential geometry to curvature stresses, Chem. Phys. Lipids **185**, 11 (2015).

[137] K. Sekimoto and L. Leibler, A mechanism for shear thickening of polymer-bearing surfaces: Elasto-hydrodynamic coupling, Europhys. Lett. **23**, 113 (1993).

[138] S. J. Weekley, S. L. Waters, and O. E. Jensen, Transient elastohydrodynamic drag on a particle moving near a deformable wall, Quart. J. Mech. Appl. Math. **59**, 277 (2006).

[139] T. Salez and L. Mahadevan, Elastohydrodynamics of a sliding, spinning and sedimenting cylinder near a soft wall, J. Fluid Mech. **779**, 181 (2015).

[140] B. Saintyves, T. Jules, T. Salez, and L. Mahadevan, Self-sustained lift and low friction via soft lubrication, Proc. Natl. Acad. Sci. USA **113**, 5847 (2016).

[141] B. Rallabandi, B. Saintyves, T. Jules, T. Salez, C. Schönecker, L. Mahadevan, and H. A. Stone, Rotation of an immersed cylinder sliding near a thin elastic coating, Phys. Rev. Fluids **2**, 074102 (2017).

[142] A. Daddi-Moussa-Ider, B. Rallabandi, S. Gekle, and H. A. Stone, Reciprocal theorem for the prediction of the normal force induced on a particle translating parallel to an elastic membrane, Phys. Rev. Fluids **3**, 084101 (2018).

[143] B. Rallabandi, N. Oppenheimer, M. Y. B. Zion, and H. A. Stone, Membrane-induced hydroelastic migration of a particle surfing its own wave, Nat. Phys. 1 (2018).

[144] Z. Zhang, V. Bertin, M. Arshad, E. Raphaël, T. Salez, and A. Maali, Direct measurement of the elastohydrodynamic lift force at the nanoscale (unpublished).

[145] A. J. T. M. Mathijssen, A. Doostmohammadi, J. M. Yeomans, and T. N. Shendruk, Hydrodynamics of micro-swimmers in films, J. Fluid Mech. **806**, 35 (2016).

[146] A. Daddi-Moussa-Ider, M. Lisicki, and S. Gekle, Mobility of an axisymmetric particle near an elastic interface, J. Fluid Mech. **811**, 210 (2017).

[147] S. D. Ryan, B. M. Haines, L. Berlyand, F. Ziebert, and I. S. Aranson, Viscosity of bacterial suspensions: Hydrodynamic interactions and self-induced noise, Phys. Rev. E **83**, 050904(R) (2011).

[148] E. Clement, A. Lindner, C. Douarche, and H. Auradou, Bacterial suspensions under flow, Eur. Phys. J. Special Topics **225**, 2389 (2016).

[149] A. Košmrlj and D. R. Nelson, Statistical Mechanics of Thin Spherical Shells, Phys. Rev. X **7**, 011002 (2017).
[150] A. Daddi-Moussa-Ider and S. Gekle, Hydrodynamic mobility of a solid particle near a spherical elastic membrane: Axisymmetric motion, Phys. Rev. E **95**, 013108 (2017).
[151] A. Daddi-Moussa-Ider, M. Lisicki, and S. Gekle, Hydrodynamic mobility of a solid particle near a spherical elastic membrane. II. Asymmetric motion, Phys. Rev. E **95**, 053117 (2017).
[152] A. Daddi-Moussa-Ider, H. Löwen, and S. Gekle, Creeping motion of a solid particle inside a spherical elastic cavity, Eur. Phys. J. E **41**, 104 (2018).
[153] C. Hoell, H. Löwen, A. M. Menzel, and A. Daddi-Moussa-Ider, Creeping motion of a solid particle inside a spherical elastic cavity. II. Asymmetric motion, Eur. Phys. J. E **42**, 89 (2019).
[154] H. C. Berg, *E. coli in Motion* (Springer, New York, 2008).
[155] F. F. V. Chevance and K. T. Hughes, Coordinating assembly of a bacterial macromolecular machine, Nat. Rev. Microbiol. **6**, 455 (2008).
[156] M. Lisicki, M. Velho Rodrigues, R. Goldstein, and E. Lauga, Swimming eukaryotic microorganisms exhibit a universal speed distribution, eLife **8**, e44907 (2019).
[157] K. Drescher, R. E. Goldstein, N. Michel, M. Polin, and I. Tuval, Direct Measurement of the Flow Field Around Swimming Microorganisms, Phys. Rev. Lett. **105**, 168101 (2010).
[158] A. M. Menzel, A. Saha, C. Hoell, and H. Löwen, Dynamical density functional theory for microswimmers, J. Chem. Phys. **144**, 024115 (2016).
[159] C. Hoell, H. Löwen, and A. M. Menzel, Dynamical density functional theory for circle swimmers, New J. Phys. **19**, 125004 (2017).
[160] T. C. Adhyapak and S. Jabbari-Farouji, Flow properties and hydrodynamic interactions of rigid spherical microswimmers, Phys. Rev. E **96**, 052608 (2017).
[161] A. Daddi-Moussa-Ider and A. M. Menzel, Dynamics of a simple model microswimmer in an anisotropic fluid: Implications for alignment behavior and active transport in a nematic liquid crystal, Phys. Rev. Fluids **3**, 094102 (2018).
[162] F. J. Schwarzendahl and M. G. Mazza, Maximum in density heterogeneities of active swimmers, Soft Matter **14**, 4666 (2018).
[163] M. T. Downton and H. Stark, Simulation of a model microswimmer, J. Phys.: Condens. Matter **21**, 204101 (2009).
[164] T. Pedley, Spherical squirmers: Models for swimming microorganisms, IMA J. Appl. Math. **81**, 488 (2016).
[165] A. Zöttl and H. Stark, Simulating squirmers with multiparticle collision dynamics, Eur. Phys. J. E **41**, 61 (2018).
[166] O. S. Pak and E. Lauga, Generalized squirming motion of a sphere, J. Eng. Math. **88**, 1 (2014).
[167] T. Ishikawa, G. Sekiya, Y. Imai, and T. Yamaguchi, Hydrodynamic interactions between two swimming bacteria, Biophys. J. **93**, 2217 (2007).
[168] I. O. Götze and G. Gompper, Mesoscale simulations of hydrodynamic squirmer interactions, Phys. Rev. E **82**, 041921 (2010).
[169] A. Zöttl and H. Stark, Nonlinear Dynamics of a Microswimmer in Poiseuille Flow, Phys. Rev. Lett. **108**, 218104 (2012).
[170] A. Zöttl and H. Stark, Periodic and quasiperiodic motion of an elongated microswimmer in Poiseuille flow, Eur. Phys. J. E **36**, 4 (2013).
[171] C. Datt, L. Zhu, G. J. Elfring, and O. S. Pak, Squirming through shear-thinning fluids, J. Fluid Mech. **784**, R1 (2015).
[172] H. Nganguia, K. Pietrzyk, and O. S. Pak, Swimming efficiency in a shear-thinning fluid, Phys. Rev. E **96**, 062606 (2017).
[173] H. Nganguia and O. S. Pak, Squirming motion in a Brinkman medium, J. Fluid Mech. **855**, 554 (2018).
[174] K. Pietrzyk, H. Nganguia, C. Datt, L. Zhu, G. J. Elfring, and O. S. Pak, Flow around a squirmer in a shear-thinning fluid, J. Nonnewton Fluid Mech. **268**, 101 (2019).
[175] S. D. Ryan, L. Berlyand, B. M. Haines, and D. Karpeev, A kinetic model for semidilute bacterial suspensions, Multiscale Model. Simul. **11**, 1176 (2013).
[176] A. P. Berke, L. Turner, H. C. Berg, and E. Lauga, Hydrodynamic Attraction of Swimming Microorganisms by Surfaces, Phys. Rev. Lett. **101**, 038102 (2008).
[177] B. Liebchen and H. Löwen, Which interactions dominate in active colloids? J. Chem. Phys. **150**, 061102 (2019).
[178] Q. Liao, G. Subramanian, M. P. DeLisa, D. L. Koch, and M. Wu, Pair velocity correlations among swimming *Escherichia coli* bacteria are determined by force-quadrupole hydrodynamic interactions, Phys. Fluids **19**, 061701 (2007).
[179] D. J. Smith, E. A. Gaffney, J. R. Blake, and J. C. Kirkman-Brown, Human sperm accumulation near surfaces: A simulation study, J. Fluid Mech. **621**, 289 (2009).
[180] W. R. DiLuzio, L. Turner, M. Mayer, P. Garstecki, D. B. Weibel, H. C. Berg, and G. M. Whitesides, *Escherichia coli* swim on the right-hand side, Nature (London) **435**, 1271 (2005).
[181] J. Dunstan, G. Mino, E. Clement, and R. Soto, A two-sphere model for bacteria swimming near solid surfaces, Phys. Fluids **24**, 011901 (2012).
[182] A. Daddi-Moussa-Ider, M. Lisicki, S. Gekle, A. M. Menzel, and H. Löwen, Hydrodynamic coupling and rotational mobilities near planar elastic membranes, J. Chem. Phys. **149**, 014901 (2018).
[183] A. I. Campbell and S. J. Ebbens, Gravitaxis in spherical Janus swimming devices, Langmuir **29**, 14066 (2013).
[184] B. ten Hagen, F. Kümmel, R. Wittkowski, D. Takagi, H. Löwen, and C. Bechinger, Gravitaxis of asymmetric self-propelled colloidal particles, Nat. Commun. **5**, 4829 (2014).
[185] A. I. Campbell, R. Wittkowski, B. ten Hagen, H. Löwen, and S. J. Ebbens, Helical paths, gravitaxis, and separation phenomena for mass-anisotropic self-propelling colloids: Experiment versus theory, J. Chem. Phys. **147**, 084905 (2017).
[186] J.-T. Kuhr, J. Blaschke, F. Rühle, and H. Stark, Collective sedimentation of squirmers under gravity, Soft Matter **13**, 7548 (2017).
[187] S. E. Spagnolie, G. R. Moreno-Flores, D. Bartolo, and E. Lauga, Geometric capture and escape of a microswimmer colliding with an obstacle, Soft Matter **11**, 3396 (2015).
[188] M. Abramowitz and I. A. Stegun, *Handbook of Mathematical Functions* (Dover, New York, 1972), Vol. 1.
[189] J. R. Blake, A note on the image system for a Stokeslet in a no-slip boundary, Math. Proc. Camb. Phil. Soc. **70**, 303 (1971).
[190] J. Blake and A. Chwang, Fundamental singularities of viscous flow, J. Eng. Math. **8**, 23 (1974).

Chapter 6

Concluding remarks

In this chapter, I briefly summarize the most important research contributions of this thesis, and I add a short perspective. The here-presented studies in the field of active soft matter physics have focused on microswimmers, that is, active particles suspended in a low-Reynolds-number medium and self-propelling by creating fluid flows in the surrounding liquid. This way, the corresponding self-propulsion mechanisms affect the surrounding environment, in particular other microswimmers. Consequently, hydrodynamic interactions between the swimmers arise, the effects of which we have analyzed.

First, Publications **P1**–**P4** present our statistical framework for (semi)dilute microswimmer suspensions and the associated modeling of swimming at low Reynolds numbers. Specifically, minimal microswimmer models on the basis of force dipoles have been introduced, for straight-propelling swimmers [**P1**] and also for circle swimmers [**P2**]. In these models, both pushers and pullers can be constructed [**P1**, **P2**]. The concrete mathematical description concerning the involved fluid flow is confined to the level of far-field hydrodynamics [31–33]. On this premise, corresponding dynamical density functional theories (DDFTs) have been derived [**P1**, **P2**] that include the effects of active self-propulsion, thermal noise, and external potentials, as well as steric and hydrodynamic interactions between swimmers. Additionally, an extension to multi-species systems has been formulated [**P3**], covering both swimmer–swimmer and active–passive mixtures. In all three cases, numerical evaluations for planar example situations have been performed [**P1**–**P3**], showcasing the applicability of our framework. They include the effect of circularly symmetric external trapping potentials confining the swimmers [**P1**–**P3**], for which the theory qualitatively reproduces the previous results of particle-based computer simulations [85, 163]. Especially, hydrodynamic interactions can cause spontaneous symmetry breaking in the spatial distribution of the swimmers at the effective boundaries of the trap, with the swimmers self-organizing into a high-density spot acting as a hydrodynamic fluid pump [**P1**]. Depending on the system parameters, further activity-induced instabilities can occur [**P1**–**P3**]. In contrast to that, circle swimmers, in general, become localized near the center of the circular trap, if the inherent curvature of their trajectories is large enough [**P2**]. Furthermore, we have described swimmers inside a circular shear cell, with externally driven particles on the rim of the cell creating the internal fluid flow [**P3**].

Moreover, we have studied hydrodynamically-induced polar orientational ordering of swimmers [**P4**], inspired by corresponding particle-based approaches [51,176]. For this purpose, a test-particle method [181] has been newly adapted from equilibrium to our system of active particles, creating a possibility to obtain full orientation-dependent swimmer–swimmer pair distribution functions [**P4**]. The above problem is treated via a linear stability analysis using appropriate approximations [**P4**]. We find that pure puller systems can develop polar orientational order across the considered length scale, while disordered suspensions of pushers are linearly stable. We have provided a quantitative criterion for the occurrence of the instability of the uniform, disordered state [**P4**]. If enough pullers are present and sufficiently strong, also binary mixtures of pushers and pullers can develop such a polar order [**P3**], in qualitative accordance with previous particle simulations [51].

Concerning discrete-particle models, an individual three-sphere swimmer propelling by shape changes and its hydrodynamic interaction with nearby planar walls (featuring no-slip boundary conditions) have been regarded [**P5**, **P6**]. Specifically, setups featuring only one wall [**P5**] and a channel consisting of two parallel walls [**P6**] were investigated. On the basis of corresponding, carefully calculated mobility tensors that describe the translational and rotational response of each sphere to a force or torque acting on one sphere, the subsequent swimmer trajectories (in the absence of thermal noise) have been ordered into state diagrams [**P5**, **P6**].

Furthermore, the situation of a one-dimensional model membrane subject to possible penetrations has been studied. Here, the model membrane consists of discrete freely-orientable spherical particles that are subject to mutual steric, elastic, and dipolar interactions [**P7**]. We have investigated whether an active particle approaching the membrane is held back by the membrane or penetrates it, depending on the system parameters [**P7**]. A corresponding mathematical description has been developed as well [**P7**], which subsequently has been extended to describing the situation for a two-dimensional model membrane [287].

Finally, hydrodynamic interactions of (active) particles with elastic interfaces have been considered. First, a driven particle within a corresponding spherical cavity in a specific non-axisymmetric setup has been described via an analytical approach, obtaining the relevant mobility tensors that connect the driving force on the particle to the resulting motions of the particle and the cavity [**P8**]. Second, for a general microswimmer, represented by a set of hydrodynamic singularities, near an infinite planar elastic interface, we have determined the corresponding contributions of, e.g., a force dipole and a source dipole [**P9**].

In this thesis, DDFT-based studies on suspensions of hydrodynamically interacting microswimmers [**P1**–**P4**] are formally combined with discrete-particle models [**P5**–**P9**]. Beyond the given specific examples, the former statistical approach constitutes a quite general theoretical framework for many-swimmer systems, and should provide a versatile tool in the future, as indicated by the outlook in Sec. 3.4. For example, the DDFT could be adjusted for setups featuring nearby rigid walls, similar to those discussed in Publication [**P5**, **P6**] using a discrete-particle model. Further work could include, e.g., more complex geometries for the situations discussed in Publications **P5**–**P9** because typical confinements, e.g., blood vessels or cell membranes, can feature significantly more irregular shapes. Foremost, however, we would be interested in experimental tests of our various predictions.

In conclusion, as the study of active microswimmers is still a relatively young field of research, it is to be expected that there is a lot left to be discovered. I humbly hope that the here-presented work can contribute to this progress.

References

[1] C. Bechinger, R. Di Leonardo, H. Löwen, C. Reichhardt, G. Volpe, and G. Volpe, *Active particles in complex and crowded environments*, Rev. Mod. Phys. **88**, 045006 (2016).

[2] E. M. Purcell, *Life at low Reynolds number*, Am. J. Phys. **45**, 3 (1977).

[3] J. O. Kessler, *Hydrodynamic focusing of motile algal cells*, Nature **313**, 218 (1985).

[4] M. Eisenbach and L. C. Giojalas, *Sperm guidance in mammals — an unpaved road to the egg*, Nat. Rev. Mol. Cell Biol. **7**, 276 (2006).

[5] M. Engstler, T. Pfohl, S. Herminghaus, M. Boshart, G. Wiegertjes, N. Heddergott, and P. Overath, *Hydrodynamic flow-mediated protein sorting on the cell surface of trypanosomes*, Cell **131**, 505 (2007).

[6] H. C. Berg, *E. coli in Motion* (Springer-Verlag New York, New York, 2008).

[7] M. Polin, I. Tuval, K. Drescher, J. P. Gollub, and R. E. Goldstein, *Chlamydomonas swims with two "gears" in a eukaryotic version of run-and-tumble locomotion*, Science **325**, 487 (2009).

[8] W. M. Durham, J. O. Kessler, and R. Stocker, *Disruption of vertical motility by shear triggers formation of thin phytoplankton layers*, Science **323**, 1067 (2009).

[9] M. Mussler, S. Rafaï, P. Peyla, and C. Wagner, *Effective viscosity of non-gravitactic Chlamydomonas reinhardtii microswimmer suspensions*, EPL (Europhys. Lett.) **101**, 54004 (2013).

[10] R. E. Goldstein, *Green algae as model organisms for biological fluid dynamics*, Annu. Rev. Fluid Mech. **47**, 343 (2015).

[11] R. Sender, S. Fuchs, and R. Milo, *Are we really vastly outnumbered? Revisiting the ratio of bacterial to host cells in humans*, Cell **164**, 337 (2016).

[12] R. Sender, S. Fuchs, and R. Milo, *Revised estimates for the number of human and bacteria cells in the body*, PLOS Biol. **14**, e1002533 (2016).

[13] W. F. Paxton, K. C. Kistler, C. C. Olmeda, A. Sen, S. K. St. Angelo, Y. Cao, T. E. Mallouk, P. E. Lammert, and V. H. Crespi, *Catalytic nanomotors: autonomous movement of striped nanorods*, J. Am. Chem. Soc. **126**, 13424 (2004).

[14] J. R. Howse, R. A. L. Jones, A. J. Ryan, T. Gough, R. Vafabakhsh, and R. Golestanian, *Self-motile colloidal particles: from directed propulsion to random walk*, Phys. Rev. Lett. **99**, 048102 (2007).

[15] I. Buttinoni, G. Volpe, F. Kümmel, G. Volpe, and C. Bechinger, *Active Brownian motion tunable by light*, J. Phys.: Condens. Matter **24**, 284129 (2012).

[16] A. Walther and A. H. Müller, *Janus particles: synthesis, self-assembly, physical properties, and applications*, Chem. Rev. **113**, 5194 (2013).

[17] S. Samin and R. van Roij, *Self-propulsion mechanism of active Janus particles in near-critical binary mixtures*, Phys. Rev. Lett. **115**, 188305 (2015).

[18] J. L. Moran and J. D. Posner, *Phoretic self-propulsion*, Annu. Rev. Fluid Mech. **49**, 511 (2017).

[19] J. Wang and W. Gao, *Nano/microscale motors: biomedical opportunities and challenges*, ACS Nano **6**, 5745 (2012).

[20] D. Patra, S. Sengupta, W. Duan, H. Zhang, R. Pavlick, and A. Sen, *Intelligent, self-powered, drug delivery systems*, Nanoscale **5**, 1273 (2013).

[21] L. K. Abdelmohsen, F. Peng, Y. Tu, and D. A. Wilson, *Micro- and nano-motors for biomedical applications*, J. Mater. Chem. B **2**, 2395 (2014).

[22] X. Ma, K. Hahn, and S. Sanchez, *Catalytic mesoporous Janus nanomotors for active cargo delivery*, J. Am. Chem. Soc. **137**, 4976 (2015).

[23] A. F. Demirörs, M. T. Akan, E. Poloni, and A. R. Studart, *Active cargo transport with Janus colloidal shuttles using electric and magnetic fields*, Soft Matter **14**, 4741 (2018).

[24] B. J. Nelson, I. K. Kaliakatsos, and J. J. Abbott, *Microrobots for minimally invasive medicine*, Annu. Rev. Biomed. Eng. **12**, 55 (2010).

[25] W. Xi, A. A. Solovev, A. N. Ananth, D. H. Gracias, S. Sanchez, and O. G. Schmidt, *Rolled-up magnetic microdrillers: towards remotely controlled minimally invasive surgery*, Nanoscale **5**, 1294 (2013).

[26] V. Magdanz, S. Sanchez, and O. G. Schmidt, *Development of a sperm-flagella driven micro-bio-robot*, Adv. Mater. **25**, 6581 (2013).

[27] R. Di Leonardo, L. Angelani, D. Dell'Arciprete, G. Ruocco, V. Iebba, S. Schippa, M. P. Conte, F. Mecarini, F. De Angelis, and E. Di Fabrizio, *Bacterial ratchet motors*, Proc. Natl. Acad. Sci. U.S.A. **107**, 9541 (2010).

[28] A. Sokolov, M. M. Apodaca, B. A. Grzybowski, and I. S. Aranson, *Swimming bacteria power microscopic gears*, Proc. Natl. Acad. Sci. U.S.A **107**, 969 (2010).

[29] C. Maggi, J. Simmchen, F. Saglimbeni, J. Katuri, M. Dipalo, F. De Angelis, S. Sanchez, and R. Di Leonardo, *Self-assembly of micromachining systems powered by Janus micromotors*, Small **12**, 446 (2016).

[30] A. M. Menzel, *Tuned, driven, and active soft matter*, Phys. Rep. **554**, 1 (2015).

[31] J. K. G. Dhont, *An Introduction to Dynamics of Colloids* (Elsevier, Amsterdam, Netherlands, 1996).

[32] J. Happel and H. Brenner, *Low Reynolds Number Hydrodynamics: with Special Applications to Particulate Media* (Springer Science & Business Media, New York, New York, 2012).

[33] S. Kim and S. J. Karrila, *Microhydrodynamics: Principles and Selected Applications* (Dover Publications, Mineola, New York, 2013).

[34] M. Saadat, M. Mirzakhanloo, J. Shen, M. Tomizuka, and M.-R. Alam, *The experimental realization of an artificial low-Reynolds-number swimmer with three-dimensional maneuverability*, arXiv:1905.05893 (2019).

[35] C. Scholz, S. Jahanshahi, A. Ldov, and H. Löwen, *Inertial delay of self-propelled particles*, Nat. Commun. **9**, 5156 (2018).

[36] S. Mandal, B. Liebchen, and H. Löwen, *Motility-induced temperature difference in coexisting phases*, arXiv:1902.06116 (2019).

[37] H. Löwen, *Active particles in noninertial frames: how to self-propel on a carousel*, Phys. Rev. E **99**, 062608 (2019).

[38] A. Ivlev, H. Löwen, G. Morfill, and C. P. Royall, *Complex Plasmas and Colloidal Dispersions: Particle-resolved Studies of Classical Liquids and Solids* (World Scientific, Singapore, Singapore, 2012).

[39] M. N. Popescu, W. E. Uspal, and S. Dietrich, *Self-diffusiophoresis of chemically active colloids*, Eur. Phys. J. Spec. Top. **225**, 2189 (2016).

[40] B. Liebchen and H. Löwen, *Which interactions dominate in active colloids?*, J. Chem. Phys. **150**, 061102 (2019).

[41] S. Ramaswamy, *The mechanics and statistics of active matter*, Annu. Rev. Condens. Matter Phys. **1**, 323 (2010).

[42] A. Doostmohammadi, S. P. Thampi, T. B. Saw, C. T. Lim, B. Ladoux, and J. M. Yeomans, *Celebrating Soft Matter's 10th anniversary: Cell division: a source of active stress in cellular monolayers*, Soft Matter **11**, 7328 (2015).

[43] A. Doostmohammadi, S. P. Thampi, and J. M. Yeomans, *Defect-mediated morphologies in growing cell colonies*, Phys. Rev. Lett. **117**, 048102 (2016).

[44] D. Dell'Arciprete, M. L. Blow, A. T. Brown, F. D. C. Farrell, J. S. Lintuvuori, A. F. McVey, D. Marenduzzo, and W. C. K. Poon, *A growing bacterial colony in two dimensions as an active nematic*, Nat. Commun. **9**, 4190 (2018).

[45] H. M. Al-Saedi, A. J. Archer, and J. Ward, *Dynamical density-functional-theory-based modeling of tissue dynamics: application to tumor growth*, Phys. Rev. E **98**, 022407 (2018).

[46] T. Vicsek, A. Czirók, E. Ben-Jacob, I. Cohen, and O. Shochet, *Novel type of phase transition in a system of self-driven particles*, Phys. Rev. Lett. **75**, 1226 (1995).

[47] J. Toner and Y. Tu, *Long-range order in a two-dimensional dynamical XY model: how birds fly together*, Phys. Rev. Lett. **75**, 4326 (1995).

[48] N. D. Mermin and H. Wagner, *Absence of ferromagnetism or antiferromagnetism in one-or two-dimensional isotropic Heisenberg models*, Phys. Rev. Lett. **17**, 1133 (1966).

[49] M. E. Cates, *Diffusive transport without detailed balance in motile bacteria: does microbiology need statistical physics?*, Rep. Prog. Phys. **75**, 042601 (2012).

[50] D. L. Ermak and J. A. McCammon, *Brownian dynamics with hydrodynamic interactions*, J. Chem. Phys. **69**, 1352 (1978).

[51] G. Pessot, H. Löwen, and A. M. Menzel, *Binary pusher–puller mixtures of active microswimmers and their collective behaviour*, Mol. Phys. **116**, 3401 (2018).

[52] T. Speck, *Collective behavior of active Brownian particles: from microscopic clustering to macroscopic phase separation*, Eur. Phys. J. Spec. Top. **225**, 2287 (2016).

[53] B. ten Hagen, R. Wittkowski, D. Takagi, F. Kümmel, C. Bechinger, and H. Löwen, *Can the self-propulsion of anisotropic microswimmers be described by using forces and torques?*, J. Phys.: Condens. Matter **27**, 194110 (2015).

[54] J. Bialké, T. Speck, and H. Löwen, *Crystallization in a dense suspension of self-propelled particles*, Phys. Rev. Lett. **108**, 168301 (2012).

[55] B. ten Hagen, S. van Teeffelen, and H. Löwen, *Non-Gaussian behaviour of a self-propelled particle on a substrate*, Condens. Matter Phys. **12**, 725 (2009).

[56] B. ten Hagen, S. van Teeffelen, and H. Löwen, *Brownian motion of a self-propelled particle*, J. Phys.: Condens. Matter **23**, 194119 (2011).

[57] G. Li and J. X. Tang, *Accumulation of microswimmers near a surface mediated by collision and rotational Brownian motion*, Phys. Rev. Lett. **103**, 078101 (2009).

[58] C. F. Lee, *Active particles under confinement: aggregation at the wall and gradient formation inside a channel*, New J. Phys. **15**, 055007 (2013).

[59] G. Volpe, S. Gigan, and G. Volpe, *Simulation of the active Brownian motion of a microswimmer*, Am. J. Phys. **82**, 659 (2014).

[60] J. Palacci, C. Cottin-Bizonne, C. Ybert, and L. Bocquet, *Sedimentation and effective temperature of active colloidal suspensions*, Phys. Rev. Lett. **105**, 088304 (2010).

[61] B. ten Hagen, F. Kümmel, R. Wittkowski, D. Takagi, H. Löwen, and C. Bechinger, *Gravitaxis of asymmetric self-propelled colloidal particles*, Nat. Commun. **5**, 4829 (2014).

[62] S. Hermann and M. Schmidt, *Active ideal sedimentation: exact two-dimensional steady states*, Soft Matter **14**, 1614 (2018).

[63] B. ten Hagen, R. Wittkowski, and H. Löwen, *Brownian dynamics of a self-propelled particle in shear flow*, Phys. Rev. E **84**, 031105 (2011).

[64] B. Liebchen and H. Löwen, *Optimal control strategies for active particle navigation*, EPL (Europhys. Lett.) **127**, 34003 (2019).

[65] I. Buttinoni, J. Bialké, F. Kümmel, H. Löwen, C. Bechinger, and T. Speck, *Dynamical clustering and phase separation in suspensions of self-propelled colloidal particles*, Phys. Rev. Lett. **110**, 238301 (2013).

[66] M. E. Cates and J. Tailleur, *When are active Brownian particles and run-and-tumble particles equivalent? Consequences for motility-induced phase separation*, EPL (Europhys. Lett.) **101**, 20010 (2013).

[67] J. Bialké, H. Löwen, and T. Speck, *Microscopic theory for the phase separation of self-propelled repulsive disks*, EPL (Europhys. Lett.) **103**, 30008 (2013).

[68] J. Bialké, T. Speck, and H. Löwen, *Active colloidal suspensions: clustering and phase behavior*, J. Non-Cryst. Solids **407**, 367 (2015).

[69] M. E. Cates and J. Tailleur, *Motility-induced phase separation*, Annu. Rev. Condens. Matter Phys. **6**, 219 (2015).

[70] A. Solon, J. Stenhammar, M. E. Cates, Y. Kafri, and J. Tailleur, *Generalized thermodynamics of motility-induced phase separation: phase equilibria, Laplace pressure, and change of ensembles*, New J. Phys. **20**, 075001 (2018).

[71] P. Digregorio, D. Levis, A. Suma, L. F. Cugliandolo, G. Gonnella, and I. Pagonabarraga, *Full phase diagram of active Brownian disks: from melting to motility-induced phase separation*, Phys. Rev. Lett. **121**, 098003 (2018).

[72] T. Speck, J. Bialké, A. M. Menzel, and H. Löwen, *Effective Cahn-Hilliard equation for the phase separation of active Brownian particles*, Phys. Rev. Lett. **112**, 218304 (2014).

[73] T. Speck, A. M. Menzel, J. Bialké, and H. Löwen, *Dynamical mean-field theory and weakly non-linear analysis for the phase separation of active Brownian particles*, J. Chem. Phys. **142**, 224109 (2015).

[74] R. Wittkowski, J. Stenhammar, and M. E. Cates, *Nonequilibrium dynamics of mixtures of active and passive colloidal particles*, New J. Phys. **19**, 105003 (2017).

[75] R. Wittkowski, A. Tiribocchi, J. Stenhammar, R. J. Allen, D. Marenduzzo, and M. E. Cates, *Scalar φ^4 field theory for active-particle phase separation*, Nat. Commun. **5**, 4351 (2014).

[76] A. Tiribocchi, R. Wittkowski, D. Marenduzzo, and M. E. Cates, *Active model H: scalar active matter in a momentum-conserving fluid*, Phys. Rev. Lett. **115**, 188302 (2015).

[77] T. F. Farage, P. Krinninger, and J. M. Brader, *Effective interactions in active Brownian suspensions*, Phys. Rev. E **91**, 042310 (2015).

[78] R. Wittmann and J. M. Brader, *Active Brownian particles at interfaces: an effective equilibrium approach*, EPL (Europhys. Lett.) **114**, 68004 (2016).

[79] A. Sharma, R. Wittmann, and J. M. Brader, *Escape rate of active particles in the effective equilibrium approach*, Phys. Rev. E **95**, 012115 (2017).

[80] R. Wittmann, C. Maggi, A. Sharma, A. Scacchi, J. M. Brader, and U. M. B. Marconi, *Effective equilibrium states in the colored-noise model for active matter I. Pairwise forces in the Fox and unified colored noise approximations*, J. Stat. Mech.: Theory Exp. **11**, 113207 (2017).

[81] R. Wittmann, U. M. B. Marconi, C. Maggi, and J. Brader, *Effective equilibrium states in the colored-noise model for active matter II. A unified framework for phase equilibria, structure and mechanical properties*, J. Stat. Mech.: Theory Exp. **11**, 113208 (2017).

[82] L. Caprini, U. M. B. Marconi, and A. Vulpiani, *Linear response and correlation of a self-propelled particle in the presence of external fields*, J. Stat. Mech.: Theory Exp. **2018**, 033203 (2018).

[83] L. Caprini, E. Hernández-García, C. López, and U. M. B. Marconi, *A comparative study between two models of active cluster-crystals*, arXiv:1906.03016 (2019).

[84] S. van Teeffelen and H. Löwen, *Dynamics of a Brownian circle swimmer*, Phys. Rev. E **78**, 020101 (2008).

[85] R. W. Nash, R. Adhikari, J. Tailleur, and M. E. Cates, *Run-and-tumble particles with hydrodynamics: sedimentation, trapping, and upstream swimming*, Phys. Rev. Lett. **104**, 258101 (2010).

[86] H. Chaté, F. Ginelli, G. Grégoire, and F. Raynaud, *Collective motion of self-propelled particles interacting without cohesion*, Phys. Rev. E **77**, 046113 (2008).

[87] T. Ohta and S. Yamanaka, *Traveling bands in self-propelled soft particles*, Eur. Phys. J. Spec. Top. **223**, 1279 (2014).

[88] A. Zampetaki, P. Schmelcher, H. Löwen, and B. Liebchen, *Taming polar active matter with moving substrates: directed transport and counterpropagating macrobands*, New J. Phys. **21**, 013023 (2019).

[89] M. J. Lighthill, *On the squirming motion of nearly spherical deformable bodies through liquids at very small Reynolds numbers*, Commun. Pure Appl. Math. **5**, 109 (1952).

[90] M. T. Downton and H. Stark, *Simulation of a model microswimmer*, J. Phys.: Condens. Matter **21**, 204101 (2009).

[91] A. Zöttl and H. Stark, *Hydrodynamics determines collective motion and phase behavior of active colloids in quasi-two-dimensional confinement*, Phys. Rev. Lett. **112**, 118101 (2014).

[92] A. Najafi and R. Golestanian, *Simple swimmer at low Reynolds number: three linked spheres*, Phys. Rev. E **69**, 062901 (2004).

[93] R. Ledesma-Aguilar, H. Löwen, and J. M. Yeomans, *A circle swimmer at low Reynolds number*, Eur. Phys. J. E **35**, 70 (2012).

[94] A. Baskaran and M. C. Marchetti, *Statistical mechanics and hydrodynamics of bacterial suspensions*, Proc. Natl. Acad. Sci. U.S.A. **106**, 15567 (2009).

[95] R. A. Simha and S. Ramaswamy, *Hydrodynamic fluctuations and instabilities in ordered suspensions of self-propelled particles*, Phys. Rev. Lett. **89**, 058101 (2002).

[96] Y. Hatwalne, S. Ramaswamy, M. Rao, and R. A. Simha, *Rheology of active-particle suspensions*, Phys. Rev. Lett. **92**, 118101 (2004).

[97] R. Golestanian, *Three-sphere low-Reynolds-number swimmer with a cargo container*, Eur. Phys. J. E **25**, 1 (2008).

[98] A. J. T. M. Mathijssen, J. Culver, M. S. Bhamla, and M. Prakash, *Collective intercellular communication through ultra-fast hydrodynamic trigger waves*, Nature **571**, 560 (2019).

[99] E. Lauga and T. R. Powers, *The hydrodynamics of swimming microorganisms*, Rep. Prog. Phys. **72**, 096601 (2009).

[100] K. Drescher, J. Dunkel, L. H. Cisneros, S. Ganguly, and R. E. Goldstein, *Fluid dynamics and noise in bacterial cell–cell and cell–surface scattering*, Proc. Natl. Acad. Sci. U.S.A. **108**, 10940 (2011).

[101] K. Drescher, R. E. Goldstein, N. Michel, M. Polin, and I. Tuval, *Direct measurement of the flow field around swimming microorganisms*, Phys. Rev. Lett. **105**, 168101 (2010).

[102] T. C. Adhyapak and S. Jabbari-Farouji, *Flow properties and hydrodynamic interactions of rigid spherical microswimmers*, Phys. Rev. E **96**, 052608 (2017).

[103] A. Kaiser and H. Löwen, *Vortex arrays as emergent collective phenomena for circle swimmers*, Phys. Rev. E **87**, 032712 (2013).

[104] S. Babel, B. ten Hagen, and H. Löwen, *Swimming path statistics of an active Brownian particle with time-dependent self-propulsion*, J. Stat. Mech. Theory Exp. **2014**, P02011 (2014).

[105] H. Löwen, *Chirality in microswimmer motion: from circle swimmers to active turbulence*, Eur. Phys. J. Spec. Top. **225**, 2319 (2016).

[106] S. Jahanshahi, H. Löwen, and B. ten Hagen, *Brownian motion of a circle swimmer in a harmonic trap*, Phys. Rev. E **95**, 022606 (2017).

[107] C. Kurzthaler and T. Franosch, *Intermediate scattering function of an anisotropic Brownian circle swimmer*, Soft Matter **13**, 6396 (2017).

[108] S. van Teeffelen, U. Zimmermann, and H. Löwen, *Clockwise-directional circle swimmer moves counter-clockwise in Petri dish-and ring-like confinements*, Soft Matter **5**, 4510 (2009).

[109] R. Wittkowski and H. Löwen, *Self-propelled Brownian spinning top: dynamics of a biaxial swimmer at low Reynolds numbers*, Phys. Rev. E **85**, 021406 (2012).

[110] R. Kirchhoff and H. Löwen, *T-structured fluid and jamming in driven Brownian rotators*, EPL (Europhys. Lett.) **69**, 291 (2004).

[111] R. Kirchhoff and H. Löwen, *Tracer diffusion and cluster formation in mixtures of spheres and rotating rods*, J. Phys.: Condens. Matter **17**, 7805 (2005).

[112] R. Evans, *The nature of the liquid-vapour interface and other topics in the statistical mechanics of non-uniform, classical fluids*, Adv. Phys. **28**, 143 (1979).

[113] R. Evans. *Density functionals in the theory of nonuniform fluids.* in *Fundamentals of Inhomogeneous Fluids*, edited by D. Henderson, pages 85–176. Marcel Dekker, New York, (1992).

[114] U. M. B. Marconi and P. Tarazona, *Dynamic density functional theory of fluids*, J. Chem. Phys. **110**, 8032 (1999).

[115] U. M. B. Marconi and P. Tarazona, *Dynamic density functional theory of fluids*, J. Phys.: Condens. Matter **12**, A413 (2000).

[116] A. J. Archer and R. Evans, *Dynamical density functional theory and its application to spinodal decomposition*, J. Chem. Phys. **121**, 4246 (2004).

[117] G. K.-L. Chan and R. Finken, *Time-dependent density functional theory of classical fluids*, Phys. Rev. Lett. **94**, 183001 (2005).

[118] P. Español and H. Löwen, *Derivation of dynamical density functional theory using the projection operator technique*, J. Chem. Phys. **131**, 244101 (2009).

[119] R. Evans. *Density functional theory for inhomogeneous fluids I: simple fluids in equilibrium.* in *Lecture Notes 3rd Warsaw School of Statistical Physics*, edited by B. Cichocki, M. Napiórkowski, and J. Piasecki, pages 43–85. Warsaw University Press, Warsaw, Poland, (2010).

[120] H. Löwen. *Density functional theory for inhomogeneous fluids II: statics, dynamics, and applications.* in *Lecture Notes 3rd Warsaw School of Statistical Physics*, edited by B. Cichocki, M. Napiórkowski, and J. Piasecki, pages 87–121. Warsaw University Press, Warsaw, Poland, (2010).

[121] R. Wittkowski and H. Löwen, *Dynamical density functional theory for colloidal particles with arbitrary shape*, Mol. Phys. **109**, 2935 (2011).

[122] R. Evans, M. Oettel, R. Roth, and G. Kahl, *New developments in classical density functional theory*, J. Phys.: Condens. Matter **28**, 240401 (2016).

[123] J.-P. Hansen and I. R. McDonald, *Theory of Simple Liquids* (Elsevier, Amsterdam, Netherlands, 1990).

[124] P. Tarazona, *Free-energy density functional for hard spheres*, Phys. Rev. A **31**, 2672 (1985).

[125] W. A. Curtin and N. W. Ashcroft, *Weighted-density-functional theory of inhomogeneous liquids and the freezing transition*, Phys. Rev. A **32**, 2909 (1985).

[126] Y. Singh, *Density-functional theory of freezing and properties of the ordered phase*, Phys. Rep. **207**, 351 (1991).

[127] H. Löwen, *Melting, freezing and colloidal suspensions*, Phys. Rep. **237**, 249 (1994).

[128] P. Hohenberg and W. Kohn, *Inhomogeneous electron gas*, Phys. Rev. **136**, B864 (1964).

[129] W. Kohn and L. J. Sham, *Self-consistent equations including exchange and correlation effects*, Phys. Rev. **140**, A1133 (1965).

[130] R. G. Parr. *Density functional theory of atoms and molecules.* in *Horizons of Quantum Chemistry*, pages 5–15. Springer Netherlands, Dordrecht, Netherlands, (1980).

[131] R. Wittkowski, H. Löwen, and H. R. Brand, *Microscopic approach to entropy production*, J. Phys. A **46**, 355003 (2013).

[132] M. Schmidt and J. M. Brader, *Power functional theory for Brownian dynamics*, J. Chem. Phys. **138**, 214101 (2013).

[133] A. Fortini, D. de las Heras, J. M. Brader, and M. Schmidt, *Superadiabatic forces in Brownian many-body dynamics*, Phys. Rev. Lett. **113**, 167801 (2014).

[134] D. de las Heras and M. Schmidt, *Velocity gradient power functional for Brownian dynamics*, Phys. Rev. Lett. **120**, 028001 (2018).

[135] S. van Teeffelen, R. Backofen, A. Voigt, and H. Löwen, *Derivation of the phase-field-crystal model for colloidal solidification*, Phys. Rev. E **79**, 051404 (2009).

[136] A. M. Menzel and H. Löwen, *Traveling and resting crystals in active systems*, Phys. Rev. Lett. **110**, 055702 (2013).

[137] A. M. Menzel, T. Ohta, and H. Löwen, *Active crystals and their stability*, Phys. Rev. E **89**, 022301 (2014).

[138] H. Emmerich, H. Löwen, R. Wittkowski, T. Gruhn, G. I. Tóth, G. Tegze, and L. Gránásy, *Phase-field-crystal models for condensed matter dynamics on atomic length and diffusive time scales: an overview*, Adv. Phys. **61**, 665 (2012).

[139] F. Alaimo and A. Voigt, *Microscopic field-theoretical approach for mixtures of active and passive particles*, Phys. Rev. E **98**, 032605 (2018).

[140] S. Heidenreich, J. Dunkel, S. H. L. Klapp, and M. Bär, *Hydrodynamic length-scale selection in microswimmer suspensions*, Phys. Rev. E **94**, 020601 (2016).

[141] H. Reinken, S. H. L. Klapp, M. Bär, and S. Heidenreich, *Derivation of a hydrodynamic theory for mesoscale dynamics in microswimmer suspensions*, Phys. Rev. E **97**, 022613 (2018).

[142] H. Reinken, S. Heidenreich, M. Bär, and S. H. L. Klapp, *Anisotropic mesoscale turbulence and pattern formation in microswimmer suspensions induced by orienting external fields*, New J. Phys. **21**, 013037 (2019).

[143] H. H. Wensink and H. Löwen, *Aggregation of self-propelled colloidal rods near confining walls*, Phys. Rev. E **78**, 031409 (2008).

[144] M. Rex and H. Löwen, *Dynamical density functional theory with hydrodynamic interactions and colloids in unstable traps*, Phys. Rev. Lett. **101**, 148302 (2008).

[145] M. Rex and H. Löwen, *Dynamical density functional theory for colloidal dispersions including hydrodynamic interactions*, Eur. Phys. J. E **28**, 139 (2009).

[146] M. Rauscher, *DDFT for Brownian particles and hydrodynamics*, J. Phys.: Condens. Matter **22**, 364109 (2010).

[147] B. D. Goddard, A. Nold, N. Savva, G. A. Pavliotis, and S. Kalliadasis, *General dynamical density functional theory for classical fluids*, Phys. Rev. Lett. **109**, 120603 (2012).

[148] B. D. Goddard, A. Nold, N. Savva, P. Yatsyshin, and S. Kalliadasis, *Unification of dynamic density functional theory for colloidal fluids to include inertia and hydrodynamic interactions: derivation and numerical experiments*, J. Phys.: Condens. Matter **25**, 035101 (2012).

[149] B. D. Goddard, A. Nold, and S. Kalliadasis, *Dynamical density functional theory with hydrodynamic interactions in confined geometries*, J. Chem. Phys. **145**, 214106 (2016).

[150] M. Doi and S. F. Edwards, *The Theory of Polymer Dynamics* (Oxford University Press, Oxford, England, 1988).

[151] J. Rotne and S. Prager, *Variational treatment of hydrodynamic interaction in polymers*, J. Chem. Phys. **50**, 4831 (1969).

[152] M. Reichert and H. Stark, *Hydrodynamic coupling of two rotating spheres trapped in harmonic potentials*, Phys. Rev. E **69**, 031407 (2004).

[153] J. Yvon, *La théorie statistique des fluides et l'équation d'état* (Hermann, Paris, France, 1935).

[154] N. N. Bogolubov, *Kinetic equations*, J. Exp. Theor. Phys. **16**, 691 (1946).

[155] J. G. Kirkwood, *The statistical mechanical theory of transport processes I. General theory*, J. Chem. Phys. **14**, 180 (1946).

[156] M. Born and H. S. Green, *A general kinetic theory of liquids I. The molecular distribution functions*, Proc. Royal Soc. A London **188**, 10 (1946).

[157] J. G. Kirkwood, *The statistical mechanical theory of transport processes II. Transport in gases*, J. Chem. Phys. **15**, 72 (1947).

[158] C. G. Gray and K. E. Gubbins, *Theory of Molecular Fluids: I: Fundamentals* (Oxford University Press, Oxford, England, 1984).

[159] L. Onsager, *The effects of shape on the interaction of colloidal particles*, Ann. N. Y. Acad. Sci. **51**, 627 (1949).

[160] J. E. Guyer, D. Wheeler, and J. A. Warren, *FiPy: partial differential equations with Python*, Comput. Sci. Eng. **11**, 6 (2009).

[161] B. M. Mladek, D. Gottwald, G. Kahl, M. Neumann, and C. N. Likos, *Formation of polymorphic cluster phases for a class of models of purely repulsive soft spheres*, Phys. Rev. Lett. **96**, 045701 (2006).

[162] A. J. Archer, M. C. Walters, U. Thiele, and E. Knobloch, *Solidification in soft-core fluids: disordered solids from fast solidification fronts*, Phys. Rev. E **90**, 042404 (2014).

[163] M. Hennes, K. Wolff, and H. Stark, *Self-induced polar order of active Brownian particles in a harmonic trap*, Phys. Rev. Lett. **112**, 238104 (2014).

[164] A. M. Menzel, *Focusing by blocking: repeatedly generating central density peaks in self-propelled particle systems by exploiting diffusive processes*, EPL (Europhys. Lett.) **110**, 38005 (2015).

[165] W. Yan and J. F. Brady, *The force on a boundary in active matter*, J. Fluid Mech. **785**, R1 (2015).

[166] B. Liebchen and D. Levis, *Collective behavior of chiral active matter: pattern formation and enhanced flocking*, Phys. Rev. Lett. **119**, 058002 (2017).

[167] D. Levis and B. Liebchen, *Micro-flock patterns and macro-clusters in chiral active Brownian disks*, J. Phys.: Condens. Matter **30**, 084001 (2018).

[168] J.-j. Liao, X.-q. Huang, and B.-q. Ai, *Transport of the moving barrier driven by chiral active particles*, J. Chem. Phys. **148**, 094902 (2018).

[169] A. J. Archer, P. Hopkins, and M. Schmidt, *Dynamics in inhomogeneous liquids and glasses via the test particle limit*, Phys. Rev. E **75**, 040501 (2007).

[170] P. Hopkins, A. Fortini, A. J. Archer, and M. Schmidt, *The van Hove distribution function for Brownian hard spheres: dynamical test particle theory and computer simulations for bulk dynamics*, J. Chem. Phys. **133**, 224505 (2010).

[171] A. J. Archer, *Dynamical density functional theory: binary phase-separating colloidal fluid in a cavity*, J. Phys.: Condens. Matter **17**, 1405 (2005).

[172] B. D. Goddard, A. Nold, and S. Kalliadasis, *Multi-species dynamical density functional theory*, J. Chem. Phys. **138**, 144904 (2013).

[173] A. Härtel, M. Kohl, and M. Schmiedeberg, *Anisotropic pair correlations in binary and multicomponent hard-sphere mixtures in the vicinity of a hard wall: a combined density functional theory and simulation study*, Phys. Rev. E **92**, 042310 (2015).

[174] S. Babel, M. H. Eikerling, and H. Löwen, *Impedance resonance in narrow confinement*, J. Phys. Chem. C **122**, 21724 (2018).

[175] W. R. C. Somerville, J. L. Stokes, A. M. Adawi, T. S. Horozov, A. J. Archer, and D. M. A. Buzza, *Density functional theory for the crystallization of two-dimensional dipolar colloidal alloys*, J. Phys.: Condens. Matter **30**, 405102 (2018).

[176] F. Alarcón and I. Pagonabarraga, *Spontaneous aggregation and global polar ordering in squirmer suspensions*, J. Mol. Liq. **185**, 56 (2013).

[177] M. P. Allen and D. J. Tildesley, *Computer Simulation of Liquids* (Oxford University Press, Oxford, England, 2017).

[178] A. Härtel, D. Richard, and T. Speck, *Three-body correlations and conditional forces in suspensions of active hard disks*, Phys. Rev. E **97**, 012606 (2018).

[179] N. de Macedo Biniossek, H. Löwen, T. Voigtmann, and F. Smallenburg, *Static structure of active Brownian hard disks*, J. Phys.: Condens. Matter **30**, 074001 (2018).

[180] F. J. Schwarzendahl and M. G. Mazza, *Hydrodynamic interactions dominate the structure of active swimmers' pair distribution functions*, J. Chem. Phys. **150**, 184902 (2019).

[181] J. K. Percus, *Approximation methods in classical statistical mechanics*, Phys. Rev. Lett. **8**, 462 (1962).

[182] A. J. Archer, B. Chacko, and R. Evans, *The standard mean-field treatment of inter-particle attraction in classical DFT is better than one might expect*, J. Chem. Phys. **147**, 034501 (2017).

[183] J. Blake, *A note on the image system for a Stokeslet in a no-slip boundary*, Math. Proc. Camb. Philos. Soc. **70**, 303 (1971).

[184] U. Zimmermann, F. Smallenburg, and H. Löwen, *Flow of colloidal solids and fluids through constrictions: dynamical density functional theory versus simulation*, J. Phys.: Condens. Matter **28**, 244019 (2016).

[185] M. P. N. Juniper, U. Zimmermann, A. V. Straube, R. Besseling, D. G. A. L. Aarts, H. Löwen, and R. P. Dullens, *Dynamic mode locking in a driven colloidal system: experiments and theory*, New J. Phys. **19**, 013010 (2017).

[186] Y. Rosenfeld, *Free-energy model for the inhomogeneous hard-sphere fluid mixture and density-functional theory of freezing*, Phys. Rev. Lett. **63**, 980 (1989).

[187] Y. Rosenfeld, M. Schmidt, H. Löwen, and P. Tarazona, *Dimensional crossover and the freezing transition in density functional theory*, J. Phys.: Condens. Matter **8**, L577 (1996).

[188] Y. Rosenfeld, M. Schmidt, H. Löwen, and P. Tarazona, *Fundamental-measure free-energy density functional for hard spheres: dimensional crossover and freezing*, Phys. Rev. E **55**, 4245 (1997).

[189] R. Roth, R. Evans, A. Lang, and G. Kahl, *Fundamental measure theory for hard-sphere mixtures revisited: the White Bear version*, J. Phys.: Condens. Matter **14**, 12063 (2002).

[190] H. Hansen-Goos and R. Roth, *Density functional theory for hard-sphere mixtures: the White Bear version Mark II*, J. Phys.: Condens. Matter **18**, 8413 (2006).

[191] R. Roth, *Fundamental measure theory for hard-sphere mixtures: a review*, J. Phys.: Condens. Matter **22**, 063102 (2010).

[192] Y. Rosenfeld, *Density functional theory of molecular fluids: free-energy model for the inhomogeneous hard-body fluid*, Phys. Rev. E **50**, R3318 (1994).

[193] H. Hansen-Goos and K. Mecke, *Fundamental measure theory for inhomogeneous fluids of nonspherical hard particles*, Phys. Rev. Lett. **102**, 018302 (2009).

[194] H. Hansen-Goos and K. Mecke, *Tensorial density functional theory for non-spherical hard-body fluids*, J. Phys.: Condens. Matter **22**, 364107 (2010).

[195] A. Härtel and H. Löwen, *Fundamental measure density functional theory for hard spherocylinders in static and time-dependent aligning fields*, J. Phys.: Condens. Matter **22**, 104112 (2010).

[196] M. Marechal and H. Löwen, *Density functional theory for hard polyhedra*, Phys. Rev. Lett. **110**, 137801 (2013).

[197] R. Wittmann, C. E. Sitta, F. Smallenburg, and H. Löwen, *Phase diagram of two-dimensional hard rods from fundamental mixed measure density functional theory*, J. Chem. Phys. **147**, 134908 (2017).

[198] H. Löwen, *Structure and Brownian dynamics of the two-dimensional Yukawa fluid*, J. Phys.: Condens. Matter **4**, 10105 (1992).

[199] H. Löwen, *Interaction between charged rodlike colloidal particles*, Phys. Rev. Lett. **72**, 424 (1994).

[200] H. Löwen, *Charged rodlike colloidal suspensions: an ab initio approach*, J. Chem. Phys. **100**, 6738 (1994).

[201] R. Ni, M. A. C. Stuart, and M. Dijkstra, *Pushing the glass transition towards random close packing using self-propelled hard spheres*, Nat. Commun. **4**, 2704 (2013).

[202] D. Levis, J. Codina, and I. Pagonabarraga, *Active Brownian equation of state: metastability and phase coexistence*, Soft Matter **13**, 8113 (2017).

[203] J. U. Klamser, S. C. Kapfer, and W. Krauth, *Thermodynamic phases in two-dimensional active matter*, Nat. Commun. **9**, 5045 (2018).

[204] J. U. Klamser, S. C. Kapfer, and W. Krauth, *A kinetic-Monte Carlo perspective on active matter*, J. Chem. Phys. **150**, 144113 (2019).

[205] J. Voß and R. Wittkowski, *Hydrodynamic resistance matrices of colloidal particles with various shapes*, arXiv:1811.01269 (2018).

[206] B. Liebchen and H. Löwen, *Synthetic chemotaxis and collective behavior in active matter*, Acc. Chem. Res. **51**, 2982 (2018).

[207] C. Lozano, B. ten Hagen, H. Löwen, and C. Bechinger, *Phototaxis of synthetic microswimmers in optical landscapes*, Nat. Commun. **7**, 12828 (2016).

[208] C. Lozano, B. Liebchen, B. ten Hagen, C. Bechinger, and H. Löwen, *Propagating density spikes in light-powered motility-ratchets*, Soft Matter **15**, 5185 (2019).

[209] A. Sharma and J. M. Brader, *Brownian systems with spatially inhomogeneous activity*, Phys. Rev. E **96**, 032604 (2017).

[210] B. Liebchen, P. Monderkamp, B. ten Hagen, and H. Löwen, *Viscotaxis: microswimmer navigation in viscosity gradients*, Phys. Rev. Lett. **120**, 208002 (2018).

[211] C. Ferreiro-Córdova, J. Toner, H. Löwen, and H. H. Wensink, *Long-time anomalous swimmer diffusion in smectic liquid crystals*, Phys. Rev. E **97**, 062606 (2018).

[212] A. Daddi-Moussa-Ider and A. M. Menzel, *Dynamics of a simple model microswimmer in an anisotropic fluid: implications for alignment behavior and active transport in a nematic liquid crystal*, Phys. Rev. Fluids **3**, 094102 (2018).

[213] T. Bäuerle, A. Fischer, T. Speck, and C. Bechinger, *Self-organization of active particles by quorum sensing rules*, Nat. Commun. **9**, (2018).

[214] F. A. Lavergne, H. Wendehenne, T. Bäuerle, and C. Bechinger, *Group formation and cohesion of active particles with visual perception-dependent motility*, Science **364**, 70 (2019).

[215] S. Tarama, S. U. Egelhaaf, and H. Löwen, *Traveling band formation in feedback-driven colloids*, Phys. Rev. E **100**, 022609 (2019).

[216] P. P. Ewald, *Die Berechnung optischer und elektrostatischer Gitterpotentiale*, Ann. Phys. (Berlin) **369**, 253 (1921).

[217] C. W. J. Beenakker, *Ewald sum of the Rotne–Prager tensor*, J. Chem. Phys. **85**, 1581 (1986).

[218] J. F. Brady, R. J. Phillips, J. C. Lester, and G. Bossis, *Dynamic simulation of hydrodynamically interacting suspensions*, J. Fluid Mech. **195**, 257 (1988).

[219] M. Rex and H. Löwen, *Influence of hydrodynamic interactions on lane formation in oppositely charged driven colloids*, Eur. Phys. J. E **26**, 143 (2008).

[220] J. Bleibel, *Ewald sum for hydrodynamic interactions with periodicity in two dimensions*, J. Phys. A **45**, 225002 (2012).

[221] T. C. Adhyapak and S. Jabbari-Farouji, *Ewald sum for hydrodynamic interactions of rigid spherical microswimmers*, J. Chem. Phys. **149**, 144110 (2018).

[222] A. Zöttl and H. Stark, *Nonlinear dynamics of a microswimmer in Poiseuille flow*, Phys. Rev. Lett. **108**, 218104 (2012).

[223] A. Zöttl and H. Stark, *Periodic and quasiperiodic motion of an elongated microswimmer in Poiseuille flow*, Eur. Phys. J. E **36**, 4 (2013).

[224] M. Tarama, A. M. Menzel, B. ten Hagen, R. Wittkowski, T. Ohta, and H. Löwen, *Dynamics of a deformable active particle under shear flow*, J. Chem. Phys. **139**, 104906 (2013).

[225] M. Tarama, A. M. Menzel, and H. Löwen, *Deformable microswimmer in a swirl: capturing and scattering dynamics*, Phys. Rev. E **90**, 032907 (2014).

[226] N. Küchler, H. Löwen, and A. M. Menzel, *Getting drowned in a swirl: deformable bead-spring model microswimmers in external flow fields*, Phys. Rev. E **93**, 022610 (2016).

[227] A. J. T. M. Mathijssen, T. N. Shendruk, J. M. Yeomans, and A. Doostmohammadi, *Upstream swimming in microbiological flows*, Phys. Rev. Lett. **116**, 028104 (2016).

[228] G. Junot, N. Figueroa-Morales, T. Darnige, A. Lindner, R. Soto, H. Auradou, and E. Clément, *Swimming bacteria in Poiseuille flow: the quest for active Bretherton-Jeffery trajectories*, EPL (Europhys. Lett.) **126**, 44003 (2019).

[229] H. M. López, J. Gachelin, C. Douarche, H. Auradou, and E. Clément, *Turning bacteria suspensions into superfluids*, Phys. Rev. Lett. **115**, 028301 (2015).

[230] M. Guzmán and R. Soto, *Nonideal rheology of semidilute bacterial suspensions*, Phys. Rev. E **99**, 012613 (2019).

[231] J. M. Brader and M. Krüger, *Density profiles of a colloidal liquid at a wall under shear flow*, Mol. Phys. **109**, 1029 (2011).

[232] A. A. Aerov and M. Krüger, *Driven colloidal suspensions in confinement and density functional theory: microstructure and wall-slip*, J. Chem. Phys. **140**, 094701 (2014).

[233] A. Scacchi, A. J. Archer, and J. M. Brader, *Dynamical density functional theory analysis of the laning instability in sheared soft matter*, Phys. Rev. E **96**, 062616 (2017).

[234] A. Scacchi and J. M. Brader, *Flow induced crystallisation of penetrable particles*, J. Phys.: Condens. Matter **30**, 095102 (2018).

[235] D. Stopper and R. Roth, *Nonequilibrium phase transitions of sheared colloidal microphases: results from dynamical density functional theory*, Phys. Rev. E **97**, 062602 (2018).

[236] G. K. Batchelor and J.-T. Green, *The hydrodynamic interaction of two small freely-moving spheres in a linear flow field*, J. Fluid Mech. **56**, 375 (1972).

[237] M. Rauscher, A. Domínguez, M. Krüger, and F. Penna, *A dynamic density functional theory for particles in a flowing solvent*, J. Chem. Phys. **127**, 244906 (2007).

[238] C. W. J. Beenakker and P. Mazur, *Self-diffusion of spheres in a concentrated suspension*, Physica A **120**, 388 (1983).

[239] C. W. J. Beenakker and P. Mazur, *Diffusion of spheres in a concentrated suspension II*, Physica A **126**, 349 (1984).

[240] G. Nägele, *On the dynamics and structure of charge-stabilized suspensions*, Phys. Rep. **272**, 215 (1996).

[241] G. Nägele and P. Baur, *Long-time dynamics of charged colloidal suspensions: hydrodynamic interaction effects*, Physica A **245**, 297 (1997).

[242] A. J. Banchio, J. Gapinski, A. Patkowski, W. Häußler, A. Fluerasu, S. Sacanna, P. Holmqvist, G. Meier, M. P. Lettinga, and G. Nägele, *Many-body hydrodynamic interactions in charge-stabilized suspensions*, Phys. Rev. Lett. **96**, 138303 (2006).

[243] A. Malevanets and R. Kapral, *Mesoscopic model for solvent dynamics*, J. Chem. Phys. **110**, 8605 (1999).

[244] R. Kapral, *Multiparticle collision dynamics: simulation of complex systems on mesoscales*, Adv. Chem. Phys. **140**, 89 (2008).

[245] G. Gompper, T. Ihle, D. M. Kroll, and R. G. Winkler. *Multi-particle collision dynamics: a particle-based mesoscale simulation approach to the hydrodynamics of complex fluids.* in *Advanced Computer Simulation Approaches for Soft Matter Sciences III*, pages 1–87. Springer, Berlin / Heidelberg, Germany, (2009).

[246] F. Rühle, J. Blaschke, J.-T. Kuhr, and H. Stark, *Gravity-induced dynamics of a squirmer microswimmer in wall proximity*, New J. Phys. **20**, 025003 (2018).

[247] T. Ihle and D. M. Kroll, *Stochastic rotation dynamics: a Galilean-invariant mesoscopic model for fluid flow*, Phys. Rev. E **63**, 020201 (2001).

[248] G. R. McNamara and G. Zanetti, *Use of the Boltzmann equation to simulate lattice-gas automata*, Phys. Rev. Lett. **61**, 2332 (1988).

[249] M. Kuron, P. Stärk, C. Burkard, J. de Graaf, and C. Holm, *A lattice Boltzmann model for squirmers*, J. Chem. Phys. **150**, 144110 (2019).

[250] D. Bardfalvy, H. Nordanger, C. Nardini, A. Morozov, and J. Stenhammar, *Particle-resolved lattice Boltzmann simulations of 3-dimensional active turbulence*, Soft Matter **15**, 7747 (2019).

[251] J. Stenhammar, R. Wittkowski, D. Marenduzzo, and M. E. Cates, *Activity-induced phase separation and self-assembly in mixtures of active and passive particles*, Phys. Rev. Lett. **114**, 018301 (2015).

[252] F. Kümmel, P. Shabestari, C. Lozano, G. Volpe, and C. Bechinger, *Formation, compression and surface melting of colloidal clusters by active particles*, Soft Matter **11**, 6187 (2015).

[253] A. Wysocki, R. G. Winkler, and G. Gompper, *Propagating interfaces in mixtures of active and passive Brownian particles*, New J. Phys. **18**, 123030 (2016).

[254] P. Krinninger, M. Schmidt, and J. M. Brader, *Nonequilibrium phase behavior from minimization of free power dissipation*, Phys. Rev. Lett. **117**, 208003 (2016).

[255] P. Krinninger, M. Schmidt, and J. M. Brader, *Erratum: Nonequilibrium phase behavior from minimization of free power dissipation [Phys. Rev. Lett.* **117***, 208003 (2016)]*, Phys. Rev. Lett. **119**, 029902 (2017).

[256] P. Krinninger and M. Schmidt, *Power functional theory for active Brownian particles: general formulation and power sum rules*, J. Chem. Phys. **150**, 074112 (2019).

[257] E. Lauga, *Propulsion in a viscoelastic fluid*, Phys. Fluids **19**, 083104 (2007).

[258] L. Zhu, E. Lauga, and L. Brandt, *Self-propulsion in viscoelastic fluids: pushers vs. pullers*, Phys. Fluids **24**, 051902 (2012).

[259] J. R. Gomez-Solano, A. Blokhuis, and C. Bechinger, *Dynamics of self-propelled Janus particles in viscoelastic fluids*, Phys. Rev. Lett. **116**, 138301 (2016).

[260] C. Lozano, J. R. Gomez-Solano, and C. Bechinger, *Run-and-tumble-like motion of active colloids in viscoelastic media*, New J. Phys. **20**, 015008 (2018).

[261] N. Narinder, C. Bechinger, and J. R. Gomez-Solano, *Memory-induced transition from a persistent random walk to circular motion for achiral microswimmers*, Phys. Rev. Lett. **121**, 078003 (2018).

[262] M. Puljiz and A. M. Menzel, *Memory-based mediated interactions between rigid particulate inclusions in viscoelastic environments*, Phys. Rev. E **99**, 012601 (2019).

[263] N. Narinder, J. R. Gomez-Solano, and C. Bechinger, *Active particles in geometrically confined viscoelastic fluids*, arXiv:1908.10339 (2019).

[264] S. A. M. Loos and S. H. L. Klapp, *Fokker-Planck equations for time-delayed systems via Markovian Embedding*, J. Stat. Phys. **177**, 95 (2019).

[265] A. Liluashvili, J. Ónody, and T. Voigtmann, *Mode-coupling theory for active Brownian particles*, Phys. Rev. E **96**, 062608 (2017).

[266] G. Szamel, *Mode-coupling theory for the steady-state dynamics of active Brownian particles*, J. Chem. Phys. **150**, 124901 (2019).

[267] L. M. C. Janssen, *Active glasses*, J. Phys.: Condens. Matter **31**, 503002 (2019).

[268] R. Golestanian and A. Ajdari, *Analytic results for the three-sphere swimmer at low Reynolds number*, Phys. Rev. E **77**, 036308 (2008).

[269] M. Leoni, J. Kotar, B. Bassetti, P. Cicuta, and M. C. Lagomarsino, *A basic swimmer at low Reynolds number*, Soft Matter **5**, 472 (2009).

[270] G. Grosjean, M. Hubert, G. Lagubeau, and N. Vandewalle, *Realization of the Najafi-Golestanian microswimmer*, Phys. Rev. E **94**, 021101 (2016).

[271] B. Nasouri, A. Vilfan, and R. Golestanian, *Efficiency limits of the three-sphere swimmer*, Phys. Rev. Fluids **4**, 073101 (2019).

[272] B. Cichocki, R. Jones, R. Kutteh, and E. Wajnryb, *Friction and mobility for colloidal spheres in Stokes flow near a boundary: the multipole method and applications*, J. Chem. Phys. **112**, 2548 (2000).

[273] M. Kędzierski and E. Wajnryb, *Precise multipole method for calculating many-body hydrodynamic interactions in a microchannel*, J. Chem. Phys. **133**, 154105 (2010).

[274] R. Zargar, A. Najafi, and M. Miri, *Three-sphere low-Reynolds-number swimmer near a wall*, Phys. Rev. E **80**, 026308 (2009).

[275] W. R. DiLuzio, L. Turner, M. Mayer, P. Garstecki, D. B. Weibel, H. C. Berg, and G. M. Whitesides, *Escherichia coli swim on the right-hand side*, Nature **435**, 1271 (2005).

[276] E. Lauga, W. R. DiLuzio, G. M. Whitesides, and H. A. Stone, *Swimming in circles: motion of bacteria near solid boundaries*, Biophys. J. **90**, 400 (2006).

[277] N. Liron and S. Mochon, *Stokes flow for a Stokeslet between two parallel flat plates*, J. Eng. Math. **10**, 287 (1976).

[278] A. J. T. M. Mathijssen, A. Doostmohammadi, J. M. Yeomans, and T. N. Shendruk, *Hydrodynamics of micro-swimmers in films*, J. Fluid Mech. **806**, 35 (2016).

[279] G. P. Alexander, C. M. Pooley, and J. M. Yeomans, *Hydrodynamics of linked sphere model swimmers*, J. Phys.: Condens. Matt. **21**, 204108 (2009).

[280] K. T. Kaljot, R. D. Shaw, D. H. Rubin, and H. B. Greenberg, *Infectious rotavirus enters cells by direct cell membrane penetration, not by endocytosis*, J. Virol. **62**, 1136 (1988).

[281] G. Seisenberger, M. U. Ried, T. Endress, H. Büning, M. Hallek, and C. Bräuchle, *Real-time single-molecule imaging of the infection pathway of an adeno-associated virus*, Science **294**, 1929 (2001).

[282] K. Saar, M. Lindgren, M. Hansen, E. Eiríksdóttir, Y. Jiang, K. Rosenthal-Aizman, M. Sassian, and Ü. Langel, *Cell-penetrating peptides: a comparative membrane toxicity study*, Analyt. Biochem. **345**, 55 (2005).

[283] Y. Xia, *Nanomaterials at work in biomedical research*, Nat. Mater. **7**, 758 (2008).

[284] D. K. Kirui, D. A. Rey, and C. A. Batt, *Gold hybrid nanoparticles for targeted phototherapy and cancer imaging*, Nanotechnology **21**, 105105 (2010).

[285] J. S. Suk, Q. Xu, N. Kim, J. Hanes, and L. M. Ensign, *PEGylation as a strategy for improving nanoparticle-based drug and gene delivery*, Adv. Drug Deliv. Rev. **99**, 28 (2016).

[286] A. Sommerfeld, *Partial Differential Equations in Physics, Vol. 1* (Academic Press, Cambridge, Massachusetts, 1949).

[287] A. Daddi-Moussa-Ider, B. Liebchen, A. M. Menzel, and H. Löwen, *Theory of active particle penetration through a planar elastic membrane*, New J. Phys. **21**, 083014 (2019).

[288] A. Daddi-Moussa-Ider and S. Gekle, *Hydrodynamic interaction between particles near elastic interfaces*, J. Chem. Phys. **145**, 014905 (2016).

[289] A. Daddi-Moussa-Ider, A. Guckenberger, and S. Gekle, *Particle mobility between two planar elastic membranes: Brownian motion and membrane deformation*, Phys. Fluids **28**, 071903 (2016).

[290] A. Daddi-Moussa-Ider, M. Lisicki, and S. Gekle, *Mobility of an axisymmetric particle near an elastic interface*, J. Fluid Mech. **811**, 210 (2017).

[291] A. Daddi-Moussa-Ider and S. Gekle, *Hydrodynamic mobility of a solid particle near a spherical elastic membrane: axisymmetric motion*, Phys. Rev. E **95**, 013108 (2017).

[292] A. Daddi-Moussa-Ider, M. Lisicki, and S. Gekle, *Hydrodynamic mobility of a solid particle near a spherical elastic membrane. II. Asymmetric motion*, Phys. Rev. E **95**, 053117 (2017).

[293] A. Daddi-Moussa-Ider, M. Lisicki, S. Gekle, A. M. Menzel, and H. Löwen, *Hydrodynamic coupling and rotational mobilities near planar elastic membranes*, J. Chem. Phys. **149**, 014901 (2018).

[294] A. Daddi-Moussa-Ider, H. Löwen, and S. Gekle, *Creeping motion of a solid particle inside a spherical elastic cavity*, Eur. Phys. J. E **41**, 104 (2018).

[295] A. Daddi-Moussa-Ider, H. Löwen, and B. Kaoui, *Axisymmetric flow due to a Stokeslet near a finite-sized elastic membrane*, J. Phys. Soc. Jpn. **88**, 054401 (2019).

[296] R. Skalak, A. Tozeren, R. P. Zarda, and S. Chien, *Strain energy function of red blood cell membranes*, Biophys. J. **13**, 245 (1973).

[297] W. Helfrich, *Elastic properties of lipid bilayers: theory and possible experiments*, Z. Naturforsch. C **28**, 693 (1973).

[298] J. Dunstan, G. Mino, E. Clement, and R. Soto, *A two-sphere model for bacteria swimming near solid surfaces*, Phys. Fluids **24**, 011901 (2012).